Title
Structural modifications for the development of shortwave infrared polymethine dyes

Author
Pengshung, Monica Hui

Publication Date
2021

Peer reviewed|Thesis/dissertation

UNIVERSITY OF CALIFORNIA

Los Angeles

Structural modifications for the development of shortwave infrared polymethine dyes

A dissertation submitted in partial satisfaction of the

requirements for the degree Doctor of Philosophy

in Chemistry

by

Monica Hui Pengshung

2021

ABSTRACT OF THE DISSERTATION

Structural modifications for the development of shortwave infrared polymethine dyes

by

Monica Hui Pengshung

Doctor of Philosophy in Chemistry

University of California, Los Angeles, 2021

Professor Ellen May Sletten, Chair

The electromagnetic spectrum has been exploited for centuries by scientists and engineers to develop new technologies. The visible (VIS, 400-700 nm) and near infrared (NIR, 700-1000 nm) regions have been widely explored for photoactive materials. Beyond that lies the shortwave infrared (SWIR, 1000-2000 nm) region of the electromagnetic spectrum which has garnered interest for military purposes, quality assurance, telecommunications and diagnostics. Photoactive SWIR materials consists of carbon nanotubes, rare earth doped nanoparticles, quantum dots, conjugated polymers and small molecules. Of particular interest are polymethine fluorophores, which are one of the few classes of small molecules for the SWIR region, but development of these dyes that can absorb and emit within the SWIR region is still in its infancy. In this dissertation,

long wavelength absorbing and emitting polymethine dyes are synthesized and studied to develop an understanding of structural modifications and their impact on photophysical properties.

Chapter One is a perspective on the polymethine dye scaffold and its utility for the SWIR region. Chapter Two focuses on tuning a flavylium heptamethine dye scaffold through substituent identity to match excitation lasers to obtain real-time excitation multiplexing *in vivo.* In Chapter Three, we further modify the flavylium heptamethine scaffold by changing the substituent position in order to gain a better understanding of the effect of electron donors on the spectral properties.

In Chapters Two and Three, we observed that small structural modifications gave small red shifts in λ_{max}, thus in Chapter Four, we explored heteroatom exchange from oxygen to silicon in a xanthene based polymethine fluorophore to induce a red shift of 100 nm. In Chapter Five, further studies on the structural modification of the flavylium heptamethine scaffold at the 6-position and post-synthetic counterion exchange were explored to help improve excitation multiplexed imaging. Finally in Chapter Six, supramolecular methods were explored in the form of J-aggregation as a route to SWIR materials. Small structural modifications were made on a thiazole cyanine scaffold to examine their effect on aggregation properties. The fundamental understanding developed within those studies were applied back to the flavylium heptamethine scaffold to yield an aggregate with $\lambda_{max,abs}$ at 1350 nm.

The dissertation of Monica Hui Pengshung is approved.

Kendall N. Houk

Andrea Kasko

Yi Tang

Ellen May Sletten, Committee Chair

University of California, Los Angeles

2021

This dissertation is dedicated to my parents, Ming and Mimi and sister, Michelle.

TABLE OF CONTENTS

LIST OF FIGURES

CHAPTER ONE

CHAPTER TWO

LIST OF SCHEMES

LIST OF TABLES

ACKNOWLEDGEMENTS

I would like to thank first and foremost my PhD advisor, Professor Ellen Sletten. She is someone who I greatly admire and respect for her abilities as a scientist, as an advisor and as a human being. She has taught me so much within the last five years and has helped me grow immensely. Coming into graduate school with no synthetic chemistry experience, she patiently helped me through my first reactions in the lab and always pushed me to pursue more; for that I am eternally grateful.

I would also like to thank my committee members, Professor Kendall Houk, Professor Andrea Kasko and Professor Yi Tang for their guidance and advice in my career. Their expertise and guidance in science and navigating graduate school has been instrumental to my success. I have also been blessed with wonderful collaborators who were willing to bring their expertise but also share their excitement with science with me. To Professor Steven Lopez, I am grateful for your willingness to provide valuable computational insight and for your patience as we tried to figure out complicated photophysical processes. To Professor Justin Caram, your genuine curiosity in science and excitement has made collaborating with you a true joy. I am especially appreciative that when I felt pessimistic about research, that you always had an optimistic attitude and positive nature that helped me feel appreciate the work I was doing.

I am extremely grateful for the friends I have made while in graduate school, specifically the Bobo Gang: Gina Lee and Katherine Bay. We met during orientation week and five years later, here we are about to graduate. Gina, my roommate, lab mate and friend who has always been there through my struggles. Somebody who has taught me to be confident, be free-spirited and be caring towards others. I truly believe that meeting Gina has made me a better person and I am grateful for her friendship. Kat, my first real friend in graduate school, who I could talk to about anything.

She never steps down from a challenge and has always inspired me to pursue what I am passionate about. Her skills as a teacher, a researcher, and as a genuinely amazing person is something I have always admired. I don't think I would have been able to get through my Ph.D without the support and friendship of these very two important people.

I would also like to thank the Sletten lab members who started this lab together and helped build the foundation of our research group through all the struggles and hardships. Maly Cosco graciously welcomed me into the lab and taught me so much as a lab hood "neighbor" when I first started as a graduate student. I have always been in awe her abilities as a chemist, a biologist, and as a scientist but also her dedication to Taylor Swift. My other lab mates within my year have been crucial to my time as a graduate student. Joe Jaye, who started in the Harran lab with me during the summer and somehow we both coincidentally found our way to the Sletten lab has become a trusted and life-long friend throughout my graduate career. His ability as a synthetic/polymer chemist is unrivaled and I have always admired his intelligence and creativity when it comes to research. I will also never forget the memes and dad jokes which never fail to put a smile on my face. Margeaux Miller is someone I greatly admire because she is so incredibly talented, and I have always wished I had even half her skills in synthetic chemistry. Her ability to run two columns simultaneously is something I will always be in awe of. Furthermore, her willingness to talk through my synthesis struggles but also let me vent about life has made her an indispensable friend. Dan Estabrook is one of the best polymer chemists I have ever met. His work ethic, drive and amazing taste in fashion is something I have always aspired to have, and I will sorely miss his "pants of the month" and the nickname "Enzos". I am grateful for Rachael Day for allowing me to ask basic biology questions all the time and showing me how to be incredibly patient, kind and caring. I will miss those days when we would be in the instrument room together doing

experiments side by side. To Anna Kataki, I have always admired your confidence and knowledge about all things in relation to chemical biology. I am extremely appreciative for having the opportunity to work in a lab with all of these amazing scientists as we struggled through starting a research lab.

The other members of the Sletten lab have also made me incredibly proud to see how our lab has grown and changed since I started. Irene Lim is an inspiration to me as someone who is always confident in herself and always willing to laugh at her own jokes. She is my go-to person to discuss experiments with and was always willing to let me pick her brain for ideas. To Anthony Spearman, I am grateful for having someone who shares so many similar interests such as video games, music and memes and I am forever happy that he took on the role of DJ for the 4224 office. I am thankful for Cesar Garcia, who has shown me you can be laidback but also work hard. His ability to maintain a calm and collected demeanor even through the most stressful of situations is something I greatly admire. I was also lucky to have crossed paths with some amazing postdocs; Dr. Wei Cao, Dr. John Axtell, Dr. Shang Jia, Dr. Heidi van de Wouw who have been wonderful mentors and always encouraged me to be proud of my research. Finally, I am thankful for the second and first year within our lab who allowed us older students to take lab time during quarantine and will carry on our legacy.

I would also like to thank Gina's cats, Gumbo and Wumbo who she adopted during our time in quarantine. They have both provided me great comfort and joy during the pandemic. I will never forget them stepping on my laptop during meetings or sitting on my desk to stop me from working. These little disruptions reminded me to take a break and take time for myself during the most difficult of times.

Finally, this would not have been possible without the support of my family. I am especially grateful to my extended family who lives here in L.A for always making sure I felt at home during my time here. I never felt far from family and always knew I had somewhere to go during the holidays. I would also like to thank my older sister, Michelle who has always been a role model to me. I would never have pursued my passion and obtained a Ph.D without her constant support. I will always be thankful for her talking me through my panic attacks and anxiety. Her constant reassurance that I am worthy is something that has helped me to where I am today. To my parents, who have always shown me unwavering support and love. They have helped me through some of the most difficult times of my life and I don't think I would be the person I am today without their encouragement.

I am where I am today only with the support and guidance of those around me. There will never be enough words to truly express how grateful I am to all those within my life.

Chapter One is an unpublished perspective written by Pengshung.

Chapter Two is a version of Cosco, E. D.; Spearman, A. L.; Ramakrishnan, S.; Lingg, J. G. P.; Saccomano, M.; Pengshung, M.; Arús, B. A.; Wong, K. C. Y.; Glasl, S.; Ntziachristos, V.; Warmer, M. McLaughlin, R. R.; Bruns, O. T.; Sletten, E. M. Shortwave Infrared Polymethine Fluorophores Matched to Excitation Lasers Enable Non-Invasive, Multicolour in Vivo Imaging in Real Time. *Nat. Chem.* **2020**, *12*, 1123–1130. Pengshung, Cosco, Spearman, Ramakrishnan, Lingg, Saccomano, Arús, Wong, Glasl, Warmer and McLaughlin contributed to experimental work. Cosco, Sletten and Bruns contributed to writing.

Chapter Three is a version of Pengshung, M.; Li, J.; Mukdaum, F.; Lopez, S. A.; Sletten, E. M. Photophysical Tuning of Shortwave Infrared Flavylium Heptamethine Dyes via Substituent

Placement. *Org. Lett.* **2020**, *22 (15)*, 6150-6154. Pengshung, Li and Mukadum contributed to experimental work. Pengshung, Li, Lopez and Sletten contributed to writing.

Chapter Four is a version of Pengshung, M.; Neal, P.; Atallah, T. L.; Kwon, J.; Caram, J. r.; Lopez, S. A.; Sletten, E. M. Silicon Incorporation in Polymethine Dyes. *Chem. Commun.* **2020**, *56*, 6110-6113. Pengshung, Neal, Atallah and Kwon contributed to experimental work. Pengshung, Lopez and Sletten contributed to writing.

Chapter Five is unpublished studies and a version of an unpublished manuscript, Pengshung, M.; Cosco, E. D.; Zhang, Z.; Sletten, E. M. Counterion pairing effects on a flavylium heptamethine dye. Pengshung, Cosco and Zhang contributed to experimental work. Pengshung, Cosco and Sletten contributed to writing.

Chapter Six is unpublished studies with authors Pengshung, M. Bailey, A. D.; Garcia, C. All authors contributed to experimental work. Pengshung is responsible for writing.

BIOGRAPHICAL SKETCH

Education:
University of California, Los Angeles, Los Angeles, CA
MS in Chemistry, 2018

University of Portland, Portland Oregon
BS in Biology with Honors, *magna cum laude*, 2016
Thesis title: Identification of flavonoid compounds in Dahlia variabilis.
Thesis advisor: Angela Hoffman

Professional and Academic Experience:
Graduate Research Assistant
University of California, Los Angeles, Department of Chemistry and Biochemistry, 2016–2021
Advisor: Prof. Ellen M. Sletten
- Design and synthesis of polymethine fluorophores for the shortwave infrared.
- Investigation of structure-property relationships by photophysical characterization.

Pharmacological Science Summer Diversity Research Intern
University of Washington, Department of Pharmaceutics, May 2015 – August 2015
Advisor: Prof. Joanne Wang
- Investigation of substrate-dependent inhibition caused by drug-drug interactions in renal transporters (OCT2 and MATE1).

Undergraduate Research Assistant
University of Portland, Department of Chemistry and Biochemistry, 2014-2016
Advisor: Prof. Angela Hoffman
- Isolation and identification of novel flavonoid compounds.

OHSU Summer Equity Research Intern
Oregon Health Science University, Behavioral Neuroscience Department, May 2014- August 2014
Advisor: Dr. Suzanne Mitchell
- Exploring impulsive behavior in mice using models of delay discounting..

Honors and Awards:
UCLA Chemists Association Dissertation Award, 2021
UCLA Chemistry and Biochemistry Excellence in Research Fellowship, 2020
UCLA ACS Research Showcase Fellowship Award, 2019
Les and Phyllis Dejardin Annual Grant, 2015
University of Portland's President Scholarship, 2015
Don. V. Rommaggi Endowed Scholarship in Science, 2015

Publications:

4. Pengshung, M.; Cosco, E. D.; Zhang, Z.; Sletten, E. M. Counterion Pairing Effects on a Flavylium Heptamethine Dye. *Manuscript in preparation*

3. Pengshung, M.; Li, J.; Mukdaum, F.; Lopez, S. A.; Sletten, E. M. Photophysical Tuning of Shortwave Infrared Flavylium Heptamethine Dyes via Substituent Placement. *Org. Lett.* **2020**, *22*, 6150-6154.

2. Pengshung, M.; Neal, P.; Atallah, T. L.; Kwon, J.; Caram, J. R.; Lopez, S. A.; Sletten, E. M. Silicon Incorporation in Polymethine Dyes. *Chem. Commun.* **2020**, *56* (45), 6110-6113.

1. Cosco, E. D.; Spearman, A. L.; Ramakrishnan, S.; Lingg, J. G. P.; Saccomano, M.; Pengshung, M.; Arús, B. A.; Wong, K. C. Y.; Glasl, S.; Ntziachristos, V.; Warmer, M. McLaughlin, R. R.; Bruns, O. T.; Sletten, E. M. Shortwave Infrared Polymethine Fluorophores Matched to Excitation Lasers Enable Non-Invasive, Multicolour in Vivo Imaging in Real Time. *Nat. Chem.* **2020**, *12*, 1123–1130.

CHAPTER ONE

Structural Modifications to the Polymethine Dye Scaffold; A Journey Toward more Red-Shifted Fluorophores

1.1 Perspective

1.1.1 Introduction

Technology utilizing different frequencies of electromagnetic radiation has been one of humanity's greatest advancements. By developing technologies that can emit or detect this radiation, researchers have developed tools to study physical phenomena ranging from stars to cells. The UV-Visible (UV-VIS, 200-700 nm) and near-infrared (NIR, 700 – 1000 nm) regions of the electromagnetic spectrum have been explored extensively for their utility in photoactive materials (Figure 1.1A). Beyond this, lies the shortwave infrared (SWIR, 1000- 2000 nm) region of the electromagnetic spectrum (Figure 1.1A). Promising for applications ranging from materials to biological sciences, the SWIR region has few other sources of confounding radiation, high depth penetration through heterogenous materials and lowered energy of radiation.[1–4] However, detection of longer wavelengths of light have been limited due to expensive and inadequate detectors. Advancements in SWIR detection (*e.g.* InGaAs cameras) have expanded commercial interest in applications within this area. In parallel, the growth of materials for the SWIR region has been severely lacking. Thus, developing fluorophores for the SWIR has become an important field of research. There are a limited number of materials that can successively be utilized within this region of the electromagnetic spectrum, the current options being carbon nanotubes[5,6], quantum dots[7,8], rare earth doped nanoparticles[9] and a select few small molecule dyes, including polymethine fluorophores[10–13].

Polymethine dyes are a class of charged fluorophores consisting of two heterocycles connected by varying lengths of a methine chain, that have tunable λ_{max} within the ranges of the VIS to the SWIR, narrow absorption and emission bands, high absorption coefficients ($\varepsilon = \sim 10^5$ M^{-1} cm^{-1}) and moderate quantum yields of fluorescence (Φ_F) (Figure 1.1B).[14] First discovered accidentally in 1856 by C. H. Gerville Williams, when reacting crude quinoline with 1-iodopentane in excess ammonia. It was later determined that the crude quinoline contained lepidine, a 4-methyl derivative, as an impurity which formed the first "cyanine" dye (Figure 1.1C, **1.1**).[15] The name "cyanine" was based off the vibrant blue color and has since been used as a common name for any polymethine fluorophore containing a nitrogen heterocycle. However, the term "cyanine" also often refers to the most commonly commercially available variant: indole-based polymethine dyes, consisting of HICI (1,1′,3,3,3′,3′-hexamethyl indocarbocyanine iodide), HIDCI (1,1′,3,3,3′,3′-hexamethyl indodicarbocyanine iodide), and HITCI (1,1′,3,3,3′,3′-hexamethyl indotricarbocyanine iodide) (Figure 1.1C, **1.2-1.4**) which are utilized mainly for fluorescence imaging in biological systems due to their brightness and variable λ_{max}.[16,17] Though cyanine dyes are the most common polymethine fluorophores, a wide range of other motifs that constitute the polymethine scaffold have been synthesized. Subtle changes in photophysical properties can be achieved by structural modifications. However, obtaining polymethine fluorophores for the SWIR region is non-trivial and will be the focus of this thesis.

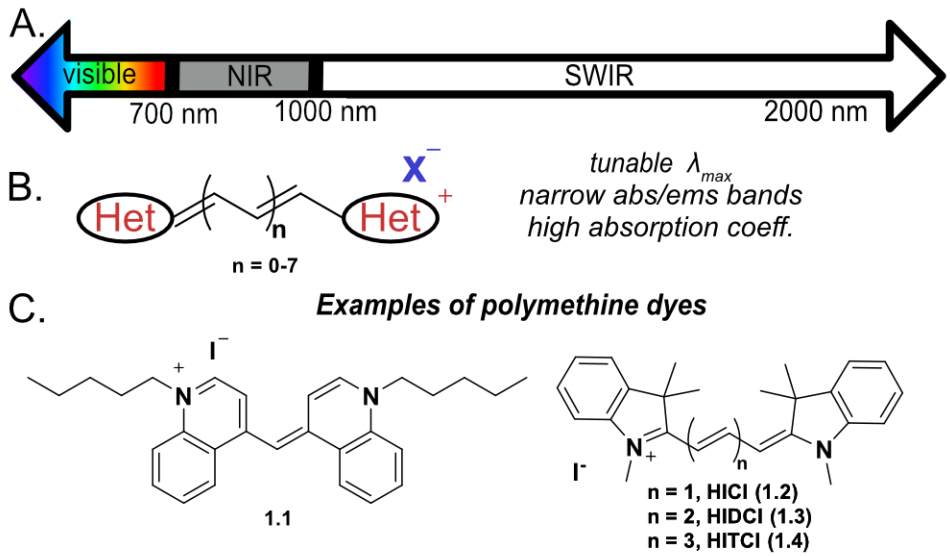

Figure 1.1. A) Electromagnetic spectrum. B) General structure of the polymethine scaffold consists of a heterocycle (HET, red), methine linker of varying lengths (n) and counterion (X^-, blue). C) Representative polymethine dyes; **1.1** and commercially available indole-based variants HICI, HIDCI, and HITCI (**1.2-1.4**).

To access polymethine fluorophores for the SWIR requires an understanding of how to make predictable structural modifications. Polymethine dyes consist of three easily interchangeable components: the heterocycle (Figure 1.1B, HET, red), the polymethine bridge (Figure 1.1B, n, black), and the counterion (Figure 1.1B, X^-, blue). Generally, these dyes are synthesized by the addition of a nucleophilic heterocycle to an electrophilic linker in the presence of base. As these dyes are synthesized in a convergent manner, the options for modifications to each component are extensive and crucial for fluorophore design.

1.1.2 Linker modification

The namesake of polymethine dyes comes from the linker chain which is a conjugated system that can be linear or cyclic with varying lengths (Figure 1.1B, n = 0-7).[18] Commonly, polymethine molecules can be referenced by the number of methine units within their

linker, e.g. a seven-carbon chain is called heptamethine. Increasing the length of the linker by a methine unit reliably invokes a bathochromic shift of approximately 100 nm (Figure 1.2A).[19,20] This effect known as the "vinylene shift" is best maintained in symmetrical polymethine dyes[19,21], whereas asymmetric polymethine dyes possess a stunted vinylene shift (< 100 nm)[21], shown to be largely heterocycle dependent and worsens upon increasing the chain length. The vinylene effect is maintained to a similar degree with nearly all heterocycles.[22] For example, a series of benzothiazole polymethine dyes have been synthesized, with the shortest (n = 1, **1.5,** Figure 1.2A) absorbing at 558 nm, and the longest being a pentadecamethine dye (n = 7, **1.6**, Figure 1.2A) with a reported λ_{max} of 1250 nm in DCM.[20] However, a major limitation of the vinylene shift includes low stability of the dye as the chain length increases, thus limiting this method for the development of SWIR fluorophores.[21,23]

Extended polymethine fluorophores can also suffer from symmetry breaking, a state in which the electron delocalization is asymmetrically distributed across the molecule. Commonly, when the charge is completely delocalized, also known as the "ideal polymethine state (IPS)" or "cyanine limit", characteristically narrow absorption/emission bands are observed as well as a lack of bond length alternation (BLA). Upon breaking this symmetric state, a broadened blue-shifted absorption spectra, no emission and maximal BLA which can be described as a "polyene-like state".[24] First observed within long chain polymethines dyes (n > 3)[25,26], instances of this phenomena can also be observed in examples of shorter fluorophores if the heterocycle moiety can effectively contain the charge.[27,28] The presence of an asymmetric state effectively reduces the advantageous photophysical properties of polymethine dyes and prevention can be incredibly beneficial in the design of future molecules.

If maintained, the symmetric state of polymethine dyes is highly beneficial for a number of reasons, such as having high absorption coefficients. Penta- and heptamethine dyes show excellent absorption coefficients (ε) within the range of ~10^5 M^{-1} cm^{-1}, while trimethine dyes are commonly lowered by one order of magnitude (~10^4). The relationship between absorption coefficients and structure is not always well understood due to difficulties in prediction of the transition dipole moment which dictates the magnitude of absorption coefficients. Thus, current understanding on how to tune this property effectively is limited. The high absorption coefficients of polymethine dyes enable them to be bright fluorophores, even without an extremely high quantum yield of fluorescence as brightness is a product of the two properties (brightness = $\Phi_F \cdot \varepsilon$).

A high Φ_F is not essential if absorption coefficient is sufficiently large enough at the desired wavelength of excitation which is advantageous for SWIR-emitting materials. As the difference between the ground state (S_0) and excited state (S_1) get smaller with longer wavelengths, the overlap between the energy wavefunctions give way to more instances of non-radiative decay. This phenomenon known as the "energy gap law" effectively lowers the Φ_F for SWIR fluorophores and can be difficult to overcome. However, high absorption coefficients and selective excitation enable SWIR polymethine fluorophores to still be bright and effective imaging agents. Thus, it is of considerable interest to understand how to develop molecules for the SWIR region, however due to the limitations of the linker for effecting large red shifts while maintaining advantageous photophysical properties, other aspects of the polymethine fluorophore should be also explored.

1.1.3 Heterocycle modification

The options for heterocycles for the polymethine scaffold vary in structure, but often contain a conjugated system with a heteroatom to stabilize the charge of the molecule. The most

classic heterocycle has already been discussed (indole) but variations have also been developed.[29,30] For example, IR-820 is an annulated [e]-benzindole (Figure 1.2B, **1.7**) which has a $\lambda_{max,abs}$ at 820 nm (MeOH), a ~60 nm red-shift from HITCI.[31,32] Benzannulation at the [cd] position has also been developed into commercial SWIR fluorophore FD-1080 (Figure 1.2B, **1.8**) with a $\lambda_{max,abs}$ at 1018 nm (EtOH), a 200 nm red-shift from HITCI.[10] Increasing conjugation length of the heterocycle, specifically at certain positions is a viable method for red-shifting fluorophores. This is further shown, though to a lesser degree, with additional substituents in which electron withdrawing or donating groups can alter photophysical properties, depending on their identity and position (Figure 1.2C, **1.9-1.12**).[33]

Other heterocycles not based on indoles have also been explored. Pyryliums, for example, are another popular scaffold, with the heptamethine variant having a $\lambda_{max,\ abs}$ at approximately 940 nm in DCM (Figure 1.2D, **1.13**). Exchanging the oxygen heteroatom for a more electropositive sulfur shows a red-shift of ~60 nm (Figure 1.2D, **1.14-1.5**). This avenue of modification proves effective when continuing down the periodic table with both selenium and teryllium showing an even more significant red-shift in $\lambda_{max,\ abs}$ (Figure 1.2D, **1.16-1.17**) but ultimately comes with the cost of decreasing Φ_F due to an increasing heavy atom effect.[34]

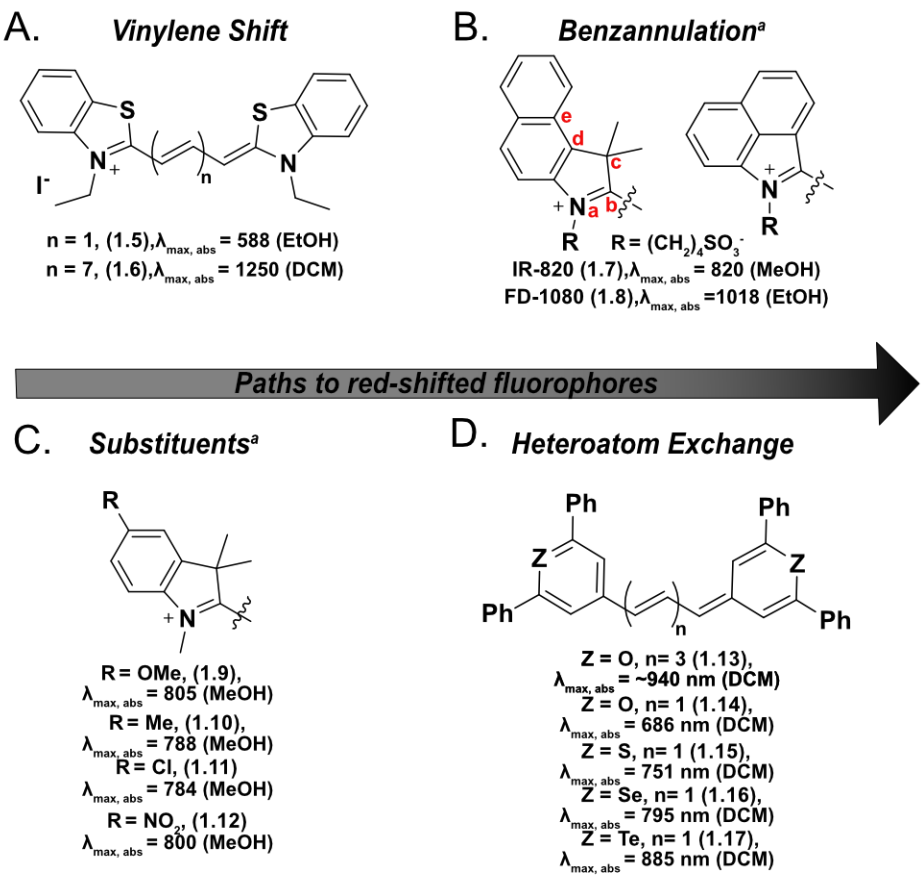

Figure 1.2. Structural modifications to polymethine dyes. A) Modifications to the methine linker, such as vinylene shift or increasing methine units (**1.5-1.8**) and cyclization of the linker **(1.9-1.11**). B) Structural modifications to the heterocycle such as benzannulation (**1.12-1.13**), addition of substituents (**1.14-1.17**) and heteroatom exchange **(1.19-1.22**)

1.1.4 Counterion Modification

There are two major subclasses of polymethine fluorophores depending on the charge: neutral (zwitterionic or merocyanine) or charged (cationic and anionic).[24] Generally polymethine fluorophores are cationic, however more recent examples of neutral and anionic molecules have shown charge can play an important role in photophysical and molecular properties. The charged nature of polymethine dyes warrants an oppositely charged counterion. Importantly, the position of the counterion in relation to the dye scaffold dictates whether a symmetric or asymmetric polymethine state is achieved. Different sizes, identity and hydrophobicity of counterion can also

control how intimate the pairing relationship and can be influenced by solvent polarity.[35] This interaction between fluorophore and counterion can effect solubility, photophysical state and stability. Ultimately the different components of polymethine dyes; linker, heterocycle and counterion can all be independently tuned to impact photophysical and molecular properties.

An example of utilizing this methodology can be seen through Flav7 (Figure 1.3, **1.20**) in which commercially available IR-26 (Figure 1.3, **1.18**) was altered to have more favorable photophysical properties for *in vivo* imaging. By exchanging the sulfur heteroatom to oxygen (Figure 1.3, IR-27, **1.19**), a higher Φ_F could be achieved. Furthermore, addition of an electron donating dimethylamino group maintained $\lambda_{max,\ abs}$ in the SWIR.[36] Thus, predictable measures can be applied to existing scaffolds in order to develop novel dyes for different applications.

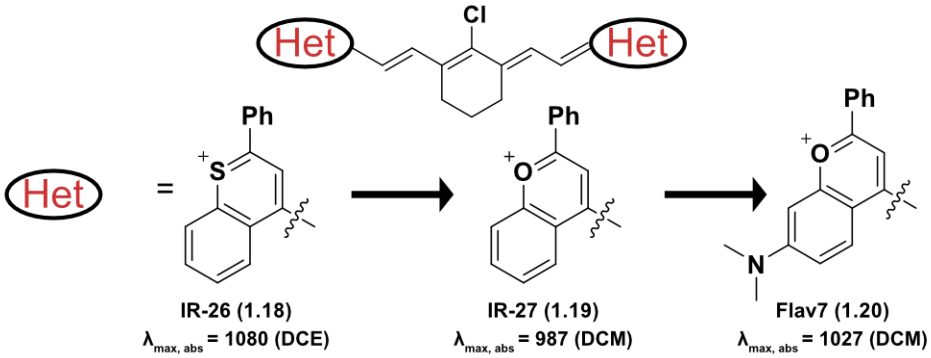

Figure 1.3 Development of Flav7 (**1.20**) exhibits the principles of predictive design of polymethine fluorophores. Starting from IR-26 (**1.18**), exchange of heteroatom yields IR-27 (**1.19**) and addition of dimethylamino produces Flav7 (**1.20**).

1.1.5 Aggregation states

Beyond the direct influence of structural modifications to the photophysical properties in the monomeric state, subtle changes can also affect photophysical characteristics within supramolecular polymers of fluorophores. The dipolar nature of dyes favor π-π stacking of monomeric molecules in the solution or solid state.[37] These aggregated states can come in many

forms, but the two common classifications are H-aggregates and J-aggregates.[38] Face to face stacked aggregation (H-aggregates) result in blue-shifted absorption spectrum, decreased quantum yields and lowered absorption coefficients. Alternately, J-aggregation, in which monomers are slip stacked allow for the lowest energy alignment of transition dipole moments (TDM) to oscillate collectively in phase. Photophysical consequences include narrow absorption bands, small Stokes shifts, and bathochromic shifts coupled with enhanced quantum yields.[37,39] Thus, J-aggregates can reach photophysical heights that could never be achieved with monomeric fluorophores alone.

Both natural and synthetic chromophores such as porphyrins[39], perylene bisimides[40], and BODIPYS[41] have been shown to form J-aggregates. However, polymethine dyes are especially promising for aggregation due to their high transition dipole moment, polarizability and planarity, all which promote higher aggregate structural stability.[37] Most exploration in this field has been focused in the visible region, but more recently fluorophores that can aggregate into the NIR and SWIR have been realized mainly due to the utility of the polymethine scaffold.[42–44] Though still in its infancy, the utilization of J-aggregates for SWIR applications shows potential for developing extremely red-shifted materials that could absorb beyond 1300 nm.

A major difficulty in employing J-aggregates for the SWIR is the lack of understanding on how to tune aggregates through structural modifications and environmental conditions. Favoring the slip stack formation can be extremely precarious and methodology of aggregation can vary widely with differing results. External properties such as temperature, salt concentration, solvent ratio and concentration of monomer can effect aggregate formation and morphology.[45] Simple structural modifications have also been explored briefly such as steric bulk[46] and amphiphilicity[47] but these were performed on visible absorbing polymethine fluorophores. A deeper understanding

of how modifications on the structure can affect morphology at the supramolecular level would help propel aggregates into new frontiers, especially for the SWIR.

To parallel the advances in engineering and technology that has allowed for wide-spread SWIR detection, fluorophore development must reach the same heights. Despite the history of polymethine fluorophores, there is still a major lack of understanding of what structural modifications can reliably alter photophysical properties. Thus, a relationship between structure and photophysical characteristics allows for the design of novel fluorophores and the ability to fine-tune properties to tailor to applications. To accomplish this goal, work encompassed here will reflect systematic structural modifications and an exploration of their impact on photophysical features with an emphasis on developing fluorophores for the SWIR.

1.2 References

(1) Smith, A. M.; Mancini, M. C.; Nie, S. Bioimaging: Second Window for in Vivo Imaging. *Nature Nanotechnology*. 2009, pp 710–711.

(2) Frangioni, J. V.; John V. Frangioni. In Vivo Near-Infrared Fluorescence Imaging. *Curr. Opin. Chem. Biol.* **2003**, *7* (5), 626–634.

(3) Wang, S.; Li, B.; Zhang, F. Molecular Fluorophores for Deep-Tissue Bioimaging. *ACS Cent. Sci.* **2020**, *6* (8).

(4) He, S.; Song, J.; Qu, J.; Cheng, Z. Crucial Breakthrough of Second Near-Infrared Biological Window Fluorophores: Design and Synthesis toward Multimodal Imaging and Theranostics. *Chem. Soc. Rev*. **2018**, *47*, 4258–4278.

(5) Hong, G.; Lee, J. C.; Robinson, J. T.; Raaz, U.; Xie, L.; Huang, N. F.; Cooke, J. P.; Dai,

H. Multifunctional in Vivo Vascular Imaging Using Near-Infrared II Fluorescence. *Nat. Med.* **2012**, *18* (12), 1841–1846.

(6) Robinson, J. T.; Hong, G.; Liang, Y.; Zhang, B.; Yaghi, O. K.; Dai, H. In Vivo Fluorescence Imaging in the Second Near-Infrared Window with Long Circulating Carbon Nanotubes Capable of Ultrahigh Tumor Uptake. *J. Am. Chem. Soc.* **2012**, *134* (25), 10664–10669.

(7) Bruns, O. T.; Bischof, T. S.; Harris, D. K.; Franke, D.; Shi, Y.; Riedemann, L.; Bartelt, A.; Jaworski, F. B.; Carr, J. A.; Rowlands, C. J.; et al. Next-Generation in Vivo Optical Imaging with Short-Wave Infrared Quantum Dots. *Nat. Biomed. Eng.* **2017**, *1* (4), 56.

(8) Dong, B.; Li, C.; Chen, G.; Zhang, Y.; Zhang, Y.; Deng, M.; Wang, Q. Facile Synthesis of Highly Photoluminescent Ag2Se Quantum Dots as a New Fluorescent Probe in the Second Near-Infrared Window for in Vivo Imaging. *Chem. Mater.* **2013**, *25* (12), 2503–2509.

(9) Naczynski, D. J.; Tan, M. C.; Zevon, M.; Wall, B.; Kohl, J.; Kulesa, A.; Chen, S.; Roth, C. M.; Riman, R. E.; Moghe, P. V. Rare-Earth-Doped Biological Composites as in Vivo Shortwave Infrared Reporters. *Nat. Commun.* **2013**, *4*, 2100.

(10) Li, B.; Lu, L.; Zhao, M.; Lei, Z.; Zhang, F. An Efficient 1064 Nm NIR-II Excitation Fluorescent Molecular Dye for Deep-Tissue High-Resolution Dynamic Bioimaging. **2018**, *57* (25), 7483–7487.

(11) Godard, A.; Kalot, G.; Pliquett, J.; Busser, B.; Le Guével, X.; Wegner, K. D.; Resch-Genger, U.; Rousselin, Y.; Coll, J.-L.; Denat, F.; et al. Water-Soluble Aza-BODIPYs:

Biocompatible Organic Dyes for High Contrast *In Vivo* NIR-II Imaging. *Bioconjug. Chem.* **2020**, *31* (4), 1088-1092.

(12) Antaris, A. L.; Chen, H.; Cheng, K.; Sun, Y.; Hong, G.; Qu, C.; Diao, S.; Deng, Z.; Hu, X.; Zhang, B.; et al. A Small-Molecule Dye for NIR-II Imaging. *Nat. Mater.* **2016**. *15*, 235-242.

(13) Ding, B.; Xiao, Y.; Zhou, H.; Zhang, X.; Qu, C.; Xu, F.; Deng, Z.; Cheng, Z.; Hong, X. Polymethine Thiopyrylium Fluorophores with Absorption beyond 1000 Nm for Biological Imaging in the Second Near-Infrared Subwindow. *J. Med. Chem.* **2019**, *62*, 2049–2059.

(14) Julia L. Bricks; Alexei D.Kachkovskii; Yurii L.Slominskii; Andrii O.Gerasov; Sergei V.Popov; Bricks, J. L.; Kachkovskii, A. D.; Slominskii, Y. L.; Gerasov, A. O.; Popov, S. V. Molecular Design of near Infrared Polymethine Dyes: A Review. *Dye. Pigment.* **2015**, *121*, 238–255.

(15) Williams, C. G. XXVI.— Researches on Chinoline and Its Homologues. *Trans. R. Soc. Edinburgh* **1857**, *21* (3), 377–401.

(16) Levitus, M.; Ranjit, S. Cyanine Dyes in Biophysical Research: The Photophysics of Polymethine Fluorescent Dyes in Biomolecular Environments. *Q. Rev. Biophys.* **2011**, *44* (1), 123–151.

(17) Elana M. S. Stennett; Monika A. Ciuba; Marcia Levitus; Stennett, E. M. S.; Ciuba, M. A.; Levitus, M. Photophysical Processes in Single Molecule Organic Fluorescent Probes. *Chem. Soc. Rev.* **2014**, *43* (4), 1057–1075.

(18) Ishchenko, A. A. Structure and Spectral-Luminescent Properties of Polymethine Dyes

Related Content Structure and Spectral-Luminescent Properties of Polymethine Dyes. *Russ. Chem. Rev.* **1991**, *60* (8), 865.

(19) König, W. Über Den Begriff Der "Polymethinfarbstoffe" Und Eine Davon Ableitbare Allgemeine Farbstoff-Formel Als Grundlage Einer Neuen Systematik Der Farbenchemie. *J. für Prakt. Chemie* **1926**, *112* (1), 1–36.

(20) Jurgen Fablan; Fabian, J.; Nakazumi, H.; Matsuoka, M. Near-Infrared Absorbing Dyes. *Chem. Rev.* **1992**, *92* (6), 1197–1226.

(21) Brooker, L. G. S. Absorption and Resonance in Dyes. *Rev. Mod. Phys.* **1942**, *14* (2–3), 275–293.

(22) Mostovnikov, V. A.; Rubinov, A. N.; Al'perovich, M. A.; Avdeeva, V. I.; Levkoev, I. I.; Loiko, M. M. Dependence of the Luminescence and Generation Properties of Solutions of Polymethine Dyes on Their Structure. *J. Appl. Spectrosc.* **1974**, *20* (1), 31–35.

(23) Ishchenko, A. A. The Length of the Polymethine Chain and the Spectral-Luminescent Properties of Symmetrical Cyanine Dyes. *Russ. Chem. Bull.* **1994**, *43* (7), 1161–1174.

(24) Bouit, P. A.; Aronica, C.; Toupet, L.; Guennic, B. Le; Andraud, C.; Maury, O. Continuous Symmetry Breaking Induced by Ion Pairing Effect in Heptamethine Cyanine Dyes: Beyond the Cyanine Limit. *J. Am. Chem. Soc.* **2010**, *132* (12), 4328–4335.

(25) Tolbert, L. M.; Zhao, X. Beyond the Cyanine Limit: Peierls Distortion and Symmetry Collapse in a Polymethine Dye. *J. Am. Chem. Soc.* **1997**, *119* (14), 3253–3258.

(26) Lepkowicz, R. S.; Przhonska, O. V.; Hales, J. M.; Fu, J.; Hagan, D. J.; Van Stryland, E.

W.; Bondar, M. V.; Slominsky, Y. L.; Kachkovski, A. D. Nature of the Electronic Transitions in Thiacarbocyanines with a Long Polymethine Chain. *Chem. Phys.* **2004**, *305* (1–3), 259–270.

(27) Vasyluk, S. V.; Viniychuk, O. O.; Poronik, Y. M.; Kovtun, Y. P.; Shandura, M. P.; Yashchuk, V. M.; Kachkovsky, O. D. Breaking of Symmetrical Charge Distribution in Xanthylocyanine Chromophores Detecting by Their Absorption Spectra. *J. Mol. Struct.* **2011**, *990* (1–3), 6–13.

(28) Pengshung, M.; Neal, P.; Atallah, T. L.; Kwon, J.; Caram, J. R.; Lopez, S. A.; Sletten, E. M. Silicon Incorporation in Polymethine Dyes. *Chem. Commun.* **2020**, *56* (45), 6110–6113.

(29) Marshall, M. V.; Rasmussen, J. C.; Tan, I.-C.; Aldrich, M. B.; Adams, K. E.; Wang, X.; Fife, C. E.; Maus, E. A.; Smith, L. A.; Sevick-Muraca, E. M. Near-Infrared Fluorescence Imaging in Humans with Indocyanine Green: A Review and Update. *Open Surg. Oncol. J.* **2010**, *2* (1), 12–25.

(30) Hu, Z.; Fang, C.; Li, B.; Zhang, Z.; Cao, C.; Cai, M.; Su, S.; Sun, X.; Shi, X.; Li, C.; et al. First-in-Human Liver-Tumour Surgery Guided by Multispectral Fluorescence Imaging in the Visible and near-Infrared-I/II Windows. *Nat. Biomed. Eng.* **2020**, *4* (3), 259–271.

(31) Ghann, W.; Kang, H.; Emerson, E.; Oh, J.; Chavez-Gil, T.; Nesbitt, F.; Williams, R.; Uddin, J. Photophysical Properties of Near-IR Cyanine Dyes and Their Application as Photosensitizers in Dye Sensitized Solar Cells. *Inorganica Chim. Acta* **2017**, *467*, 123–131.

(32) Feng, Z.; Yu, X.; Jiang, M.; Zhu, L.; Zhang, Y.; Yang, W.; Xi, W.; Li, G.; Qian, J. Excretable IR-820 for in Vivo NIR-II Fluorescence Cerebrovascular Imaging and Photothermal Therapy of Subcutaneous Tumor. *Theranostics* **2019**, *9* (19), 5706–5719.

(33) Li, Q.; Tan, J.; Peng, B.-X. Synthesis and Characterization of Heptamethine Cyanine Dyes. *Molecules* **1997**, *2*, 91–98.

(34) Detty, M. R.; Murray, B. J. Telluropyrylium Dyes. 2,6-Diphenyltelluropyrylium Dyes. *J. Org. Chem.* **1982**, *47* (27), 5235–5238.

(35) Bouit, P.-A.; Aronica, C.; Le Guennic, B.; Andraud, C.; Maury, O. Continuous Symmetry Breaking Induced by Ion Pairing Effect in Heptamethine Cyanine Dyes: Beyond the Cyanine Limit. *J. Amer. Chem. Soc.* **2010**, *132*, 4328-4335.

(36) Cosco, E. D.; Caram, J. R.; Bruns, O. T.; Franke, D.; Day, R. A.; Farr, E. P.; Bawendi, M. G.; Sletten, E. M. Flavylium Polymethine Fluorophores for Near- and Shortwave Infrared Imaging. *Angew. Chemie - Int. Ed.* **2017**, *56* (42), 13126–13129.

(37) Bricks, J. L.; Slominskii, Y. L.; Panas, I. D.; Demchenko, A. P. Fluorescent J-Aggregates of Cyanine Dyes: Basic Research and Applications Review. *Methods Appl. Fluoresc.* **2018**, *6* (1).

(38) Hestand, N. J.; Spano, F. C. Expanded Theory of H- and J-Molecular Aggregates: The Effects of Vibronic Coupling and Intermolecular Charge Transfer. *Chem. Rev.* **2018**, *118*, 7069-7163.

(39) Würthner, F.; Kaiser, T. E.; Saha-Möller, C. R. J-Aggregates: From Serendipitous Discovery to Supramolecular Engineering of Functional Dye Materials. *Angew. Chemie*

Int. Ed. **2011**, *50* (15), 3376–3410.

(40) Kaiser, T. E.; Stepanenko, V.; Würthner, F. Fluorescent J-Aggregates of Core-Substituted Perylene Bisimides: Studies on Structure-Property Relationship, Nucleation-Elongation Mechanism, and Sergeants-and-Soldiers Principle. *J. Am. Chem. Soc.* **2009**, *131* (19) 6719-6732.

(41) Chen, Z.; Liu, Y.; Wagner, W.; Stepanenko, V.; Ren, X.; Ogi, S.; Würthner, F. Near-IR Absorbing J-Aggregate of an Amphiphilic BF_2 -Azadipyrromethene Dye by Kinetic Cooperative Self-Assembly. *Angew. Chemie Int. Ed.* **2017**, *56* (21), 5729–5733.

(42) Sun, C.; Li, B.; Zhao, M.; Wang, S.; Lei, Z.; Lu, L.; Zhang, H.; Feng, L.; Dou, C.; Yin, D.; et al. J-Aggregates of Cyanine Dye for NIR-II in Vivo Dynamic Vascular Imaging beyond 1500 Nm. *J. Am. Chem. Soc.* **2019**, *141* (49), 19221–19225.

(43) Xu, S.; Liu, H.; Huan, S.; Yuan, L.; Zhang, X. Recent Progress in Utilizing Near-Infrared J-Aggregates for Imaging and Cancer Therapy. *Mater. Chem. Front.* **2020**.

(44) Chen, W.; Cheng, C. A.; Cosco, E. D.; Ramakrishnan, S.; Lingg, J. G. P.; Bruns, O. T.; Zink, J. I.; Sletten, E. M. Shortwave Infrared Imaging with J-Aggregates Stabilized in Hollow Mesoporous Silica Nanoparticles. *J. Am. Chem. Soc.* **2019**, *141* (32), 12475–12480.

(45) Deshmukh, A. P.; Bailey, A. D.; Forte, L. S.; Shen, X.; Geue, N.; Sletten, E. M.; Caram, J. R. Thermodynamic Control over Molecular Aggregate Assembly Enables Tunable Excitonic Properties across the Visible and Near-Infrared. *J. Phys. Chem. Lett* **2020**, *11*, 8033.

(46) Shapiro, B. I.; Sokolova, L. S.; Kuz'min, V. A.; Tolmachev, A. I.; Slominskii, Y. L.; Briks, Y. L. Effect of Meso-Alkyl Substituents in the Polymethine Chain of Thiacarbocyanines on the Morphology of Dye Aggregates. *Nanotechnologies Russ.* **2012**, *7* (5–6), 205–212.

(47) Kirstein, S.; Daehne, S. J-Aggregates of Amphiphilic Cyanine Dyes: Self-Organization of Artificial Light Harvesting Complexes. *Int. J. Photoenergy* **2006**, *2006*, 1–21.

CHAPTER TWO

Multicolor in vivo Imaging in Real Time using Excitation-Multiplexing with Shortwave Infrared Polymethine Fluorophores

Material in Chapter Two is adapted from: Emily D. Cosco, Anthony L. Spearman, Shyam Ramakrishnan, Jakob G. P. Lingg, Mara Saccomano, Sarah Glasl, Monica Pengshung, Bernardo A. Arús, Kelly C. Y. Wong, Vasilis Ntziachristos, Martin Warmer, Ryan R. McLaughlin, Oliver T. Bruns,* and Ellen M. Sletten* Shortwave infrared polymethine fluorophores matched to excitation lasers enable non-invasive, multicolor in vivo imaging in real time. *Nat. Chem.* **2020**, *12*, 1123–1130. DOI: 10.1038/s41557-020-00554-5

2.1 Abstract

Transitioning high resolution multiplexed imaging experiments from *in cellulo* into *in vivo* is challenging due to substantial scattering and autofluorescence in tissue at visible (350–700 nm) and near-infrared (700–1,000 nm) wavelengths. By designing optical contrast agents for the shortwave infrared (SWIR, 1,000–2,000 nm) region and complementary advances in imaging technologies, we can enable real-time, non-invasive multicolor imaging experiments. We developed tunable, SWIR-emissive flavylium polymethine dyes and established a relationship between structure and photophysical properties. In parallel, an imaging system with variable near-infrared/SWIR excitation and single-channel detection was developed to facilitate video-rate multicolor SWIR imaging for imaging of awake and moving mice with multiplexed detection. Optimized dyes matched to 980 nm and 1064 nm lasers, combined with the clinically approved

indocyanine green, enabled real-time, three-color imaging with high temporal and spatial resolutions.

2.2 Introduction

Fluorescence imaging has revolutionized the way in which scientists have been able to study biological systems.[1] Advancements in imaging technologies and optical probes has vastly improved our understanding of cells and small model organisms such as zebrafish and *C*. elegans. However, translation of these tools to more complex biological systems, like mammals, have proven difficult due to the limitation of currently available fluorophores. Commonly utilized imaging agents absorb and emit in the visible (VIS, 350-700 nm) region of the electromagnetic spectrum but have high background autofluorescence and lack tissue depth penetration.[2] For these reasons, fluorescence imaging in mammals has turned to the near-infrared (NIR, 700-1000 nm) and shortwave infrared (SWIR, 1000- 2000 nm) regions of the electromagnetic spectrum in which these limitations are overcome.[3,4] Nonetheless, the state of fluorescence imaging in these regions has yet to rival that of what is achievable with the visible.

Multicolor fluorescence imaging experiments are one of the major advantages of fluorescence imaging *in cellulo*. Though this technique has been realized in mice with quantum dots[5], fluorescently labeled silica nanoparticles[6], fluorescent proteins[7] and surface-enhanced Raman scattering nanoparticles[8], there are still challenges with low spatial and temporal resolution. To enable robust, real-time, multiplexed imaging in animals it is necessary to (1) detect within the SWIR region; (2) establish efficient, orthogonal excitation and/or detection of bright fluorophores; and (3) rapidly detect each channel on the millisecond timescale. Key to this technique is the implementation of excitation multiplexing and ‘color-blind’ single-channel detection of low-

energy shortwave infrared (SWIR, 1,000–2,000 nm) light emitted by bright, 'excitation-matched' polymethine fluorophores (Figure 2.1A).

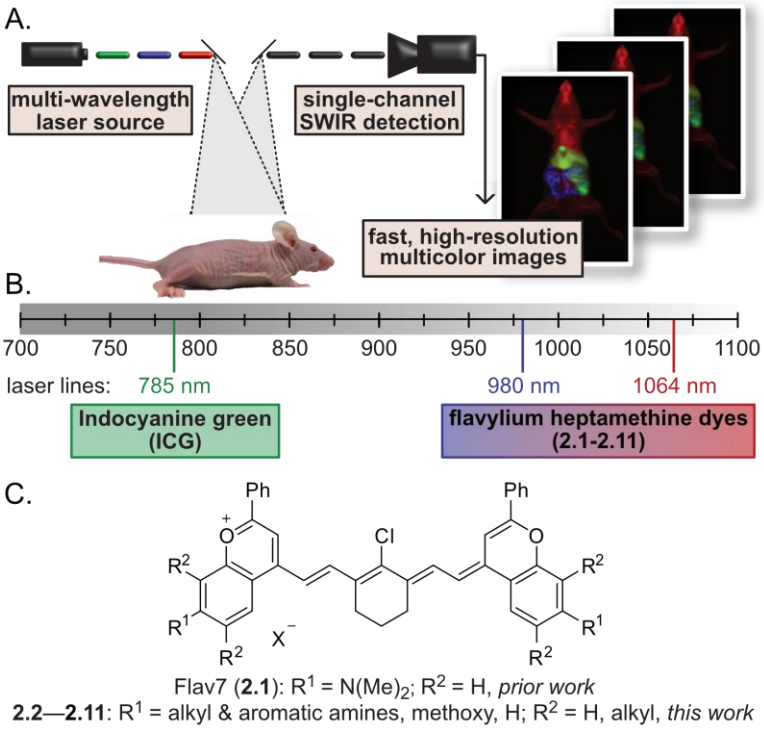

Figure 2.1 Real-time excitation-multiplexed SWIR imaging design. A) Multiple laser sources are pulsed and delivered to the biological sample. Single-channel SWIR detection (InGaAs, 1100–1700 nm) acquires frames that are temporally separated by color on the millisecond timescale. Fast frame rates produce real-time multicolor *in vivo* images at up to 50 fps. B) Relevant portions of the NIR and SWIR regions of the electromagnetic spectrum, lasers used for excitation and dyes used and/or presented in this study that are excited by the distinct laser lines. C) Flavylium polymethine scaffold explored here to match bright SWIR dyes to appropriate lasers.

Classic approaches to multiplexed imaging employ a common excitation wavelength and different detection window which can result in different resolutions for each channel due to dramatic changes in the contrast and resolution that occur throughout wavelength bands of the NIR and SWIR regions.[9–14] Furthermore, fast imaging speeds can be impeded by low photon throughput in sectioned regions of the electromagnetic spectrum or by mechanical components, such as filter wheels. Instead of these approaches, we differentiate the contrast agents via excitation wavelength

and employ a single SWIR detection channel, a technique known as excitation multiplexing, allowing for consistent resolution in all channels, high photon efficiency and ease of rapid collection of each frame on a single detector.[15,16] Excitation multiplexing has been applied to single-molecule spectroscopy methods and microscopy but have yet to be adapted for animals.[17–19] The implementation of excitation multiplexing in the SWIR is particularly beneficial as excitation can be optimized for each fluorophore and photons can be detected over a wide range of wavelengths, maximizing the signal obtained from SWIR contrast agents, which have inherently low quantum yields when compared to those in the VIS and NIR regions.[20]

To perform real-time excitation multiplexing in animals, bright SWIR-emissive contrast agents with absorption spectra compatible with common and cost-efficient laser lines are required (Figure 2.1B/C). However, the availability of differentiable NIR and SWIR fluorophores that can be utilized for this technique is limited. We turned to polymethine dyes as a solution as they have characteristically narrow absorption bands and high absorption coefficients.[21] We envisioned that polymethine dyes with both well-separated and laser-line-compatible absorption could enable efficient multicolor SWIR imaging via excitation multiplexing. Our lab has previously developed a flavylium heptamethine dye, Flav7, for SWIR optical imaging that showed both SWIR absorption and high brightness for this region.[22] To realize a multiplexing strategy, structural modifications to Flav7 were employed to tune the maximum absorption ($\lambda_{max,abs}$) to match accessible laser wavelengths used for SWIR imaging (980 nm and 1064 nm). This work allowed access to a set of dyes that were optimal for real-time, multicolor SWIR imaging (Figure 2.1C). Addition of ICG, an FDA approved polymethine dye, with $\lambda_{max,abs}$ matched to the 785 nm laser, provided a third color and enabled excitation multiplexed imaging *in vivo*.

2.3 Results and Discussion

2.3.1 Design and Synthesis of Flavylium Heptamethine Dyes[1]

Flavylium polymethine dyes are synthesized via the reaction of a flavylium heterocycle and heptamethine linker in the presence of base. To tune the absorption properties of flavylium polymethine dyes for excitation multiplexing, robust synthetic approaches towards flavylium heterocycles were necessary. We developed an approach relying on key 7-substituted flavone intermediate (**2.13**) that could be converted to the desired heterocycles by methyl Grignard addition[23] (Scheme 2.1). Three general routes lead to varying 7-aminoflavones, (1) Mentzer pyrone synthesis[24], (2) functionalization of 7-hydroxyflavone by Buchwald–Hartwig coupling of the corresponding triflate[25] and (3) acylation of the commercial 7-aminoflavone (**2.13a-i**). These derivatives were explored in an attempt to red-shifted $\lambda_{max,abs}$ of Flav7 to match the commericially available 1064 nm laser. Alternatively, a 7-methoxyflavylium (**2.12j**) was synthesized based off of previous literature precedence to develop a blue-shifted fluorophore that would match the 980 nm laser.[26] The heptamethine dyes **2.1**–**2.11** were then obtained through the base-promoted reaction of each flavylium heterocycle (**2.12a-j**) with the relevant bis(phenylimine) polymethine chain (**2.19**) (Table 2.1).

Notably, we struggled while obtaining MeOFlav7 (**2.10**) as it behaved very differently than the amino counterparts. We started with a similar procedure which utilized 2,6-di-*tert*-butyl-4-methylpyridine and n-butanol:toluene as the base and solvent, respectively. This provided us excellent conversion when monitored by UV-VIS absorption for dye formation (984 nm) and loss of linker (550 nm). However, attempts to purify **2.10** through silica gel chromatography in DCM:EtOH resulted in slight degradation of product, apparent by a consistent peak at 350 nm that

[1] Emily Cosco, Anthony Spearman and Ryan McLaughlin contributed to this section.

could not be removed. High performance liquid chromatography (HPLC) also proved unsuccessful due to similar retention times between product and impurities. Thus, to obtain pure dye, we took a step back and examined our reaction conditions. Interestingly, n-butanol:toluene was chosen as a solvent combination due to the solubility of reagents in n-butanol but the insolubility of product in toluene which helped influence the equilibrium of the reaction. Thus, we thought that addition of excess toluene could help promote precipitation of product out of solution. We were happy to find that upon cooling the reaction on ice and addition of excess toluene produced a dark magenta solid that could be collected via vacuum filtration.

Due to the difficulties with silica gel chromatography and HPLC, we opted for a different method of purification for **2.10**. The low solubility of desired fluorophore in solvents like toluene, Et_2O and THF but higher solubility of impurities prompted us to utilizing washing as a route to isolate **2.10**. Boiling toluene was the most effective at removing impurities and we found that Soxhlet extraction overnight with refluxing toluene provided pure **2.10** as a dark red-magenta solid. Discovery of this new route of isolation expeditated future synthesis of similar fluorophores and allowed for purification of unstable dyes.

Scheme 2.1 Retrosynthesis of 7-substituted flavylium heterocycles.

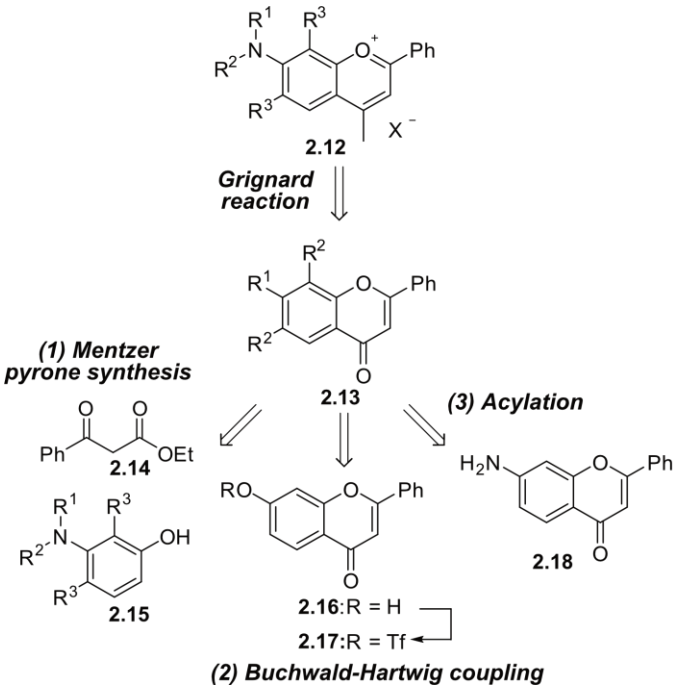

Table 2.1 Synthesis of flavylium heptamethine dyes **2.1**–**2.11**.

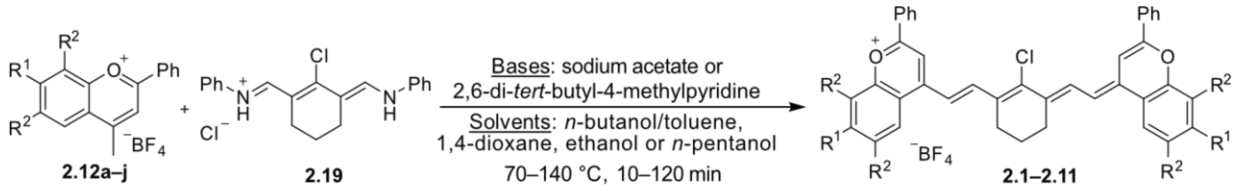

2.12a–j + **2.19** → **2.1–2.11**

Flavylium (2.12)	*R^1*	*R^2*	*base*[a]	*solvent*	*temp (°C)*	*time (min)*	*yield # (%)*	*dye*
2.12a		H	A	*n*-butanol/toluene	100	15	51	**2.1**
2.12b		H	A	*n*-butanol/toluene	100	10	40	**2.2**
2.12c	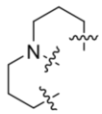		A	ethanol	70	120	37	**2.3**
2.12d		H	A	*n*-butanol/toluene	100	10	37	**2.4**
2.12e		H	B	*n*-pentanol	140	50	8	**2.5**
2.12f		H	B	*n*-butanol/toluene	100	120	26	**2.6**
2.12g		H	B	1,4-dioxane	100	15	11	**2.7**
2.12h	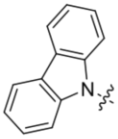	H	B	1,4-dioxane	90	15	13	**2.8**
2.12i	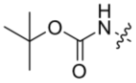	H	B	1,4-dioxane	95	15	33[b]	**2.9**
2.12j[c]		H	B	*n*-butanol/toluene	100	15	33	**2.10**
–		H	B	*n*-butanol/toluene	90	45	5	**2.11**

[a]base: A = sodium acetate; B = 2,6-di-*tert*-butyl-4-methylpyridine
[b]yield over two steps, flavylium **2.12**i not isolated.
[c]counterion is Cl^-

2.3.2 Photophysical Characterization of Flavylium Heptamethine dyes[2]

To enable excitation multiplexing, differences in $\lambda_{max,abs}$ between fluorophores are essential. We characterized the photophysical properties of **2.1**–**2.11** in dichloromethane (DCM) and found that the flavylium heptamethine dyes have absorption/emission ranging from 984 nm to 1061 nm (Figure 2.2A, Table 2.2). Compared to Flav7 (**2.1**), with $\lambda_{max,abs}$ = 1027 nm, **2.9** and **2.10** underwent hypsochromic shifts, with **2.10** being ~43 nm blue-shifted from Flav7 ($\lambda_{max,abs}$ = 984 nm), similar to unsubstituted flavylium heptamethine dye **2.11** (IR-27)[27]. Conversely, dyes **2.3** and **2.7** displayed bathochromic shifts compared to Flav7. The diphenylamino-substituted **2.7** is ~23 nm red-shifted ($\lambda_{max,abs}$ = 1047 nm), while julolidine derivative **2.3** is red-shifted by ~35 nm ($\lambda_{max,abs}$ = 1061 nm). Linear and cyclic aliphatic amine-substituted dyes **2.2** and **2.4**–**2.6** exhibited minor redshifts. Plotting absorption/emission wavelengths of nine dyes in the series against Hammett σ_m values[28] resulted in a strong correlation (R^2 = 0.96; Figure 2.2B). By increasing our understanding of the relationship between structure and λ_{max}, more predictive measures of fluorophore properties based on structure could be established.

Further characterization of the panel of flavylium polymethine dyes was necessary to determine their maximum brightness (brightness (ε_λ) = $\varepsilon_\lambda \times \Phi_F$). Absorption coefficients (ε) varied from ~110000 to ~240000 $M^{-1}cm^{-1}$, in line with the high-absorption cross-sections characteristic for polymethine fluorophores.[21] The fluorescence quantum yields (Φ_F; relative measurements to dye IR-26 = 0.05%[29]) remain rather constant, in the ~0.4–0.6% range. Notably, we had obtained flavylium heptamethine dyes that matched the 980 nm and 1064 nm laser line, MeOFlav7 (**2.10**) and JuloFlav7 (**2.3**), respectively, that maintained high and relatively consistent ε and Φ_F values (Figure 2.2C).

[2] All photophysical characterization was performed by Emily Cosco.

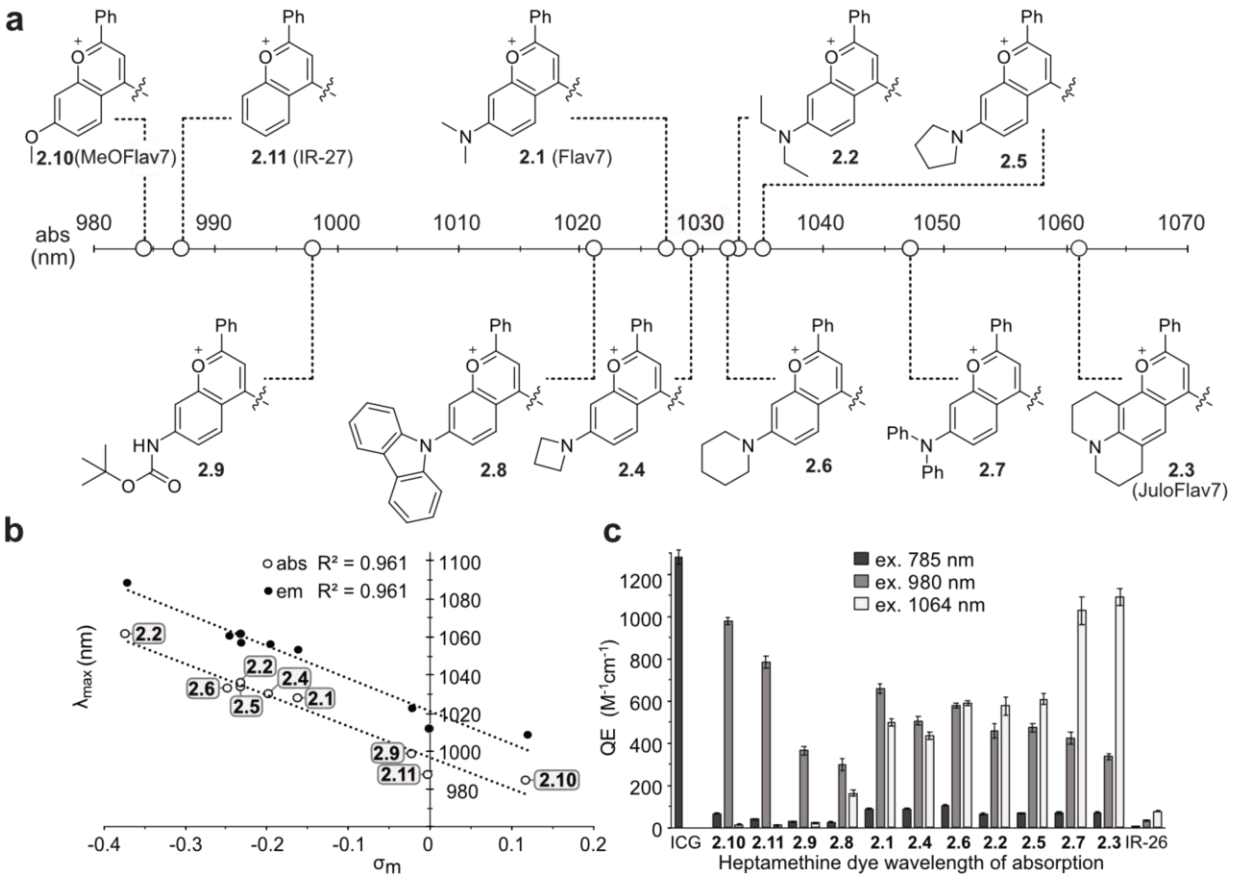

Figure 2.2 Panel of flavylium heptamethine dyes and their photophysical properties. A) Heterocycle structures and absorption wavelength maxima visualized graphically on the electromagnetic spectrum. B) Hammett plot relating σ_m substituent constants[28] to absorption and emission wavelengths of dyes **2.1**–**2.6** and **2.9**–**2.11**. C) Brightness (defined as $\varepsilon_\lambda \times \Phi_F$) of the heptamethine derivatives at relevant excitation wavelengths (λ = 785 nm (dark grey), λ = 980 nm (light grey) and λ = 1,064 nm (white)). Error bars represent the propagated error from standard deviations in ε and Φ_F measurements.

Table 2.2 Photophysical properties of flavylium heptamethine dyes

dye	$\lambda_{max,abs}$ (nm)	ε_{max} ($M^{-1}cm^{-1}$)	$\lambda_{max,em}$ (nm)	Φ_F (%)	Brightness(ε_{max}) ($M^{-1}cm^{-1}$)
2.1 (Flav7)	1027	241,000 ± 1,000	1053	0.61 ± 0.02	1470 ± 50
2.2	1033	190,000 ± 10,000	1057	0.62 ± 0.02	1180 ± 70
2.3 (JuloFlav7)	1061	238,000 ± 7,000	1088	0.46 ± 0.01	1090 ± 40
2.4	1029	207,000 ± 1,000	1056	0.51 ± 0.02	1060 ± 40
2.5	1034	247,000 ± 1,000	1061	0.48 ± 0.02	1190 ± 50
2.6	1032	110,000 ± 10,000	1060	0.54 ± 0.01	590 ± 60
2.7	1047	210,000 ± 10,000	1078	0.58 ± 0.02	1220 ± 70
2.8	1021	140,000 ± 10,000	1048	0.45 ± 0.01	630 ± 40
2.9	998	108,000 ± 4,000	1022	0.42 ± 0.02	450 ± 30
2.10 (MeOFlav7)	984	190,000 ± 1,000	1008	0.52 ± 0.01	990 ± 20
2.11 (IR-27)	987	231,000 ± 6,000	1011	0.35 ± 0.01	810 ± 30
ICG	787[a]	194,000[a] ± 5,000	818[a]	0.66[a,b] ± 0.01	1,280 ± 30[b]
IR-26	1080	171,000 ± 5,000	1114	0.05[c]	86 ± 3

[a]data taken from Rurack, K. & Spieles, M. *Anal. Chem.* **83**, 1232–1242 (2011). (measured in EtOH)
[b]value includes only the % emission between 1000–1300 nm (5%), from Carr, J. A. *et al. Proc. Natl. Acad. Sci. USA* **115**, 4465–4470 (2018).
[c]value from Semonin, O. E. et al. *J. Phys. Chem. Lett.* 1, 2445–2450 (2010). and treated as a constant for relative Φ_F measurements.

2.3.3 Excitation Multiplexing with Flavylium SWIR Dyes[3]

The development of MeOFlav7 (**2.10**) and JuloFlav7 (**2.3**) gave two fluorophores for SWIR excitation multiplexed imaging. With the addition of ICG, we had three distinct fluorophores that could be individually excited, but emission could be collected with one detector (Figure 2.3A). To perform excitation multiplexing with single-channel SWIR detection, a custom SWIR imaging configuration with three lasers and a fast InGaAs camera was constructed (Figure

[3] Excitation multiplexing performed by Emily Cosco, Mara Saccomano, Bernardo Arús, and Sarah Glasl.

2.4). With 785, 980 and 1064 nm lasers, tailored excitation could preferentially excite, while emission is detected in a color-blind fashion using identical filters and settings for all channels. This method enables fast acquisition of all channels in each imaging frame by using rapidly modulated excitation sources and identical acquisition settings in a single detector.

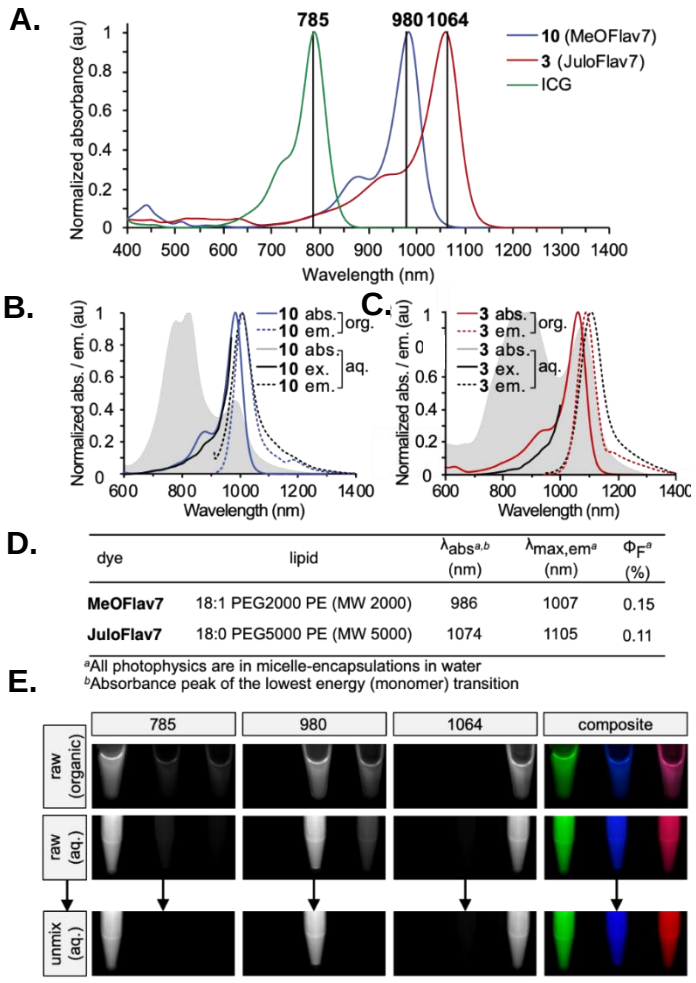

Figure 2.3 Excitation-multiplexed SWIR imaging. A) Absorption profiles of dyes used in imaging experiments plotted against excitation wavelengths employed. B-C) Absorption spectra (grey); emission spectra (excitation at 880 nm (B) and 900 nm (C), black dotted line); and excitation spectra (emission monitored at 1008 nm (B) and 1088 nm (C), black solid line) of micelle-encapsulated **2.10** (B) and **2.3** (C) overlaid with absorption traces of dyes in DCM (colored). D) Photophysics of the micelle-encapsulated dyes in water. E) Raw and unmixed images of successive frames and merged three-color images of vials containing ICG (left), **2.10** (center) and **2.3** (right) in ethanol or DCM (top) and in micelles in water (middle and bottom). Arrows indicate linear unmixing procedure.

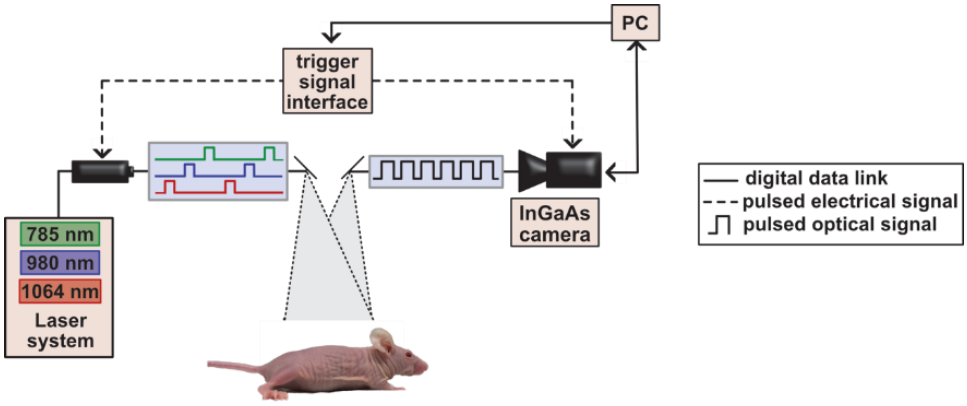

Figure 2.4 Electronic trigger-controlled excitation-multiplexed shortwave infrared imaging system.

Due to the hydrophobicity of flavylium heptamethine dyes, JuloFlav7 (**2.3**) and MeOFlav7 (**2.10**) were encapsulated in polyethylene glycol-coated micelles to impart water solubility (Figure 2.5). The aqueous-soluble formulations of **2.3** and **2.10** display aggregation, which decreases the concentration of emissive species present in the aqueous environment but does not substantially alter their excitation or emission profiles (Figure 2.4B,C).We verified that excitation multiplexing proceeded in both organic and aqueous environments by imaging tubes containing ICG (Figure 2.4E, left), MeOFlav7 (**2.10**; center) and JuloFlav7 (**2.3**; right) in organic solvent (top), and micelle encapsulations in water (middle). In each case, three successive frames collected with 785, 980 and 1064 nm lasers show high intensities in the left, center and right samples, respectively. Merging the three frames together yields a three-color image representing one effective multiplexed frame. Because molecules absorb minimal light at energies lower than their S_0 to S_1 transition, cross-talk occurs primarily in one direction. Linear unmixing can correct for minor signal overlaps between channels as seen in Figure 2.4E (bottom).

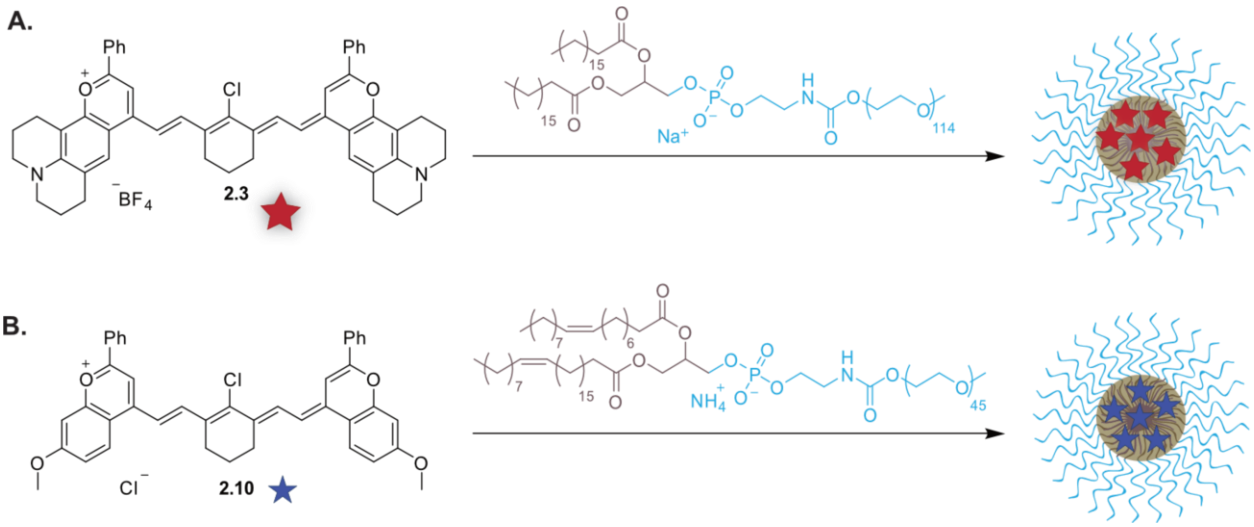

Figure 2.5 Assembly of PEG-phospholipid micelles. A) Encapsulation of JuloFlav7 (**2.3**) in 1,2-distearoyl-*sn*-glycero-3-phosphoethanolamine-*N*-[methoxy(polyethylene glycol)-5000] (sodium salt) lipid (abbreviated 18:0 PEG5000 PE) micelles. B) Encapsulation of MeOFlav7 (**2.10**) in 1,2-dioleoyl-*sn*-glycero-3-phosphoethanolamine-*N*-[methoxy(polyethylene glycol)-2000] (ammonium salt) lipid (abbreviated 18:1 PEG2000 PE) micelles.

2.3.4 In vivo Demonstration of Multicolor SWIR imaging[4]

We performed three-color imaging *in vivo* by first performing an intraperitoneal (i.p.) injection of MeOFlav7 (**2.10**), followed by i.v. injections of JuloFlav7 (**2.3**) and finally ICG (Figure 2.6A). Representative time points of the three-color video are displayed in Figure 2.6B. Herein, we have established a new imaging setup as well as molecular tools for high resolution real-time multiplexed imaging *in vivo*. This was achieved through the design of SWIR fluorophores based off a flavylium heptamethine scaffold. Subtle structural modifications allowed for varying $\lambda_{max,\ abs}$ to be obtained which enabled precise excitation with commercially available laser lines.

[4] Performed by Emily Cosco.

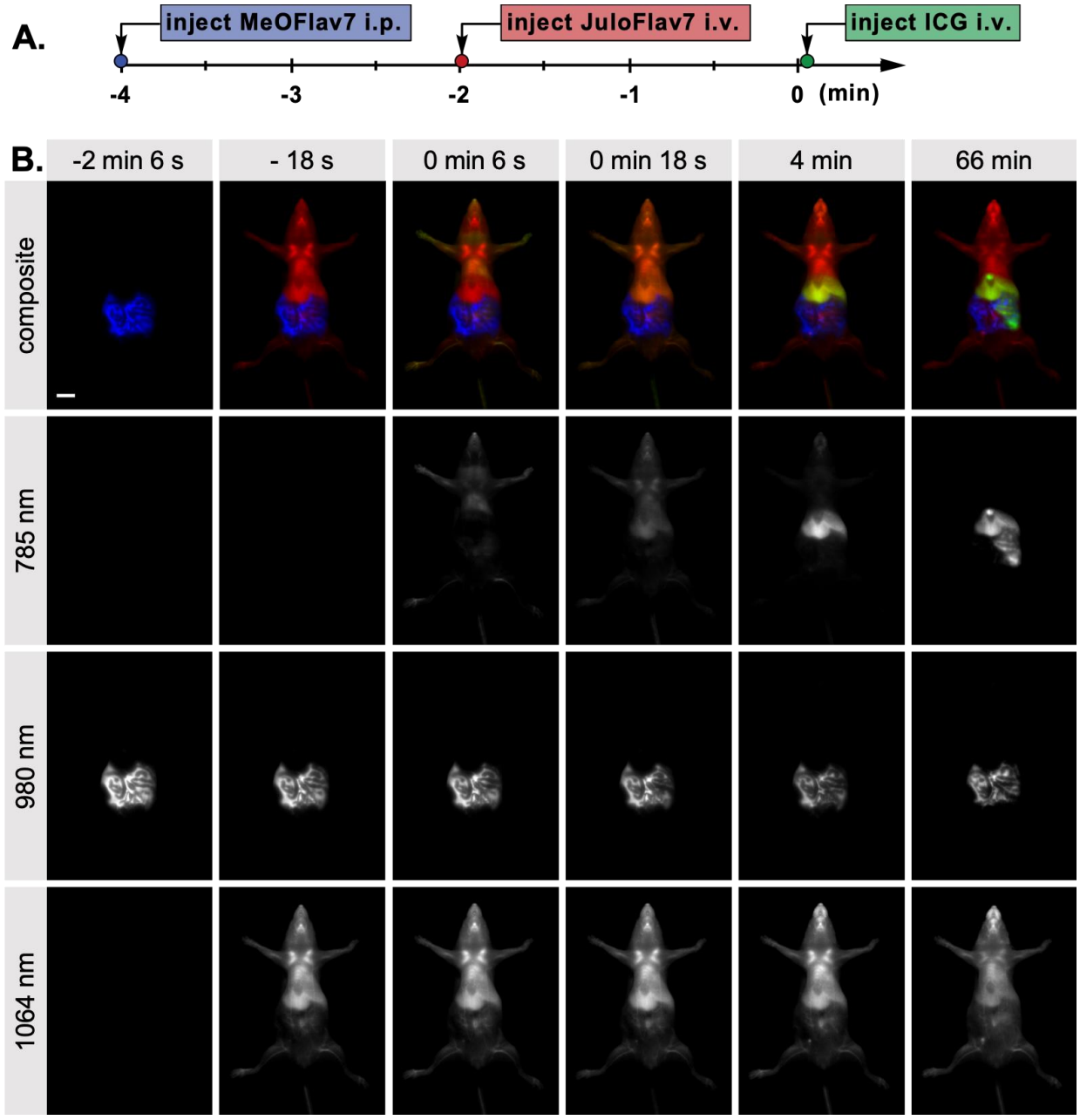

Figure 2.6 Video-rate multiplexed imaging *in vivo*. Imaging occurred after delivery of probes **2.10** (i.p, 211 nmol in micelles), **2.3** (i.v. 50 nmol in micelles) and ICG (i.v., 6.5 nmol). Acquisition parameters were excitation for three channels at 785 nm (78 $mWcm^{-1}$), 980 nm (77 $mWcm^{-1}$), and 1,064 nm (79 $mWcm^{-1}$) and 1150–1700 nm collection (10 ms exposure time, 27.8 fps). Displayed images are averaged over 5 frames. Data are representative of two replicate experiments. Scale bar represents 1 cm.

2.4 Conclusions

Despite the large set of optical tools developed for the VIS and NIR regions of the electromagnetic spectrum, non-invasive, multicolor imaging in mammals with high resolution is still a considerable challenge. To overcome this, we developed tunable SWIR polymethine fluorophores, along with a triggered multi-excitation SWIR optical configuration to demonstrate multicolor whole-animal imaging. This approach of excitation multiplexing with single-channel SWIR detection minimizes the challenges of low quantum yields of SWIR fluorophores by using efficient excitation and detection, while also expanding the wavelengths of the electromagnetic spectrum compatible with multicolor deep-tissue imaging.

The ability to fine-tune the spectral properties of the fluorophores such that they could be matched with relevant lasers was accomplished by systematic functional group substitution on a flavylium heptamethine scaffold. These studies revealed that structural modifications could alter absorption/emission using physical organic chemistry principles and produced MeOFlav7 (**2.10**), and JuloFlav7 (**2.3**), which were well matched to laser lines at 980 nm and 1064 nm, respectively. These dyes, along with FDA-approved ICG, enable single-channel imaging at 100 fps and two- or three-color imaging at video-rate speeds (≥27 fps). We envision that excitation-matching will be an essential design principle for the future of multiplexed imaging. The predictive measures described herein, could be further applied to develop polymethine dyes for the SWIR and expand the current channels for multiplexed imaging. Advancing the field of polymethine-based fluorophores and the development of clinical imaging systems will enable superior surgical, diagnostic and biomedical studies.

2.5 Experimental Procedures

2.5.1 General Experimental Procedures

Materials. Chemical reagents were purchased from Accela, Acros Organics, Alfa Aesar, Carl Roth, Fisher Scientific, Sigma-Aldrich or TCI and used without purification unless noted otherwise. Lipids were purchased from Laysan Bio and Avanti Polar Lipids. Anhydrous and deoxygenated solvents (toluene, THF) were dispensed from a Grubb's-type Phoenix Solvent Drying System constructed by J. C. Meyer. Anhydrous solvents were prepared by drying over 4 Å molecular sieves for at least three days (1,4-dioxane, ethanol, n-butanol, n-pentanol) or dried with $CaCl_2$, followed by $MgSO_4$ and distilled (EtOAc). Oxygen was removed by three consecutive freeze–pump–thaw cycles in air-free glassware directly before use.

Instrumentation. Thin layer chromatography was performed using Silica Gel 60 F254 (EMD Millipore) plates. Flash chromatography was executed with technical grade silica gel with 60 Å pores and 40–63 μm mesh particle size (Sorbtech Technologies). Solvent was removed under reduced pressure with a Büchi Rotavapor with a Welch self-cleaning dry vacuum pump and further dried with a Welch DuoSeal pump. Bath sonication was performed using a Branson 3800 ultrasonic cleaner or an Elma S15Elmasonic. Nuclear magnetic resonance (^{1}H NMR, ^{13}C NMR and ^{19}F NMR) spectra were taken on a Bruker Avance 300, AV-400, AV-500 or AV-600 instrument and processed with MestReNova or TopSpin software. All ^{1}H NMR and ^{13}C NMR peaks are reported in ppm in reference to their respective solvent signals. The ^{19}F NMR spectra are reported in ppm in reference to α,α,α-trifluorotoluene at −63.90 ppm as an external standard. High-resolution mass spectra (electrospray ionization) were obtained on a Thermo Scientific Q Exactive Plus Hybrid Quadrupole-Orbitrap M with Dionex UltiMate 3000 RSLCnano System. Infrared spectra were obtained on a PerkinElmer UATR Two FT-IR spectrometer and are reported

in terms of frequency of absorption (cm^{-1}). Nanomaterial size was analyzed with a Malvern Zetasizer Nano dynamic light scattering instrument in plastic 1 cm cuvettes. Absorption spectra were collected on a JASCO V-770 UV–visible/NIR spectrophotometer with a 2,000 nm min^{-1} scan rate after blanking with the appropriate solvent. Photoluminescence spectra were obtained on a Horiba Instruments PTI QuantaMaster Series fluorometer. Quartz cuvettes (10 mm × 10 mm, 2 mm × 10 mm or 3 mm × 3 mm; Starna Cells or Thorlabs) were used for absorption and photoluminescence measurements. All spectra were obtained at ambient temperature. Normalized spectra are displayed for clarity. Absorption coefficient (ε_{max}) values in DCM were calculated using serial dilutions with Hamilton syringes in volumetric glassware and are displayed as the mean ± standard deviation (n = 3 measurements). Relative quantum yields were determined in DCM relative to IR-26 in DCM. See Section 2.6.3 for a detailed discussion of quantum yield measurements.

General synthetic procedures. Flavones **2.13a–c** were synthesized by subjecting the corresponding 3-aminophenol (150–750 mg scale, 1.0 equiv.) to ethyl benzoylacetate (1.75–2.0 equiv.) and heating at 180 °C for 15–48 h. Compounds were purified by column chromatography with a hexanes/EtOAc solvent gradient (51–55% yield). Flavone **2.17** was synthesized following a known procedure[30] from 7-hydroxyflavone **2.16**. Flavones **2.13d–h** were synthesized by subjecting flavone **2.17** (50–180 mg scale, 1.0 equiv.) to the corresponding secondary amine (1.5–2.8 equiv.), RuPhos Pd G3 (0.1 equiv.), RuPhos (0.1 equiv.) and cesium carbonate (1.5 equiv.), in either toluene (at 100–110 °C; 0.1–0.3 M) or THF (at 50 °C; 0.1–0.3 M) for 5.5–22 h. Compounds were purified by column chromatography with a hexanes/EtOAc solvent gradient (63–83% yield). Flavone **2.13i** was synthesized by subjecting 7-aminoflavone (**2.18**) (180 mg scale, 1.0 equiv.) to di-*tert*-butyl dicarbonate (3.2 equiv.), triethylamine (2.5 equiv.) and dimethylamino pyridine (0.3

equiv.) in THF (0.2 M), and heating to reflux for 48 h. The compound was purified by column chromatography with a hexanes/EtOAc solvent gradient (66% yield).

Flavyliums **2.12a–i** were synthesized by subjecting the corresponding flavone (**2.13a–i**) (20–770 mg scale, 1.0 equiv.) to methyl magnesium bromide (1.5–3.2 equiv.) in THF (0.05–0.1 M) at 0 °C, warming to room temperature and stirring for 12–24 h. The reaction was quenched with aqueous fluoroboric acid, extracted with DCM and aqueous fluoroboric acid, dried and filtered. The compounds were purified by trituration with EtOAc or with diethyl ether and toluene (39–86% yield, **2.12i** not isolated for yield). Flavylium **2.12j** was synthesized following a literature procedure.[26]

Heptamethine dyes **2.1**–**2.11** were synthesized by subjecting the corresponding flavylium (**2.12a**–**j**) (10–150 mg scale, 1.0 equiv.) to *N*-((3-(anilinomethylene)-2-chloro-1-cyclohexen-1-yl)methylene)aniline hydrochloride (**2.19**) (0.40–0.49 equiv.) with either sodium acetate or 2,6-di-*tert*-butyl-4-methylpyridine (1.5–5.6 equiv.) in either *n*-butanol/toluene, 1,4-dioxane, ethanol or *n*-pentanol (0.05–0.1 M) at 70–140 °C for 10–120 min. Compounds were purified by a mixture of column chromatography (with a gradient of either DCM/EtOH, DCM/acetone, DCM/MeCN or DCM/toluene/EtOH), trituration (in toluene and THF) and Soxhlet extraction (compound **2.10**, in toluene). Compounds were isolated in 5–51% yield. See the specific experimental procedures in *Section 2.5.2* for individual procedures used to obtain each flavone, flavylium and heptamethine dye and the full characterization of all new compounds.

Animal procedures. Animal experiments were conducted in conformity with the institutional guidelines. Non-invasive whole mouse imaging was performed on athymic nude female mice (6–16 weeks old, weight between 20–25 g), purchased from Envigo. Mice were anaesthetized with an i.p. injection of a ketamine/xylazine mixture. Tail vein injections were performed with a catheter

assembled from a 30-gauge needle connected through plastic tubing to a syringe prefilled with isotonic saline solution. The bevel of the needle was then inserted into the tail vein and secured using tissue adhesive. The plastic tubing was then connected to a syringe (30-gauge needle) prefilled with the probe of interest. All probes were filtered through a 0.22 μm syringe filter prior to i.v. injection.

SWIR imaging apparatus. For whole mouse imaging, a custom-built set-up was used. Lumics laser units (LU1064DLD350-S70AN03 (35 W), 1064 nm; LU0980D350-D30AN (35 W), 980 nm; and LU0785DLU250-S70AN03 (25 W), 785 nm) were used for excitation. Laser modules are specced to ±10 nm. Laser outputs were coupled in a 4 × 1 fan-out fibre-optic bundle (Thorlabs BF46LS01) of 600 μm core diameter for each optical path. The output from the fibre was fixed in an excitation cube (Thorlabs KCB1EC/M), reflected off of a mirror (Thorlabs BBE1-E03) and passed through a positive achromat (Thorlabs AC254-050-B), SP filter (if necessary) and ground glass diffuser (Thorlabs DG10-120-MD) or an engineered diffuser (Thorlabs ED1-S20-MD) to provide uniform illumination over the working area. In a typical experiment, the excitation flux at the object was adjusted to be close to 100 mW cm^{-2} with an error of ±3% (the power density used is defined separately in each experiment). The working area was covered by a heating mat coated with blackout fabric (Thorlabs BK5). Emitted light was directed onto an Allied Vision Goldeye G-032 Cool TEC2 camera with a sensor temperature set point of −20 °C. Two lens systems were used, as follows:

Lens system A: emitted light was directed through a four-inch square first-surface silver mirror (Edmund Optics, 84448) with a custom filter set (defined for each experiment) and a C-mount camera lens (Navitar, SWIR-35).

Lens system B: the custom lens system consists of a 4f configuration with three

lenses with focal length (f) = 500.0 mm (Thorlabs LB1909-C) and two f = 200.0 mm lenses (Thorlabs LB1199-C) with a custom filter set (defined for each experiment). For ergonomic reasons, a 2-inch protected silver-coated elliptical mirror (PFE20-P01) mounted to a kinematic mount (Thorlabs KCB2EC/M) was used.

The assembly was partially enclosed to avoid excess light while enabling manipulation of the field of view during operation. The image acquisition toolbox of the MATLAB programming environment was used in combination with a custom MATLAB script to preview and collect the required image data in 8-bit or 12-bit format. The prepared MATLAB script allows users to access basic functionalities of the image acquisition device by establishing the necessary communication layer and a stable streaming link between the host computer and the imaging device.

Multiplexed imaging acquisition. To facilitate real-time multiplexed imaging, a programmable trigger controller was implemented using an Arduino Nano Rev 3 (A000005) microcontroller unit. Predetermined triggering sequences written in C language were compiled using the Arduino Integrated Development Environment in the host computer and uploaded via USB interface to the microcontroller unit. The pre-programmed trigger controller was then used to deliver the sequential electrical voltage signals of 5 V to the laser driver units and InGaAs camera to perform multiplexed image acquisition. A semi-automatic imaging algorithm adopted in MATLAB (see above, SWIR imaging apparatus), in combination with manual control of laser parameters via the individual laser modules, and the programmed microcontroller unit facilitate excitation-synchronized imaging. Excitation-synchronized frames are collected by the camera and transferred to the personal computer via the GigE interface. Further information and illustrative figures can be found in Section 2.6.5.

Image processing procedures. Images were processed using the Fiji distribution[31] of ImageJ[32]. All images were background corrected with a ten-frame averaged background file to correct for non-linearities in the detector and/or excitation. Raw images underwent no further processing. Unmixed images were image subtracted according to the relative contribution of each channel, determined separately for each experiment, and detailed in the figure experimental procedures, Section 2.5.3. All still images were averaged over five frames and converted to 8-bit PNG files for display, unless stated otherwise.

2.5.2 Experimental Procedures

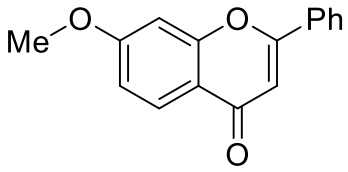

7-methoxy-4-methyl-2-phenylchromenylium chloride (2.12j): 3-methoxy flavone (1.00 g, 8.06 mmol, 1.0 equiv.), benzoyl acetone (1.31 g, 8.06 mmol, 1.0 equiv.), were dissolved in EtOAc (40 mL) and placed in a 100 mL 3-neck flask. After bubbling HCl(*g*) for 3 h, the reaction was stirred at rt for an additional 24 h under a N_2 atmosphere. The reaction mixture was filtered and rinsed with additional EtOAc to yield a bright yellow solid (814 mg, 2.84 mmol, 35%). ^{1}H NMR (500 MHz, Acetonitrile-d_3) δ 8.45 – 8.39 (m, 3H), 8.35 (d, *J*= 9.3 Hz, 1H), 7.90 – 7.84 (m, 1H), 7.79 – 7.75 (m, 3H), 7.57 (dd, *J*= 9.3, 2.4 Hz, 1H), 4.14 (s, 3H), 3.07 (s, 3H). ^{13}C NMR (126 MHz, Acetonitrile-d_3) δ 172.1, 171.5, 170.5, 160.1, 137.1, 131.2, 130.1, 130.0, 129.8, 122.9, 121.2, 117.1, 101.7, 58.5, 21.4. HRMS (ESI$^+$) calcd for $C_{17}H_{15}O_2^+$ [M]$^+$: 251.1067, found: 251.1061. Absorbance (CH_2Cl_2): 228, 265, 303, 428 nm. Emission (CH_2Cl_2, ex. 390 nm): 460 nm.

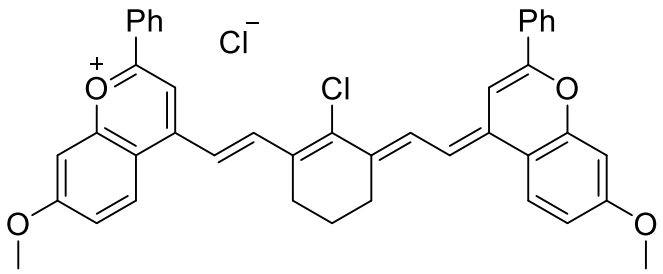

4-((E)-2-((E)-2-chloro-3-(2-((E)-7-methoxy-2-phenyl-4H-chromen-4-ylidene)ethylidene)cyclohex-1-en-1-yl)vinyl)-7-methoxy-2-phenylchromenylium chloride (2.10, MeOFlav7): Flavylium **2.12j** (150 mg, 0.523 mmol, 1.0 equiv.), *N*-[(3-(anilinomethylene)-2-chloro-1-cyclohexen-1-yl)methylene]aniline hydrochloride (**2.19**) (75 mg, 0.21 mmol, 0.40 equiv.) and 2,6-di-*tert*-butyl-4-methylpyridine (327 mg, 1.59 mmol, 3.0 equiv.) were dissolved in toluene (4.05 mL) and *n*-butanol (1.25 mL) and heated to 100 °C for 15 min. The solution was cooled to rt then cooled with ice. Toluene (10 mL) was added and a reddish brown solid precipitated and was collected through filtration and washed with an additional 25 mL of toluene. The crude product was purified through Soxhlet extraction with toluene for 4 hours at 130 °C to give a brick red solid. (47 mg, 0.070 mmol, 33%). R_f = 0.4 in 9:1 DCM/EtOH. ^{1}H NMR (400 MHz, Methylene Chloride-d_2) δ 8.55 (d, J = 13.6 Hz, 2H), 8.14 – 8.02 (m, 4H), 7.69 (s, 2H), 7.65 (t, J = 6.8 Hz, 4H), 7.40 – 7.23 (m, 6H), 7.25 – 7.09 (m, 4H), 4.01 (s, 3H), 2.93 – 2.84 (m, 4H), 2.08 – 1.96 (m, 2H). HRMS (ESI$^+$) Calculated for $C_{42}H_{34}ClNO_4^+$ $[M]^+$: 637.2140; found: 637.2124. Absorbance (CH_2Cl_2): 441 nm, 880 nm, 984 nm. Emission (CH_2Cl_2, ex. 885 nm): 1008 nm.

2.7 Spectra Relevant to Chapter Two

2.7.1 ^{1}H NMR Spectra

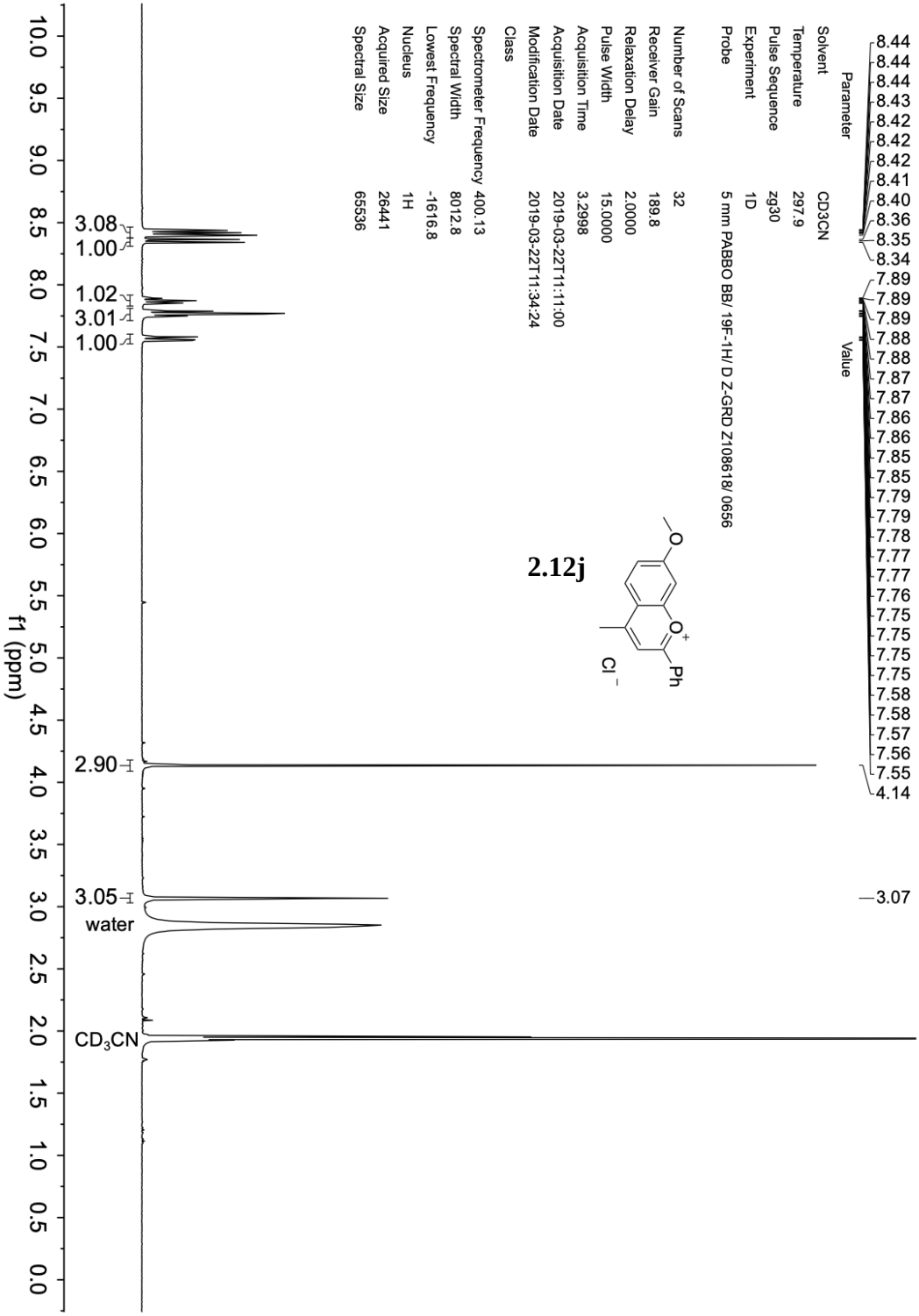

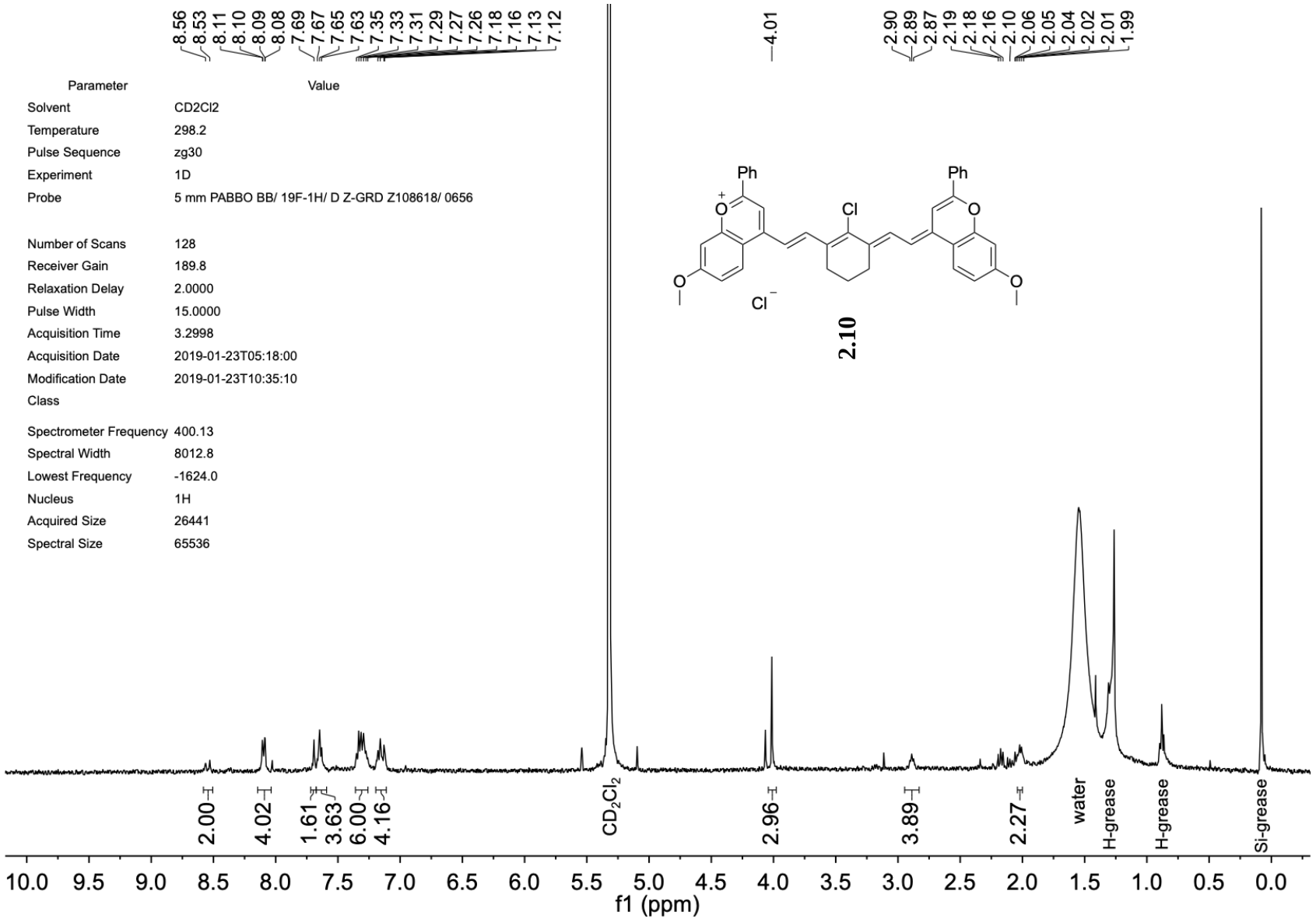
8.56
8.53
8.11
8.10
8.09
8.08
7.69
7.67
7.65
7.63
7.35
7.33
7.31
7.29
7.27
7.26
7.18
7.16
7.13
7.12
4.01
2.90
2.89
2.87
2.19
2.18
2.16
2.10
2.06
2.05
2.04
2.02
2.01
1.99
Parameter
Value
Solvent CD2Cl2
Temperature 298.2
Pulse Sequence zg30
Experiment 1D
Probe 5 mm PABBO BB/ 19F-1H/ D Z-GRD Z108618/ 0656
Number of Scans 128
Receiver Gain 189.8
Relaxation Delay 2.0000
Pulse Width 15.0000
Acquisition Time 3.2998
Acquisition Date 2019-01-23T05:18:00
Modification Date 2019-01-23T10:35:10
Class
Spectrometer Frequency 400.13
Spectral Width 8012.8
Lowest Frequency -1624.0
Nucleus 1H
Acquired Size 26441
Spectral Size 65536
Ph
Ph
Cl
O
O
O
O
Cl⁻
2.10
2.00
4.02
1.61
3.63
6.00
4.16
CD2Cl2
2.96
3.89
2.27
water
H-grease
H-grease
Si-grease
10.0 9.5 9.0 8.5 8.0 7.5 7.0 6.5 6.0 5.5 5.0 4.5 4.0 3.5 3.0 2.5 2.0 1.5 1.0 0.5 0.0
f1 (ppm)

2.7.2 ^{13}C NMR Spectra

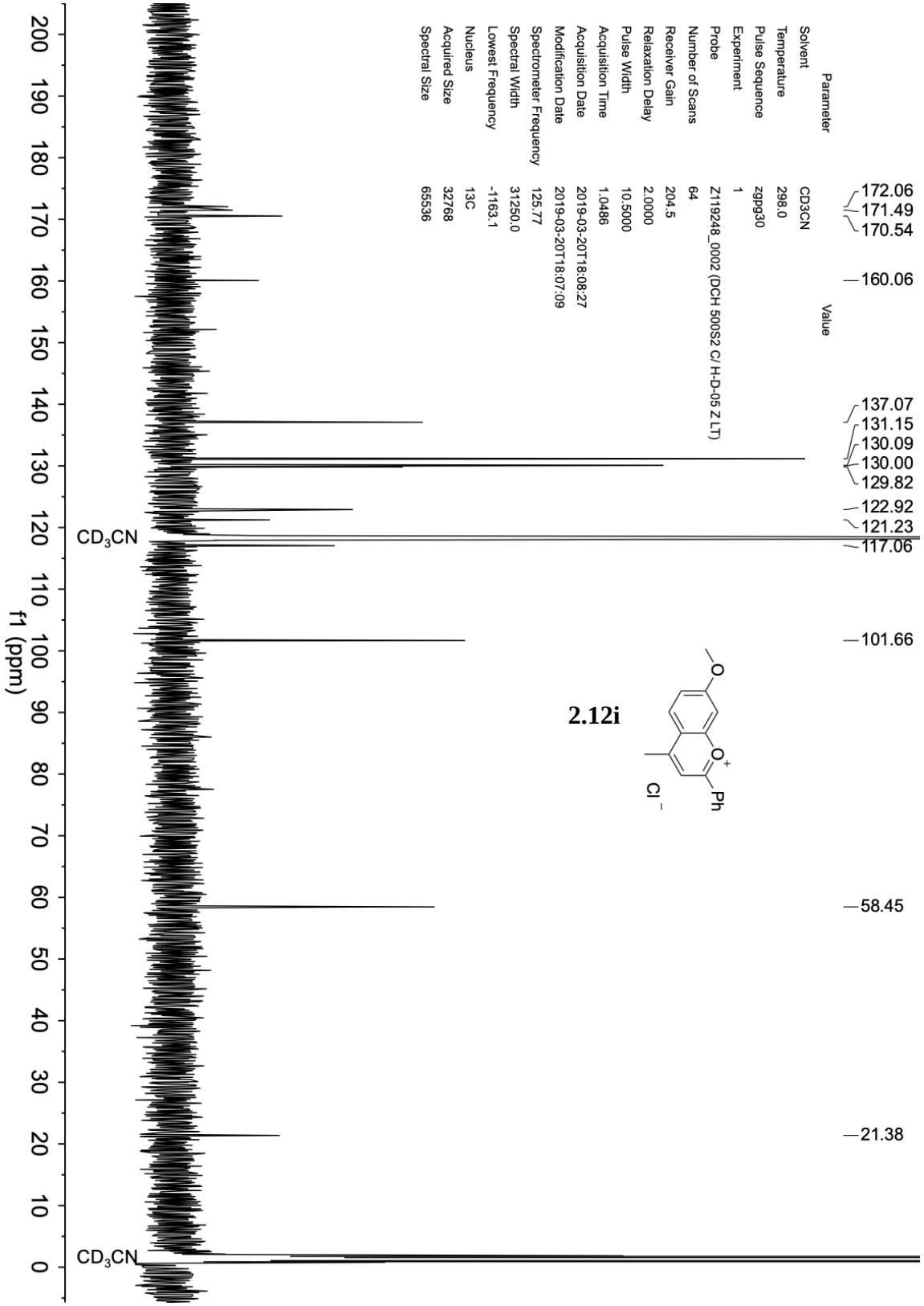

2.7.3 Absorption and Emission Spectra

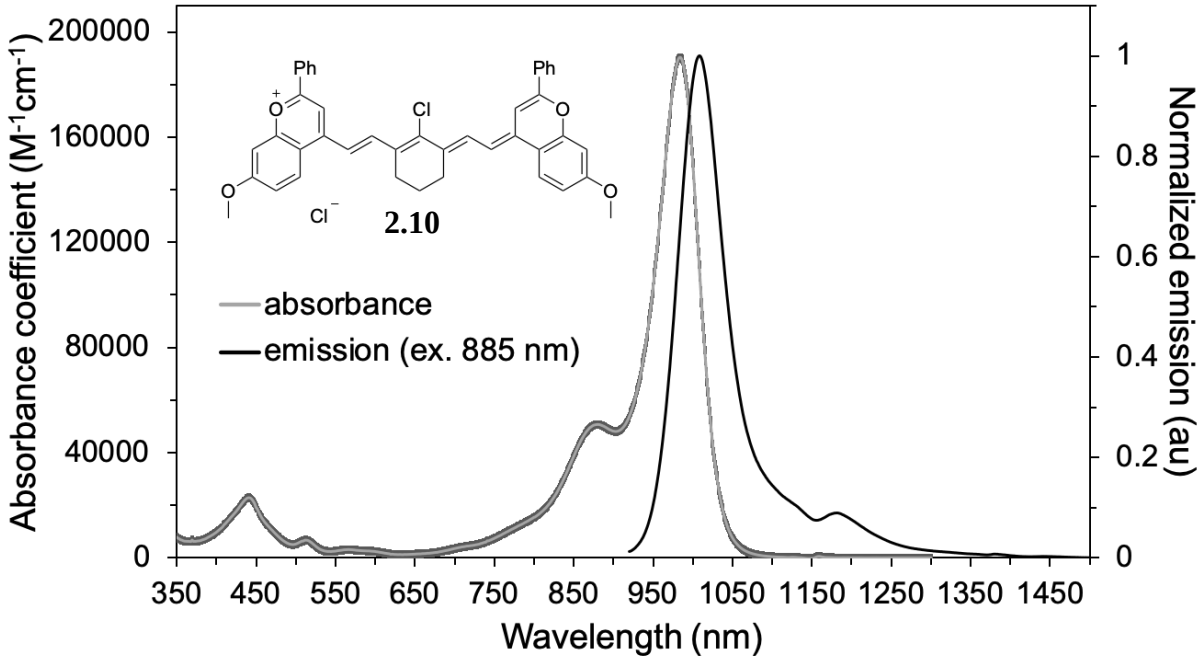

2.8 Data and Code Availability

Image datasets, including all raw and processed imaging data generated in this Chapter, are available at BioImage Archive (accession number: S-BIAD27). Custom computer programs used for the work are available at GitHub (https:// gitlab.com/brunslab/ccda).

2.9 References

(1) Kevin M Dean; Amy M. Palmer. Advances in Fluorescence Labeling Strategies for Dynamic Cellular Imaging. *Nat. Chem. Bio.* **2014,** *10*, 512–523.

(2) Lavis, L. D.; Raines, R. T. Bright Ideas for Chemical Biology. *ACS Chem. Bio.* **2008**, *3* (3), 142-155.

(3) Smith, A. M.; Mancini, M. C.; Nie, S. *Bioimaging: Second Window for in Vivo Imaging*; *Nature Nanotech.* **2009**, *4*, 710-711.

(4) Weissleder, R. A Clearer Vision for in Vivo Imaging. *Nat. Biotechnol.* **2001**, *19* (4), 316–317.

(5) Kosaka, N.; Ogawa, M.; Sato, N.; Choyke, P. L.; Kobayashi, H. In Vivo Real-Time, Multicolor, Quantum Dot Lymphatic Imaging. *J. Invest. Dermatol.* **2009**, *129* (12), 2818–2822.

(6) Erogbogbo, F.; Yong, K. T.; Roy, I.; Hu, R.; Law, W. C.; Zhao, W.; Ding, H.; Wu, F.; Kumar, R.; Swihart, M. T.; et al. In Vivo Targeted Cancer Imaging, Sentinel Lymph Node Mapping and Multi-Channel Imaging with Biocompatible Silicon Nanocrystals. *ACS Nano* **2011**, *5* (1), 413–423.

(7) Shcherbakova, D. M.; Verkhusha, V. V. Near-Infrared Fluorescent Proteins for Multicolor in Vivo Imaging. *Nat. Methods* **2013**, *10* (8), 751–754.

(8) Zavaleta, C. L.; Smith, B. R.; Walton, I.; Doering, W.; Davis, G.; Shojaei, B.; Natan, M. J.; Gambhir, S. S. Multiplexed Imaging of Surface Enhanced Raman Scattering Nanotags in Living Mice Using Noninvasive Raman Spectroscopy. *Proc. Natl. Acad. Sci. U. S. A.* **2009**, *106* (32), 13511–13516.

(9) Ma, L.; Zhai, X.; Du, G.; Zhou, J. Orthogonal Shortwave Infrared Emission Based on Rare Earth Nanoparticles for Interference-Free Logical Codes and Bio-Imaging. *Chem. Sci.* **2019**, *10*, 3281-3288.

(10) Naczynski, D. J.; Tan, M. C.; Zevon, M.; Wall, B.; Kohl, J.; Kulesa, A.; Chen, S.; Roth, C. M.; Riman, R. E.; Moghe, P. V. Rare-Earth-Doped Biological Composites as in Vivo Shortwave Infrared Reporters. *Nat. Commun.* **2013**, *4*, 2199.

(11) Zhu, S.; Herraiz, S.; Yue, J.; Zhang, M.; Wan, H.; Yang, Q.; Ma, Z.; Wang, Y.; He, J.;

Antaris, A. L.; et al. 3D NIR-II Molecular Imaging Distinguishes Targeted Organs with High-Performance NIR-II Bioconjugates. *Adv. Mater.* **2018**, *30* (13), 1705799.

(12) Wan, H.; Yue, J.; Zhu, S.; Uno, T.; Zhang, X.; Yang, Q.; Yu, K.; Hong, G.; Wang, J.; Li, L.; et al. A Bright Organic NIR-II Nanofluorophore for Three-Dimensional Imaging into Biological Tissues. *Nat. Commun.* **2018**, *9* (1), 1–9.

(13) Wang, F.; Wan, H.; Ma, Z.; Zhong, Y.; Sun, Q.; Tian, Y.; Qu, L.; Du, H.; Zhang, M.; Li, L.; et al. Light-Sheet Microscopy in the near-Infrared II Window. *Nat. Methods* **2019**, *16* (6), 545–552.

(14) Zhu, S.; Yang, Q.; Antaris, A. L.; Yue, J.; Ma, Z.; Wang, H.; Huang, W.; Wan, H.; Wang, J.; Diao, S.; et al. Molecular Imaging of Biological Systems with a Clickable Dye in the Broad 800- to 1,700-Nm near-Infrared Window. *Proc. Natl. Acad. Sci. U. S. A.* **2017**, *114* (5), 962–967.

(15) Kapanidis, A. N.; Laurence, T. A.; Nam, K. L.; Margeat, E.; Kong, X.; Weiss, S. Alternating-Laser Excitation of Single Molecules. *Acc. Chem. Res.* **2005**, *38* (7), 523–533.

(16) Müller, B. K.; Zaychikov, E.; Bräuchle, C.; Lamb, D. C. Pulsed Interleaved Excitation. *Biophys. J.* **2005**, *89* (5), 3508–3522.

(17) Lewis, E. K.; Haaland, W. C.; Nguyen, F.; Heller, D. A.; Allen, M. J.; MacGregor, R. R.; Berger, C. S.; Willingham, B.; Burns, L. A.; Scott, G. B. I.; et al. Color-Blind Fluorescence Detection for Four-Color DNA Sequencing. *Proc. Natl. Acad. Sci. U. S. A.* **2005**, *102* (15), 5346–5351.

(18) Garbacik, E. T.; Sanz-Paz, M.; Borgman, K. J. E.; Campelo, F.; Garcia-Parajo, M. F. Frequency-Encoded Multicolor Fluorescence Imaging with Single-Photon-Counting

Color-Blind Detection. *Biophys. J.* **2018**, *115* (4), 725–736.

(19) Gómez-García, P. A.; Garbacik, E. T.; Otterstrom, J. J.; Garcia-Parajo, M. F.; Lakadamyali, M. Excitation-Multiplexed Multicolor Superresolution Imaging with Fm-STORM and Fm-DNA-PAINT. *Proc. Natl. Acad. Sci. U. S. A.* **2018**, *115* (51), 12991–12996.

(20) Thimsen, E.; Sadtler, B.; Berezin, M. Y. Shortwave-Infrared (SWIR) Emitters for Biological Imaging: A Review of Challenges and Opportunities. *Nanophotonics* **2017**, *6* (5), 1043–1054.

(21) Julia L. Bricks; Alexei D.Kachkovskii; Yurii L.Slominskii; Andrii O.Gerasov; Sergei V.Popov; Bricks, J. L.; Kachkovskii, A. D.; Slominskii, Y. L.; Gerasov, A. O.; Popov, S. V. Molecular Design of near Infrared Polymethine Dyes: A Review. *Dye. Pigment.* **2015**, *121*, 238–255.

(22) Cosco, E. D.; Caram, J. R.; Bruns, O. T.; Franke, D.; Day, R. A.; Farr, E. P.; Bawendi, M. G.; Sletten, E. M. Flavylium Polymethine Fluorophores for Near- and Shortwave Infrared Imaging. *Angew. Chemie - Int. Ed.* **2017**, *56* (42), 13126–13129.

(23) Roehri-Stoeckel, C.; Gonzalez, E.; Fougerousse, A.; Brouillard, R. Synthetic Dyes: Simple and Original Ways to 4-Substituted Flavylium Salts and Their Corresponding Vitisin Derivatives. *Can. J. Chem.* **2001**, *79* (7), 1173–1178.

(24) Seijas, J. A.; Vázquez-Tato, M. P.; Carballido-Reboredo, R. Solvent-Free Synthesis of Functionalized Flavones under Microwave Irradiation. *J. Org. Chem.* **2005**, *70* (7), 2855–2858.

(25) Kónya, K.; Pajtás, D.; Kiss-Szikszai, A.; Patonay, T. Buchwald-Hartwig Reactions of

Monohaloflavones. *European J. Org. Chem.* **2015**, *2015* (4), 828–839.

(26) Chen, J. R.; Wong, J. B.; Kuo, P. Y.; Yang, D. Y. Synthesis and Characterization of Coumarin-Based Spiropyran Photochromic Colorants. *Org. Lett.* **2008**, *10* (21), 4823–4826.

(27) Kopainsky, B.; Qiu, P.; Kaiser, W.; Sens, B.; Drexhage, K. H. Lifetime, Photostability, and Chemical Structure of IR Heptamethine Cyanine Dyes Absorbing beyond 1 Mm. *Appl. Phys. B Photophysics Laser Chem.* **1982**, *29* (1), 15–18.

(28) Hansch, C.; Leo, A.; Taft, R. W. A Survey of Hammett Substituent Constants and Resonance and Field Parameters. *Chem. Rev.* **1991**, *91*, 165-195.

(29) Semonin, O. E.; Johnson, J. C.; Luther, J. M.; Midgett, A. G.; Nozik, A. J.; Beard, M. C. Absolute Photoluminescence Quantum Yields of IR-26 Dye, PbS, and PbSe Quantum Dots. *J. Phys. Chem. Lett.* **2010**, *1* (16), 2445–2450.

(30) Kövér, J.; Antus, S. Facile Deoxygenation of Hydroxylated Flavonoids by Palladium-Catalysed Reduction of Its Triflate Derivatives. *Zeitschrift fur Naturforsch. - Sect. B J. Chem. Sci.* **2005**, *60* (7), 792–796.

(31) Schindelin, J.; Arganda-Carreras, I.; Frise, E.; Kaynig, V.; Longair, M.; Pietzsch, T.; Preibisch, S.; Rueden, C.; Saalfeld, S.; Schmid, B.; et al. Fiji: An Open-Source Platform for Biological-Image Analysis. *Nature Methods*. **2012**, *9* (7), 676-682.

(32) Rueden, C. T.; Schindelin, J.; Hiner, M. C.; DeZonia, B. E.; Walter, A. E.; Arena, E. T.; Eliceiri, K. W. ImageJ2: ImageJ for the next Generation of Scientific Image Data. *BMC Bioinformatics* **2017**, *18* (1), 529.

CHAPTER THREE

Photophysical Tuning of Shortwave Infrared Flavylium Heptamethine Dyes via Substituent Placement

Adapted from: Monica Pengshung, Jingbai, Li, Fatemah Mukadum, Steven A. Lopez, Ellen M. Sletten*. Photophysical Tuning of Shortwave Infrared Flavylium Heptamethine Dyes via Substituent Placement. *Org. Lett.* **2020**, *22 (15)*, 6150-6154. DOI: 10.1021/acs.orglett.0c02213

3.1 Abstract

Optical imaging in the shortwave infrared (SWIR, 1000–2000 nm) region of the electromagnetic spectrum provides high resolution imaging in complex systems. Here, we explore substituent placement on dimethylamino flavylium polymethine dyes, a class of SWIR fluorophores. We find that the position of substituent affects the λ_{max} and fluorescence quantum yield. Quantum mechanical calculations suggest that steric clashes control the extent of π-conjugation. These insights provide a design principle for the development of novel fluorophores for enhanced SWIR imaging.

3.2 Introduction

Fluorophores in the shortwave infrared (SWIR, 1000–2000 nm) region of the electromagnetic spectrum have recently garnered excitement as tools for biological imaging.[1–3] The SWIR region is advantageous for optical imaging in complex systems because of the increased depth penetration of light through tissue, enhanced image resolution, and low energy photons as compared with the visible and near-infrared regions.[4,5] Imaging in the SWIR originally necessitated single-wall

carbon nanotubes (SWCNT)[6–9], rare earth nanomaterials[10–12] and quantum dots[13–15] as contrast agents, which have biocompatibility or bioaccumulation concerns.[16–20] In contrast with these nanostructures, small molecule fluorophores have low toxicity and are readily cleared from the body.[21] However, it is challenging to obtain fluorophores with absorption and emission above 1000 nm with fluorescence quantum yields (Φ_F) greater than ~0.3%.[22–24]

In 2017, we reported a bright flavylium heptamethine SWIR fluorophore, deemed **Flav7** (**3.1**, Figure 3.1).[25] **Flav7** contains a dimethylamino substituent at the seven-position, which provided a λ_{max} above 1000 nm. In Chapter Two, we have varied the electron-donating substituent at the seven-position and found that the $\lambda_{max,abs}$ can be modulated by ~80 nm and form a linear free energy relationship with σ *meta* Hammett constants.[26] The identity of the substituent had minimal effect on the quantum yield of the series analyzed (Φ_F = 0.42–0.62%). Finding that the seven-position represented the *meta*-position prompted our interest in placing the dimethylamino group at other positions on the flavylium heterocycle (Figure 3.1). Additional π-donation resulting from *para* and *ortho* substitution can lead to more significant electronic contributions from substituents, although the *ortho* position can be complicated by sterics.[27] In Chapter Three, we report how dimethylamino substituents at putative *ortho*-, *meta*-, and *para*-positions on flavylium heptamethine fluorophores affect photophysical properties exploring experimental and quantum mechanical analyses.

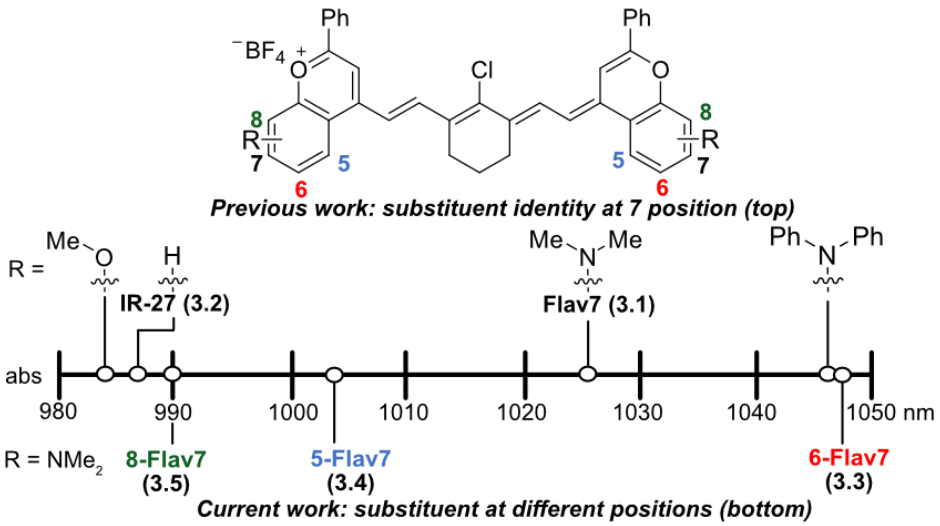

Figure 3.1. Systematic exploration of structural modifications of Flav7 (**3.1**). Previous work on derivatives at the seven-position, including methoxy and diphenylamine with a shift in λ_{max}.[26] Current work on exploring dimethylamino substitutions at different positions (five-, six-, and eight- on the heterocycle (**3.3-3.5**).

3.3 Results and Discussion

The dimethylamino flavylium heptamethine dyes were synthesized by leveraging chemistry developed to access **Flav7** derivatives.[26] The dimethylamino group was installed through a Buchwald Hartwig amination from either triflated or brominated flavones (**3.6a-3.6c**) to provide dimethylamino substituents at the five-, six-, or eight-position (**3.7a-3.7c**), respectively (Scheme 3.1). The addition of methyl-Grignard followed by quenching with tetrafluoroboric acid yielded flavylium hetereocycles (**3.8a-3.8c**), which could then be treated with linker **3.9** and 2,4-di-*tert*-butyl-4-methylpyridine to provide **5-, 6-,** and **8-Flav7** (**3.3-3.5**, respectively). These dyes are named with the first number representing the position of the dimethylamino substituent on the flavylium heterocycle, and Flav7 references the flavylium heptamethine.

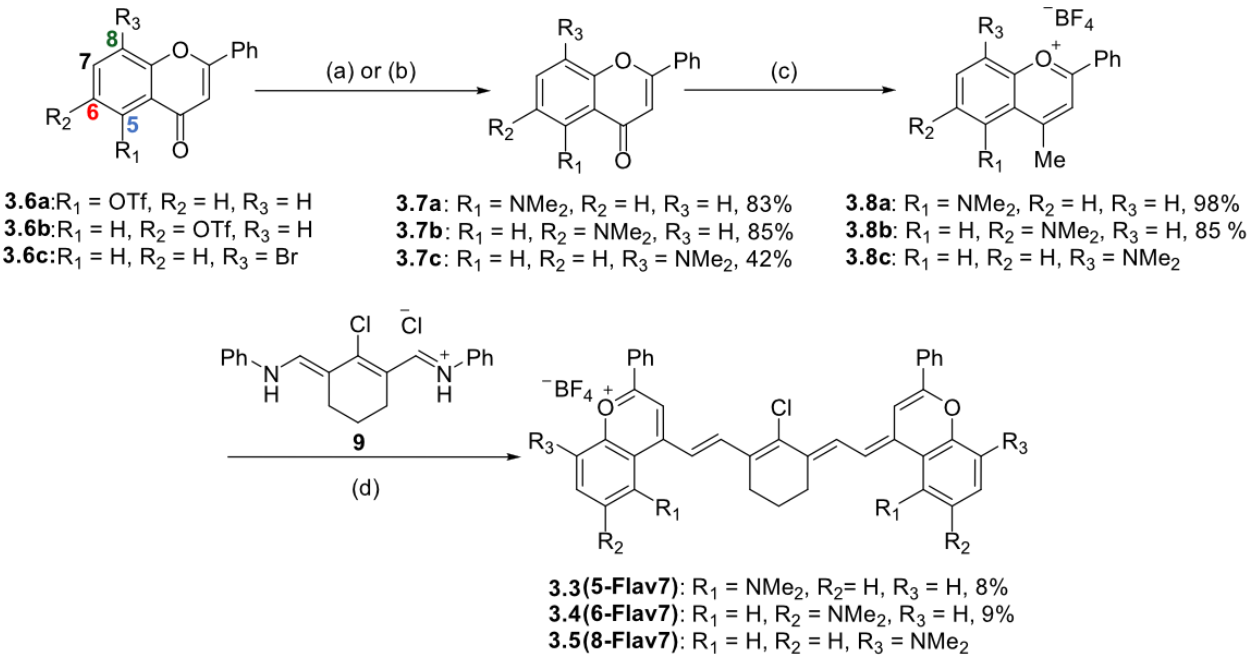

Scheme 3.1. Synthetic scheme for dimethylamino flavylium heptamethines **3–5** with substituents at the five-, six-, and eight- positions. (a) RuPhos Pd G3 (0.10 eq), RuPhos (0.10 eq), Cs_2Co_3, $HNMe_2$, toluene, 110 °C, 24 h. for **6a** and **6b**. (b) SPhos Pd G3 (0.10 eq), SPhos (0.10 eq) Cs_2Co_3, $HNMe_2$, toluene, 110 °C, 24 h. for **6c**. (c) MeMgBr (1.4M), THF, r.t. d) 2,6-di-*tert*-butyl-4methyl-pyridine, *n*-butanol/toluene or acetic anhydride, 100 °C, 15 min. Refer to SI for further experimental details.

We isolated pure **5-Flav7** (**3.3**) and **6-Flav7** (**3.4**). However, the eight-substituted flavylium (**3.8c**) readily reacted with oxygen to form a monomethine dye, characterized by an absorption peak at 722 nm (Figure 3.2).[25] To minimize this, crude **3.8c** was immediately taken to the next reaction. The resulting **8-Flav7 (3.5)** proved difficult to purify due to its instability.[28] Thus, we gained as much photophysical information as possible from the crude sample. The absorption coefficient (ε) was not determined due to insufficient purity.

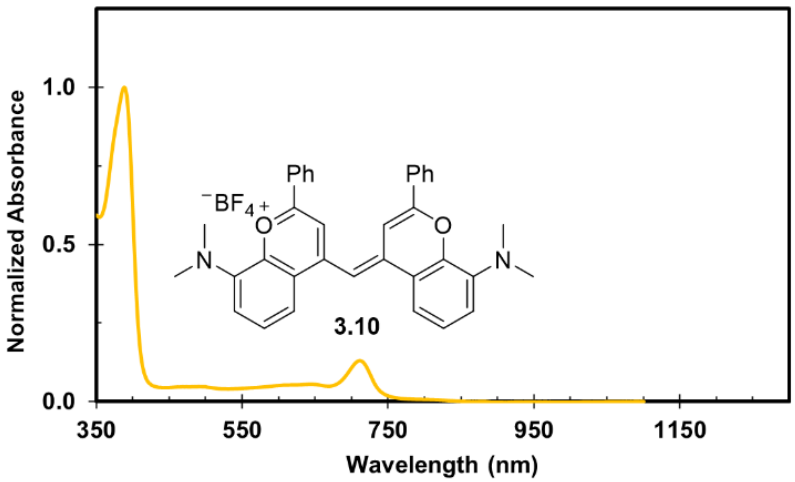

Figure 3.2. Normalized absorption spectra of **3.8c** shows the presence of a species that absorbs at 722 nm, which we attribute to monomethine dye (**3.10**) impurity.

We evaluated the photophysical properties of the newly synthesized dyes in comparison with **Flav7** (**3.1,** Figure 3.3). The absorbance and emission spectra clearly show that the position of the dimethylamino affect the $\lambda_{max,abs}$ and $\lambda_{max,em}$. Previously, we correlated the seven-position with the *meta* position through Hammett analysis.[25] We expected that the six-position would correspond to the *para*-position and that substitution at this position would show pronounced effects due to enhanced π-donation. Indeed, we observed this result, as **6-Flav7** (**3.4**, Figure 3.3, red) is 20 nm bathochromically shifted from **Flav7** (**3.1,** Figure 3.3, black).

We then reasoned that the five-position could serve as the other *meta* position and the eight-position would be the *ortho* position. We expected that the absorption and emission of **5-Flav7** (**3.3**) would be similar to **Flav7** (**3.1**), and the same comparison could be drawn for **8-Flav7** (**3.5**) and **6-Flav7** (**3.4**). However, we observed that both **3.3** and **3.5** were hypsochromically shifted in comparison to **Flav7** (**3.1**). **5-Flav7** (**3.3**, Figure 3.3, blue) has a $\lambda_{max,abs}$ of 1004 nm, a blue shift of 23 nm from **Flav7** (**3.1**). **8-Flav7** (**3.5,** Figure 3.3, green) has a $\lambda_{max,abs}$ at 990 nm, nearly identical

to parent dye **IR-27** (**3.2**). These results were counterintuitive to predicted $\lambda_{max,abs}$ based on Hammett parameters and prompted a quantum mechanical study.

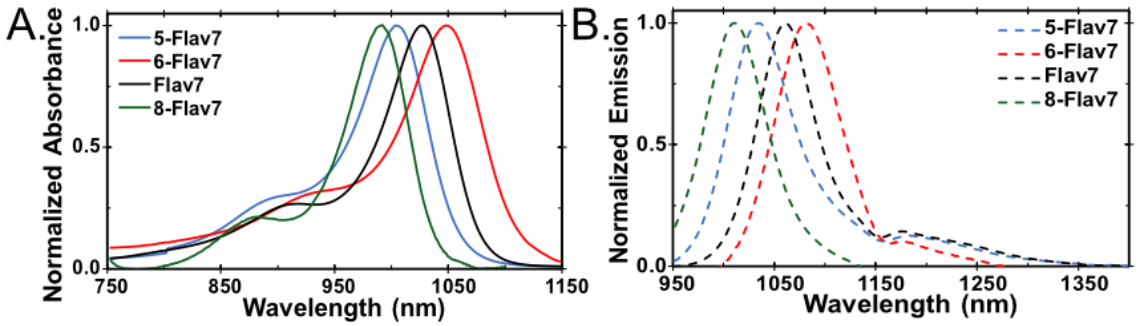

C.

Compound	$\lambda_{max,\ abs}$ (nm)	$\lambda_{max,em}$ (nm)	Φ_F (%)	ε (x 10^5 M^{-1} cm^{-1})
IR-27 (3.2)[a]	987	1011	0.35 ± 0.01	2.31 ± 0.06
5-Flav7 (3.3)	1004	1036	0.14 ± 0.01	0.79 ± 0.09
6-Flav7 (3.4)	1048	1080	0.12 ± 0.01	1.6 ± 0.3
Flav7 (3.1)[a]	1027	1053	0.61 ± 0.02	2.41 ± 0.01
8-Flav7 (3.5)[b]	990	1015	0.16 ± 0.01	N/A

Figure 3.3. Normalized (A) absorbance and (B) emission of the flavylium polymethines discussed. (C) Photophysical data of unsubstituted (**IR-27**, **3.2**) and dimethylamino substituted heptamethines (**3.1**, **3.3–3.5**). All samples were taken in dichloromethane. [a]Data was previously reported.[26] [b]Photophysical data was taken with crude sample.

We performed a conformational search of 10,000 structures enforcing the all-*trans* configuration along the polymethine chain while searching conformational flexibility of the phenyl groups. We optimized the ten lowest conformers of each molecule with the M06-2X[29] density functional and the 6-31+G(d,p) basis set. We used the integral equation formalism polarizable continuum model (IEFPCM)[30] for all calculations in the presence of dichloromethane. The computed range of free energies between the ten lowest energy conformers is 0.0–0.7 kcal mol^{-1} (Figure 3.4).

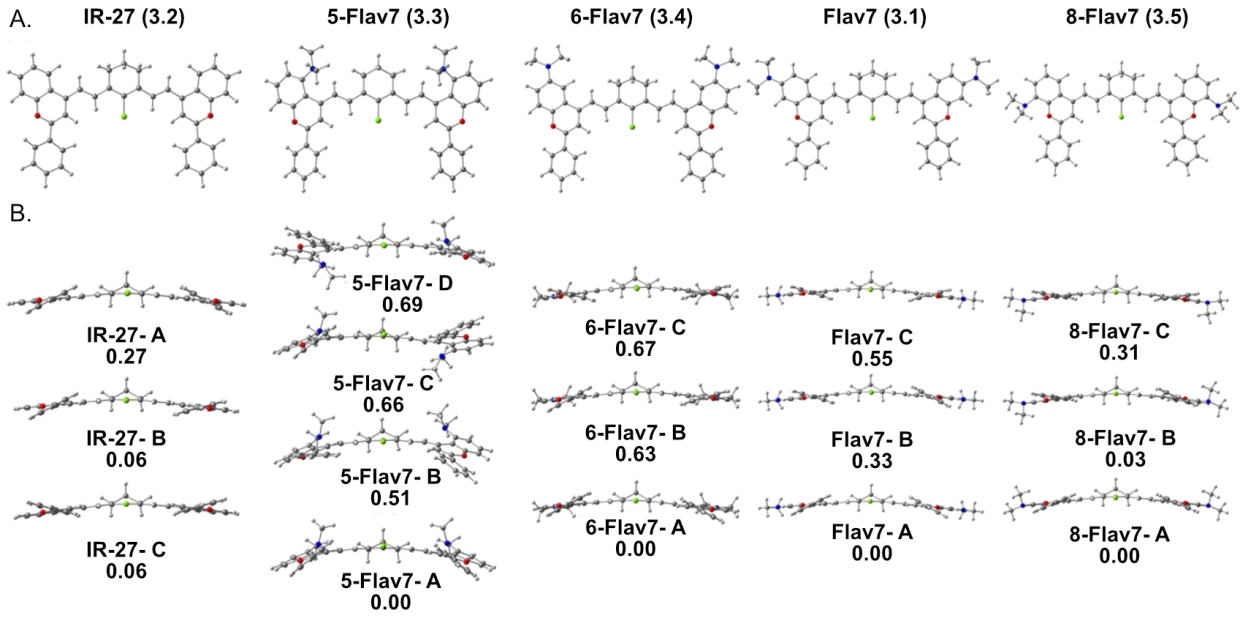

Figure 3.4. A) The global minimum geometries of **IR-27** (**3.2**), **5-Flav7** (**3.3**), **6-Flav7** (**3.4**), **Flav7** (**3.1**), and **8-Flav7** (**3.5**) dyes optimized at M062X/6-31+G(d,p) level of theory. B) The comparison of the optimized local minimum geometries (A-D) of **IR-27** (**3.2**), **5-Flav7** (**3.3**), **6-Flav7** (**3.4**), **Flav7** (**3.1**), and **8-Flav7** (**3.5**) dyes. The relative energies are in kcal·mol^{-1}, corrected with Gibbs free energy at 298.15 K.

To evaluate the photophysical properties, we used the global minima for **Flav7** dyes (**3.1**, **3.3–3.5**) as well as unmodified **IR-27** (**3.2**). The conjugated C-C bonds in the polymethine chains ranged from 1.39–1.41 Å. However, the substituents altered the planarity of the π-system along the polymethine chain and the flavylium heterocycle. We deconvoluted these effects with two angular parameters, α and β (Figure 3.5A,B). We define α as the angle between the plane of the polymethine and the plane of the flavylium, whereas β is the angle between the plane of the flavylium and the substituent. Analysis of the α angles shows little distortion between the polymethine plane and the flavylium heterocycles when the dimethylamino group is at the six-, seven-, or right- position (α = 5°–7°, Figure 3.5B). At the five-position, the NMe_2 C-H bonds clash with the vinyl C-H bond of the polymethine chain, which results in a larger angle of 18°.

The NMe_2 substituents also alter the geometries near the vicinity of the flavylium heterocycle. The torsion angle β in **Flav7** (**3.1**) and **6-Flav7** (**3.4**) are nearly planar (5° and 1°, respectively). **5-Flav7** (**3.3**) and **8-Flav7** (**3.5**) have β angles of 46° and 44°, respectively, which indicate significant out-of-plane distortions. The NMe_2 groups rotate to minimize closed-shell repulsion to the vinyl C-H bond in **5-Flav7** (**3.3,** Figure 3.5C) and to the oxygen lone pair and adjacent C-H bond of the phenyl group in **8-Flav7** (**3.5,** Figure 3.5D).

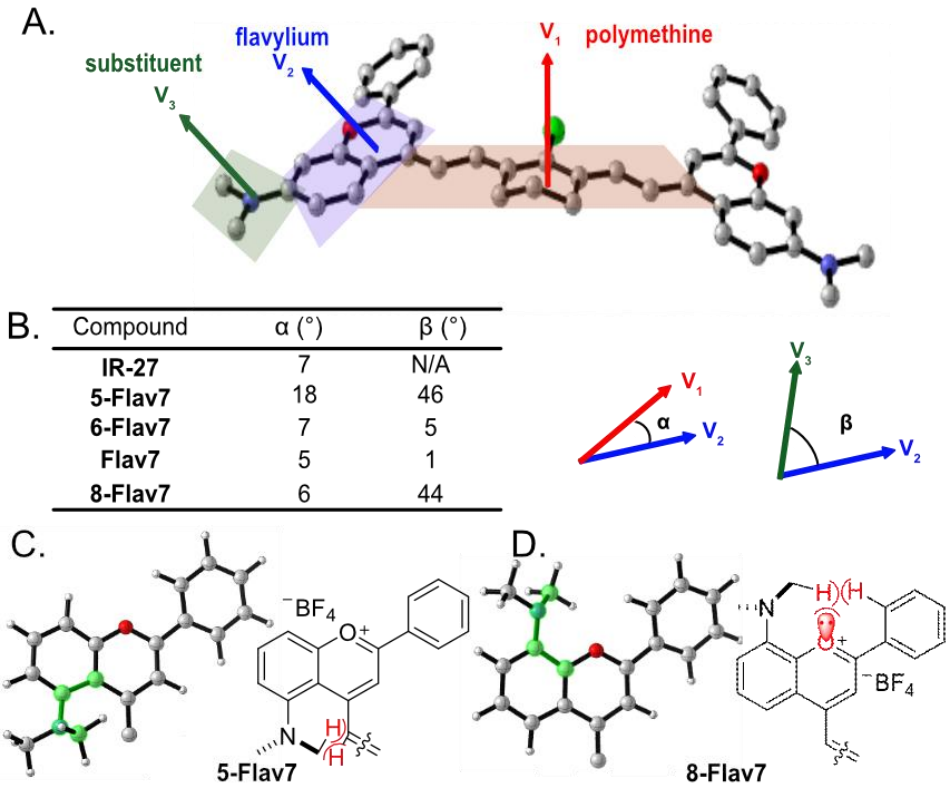

Figure 3.5. (A) Represented by **Flav7**; torsion angles are defined by α (V_1 to V_2, red to blue) and β (V_3 to V_2, green to blue) using the normal of the plane of the polymethine (V_1), flavylium (V_2) and substituent (V_3). (B) Table of α and β angles for **Flav7** dyes. (C,D) Heterocycle structures of (C) **5-Flav7** and (D) **8-Flav7** at the S_0 state, optimized with M06-2X/6-31+G(d,p). The polymethine chain is omitted for clarity. The dihedral angles at the substituted positions of the flavylium heterocycles are highlighted in green to show the rotation of the NMe_2 group in **5-Flav7** and **8-Flav7**.

We computed the frontier molecular orbitals (FMOs) to illustrate the differences in the electronic structures of these fluorophores. Displayed in Figures 3.6A and Figure 3.7 are the highest occupied molecular orbitals and lowest unoccupied molecular orbitals (HOMOs and LUMOs). The FMOs show that the extent of π-conjugation in the flavylium heterocycles varies with respect to the substituent site. **Flav7** (**3.1**) and **6-Flav7** (**3.4**) have dimethylamino substituents that are nearly coplanar with flavylium heterocycles, allowing for the NMe_2 to maximally extended orbital overlap in the HOMOs and LUMOs. This results in reduced HOMO-LUMO gaps and longer $\lambda_{max,abs}$. The 46° out-of-plane torsion in **5-Flav7** (**3.3**) results in decreased π-conjugation of the nitrogen lone pair to the chromophore. The substantial out-of-plane distortion of **8-Flav7** (**3.5**) nearly eliminates π-conjugation of the nitrogen lone pair, which leads to unperturbed $\lambda_{max,abs}$ relative to parent dye, **IR-27** (**3.2**).

The predicted $\lambda_{max,abs}$ values of dyes were calculated using configuration interactions of singles with corrections to doubles method (CIS(D))[31,32] and the cc-pVDZ basis sets. The computed HOMO–LUMO gaps match the experimentally observed trend (Figure 4B). **6-Flav7** (**3.4**) has the smallest gap (2.94 eV), which correlates with the longest $\lambda_{max,abs,}$ whereas **8-Flav7** (**3.5**) has the largest gap (3.03 eV) and the shortest experimentally determined $\lambda_{max,abs}$. The predicted $\lambda_{max,abs}$ is systematically blue-shifted 159–190 nm relative to experimental values, likely due to contributions from double excitation that are unaccounted for with single-reference quantum mechanical methods.[33,34]

A.

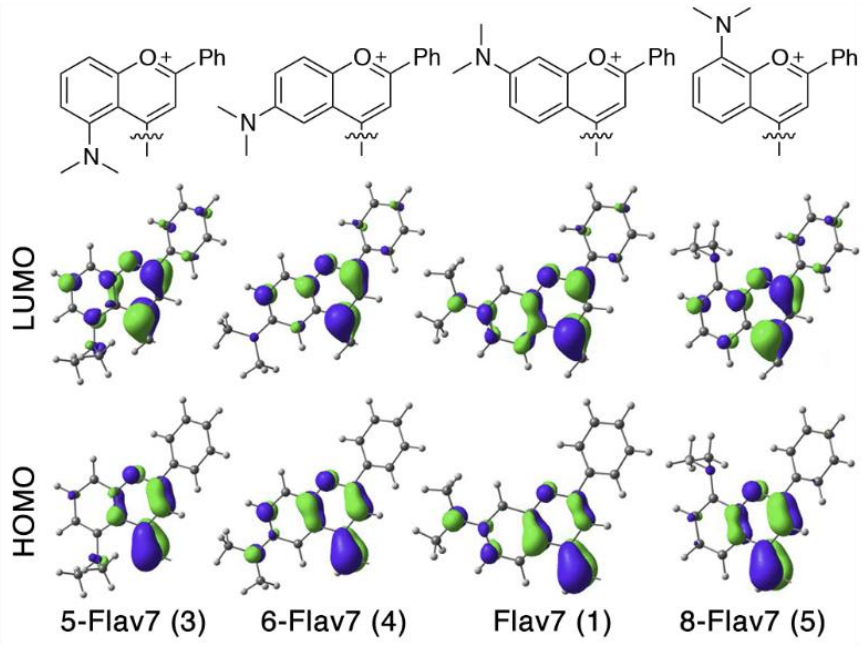

B.

Compound	Δ (nm)	HOMO-LUMO gap (eV)	$\lambda_{max,\ calc.\ abs}$ (nm)
IR-27 (3.2)	165	3.03	822
5-Flav7 (3.3)	169	2.99	835
6-Flav7 (3.4)	190	2.94	858
Flav7 (3.1)	163	2.98	864
8-Flav7 (3.5)	159	3.03	831

Figure 3.6. (A) HOMOs and LUMOs of **Flav7** (**3.1**) and (**5**,**6** and **8**)**-Flav7** (**3.3-3.5**) at M06-2X/6-31+G(d,p) level of theory. Polymethine chains were omitted for clarity. (B) Table of calculated $\lambda_{max,calc,abs}$ (nm) determined by theoretical HOMO-LUMO gap (eV). Δ is the difference between experimental and calculated $\lambda_{max,abs}$.

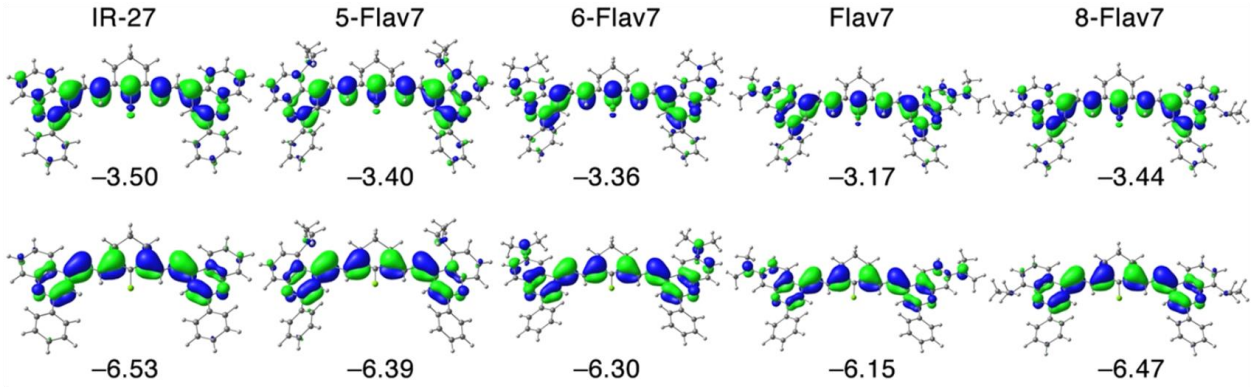

Figure 3.7. The frontier molecular orbitals (HOMO/top and LUMO/bottom) of **IR-27** (**3.2**), **5-Flav7** (**3.3**), **6-Flav7** (**3.4**), **Flav7** (**3.1**), and **8-Flav7** (**3.5**) dyes in their global minimum computed at M062X/6-31+G(d,p). The orbital energies are in eV.

Our analysis of the λ_{max} show that the position of substituents on the flavylium ring can affect $\lambda_{max,}$ comparable to the magnitude observed by varying the electronics at the seven-position. However, the major limitation of small molecule fluorophores in the SWIR is their low $\Phi_{F.}$[22] At 0.61%, **Flav7** (**3.1**) has a respectable Φ_F for polymethine SWIR fluorophores. It is of interest to gain an understanding of how structural modifications impact Φ_F to develop brighter probes. Previously, we found that functional groups at the seven-position showed little change in quantum yield of fluorescence.[25] However, here we see that substituent placement can greatly alter the Φ_F (Figure 3.3).

We measured Φ_F values for **5-Flav7**, **6-Flav7**, and **8-Flav7** (**3.3-3.5**). All three were significantly less fluorescent than **Flav7** (**3.1**), with Φ_F ranging from 0.12–0.16%. We were particularly interested in the large difference between **Flav7** (**3.1**) and **6-Flav7** (**3.4**)**,** which are conformationally similar. Flavylium heterocycles are structurally similar to coumarin heterocycles, and large differences in Φ_F between six- and seven-position substituted coumarin fluorophores has previously been observed.[27] The low Φ_F in 6-aminocoumarins (**3.11**) compared to 7-aminocoumarins (**3.12**) was attributed to a significant contribution of a twisted intermolecular charge transfer (TICT) state in which the amine donor twists out of plane by ~90° upon photoexcitation, forming a non-emissive species.[35] We hypothesized a similar phenomenon could contribute to the loss of fluorescence in **6-Flav7** (**3.4**), as compared with the parent **Flav7** (**3.1**).

To gain insight into whether TICT was contributing to observed differences in fluorescence **3.1** and **3.4**, we synthesized a flavylium heptamethine that contained an azetidine at the six-position. Azetidines have been shown to minimize TICT states by preventing the substituent from twisting out of plane.[36] **Azet-6-Flav7** (**3.15,** Figure 3.8A) was synthesized following a similar procedure to **6-Flav7** (Scheme 3.2). We found the Φ_F to be 0.21%, 1.75 times higher than the dimethylamino

derivative. In contrast, azetidine at the 7-position (**3.16**) resulted in a slight decrease in Φ_F compared with **Flav7** (**3.1**) (0.51% vs. 0.61%, Figure 5C).[26] We calculated fold change of Φ_F for each of the pairs of six- and seven-substituted fluorophores (**3.4** vs **3.1**, **3.12** vs **3.13, 3.10** vs **3.11;** Figure 3.8D) and found that the NMe_2 variants of both flavylium heptamethine and coumarin dyes had similar changes, whereas the azetidine functionalized Flav7 dyes displayed a reduced change. These data support the notion that TICT could be playing a larger role at the six-position, contributing to the observed difference in Φ_F between **Flav7 (3.1)** and **6-Flav74** vs (**3.4**).

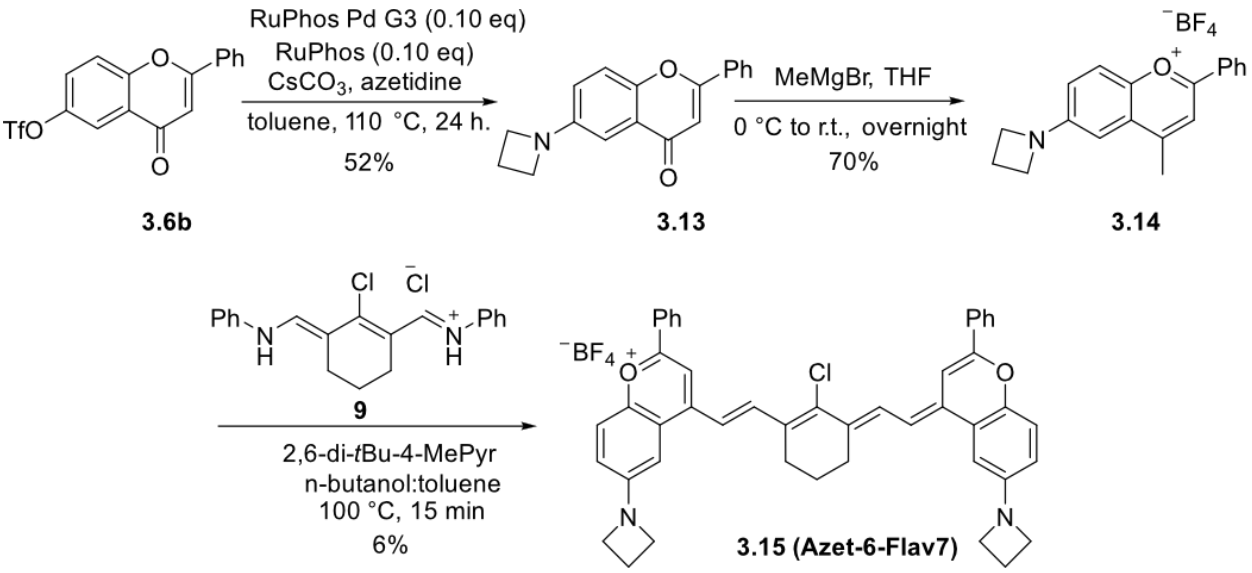

Scheme 3.2. Synthesis of Azet-6-Flav7 **3.15**.

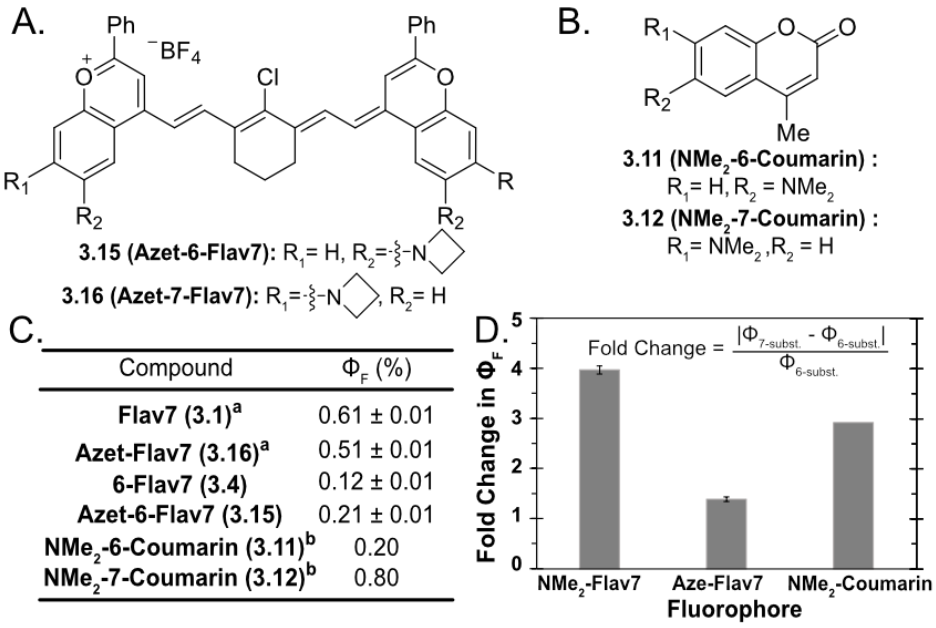

Compound	Φ_F (%)
Flav7 (3.1)[a]	0.61 ± 0.01
Azet-Flav7 (3.16)[a]	0.51 ± 0.01
6-Flav7 (3.4)	0.12 ± 0.01
Azet-6-Flav7 (3.15)	0.21 ± 0.01
NMe_2-6-Coumarin (3.11)[b]	0.20
NMe_2-7-Coumarin (3.12)[b]	0.80

Figure 3.8. (A) Structures of azetidine-substituted flavylium heptamethines (**3.12, 3.13**). (B) Structure of 6- and 7-aminocoumarins (**3.10, 3.11**). (C) Φ_F of flavylium heptamethine and coumarin dyes in dichloromethane and decanol, respectively. [a]Previously reported by our group.[26] [b]Previously reported.[35] (D) Fold change of Φ_F between six- and seven-substituted flavylium heptamethine or coumarin fluorophore.

3.4 Conclusions

In conclusion, we have demonstrated that dimethylamino substituent placement significantly influences the photophysical properties of flavylium heptamethine dyes. Substituent steric effects impact the degree of conjugation and alter the $\lambda_{max,abs.}$ We have used density functional theory calculations to understand the origin of these unique photophysical properties. The seven-position appears to be advantageous for obtaining a high quantum yield and maintaining SWIR absorption maxima; however, further red-shifted dyes can be obtained by substituting the six-position. The insights garnered herein can contribute to the design of novel fluorophores to be utilized for high resolution SWIR *in vivo* imaging.

3.5 Experimental Procedures

3.5.1 Photophysical Procedures

Absorbance spectra were collected on a JASCO V-770 UV-Visible/NIR spectrophotometer with a 2000 nm/min scan rate after blanking with the appropriate solvent. Photoluminescence spectra were obtained on a Horiba Instruments PTI QuantaMaster Series fluorometer. Quartz cuvettes (1 cm) were used for absorbance and photoluminescence measurements. Absorption coefficients in dichloromethane were calculated with serial dilutions with Hamilton syringes in volumetric glassware. Error was taken as the standard deviation of the triplicate experiments. Relative quantum yields were determined in dichloromethane relative to IR-26.

Fluorescence quantum yield measurements:

The fluorescence quantum yield (Φ_F) of a molecule or material is defined as follows:

$$\Phi_F = \frac{P_E}{P_A} \qquad (1)$$

Where P_E and P_A represent the number of photons emitted and absorbed, respectively. To determine the quantum yield, we used a relative method with IR-26 as a known standard in the same region of the electromagnetic spectrum.

To compare an unknown to a reference with a known quantum yield, the following relationship was used:

$$\Phi_{F,x} = \Phi_{F,r}\,(m_x / m_r)(\eta_x^2 / \eta_r^2)$$

Where m represents the slope of the line (y = mx + b) obtained from graphing integrated fluorescence intensity versus optical density across a series of samples, η is the refractive index

of the solvent and the subscripts *x* and *r* represent values of the unknown and reference, respectively.

The $\Phi_{F,r}$ of IR-26 was taken to be 0.05%, as previously determined.[37]

To obtain a plot of integrated fluorescence intensity versus absorbance for the reference and unknown, five solutions and a solvent blank were prepared with absorbance maxima between 0.01 and 0.1 au. Absorbance and emission spectra (with an excitation wavelength of 885 nm) were acquired for all samples. IR-26 and the unknown dyes were diluted in dichloromethane to concentrations with optical densities less than 0.1 to minimize effects of reabsorption. The baseline corrected (at 1500 nm) fluorescence traces were integrated, and the raw integrals were corrected by subtracting the integral over an identical range from fluorescence traces of the blank solvent. The integrated fluorescence intensities were then plotted against the baseline corrected absorbance values at the relevant wavelength (885 nm), and the slope and error in slope were obtained ($R^2 > 0.99$ for all traces).

3.5.2 Synthetic Procedures

Materials Chemical reagents were purchased from Acros Organics, Alfa Aesar, Fisher Scientific, Sigma-Aldrich, or TCI and used without purification unless noted otherwise. Anhydrous and deoxygenated solvents (THF, toluene) were dispensed from a Grubb's-type Phoenix Solvent Drying System constructed by J.C. Meyer. Oxygen was removed by three consecutive freeze pump–thaw cycles in air-free glassware directly before use. Thin layer chromatography was performed using Silica Gel 60 F254 (EMD Millipore) plates. Flash chromatography was executed with technical grade silica gel with 60 Å pores and 40 – 63 μm mesh particle size (Sorbtech Technologies).

Instrumentation Solvent was removed under reduced pressure with a Büchi Rotovapor with a Welch self-cleaning dry vacuum pump and further dried with a Welch DuoSeal pump. Nuclear magnetic resonance (^{1}H-NMR, ^{13}C-NMR) spectra were taken on Bruker Advance AV-400, AV-500 and processed with MestReNova or TopSpin software. All ^{1}H-NMR and ^{13}C-NMR peaks are reported in ppm in reference to their respective solvent signals. High resolution mass spectra (electrospray ionization (ESI)) were obtained on a Thermo Scientific Q Exactive™ Plus Hybrid Quadrupole-Orbitrap™ with Dionex UltiMate 3000 RSLCnano System.

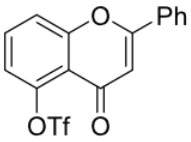

4-oxo-2-phenyl-4*H*-chromen-5-yl trifluoromethanesulfonate (3.6a)

Triflic anhydride (0.60 mL, 3.0 mmol, 4 eq) was added slowly dropwise to a solution of 5-hydroxyflavone (200 mg, 0.8 mmol, 1 eq) in anhydrous pyridine (2.5 mL, 30 mmol, 40 eq) at 0 °C. The reaction was warmed to room temperature and left to stir for 1 hr. The solution was quenched with saturated $NaHCO_3$ (15 mL), extracted with ethyl acetate (3 x 20 mL), dried over $NaSO_4$, filtered and evaporated to give a yellow crystalline solid. The crude product was purified via silica gel chromatography with hexane: ethyl acetate (9:1) to afford pure **4-oxo-2-phenyl-4*H*-chromen-5-yl trifluoromethanesulfonate** (260 mg, 3.0 mmol, 85%) as a beige solid. ^{1}H-NMR (400 MHz, Chloroform-*d*) δ 7.93 – 7.87 (m, 2H), 7.76 – 7.70 (m, 1H), 7.65 (dd, *J* = 8.6, 1.2 Hz, 1H), 7.58 – 7.51 (m, 3H), 7.23 (s, 1H), 6.81 (s, 1H). NMR matched the literature.[38]

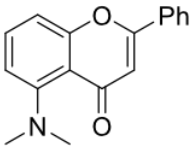

5-(dimethylamino)-2-phenyl-4*H*-chromen-4-one (3.7a)

Flavone **3.6a** (200 mg, 0.50 mmol, 1 eq), RuPhos-Pd-G3 (45 mg, 0.10 mmol, 0.1 eq), RuPhos (20 mg, 0.10 mmol, 0.1 eq) and cesium carbonate (240 mg, 0.80 mmol, 1.5 eq) was evacuated and subsequently purged with nitrogen for three cycles. Anhydrous toluene (5 mL) was added to solubilize all solids and then dimethylamine (0.40 mL, 0.80 mmol, 1.5 eq) was added. The solution was heated to 110 °C in a heating block and turned from a cloudy brown to clear orange-yellow. After 24 hours of stirring, the solution was concentrated down to give an orange red solid. The crude product was purified via silica gel chromatography with hexanes: ethyl acetate (9:1→ 4:1) to afford pure **5-(dimethylamino)-2-phenyl-4*H*-chromen-4-one** (110 mg, 0.40 mmol, 83%) as a yellow/green solid. ^{1}H-NMR (400 MHz, Chloroform-*d*): δ 7.84 – 7.75 (m, 2H), 7.45 – 7.30 (m, 4H), 6.92 (dd, *J* = 8.3, 1.0 Hz, 1H), 6.74 (dd, *J* = 8.2, 1.2 Hz, 1H), 6.62 (s, 1H), 2.89 (d, *J* = 1.3 Hz, 6H). ^{13}C-NMR (101 MHz, Chloroform-*d*) δ 177.9, 160.3, 159.1, 152.9, 133.1, 131.6, 131.1, 128.9, 125.9, 115.2, 111.6, 108.6, 108.6, 44.7. HRMS (ESI) m/z: $[M+H]^+$ Calcd for $C_{17}H_{16}NO_2^+$ 266.1103; Found 266.1093.

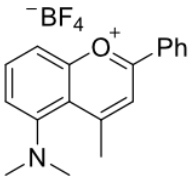

5-(dimethylamino)-4-methyl-2-phenylchromenylium (3.8a)

5-(dimethylamino)-2-phenyl-4*H*-chromen-4-one **3.7a** (110 mg, 0.40 mmol, 1 eq) was dissolved in THF (5.3 mL, anhydrous) and cooled to 0 °C. MeMgBr (1.4 M in THF/toluene, 0.60 mL, 0.80

mmol, 2 eq) was added dropwise over 30 min turning the solution from yellow to orange brown. The mixture was warmed to room temperature and left to stir overnight, at which point was quenched with 5% fluoroboric acid solution, turning the solution purple, then extracted with dichloromethane (3 x 15 mL), dried over $NaSO_4$, filtered and evaporated. The crude solid was washed with cold ethyl acetate (50 mL) to afford pure **3.3a** as a purple solid (96 mg, 0.35 mmol, 98%). ^{1}H-NMR (400 MHz, Acetonitrile-d_3): δ 8.36 (dd, J = 8.5, 1.3 Hz, 2H), 8.14 (s, 1H), 8.07 (t, J = 8.3 Hz, 1H), 7.85 – 7.79 (m, 1H), 7.78 – 7.67 (m, 1H), 7.58 (dd, J = 8.3, 1.0 Hz, 1H), 7.36 (dd, J = 8.4, 1.0 Hz, 1H), 3.15 (s, 3H), 2.99 (s, 6H). ^{13}C-NMR (101 MHz, Acetonitrile-d_3) δ 172.6, 168.3, 157.5, 155.5, 139.8, 135.8, 130.0, 129.0, 128.6, 120.3, 116.5, 116.4, 109.3, 44.6, 23.2. HRMS (ESI) m/z: $[M+H]^+$ Calcd for $C_{18}H_{19}NO$ 265.1383; Found 265.1375.

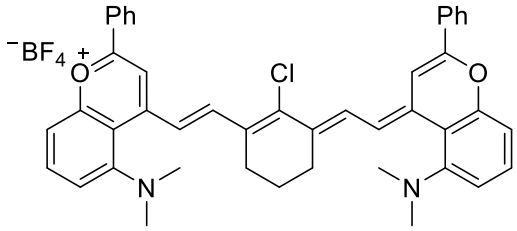

4-((E)-2-((E)-2-chloro-3-(2-((E)-5-(dimethylamino)-2-phenyl-4*H*-chromen-4-ylidene)ethylidene)cyclohex-1-en-1-yl)vinyl)-5-(dimethylamino)-2-phenylchromenylium tetrafluoroborate (5-Flav7, 3.3)

A Schlenk flask was charged with flavylium **3.8a** (80 mg, 0.20 mmol, 1 eq), 2,6-di-*tert*-butyl-4-methylpyridine (240 mg, 1.1 mmol, 5 eq), N-[(3-(anilinomethylene)-2-chloro-1-cyclohexen-1-yl)methylene]aniline hydrochloride **3.9** (25 mg, 0.1 mmol, 0.3 eq) and acetic anhydride (2.5 mL). The dark magenta solution was freeze pump thawed 3x and then heated to 100 °C in an oil bath for 10 min. The reaction was monitored by UV-Vis for the disappearance of the 500 nm peak and formation of 1004 nm peak. Upon completion, the solution was cooled to r.t

and dried immediately onto silica. The product was purified via silica gel chromatography twice with dichloromethane: ethanol (99.5: 0.5 → 99.25: 0.75 → 99:1) to afford pure **5-Flav7** as a dark green-brown solid (4 mg, 0.01 mmol, 8%). ^{1}H-NMR (400 MHz, Methylene Chloride-d_2) δ 7.96 – 7.69 (m, 5H), 7.51 (dd, J = 5.5, 1.9 Hz, 9H), 7.19 (s, 5H), 7.04 (s, 3H), 3.09 (s, 12H), 2.40 (s, 4H), 1.72 (d, J = 7.2 Hz, 2H). HRMS (ESI) m/z: $[M]^+$ Calcd for $C_{44}H_{40}ClN_2O_2^+$: 663.2278; Found 663.2264. Absorbance (dichloromethane, λ_{max}/nm) = 1004 nm. Emission (dichloromethane, λ_{max}/nm) = 1038 nm.

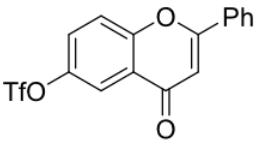

4-oxo-2-phenyl-4*H*-chromen-6-yl trifluoromethanesulfonate (3.6b)

Triflic anhydride (0.42 mL, 2.5 mmol, 4 eq) was added dropwise to a solution of 6-hydroxyflavone (150 mg, 0.60 mmol, 1 eq) in anhydrous pyridine (2.0 mL, 24 mmol, 60 eq) at 0 °C. The solution was warmed to room temperature and left to stir for 1 hr, at which point it was quenched with saturated $NaHCO_3$ (10 mL), extracted with ethyl acetate (3 x 15 mL), dried over $NaSO_4$, filtered and evaporated to give an orange solid. The crude product was purified via silica gel chromatography with hexane: ethyl acetate (9:1) to afford pure **4-oxo-2-phenyl-4*H*-chromen-6-yl trifluoromethanesulfonate** as a white fluffy solid (185 mg, 0.50 mmol, 83%).^{1}H-NMR (400 MHz, Chloroform-*d*) δ 8.11 (d, J = 3.0 Hz, 1H), 7.91 (dd, J = 8.1, 1.7 Hz, 2H), 7.68 (d, J = 9.1 Hz, 1H), 7.63 – 7.50 (m, 4H), 6.84 (s, 1H). ^{13}C-NMR (101 MHz, Chloroform-*d*) δ 176.7, 164.1, 154.9, 146.2, 132.1, 131.1, 129.2, 127.1, 126.4, 125.1, 120.8, 120.3, 118.3, 117.1, 107.4. HRMS (ESI) m/z: $[M+H]^+$ Calcd for $C_{16}H_{10}F_3O_5S^+$ 371.0123; Found 371.0120.

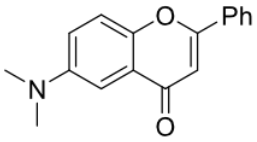

6-(dimethylamino)-2-phenyl-4*H*-chromen-4-one (3.7b)

Flavone **3.6b** (200 mg, 0.5 mmol, 1 eq), RuPhos-Pd-G3 (50 mg, 0.05 mmol, 0.1 eq), RuPhos (20 mg, 0.05 mmol, 0.1 eq) and cesium carbonate (260 mg, 0.80 mmol, 1.5 eq) was put on a high vac and subsequently purged with nitrogen for three cycles. Toluene (5.0 mL, anhydrous) was added to solubilize all solids and then dimethylamine (0.4 mL, 0.8 mmol, 1.5 eq) was added. The solution was heated to 110 °C in a heating block, turning the solution a deeper orange color. After 24 hours of stirring, the solution was concentrated down to give an orange yellow solid. The crude product was purified via silica gel chromatography with hexanes: ethyl acetate (9:1 → 4:1) to afford pure **6-(dimethylamino)-2-phenyl-4*H*-chromen-4-one** as a yellow/green solid (122 mg, 0.5 mmol, 85%). ^{1}H-NMR (400 MHz, Chloroform-*d*) δ 7.93 – 7.89 (m, 2H), 7.53 – 7.49 (m, 3H), 7.46 (d, *J* = 9.1 Hz, 1H), 7.34 (d, *J* = 3.2 Hz, 1H), 7.15 (dd, *J* = 9.2, 3.2 Hz, 1H), 6.78 (s, 1H), 3.03 (s, 6H). ^{13}C-NMR (101 MHz, Chloroform-*d*) δ 178.8, 162.7, 148.9, 148.2, 132.2, 131.2, 128.9, 126.2, 124.5, 119.8, 118.7, 106.6, 105.0, 40.9. HRMS (ESI) m/z: $[M+H]^+$ Calcd for $C_{18}H_{19}NO^+$ 266.1103; Found 265.1095.

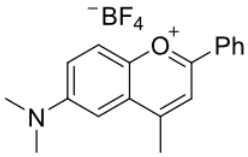

6-(dimethylamino)-4-methyl-2-phenylchromenylium (3.8b)

6-(dimethylamino)-2-phenyl-4*H*-chromen-4-one **3.7b** (120 mg, 0.5 mmol, 1 eq) was dissolved in THF (5.7 mL, anhydrous) and cooled to 0 °C. MeMgBr (1.0 M in THF, 1.0 mL, 1.0 mmol, 2 eq) was added dropwise over 30 min turning the solution from yellow to orange brown. The solution

was warmed to room temperature and left to stir overnight. The following morning the reaction mixture was quenched with 5% fluoroboric acid solution, turning the solution blue-purple, then extracted with dichloromethane (3 x 5 mL), dried over $NaSO_4$, filtered and evaporated to afford pure **3.8b** as a blue-purple solid (110 mg, 0.4 mmol, 85%). ^{1}H-NMR (400 MHz, Acetonitrile-*d*$_3$) δ 8.43 – 8.22 (m, 3H), 8.08 (d, *J* = 9.6 Hz, 1H), 7.82 – 7.77 (m, 2H), 7.70 (ddd, *J* = 8.3, 6.7, 1.4 Hz, 2H), 6.92 (d, *J* = 3.1 Hz, 1H), 3.15 (s, 6H), 2.97 (s, 3H). ^{13}C-NMR (101 MHz, Acetonitrile-*d*$_3$) δ 167.5, 150.5, 149.6, 135.5, 130.1, 129.1, 128.7, 127.1, 126.8, 120.3, 117.9, 100.6, 39.8, 20.6. HRMS (ESI) m/z: $[M+H]^+$ Calcd for $C_{18}H_{19}NO^+$ 265.1383; Found 264.1379.

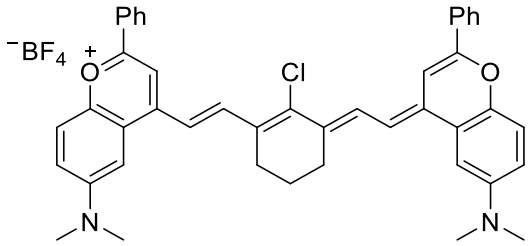

4-((E)-2-((E)-2-chloro-3-(2-((E)-6-(dimethylamino)-2-phenyl-4*H*-chromen-4-ylidene)ethylidene)cyclohex-1-en-1-yl)vinyl)-6-(dimethylamino)-2-phenylchromenylium tetrafluoroborate (6-Flav7, 3.4)

A Schlenk flask was charged with **3.8b** (70 mg, 0.2 mmol, 1 eq), 2,6-di-*tert*-butyl-4-methylpyridine (210 mg, 1.0 mmol, 5 eq), *N*-[(3-(anilinomethylene)-2-chloro-1-cyclohexen-1-yl)methylene]aniline hydrochloride **9** (20 mg, 0.06 mmol, 0.3 eq) and n-butanol:toluene (0.4 mL: 1.6 mL). The dark purple solution was freeze pump thawed 3x and then heated to 100 °C in an oil bath for 10 min. The reaction was monitored by UV-Vis for the disappearance of the 500 nm peak and formation of 1048 nm peak. Upon completion, the solution was cooled to r.t. Excess toluene (30 mL) was added at 0 °C and solid precipitate was collected via vacuum filtration and washed with toluene. The crude product was purified via silica gel chromatography twice with

dichloromethane: ethanol (99.5: 0.50 → 99.25: 0.75 → 99:) to afford pure **6-Flav7** as a dark blue-black solid (4 mg, 0.01 mmol, 9%). ^{1}H-NMR (400 MHz, Methylene Chloride-d_2) δ 8.54 (d, J = 13.7 Hz, 2H), 8.09 – 8.04 (m, 6H), 7.73 (s, 2H), 7.63 – 7.56 (m, 8H), 7.31 (dd, J = 9.3, 2.9 Hz, 2H), 7.08 (d, J = 13.8 Hz, 2H), 7.04 (d, J = 2.9 Hz, 2H), 3.14 (s, 12H), 2.90 (t, J = 6.2 Hz, 4H), 2.32 (t, J = 7.5 Hz, 2H). HRMS (ESI) m/z: $[M]^+$ Calcd for $C_{44}H_{40}ClN_2O_2^+$: 663.2278; Found 663.2265. Absorbance (dichloromethane, λ_{max}/nm) = 1048 nm. Emission (dichloromethane, λ_{max}/nm) = 1080 nm.

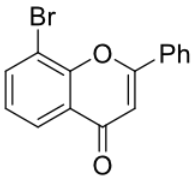

8-bromo-2-phenyl-4*H*-chromen-4-one (3.6c)

3'-bromo-2'-hydroxylacetophenone (300 mg, 1.0 mmol, 1 eq) was dissolved in THF (2.8 mL, anhydrous) to give a pale-yellow solution. LiHMDS (1M in THF, 5.6 mL, 5.6 mmol, 4 eq) was added slowly at -78 °C, turning the solution brown. The reaction was left to warm up to r.t. for two hours then cooled back down to -78 °C. Benzoyl chloride (0.10 mL, 1.4 mmol, 1 eq) was added and the reaction was left stirring at -78 °C for 1hr. The reaction was quenched with 2M HCl (5 mL), then extracted into dichloromethane (3 x 15 mL), dried over $NaSO_4$, filtered and evaporated to give a yellow solid. The solid was dissolved in a solution of conc. H_2SO_4 and AcOH (2.8 mL: 2.8 mL) and heated to reflux in an oil bath. After ten minutes, the reaction was cooled to r.t and water was added. Beige solid **8-bromo-2-phenyl-4*H*-chromen-4-one** (110 mg, 0.80 mmol, 60%) was collected via vacuum filtration. ^{1}H-NMR (300 MHz, Chloroform-*d*) δ 8.23 (dd, J = 8.0, 1.6 Hz, 1H), 8.16 (dd, J = 8.4, 1.4 Hz, 1H), 8.10 – 8.05 (m, 1H), 7.97 (dd, J = 7.8, 1.6 Hz, 1H), 7.69

– 7.57 (m, 2H), 7.52 (dd, *J* = 8.3, 6.7 Hz, 1H), 7.35 (t, *J* = 7.9 Hz, 1H), 6.94 (s, 1H). NMR matched literature.[39]

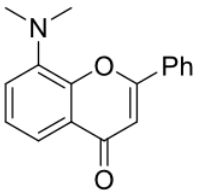

8-(dimethylamino)-2-phenyl-4*H*-chromen-4-one (3.7c)

8-bromo-2-phenyl-4*H*-chromen-4-one **6c** (200 mg, 0.7 mmol, 1 eq), SPhos-Pd-G3 (60 mg, 0.07 mmol, 0.1 eq), SPhos (30 mg, 0.07 mmol, 0.1 eq) and cesium carbonate (300 mg, 1.0 mmol, 1.5 eq) was put on a high vac and subsequently purged with nitrogen for three cycles. Toluene (4.0 mL, anhydrous) was added to solubilize all solids and then dimethylamine (1.0 mL, 2.0 mmol, 3 eq) was added. The solution was heated to 110 °C in a heating block, turning the solution a cloudy brown/orange color. After 24 hours of stirring, the solution was concentrated down to give an orange yellow solid. The crude product was purified via silica gel chromatography with hexanes: ethyl acetate (9:1 → 4:1) to afford pure **8-(dimethylamino)-2-phenyl-4*H*-chromen-4-one** as a yellow solid (75 mg, 0.30 mmol, 42%). ^{1}H NMR (400 MHz, Chloroform-*d*) δ 7.95 (dd, *J* = 6.7, 3.1 Hz, 2H), 7.79 (dd, *J* = 7.9, 1.6 Hz, 1H), 7.57 – 7.47 (m, 3H), 7.28 (t, J = 7.8 Hz, 1H), 7.21 (d, J = 1.6 Hz, 1H), 6.82 (s, 1H), 2.97 (s, 6H). ^{13}C NMR (101 MHz, Chloroform-*d*) δ 178.9, 162.7, 149.4, 142.9, 132.0, 131.5, 129.1, 126.2, 124.9, 121.5, 117.6, 107.3, 43.6. HRMS (ESI) m/z: $[M+H]^+$ Calcd for $C_{17}H_{16}NO_2^+$ 266.1103; Found 266.1094.

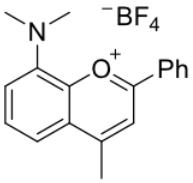

8-(dimethylamino)-4-methyl-2-phenylchromenylium (3.8c)

8-(dimethylamino)-2-phenyl-4*H*-chromen-4-one **3.7c** (50 mg, 0.2 mmol, 1 eq) was dissolved in THF (2.20 mL, anhydrous) and cooled to 0 °C. MeMgBr (1.0 M in THF, 0.3 mL, 0.4 mmol, 2 eq) was added dropwise over 30 min turning the solution from yellow to orange brown. The mixture was warmed to room temperature and left to stir overnight, at which point it was quenched with 5% fluoroboric acid solution, turning the solution purple, and extracted with dichloromethane (3 x 5 mL), dried over $NaSO_4$, filtered and evaporated to afford **3.8c** as a brown solid that was pushed forward crude due to instability in air. ^{1}H NMR (400 MHz, Acetonitrile-d_3) δ 8.81 – 8.71 (m, 1H), 8.53 (dd, J = 8.6, 1.3 Hz, 2H), 8.47 (dd, J = 20.1, 8.0 Hz, 2H), 8.11 (t, J = 8.2 Hz, 1H), 8.04 – 7.97 (m, 1H), 7.84 (dd, J = 8.6, 7.4 Hz, 2H), 3.48 (s, 6H), 3.19 (d, J = 0.8 Hz, 3H). HRMS (ESI) m/z: $[M+H]^+$ Calcd for $C_{18}H_{19}NO_2^+$ 265.1383; Found 265.1379.

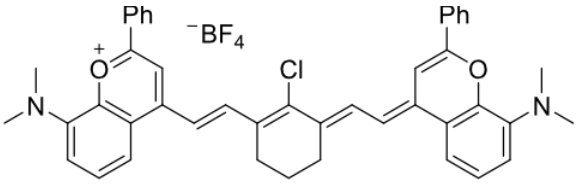

2-((E)-2-chloro-3-(2-((E)-8-(dimethylamino)-2-phenyl-4*H*-chromen-4-ylidene)ethylidene)cyclohex-1-en-1-yl)vinyl)-8-(dimethylamino)-2-phenylchromenylium tetrafluoroborate (8-Flav7, 3.5)

A Schlenk flask was charged with **3.8c** (30 mg, 0.10 mmol, 1 eq), 2,6-di-*tert*-butyl-4-methylpyridine (100 mg, 0.5 mmol, 3 eq), N-[(3-(anilinomethylene)-2-chloro-1-cyclohexen-1-yl)methylene]aniline hydrochloride **9** (7 mg, 0.02 mmol, 0.3 eq) and acetic anhydride (0.50 mL). The magenta solution was freeze pump thawed 3x and then heated to 100 °C in an oil bath for 10 min. The reaction was monitored by UV-Vis for the disappearance of 500 peak and formation of 990 nm peak. Upon completion of the reaction by UV-Vis, the solution was cooled to r.t. Excess toluene (10 mL) was added and solid precipitate was collected via vacuum

filtration and washed with toluene. The crude product was unable to be purified and fully characterized due to instability of the compound. HRMS (ESI) m/z: $[M]^+$ Calcd for $C_{44}H_{40}ClN_2O_2^+$: 663.2278; Found 663.2269. Absorbance (dichloromethane, λ_{max}/nm) = 990 nm. Emission (dichloromethane, λ_{max}/nm) = 1015 nm.

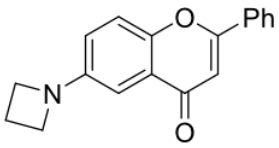

6-(azetidin-1-yl)-2-phenyl-4*H*-chromen-4-one (3.14)

Flavone **3.6b** (25 mg, 0.10 mmol, 1 eq), RuPhos-Pd-G3 (60 mg, 0.01 mmol, 0.1 eq), RuPhos (3 mg, 0.01 mmol, 0.1 eq), cesium carbonate (30 mg, 0.10 mmol, 1.5 eq) and azetidine hydrochloride (10 mg, 0.1 mmol, 1.5 eq) was put on a high vac and subsequently purged with nitrogen for three cycles. Toluene (0.30 mL, anhydrous) was added to solubilize all solids. The solution was heated to 110 °C in a heating block, turning the solution a deep brown color. After 24 hours of stirring, the solution was concentrated down to give a dark black solid. The crude product was purified via silica gel chromatography with hexanes: ethyl acetate (9:1 → 4:1) to afford pure **6-(azetidin-1-yl)-2-phenyl-4*H*-chromen-4-one (3.15)** as a yellow solid. (10 mg, 0.04 mmol, 52%).^{1}H NMR (400 MHz, Chloroform-*d*) δ 7.93 – 7.87 (m, 2H), 7.50 (dd, *J* = 5.2, 1.8 Hz, 3H), 7.44 (d, *J* = 8.9 Hz, 1H), 7.10 (d, *J* = 2.9 Hz, 1H), 6.83 (dd, *J* = 8.9, 2.9 Hz, 1H), 6.78 (s, 1H), 3.95 (t, *J* = 7.2 Hz, 4H), 2.58 – 2.24 (m, 2H). ^{13}C NMR (101 MHz, Chloroform-*d*) δ 178.7, 162.8, 149.6, 149.4, 132.2, 131.3, 128.9, 126.2, 124.5, 118.7, 118.5, 106.6, 104.1, 52.7, 29.7, 16.9. HRMS (ESI) m/z: $[M+H]^+$ Calcd for $C_{18}H_{16}NO_2^+$ 278.1103; Found 278.1090

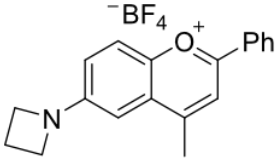

6-(azetidin-1-yl)-4-methyl-2-phenylchromenylium (3.15)

6-(azetidin-1-yl)-2-phenyl-4*H*-chromen-4-one **3.15** (30 mg, 0.08 mmol, 1 eq) was dissolved in THF (1.0 mL, anhydrous) and cooled to 0 °C. MeMgBr (1.4 M in THF/toluene, 0.2 mL, 0.3 mmol, 2 eq) was added dropwise over 30 min turning the solution from yellow to orange brown. The reaction was warmed to room temperature and left to stir overnight. The reaction was quenched with 5% fluoroboric acid solution, turning the solution blue-purple, then extracted with dichloromethane (3 x 5 mL), dried over $NaSO_4$, filtered and evaporated to afford pure **3.16** as a blue-purple solid (20 mg, 0.06 mmol, 70%).^{1}H NMR (400 MHz, Acetonitrile-d_3) δ 8.41 – 8.30 (m, 4H), 8.09 (d, J = 9.3 Hz, 1H), 7.81 (d, J = 7.4 Hz, 1H), 7.72 (t, J = 7.7 Hz, 2H), 7.44 (dd, J = 9.3, 2.8 Hz, 1H), 6.74 (d, J = 2.8 Hz, 1H), 4.20 – 4.02 (m, 4H), 2.96 (d, J = 0.8 Hz, 3H), 2.48 (p, J = 7.4 Hz, 2H). ^{13}C-NMR (101 MHz, Acetonitrile-d_3) δ 167.8, 167.3, 151.3, 150.0, 135.5, 130.1, 129.2, 128.7, 126.9, 125.7, 120.5, 118.1, 99.3, 51.9, 20.6, 16.0. HRMS (ESI) m/z: $[M+H]^+$ Calcd for $C_{19}H_{19}NO^+$ 277.1383; Found 277.1381

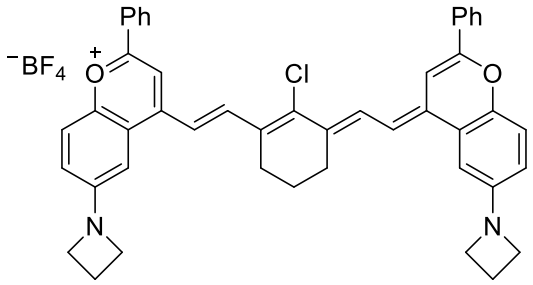

6-(azetidin-1-yl)-4-((E)-2-((E)-3-(2-((E)-6-(azetidin-1-yl)-2-phenyl-4*H*-chromen-4-ylidene)ethylidene)-2-chlorocyclohex-1-en-1-yl)vinyl)-2-phenylchromenylium tetrafluoroborate (Azet-6-Flav7, 3.16)

A Schlenk flask was charged with **3.15** (80 mg, 0.2 mmol, 1 eq), 2,6-di-*tert*-butyl-4-methylpyridine (210 mg, 1.0 mmol, 5 eq), *N*-[(3-(anilinomethylene)-2-chloro-1-cyclohexen-1-

yl)methylene]aniline hydrochloride **3.9** (20 mg, 0.07 mmol, 0.3 eq) and n-butanol:toluene (0.4 mL: 1.6 mL). The dark purple solution was freeze pump thawed 3x and then heated to 100 °C in an oil bath for 10 min. The reaction was monitored by UV-Vis for the disappearance of the 500 nm peak and formation of 1039 nm peak. Upon completion, the solution was cooled to r.t. Excess toluene (30 mL) was added at 0 °C and solid precipitate was collected via vacuum filtration and washed with toluene. The crude product was purified via silica gel chromatography twice with dichloromethane: ethanol (99.5: 0.50 → 99.25: 0.75 → 99:1) to afford pure **Azet-6-Flav7** as a dark green-black solid (3 mg, 0.004 mmol, 6%).^{1}H-NMR (400 MHz, Methylene Chloride-d_2) δ 8.49 (d, J = 14.0 Hz, 2H), 8.08 – 8.01 (m, 6H), 7.69 (s, 2H), 7.51 (d, J = 8.8 Hz, 4H), 7.22 – 7.15 (m, 4H), 7.11 (d, J = 13.5 Hz, 4H), 3.76 (t, J = 6.0 Hz, 8H), 2.89 (s, 4H), 2.32 (t, J = 7.5 Hz, 4H), 1.82 (d, J = 6.6 Hz, 2H). HRMS (ESI) m/z: $[M]^+$ Calcd for $C_{46}H_{40}ClN_2O_2^+$: 687.2773; Found 687.2765. Absorbance (dichloromethane, λ_{max}/nm) = 1039 nm. Emission (dichloromethane, λ_{max}/nm) = 1080 nm.

3.5.3 Computational Procedures (Performed by Jingbai, Li and Fatemah Mukadum)

The conformations of **Flav7** dyes (**3.1**, **3.3–3.5)** were searched using the OPLS3e force field potential implemented in the Schrödinger release 2019-2 program suite.[40] The conformational search used Mixed torsional/Low-mode sampling method and removed the redundant conformers based on the maximum atom deviation of 1 Å. The probability of a torsion rotation and molecule translation was set to 0.5 and the distance range of the low-mode move was 3.0–12.0. For each rotatable bond, the conformers were further searched in 100 steps. The 10 lowest conformers were found after 10,000 iterations within an energy window of 47.8 kcal mol^{-1} (200 kJ mol^{-1}). The lowest 10 conformers were optimized to the ground-state minimum with M06-2X/6-31+G(d,p). The polarizable continuum model (PCM) was utilized to include the solvent effect of

dichloromethane. All stationary points were confirmed by the computations of the Hessian matrix that all vibrational frequencies are positive and real. The conformers were sorted according to the calculated Gibbs free energy at 298.15 K. The geometry optimization and thermochemistry calculations were done by Gaussian16. B01.[41] The global minimum geometries were used for excited-state calculations. The vertical excitation energies were computed using CIS(D)/cc-pVDZ. In order to speed up the calculations, the resolution of identity (RI) approximation RIJCOSX (RI for Coulomb integral and COSX numerical integration for HF-exchange) was used together with the cc-pVDZ/C auxiliary basis sets. The CIS(D) single point calculations were performed by ORCA 4.2.1 program package.[42]

Cartesian coordinates for optimized structures and calculated thermodynamics energies with the first 10 vibrational frequencies.

IR-27-A

C	0.000004	-4.008458	0.965780
C	-1.251704	-3.434080	0.315814
C	1.251658	-3.434065	0.315736
H	-2.135549	-3.793980	0.848997
H	1.335146	-3.792390	-0.719546
C	-1.247269	-1.918994	0.325379
C	1.247191	-1.918989	0.325283
C	-0.000012	-1.261953	0.372243
H	0.000027	-3.759949	2.033555
Cl	-0.000032	0.491933	0.447708
H	-1.335248	-3.792398	-0.719463
H	0.000010	-5.098310	0.882578
H	2.135550	-3.793946	0.848858
C	-2.446041	-1.205811	0.238235
H	-2.375268	-0.125124	0.265503
C	-3.712415	-1.777798	0.092814
H	-3.782504	-2.855941	0.038720
C	2.446005	-1.205806	0.238061
H	2.375222	-0.125119	0.265273
C	3.712311	-1.777823	0.092587
H	3.782374	-2.855960	0.038381
C	-4.900277	-1.042328	-0.003081
C	-4.941615	0.383627	0.033589
C	-6.111854	1.077424	-0.053505
O	-7.292412	0.452487	-0.195704

C	-7.347705	-0.907391	-0.257213
C	-6.194003	-1.701396	-0.161117
C	-6.374288	-3.099777	-0.229791
C	-7.631182	-3.651855	-0.384792
C	-8.762372	-2.824142	-0.477737
C	-8.624576	-1.449954	-0.413917
H	-4.030291	0.959355	0.107276
H	-9.474833	-0.780466	-0.480222
H	-9.747664	-3.260922	-0.599046
H	-7.743274	-4.729096	-0.434341
H	-5.518336	-3.759665	-0.160795
C	4.900242	-1.042364	-0.003282
C	4.941603	0.383568	0.033722
C	6.111864	1.077359	-0.053365
O	7.292361	0.452378	-0.195823
C	7.347621	-0.907460	-0.257585
C	6.193890	-1.701458	-0.161562
C	6.374117	-3.099836	-0.230553
C	7.630976	-3.651922	-0.385762
C	8.762194	-2.824226	-0.478600
C	8.624458	-1.450053	-0.414484
H	4.030294	0.959274	0.107696
H	9.474731	-0.780574	-0.480706
H	9.747465	-3.261008	-0.600065
H	7.743009	-4.729158	-0.435556
H	5.518149	-3.759711	-0.161655
C	-6.240143	2.542485	-0.028082
C	-7.369246	3.153964	-0.590886
C	-5.241380	3.336516	0.553148
C	-7.485279	4.540615	-0.587651
C	-5.365226	4.721552	0.556060
C	-6.484604	5.327026	-0.016984
H	-8.145399	2.543131	-1.038478
H	-4.380476	2.876943	1.027607
H	-8.357722	5.007227	-1.032752
H	-4.591845	5.328314	1.014911
H	-6.578764	6.408056	-0.013048
C	6.240255	2.542395	-0.027595
C	7.369425	3.153928	-0.590216
C	5.241530	3.336359	0.553796
C	7.485556	4.540566	-0.586644
C	5.365485	4.721387	0.557053
C	6.484923	5.326914	-0.015811
H	8.145544	2.543153	-1.037943
H	4.380572	2.876752	1.028115
H	8.358043	5.007220	-1.031612
H	4.592133	5.328089	1.016032
H	6.579167	6.407935	-0.011609

	Energies (Hartree)
E(M06-2X)	-2152.12197769
E(M06-2X)+ZPE	-2151.53294900
E(M06-2X)+U	-2151.49791000
E(M06-2X)+H	-2151.49696500
E(M06-2X)+G	-2151.60589200
Number of imaginary frequencies	0
Top 10 frequencies (cm^{-1})	
1	8.0881
2	12.6565
3	13.1359
4	21.7115
5	27.6595
6	33.7767
7	35.2910
8	47.4242
9	56.4398
10	57.0378

IR-27-B

C	-0.000489	-3.976896	1.039103
C	-1.255931	-3.420309	0.381106
C	1.247446	-3.422313	0.364869
H	-2.136316	-3.759062	0.933680
H	1.320730	-3.805538	-0.662269
C	-1.248387	-1.905641	0.339030
C	1.246047	-1.907449	0.338709
C	-0.001129	-1.248414	0.365482
H	-0.002043	-5.068686	0.987035
Cl	-0.000218	0.506874	0.388180
H	-1.349537	-3.812959	-0.640790
H	0.007059	-3.698196	2.099358
H	2.134657	-3.771955	0.899062
C	-2.447120	-1.195236	0.226359
H	-2.376757	-0.114138	0.213932
C	-3.712293	-1.772663	0.095401
H	-3.780465	-2.851860	0.064607
C	2.445850	-1.197902	0.241743
H	2.376708	-0.116744	0.248522
C	3.712005	-1.774290	0.109148
H	3.779678	-2.853046	0.065316
C	-4.900428	-1.040952	-0.026163
C	-4.947702	0.384188	0.024401
C	-6.115156	1.075833	-0.108421
O	-7.290649	0.447113	-0.273456
C	-7.344529	-0.913649	-0.309419
C	-6.189804	-1.704255	-0.198855

C	-6.366135	-3.103593	-0.258993
C	-7.620650	-3.659661	-0.418551
C	-8.753182	-2.835294	-0.524764
C	-8.619010	-1.460320	-0.471490
H	-4.049380	0.957910	0.201222
H	-9.469999	-0.793343	-0.552129
H	-9.736522	-3.275317	-0.650129
H	-7.729851	-4.737451	-0.462223
H	-5.509032	-3.760913	-0.180108
C	4.901780	-1.042734	0.011406
C	4.947840	0.383179	0.050813
C	6.120252	1.073299	-0.034042
O	7.298897	0.444832	-0.178045
C	7.349604	-0.915088	-0.243274
C	6.193403	-1.705615	-0.148744
C	6.368906	-3.104294	-0.223062
C	7.623878	-3.660087	-0.380591
C	8.757802	-2.835870	-0.470876
C	8.624566	-1.461446	-0.402385
H	4.038543	0.961425	0.129419
H	9.477009	-0.794574	-0.467030
H	9.741582	-3.275481	-0.594230
H	7.732228	-4.737494	-0.434660
H	5.510620	-3.761535	-0.157486
C	-6.251141	2.539889	-0.069825
C	-7.486795	3.117726	0.253972
C	-5.155176	3.366561	-0.355382
C	-7.616032	4.502076	0.308644
C	-5.291877	4.749328	-0.301760
C	-6.520469	5.320350	0.033365
H	-8.337661	2.481880	0.472097
H	-4.202696	2.936111	-0.646340
H	-8.573247	4.941969	0.567855
H	-4.441053	5.381868	-0.531659
H	-6.624407	6.399718	0.073808
C	6.253809	2.537829	-0.002305
C	7.385820	3.147580	-0.561115
C	5.257564	3.333084	0.581589
C	7.507271	4.533747	-0.551249
C	5.386820	4.717601	0.591162
C	6.509151	5.321400	0.022153
H	8.160122	2.535828	-1.010648
H	4.394397	2.874767	1.053124
H	8.382045	4.999011	-0.993179
H	4.615393	5.325174	1.052232
H	6.607635	6.402012	0.031449

	Energies (Hartree)
E(M06-2X)	-2152.12198105
E(M06-2X)+ZPE	-2151.53292500
E(M06-2X)+U	-2151.49787700
E(M06-2X)+H	-2151.49693300
E(M06-2X)+G	-2151.60623400
Number of imaginary frequencies	0
Top 10 frequencies (cm^{-1})	
1	7.2853
2	11.4128
3	13.0340
4	20.4640
5	26.9581
6	32.0415
7	36.5838
8	44.9773
9	55.5552
10	56.2697

IR-27-C (Global Minimum)

C	0.000084	-3.951233	1.100492
C	-1.251816	-3.409879	0.423091
C	1.251625	-3.409961	0.422350
H	-1.335619	-3.819774	-0.592911
H	1.334652	-3.819640	-0.593806
C	-1.247206	-1.896125	0.356285
C	1.247159	-1.896196	0.355908
C	0.000006	-1.237627	0.367704
H	0.000028	-5.043887	1.071473
Cl	0.000037	0.517741	0.350659
H	-2.135534	-3.742049	0.974145
H	0.000420	-3.650284	2.154665
H	2.135654	-3.742410	0.972726
C	-2.446814	-1.188980	0.236859
H	-2.378245	-0.107972	0.211418
C	-3.711582	-1.769760	0.113365
H	-3.777629	-2.849273	0.089211
C	2.446801	-1.189083	0.236480
H	2.378259	-0.108065	0.211364
C	3.711520	-1.769851	0.112639
H	3.777556	-2.849355	0.088141
C	-4.901038	-1.041232	-0.010722
C	-4.952143	0.383908	0.041567
C	-6.121392	1.072553	-0.089978
O	-7.295236	0.440989	-0.256973
C	-7.345238	-0.919883	-0.296488
C	-6.188529	-1.707609	-0.186489

C	-6.360768	-3.107188	-0.251793
C	-7.613523	-3.666341	-0.414667
C	-8.748256	-2.844869	-0.519382
C	-8.617969	-1.469676	-0.461725
H	-4.055717	0.959532	0.221855
H	-9.470721	-0.804845	-0.541489
H	-9.730207	-3.287236	-0.647385
H	-7.719532	-4.744276	-0.462474
H	-5.501740	-3.762283	-0.175141
C	4.900991	-1.041296	-0.011309
C	4.952122	0.383812	0.041586
C	6.121398	1.072493	-0.089580
O	7.295222	0.440945	-0.256796
C	7.345172	-0.919895	-0.297077
C	6.188430	-1.707638	-0.187516
C	6.360594	-3.107189	-0.253668
C	7.613321	-3.666302	-0.416867
C	8.748097	-2.844817	-0.521075
C	8.617880	-1.469655	-0.462622
H	4.055694	0.959353	0.222119
H	9.470669	-0.804825	-0.541996
H	9.730027	-3.287158	-0.649329
H	7.719285	-4.744211	-0.465332
H	5.501526	-3.762284	-0.177460
C	-6.261690	2.536101	-0.046421
C	-7.499184	3.109173	0.278785
C	-5.167922	3.367036	-0.327971
C	-7.632415	4.492934	0.338821
C	-5.308570	4.749188	-0.268922
C	-6.538999	5.315412	0.067612
H	-8.348363	2.470065	0.493930
H	-4.213983	2.940411	-0.619808
H	-8.591050	4.929070	0.599139
H	-4.459350	5.385061	-0.495558
H	-6.646002	6.394309	0.112376
C	6.261777	2.536008	-0.045336
C	7.499338	3.108864	0.280001
C	5.168023	3.367143	-0.326367
C	7.632653	4.492588	0.340672
C	5.308755	4.749258	-0.266682
C	6.539254	5.315257	0.069976
H	8.348509	2.469617	0.494759
H	4.214019	2.940730	-0.618297
H	8.591343	4.928545	0.601084
H	4.459542	5.385282	-0.492917
H	6.646324	6.394126	0.115235

	Energies (Hartree)
E(M06-2X)	-2152.12198024

E(M06-2X)+ZPE	-2151.53288300
E(M06-2X)+U	-2151.49784300
E(M06-2X)+H	-2151.49689900
E(M06-2X)+G	-2151.60632700
Number of imaginary frequencies	0
Top 10 frequencies (cm^{-1})	
1	6.3769
2	10.4480
3	14.1495
4	21.5123
5	25.2992
6	32.7785
7	36.6316
8	43.4580
9	55.3467
10	55.6913

5-Flav7-A (Global Minimum)

C	-1.245789	-1.342661	0.212040
C	-1.257151	-2.831848	-0.069522
C	-0.001401	-3.518219	0.450332
C	1.244942	-2.833884	-0.094914
C	1.249775	-1.348334	0.205592
C	-0.002291	-0.709688	0.372666
Cl	0.003202	1.002599	0.768876
C	-2.451556	-0.624373	0.257589
C	2.448473	-0.637965	0.257440
C	3.712082	-1.195632	0.021671
C	-3.706066	-1.183202	0.035632
C	4.909230	-0.470954	0.008244
C	-4.913124	-0.457481	0.013478
C	-4.926168	0.968053	0.108505
C	-6.044515	1.697354	-0.151708
O	-7.177405	1.100373	-0.552279
C	-7.275813	-0.258068	-0.596236
C	-6.208579	-1.094570	-0.203103
C	6.207916	-1.084527	-0.283102
C	7.254954	-0.218922	-0.661675
O	7.148960	1.136729	-0.553117
C	6.027451	1.700045	-0.068611
C	4.927190	0.951261	0.195215
C	6.497494	-2.492382	-0.316468
C	-6.483288	-2.507114	-0.155595
C	6.132421	3.161530	0.070355
C	5.259565	3.861175	0.915438
C	5.356811	5.243640	1.030439
C	6.325944	5.941571	0.307882
C	7.202699	5.248892	-0.526563

C	7.111989	3.864876	-0.643983
C	-6.151395	3.162952	-0.097578
C	-5.241746	3.914459	0.659823
C	-5.342166	5.300856	0.695847
C	-6.350082	5.949951	-0.019028
C	-7.262773	5.205725	-0.766317
C	-7.169474	3.817807	-0.804493
H	-1.356767	-2.998005	-1.151066
H	-2.138463	-3.279446	0.399145
H	-0.005599	-4.573874	0.166358
H	0.009758	-3.472096	1.545830
H	2.135166	-3.294131	0.342192
H	1.310965	-2.986311	-1.181138
H	2.379966	0.419403	0.482227
H	-3.781774	-2.243779	-0.156945
H	-4.015875	1.510504	0.317664
H	4.029471	1.473560	0.491857
H	4.519631	3.327411	1.503075
H	4.681790	5.775640	1.692512
H	6.400434	7.020210	0.400110
H	7.959218	5.786559	-1.088526
H	7.792208	3.327703	-1.295525
H	-4.470502	3.419786	1.241293
H	-4.638884	5.874651	1.289933
H	-6.426365	7.031965	0.011270
H	-8.048688	5.706351	-1.321936
H	-7.876929	3.239866	-1.388612
C	-8.670125	-2.101313	-1.151214
H	-9.602248	-2.504110	-1.533275
C	8.661041	-2.017587	-1.331773
H	9.589487	-2.390224	-1.751539
C	8.466274	-0.656410	-1.192647
H	9.212050	0.074668	-1.481183
C	-8.492903	-0.732018	-1.077776
H	-9.255051	-0.024770	-1.381967
C	7.697804	-2.925073	-0.884063
H	7.913836	-3.984048	-0.939547
C	-7.688093	-2.977654	-0.682970
H	-7.894910	-4.039858	-0.683570
N	5.585389	-3.412993	0.214024
N	-5.557041	-3.387774	0.405502
C	5.745057	-4.810261	-0.156494
H	4.848290	-5.348628	0.159558
H	5.841983	-4.904596	-1.239661
H	6.614376	-5.282733	0.327184
C	5.288704	-3.270238	1.641451
H	6.053415	-3.780202	2.245408
H	4.314130	-3.717194	1.859620
H	5.259190	-2.220859	1.930905
C	-5.189117	-3.154551	1.804206

H	-5.884557	-3.681515	2.472794
H	-4.176102	-3.526172	1.987619
H	-5.215917	-2.092716	2.043654
C	-5.707719	-4.806078	0.121147
H	-5.828621	-4.965252	-0.951882
H	-4.796858	-5.314405	0.446256
H	-6.559482	-5.257121	0.653178
H	-2.380023	0.434315	0.475955
H	3.784047	-2.251027	-0.198574

	Energies (Hartree)
E(M06-2X)	-2419.94066256
E(M06-2X)+ZPE	-2419.20426100
E(M06-2X)+U	-2419.16115300
E(M06-2X)+H	-2419.16020900
E(M06-2X)+G	-2419.28635900
Number of imaginary frequencies	0
Top 10 frequencies (cm^{-1})	
1	6.7374
2	8.7196
3	14.1953
4	20.4989
5	25.1626
6	27.5456
7	31.6595
8	36.5387
9	39.0069
10	47.7465

5-Flav7-B

C	1.246385	-1.353931	0.176080
C	1.224052	-2.833623	-0.151198
C	-0.000070	-3.522207	0.437775
C	-1.274911	-2.836907	-0.034333
C	-1.249188	-1.344576	0.227941
C	-0.014415	-0.713485	0.366998
Cl	0.003311	0.999328	0.761796
C	2.438477	-0.651435	0.226402
C	-2.464079	-0.620053	0.274896
C	-3.711664	-1.178335	0.076767
C	3.706478	-1.208334	-0.047705
C	-4.924427	-0.441968	0.039704
C	4.896556	-0.491288	-0.040754
C	4.935334	0.910331	0.294178
C	6.005136	1.687882	0.008705
O	7.097884	1.175601	-0.595627
C	7.216979	-0.172975	-0.777498
C	6.191139	-1.071940	-0.425657

C	-6.221937	-1.086515	-0.068655
C	-7.303775	-0.281536	-0.493372
O	-7.198781	1.074363	-0.557389
C	-6.049303	1.695890	-0.269097
C	-4.919100	0.980126	-0.002310
C	-6.492928	-2.491106	0.109326
C	6.489934	-2.469425	-0.561708
C	-6.144862	3.159920	-0.340823
C	-5.187945	3.963827	0.295007
C	-5.278282	5.348898	0.215707
C	-6.322165	5.943510	-0.494765
C	-7.280899	5.147498	-1.121790
C	-7.198414	3.760924	-1.044082
C	6.130686	3.129470	0.285181
C	4.992510	3.925639	0.475062
C	5.125722	5.280772	0.758409
C	6.393181	5.858330	0.848880
C	7.528237	5.073511	0.648613
C	7.400816	3.716567	0.364335
H	2.131436	-3.305394	0.234336
H	1.235776	-2.965689	-1.242145
H	0.051281	-3.478922	1.532223
H	-0.013857	-4.577099	0.151272
H	-2.135599	-3.275926	0.479572
H	-1.425232	-3.015832	-1.107876
H	-2.389189	0.441122	0.481878
H	3.766917	-2.250186	-0.327850
H	4.089698	1.376349	0.779550
H	-3.992397	1.526835	0.092574
H	-4.387255	3.513313	0.872225
H	-4.538703	5.964681	0.716172
H	-6.390416	7.024775	-0.554947
H	-8.094032	5.606791	-1.673722
H	-7.941239	3.142301	-1.535211
H	4.000674	3.496128	0.378907
H	4.238355	5.889311	0.897978
H	6.494099	6.916393	1.067784
H	8.516186	5.517258	0.714945
H	8.284097	3.106098	0.212511
C	8.623388	-1.911474	-1.597105
H	9.543382	-2.246152	-2.064803
C	-8.703891	-2.163523	-0.860499
H	-9.645262	-2.595918	-1.182854
C	-8.532604	-0.790808	-0.898413
H	-9.307474	-0.111906	-1.232896
C	8.416939	-0.564122	-1.368818
H	9.145341	0.192648	-1.635192
C	-7.708967	-3.001926	-0.352984
H	-7.915635	-4.060307	-0.263251
C	7.679989	-2.854818	-1.183009

H	7.901008	-3.906281	-1.313373
N	-5.558455	-3.316311	0.723816
N	5.592601	-3.432221	-0.074780
C	-5.099894	-2.945202	2.064606
H	-4.053465	-3.236798	2.198316
H	-5.708349	-3.456520	2.822786
H	-5.182957	-1.871157	2.222347
C	-5.711170	-4.755608	0.580372
H	-6.544501	-5.153050	1.179369
H	-5.863903	-5.016905	-0.468222
H	-4.788441	-5.228675	0.924112
C	5.750240	-4.797706	-0.549061
H	5.818705	-4.813180	-1.638473
H	6.634790	-5.298451	-0.124422
H	4.865386	-5.364614	-0.249174
C	5.349626	-3.396764	1.369099
H	4.391121	-3.875983	1.590752
H	6.144744	-3.933596	1.907572
H	5.313265	-2.370894	1.732861
H	2.379957	0.403206	0.467749
H	-3.797945	-2.245387	-0.075495

	Energies (Hartree)
E(M06-2X)	-2419.94066842
E(M06-2X)+ZPE	-2419.20399400
E(M06-2X)+U	-2419.16099000
E(M06-2X)+H	-2419.16004600
E(M06-2X)+G	-2419.28555300
Number of imaginary frequencies	0
Top 10 frequencies (cm^{-1})	
1	5.3820
2	12.7412
3	14.7075
4	21.9387
5	24.4691
6	29.2008
7	31.2763
8	36.4881
9	39.1389
10	47.8937

5-Flav7-C

C	1.259006	-1.241783	-0.455679
C	1.249575	-2.750470	-0.599446
C	0.006097	-3.238406	-1.331729
C	-1.252935	-2.749888	-0.628394
C	-1.236676	-1.250424	-0.409640
C	-0.012410	-0.591256	-0.386051

Cl	-0.012438	1.158201	-0.215809
C	2.445163	-0.541125	-0.342380
C	-2.459539	-0.563614	-0.201289
C	-3.686813	-1.182879	-0.091592
C	3.727505	-1.136697	-0.299675
C	-4.918139	-0.493549	0.083589
C	4.912914	-0.429670	-0.157576
C	4.932156	1.012186	-0.101859
C	6.008722	1.700912	0.339661
O	7.130437	1.062716	0.737211
C	7.264238	-0.282586	0.538332
C	6.227567	-1.071365	0.002291
C	-6.164550	-1.181959	0.362793
C	-7.359634	-0.459835	0.136828
O	-7.346019	0.882020	-0.091480
C	-6.197509	1.562413	-0.170568
C	-4.999070	0.910950	-0.117974
C	-6.307559	-2.565313	0.743682
C	6.539782	-2.448332	-0.254341
C	-6.386069	3.003934	-0.377619
C	-5.344100	3.900667	-0.100955
C	-5.524792	5.263366	-0.308655
C	-6.743568	5.742995	-0.791096
C	-7.785491	4.855059	-1.059646
C	-7.612854	3.490530	-0.851225
C	6.114690	3.165747	0.457633
C	7.376822	3.774296	0.483407
C	7.484396	5.159720	0.570785
C	6.337602	5.949828	0.640824
C	5.078506	5.347434	0.628498
C	4.965137	3.963960	0.541022
H	1.298860	-3.212043	0.396801
H	2.143495	-3.069217	-1.141252
H	0.004538	-4.330217	-1.386897
H	0.017776	-2.857015	-2.359608
H	-2.130921	-3.012706	-1.225326
H	-1.363682	-3.258257	0.340135
H	-2.398921	0.510836	-0.070794
H	3.800517	-2.214317	-0.328790
H	4.066814	1.579052	-0.414086
H	-4.107906	1.484913	-0.325769
H	-4.401514	3.541748	0.299071
H	-4.717106	5.952262	-0.085885
H	-6.881825	6.807083	-0.952547
H	-8.734019	5.225314	-1.433821
H	-8.421083	2.799865	-1.064317
H	8.269069	3.160727	0.425081
H	8.466065	5.621883	0.582676
H	6.423234	7.029298	0.711591
H	4.182694	5.955641	0.698391

H	3.980992	3.506936	0.561895
C	8.720899	-2.150777	0.789724
H	9.665144	-2.581879	1.105472
C	-8.702205	-2.408696	0.321521
H	-9.668884	-2.900066	0.288104
C	-8.620286	-1.044605	0.102083
H	-9.488839	-0.429399	-0.098615
C	8.494436	-0.796508	0.945299
H	9.230197	-0.125804	1.373241
C	-7.570162	-3.157457	0.649643
H	-7.691417	-4.204253	0.895385
C	7.762296	-2.964290	0.181257
H	7.994165	-4.008007	0.013049
N	-5.209465	-3.291661	1.185973
N	5.622129	-3.264205	-0.937204
C	-4.455255	-2.767244	2.327073
H	-3.393348	-3.008162	2.217817
H	-4.826790	-3.217066	3.257730
H	-4.559851	-1.686010	2.400928
C	-5.312137	-4.742162	1.222163
H	-4.308351	-5.148145	1.366734
H	-5.704405	-5.117345	0.275328
H	-5.947772	-5.098914	2.046469
C	5.327450	-2.856957	-2.312951
H	4.378047	-3.300302	-2.628263
H	5.243189	-1.773622	-2.388594
H	6.119636	-3.198088	-2.996174
C	5.809494	-4.703392	-0.844388
H	4.914520	-5.188161	-1.242103
H	5.930168	-5.001311	0.198895
H	6.675375	-5.061167	-1.423914
H	2.375514	0.536139	-0.250687
H	-3.742127	-2.263009	-0.116134

	Energies (Hartree)
E(M06-2X)	-2419.94075785
E(M06-2X)+ZPE	-2419.20392300
E(M06-2X)+U	-2419.16096900
E(M06-2X)+H	-2419.16002500
E(M06-2X)+G	-2419.28526600
Number of imaginary frequencies	0
Top 10 frequencies (cm^{-1})	
1	6.8042
2	11.3263
3	14.1169
4	17.2364
5	25.7601
6	30.1513
7	36.8751

8	38.6557
9	41.3806
10	48.4327

5-Flav7-D

C	-1.253209	-1.266180	-0.376234
C	-1.259602	-2.781592	-0.405764
C	0.007811	-3.341248	-1.037803
C	1.241751	-2.794594	-0.332394
C	1.240724	-1.279654	-0.283591
C	0.004241	-0.616858	-0.348196
Cl	0.012931	1.140449	-0.355182
C	-2.449651	-0.551930	-0.327366
C	2.447906	-0.578014	-0.134324
C	3.691048	-1.180587	0.032114
C	-3.720578	-1.139336	-0.273625
C	4.908948	-0.480533	0.142178
C	-4.921197	-0.428087	-0.171958
C	-4.940409	1.002673	-0.069885
C	-6.056371	1.684878	0.290594
O	-7.194101	1.037376	0.601473
C	-7.296279	-0.311805	0.426154
C	-6.227632	-1.084288	-0.073998
C	6.189523	-1.150847	0.347038
C	7.354995	-0.407328	0.058549
O	7.312436	0.934518	-0.174772
C	6.147160	1.599489	-0.167990
C	4.967058	0.935774	-0.038489
C	6.382854	-2.529880	0.713543
C	-6.508444	-2.468190	-0.344509
C	6.306593	3.047295	-0.370299
C	5.280053	3.932440	-0.011749
C	5.433548	5.298972	-0.217662
C	6.610969	5.795866	-0.778931
C	7.638449	4.919957	-1.128638
C	7.492125	3.551429	-0.922996
C	-6.164955	3.144563	0.445357
C	-5.259463	3.998499	-0.200114
C	-5.359914	5.375821	-0.036506
C	-6.364647	5.915639	0.768090
C	-7.273814	5.070760	1.404110
C	-7.179933	3.691391	1.242369
H	-2.132245	-3.129123	-0.965512
H	-1.367596	-3.165642	0.618098
H	0.040834	-3.058045	-2.096497

H	0.001312	-4.433420	-0.990524
H	2.140982	-3.137321	-0.851289
H	1.293940	-3.191534	0.691355
H	2.382946	0.503258	-0.114974
H	-3.796962	-2.217044	-0.278211
H	-4.034220	1.571860	-0.216504
H	4.058883	1.509229	-0.152089
H	4.370714	3.561295	0.449447
H	4.637236	5.977724	0.068681
H	6.728296	6.862847	-0.937998
H	8.555865	5.302178	-1.563672
H	8.289773	2.870661	-1.198590
H	-4.490714	3.593116	-0.849990
H	-4.659135	6.029201	-0.545467
H	-6.441376	6.990796	0.893360
H	-8.058053	5.485590	2.028653
H	-7.885385	3.035192	1.739889
C	-8.716521	-2.207150	0.652062
H	-9.659482	-2.656175	0.945816
C	8.753408	-2.325192	0.187118
H	9.728262	-2.794935	0.109537
C	8.626020	-0.966664	-0.036263
H	9.468081	-0.331750	-0.284020
C	-8.526246	-0.846288	0.802577
H	-9.289614	-0.188805	1.201145
C	7.652677	-3.094356	0.571378
H	7.805503	-4.138084	0.812877
C	-7.729038	-3.005815	0.070414
H	-7.940116	-4.053178	-0.101806
N	5.315652	-3.288029	1.197054
N	-5.568700	-3.261396	-1.012267
C	4.655829	-2.799673	2.410450
H	5.161054	-3.195713	3.302725
H	4.675656	-1.711880	2.454723
H	3.612339	-3.128589	2.420735
C	5.460076	-4.735125	1.212150
H	6.147253	-5.084727	1.998014
H	4.476543	-5.170699	1.403612
H	5.812953	-5.089713	0.242021
C	-5.735234	-4.704677	-0.950403
H	-4.821997	-5.167134	-1.332566
H	-5.878735	-5.024328	0.083413
H	-6.579289	-5.062789	-1.560363
C	-5.191905	-2.823388	-2.358384
H	-5.181520	-1.736693	-2.426489
H	-4.191180	-3.194932	-2.600097
H	-5.902217	-3.214760	-3.100987
H	-2.374384	0.528683	-0.317580
H	3.748265	-2.258440	0.083073

	Energies (Hartree)
E(M06-2X)	-2419.94069164
E(M06-2X)+ZPE	-2419.20412700
E(M06-2X)+U	-2419.16108500
E(M06-2X)+H	-2419.16014100
E(M06-2X)+G	-2419.28537000
Number of imaginary frequencies	0
Top 10 frequencies (cm^{-1})	
1	8.0170
2	12.3712
3	14.0882
4	19.0158
5	26.9956
6	28.2504
7	36.1168
8	38.7086
9	42.8228
10	47.3794

6-Flav7-A (Global Minimum)

C	1.245082	-1.128467	0.438670
C	1.245159	-2.643171	0.475350
C	-0.006800	-3.192978	1.146144
C	-1.258879	-2.637821	0.480256
C	-1.249815	-1.123337	0.431850
C	-0.001148	-0.469856	0.458778
Cl	0.002412	1.287727	0.469585
C	2.448387	-0.422644	0.337082
C	-2.448776	-0.412782	0.310852
C	-3.714056	-0.987705	0.184782
C	3.711262	-1.002249	0.206383
C	-4.904463	-0.257019	0.047773
C	4.907067	-0.275717	0.099742
C	4.957175	1.147537	0.138567
C	6.130529	1.839713	0.040916
O	7.300842	1.210491	-0.116011
C	7.342855	-0.151374	-0.179225
C	6.194314	-0.947064	-0.069710
C	-6.199214	-0.924884	-0.070128
C	-7.341649	-0.126057	-0.214607
O	-7.285966	1.236469	-0.238700
C	-6.108441	1.862799	-0.133227
C	-4.940923	1.166198	-0.001039
C	-6.368404	-2.321241	-0.043420
C	-7.631157	-2.917970	-0.168607
C	7.604644	-2.943190	-0.311849
C	6.348251	-2.343433	-0.144215
C	-6.226141	3.328278	-0.199268

C	-7.357252	3.912252	-0.786607
C	-7.465230	5.297281	-0.867408
C	-6.453301	6.111080	-0.358150
C	-5.330922	5.534107	0.237718
C	-5.215901	4.150528	0.319268
C	6.262751	3.305160	0.071884
C	5.273481	4.099715	0.668030
C	5.402124	5.484558	0.677636
C	6.517295	6.089838	0.096514
C	7.508664	5.302884	-0.489553
C	7.387219	3.916649	-0.499936
H	1.324745	-3.034419	-0.548480
H	2.129291	-2.989332	1.017374
H	-0.003720	-2.908832	2.205042
H	-0.009509	-4.285195	1.099959
H	-2.141910	-2.973861	1.030659
H	-1.348975	-3.035560	-0.540147
H	4.049104	1.726238	0.228587
H	-4.025976	1.739561	0.038403
H	-5.498739	-2.949204	0.079269
H	5.471356	-2.969189	-0.072802
H	-8.142173	3.280139	-1.187020
H	-8.340122	5.741245	-1.330649
H	-6.540718	7.190885	-0.420193
H	-4.547673	6.162484	0.648353
H	-4.351264	3.715681	0.809788
H	4.415698	3.640470	1.148471
H	4.635516	6.091138	1.148085
H	6.615365	7.170504	0.105766
H	8.378017	5.768861	-0.941470
H	8.156066	3.305524	-0.959743
C	8.738222	-2.087314	-0.429032
H	9.726606	-2.504384	-0.573529
C	-8.760522	-2.059039	-0.302670
C	-8.613497	-0.690262	-0.326999
C	8.605500	-0.718647	-0.359924
H	9.468436	-0.067309	-0.445655
N	7.751495	-4.306300	-0.358339
N	-7.786616	-4.281373	-0.167135
C	-9.119738	-4.855581	-0.087809
H	-9.720197	-4.580707	-0.960635
H	-9.652690	-4.538679	0.818624
H	-9.032977	-5.940853	-0.073754
C	-6.639295	-5.122048	0.118649
H	-6.222324	-4.925168	1.116589
H	-6.943743	-6.166153	0.069722
H	-5.848993	-4.967474	-0.623690
C	9.031174	-4.882493	-0.737071
H	9.353681	-4.550519	-1.732838
H	8.936273	-5.967019	-0.750975

H	9.810962	-4.624728	-0.013247
C	6.568264	-5.145510	-0.363836
H	6.874567	-6.189956	-0.388395
H	5.976218	-4.990275	0.544684
H	5.926810	-4.948225	-1.234513
H	-3.784333	-2.067132	0.180161
H	-2.375781	0.668177	0.295678
H	2.381269	0.658797	0.336376
H	3.774409	-2.081430	0.168490
H	-9.757135	-2.473200	-0.386387
H	-9.472954	-0.036572	-0.428226

	Energies (Hartree)
E(M06-2X)	-2419.95380856
E(M06-2X)+ZPE	-2419.21835500
E(M06-2X)+U	-2419.17410400
E(M06-2X)+H	-2419.17316000
E(M06-2X)+G	-2419.30434700
Number of imaginary frequencies	0
Top 10 frequencies (cm^{-1})	
1	4.2165
2	8.2699
3	11.5008
4	18.3992
5	24.7808
6	27.7695
7	29.2701
8	33.0316
9	37.7436
10	42.4027

6-Flav7-B

C	1.246926	-1.117230	0.408394
C	1.248295	-2.631045	0.472874
C	0.000296	-3.169071	1.160523
C	-1.255723	-2.628696	0.489971
C	-1.248064	-1.115535	0.409071
C	-0.001013	-0.460072	0.416788
Cl	-0.000053	1.297338	0.388479
C	2.448700	-0.411670	0.295662
C	-2.449719	-0.409623	0.280806
C	-3.712857	-0.990399	0.166632
C	3.713699	-0.991139	0.179140
C	-4.906856	-0.264512	0.030415
C	4.908310	-0.264713	0.066107
C	4.955375	1.159537	0.070815

C	6.128042	1.851676	-0.032168
O	7.301695	1.221846	-0.160922
C	7.347162	-0.141226	-0.189387
C	6.198888	-0.936640	-0.076021
C	-6.194206	-0.938060	-0.125949
C	-7.342061	-0.143417	-0.249968
O	-7.294501	1.219460	-0.244544
C	-6.124635	1.850921	-0.095980
C	-4.955797	1.158718	0.049659
C	-6.352364	-2.335785	-0.148105
C	-7.610164	-2.937291	-0.298467
C	7.616030	-2.934760	-0.254660
C	6.357619	-2.334097	-0.106215
C	-6.257132	3.316540	-0.087065
C	-5.160315	4.135335	-0.390552
C	-5.294135	5.519463	-0.365249
C	-6.521026	6.100048	-0.040896
C	-7.617611	5.289406	0.252537
C	-7.490779	3.903917	0.226758
C	6.256425	3.317838	-0.036938
C	5.259599	4.124130	0.530111
C	5.384442	5.509149	0.506546
C	6.503398	6.102989	-0.079088
C	7.502263	5.304545	-0.636193
C	7.384542	3.918107	-0.613362
H	2.135457	-2.967086	1.016181
H	1.322167	-3.040889	-0.544099
H	0.008196	-2.864257	2.213625
H	-0.001245	-4.261994	1.135722
H	-2.135602	-2.953017	1.052311
H	-1.351072	-3.048110	-0.521280
H	4.045283	1.738417	0.136123
H	-4.056617	1.735643	0.211745
H	-5.478212	-2.961158	-0.045718
H	5.483040	-2.960141	-0.011821
H	-4.208749	3.696937	-0.672622
H	-4.442032	6.145284	-0.608614
H	-6.622792	7.180246	-0.022469
H	-8.573755	5.736247	0.503977
H	-8.342373	3.274105	0.459379
H	4.398842	3.674233	1.014052
H	4.611891	6.125014	0.954695
H	6.598583	7.183816	-0.095784
H	8.374569	5.761689	-1.091442
H	8.159254	3.297870	-1.050604
C	8.751773	-2.079783	-0.354616
H	9.745035	-2.498016	-0.456126
C	-8.745527	-2.082809	-0.410382
C	-8.608873	-0.712993	-0.389887
C	8.614738	-0.710027	-0.324505

H	9.478937	-0.059133	-0.400391
N	7.761215	-4.298013	-0.307429
N	-7.755346	-4.300366	-0.342689
C	-9.084401	-4.887648	-0.303886
H	-8.988509	-5.972119	-0.317119
H	-9.635525	-4.599947	0.601256
H	-9.672173	-4.593634	-1.179405
C	-6.600812	-5.142557	-0.093533
H	-5.816338	-4.958311	-0.835650
H	-6.898971	-6.186461	-0.174146
H	-6.178427	-4.975463	0.907424
C	9.090029	-4.885018	-0.257116
H	9.631321	-4.602311	0.655604
H	8.994729	-5.969443	-0.277928
H	9.687153	-4.585775	-1.124443
C	6.606058	-5.141049	-0.063979
H	6.182641	-4.979925	0.937610
H	5.822495	-4.951952	-0.805735
H	6.903768	-6.184611	-0.150889
H	-3.778246	-2.070124	0.160856
H	-2.379859	0.670986	0.241613
H	2.379868	0.669481	0.276292
H	3.778746	-2.070717	0.159738
H	-9.738099	-2.501907	-0.515113
H	-9.472336	-0.062720	-0.478239

	Energies (Hartree)
E(M06-2X)	-2419.95383556
E(M06-2X)+ZPE	-2419.21820100
E(M06-2X)+U	-2419.17406400
E(M06-2X)+H	-2419.17312000
E(M06-2X)+G	-2419.30334200
Number of imaginary frequencies	0
Top 10 frequencies (cm^{-1})	
1	4.9248
2	9.5501
3	13.4646
4	19.8613
5	24.8933
6	26.6720
7	29.8016
8	34.1601
9	38.0890
10	41.1018

6-Flav7-C

C	1.247404	-1.091842	0.477145
C	1.253435	-2.601392	0.609256

C	0.005177	-3.113925	1.315384
C	-1.250319	-2.602848	0.621161
C	-1.247360	-1.093281	0.489333
C	-0.000363	-0.436402	0.465814
Cl	-0.001921	1.318558	0.368869
C	2.448323	-0.391444	0.321527
C	-2.450443	-0.394498	0.345019
C	-3.712587	-0.982321	0.247202
C	3.710503	-0.977345	0.215335
C	-4.908376	-0.264056	0.095307
C	4.904609	-0.257930	0.054323
C	4.958614	1.165616	0.052549
C	6.128101	1.851455	-0.114644
O	7.294560	1.213915	-0.266067
C	7.337243	-0.149232	-0.253816
C	6.188145	-0.938005	-0.107122
C	-6.190833	-0.944914	-0.071246
C	-7.340941	-0.156980	-0.214070
O	-7.301296	1.206360	-0.209963
C	-6.136370	1.844556	-0.049048
C	-4.965388	1.159407	0.109736
C	-6.339775	-2.343484	-0.101817
C	-7.593261	-2.952523	-0.256879
C	7.594870	-2.944478	-0.271859
C	6.340984	-2.336434	-0.114980
C	-6.277786	3.309440	-0.041279
C	-5.182391	4.135009	-0.331215
C	-5.324816	5.518309	-0.307014
C	-6.559023	6.091413	0.002575
C	-7.654146	5.274026	0.282400
C	-7.518614	3.889312	0.257815
C	6.265968	3.316630	-0.126972
C	7.505757	3.903506	0.162632
C	7.637987	5.288741	0.168200
C	6.540587	6.099614	-0.121455
C	5.307391	5.519389	-0.421683
C	5.168251	4.135553	-0.426811
H	2.140092	-2.908838	1.170256
H	1.333218	-3.055678	-0.388282
H	0.009934	-2.767259	2.355489
H	0.005894	-4.206964	1.334027
H	-1.338758	-3.057069	-0.375668
H	-2.131309	-2.911450	1.190368
H	4.063335	1.747698	0.217924
H	-4.071651	1.741244	0.284167
H	-5.461189	-2.963538	-0.005454
H	5.465529	-2.957362	0.002419
H	-4.224771	3.702454	-0.601599
H	-4.473545	6.149355	-0.539612
H	-6.667499	7.170975	0.020171

H	-8.615956	5.714968	0.522404
H	-8.369134	3.254307	0.480015
H	8.358100	3.273635	0.392280
H	8.599038	5.735185	0.400969
H	6.646500	7.179573	-0.118804
H	4.454340	6.145160	-0.661854
H	4.211286	3.697105	-0.689904
C	8.732094	-2.095725	-0.405268
H	9.722046	-2.519591	-0.515468
C	-8.728502	-2.104631	-0.410011
C	-8.600348	-0.733950	-0.386337
C	8.600418	-0.725199	-0.399980
H	9.465168	-0.079220	-0.505643
N	7.734174	-4.308638	-0.303174
N	-7.735356	-4.317177	-0.259614
C	-9.010258	-4.909503	-0.629609
H	-9.323012	-4.617045	-1.640872
H	-8.914156	-5.993611	-0.599792
H	-9.797498	-4.625050	0.075775
C	-6.548314	-5.150987	-0.240972
H	-5.957940	-4.968129	0.663428
H	-5.906933	-4.974803	-1.116255
H	-6.849954	-6.197080	-0.237057
C	6.578996	-5.143500	-0.033327
H	6.167587	-4.964529	0.970154
H	5.787546	-4.963845	-0.769156
H	6.872183	-6.189382	-0.106215
C	9.061207	-4.900838	-0.271654
H	8.961028	-5.985017	-0.273862
H	9.641587	-4.617341	-1.155516
H	9.622256	-4.606933	0.625364
H	-3.773905	-2.062199	0.263681
H	-2.384241	0.684804	0.274283
H	2.379637	0.687675	0.250569
H	3.773506	-2.057061	0.234411
H	-9.714463	-2.529294	-0.548745
H	-9.464171	-0.088673	-0.503295

	Energies (Hartree)
E(M06-2X)	-2419.95384087
E(M06-2X)+ZPE	-2419.21813600
E(M06-2X)+U	-2419.17398300
E(M06-2X)+H	-2419.17303900
E(M06-2X)+G	-2419.30327800
Number of imaginary frequencies	0
Top 10 frequencies (cm^{-1})	
1	4.8192
2	8.5956
3	14.3703

4	22.1717
5	25.0460
6	29.2303
7	29.6955
8	34.9430
9	38.3428
10	42.7317

Flav7-A (Global Minimum)

C	-0.000117	-3.479553	1.129915
C	-1.252343	-2.929378	0.459690
C	1.252603	-2.929282	0.460708
H	-1.337806	-3.329083	-0.560504
H	1.339261	-3.329421	-0.559215
C	-1.247782	-1.414875	0.411246
C	1.247738	-1.414795	0.411555
C	0.000045	-0.761281	0.428003
H	-0.000045	-4.572093	1.088190
Cl	-0.000017	0.999040	0.424447
H	-2.135577	-3.268875	1.007652
H	-0.000573	-3.191197	2.187767
H	2.135390	-3.268248	1.009735
C	-2.451653	-0.707844	0.305291
C	-3.716060	-1.282849	0.192144
H	-3.788039	-2.362616	0.176427
C	2.451709	-0.707690	0.305275
H	2.381181	0.373426	0.292530
C	3.715999	-1.282691	0.192512
H	3.788058	-2.362462	0.177526
C	-4.912441	-0.551649	0.084902
C	-4.944680	0.881475	0.076134
C	-6.112270	1.571393	-0.009285
O	-7.301225	0.944791	-0.107406
C	-7.362890	-0.417547	-0.129608
C	-6.194946	-1.201147	-0.032707
C	-6.398536	-2.602439	-0.062645
C	-7.645839	-3.161162	-0.177642
C	-8.815586	-2.343079	-0.272282
C	-8.637926	-0.945625	-0.244887
H	-4.029894	1.455057	0.113899
H	-9.468088	-0.254969	-0.309806
H	-7.734200	-4.239589	-0.193765
H	-5.548264	-3.270492	0.006122
C	4.912482	-0.551459	0.084838
C	4.944561	0.881588	0.074700
C	6.112144	1.571549	-0.011133
O	7.301080	0.944845	-0.108261
C	7.362884	-0.417473	-0.129169
C	6.194925	-1.201046	-0.031889

C	6.398565	-2.602390	-0.060537
C	7.645907	-3.161125	-0.174708
C	8.815675	-2.343055	-0.269721
C	8.637968	-0.945574	-0.243655
H	4.029672	1.455040	0.111662
H	9.468111	-0.254949	-0.309086
H	7.734341	-4.239559	-0.189910
H	5.548300	-3.270415	0.008542
C	-6.240779	3.038196	-0.028521
C	-7.373216	3.633816	-0.600590
C	-5.236800	3.849510	0.518199
C	-7.487666	5.020444	-0.640951
C	-5.357906	5.234436	0.476972
C	-6.481174	5.823663	-0.105285
H	-8.154092	3.009784	-1.021119
H	-4.372877	3.402781	0.999587
H	-8.363641	5.473737	-1.093102
H	-4.579236	5.854088	0.909117
H	-6.573755	6.904434	-0.135434
C	6.240651	3.038319	-0.031849
C	5.235746	3.850292	0.512212
C	7.374047	3.633300	-0.602699
C	5.356946	5.235159	0.469621
C	7.488596	5.019879	-0.644420
C	6.481220	5.823723	-0.111371
H	4.370931	3.404226	0.992595
H	8.155630	3.008820	-1.021228
H	4.577521	5.855296	0.899704
H	8.365351	5.472633	-1.095593
H	6.573868	6.904457	-0.142584
N	-10.048249	-2.896038	-0.382898
C	-11.219528	-2.037574	-0.456601
H	-11.175601	-1.383772	-1.335017
H	-12.109964	-2.658017	-0.533968
H	-11.308539	-1.413693	0.440124
C	-10.209192	-4.342657	-0.407577
H	-9.844181	-4.800351	0.518344
H	-11.267109	-4.575295	-0.510197
H	-9.676522	-4.786737	-1.255207
N	10.048354	-2.896070	-0.379442
C	10.209298	-4.342709	-0.403827
H	9.843933	-4.800206	0.522038
H	9.676955	-4.786940	-1.251585
H	11.267255	-4.575360	-0.505968
C	11.219602	-2.037633	-0.454188
H	11.175939	-1.385255	-1.333689
H	11.308216	-1.412322	0.441559
H	12.110111	-2.658137	-0.530181
H	-2.381218	0.373284	0.293145

		Energies (Hartree)
E(M06-2X)		-2419.96835111
E(M06-2X)+ZPE		-2419.23263800
E(M06-2X)+U		-2419.18847700
E(M06-2X)+H		-2419.18753200
E(M06-2X)+G		-2419.31744800
Number of imaginary frequencies		0
Top 10 frequencies (cm^{-1})		
1		4.1716
2		9.2423
3		12.3633
4		19.6019
5		25.1219
6		28.4616
7		29.3913
8		36.0974
9		44.7574
10		49.9678

Flav7-B

C	-0.000224	-3.445717	1.207913
C	1.255397	-2.912002	0.530942
C	-1.249479	-2.913933	0.517439
H	2.135509	-3.232233	1.095411
H	-2.135361	-3.243175	1.067210
C	1.248337	-1.399548	0.436728
C	-1.247130	-1.400864	0.435579
C	0.000918	-0.746471	0.435050
H	-0.006454	-3.130264	2.257977
Cl	0.000204	1.013108	0.383839
H	1.349678	-3.341788	-0.476197
H	0.000969	-4.538972	1.194278
H	-1.327040	-3.336575	-0.494148
C	2.452631	-0.695747	0.308385
C	3.715452	-1.275316	0.207736
H	3.785279	-2.355341	0.212317
C	-2.451410	-0.697217	0.318222
H	-2.382170	0.383598	0.285941
C	-3.715682	-1.275657	0.215870
H	-3.785679	-2.355671	0.212789
C	4.912567	-0.548506	0.075309
C	4.950732	0.884177	0.082370
C	6.115805	1.570474	-0.054556
O	7.299238	0.939243	-0.183356
C	7.359232	-0.423209	-0.177190
C	6.190389	-1.202783	-0.059841
C	6.389714	-2.604981	-0.080012
C	7.634415	-3.167945	-0.200927
C	8.805522	-2.353863	-0.313378

C	8.631666	-0.955675	-0.300166
H	4.047822	1.459201	0.228295
H	9.462364	-0.268006	-0.386417
H	7.719856	-4.246692	-0.208446
H	5.538344	-3.270040	0.002826
C	-4.913256	-0.548278	0.102019
C	-4.949579	0.884884	0.088846
C	-6.118817	1.571281	-0.000574
O	-7.305980	0.941176	-0.099804
C	-7.363723	-0.421459	-0.118608
C	-6.194033	-1.201593	-0.016572
C	-6.393631	-2.603405	-0.044609
C	-7.639124	-3.165907	-0.161736
C	-8.810816	-2.351316	-0.260982
C	-8.637027	-0.953358	-0.236175
H	-4.036548	1.461052	0.129624
H	-9.468885	-0.265128	-0.305099
H	-7.724352	-4.244607	-0.176423
H	-5.541599	-3.268965	0.026776
C	6.251985	3.036713	-0.059685
C	7.478931	3.626604	0.273665
C	5.163191	3.853407	-0.395606
C	7.606624	5.012556	0.287733
C	5.297441	5.237648	-0.381637
C	6.517673	5.821016	-0.037310
H	8.324915	2.998604	0.530260
H	4.217840	3.411920	-0.693610
H	8.557860	5.461188	0.554359
H	4.451333	5.861348	-0.650223
H	6.620188	6.901288	-0.028635
C	-6.251608	3.037727	-0.022192
C	-7.385246	3.629159	-0.596218
C	-5.250777	3.852910	0.524553
C	-7.503986	5.015387	-0.638439
C	-5.376139	5.237403	0.481470
C	-6.500617	5.822430	-0.102691
H	-8.163789	3.002193	-1.016698
H	-4.385978	3.409575	1.007482
H	-8.380937	5.465363	-1.092015
H	-4.599894	5.859984	0.913774
H	-6.596597	6.902868	-0.134182
N	10.035563	-2.911271	-0.428916
C	10.191728	-4.358554	-0.448595
H	11.248003	-4.594993	-0.558944
H	9.833154	-4.810742	0.482487
H	9.650494	-4.804771	-1.289670
C	11.208286	-2.056852	-0.524434
H	12.096935	-2.680538	-0.596029
H	11.303629	-1.418423	0.361227
H	11.160763	-1.417668	-1.413416

N	-10.041757	-2.907943	-0.373773
C	-11.215130	-2.052885	-0.452954
H	-12.103700	-2.675933	-0.531000
H	-11.308248	-1.426828	0.441834
H	-11.170656	-1.401289	-1.332997
C	-10.198484	-4.355018	-0.396494
H	-11.255485	-4.590889	-0.501155
H	-9.834308	-4.810168	0.531012
H	-9.662564	-4.799004	-1.242148
H	2.382845	0.384535	0.260928

	Energies (Hartree)
E(M06-2X)	-2419.96836422
E(M06-2X)+ZPE	-2419.23255600
E(M06-2X)+U	-2419.18842600
E(M06-2X)+H	-2419.18748200
E(M06-2X)+G	-2419.31692900
Number of imaginary frequencies	0
Top 10 frequencies (cm^{-1})	
1	5.2045
2	8.6358
3	14.0535
4	21.6955
5	24.8694
6	28.3178
7	34.8493
8	35.1887
9	44.6377
10	48.6914

Flav7-C

C	0.000013	-3.414011	1.283592
C	-1.252333	-2.895879	0.588575
C	1.252363	-2.895881	0.588581
H	-1.337896	-3.343254	-0.411711
H	1.337962	-3.343295	-0.411684
C	-1.247666	-1.385235	0.468949
C	1.247672	-1.385243	0.468881
C	0.000020	-0.731630	0.454409
H	0.000015	-4.507305	1.293136
Cl	0.000032	1.026476	0.366586
H	-2.135544	-3.208734	1.152195
H	0.000012	-3.076197	2.326698
H	2.135573	-3.208681	1.152235
C	-2.452226	-0.684836	0.330685
C	-3.714547	-1.267738	0.235811
H	-3.782116	-2.347822	0.249849
C	2.452246	-0.684852	0.330516

H	2.384111	0.394839	0.268529
C	3.714540	-1.267759	0.235622
H	3.782107	-2.347844	0.249665
C	-4.912564	-0.544911	0.095457
C	-4.954904	0.887880	0.098022
C	-6.121248	1.570440	-0.045660
O	-7.302460	0.935506	-0.178332
C	-7.358585	-0.427162	-0.168585
C	-6.188340	-1.203123	-0.043104
C	-6.383611	-2.605802	-0.060876
C	-7.626159	-3.172685	-0.186535
C	-8.798877	-2.362257	-0.306968
C	-8.628930	-0.963577	-0.296677
H	-4.054383	1.465660	0.247926
H	-9.461072	-0.278463	-0.389280
H	-7.708450	-4.251684	-0.192009
H	-5.530722	-3.268249	0.027347
C	4.912572	-0.544925	0.095279
C	4.954904	0.887858	0.097999
C	6.121268	1.570431	-0.045505
O	7.302487	0.935521	-0.178112
C	7.358600	-0.427154	-0.168613
C	6.188328	-1.203122	-0.043374
C	6.383588	-2.605806	-0.061448
C	7.626136	-3.172673	-0.187135
C	8.798878	-2.362233	-0.307299
C	8.628948	-0.963551	-0.296703
H	4.054383	1.465636	0.247911
H	9.461102	-0.278423	-0.389081
H	7.708419	-4.251673	-0.192822
H	5.530683	-3.268265	0.026547
C	-6.261908	3.036285	-0.053844
C	-7.492701	3.622873	0.271050
C	-5.173551	3.855999	-0.383828
C	-7.624723	5.008457	0.282705
C	-5.312079	5.239835	-0.372220
C	-6.536223	5.819906	-0.036287
H	-8.338376	2.992609	0.523036
H	-4.224917	3.417107	-0.675147
H	-8.579007	5.454440	0.542817
H	-4.466126	5.865825	-0.635943
H	-6.642049	6.899873	-0.029374
C	6.261903	3.036279	-0.053505
C	7.492598	3.622855	0.271778
C	5.173618	3.855994	-0.383716
C	7.624588	5.008441	0.283595
C	5.312116	5.239832	-0.371945
C	6.536157	5.819894	-0.035623
H	8.338214	2.992581	0.523940
H	4.225080	3.417097	-0.675342

H	8.578790	5.454424	0.544008
H	4.466227	5.865833	-0.635848
H	6.641960	6.899862	-0.028582
N	-10.026860	-2.923484	-0.427323
C	-10.178571	-4.371210	-0.445265
H	-11.233608	-4.611067	-0.560011
H	-9.632116	-4.817348	-1.283046
H	-9.822931	-4.820722	0.488242
C	-11.201302	-2.072657	-0.532451
H	-11.303134	-1.431067	0.350192
H	-12.087930	-2.698978	-0.606291
H	-11.150782	-1.436724	-1.423624
N	10.026850	-2.923454	-0.427691
C	11.201354	-2.072639	-0.532262
H	12.087971	-2.698979	-0.606056
H	11.302974	-1.431315	0.350598
H	11.151097	-1.436443	-1.423263
C	10.178534	-4.371183	-0.445896
H	11.233543	-4.611034	-0.560914
H	9.631900	-4.817146	-1.283646
H	9.823070	-4.820858	0.487603
H	-2.384099	0.394857	0.268766

		Energies (Hartree)
E(M06-2X)		-2419.96837486
E(M06-2X)+ZPE		-2419.23245300
E(M06-2X)+U		-2419.18835300
E(M06-2X)+H		-2419.18740900
E(M06-2X)+G		-2419.31657500
Number of imaginary frequencies		0
Top 10 frequencies (cm^{-1})		
1		5.9731
2		7.8644
3		14.9789
4		23.6640
5		24.2216
6		33.2668
7		34.0750
8		35.7069
9		44.2020
10		47.8972

8-Flav7-A (Global Minimum)

C	1.247281	-1.808789	0.419757
C	1.251768	-3.322111	0.496613
C	0.000025	-3.858866	1.177915
C	-1.251783	-3.322091	0.496749
C	-1.247268	-1.808771	0.419885
C	-0.000008	-1.150884	0.427792

Cl	0.000007	0.605103	0.397817
C	2.447558	-1.102758	0.295490
C	-2.447570	-1.102719	0.295716
C	-3.711394	-1.685174	0.176771
C	3.711392	-1.685226	0.176390
C	-4.905013	-0.961050	0.053092
C	4.904982	-0.961104	0.052746
C	4.953321	0.463869	0.072467
C	6.129647	1.143761	-0.033197
O	7.297357	0.498131	-0.166819
C	7.349792	-0.859462	-0.200599
C	6.189140	-1.640061	-0.112540
C	-6.189207	-1.640051	-0.111679
C	-7.349837	-0.859451	-0.200067
O	-7.297343	0.498147	-0.166932
C	-6.129619	1.143803	-0.033679
C	-4.953294	0.463918	0.072193
C	-6.330660	-3.040487	-0.221896
C	-7.577833	-3.596328	-0.411979
C	-8.647040	-1.408807	-0.358594
C	8.646964	-1.408802	-0.359441
C	7.577643	-3.596240	-0.414027
C	6.330506	-3.040435	-0.223574
C	-6.292808	2.605918	-0.031711
C	-7.485187	3.171800	-0.506442
C	-7.644161	4.554154	-0.518746
C	-6.622955	5.382398	-0.053449
C	-5.439324	4.822760	0.430073
C	-5.272789	3.442343	0.443455
C	6.292883	2.605875	-0.030582
C	7.485368	3.171925	-0.504847
C	7.644390	4.554281	-0.516547
C	6.623124	5.382368	-0.051105
C	5.439382	4.822560	0.431951
C	5.272802	3.442144	0.444728
H	2.135472	-3.650833	1.049822
H	1.335513	-3.739075	-0.516550
H	0.000017	-4.951737	1.156384
H	0.000084	-3.550802	2.230084
H	-1.335660	-3.739062	-0.516399
H	-2.135429	-3.650789	1.050064
H	2.378203	-0.021999	0.264570
H	3.775469	-2.764761	0.165476
H	4.045965	1.043970	0.156786
H	-4.045913	1.044045	0.156053
H	-5.464072	-3.686663	-0.172648
H	-7.679463	-4.672134	-0.504899
H	7.679201	-4.671998	-0.507592
H	5.463866	-3.686570	-0.174706
H	-8.278118	2.527905	-0.872222

H	-8.566481	4.984684	-0.894210
H	-6.750047	6.460023	-0.062415
H	-4.647308	5.461935	0.805581
H	-4.357162	3.022256	0.845941
H	8.278357	2.528165	-0.870738
H	8.566801	4.984930	-0.891651
H	6.750249	6.459993	-0.059596
H	4.647305	5.461600	0.807562
H	4.357070	3.021936	0.846847
C	8.727002	-2.793411	-0.475964
H	9.692589	-3.265290	-0.612965
C	-8.727153	-2.793469	-0.474351
H	-9.692766	-3.265378	-0.611072
N	9.752971	-0.548400	-0.457260
N	-9.753000	-0.548385	-0.456868
C	-10.046996	0.241419	0.744021
H	-10.762819	1.023945	0.481404
H	-9.146284	0.714701	1.131055
H	-10.487208	-0.388377	1.532207
C	-10.966731	-1.144008	-0.997220
H	-11.680222	-0.341861	-1.197087
H	-10.747853	-1.655948	-1.936684
H	-11.439164	-1.855693	-0.301065
C	10.966685	-1.143799	-0.997886
H	11.439061	-1.855869	-0.302085
H	11.680223	-0.341582	-1.197312
H	10.747815	-1.655239	-1.937624
C	10.046982	0.240837	0.743994
H	10.762745	1.023536	0.481728
H	10.487272	-0.389319	1.531849
H	9.146265	0.713874	1.131318
H	-2.378185	-0.021962	0.264763
H	-3.775482	-2.764706	0.165981

	Energies (Hartree)
E(M06-2X)	-2419.94681906
E(M06-2X)+ZPE	-2419.21032300
E(M06-2X)+U	-2419.16704300
E(M06-2X)+H	-2419.16609900
E(M06-2X)+G	-2419.29310300
Number of imaginary frequencies	0
Top 10 frequencies (cm^{-1})	
1	5.3456
2	8.8636
3	12.2326
4	19.8724
5	19.9335
6	30.5383
7	33.2592

8	39.8454
9	40.5785
10	46.4734

8-Flav7-B

C	1.248444	-1.817999	0.452494
C	1.252284	-3.332128	0.510809
C	-0.006144	-3.877119	1.172947
C	-1.251147	-3.332025	0.485905
C	-1.246006	-1.817876	0.427632
C	0.001149	-1.160205	0.455579
Cl	0.001506	0.596029	0.447492
C	2.450001	-1.110761	0.349316
C	-2.444970	-1.110027	0.301266
C	-3.708360	-1.690071	0.166718
C	3.714800	-1.692094	0.235153
C	-4.900340	-0.963403	0.042353
C	4.908200	-0.965765	0.123820
C	4.955701	0.458686	0.170217
C	6.127941	1.142459	0.044886
O	7.293253	0.500373	-0.122914
C	7.348203	-0.856842	-0.166535
C	6.194969	-1.641731	-0.032655
C	-6.184694	-1.639309	-0.133638
C	-7.343961	-0.856486	-0.220417
O	-7.289794	0.500777	-0.176925
C	-6.121700	1.143775	-0.034320
C	-4.946810	0.461479	0.071683
C	-6.327525	-3.038632	-0.255354
C	-7.574689	-3.591339	-0.454538
C	-8.641299	-1.402915	-0.387659
C	8.646654	-1.402638	-0.326532
C	7.610232	-3.598828	-0.144478
C	6.353411	-3.044683	-0.026644
C	-6.282683	2.606099	-0.022950
C	-7.472405	3.177107	-0.498212
C	-7.629127	4.559775	-0.501744
C	-6.608310	5.383214	-0.027151
C	-5.427340	4.818406	0.456865
C	-5.263050	3.437669	0.461509
C	6.292979	2.603832	0.087394
C	7.566792	3.152441	0.297355
C	7.731614	4.533203	0.348212
C	6.633753	5.377742	0.185105
C	5.366141	4.836120	-0.033867
C	5.193905	3.457302	-0.084421
H	2.130543	-3.667491	1.068690
H	1.346154	-3.736703	-0.506453
H	-0.016627	-3.581819	2.228702

H	-0.005873	-4.969644	1.138145
H	-2.140205	-3.667508	1.026312
H	-1.324909	-3.736539	-0.533071
H	2.381627	-0.029608	0.331022
H	3.778448	-2.771277	0.204483
H	4.056117	1.032798	0.337535
H	-4.039041	1.039815	0.163282
H	-5.461946	-3.686280	-0.207816
H	-7.677313	-4.666255	-0.556282
H	7.726917	-4.677034	-0.130051
H	5.495238	-3.694767	0.082173
H	-8.265059	2.536995	-0.871172
H	-8.549404	4.994311	-0.877600
H	-6.733685	6.461076	-0.029208
H	-4.635693	5.453739	0.839612
H	-4.349585	3.013406	0.864520
H	8.420394	2.495861	0.428744
H	8.718994	4.949619	0.517688
H	6.764984	6.454211	0.223607
H	4.510954	5.488676	-0.174048
H	4.206274	3.053304	-0.279618
C	8.747053	-2.790473	-0.298389
H	9.717834	-3.260305	-0.401923
C	-8.722757	-2.786534	-0.514636
H	-9.688499	-3.256080	-0.658392
N	9.748727	-0.538519	-0.434995
N	-9.745847	-0.540351	-0.482752
C	-10.042470	0.240740	0.723196
H	-9.142440	0.710260	1.116356
H	-10.756780	1.025901	0.464381
H	-10.485546	-0.394495	1.505380
C	-10.958709	-1.130258	-1.031244
H	-11.434148	-1.846557	-0.341894
H	-11.670572	-0.325691	-1.227170
H	-10.737675	-1.635385	-1.973883
C	11.050479	-1.146908	-0.200915
H	11.358152	-1.823153	-1.014667
H	11.791332	-0.348132	-0.126348
H	11.042035	-1.701665	0.739700
C	9.772613	0.305542	-1.634539
H	10.527574	1.083818	-1.499827
H	10.031005	-0.284764	-2.527024
H	8.808300	0.784908	-1.794404
H	-2.374744	-0.029047	0.283066
H	-3.773493	-2.769385	0.145593

	Energies (Hartree)
E(M06-2X)	-2419.94683115
E(M06-2X)+ZPE	-2419.21031400
E(M06-2X)+U	-2419.16704000
E(M06-2X)+H	-2419.16609600

E(M06-2X)+G	-2419.29305800
Number of imaginary frequencies	0
Top 10 frequencies (cm^{-1})	
1	5.0190
2	8.8976
3	12.9208
4	19.7627
5	20.7120
6	30.1376
7	35.2200
8	37.9451
9	41.3123
10	46.3612

8-Flav7-C

C	1.247289	-1.824348	0.471830
C	1.251739	-3.339024	0.513677
C	0.000018	-3.891300	1.182495
C	-1.251782	-3.338993	0.513866
C	-1.247275	-1.824322	0.471898
C	-0.000004	-1.166801	0.494342
Cl	-0.000004	0.589392	0.506056
C	2.447648	-1.115738	0.364544
C	-2.447646	-1.115696	0.364541
C	-3.711620	-1.695315	0.233735
C	3.711657	-1.695339	0.233768
C	-4.903759	-0.967468	0.118836
C	4.903774	-0.967484	0.118980
C	4.950988	0.456623	0.176228
C	6.121708	1.141982	0.045660
O	7.285903	0.501876	-0.136869
C	7.341322	-0.854973	-0.190385
C	6.189616	-1.641504	-0.052869
C	-6.189538	-1.641516	-0.053289
C	-7.341291	-0.855008	-0.190604
O	-7.285956	0.501826	-0.136631
C	-6.121780	1.141950	0.045899
C	-4.951010	0.456614	0.176261
C	-6.348716	-3.044366	-0.058947
C	-7.604796	-3.596951	-0.191216
C	-8.638680	-1.398879	-0.364998
C	8.638759	-1.398813	-0.364542
C	7.605029	-3.596889	-0.190057
C	6.348909	-3.044351	-0.058002
C	-6.286355	2.603076	0.097458
C	-5.185544	3.457003	-0.060312
C	-5.357361	4.835548	-0.001527
C	-6.626272	5.376424	0.211668
C	-7.725810	4.531473	0.360712

C	-7.561404	3.150992	0.301586
C	6.286254	2.603130	0.096914
C	5.185417	3.457018	-0.060871
C	5.357226	4.835578	-0.002363
C	6.626156	5.376500	0.210576
C	7.725722	4.531587	0.359639
C	7.561327	3.151095	0.300784
H	2.135527	-3.680329	1.059073
H	1.335483	-3.732541	-0.508809
H	0.000117	-3.607251	2.241369
H	-0.000011	-4.983385	1.135997
H	-2.135499	-3.680209	1.059434
H	-1.335722	-3.732581	-0.508577
H	2.378696	-0.034487	0.357440
H	3.775532	-2.774172	0.193096
H	4.052626	1.029000	0.355667
H	-4.052668	1.029000	0.355792
H	-5.491787	-3.695701	0.052159
H	-7.722091	-4.675175	-0.185797
H	7.722412	-4.675101	-0.184231
H	5.492038	-3.695711	0.053399
H	-4.196790	3.053620	-0.251074
H	-4.500785	5.488536	-0.130764
H	-6.757172	6.452681	0.256606
H	-8.714185	4.947335	0.525667
H	-8.416335	2.494049	0.422036
H	4.196644	3.053580	-0.251427
H	4.500625	5.488532	-0.131610
H	6.757063	6.452767	0.255301
H	8.714109	4.947500	0.524394
H	8.416273	2.494173	0.421242
C	8.740121	-2.786765	-0.347334
H	9.710287	-3.255263	-0.462064
C	-8.739937	-2.786854	-0.348229
H	-9.710073	-3.255365	-0.463153
N	9.739531	-0.533293	-0.475249
N	-9.739520	-0.533426	-0.475438
C	-11.043305	-1.142876	-0.255842
H	-11.042268	-1.704767	0.680570
H	-11.345157	-1.812755	-1.077013
H	-11.784295	-0.344268	-0.180788
C	-9.753893	0.319777	-1.668621
H	-8.788245	0.800004	-1.817431
H	-10.005653	-0.263558	-2.567561
H	-10.509610	1.097297	-1.533769
C	9.753819	0.319414	-1.668798
H	10.509519	1.097007	-1.534283
H	10.005554	-0.264284	-2.567504
H	8.788144	0.799560	-1.817754
C	11.043350	-1.142623	-0.255467

H	11.042346	-1.704184	0.681143
H	11.784314	-0.343967	-0.180709
H	11.345208	-1.812784	-1.076405
H	-2.378689	-0.034444	0.357351
H	-3.775482	-2.774152	0.193117

	Energies (Hartree)
E(M06-2X)	-2419.94682576
E(M06-2X)+ZPE	-2419.21025300
E(M06-2X)+U	-2419.16700600
E(M06-2X)+H	-2419.16606200
E(M06-2X)+G	-2419.29261000
Number of imaginary frequencies	0
Top 10 frequencies (cm^{-1})	
1	6.7184
2	8.3922
3	13.7188
4	19.6240
5	20.9459
6	31.3400
7	36.3008
8	39.5887
9	40.9120
10	46.5358

3.6 Spectra Relevant to Chapter Three

3.6.1 ^{1}H NMR Spectra

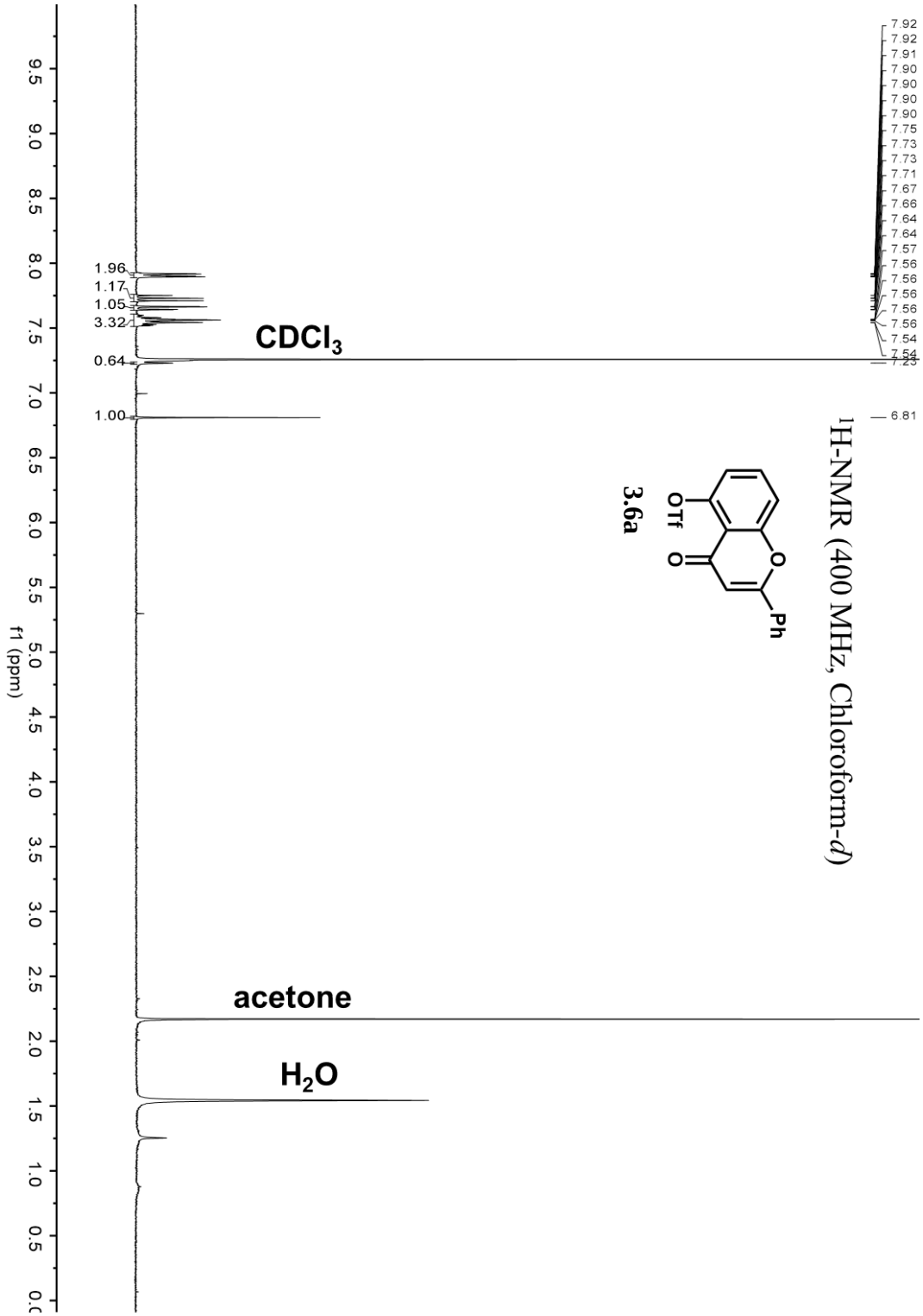

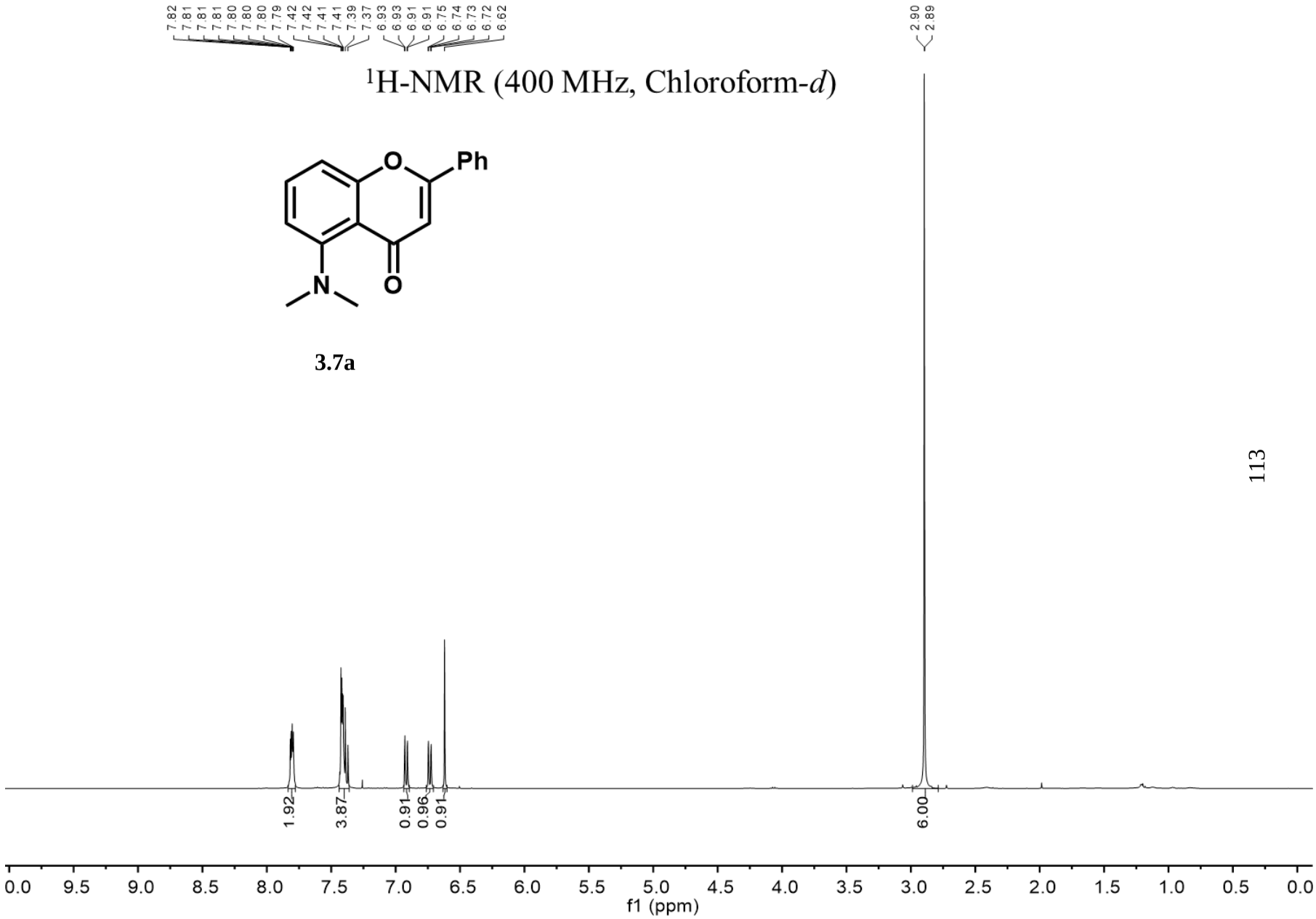
7.82
7.81
7.81
7.81
7.80
7.80
7.80
7.79
7.42
7.42
7.41
7.41
7.39
7.37
6.93
6.93
6.91
6.91
6.75
6.74
6.73
6.72
6.62
2.90
2.89
1H-NMR (400 MHz, Chloroform-d)
O
Ph
N
O
3.7a
1.92
3.87
0.91
0.96
0.91
6.00
0.0
9.5
9.0
8.5
8.0
7.5
7.0
6.5
6.0
5.5
5.0
4.5
4.0
3.5
3.0
2.5
2.0
1.5
1.0
0.5
0.0
f1 (ppm)

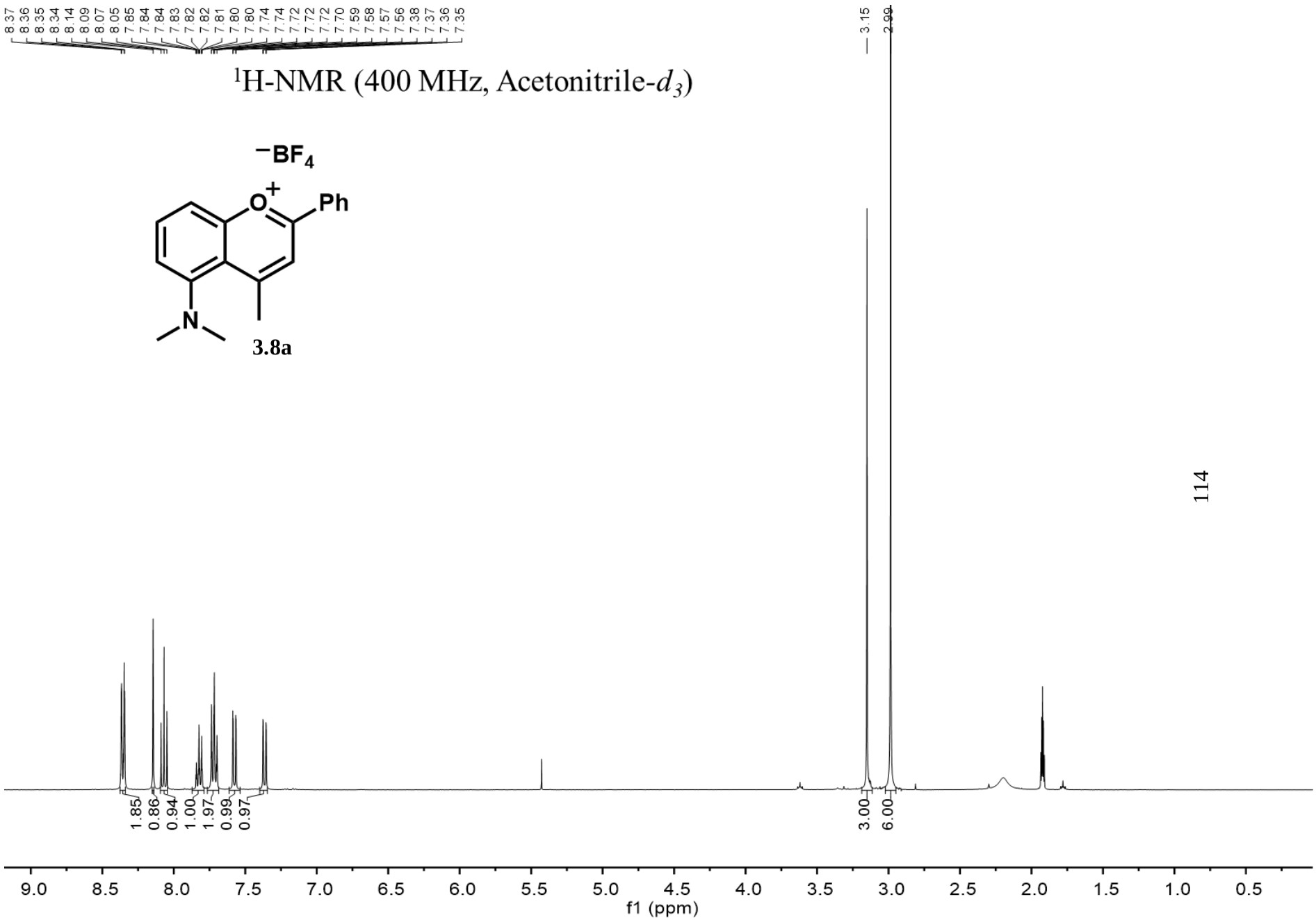
8.37
8.36
8.35
8.34
8.14
8.09
8.07
8.05
7.85
7.84
7.84
7.83
7.82
7.82
7.81
7.80
7.80
7.74
7.74
7.72
7.72
7.72
7.70
7.59
7.58
7.57
7.56
7.38
7.37
7.36
7.35
3.15
2.99
1H-NMR (400 MHz, Acetonitrile-d3)
−BF4
O+
Ph
N
3.8a
1.85
0.86
0.94
1.00
1.97
0.99
0.97
3.00
6.00
9.0
8.5
8.0
7.5
7.0
6.5
6.0
5.5
5.0
4.5
4.0
3.5
3.0
2.5
2.0
1.5
1.0
0.5
f1 (ppm)

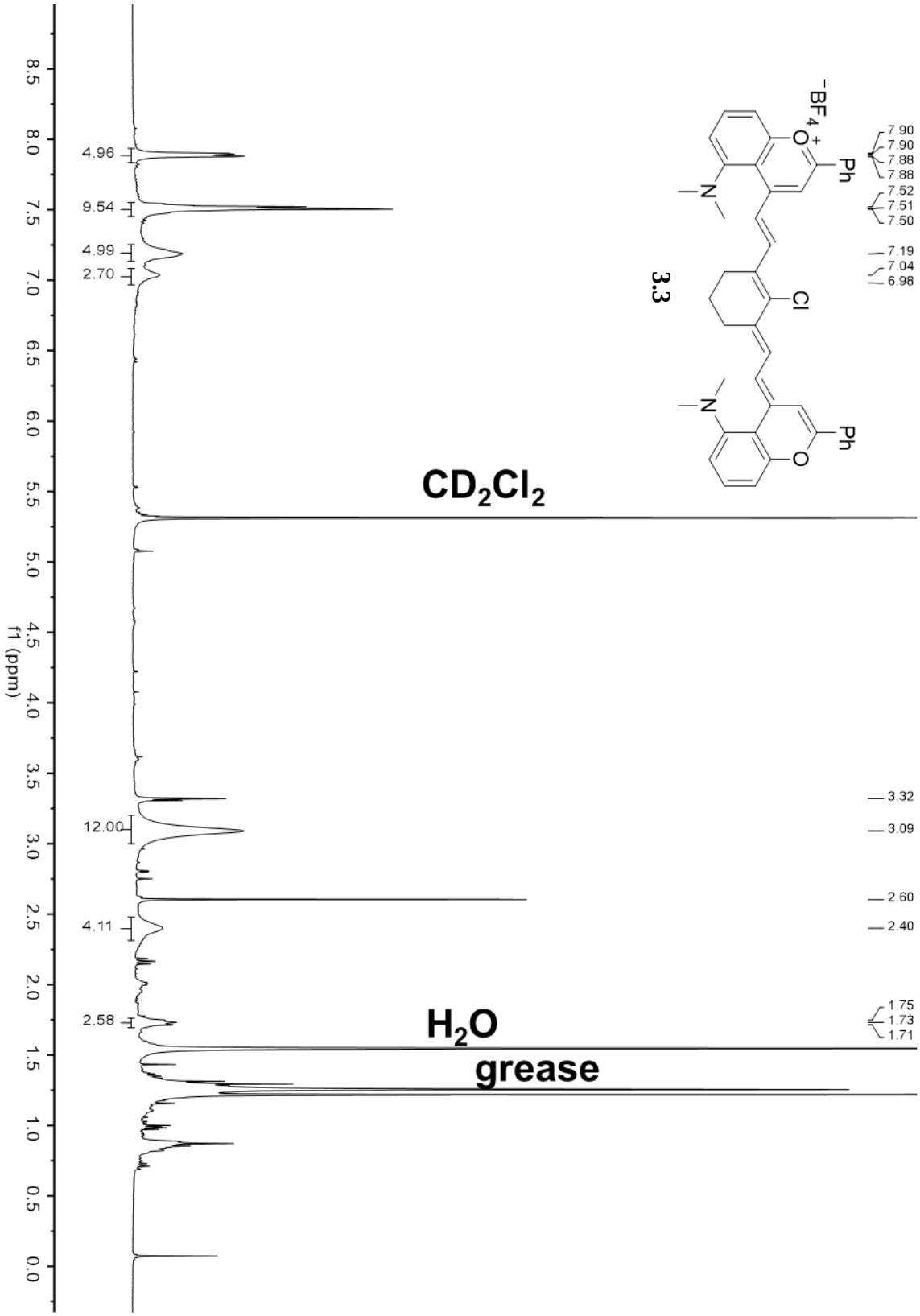

^{1}H-NMR (400 MHz, Methylene Chloride-d_2)

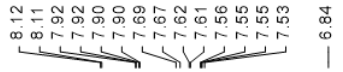

^{1}H-NMR (400 MHz, Chloroform-*d*)

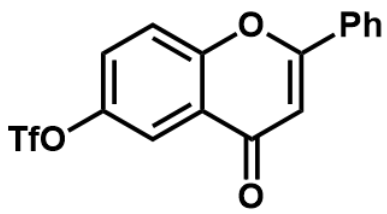

3.6b

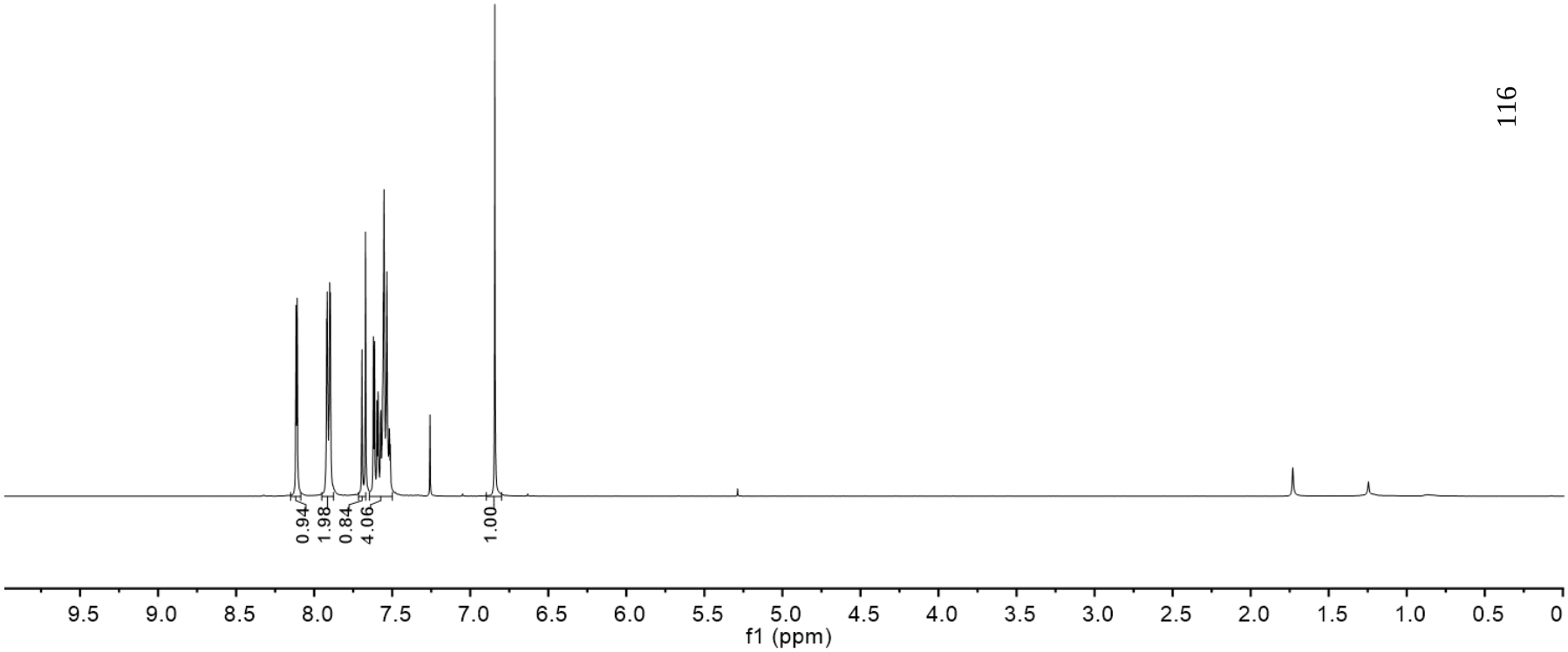

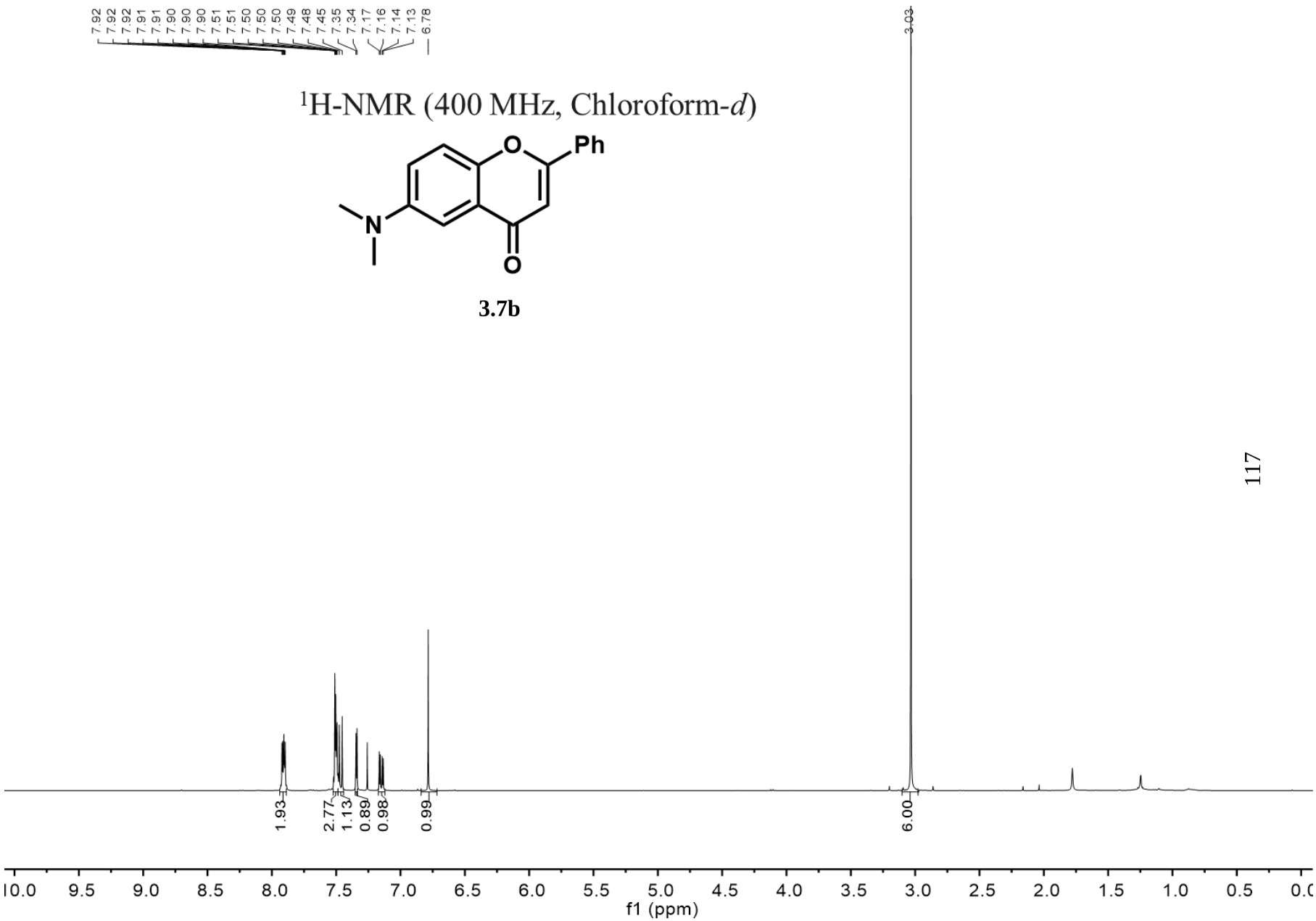
7.92
7.92
7.92
7.91
7.91
7.90
7.90
7.90
7.51
7.51
7.50
7.50
7.50
7.49
7.48
7.45
7.35
7.34
7.17
7.16
7.14
7.13
6.78
3.03
1H-NMR (400 MHz, Chloroform-d)
O
Ph
N
O
3.7b
1.93
2.77
1.13
0.89
0.98
0.99
6.00
10.0
9.5
9.0
8.5
8.0
7.5
7.0
6.5
6.0
5.5
5.0
4.5
4.0
3.5
3.0
2.5
2.0
1.5
1.0
0.5
0.0
f1 (ppm)

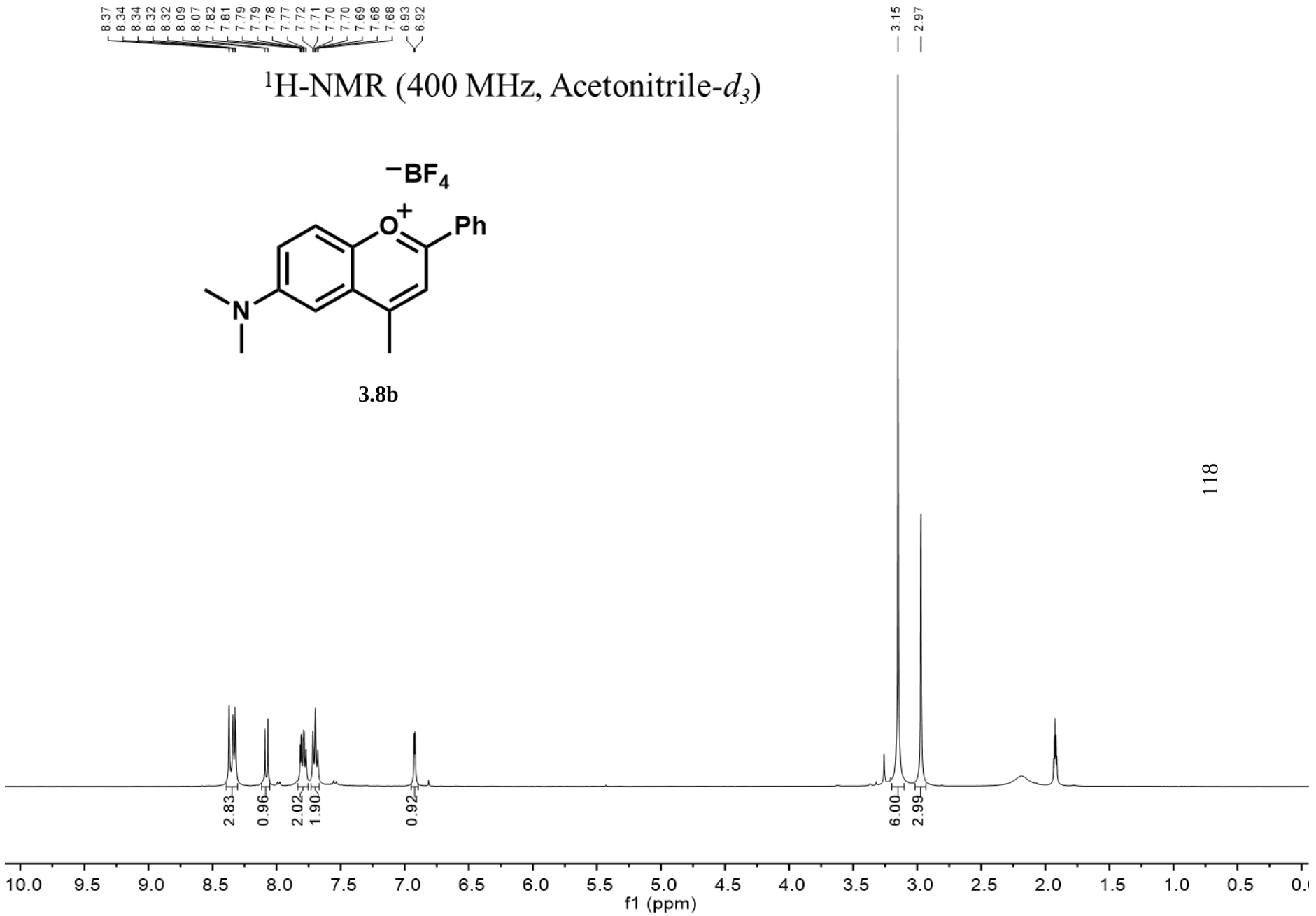
8.37
8.34
8.34
8.32
8.32
8.09
8.07
7.82
7.81
7.79
7.79
7.78
7.77
7.72
7.71
7.70
7.70
7.69
7.68
7.68
6.93
6.92
3.15
2.97
^{1}H-NMR (400 MHz, Acetonitrile-d_3)
$^-BF_4$
O$^+$
Ph
N
3.8b
2.83
0.96
2.02
1.90
0.92
6.00
2.99
10.0
9.5
9.0
8.5
8.0
7.5
7.0
6.5
6.0
5.5
5.0
4.5
4.0
3.5
3.0
2.5
2.0
1.5
1.0
0.5
f1 (ppm)

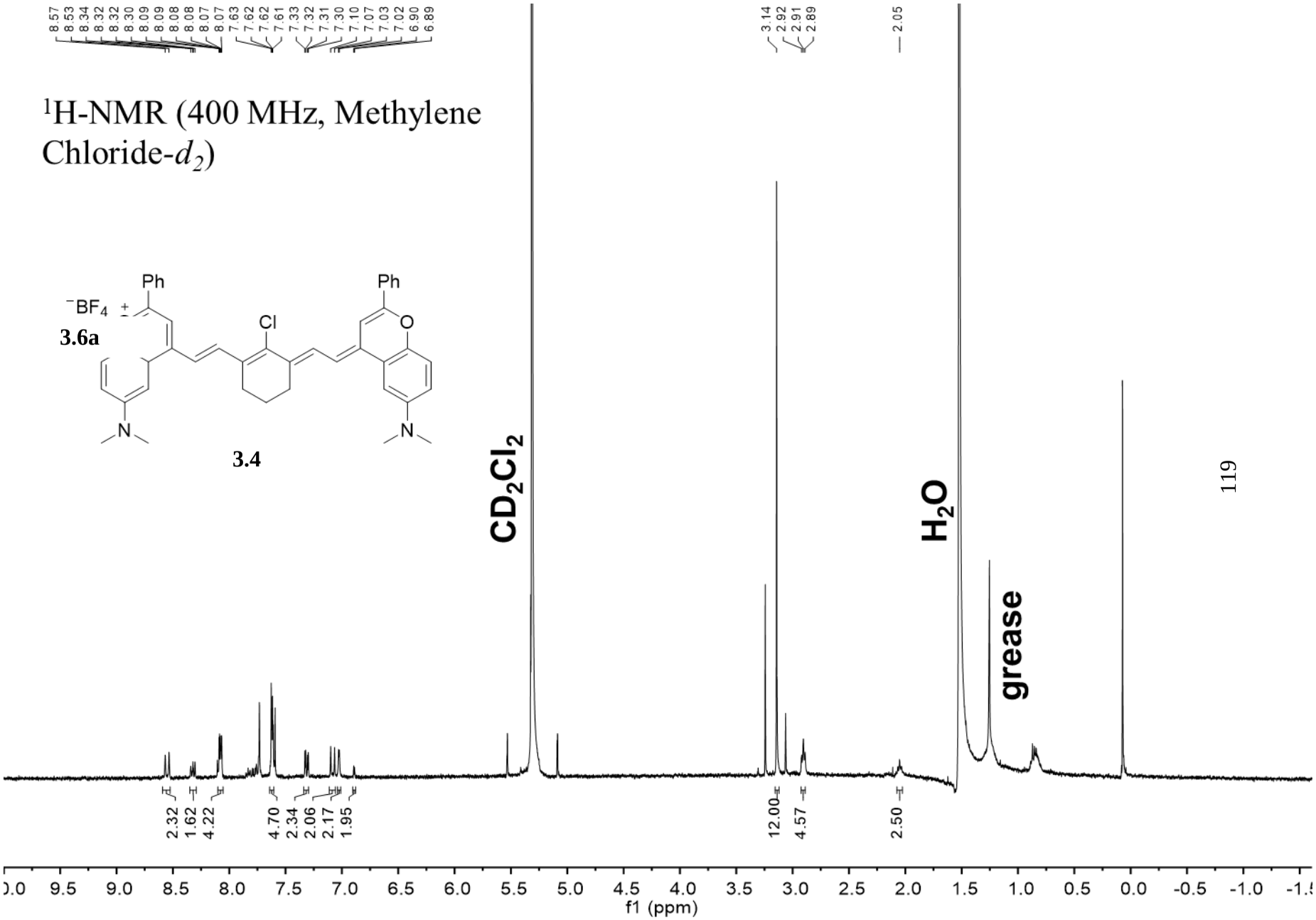
8.57
8.53
8.34
8.32
8.32
8.30
8.09
8.09
8.08
8.08
8.07
8.07
7.63
7.62
7.62
7.61
7.33
7.32
7.31
7.30
7.10
7.07
7.03
7.02
6.90
6.89
3.14
2.92
2.91
2.89
2.05
1H-NMR (400 MHz, Methylene Chloride-d2)
Ph
BF4
3.6a
Cl
Ph
O
N
N
3.4
CD2Cl2
H2O
grease
2.32
1.62
4.22
4.70
2.34
2.06
2.17
1.95
12.00
4.57
2.50
f1 (ppm)

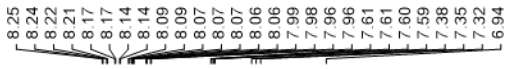

^{1}H-NMR (300 MHz, Chloroform-*d*)

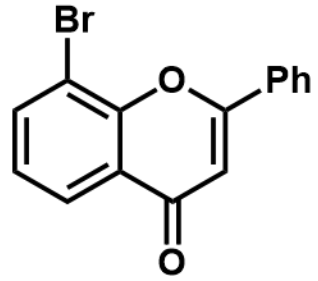

3.6c

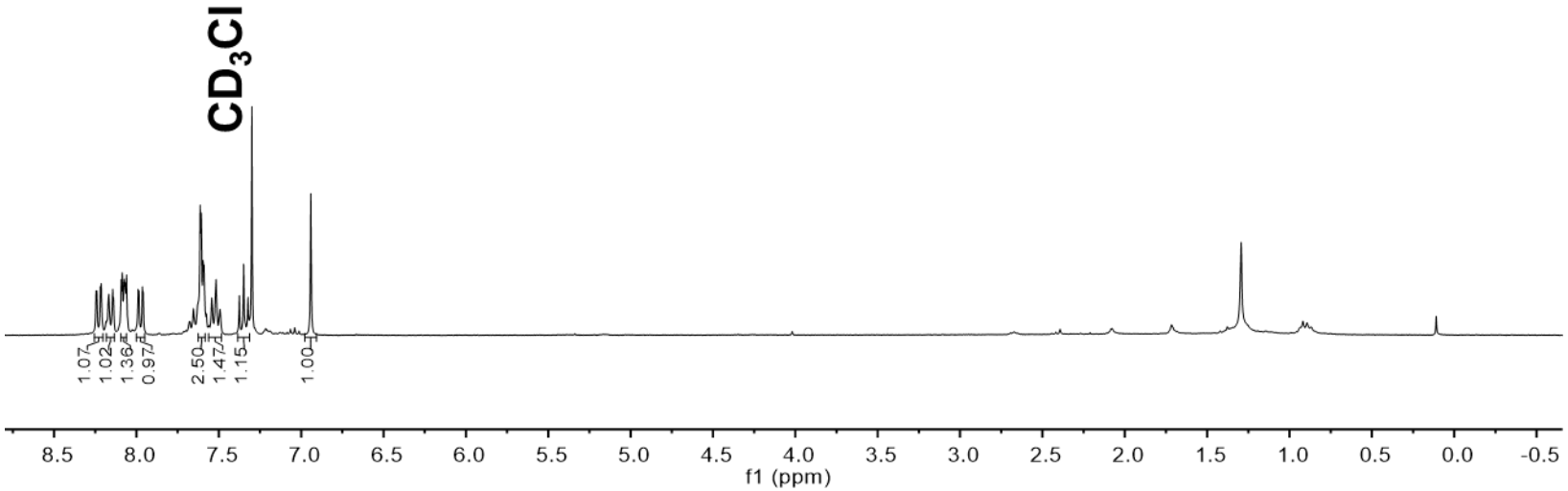

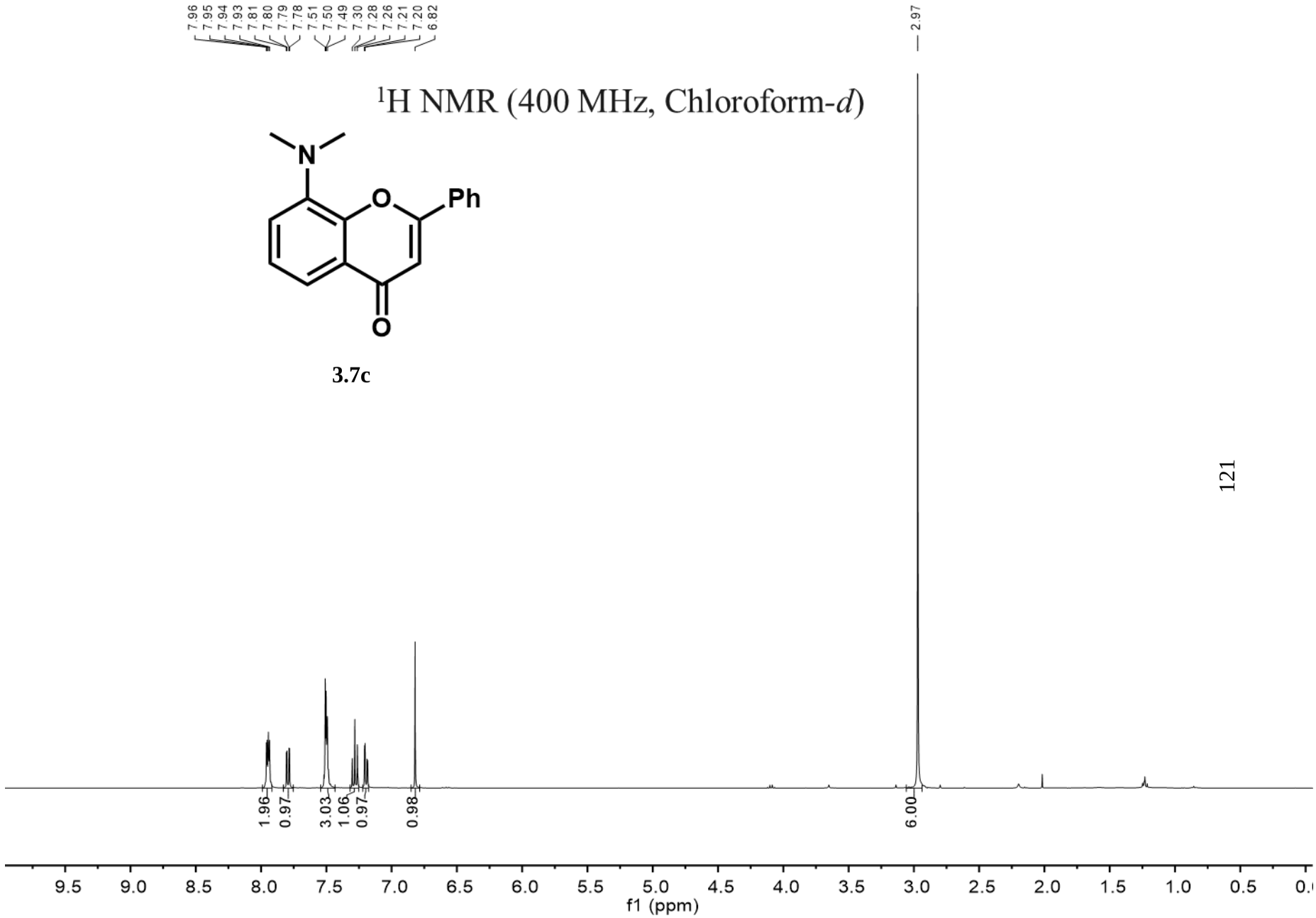
7.96
7.95
7.94
7.93
7.81
7.80
7.79
7.78
7.51
7.50
7.49
7.30
7.28
7.26
7.21
7.20
6.82
2.97
1H NMR (400 MHz, Chloroform-d)
N
O
Ph
O
3.7c
1.96
0.97
3.03
1.06
0.97
0.98
6.00
9.5
9.0
8.5
8.0
7.5
7.0
6.5
6.0
5.5
5.0
4.5
4.0
3.5
3.0
2.5
2.0
1.5
1.0
0.5
f1 (ppm)

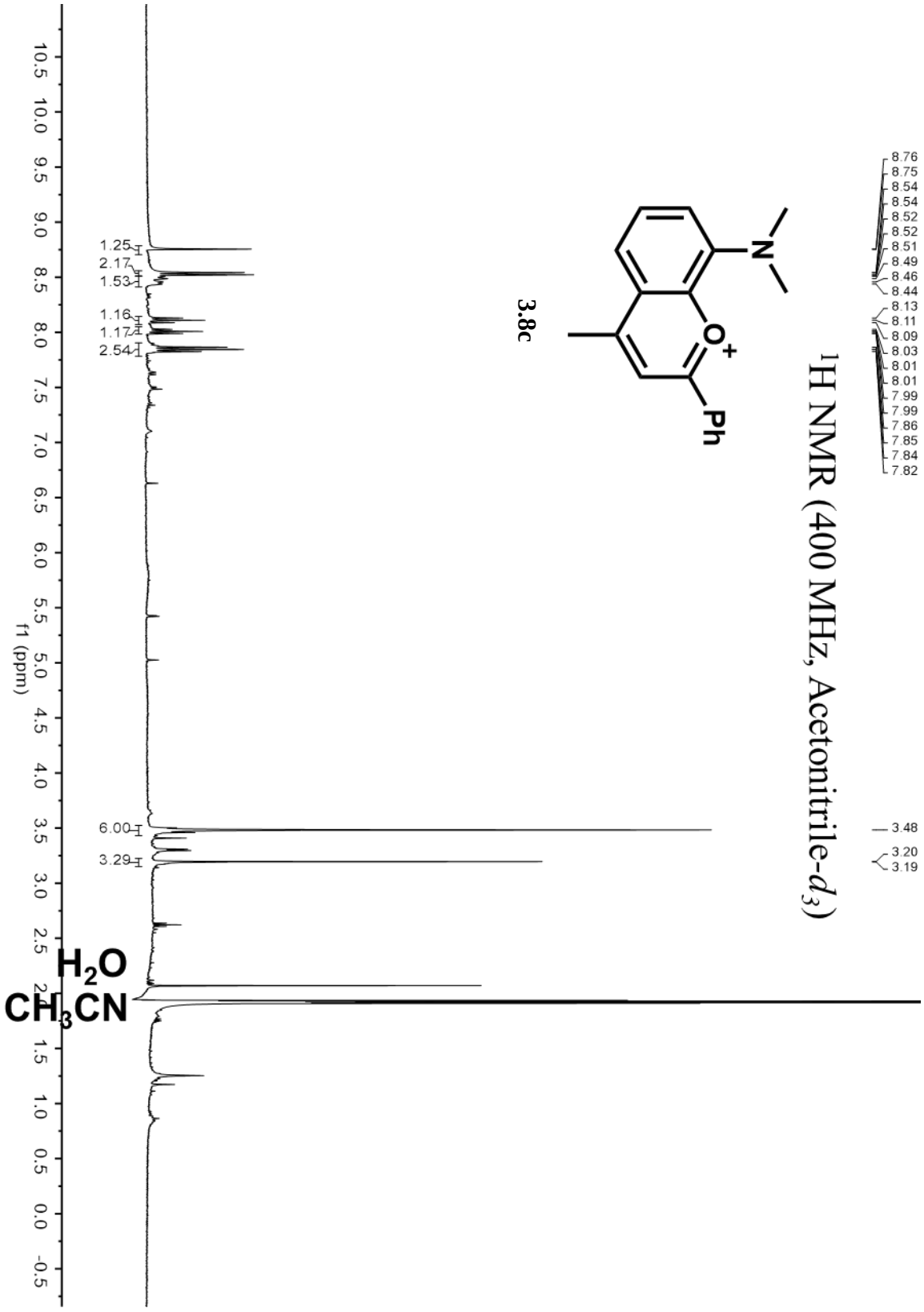
^{1}H NMR (400 MHz, Acetonitrile-d_3)
3.8c
Ph
8.76
8.75
8.54
8.54
8.52
8.52
8.51
8.49
8.46
8.44
8.13
8.11
8.09
8.03
8.01
8.01
7.99
7.99
7.86
7.85
7.84
7.82
1.25
2.17
1.53
1.16
1.17
2.54
6.00
3.29
3.48
3.20
3.19
H_2O
CH_3CN
f1 (ppm)

^{1}H NMR (400 MHz, Chloroform-*d*)

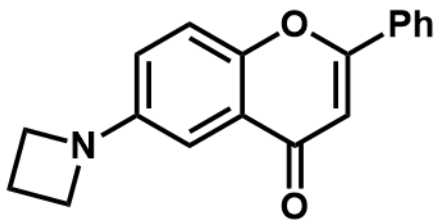

3.14

123

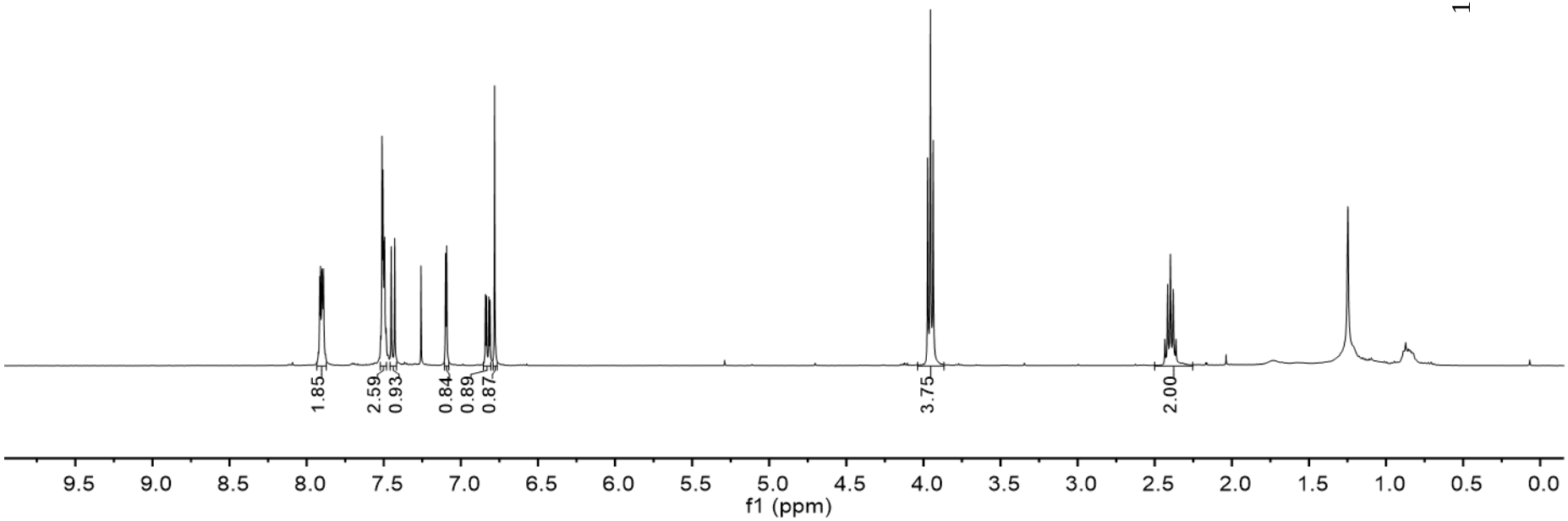

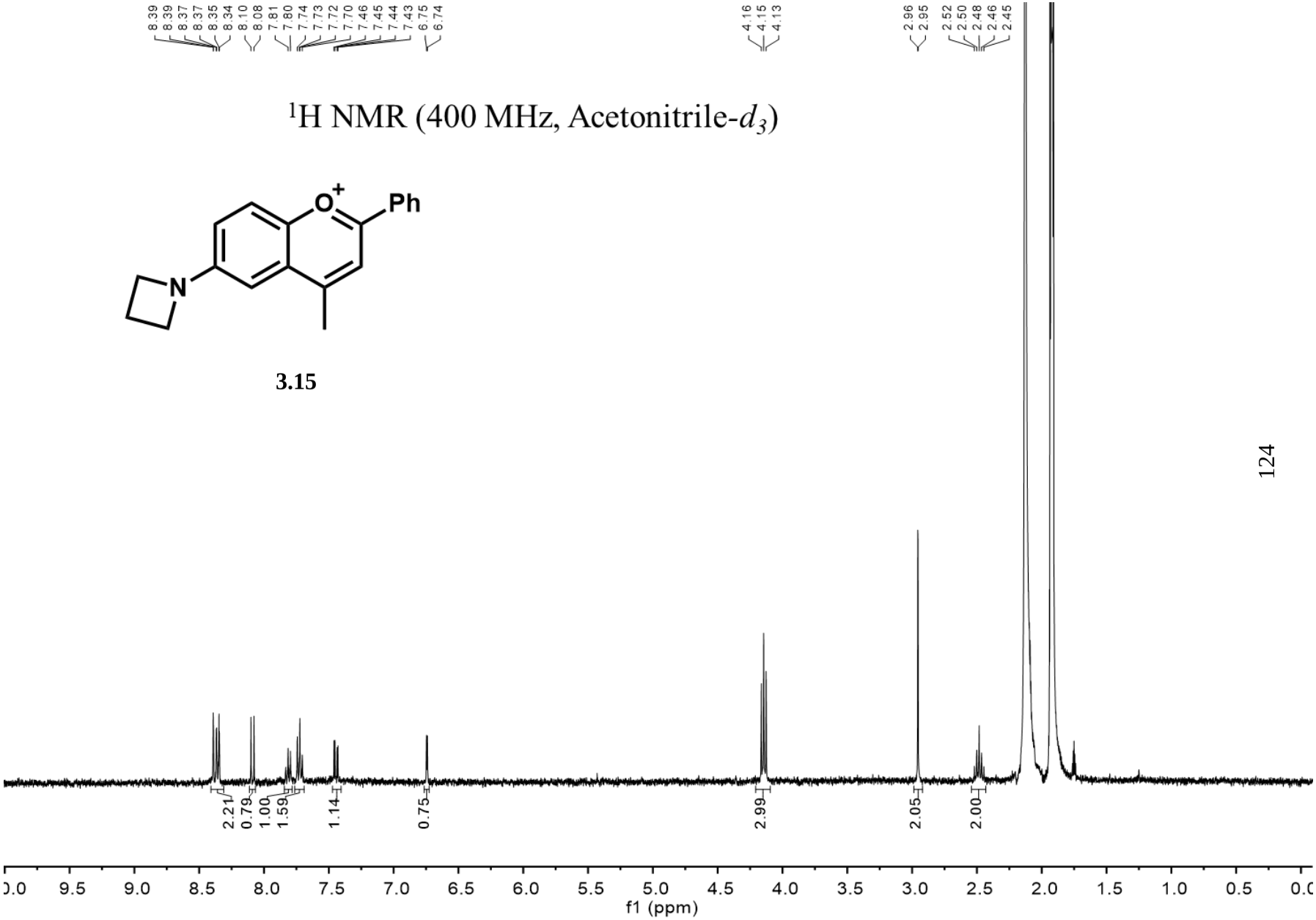

^{1}H NMR (400 MHz, Acetonitrile-d_3)

3.15

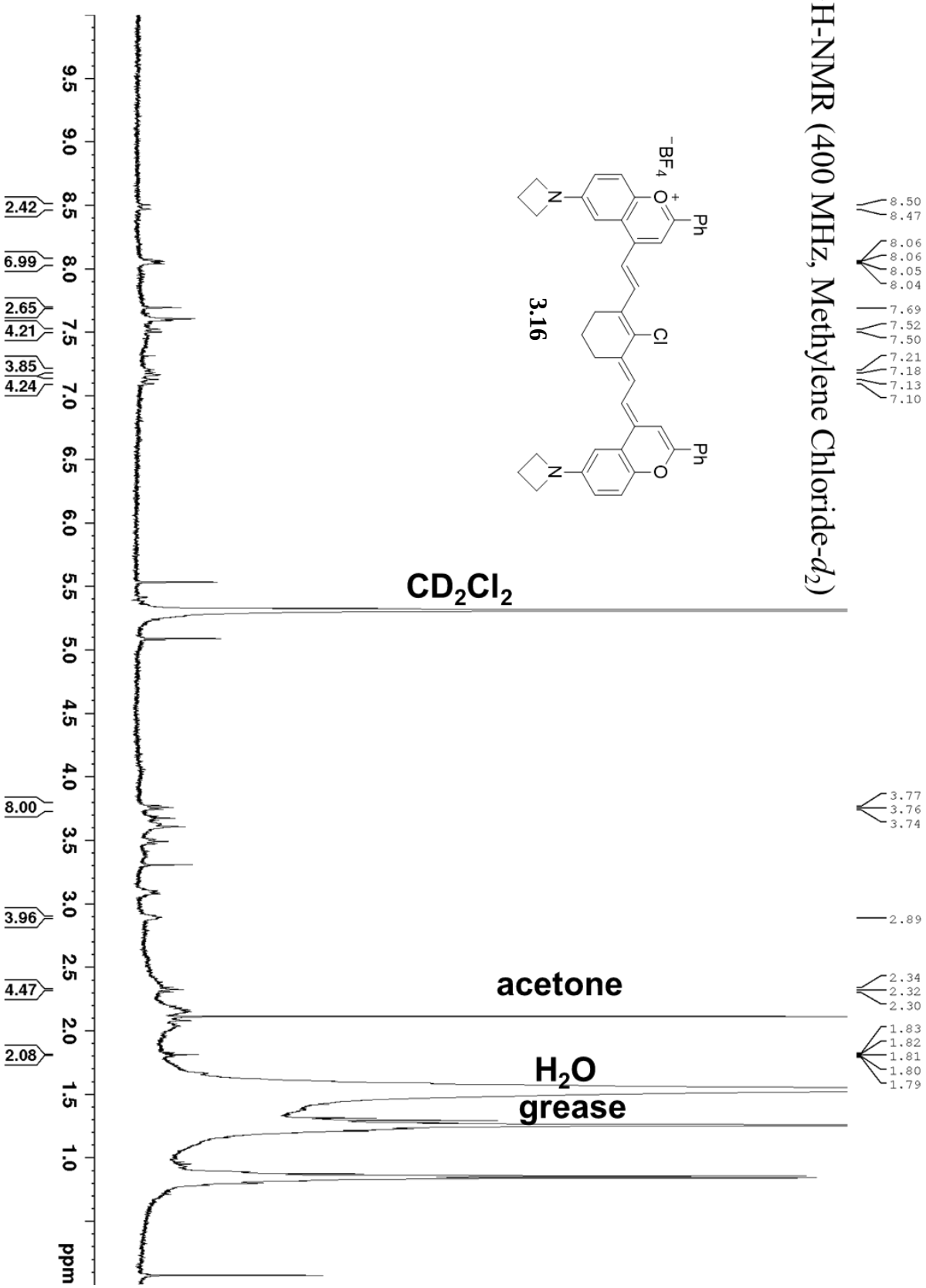
^{1}H-NMR (400 MHz, Methylene Chloride-d_2)
3.16
CD_2Cl_2
acetone
H_2O
grease
ppm

3.6.2 [1]C NMR Spectra

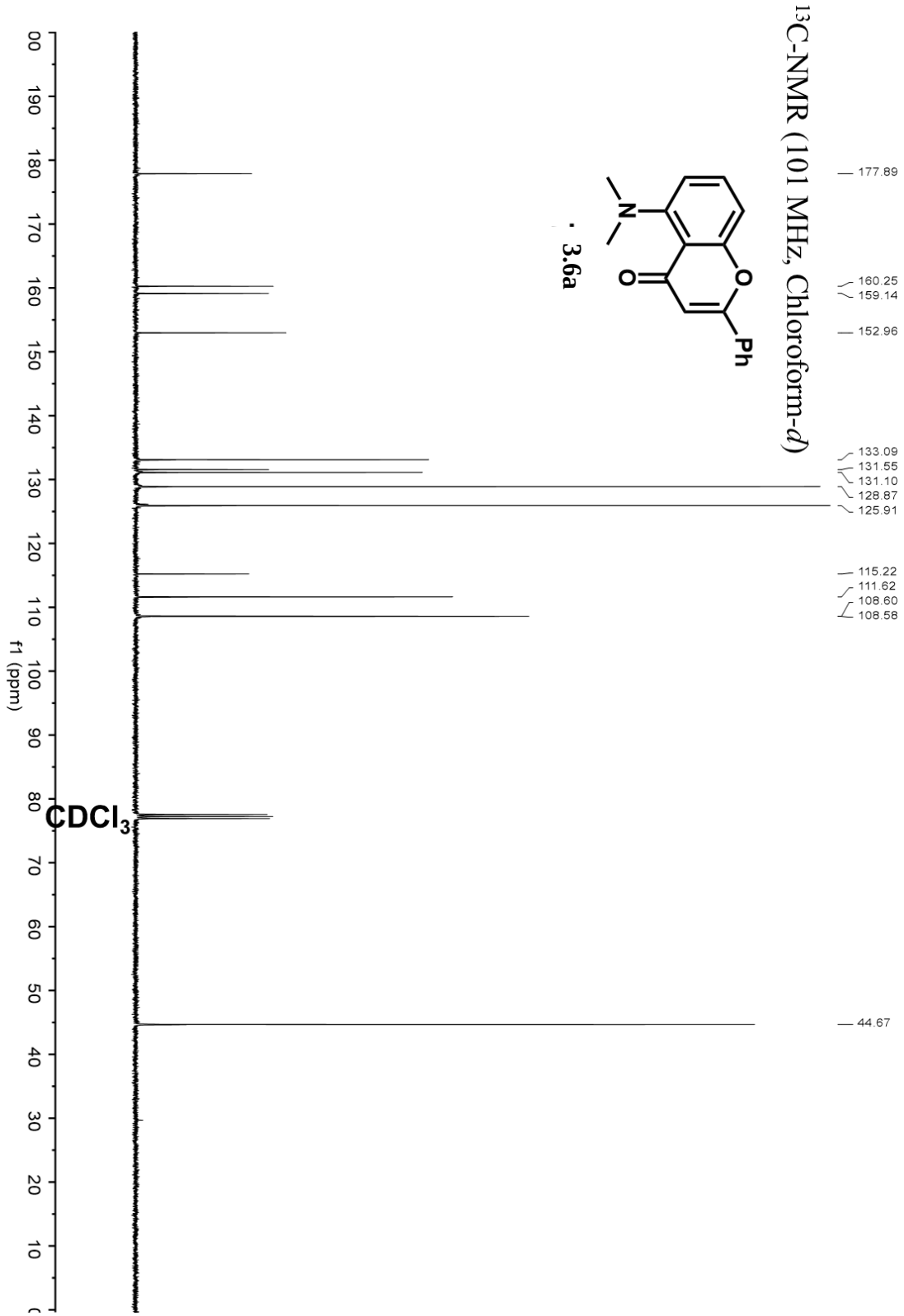

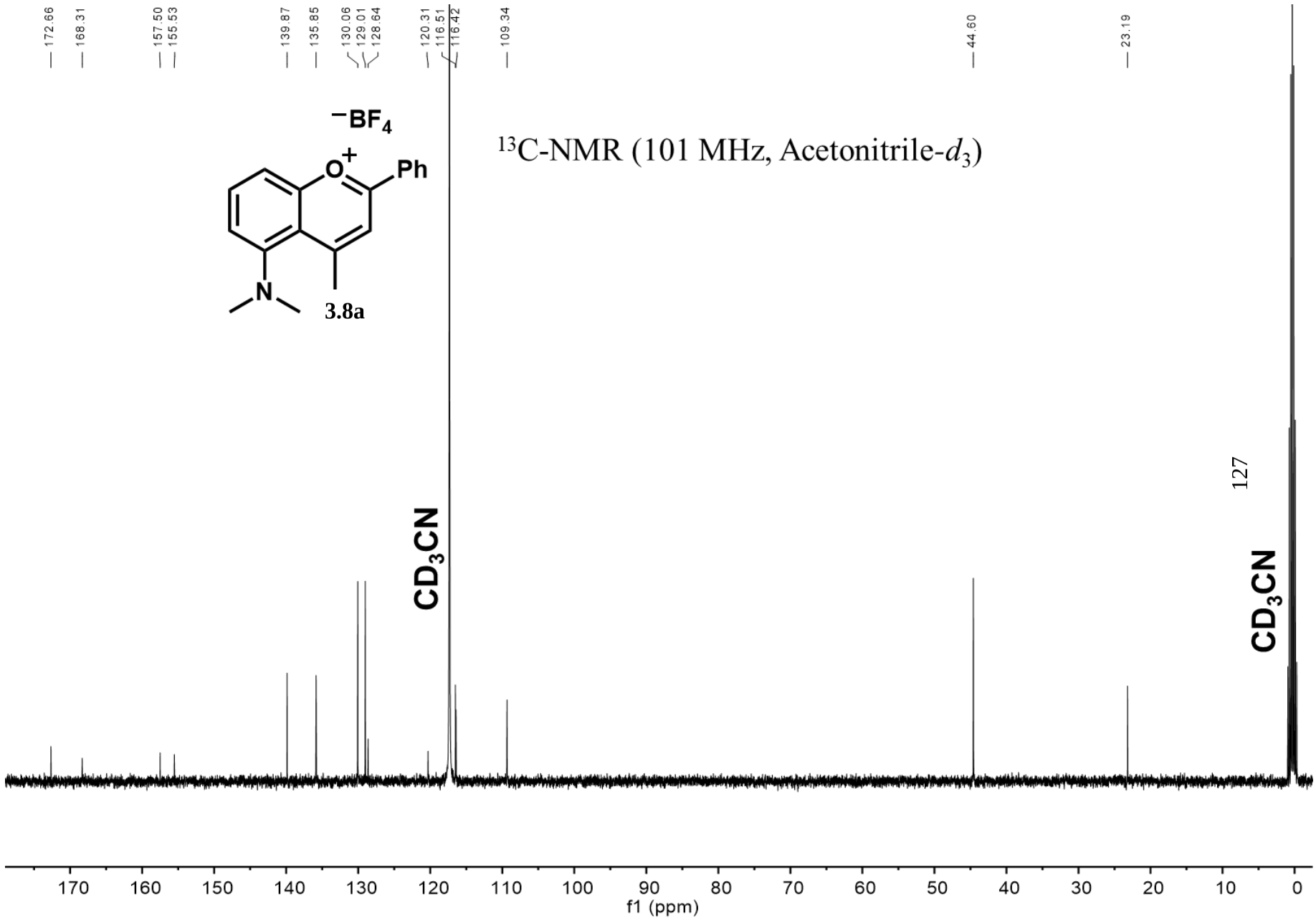
172.66
168.31
157.50
155.53
139.87
135.85
130.06
129.01
128.64
120.31
116.51
116.42
109.34
44.60
23.19
$^{-}BF_4$
O
Ph
N
3.8a
^{13}C-NMR (101 MHz, Acetonitrile-d_3)
CD_3CN
127
CD_3CN
170
160
150
140
130
120
110
100
90
80
70
60
50
40
30
20
10
0
f1 (ppm)

^{13}C-NMR (101 MHz, Chloroform-*d*)

3.6b

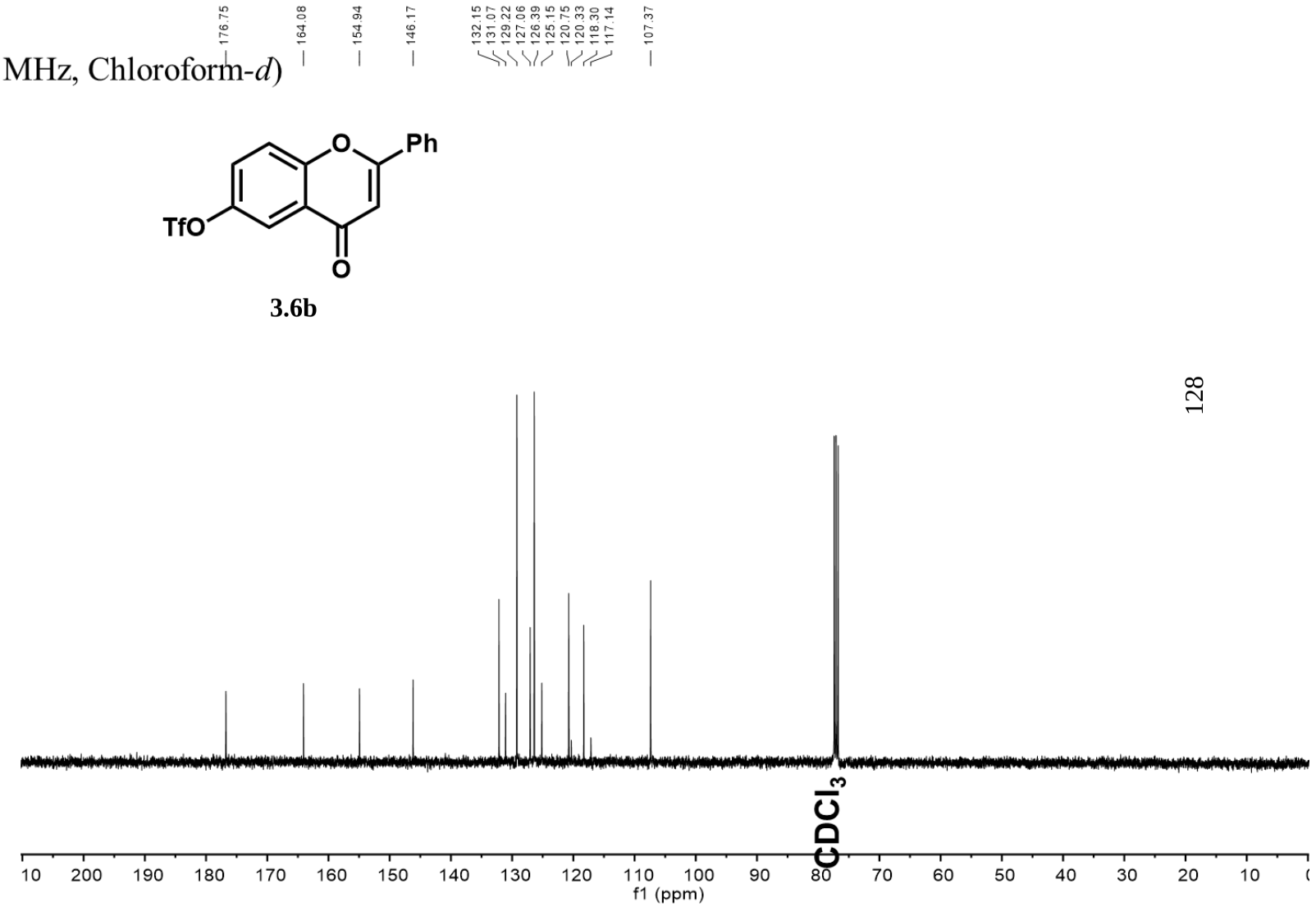

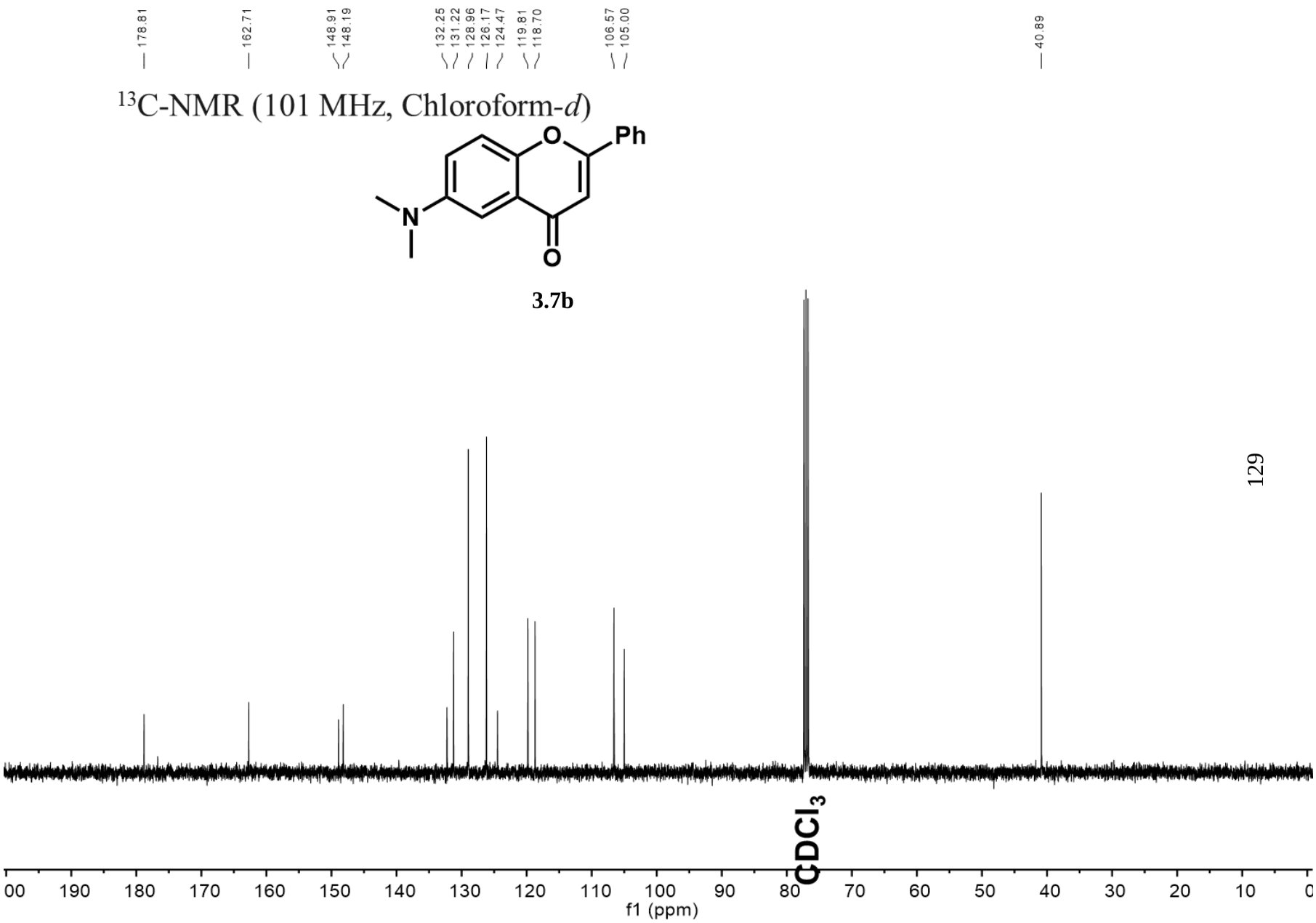
178.81
162.71
148.91
148.19
132.25
131.22
128.96
126.17
124.47
119.81
118.70
106.57
105.00
40.89
13C-NMR (101 MHz, Chloroform-d)
O
Ph
N
O
3.7b
129
CDCl3
00 190 180 170 160 150 140 130 120 110 100 90 80 70 60 50 40 30 20 10 0
f1 (ppm)

^{13}C-NMR (101 MHz, Acetonitrile-d_3)

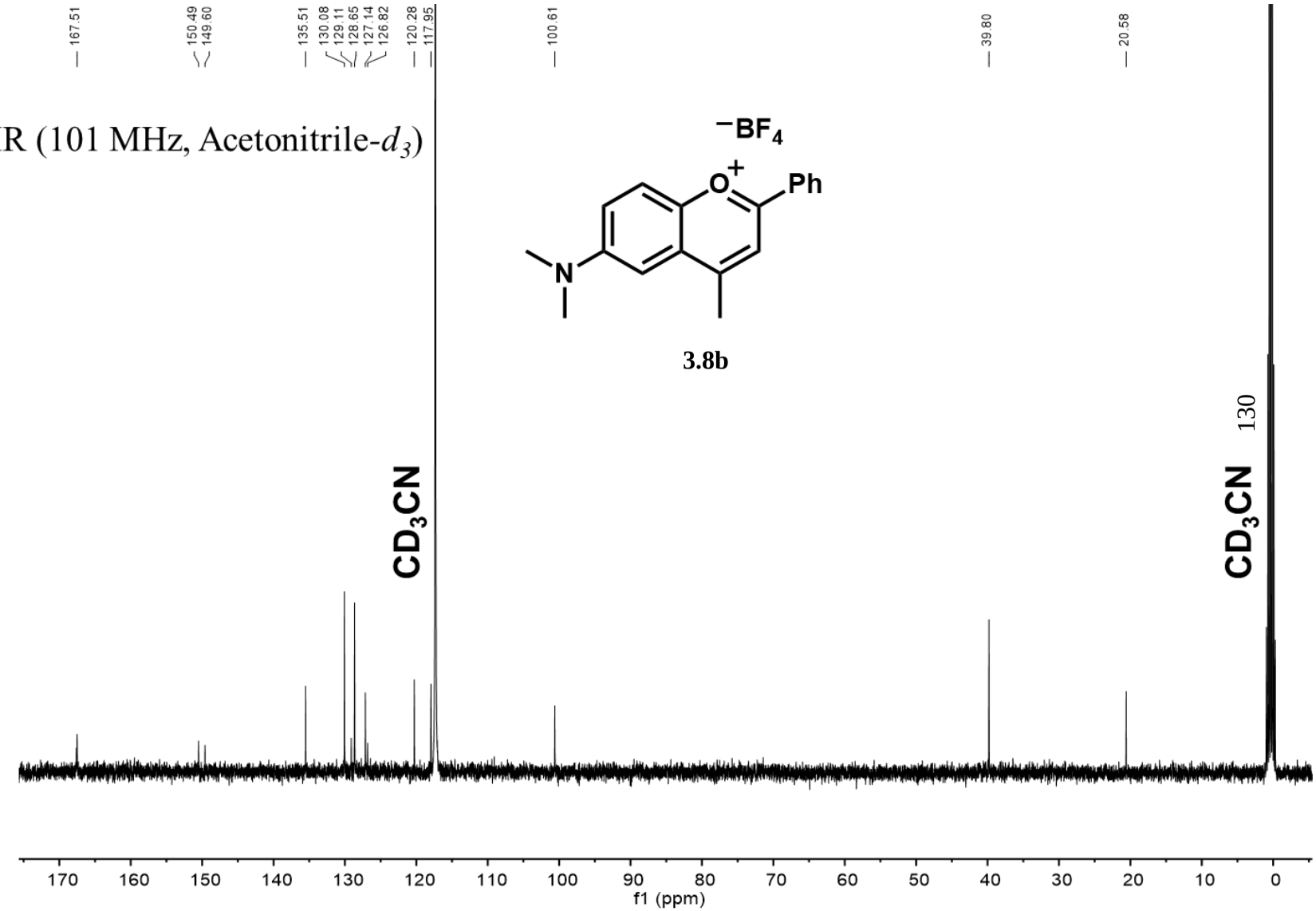

3.8b

^{1}H NMR (400 MHz, Chloroform-*d*)

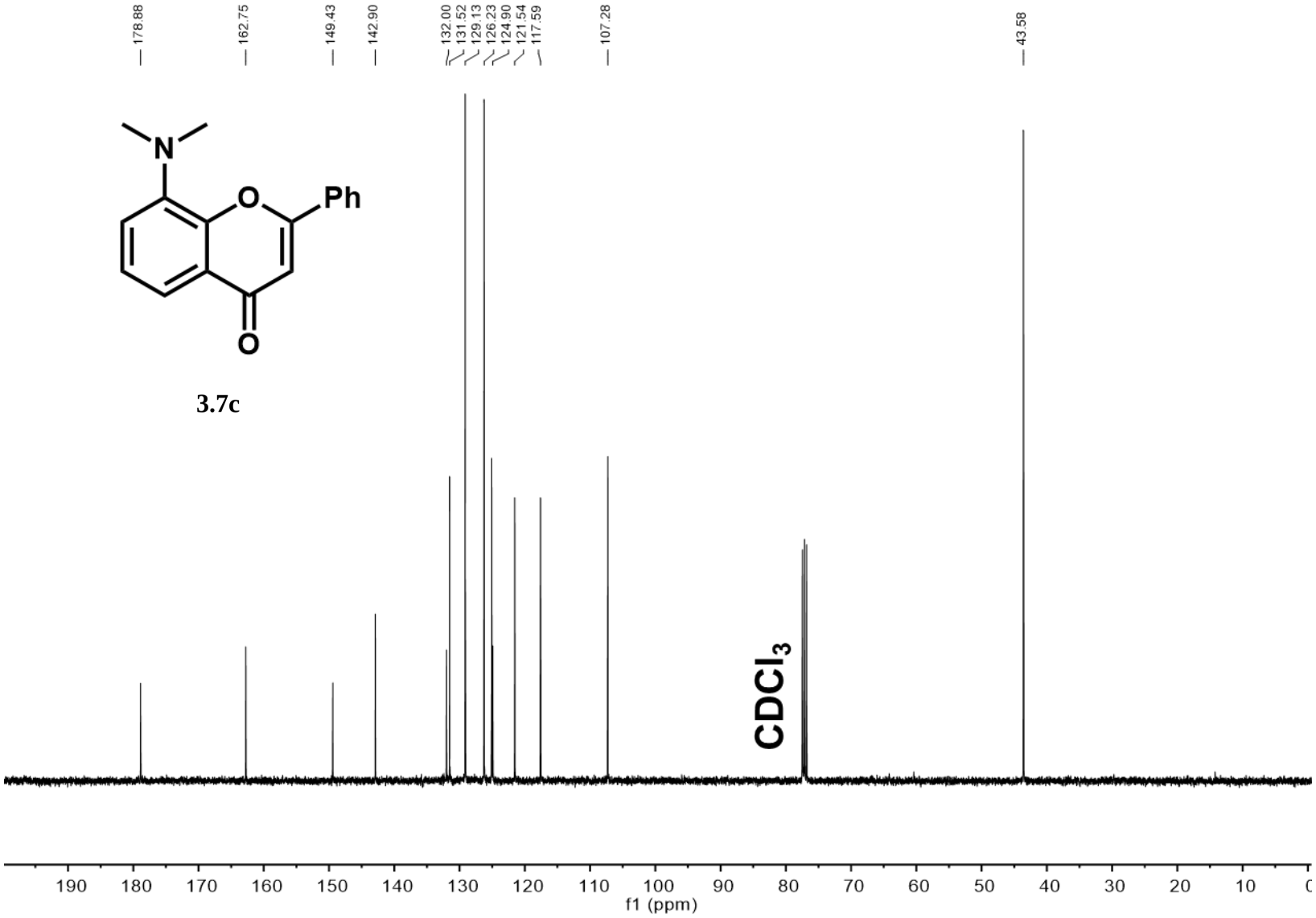

3.7c

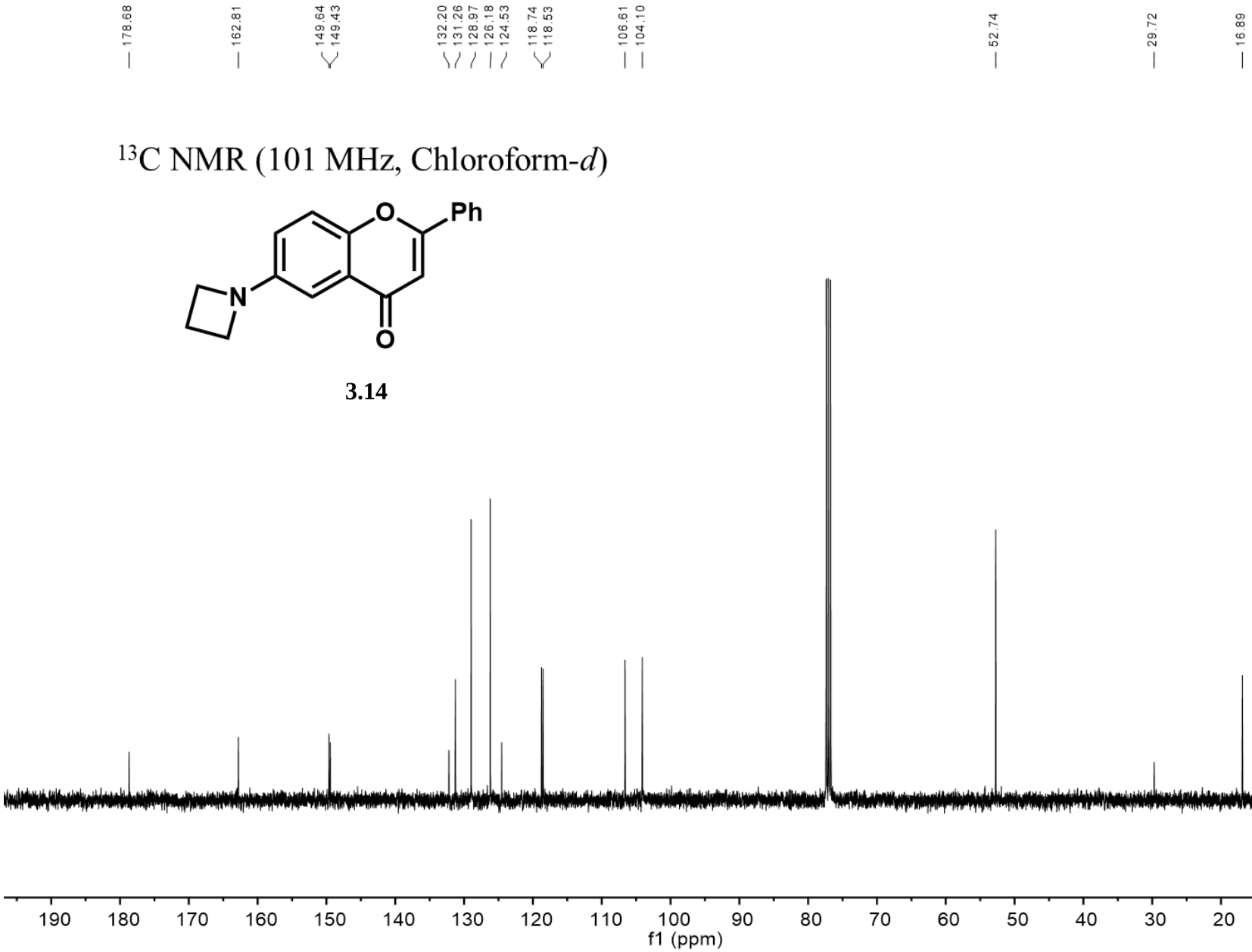

^{13}C NMR (101 MHz, Chloroform-*d*)

3.14

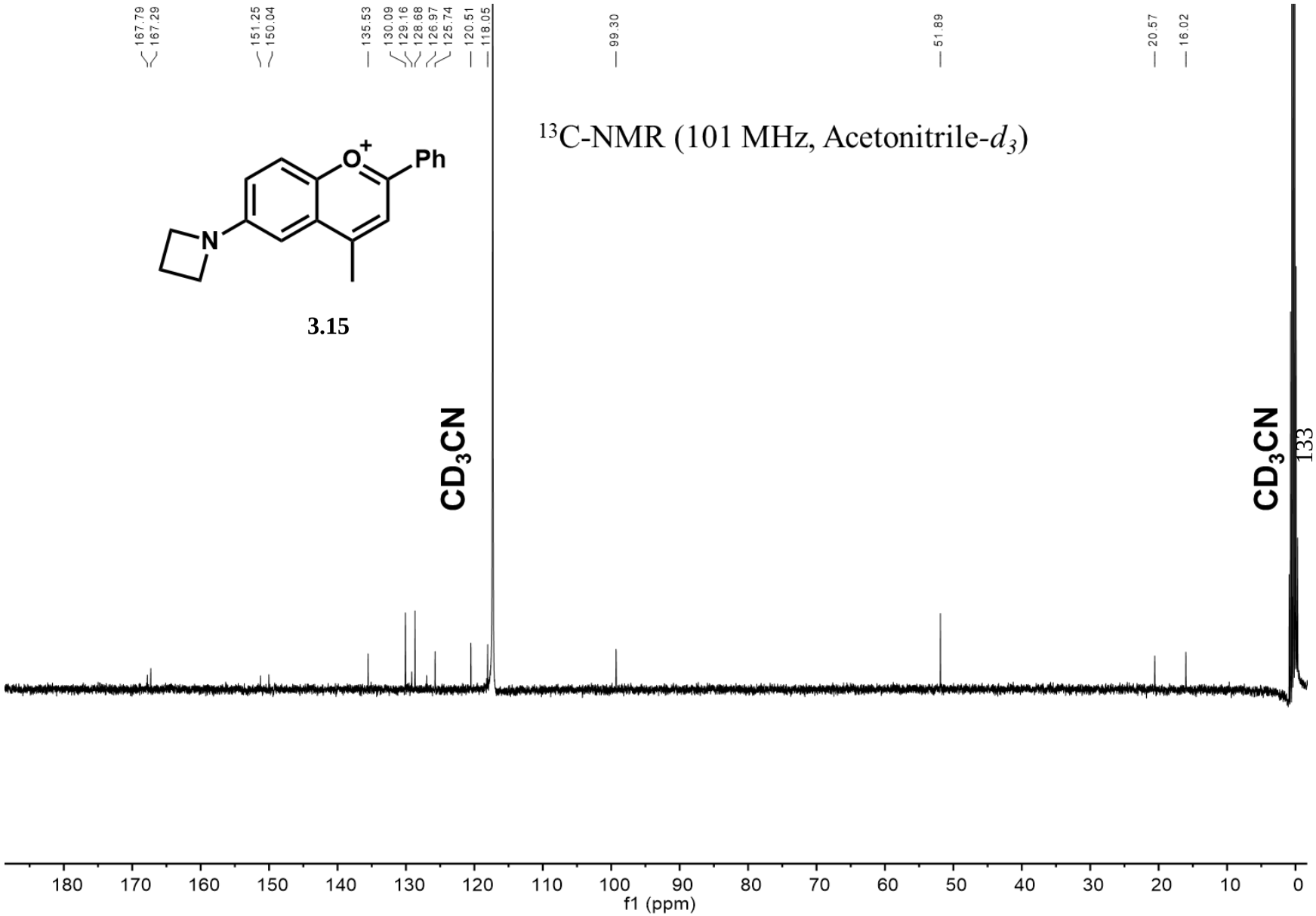
167.79
167.29
151.25
150.04
135.53
130.09
129.16
128.68
126.97
125.74
120.51
118.05
99.30
51.89
20.57
16.02
^{13}C-NMR (101 MHz, Acetonitrile-d_3)
O+
Ph
N
3.15
CD3CN
CD3CN
133
180
170
160
150
140
130
120
110
100
90
80
70
60
50
40
30
20
10
0
f1 (ppm)

3.6.3 Absorption/Emission Spectra

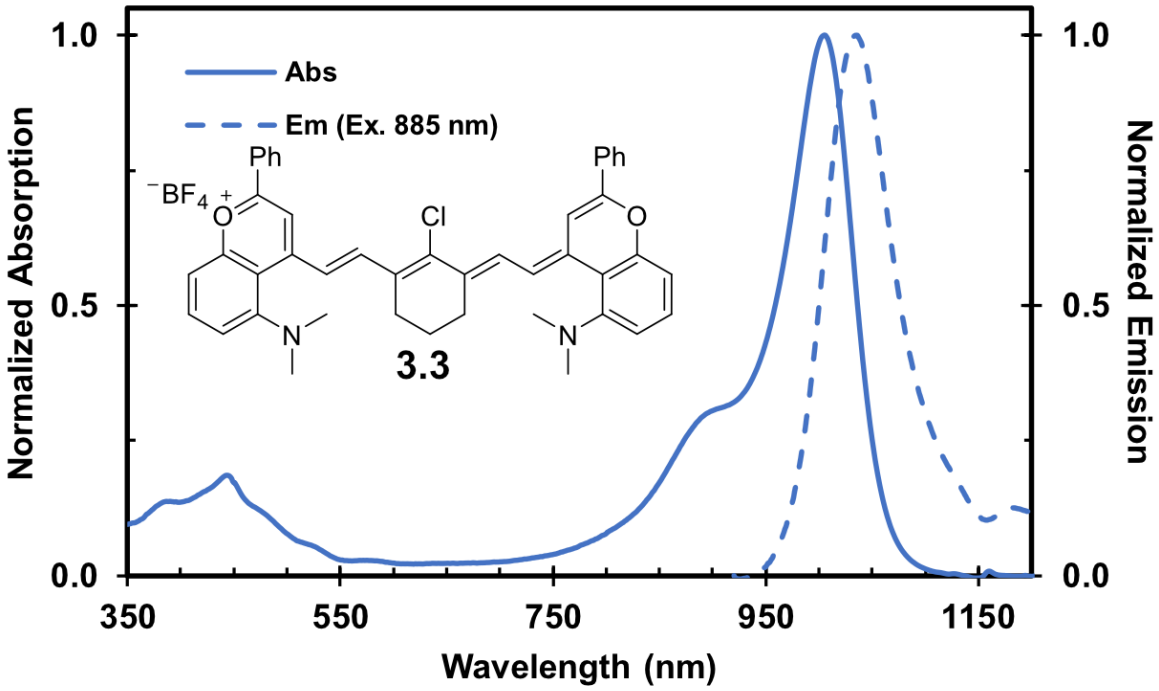

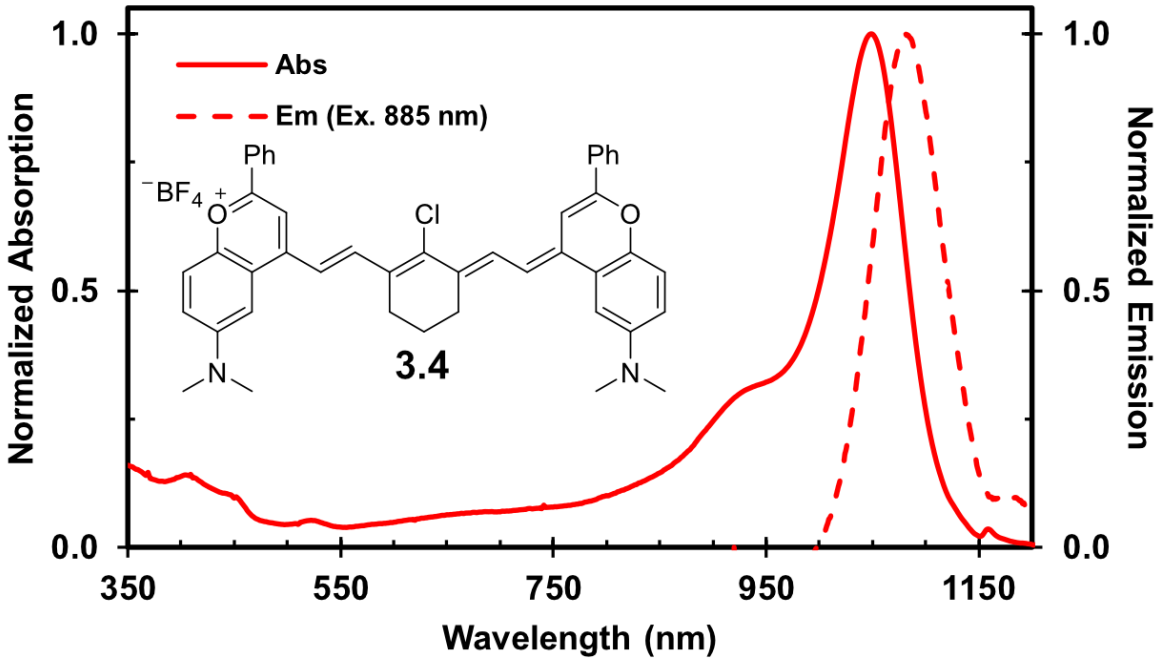

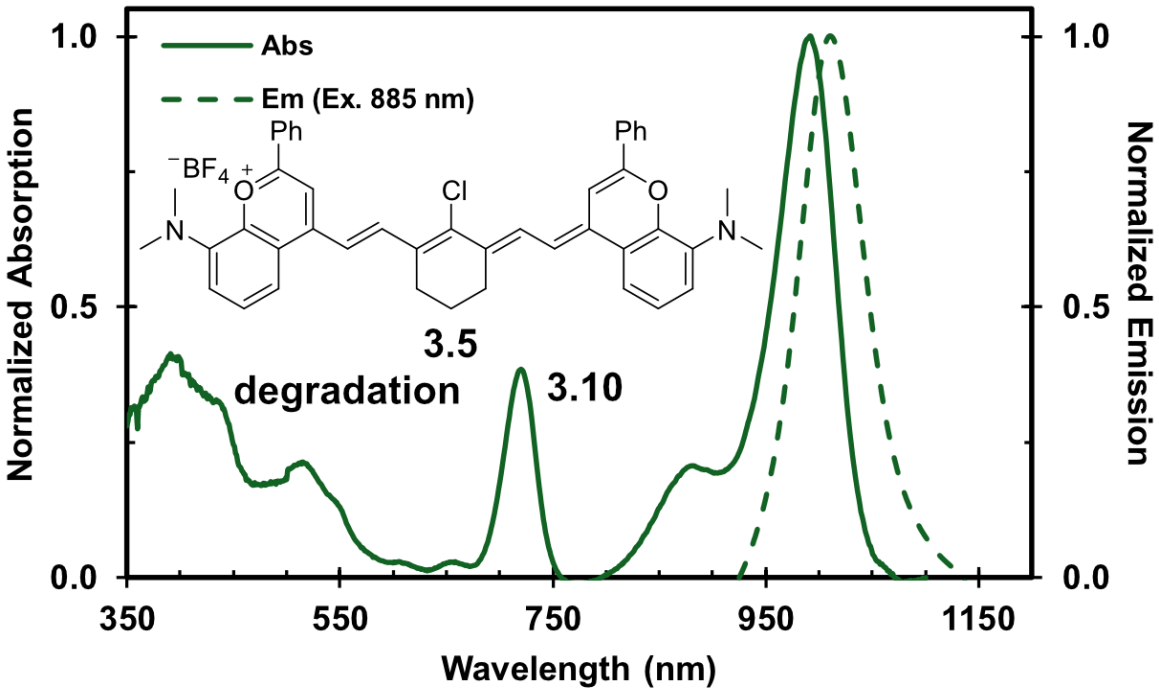
Abs
Em (Ex. 885 nm)
Ph
Ph
$^{-}BF_4$ +
O
Cl
O
N
N
3.5
degradation
3.10
Normalized Absorption
Normalized Emission
1.0
0.5
0.0
350
550
750
950
1150
Wavelength (nm)

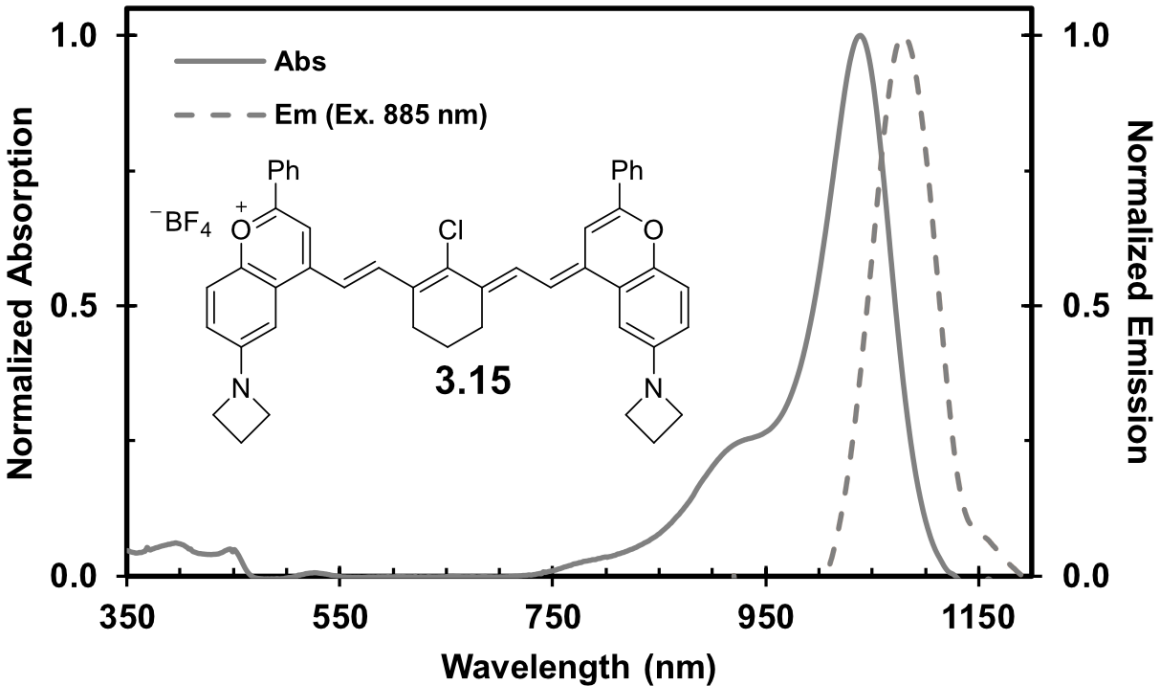
Abs
Em (Ex. 885 nm)
Ph
Ph
$^{-}BF_4$ +
O
Cl
O
N
N
3.15
Normalized Absorption
Normalized Emission
1.0
0.5
0.0
350
550
750
950
1150
Wavelength (nm)

References:

(1) Schnermann, M. J. Chemical Biology: Organic Dyes for Deep Bioimaging. *Nature*., **2017**, 176–177.

(2) Thimsen, E.; Sadtler, B.; Berezin, M. Y. Shortwave-Infrared (SWIR) Emitters for Biological Imaging: A Review of Challenges and Opportunities. *Nanophotonics* **2017**, *6* (5), 1043–1054.

(3) Weissleder, R. A Clearer Vision for in Vivo Imaging. *Nat. Biotechnol.* **2001**, *19* (4), 316–317.

(4) Smith, A. M.; Mancini, M. C.; Nie, S. *Bioimaging: Second Window for in Vivo Imaging*; *Nature Nanotech.* **2009**, *4*, 710-711.

(5) Carr, J. A.; Franke, D.; Caram, J. R.; Perkinson, C. F.; Saif, M.; Askoxylakis, V.; Datta, M.; Fukumura, D.; Jain, R. K.; Bawendi, M. G.; et al. Shortwave Infrared Fluorescence Imaging with the Clinically Approved Near-Infrared Dye Indocyanine Green. *Proc. Natl. Acad. Sci. U. S. A.* **2018**, *115*, 4465-4470.

(6) Hong, G.; Lee, J. C.; Robinson, J. T.; Raaz, U.; Xie, L.; Huang, N. F.; Cooke, J. P.; Dai, H. Multifunctional in Vivo Vascular Imaging Using Near-Infrared II Fluorescence. *Nat. Med.* **2012**, *18* (12), 1841–1846.

(7) Welsher, K.; Liu, Z.; Sherlock, S. P.; Robinson, J. T.; Chen, Z.; Daranciang, D.; Dai, H. A Route to Brightly Fluorescent Carbon Nanotubes for Near-Infrared Imaging in Mice. *Nat. Nanotechnol.* **2009**, *4* (11), 773–780.

(8) Diao, S.; Blackburn, J. L.; Hong, G.; Antaris, A. L.; Chang, J.; Wu, J. Z.; Zhang, B.; Cheng, K.; Kuo, C. J.; Dai, H. Fluorescence Imaging In Vivo at Wavelengths beyond 1500 Nm. *Angew. Chemie Int. Ed.* **2015**, *54* (49), 14758–14762.

(9) Robinson, J. T.; Hong, G.; Liang, Y.; Zhang, B.; Yaghi, O. K.; Dai, H. In Vivo Fluorescence Imaging in the Second Near-Infrared Window with Long Circulating Carbon Nanotubes Capable of Ultrahigh Tumor Uptake. *J. Am. Chem. Soc.* **2012**, *134* (25), 10664–10669.

(10) Naczynski, D. J.; Tan, M. C.; Zevon, M.; Wall, B.; Kohl, J.; Kulesa, A.; Chen, S.; Roth, C. M.; Riman, R. E.; Moghe, P. V. Rare-Earth-Doped Biological Composites as in Vivo Shortwave Infrared Reporters. *Nat. Commun.* **2013**, *4*, 2199.

(11) Naczynski, D. J.; Tan, M. C.; Riman, R. E.; Moghe, P. V. Rare Earth Nanoprobes for Functional Biomolecular Imaging and Theranostics. *Journal of Materials Chemistry B.* **2014**, *2* (20), 2958-2973.

(12) Naczynski, D. J.; Sun, C.; Türkcan, S.; Jenkins, C.; Koh, A. L.; Ikeda, D.; Pratx, G.; Xing, L. X-Ray-Induced Shortwave Infrared Biomedical Imaging Using Rare-Earth Nanoprobes. *Nano Lett.* **2015**, *15* (1), 96–102.

(13) Bruns, O. T.; Bischof, T. S.; Harris, D. K.; Franke, D.; Shi, Y.; Riedemann, L.; Bartelt, A.; Jaworski, F. B.; Carr, J. A.; Rowlands, C. J.; et al. Next-Generation in Vivo Optical Imaging with Short-Wave Infrared Quantum Dots. *Nat. Biomed. Eng.* **2017**, *1* (4).

(14) Dong, B.; Li, C.; Chen, G.; Zhang, Y.; Zhang, Y.; Deng, M.; Wang, Q. Facile Synthesis of Highly Photoluminescent Ag2Se Quantum Dots as a New Fluorescent Probe in the Second Near-Infrared Window for in Vivo Imaging. *Chem. Mater.* **2013**, *25* (12), 2503–2509.

(15) Hong, G.; Robinson, J. T.; Zhang, Y.; Diao, S.; Antaris, A. L.; Wang, Q.; Dai, H. In Vivo Fluorescence Imaging with Ag_2S Quantum Dots in the Second Near-Infrared Region. *Angew. Chemie Int. Ed.* **2012**, *51* (39), 9818–9821.

(16) Ding, F.; Zhan, Y.; Lu, X.; Sun, Y. Recent Advances in Near-Infrared II Fluorophores for Multifunctional Biomedical Imaging. *Chem. Sci.* **2018**, *19*, 4370-4380.

(17) Yang, S. T.; Wang, X.; Jia, G.; Gu, Y.; Wang, T.; Nie, H.; Ge, C.; Wang, H.; Liu, Y. Long-Term Accumulation and Low Toxicity of Single-Walled Carbon Nanotubes in Intravenously Exposed Mice. *Toxicol. Lett.* **2008**, *181* (3), 182–189.

(18) Liu, Z.; Davis, C.; Cai, W.; He, L.; Chen, X.; Dai, H. Circulation and Long-Term Fate of Functionalized, Biocompatible Single-Walled Carbon Nanotubes in Mice Probed by Raman Spectroscopy. *Proc. Natl. Acad. Sci. U. S. A.* **2008**, *105* (5), 1410–1415.

(19) Choi, H. S.; Liu, W.; Misra, P.; Tanaka, E.; Zimmer, J. P.; Bawendi, M. G.; Frangioni, J. V. Renal Clearance of Quantum Dots. *Nat. Biotechnol.* **2007**, *25* (10), 1165-1170.

(20) Fitzpatrick, J. A. J.; Andreko, S. K.; Ernst, L. A.; Waggoner, A. S.; Ballou, B.; Bruchez, M. P. Long-Term Persistence and Spectral Blue Shifting of Quantum Dots in Vivo. *Nano Lett.* **2009**, *9* (7), 2736-2741.

(21) Lavis, L. D.; Raines, R. T. Bright Ideas for Chemical Biology. *ACS Chem. Bio.* **2008**, *3* (3), 142-155.

(22) Casalboni, M.; De Matteis, F.; Prosposito, P.; Quatela, A.; Sarcinelli, F. Fluorescence Efficiency of Four Infrared Polymethine Dyes. *Chem. Phys. Lett.* **2003**, *373* (3–4), 372–378.

(23) Wang, S.; Fan, Y.; Li, D.; Sun, C.; Lei, Z.; Lu, L.; Wang, T.; Zhang, F. Anti-Quenching NIR-II Molecular Fluorophores for in Vivo High-Contrast Imaging and PH Sensing. *Nat. Commun.* **2019**, *10* (1), 1058.

(24) Hong, G.; Zou, Y.; Antaris, A. L.; Diao, S.; Wu, D.; Cheng, K.; Zhang, X.; Chen, C.; Liu, B.; He, Y.; et al. Ultrafast Fluorescence Imaging in Vivo with Conjugated Polymer

Fluorophores in the Second Near-Infrared Window. *Nat. Commun.* **2014**, *5* (1), 1–9.

(25) Cosco, E. D.; Caram, J. R.; Bruns, O. T.; Franke, D.; Day, R. A.; Farr, E. P.; Bawendi, M. G.; Sletten, E. M. Flavylium Polymethine Fluorophores for Near- and Shortwave Infrared Imaging. *Angew. Chemie - Int. Ed.* **2017**, *56* (42), 13126–13129.

(26) Cosco, E. D.; Spearman, A. L.; Ramakrishnan, S.; Lingg, J. G. P.; Saccomano, M.; Pengshung, M.; Glasl, S.; Ntziachristos, V.; Warmer, M.; McLaughlin, R.; Burns, O. T.; Sletten, E. M. Shortwave infrared polymethine fluorophores matched to excitation lasers enable non-invasive, multicolour in vivo imaging in real time. *Nat. Chem.* **2020**, *12*, 1123-1130.

(27) Hansch, C.; Leo, A.; Taft, R. W. A Survey of Hammett Substituent Constants and Resonance and Field Parameters. *Chem. Rev.* **1991**, *91*, 165-195.

(28) Purification of 8-Flav7 was attempted via silica column chromatography, HPLC, recrystallization, and washing with solvents (toluene, tetrahydrofuran, diethyl ether, ethyl acetate). No Title.

(29) Zhao, Y.; Truhlar, D. G. The M06 Suite of Density Functionals for Main Group Thermochemistry, Thermochemical Kinetics, Noncovalent Interactions, Excited States, and Transition Elements: Two New Functionals and Systematic Testing of Four M06-Class Functionals and 12 Other Functionals. *Theor. Chem. Acc.* **2008**, *120* (1–3), 215–241.

(30) Scalmani, G.; Frisch, M. J. Continuous Surface Charge Polarizable Continuum Models of Solvation. I. General Formalism. *J. Chem. Phys.* **2010**, *132* (11), 114110.

(31) Head-Gordon, M.; Rico, R. J.; Oumi, M.; Lee, T. J. A Doubles Correction to Electronic Excited States from Configuration Interaction in the Space of Single Substitutions. *Chem.*

Phys. Lett. **1994**, *219* (1–2), 21–29.

(32) Head-Gordon, M.; Maurice, D.; Oumi, M. A Perturbative Correction to Restricted Open Shell Configuration Interaction with Single Substitutions for Excited States of Radicals. *Chem. Phys. Lett.* **1995**, *246* (1–2), 114–121.

(33) Zhou, P. Why the Lowest Electronic Excitations of Rhodamines Are Overestimated by Time-Dependent Density Functional Theory. *Int. J. Quantum Chem.* **2018**, *118* (23), e25780.

(34) CIS(D) leads to smaller deviations relative to TD-DFT methods because of the built-in corrections to the doubly excited state. No Title.

(35) Rettig, W.; Klock, A. Intramolecular Fluorescence Quenching in Aminocoumarines. Identification of an Excited State with Full Charge Separation. *Can. J. Chem.* **1985**, *63*, 1649.

(36) Liu, X.; Qiao, Q.; Tian, W.; Liu, W.; Chen, J.; Lang, M. J.; Xu, Z. Aziridinyl Fluorophores Demonstrate Bright Fluorescence and Superior Photostability by Effectively Inhibiting Twisted Intramolecular Charge Transfer. *J. Am. Chem. Soc* **2016**, *138*, 6963.

(37) Semonin, O. E.; Johnson, J. C.; Luther, J. M.; Midgett, A. G.; Nozik, A. J.; Beard, M. C. Absolute Photoluminescence Quantum Yields of IR-26 Dye, PbS, and PbSe Quantum Dots. *J. Phys. Chem. Lett.* **2010**, *1* (16), 2445–2450.

(38) Fitzmaurice, R. J.; Etheridge, Z. C.; Jumel, E.; Woolfson, D. N.; Caddick, S. Microwave Enhanced Palladium Catalysed Coupling Reactions: A Diversity-Oriented Synthesis Approach to Functionalised Flavones. *Chem. Commun.* **2006**, 4814-4816.

(39) Pajtás, D.; Patonay, T.; Kónya, K. Synthesis of 8-Bromoflavone and Its Buchwald-Hartwig Reaction with Amines. *Synth.* **2016**, *48* (1), 97–102.

(40) Schrödinger Release 2019-4: Maestro, Schrödinger, LLC, New York, NY, 2019.

(41) Gaussian 16, Revision C.01, Frisch, M. J.; Trucks, G. W.; Schlegel, H. B.; Scuseria, G. E.; Robb, M. A.; Cheeseman, J. R.; Scalmani, G.; Barone, V.; Petersson, G. A.; Nakatsuji, H.; Li, X.; Caricato, M.; Marenich, A. V.; Bloino, J.; Janesko, B. G.; Gomperts, R.; Mennucci, B.; Hratchian, H. P.; Ortiz, J. V.; Izmaylov, A. F.; Sonnenberg, J. L.; Williams-Young, D.; Ding, F.; Lipparini, F.; Egidi, F.; Goings, J.; Peng, B.; Petrone, A.; Henderson, T.; Ranasinghe, D.; Zakrzewski, V. G.; Gao, J.; Rega, N.; Zheng, G.; Liang, W.; Hada, M.; Ehara, M.; Toyota, K.; Fukuda, R.; Hasegawa, J.; Ishida, M.; Nakajima, T.; Honda, Y.; Kitao, O.; Nakai, H.; Vreven, T.; Throssell, K.; Montgomery, J. A., Jr.; Peralta, J. E.; Ogliaro, F.; Bearpark, M. J.; Heyd, J. J.; Brothers, E. N.; Kudin, K. N.; Staroverov, V. N.; Keith, T. A.; Kobayashi, R.; Normand, J.; Raghavachari, K.; Rendell, A. P.; Burant, J. C.; Iyengar, S. S.; Tomasi, J.; Cossi, M.; Millam, J. M.; Klene, M.; Adamo, C.; Cammi, R.; Ochterski, J. W.; Martin, R. L.; Morokuma, K.; Farkas, O.; Foresman, J. B.; Fox, D. J. Gaussian, Inc., Wallingford CT, 2016.

(42) Neese, F. The ORCA Program System. *WIREs Comput. Mol. Sci.* **2012**, *2* (1), 73–78.

CHAPTER FOUR

Silicon Incorporation in Polymethine Dyes

Adapted from: Monica Pengshung, Patrick Neal, Timothy L. Atallah, Junho Kwon, Justin R. Caram, Steven A. Lopez, Ellen M. Sletten*. Silicon Incorporation in Polymethine Dyes. *Chem. Commun.* **2020**, *56*, 6110-6113. DOI: 10.1039/C9CC09671J

4.1 Abstract

Methods to red-shift fluorophores have garnered considerable interest due to the broad utility of low energy light. The incorporation of silicon into xanthene and coumarin scaffolds has resulted in an array of visible and near-infrared fluorophores. Here, we extend this approach to polymethine dyes, another popular fluorophore class, performing experimental and computational analyses. We found that when oxygen was replaced with $SiMe_2$, bathochromic shifts of up to 121 nm and fluorophores with emission above 900 nm were achieved.

4.2 Introduction

Fluorescence is a vital research tool for analysing molecules in complex, dilute environments.[1] Key to the success of fluorescent analyses are fluorophores which have enabled fundamental materials and biological studies; however, due to limitations of light penetration through heterogeneous materials, there has been interest in red-shifting fluorophores to the near-infrared (NIR, 700–1000 nm) region and beyond.[2,3]

In 2008, Xu and coworkers reported that the introduction of silicon into a xanthene chromophore in place of oxygen resulted in a bathochromic shift of 100 nm (Figure 4.1A).[4] Following this initial work, the use of silicon to red-shift fluorophores has been applied to oxazine,

coumarin, fluorescein and rhodamine dyes (Figure 4.1B-D).[5–10] These dyes have been shown to be bright probes with advantageous photostability. We now extend silicon incorporation to another ubiquitous class of fluorophores, polymethine dyes.

Polymethine dyes are known for their narrow absorption bands, high absorption coefficients, and readily tunable λ_{max} within the visible and near-infrared regions. The most common polymethines are cyanine dyes, which have nitrogen-containing heterocycles connected via a polymethine chain (Figure 4.1E). A widely utilized approach to significantly modulate the λ_{max} of cyanine dyes is to vary the length of the polymethine chain, which leads to a ~100 nm red-shift for each additional vinylene unit, though increasing the polymethine chain decreases stability.[11] An alternative strategy to afford large red-shifts is to replace the nitrogen with a different heteroatom such as O, S, Se, and Te.[12] Herein, we demonstrate that the incorporation of silicon into heterocycles for polymethine dyes can impart red-shifts of similar magnitude to extension of the polymethine chain, while also enhancing photostability, resulting in fluorophores with emission above 900 nm (Figure 4.1F).

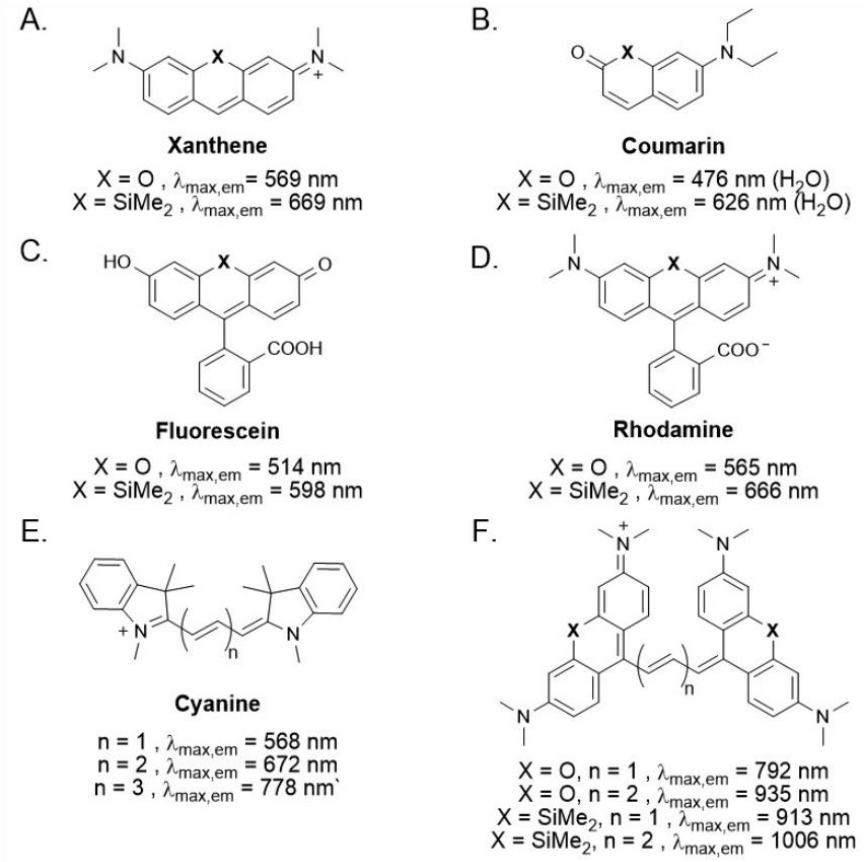

Figure 4.1 (A-E) Fluorophore scaffolds. (A). Xanthene.[4] B) Coumarin.[10] C) Fluorescein.[9] D) Rhodamine.[9] E) Cyanine.[11] F) This work on silicon polymethines and their oxygen counterparts.[13]

4.3 Results and Discussion

To prepare polymethine fluorophores, heterocycles that can readily react with electrophilic polyene linkers are necessary. We synthesized xanthone **4.1** according to literature procedures[14] and treated it with MeMgBr (Scheme 4.1A) to obtain **4.3**. Silicon xanthylium **4.3** proved to be a bright new fluorophore with $\lambda_{max,abs}$ = 646 nm and $\lambda_{max,ems}$ = 673 nm (Figure 4.2A, blue). Notably, this is 100 nm red-shifted from the oxygen congener **4.4**, which we synthesized as a control (Scheme 4.1A).

To synthesize the first generation of silicon polymethines, **4.3** was deprotonated with 2,6-lutidine and combined with diphenylformamidinine (**4.5**) in acetic anhydride (Scheme 4.1B) to

afford **7** as a dark blue solid. Trimethine **7** displayed an absorption band with $\lambda_{max,abs}$ at 854 nm and $\lambda_{max,ems}$ at 913 nm (Fig. 4.2A and Fig. 4.3A, red). We prepared pentamethine dye **10** through a similar procedure with malonaldehyde bis(phenylimine) HCl (**4.9**) to yield **4.10** (Scheme 4.1B). Pentamethine **4.10** had a $\lambda_{max,abs}$ at 938 nm and $\lambda_{max,ems}$ at 1006 nm (Figure 4.2A, black).

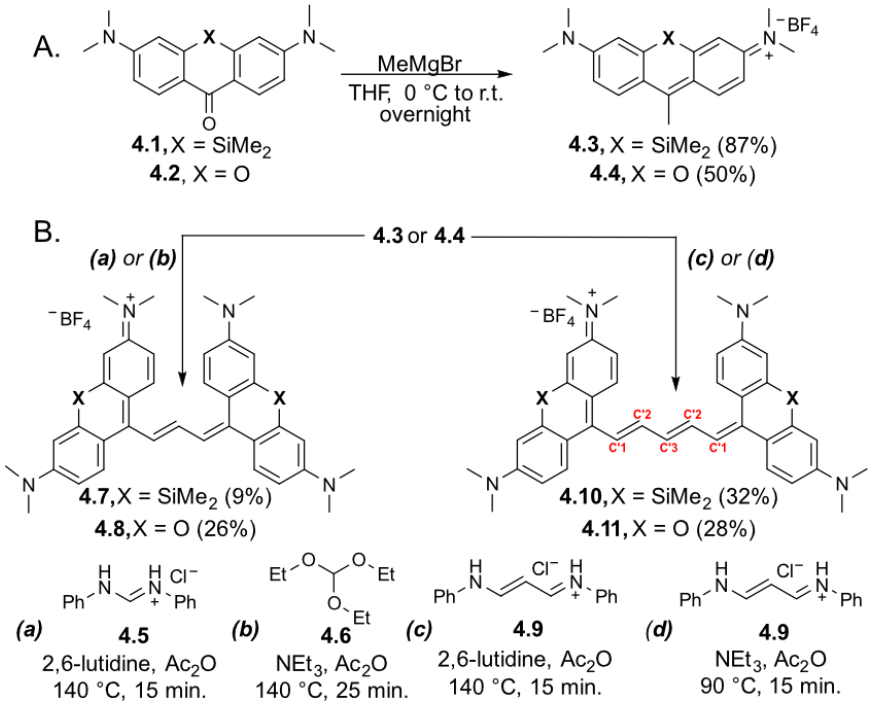

Scheme 4.1. Synthesis of silicon and oxygen fluorophores studied herein. (A) Heterocycle synthesis. (B) Polymethine dye synthesis. For **4.7**, conditions **(a)**. For **4.8**, conditions **(b)**. For **4.10**, conditions **(c)**. For **4.11**, conditions **(d)**.

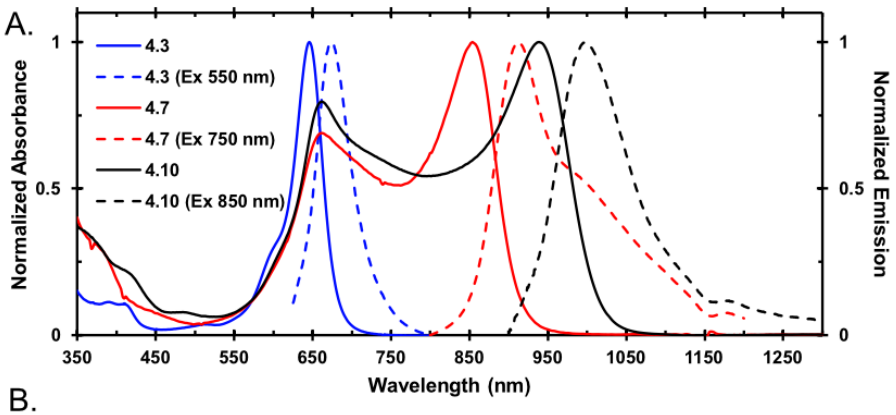

B.

Compound	$\lambda_{max, abs}$ (nm)	$\lambda_{max, ems}$ (nm)	ε (10^4, M^{-1} cm^{-1})	Φ_f (%)	τ (ps)[a]	k_r (ns)[a]	k_{nr} (ns)[a]
4.3	646	673	3.5 ± 0.4	61 ± 5	-	-	-
4.7	854	913	3.9 ± 0.4	0.26 ± 0.02	48	0.05	21
4.10	938	1006	5.9 ± 0.2	0.19 ± 0.01	43	0.03	18

Figure 4.2. Photophysical data of silicon fluorophores. (A) Normalized absorbance (solid) and emission (dotted) in dichloromethane (DCM). (B) Photophysical characterization of **4.3**, **4.7**, **4.10** in dichloromethane. [a]Error and experimental in Fig 4.6.

Attempts to synthesize a silicon xanthene heptamethine proved ultimately unsuccessful. Trials involving heptamethine linker **4.12**, acetic anhydride and pyridine or 2,6-lutidine as the base while heating at 140 °C, proved to yield little dye based on monitoring of the absoprtion spectra (Scheme **4.2**, Figure **4.3**, gray, solid). A small broad peak present around ~1035 nm was suggestive of the heptamethine formation but the presenece of two large peaks at ~850 nm and 650 nm showed a large presence of trimethine and unreacted heterocycle. Attempts to purify these crude mixtures similarily were unsuccessful due to the instable nature of **4.13**. However, emission could be obtained from the crude mixture with excitation at 950 nm, with a $\lambda_{max,ems}$ at 1119 nm (Figure **4.3**, gray, dotted)

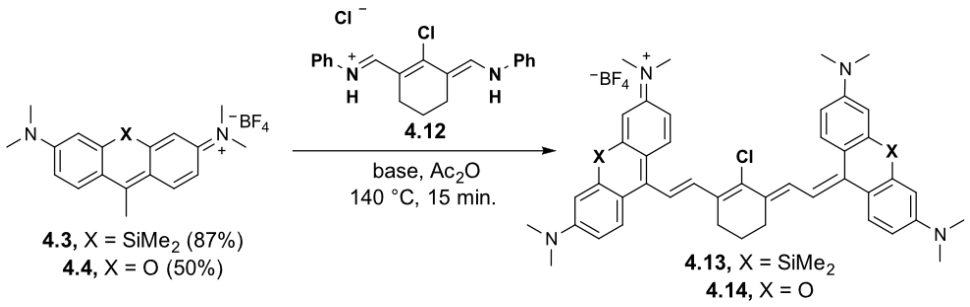

Scheme 4.2. Synthetic route for silicon xanthene heptamethine dye.

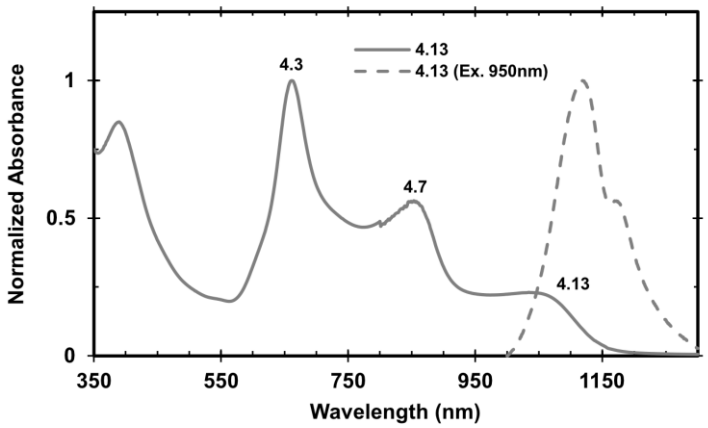

Figure 4.3 Absorbance spectra of crude mixture of **4.13** (gray, solid) and emission (gray, dotted) in dichloromethane.

Silicon polymethines **4.7** and **4.10** displayed a large absorption range (550–1000 nm) and contained two distinct peaks at 663 nm, and either 854 nm or 938 nm for **4.7** and **4.10**, respectively (Figure 4.2A). These spectra are uncharacteristic of traditional cyanine dyes, which have narrow absorbance due to complete electron delocalization (Figure 4.4A).[15] Broad absorption spectra has been observed in long chain cyanine dyes (>7 carbon units) due to ground state desymmetrization in which electron delocalization is compromised such that asymmetric electronic configurations and dipolar character are observed (Figure 4.4B).[15,16] Shorter chain polymethine dyes containing

xanthene heterocycles have also been reported to display ground state destabilization, resulting in bimodal absorbance spectra.[17]

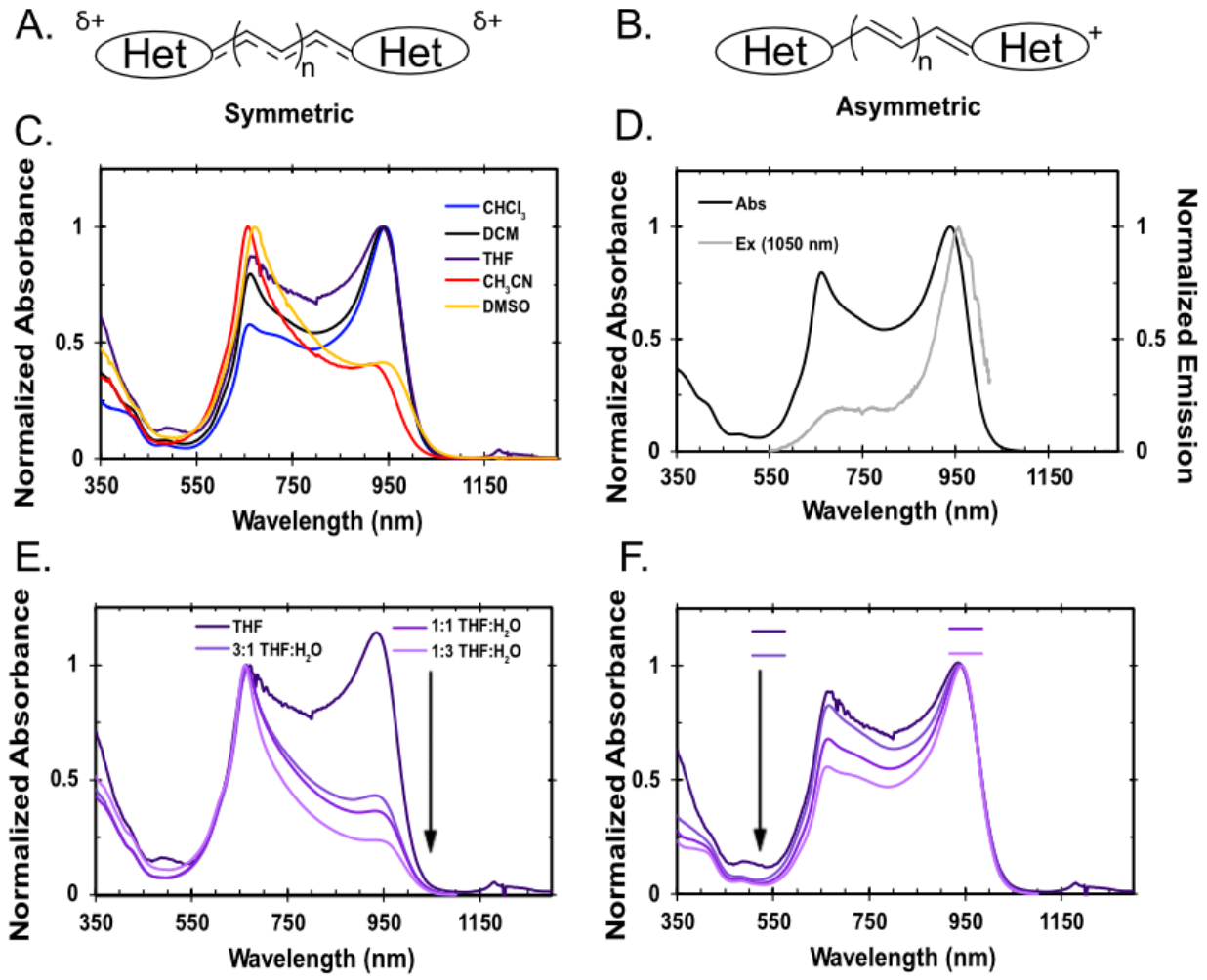

Figure 4.4. (A/B). Schematic of symmetric state (delocalized charge, (A)) and asymmetric state (dipolar, charge is localized on one heterocycle, (B)). (C) Absorbance of **4.10** (normalized to λ_{max}) in a range of nonpolar and polar solvents. (D) Normalized absorption spectra (Abs, black) and excitation spectra (Ex, grey, excitation from 515–1025 nm and collection 1050 nm) of **4.10** in DCM. (E) Absorption spectra of **4.10** normalized at 663 nm in a solution of tetrahydrofuran (THF, 0.01 mM) supplemented with increasing amounts of H_2O. (F) Absorption spectra of **10** normalized at 938 nm in a solution of THF (0.01 mM) supplemented with increasing amounts of $CHCl_3$.

The absorbance spectra of pentamethine **4.10** in dichloromethane (DCM) displays a peak ratio of 1:1.5 for absorbance at 663 nm and 938 nm. The peak ratio is concentration independent (Figure

4.5) leading us to ascribe the bimodal absorbance to the presence of asymmetric and symmetric states. We performed a solvatochromism study on **4.10** (Figure 4.4C), which revealed that polar solvents such as dimethyl sulfoxide and acetonitrile resulted in the 633 nm peak dominating by 2.5-fold (Figure 4.4C). More systematically studying the effect of polar solvents through the addition of water or chloroform to **4.10** in THF indicate the 633 nm peak is favoured as solvent polarity is increased (Figure 4.4E and 4F). Mixtures of THF and phosphate buffered saline show similar dominance of the 633 nm peak (Figure 4.6). Collectively, these results are consistent with previous findings that polar environments are able to stabilize the asymmetric state.[20] Solvatochromism studies of **4.7** are comparable to **4.10** (Figure 4.7). Interestingly, the $\lambda_{max,abs}$ of the asymmetric state of trimethine **4.7** is similar to pentamethine **4.10**, while their symmetric states differ by 84 nm. We attribute this to the asymmetric state having significant heterocycle character, with the heterocycle being a good chromophore itself.

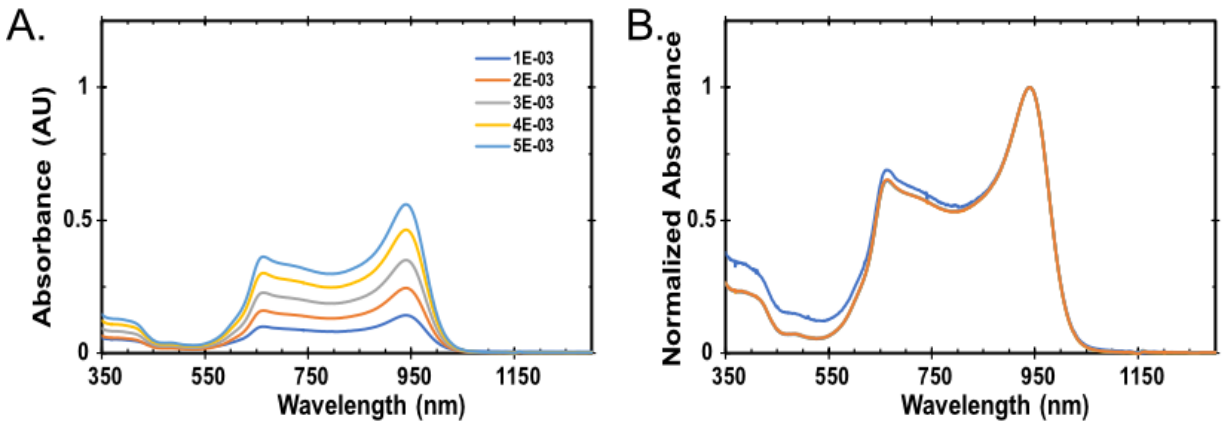

Figure 4.5 Absorbance spectra of **4.10** in DCM in A) varying concentrations (mM) as shown in legend and B) data in (A) normalized. No change in spectral shape as a function of concentration suggest no aggregation.

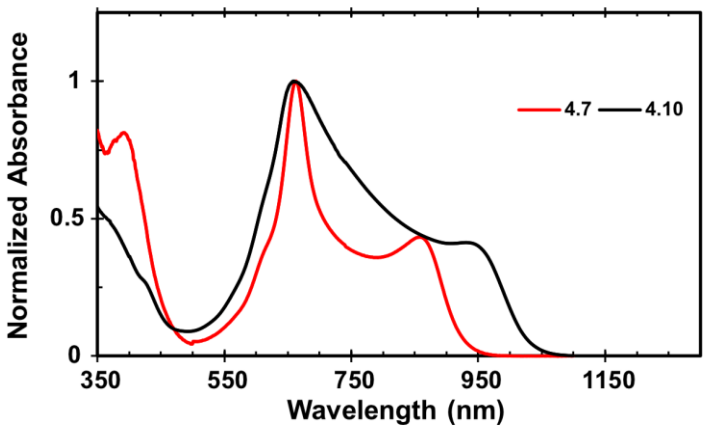

Figure 4.6 Solution of **4.7** (red) and **4.10** (black) in tetrahydofuran:PBS buffer (1:1) shows a similar absorption spectra to spectra provided in mixtures with H_2O.

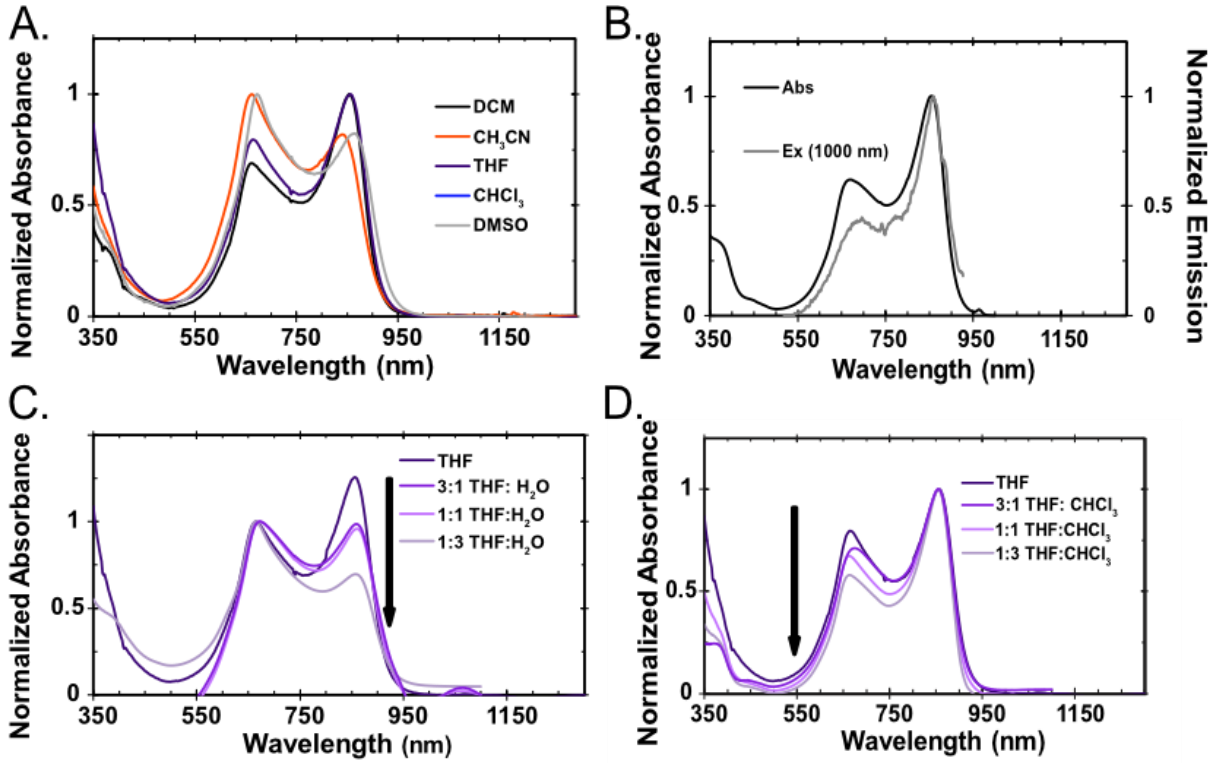

Figure 4.7. Photophysical data suggesting ground state desymmetrization of trimethine **4.7**. A) Absorbance of trimethine **4.7** (normalized to λ_{max}) in a range of nonpolar and polar solvents. B) Normalized absorbance spectra (black) of **4.7** in dichloromethane. Normalized excitation spectra (grey) of **4.7** with excitation at 515–930 nm and emission collected at 1000 nm in dichloromethane. C) Absorption spectra of trimethine **4.7** normalized at 660 nm in a solution of THF (0.01 mM) supplemented with increasing amounts of H_2O. D) Absorption spectra of trimethine **4.7** normalized at 854 nm in a solution of THF (0.01 mM) supplemented with increasing amounts of $CHCl_3$.

To further explore the hypothesis of ground state desymmetrization, we employed quantum mechanical calculations. We first performed a conformational search to identify the global and local minima of **4.10**. These structures were then optimized with the hybrid density functional M06-2X[21] with the 6-31+G(d,p) basis set in the gas phase and implicit solvent H_2O using Gaussian 16.[22] No gas phase geometries exhibited structural asymmetries nor did the lowest energy conformer in H_2O (**4.10-H_2O-A**); however, two accessible solvated conformers **4.10-H_2O-B** and **4.10-H_2O-C** at 0.6 and 1.5 kcal mol^{-1} higher in free energy, respectively, were found to display asymmetry (Figure 4.8). Computationally, bond length alternation (BLA) and charge alternation (CA) are characteristic metrics for assessing ground state desymmetrization.[17] Analysis found that **10-H_2O-B** displayed BLA and CA (Figure 4.9a and 4.9b). However, the desymmetrization was small in magnitude, with only 0.17*e* (elementary charge) transferred to one heterocycle (Figure 4.10A).

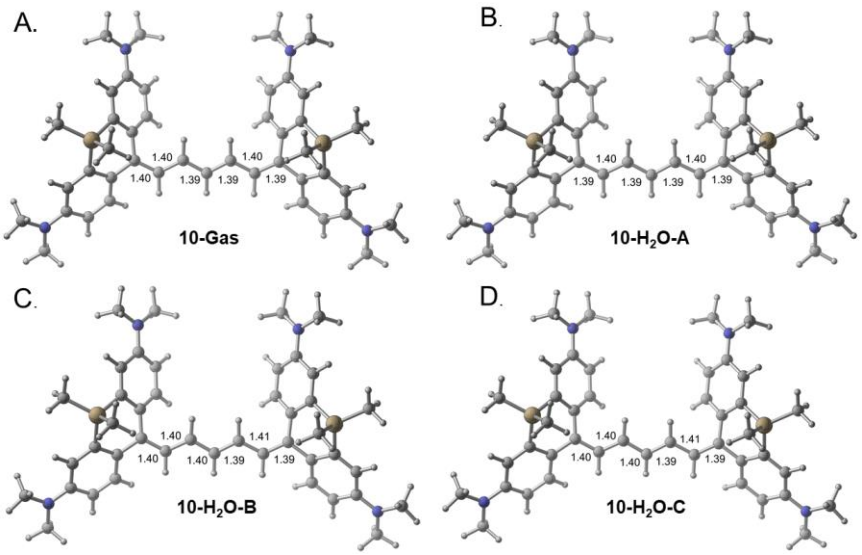

Figure 4.8. Conformers of **4.10** optimized with M062X/6-31+G(d,p). A) Lowest energy conformer in the gas phase **(4.10-gas).** B) Lowest energy conformer in water phase **(4.10-H_2O-A)** shows no bond length alternation (BLA) and *syn* geometry. C) An accessible 0.6 kcal mol^{-1} higher energy structure **(4.10-H_2O-B)** with BLA and desymmetrization. D) A second 1.5 kcal mol^{-1} higher energy structure (**4.10-H_2O-C**) with BLA and desymmetrization.

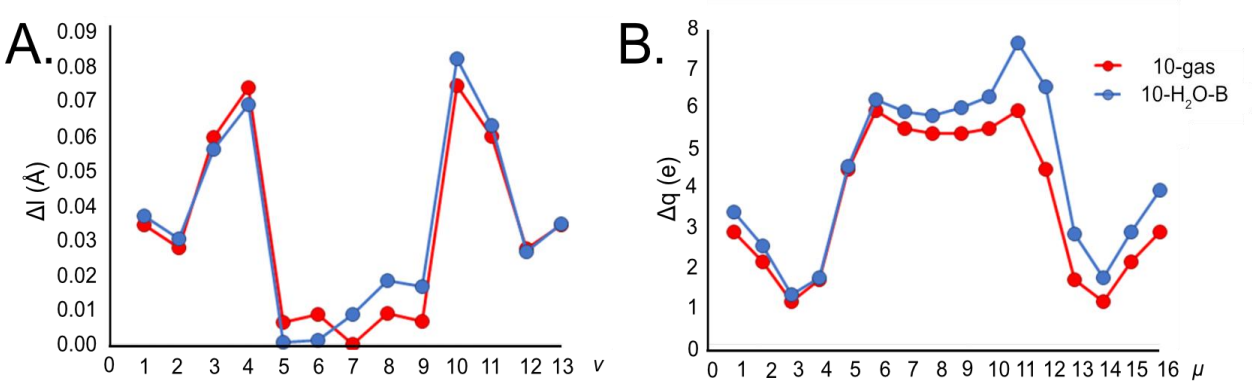

Figure 4.9. Bond length alternation (A) and charge alternation (B) for gas phase conformers (red, **4.10-gas**) and the slightly higher energy aqueous conformer (blue, **4.10-H_2O-B**).

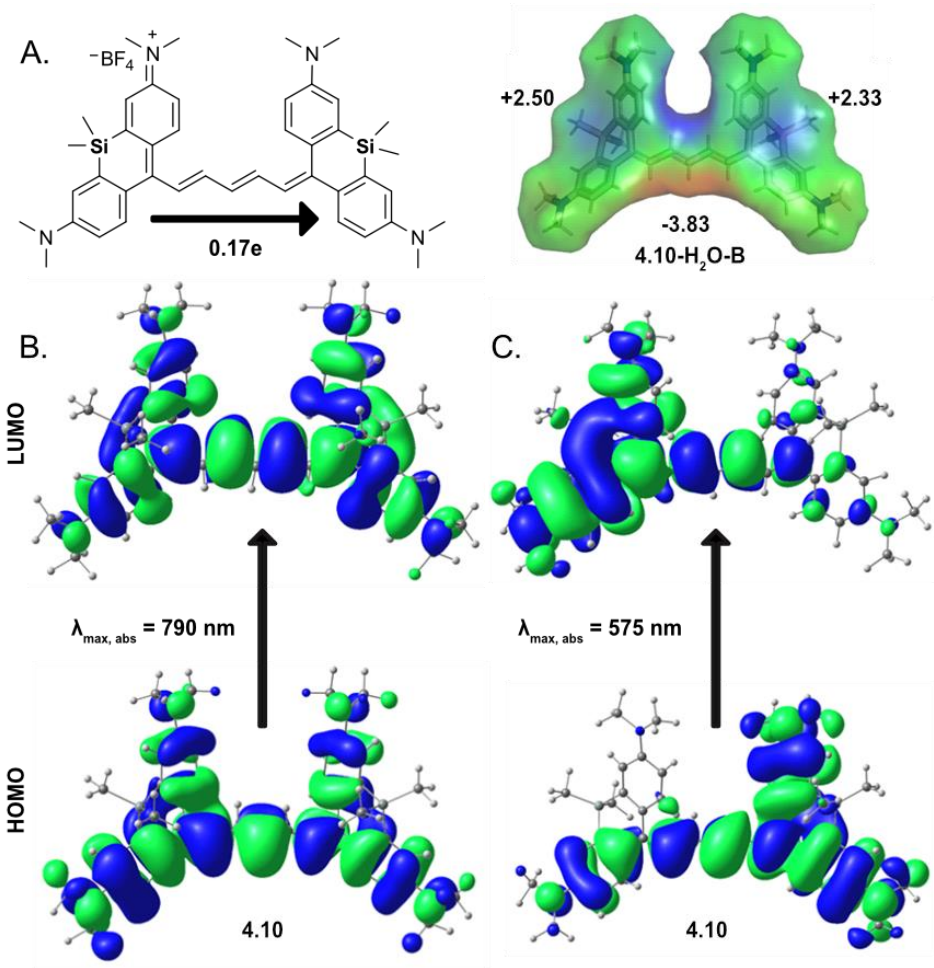

Figure 4.10. **(**A) Conformer **4.10-H_2O-B** shows desymmetrization of 0.17*e* charge transfer toward the right heterocycle represented schematically and an electron density map. (B/C) Frontier molecular orbitals of Wigner sampled structures of **4.10** computed with CIS(D)/cc-pVDZ-RI correspond to (B) $\lambda_{max,abs}$ of 790 nm, show complete electron delocalization or (C) $\lambda_{max,abs}$ of 575 nm, show asymmetric character.

As reported by Kachkovsky and co-workers,[17] substantial bond length differences in **4.11** were observed in polar solvent, indicating the importance of desymmetrization. Plotting the BLA along each index of the extended polymethine chain illustrates how either side of the molecule differs in geometry. Therefore, we plotted the BLA and CA parameters along the extended polymethine chain (Figure 4.11A and 4.11B) and computed electrostatic potential energy maps (Figure 4.11C) to determine the directionality and extent of charge transfer in **4.11-Gas** and **4.11-H_2O.**

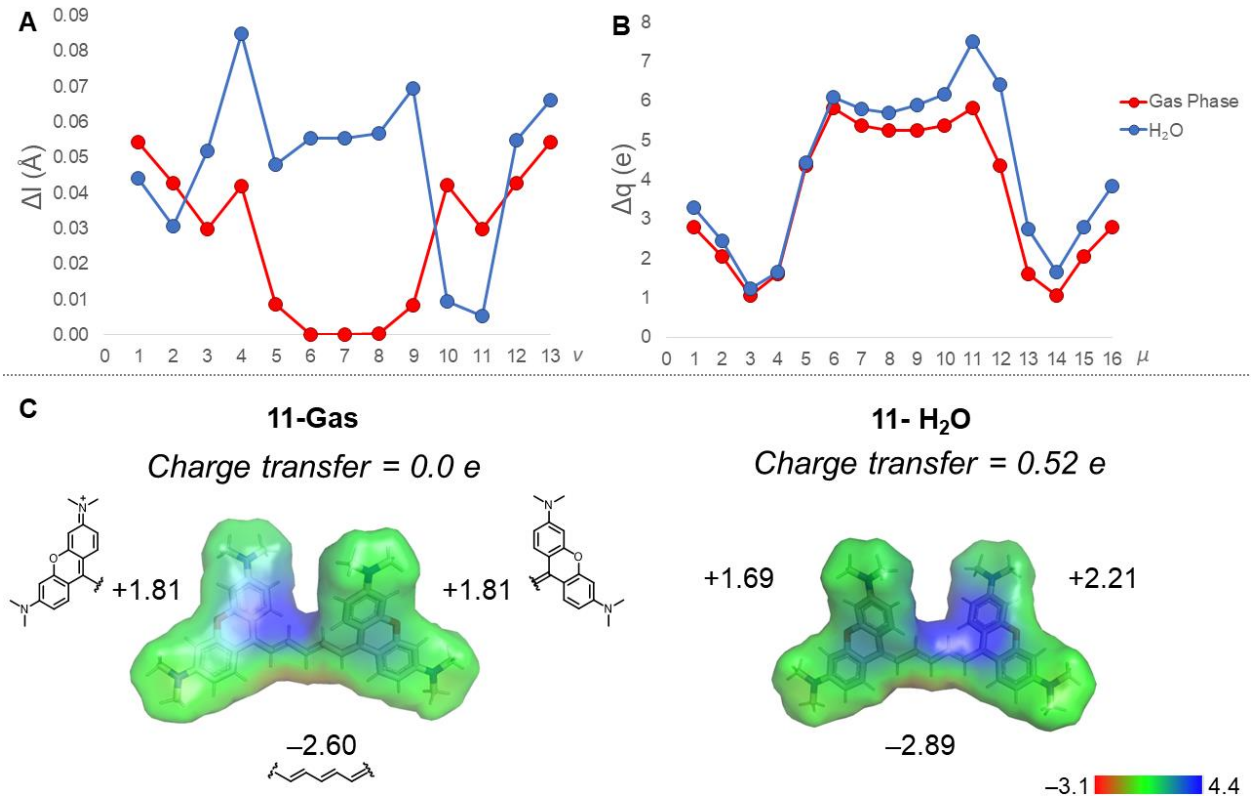

Figure 4.11. Symmetry breaking is shown in the bond length alternation (A) and charge alternation (B) in the water solvated structures, but not in the gas phase calculations. The sum of the charges of each heterocycle and the central triene respectively indicates that 0.52 e are transferred to one heterocycle.

The symmetry along the chain (shown on the x-axis) suggests that the electronic structure is delocalized; asymmetry suggests a desymmetrized electronic structure. The pattern of BLA for **4.11-H_2O** is not symmetrical about the polymethine chain: the left side peaks at 0.09 Å versus 0.07 Å on the right, and there is a dip in BLA values for index **4.10** and **4.11** on the right. Further, 0.52 e greater charge was localized to the right heterocycle of **4.11-H_2O**, while there is a symmetrical charge distribution in **4.11-Gas**. Although two higher-energy desymmetrized conformers were found in the gas phase, they are much higher in energy, at least 4.3 kcal mol-1 in free energy above **4.11-Gas**. This supports our hypothesis that polar environment stabilizes the localization of charge to the heterocycle, thereby creating the asymmetrical electronic structure.

Wigner sampling was performed to generate 50 structures from the lowest energy conformer **4.11-H_2O** which is *anti*, as well as the lowest energy *syn* conformer **4.11-H_2O-syn**, which is 0.6 kcal mol-1 higher in free energy (Figure 4.12).

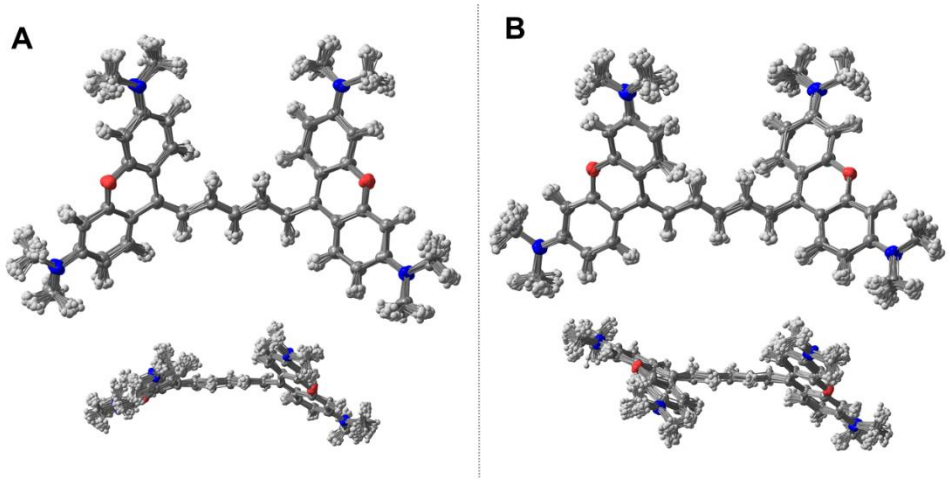

Figure 4.12. 50 sampled structures are overlaid for the minimum energy conformer **4.11-H_2O** which is anti (A) and an additional 50 structures were generated for the lowest energy geometry of the opposite conformer type, **4.11-H_2O-syn** at 0.6 kcal mol-1 higher in free energy (B).

We used the CIS(D)/cc-pvdz-RI method to compute the vertical excitation energies for each sampled geometry to simulate the absorbance spectrum for **4.11-H_2O**. As observed in **4.10**, the symmetrical and asymmetrical electronic states yield different absorbances (Figure 4.13).

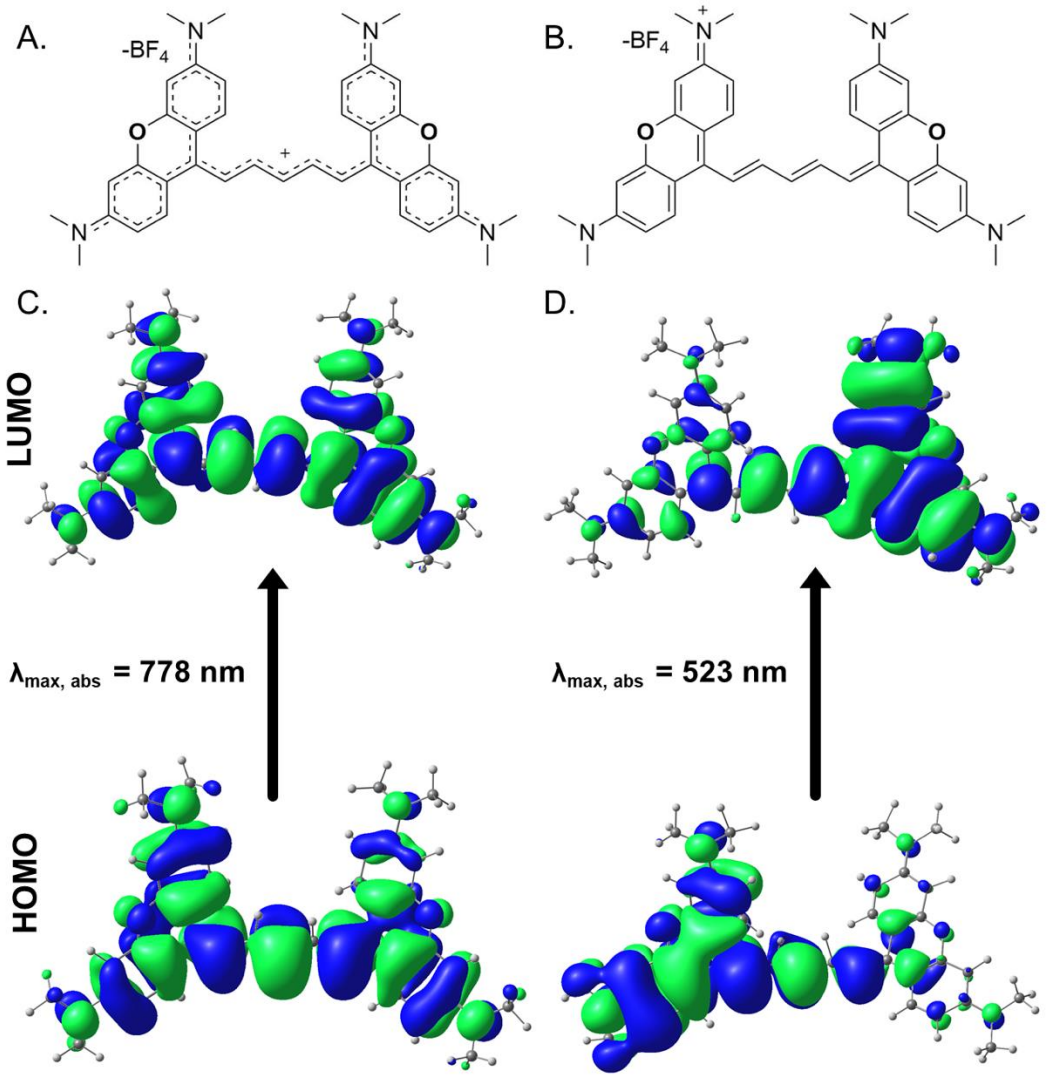

Figure 4.13. Computation of **4.11** in aqueous solvation models. A) Symmetric state (delocalized), resembles a traditional polymethine fluorophore with complete delocalized partial positive character throughout the fluorophore. B) Asymmetric state (dipolar) show localized charge towards the heterocycles. C) HOMO/LUMO levels of conformers found at CIS(D)/cc-pvdz-RI level of theory with predicted $\lambda_{max,abs}$ of 778 nm, show complete electron delocalization. D) HOMO/LUMO levels of conformers with predicted $\lambda_{max,abs}$ of 525 nm show asymmetric character in their electronic structure.

Structures with a λ_{max} near 780 nm show complete electron delocalization of the HOMO and LUMO, however, sampled geometries shifted to the 500-600 nm region correspond to a desymmetrized transition with charge transfer from one heterocycle to the other. Absorbance plots were generated from vertical excitation energies. Intensity was calculated as a function of the oscillator strength to approximate a molar absorptivity. To normalize the absorbance, all computed intensities were divided by the maximum intensity for each plot. All sampled structures are plotted in Figure 4.14 and Figure 4.15.

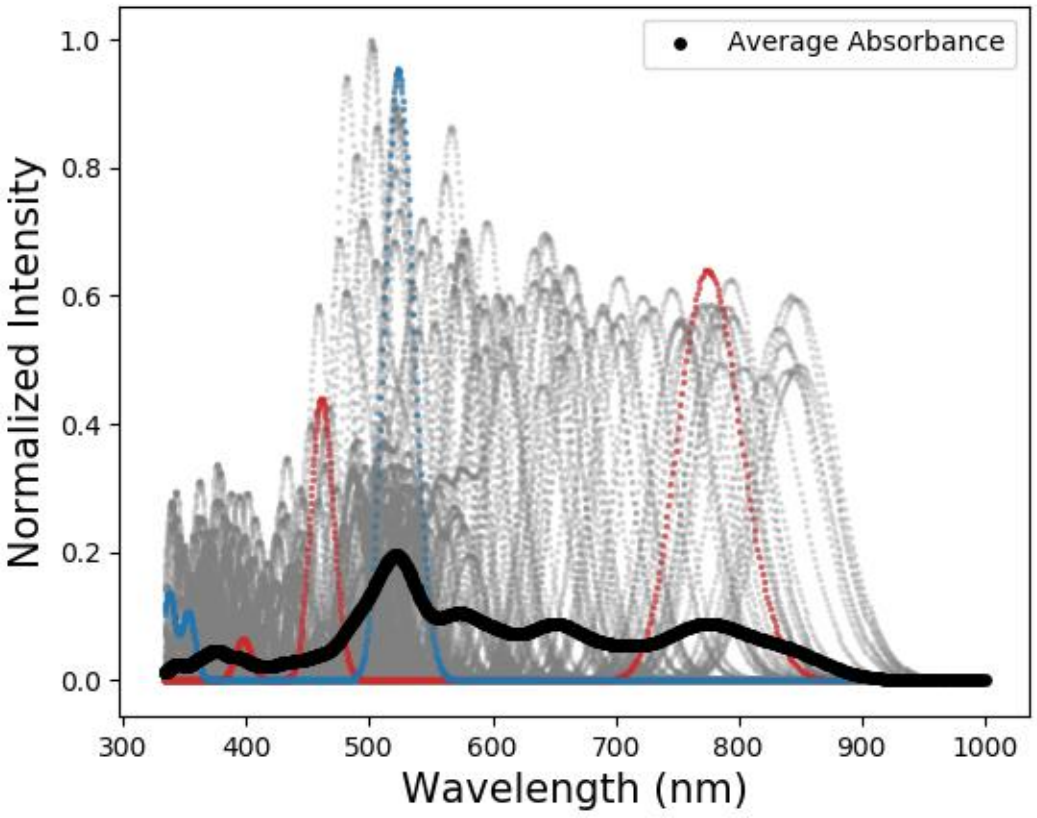

Figure 4.14. Average computed absorbance spectrum of **4.11** (A) is plotted from 100 sampled structures at the CIS(D)/cc-pvdz-RI level of theory in black. Selected peaks with at λ_{max} of 523 nm in blue and 778 nm in red are shown, as well as all other sampled structures in grey.

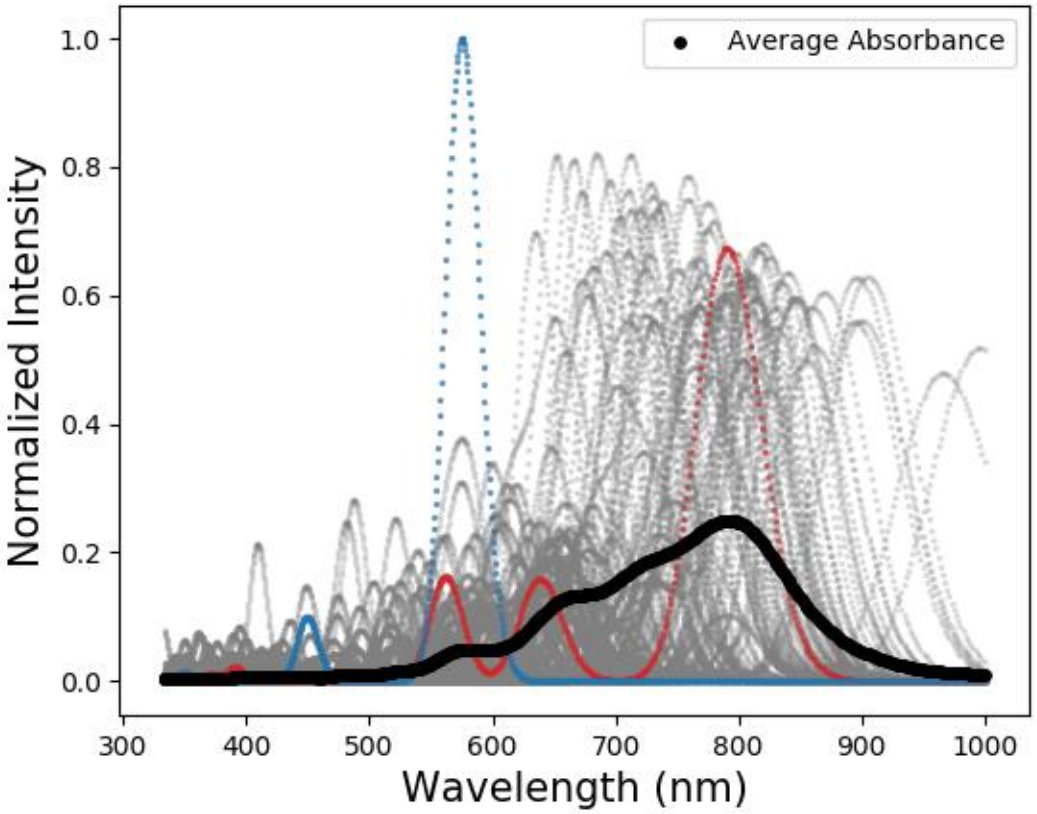

Figure 4.15. Average computed absorbance spectrum of **4.10** is plotted from 100 sampled structures at the CIS(D)/cc-pvdz-RI level of theory in black. Selected peaks with at λ_{max} of 575 nm in blue and 790 nm in red are shown, as well as all other sampled structures in grey.

Therefore, we considered the role of dynamic structures resulting from accessible vibrational modes to simulate absorbance spectra (Figure 4.16). Vertical excitations, calculated with configuration interaction of singles with a correction to doubles method [CIS(D)][23,24] with the cc-pVDZ basis set and resolution of the identity (RI) technique in ORCA 4.0.1[25,26] were computed on 50 Wigner sampled structures from the lowest energy *anti* and *syn* conformers of **10**.[‡] Structures with the most red-shifted λ_{max}, show complete electron delocalization of the highest occupied molecular orbital (HOMO) and lowest occupied molecular orbital LUMO (Figure 4.10B), whereas

sampled geometries shifted to the 550–700 nm region show a desymmetrized HOMO and LUMO (Figure 4.10C). In the desymmetrized structures, the electron density is localized on the heterocycle, consistent with the experimentally observed peak at 663 nm.

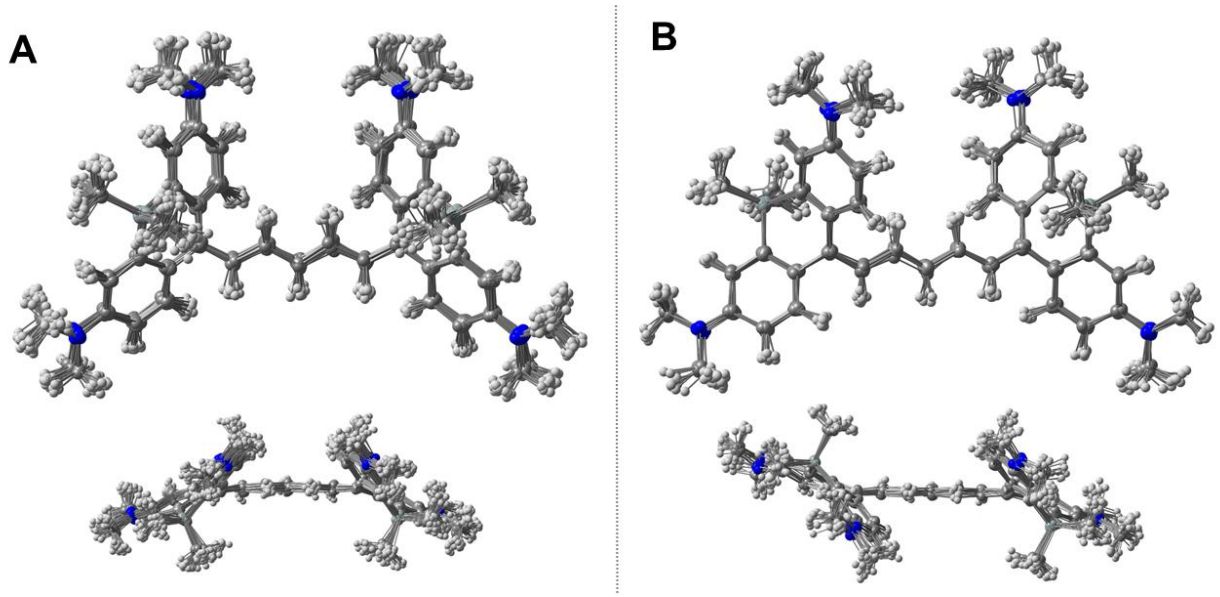

Figure 4.16. 50 Wigner sampled structures are overlaid for the minimum energy conformer **4.10-H_2O-A** which is *syn* (A) and an additional 50 structures were generated for the lowest energy geometry of the opposite conformer type, **4.10-H_2O-*anti***, at 1.5 kcal mol-1 higher in free energy (B).

While the absorption of the silicon-containing polymethine dyes was broad and bimodal, the emission was well-defined. The quantum yields were low (Φ_F < 0.30%) and excited state lifetimes ranged from 43–48 pm (Figure 4.2B and Figure 4.17).[27] The narrow emission band is attributed to emission solely from the symmetrical state, which was confirmed with the excitation spectra for both **7** and **10** (Figure 4.4D, grey and Figure 4.7B).[28]

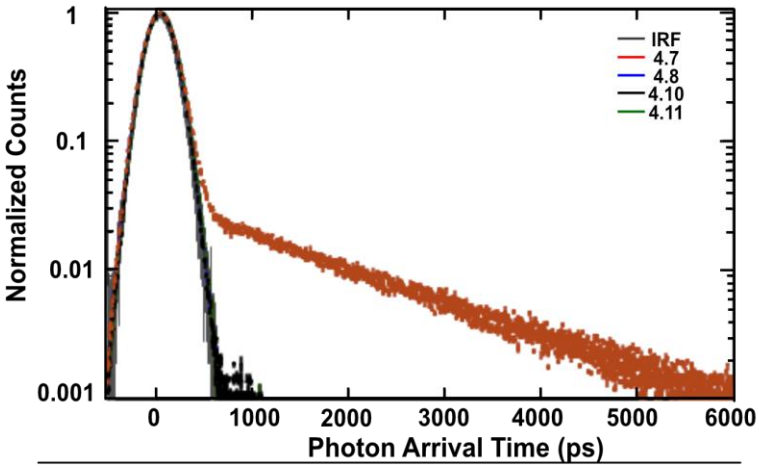

Compound	τ (ps)	k_r (ns)	k_{nr} (ns)
4.7	48.2 ± 0.01	0.05 ± 0.01	20.7 ± 0.2
4.8	47.9 ± 0.01	0.15 ± 0.01	20.7 ± 0.2
4.10	43.1 ± 0.01	0.04 ± 0.01	23.1 ± 0.2
4.11	43.0 ± 0.01	0.10 ± 0.01	23.1 ± 0.2

Figure 4.17. Excited state lifetimes plot summarizing the recorded lifetimes (after echo correction) of **4.7, 4.8, 4.10** and **4.11** and error. All measurements were done through time resolved photoluminescence. See photophysics section for more detail. Note that the fast lifetimes of the dyes are similar and close to the instrument response function so only the upper bounds for the excited state lifetimes are reported. Compound **4.7** has a prominent long-lived component which could be attributed to the presence of the charge-transfer state[18] or intersystem crossing to a triplet state resulting in thermally activated delayed fluorescence[19] or phosphorescence.

To showcase the direct benefit of silicon incorporation into the polymethine scaffold, we prepared oxygen congeners **8** and **11** (Scheme 4.1 and Figure 4.18) which were hypsochromically shifted (Figure 4.19A/B). The red-shift between silicon fluorophores and oxygen is normally attributed to a lowered LUMO energy, caused by σ*–π* conjugation.[27] However, our calculations suggest that the LUMO of **11** is higher in energy than **10** because of a destabilizing out-of-phase interaction between the oxygen lone pair and the π orbitals in **11** (Figure 4.20)**.**

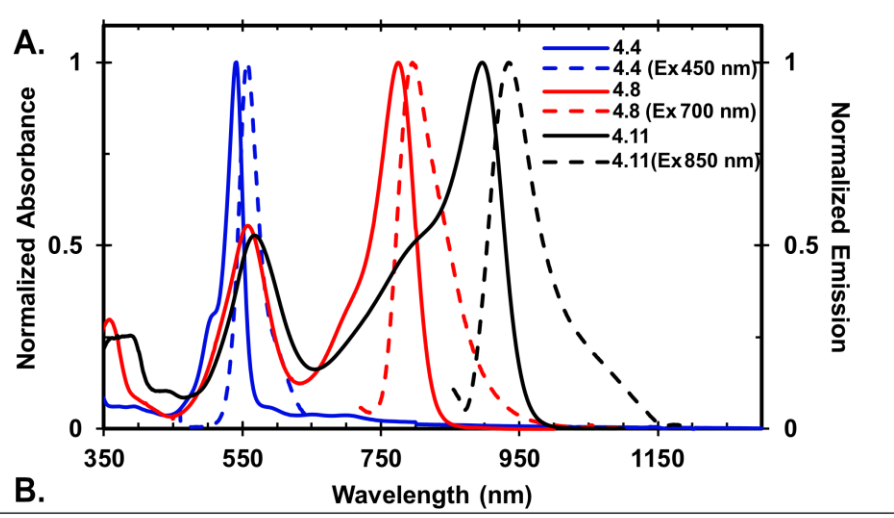

B.

Compound	$\lambda_{max,\ abs}$ (nm)	$\lambda_{max,\ ems}$ (nm)	ε (10^4, M^{-1} cm^{-1})	Φ_f (%)
4.4	542	556	1.9 ± 0.1	98 ± 5
4.8	775	792	1.8 ± 0.1	0.72 ± 0.04
4.11	896	935	14.0 ± 0.7	0.44 ± 0.03

Figure 4.18. Photophysical data of oxygen fluorophores. A) Normalized absorbance (solid) and emission (dotted) of **4.4** (blue), **4.8** (red), and **4.11** (black) in dichloromethane. B) Photophysical characterization of **4.4**, **4.8**, **4.11** in dichloromethane.

We found that the degree of red shift between the O and Si containing fluorophores decreased as the polymethine linker increased. The absorbance difference at λ_{max} for the trimethines was 79 nm (1194 cm^{-1}) while the pentamethines was only 42 nm (500 cm^{-1}) (Figure 4.19A). The difference in emission is larger for the trimethines than the pentamethines ($\Delta\lambda_{max}$ = 121 and 71 nm, respectively, Figure 4.19B). The smaller shifts in absorbance are likely due to contributions from the asymmetric state. Overall, the incorporation of silicon into polymethine fluorophores in place of oxygen results in bathochromic shifts of the symmetric state by 70–100 nm, on par with extension of the polymethine chain and consistent with incorporation of silicon into other fluorophore scaffolds.[8,9]

Finally, another advantage commonly cited for the use of silicon fluorophores is increased photostability.[5,8] We evaluated the photostability of the silicon *vs.* oxygen fluorophores, focusing

on the pair that has the most similar absorption: trimethine **4.7** and pentamethine **4.11**. We found that **4.11** began photobleaching rapidly, while **4.7** was unchanged over three hours. Upon calculation of the photobleaching rate constants, we quantified silicon-containing polymethine **4.7** to be six-fold more stable than **4.11** (Figure 4.21A). Photobleaching of pentamethine **4.10** under the same conditions showed a similar decrease as **4.7,** suggestive that silicon incorporation plays an important role in increasing the photostability. In comparison to other commercial fluorophores, **4.7** was more stable than HITCI (1,1′,3,3,3′,3′-Hexamethylindotricarbocyanine iodide) but less stable than Rhodamine B (Figure 4.21B).

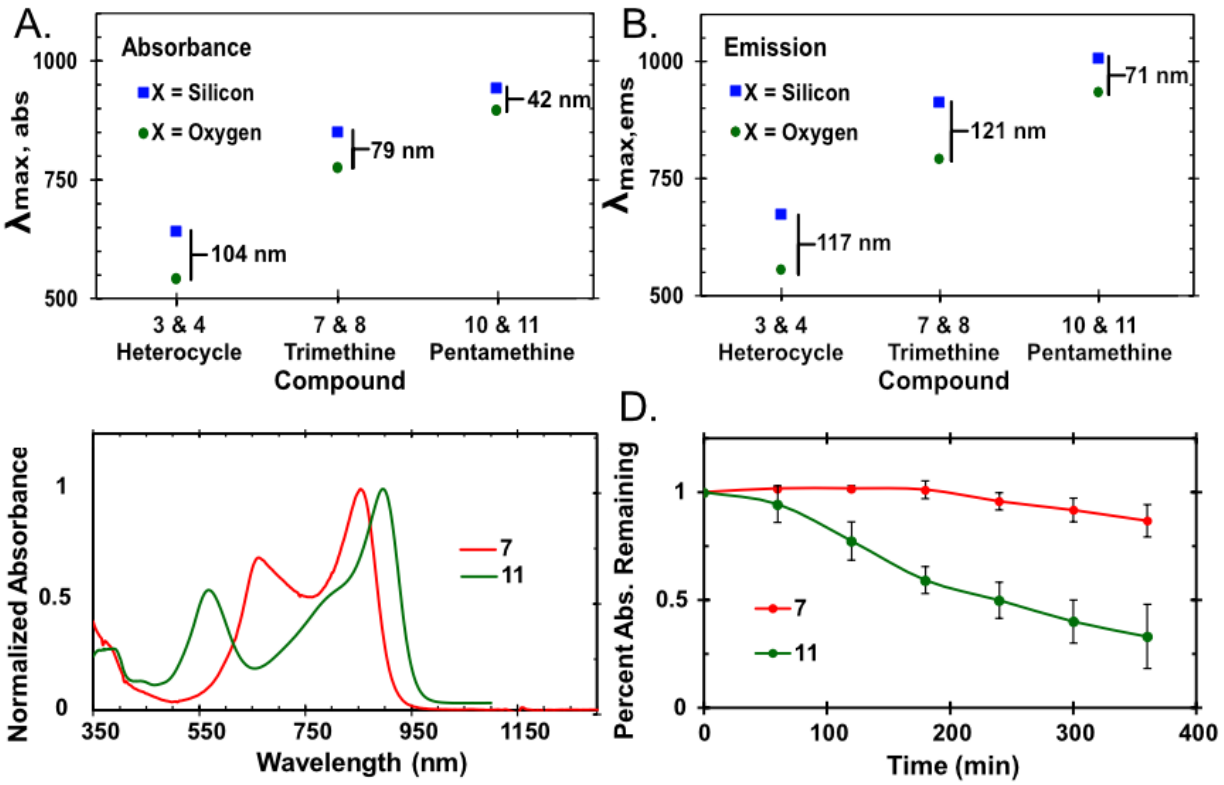

Figure 4.19. Comparison of silicon and oxygen xanthene polymethines. (A and B) λ_{max} of silicon- (blue square) and oxygen- (green circle) containing polymethine fluorophores in DCM. The values depicted on the plot indicate the degree of red-shift imparted by silicon. (A) Absorbance. (B) Emission. C) Normalized absorbance spectra of **4.7** and **4.11** in DCM. (D) Percent absorbance remaining at $\lambda_{max,abs}$ of **4.7** and **4.11** with continuous irradiation at 730 nm (146 mW cm^{-2}) over 6 hours. Error is the standard deviation of three experiments.

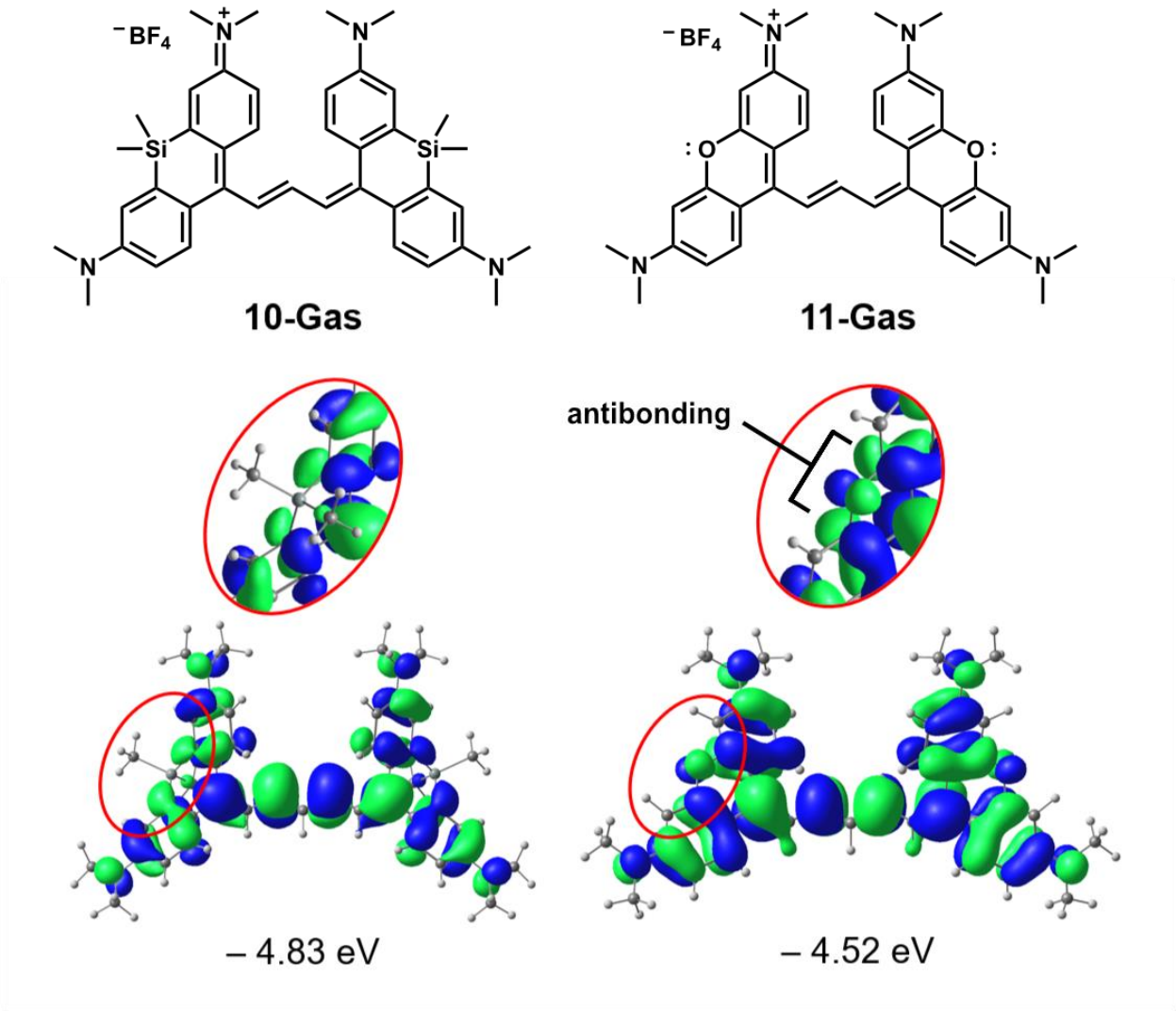

Figure 4.20. The LUMO of dyes **4.10** and **4.11** are given at the M06-2X/6-31+G(d,p) level of theory plotted with the same isolevel. Compound **4.11** shows greater antibonding interaction due to oxygen lone pairs with adjacent π bonds than **4.10**, resulting in a higher-lying LUMO energy.

A.

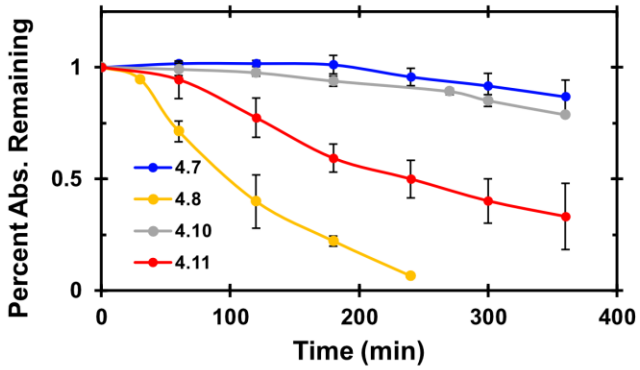

B.

Compound	k (x 10^{-4}, s^{-1})	ε (x 10^{4}, M^{-1} cm^{-1})	k_{rel} (x 10^{-3}, s^{-1})	relative stability
4.7	6.2 ± 0.6	3.9 ± 0.4	1.1 ± 0.4	1.0 ± 0.1
4.8	129.0 ± 1.0	1.9 ± 0.1	45 ± 2	10.0 ± 0.8
4.10	8.2 ± 0.2	4.3 ± 0.3	0.82 ± 0.08	2.3 ± 0.1
4.11	33.9 ± 0.6	6.5 ± 0.4	5 ± 2	6.0 ± 0.1
HITCI[a]	34.0 ± 2	13.9 ± 0.6	1.6 ± 0.1	9 ± 6
Rhodamine B[b]	13.0 ± 2	2.9 ± 0.4	5.0 ± 0.1 x 10^{-4}	5.0 ± 0.1 x 10^{-4}

Figure 4.21. Photobleaching of silicon (**4.7** and **4.10**) and oxygen (**4.8** and **4.11**) polymethine fluorophores, with continuous irradiation at 730 nm (146 mW/cm^2) over six hours in dichloromethane with $\lambda_{max, abs}$ matched at 1 au. Percent absorbance remaining is measured from t=0. Error was taken as the standard deviation of the triplicate experiments. k_{rel} was determined by taking the linear slope of the initial rate of photobleaching (k) and dividing by the relative absorption coefficient (ε) at 730 nm relative to dye **4.10** with the highest absorption coefficient at 730 nm. [a]Data was previously reported in reference 3. [b] Irradiated at 530 nm (40 mW/cm^2). Refer to photophysical procedures for more details on experimental procedure.

We further explored the pathways of degradation for these dyes. Photobleaching of cyanine dyes are generally caused by $^1O_2$ mediated photolysis of the polymethine chain.[29] Thus, **4.10** and **4.11** were subjected to $^1O_2$ and analysed for photodegradation products *via* liquid chromatography mass spectrometry (LCMS, Figure 4.22). We found that **4.11** degraded quickly (< 1 hour) and cleaved at C-1' of the polymethine chain as anticipated.[29] Surprisingly, **4.10** reacted slowly and did not display complete degradation by LCMS analysis until 17 hours. Unlike its oxygen counterpart, **4.10** degraded into a multitude of products suggesting that silicon incorporation deactivated the $^1O_2$ reactivity to the C-1'. We compared this photostability to acid and base stability

of **4.7**, **4.8**, **4.10**, and **4.11** where we found that the oxygen congeners (**4.8, 4.11**) were more stable to base and similarily stable to acid as compared to **4.7** and **4.10** (Figure 4.23-4.26)

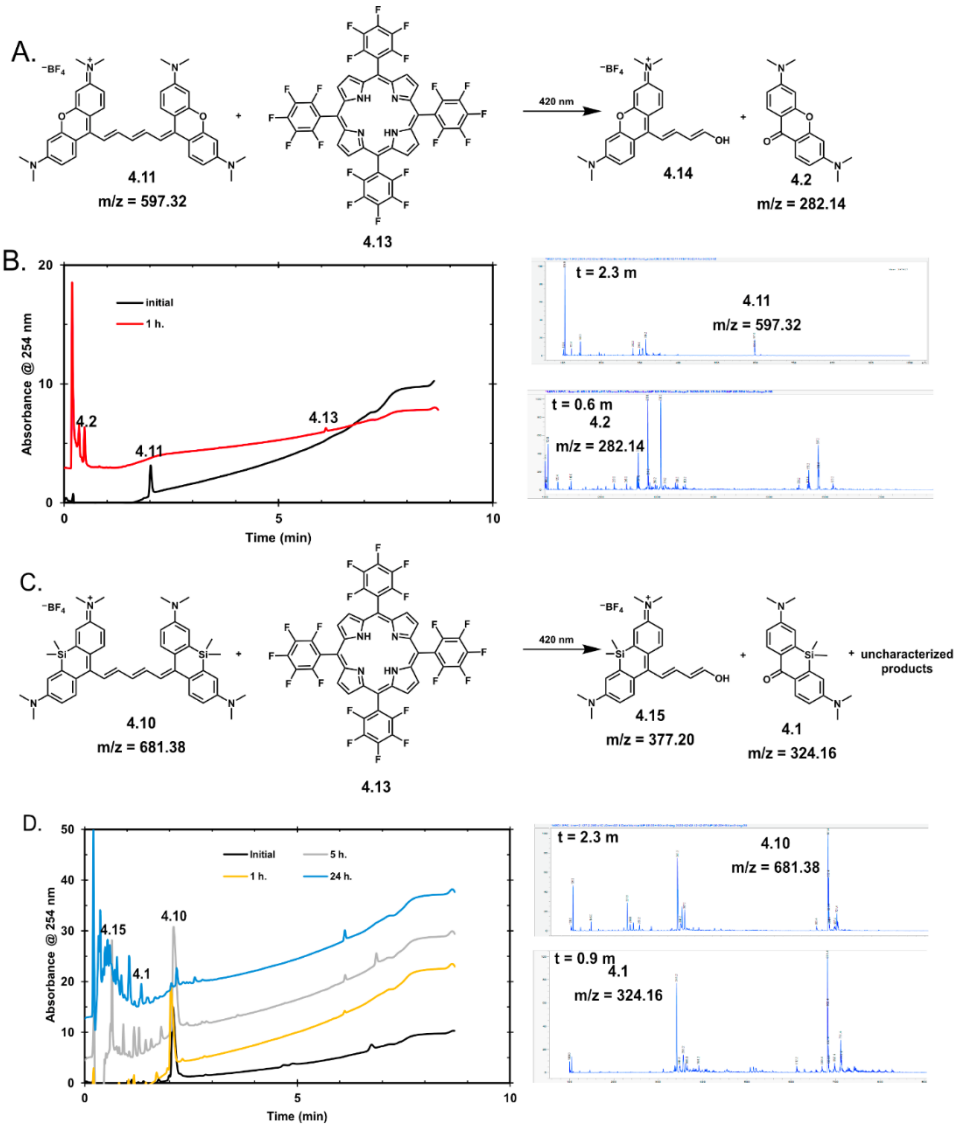

Figure 4.22. Reactivity of **4.10** and **4.11** with singlet oxygen. A) Reaction of **4.10** with singlet oxygen, sensitized by 5,10,15,20-tetrakis(pentafluorophenyl)porphyrin (**4.14,** 0.01%) in dichloromethane. B) Liquid chromatography traces (detection 254 nm) of the reaction depicted in (A) at 0 h and 1 h. LC conditions were 65% to 100% water in acetonitrile. C) Reaction of **4.10** with singlet oxygen, sensitized by 5,10,15,20-tetrakis(pentafluorophenyl)porphyrin (**4.14,** 0.01%) in dichloromethane shows degradation into many products that are not all characterized. D) Liquid chromatography traces (detection 254 nm) of the reaction depicted in (C) at 0 h, 1 h, 5 h and 17 h and m/z spectra. LC conditions were 65% to 100% water in acetonitrile.

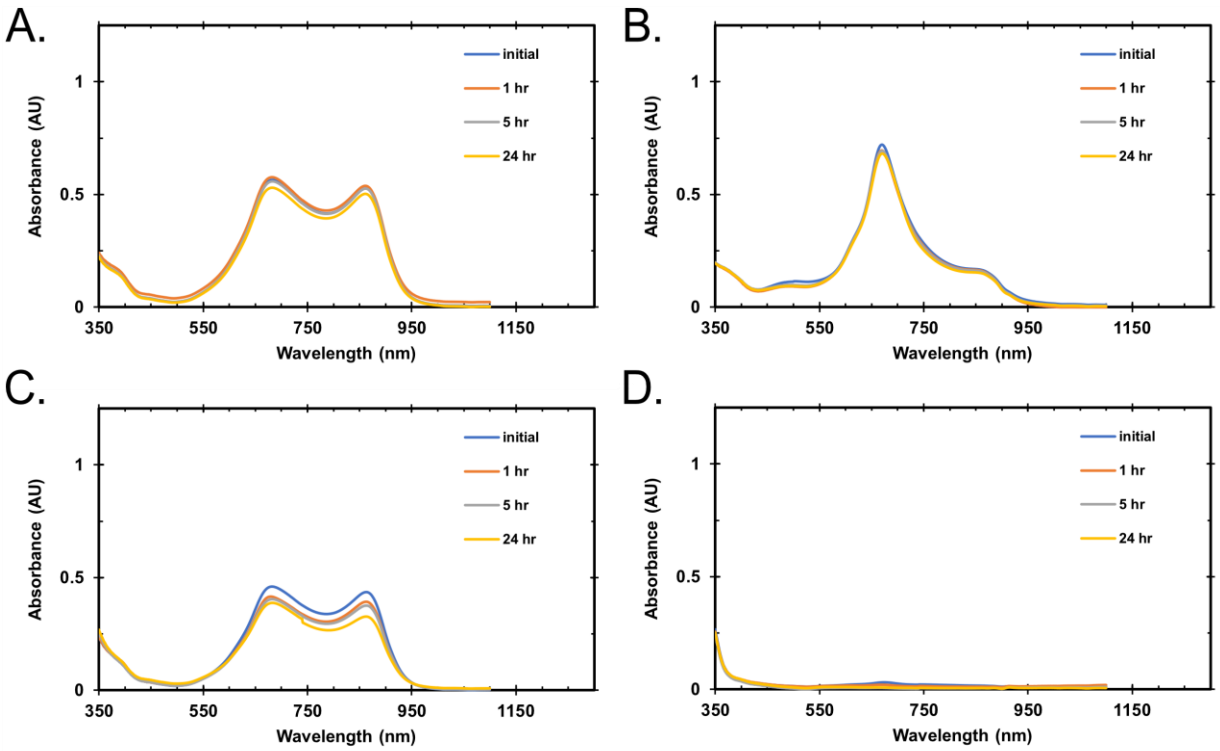

Figure 4.23. Acid and base stability of trimethine **4.7**. A solution of dye **4.7** was dissolved in dimethyl sulfoxide (0.01 mM). Ten equivalents of either acid or base was added. Absorption time points were taken at 0, 1 h, 5 h, and 24 h. A) Acetic acid. B) Trifluoroacetic acid. C) Pyridine. D) Triethylamine

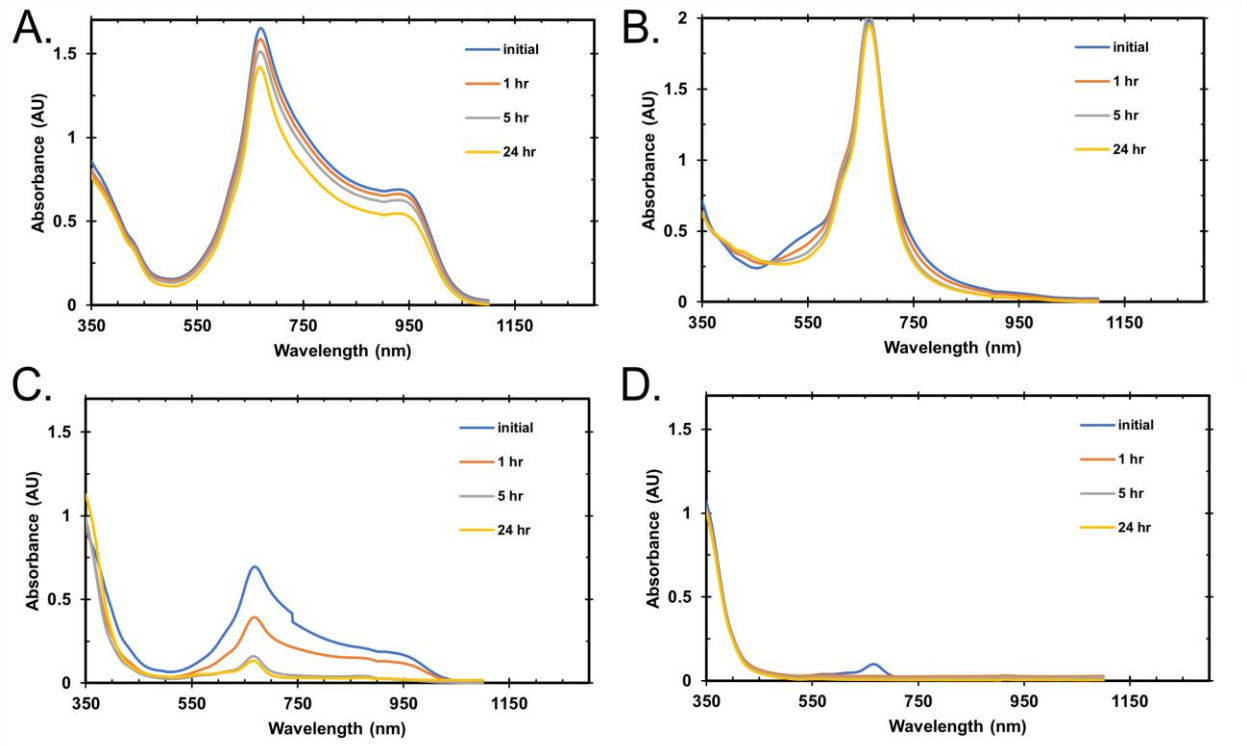

Figure 4.24. Acid and base stability of compound **4.10.** A solution of dye **4.10** was dissolved in dimethyl sulfoxide (0.01 mM). Ten equivalents of either acid or base was added. Absorption time points were taken at 0, 1 h, 5 h, and 24 h. A) Acetic acid. B) Trifluoroacetic acid. C) Pyridine. D) Triethylamine

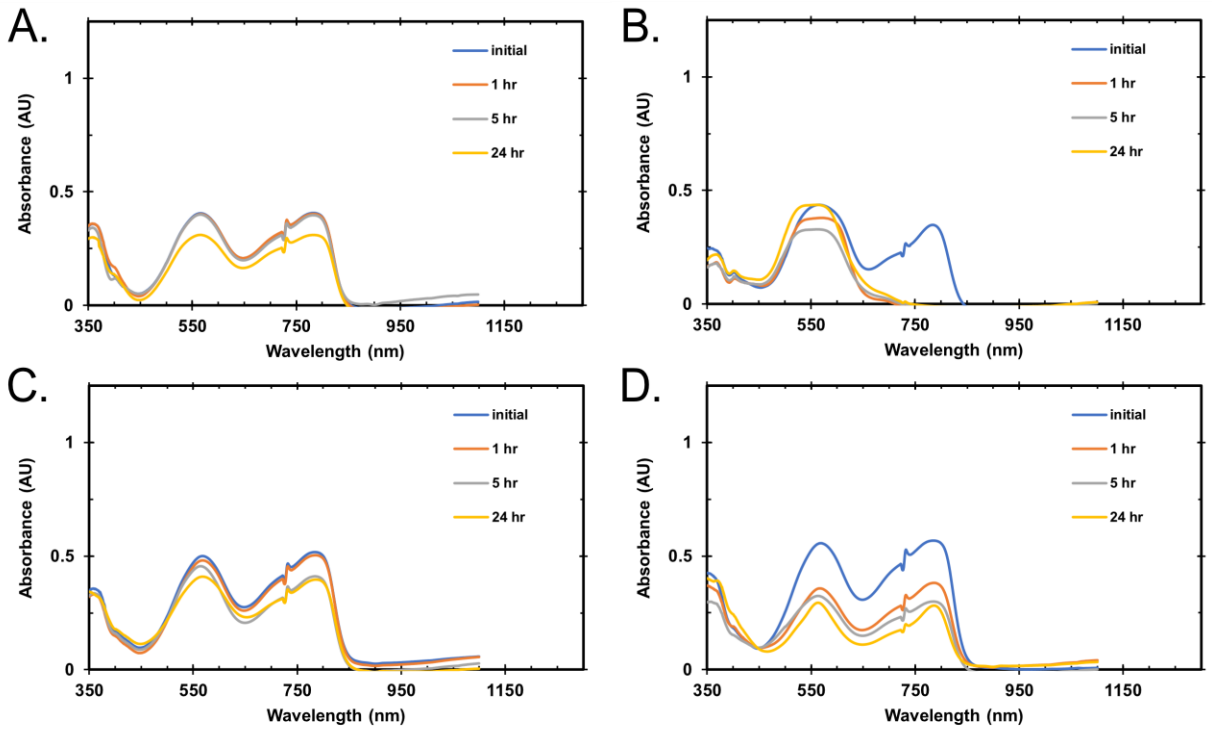

Figure 4.25. Acid and base stability of compound **4.8.** A solution of dye **4.8** was dissolved in dimethyl sulfoxide (0.01 mM). Ten equivalents of either acid or base was added. Absorption time points were taken at 0, 1 h, 5 h, and 24 h. A) Acetic acid. B) Trifluoroacetic acid. C) Pyridine. D) Triethylamine

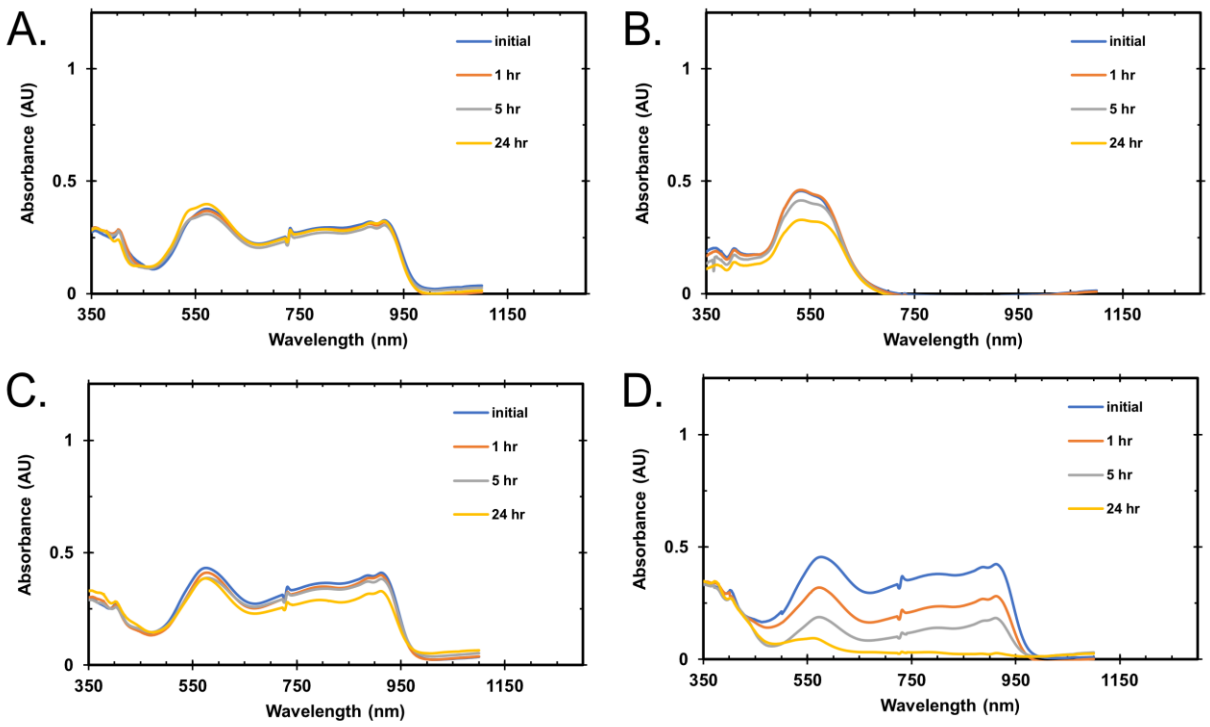

Figure 4.26. Acid and base stability of compound **4.11.** A solution of dye **4.11** was dissolved in dimethyl sulfoxide (0.01 mM). Ten equivalents of either acid or base was added. Absorption time points were taken at 0, 1 h, 5 h, and 24 h. A) Acetic acid. B) Trifluoroacetic acid. C) Pyridine. D) Triethylamine

4.4 Conclusion

In summary, we have demonstrated that incorporation of silicon into polymethine dyes is a valid approach to red shift this class of fluorophores and is on par with vinylene chain extension. We prepared tri- and pentamethines with xanthene-derived hetereocycles which were 70–100 nm red-shifted and six to ten-fold more photostable compared to oxygen analogues. The xanthene-derived heterocycles, while providing an efficient avenue for the synthesis of silicon polymethine dyes, also promoted ground state desymmetrization, which resulted in a broad, bimodal absorption spectrum and a decreased presence of the emissive species. Looking forward, the implementation of silicon into polymethine heterocycles that do not promote desymmetrization should provide avenues for the creation of deeply red-shifted (>900 nm) fluorophores with high photostability.

4.5 Experimental Procedures

4.5.1 Photophysical Procedures

Absorbance spectra were collected on a JASCO V-770 UV-Visible/NIR spectrophotometer and JASCO V-730 UV-Visible/NIR with a 2000 nm/min scan rate after blanking with the appropriate solvent. Photoluminescence spectra were obtained on a Horiba Instruments PTI QuantaMaster Series fluorometer. Quartz cuvettes (1 cm) were used for absorbance and photoluminescence measurements. Absorption coefficients in dichloromethane were calculated with serial dilutions with Hamilton syringes and volumetric glassware. Error was taken as the standard deviation of three independent replicates.

Fluorescence quantum yield measurements:

The fluorescence quantum yield (Φ_f) of a molecule or material is defined as followed:

$$\Phi_F = \frac{P_E}{P_A} \qquad (1)$$

Where P_E and P_A represent the number of photons emitted and absorbed, respectively. Absolute quantum yields were determined in an integrating sphere for **3**, **4**, **8**, and **11** in dichloromethane. Relative quantum yields were determined relative to Flav5[30] for **7** and IR-26[31] for **10** in dichloromethane.

Polarity Studies: Samples were dissolved in tetrahydrofuran with an initial concentration of 0.01 mM. From this stock was taken an aliquot (0.5 mL – 1.5 mL) and supplemented with water or chloroform in varying amounts (0.5 mL – 1.5 mL) and absorbance was recorded.

Photobleaching: A solution of sample in dichloromethane (λ_{max} = 1 au) was added to a screw-top cuvette placed in a cardboard box, 7 cm away from a 730 nm LED (M730L4 Thor Lab) with an adjustable collimation adapter (SM1P25-B). The power density was measured by Thorlab

PM100D luxometer to be 146 mW/cm^2 at this distance. Absorbance was recorded for the sample approximately every 30–60 min for six hours. The λ_{max} of absorbance at t = 0 was measured at 1 au and preceding samples were taken as a percentage of that value.

All photobleaching data was fitted to a first-order rate decay equation:

$$\ln[A] = -kt + \ln [A]_0 \qquad (2)$$

where A and A_0 represent collection at time *t* and initial absorbance collected, respectively. All R^2 values were > 0.95. Each experiment was done in triplicate and the error represents the standard deviation of the three replicates.

To compare photobleaching rates between samples with different absorption coefficients, the relative rate of decay (k_{rel}) was determined by the following equation:

$$k_{rel} = \frac{k}{\varepsilon_{730}} \qquad (3)$$

Where *k* is the raw rate determined by equation (2) and ε is the absorption coefficient at the wavelength of irradiation (730 nm) relative to the dye with the highest absorption coefficient at that wavelength.

Excited State Lifetimes: *(Performed by Timothy Atallah)*

We recorded PL lifetimes using a home-built, all-reflective epifluorescence setup. We excited the dye sample solutions at the front of a 1 cm cuvette using the pulsed laser output from an optical parametric amplifier [Spirit-OPA, MKS-Spectra Physics] pumped by ytterbium-fiber amplified pulsed laser (1040 nm, 29μJ, ~300 fs, 1 MHz) [Spirit HE 30, MKS-Spectra Physics]. The OPA excitation was tuned to 745 nm (30 nJ/cm^2, ~200 fs) and the emission was then collected and filtered with a 90:10 beamsplitter [BSX10R, Thorlabs], one 760 nm longpass filters [10CGA-760, Newport], one 800 nm longpass filter [10CGA-800, Newport, Thorlabs], and a hot mirror

[10CLVR-1, Newport] and finally reflectively coupled into a single-mode fiber [F-SMF-28-C-10FC, Newport] and detected using a superconducting nanowire single photon detector (SNSPD, IRF = 140 ps) [Quantum Opus One]. Time correlated single photon counting (TCSPC) traces were histogrammed using a HydraHarp 400 and corresponding software [Picoquant]. All measurements were carried out at room temperature.

Determining Excited State Lifetimes Through Fitting: To determine the lifetime (or decay rate, *k*) for each TCSPC trace we fit each curve to a convolution of Gaussian with exponential decay:

$$I(t) = \frac{I_0}{2} e^{-k\left((t-t_0)-\frac{\sigma^2 k}{2}\right)}\left(1 + \mathrm{erf}\left(\frac{(t-t_0)-\sigma^2 k}{\sqrt{2}\sigma}\right)\right) \qquad (4)$$

The width, σ, of the Gaussian was determined using the instrument response function (IRF) which was measured as the back-scatter off of a cuvette with solvent (i.e. DCM) without the longpass filters. The initial peak amplitude, I_0, and the rate, k, were free fitting parameters, while the time offset, t_0, and the IRF width, σ were fixed variables.

Removal of Fiber Internal Reflection Echo: It should be noted that the raw data include an artifact due to the internal reflection with fibers due to imperfect coupling between input fibers of the SNSPD resulting in an echo signal at later time. This echo signal possess all the same rate components as the original peak, however has a smaller amplitude and is offset in time. The signal was subtracted out by fitting the additional only with the free parameter of peak time position and amplitude. This correction and the fitting is demonstrated below.

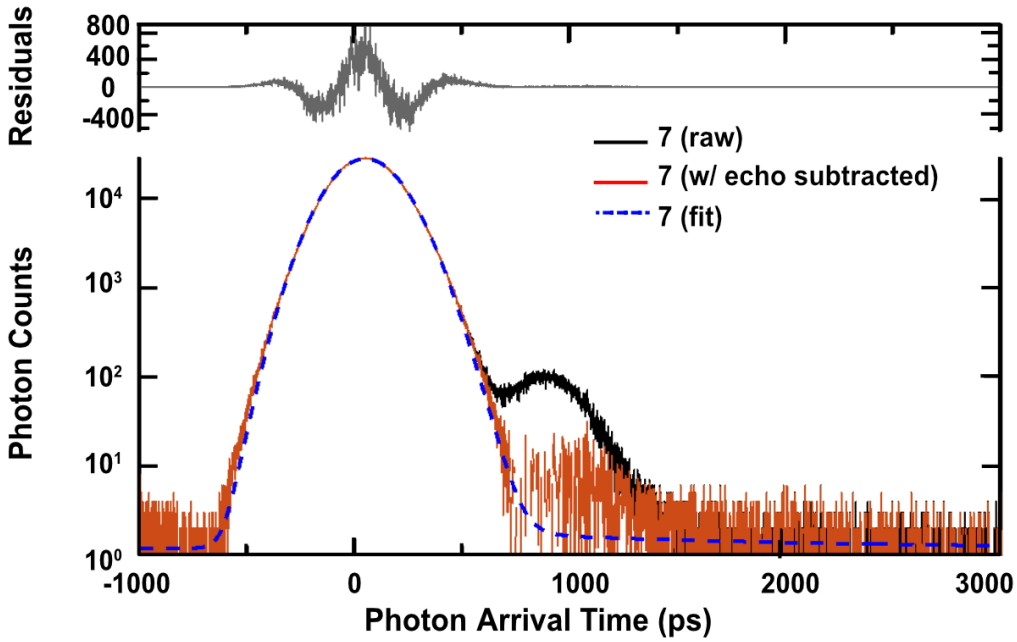

Figure 4.27. A plot showing the raw data of **4.7** with the fiber echo (black), the data after the echo is subtracted (red), the fit to equation 4 (dashed blue) and the corresponding residual of the fit (grey).

It should be noted that the fast lifetimes are roughly a third of the IRF and very similar. We are at the limit of our instrument time resolution, so our numbers represent upper bounds for the lifetimes. Compound **4.7** had a very pronounced additional long lifetime component (τ = 1612 ps), which was fit by adding another term corresponding to a new state in equation 4. This could be attributed to the presence of the (asymmetric) charge-transfer state[18] or intersystem crossing to a triplet state resulting thermally activated delayed fluorescence[19] or phosphorescence. It should be noted that the other dyes lifetimes visually appeared to have a very weak long-lived component (Figures 4.27, red trace), however, they could not be reliably fit due to poor signal-to-noise.

The radiative (k_r) and non-radiative (k_{nr}) rates were determined by utilizing the determined lifetimes and relating them to k as shown in equation 5.

$$\tau = \frac{1}{k} \qquad (5)$$

Where k is equal to both the summation of radiative and non-radiative rates. Utilizing the quantum yield of fluorescence (Φ) equation below, these rates can be solved for.

$$\Phi_F = \frac{k_r}{k_r + k_{nr}} \qquad (6)$$

4.5.2 Computational Procedures (Performed by Patrick Neal)

I. Additional computational details

Conformational searches were performed with the Schrodinger suite of programs in Maestro.[32] The search was done in both gas phase and water with the OPLS3 force field.[33] A Van der Waals radii cutoff of 12.0, electrostatic cutoff of 20.0, and H-bond cutoff of 4.0 was used. The OSVM gradient descent with 3,000 iterations was applied with a convergence threshold of 0.05. The Mixed torsional/Low-mode sampling algorithm was implemented with 10,000 structures and 100 steps per rotatable bond. The lowest energy 10 structures within 100 kJ/mol and an RMSD cutoff of 0.5 Å were selected for DFT optimization. All equilibrium geometries were optimized with M06-2X[21]/6-31+G(d,p) in gas phase and IEF-PCM^{water} (gas and H_2O, respectively) with Gaussian 16revisionA.03.[22] Only all *trans* conformers were considered. As a result, an additional constraint was applied to the central triene during the conformational search for **4.10-Gas** to prevent rotation to *cis*. Frequency calculations were performed to confirm stationary points and compute atomic polar tensor (APT)[9] charges for desymmetrization analysis. The APBS Electrostatics[10-12] plugin for PyMol was used to plot the APT charges to electrostatic potential maps. Two general classes of conformers, *anti* and *syn*, were observed. We classify structures with polymethine substituents pointed away from each as *anti*, while structures with polymethine substituents pointed towards each other as *syn*.

We sought to further understand the effect of desymmetrization on the optical properties of these dyes. To this end, we considered the role of dynamic structures resulting from accessible

vibrational modes in solution to simulate absorbance spectra. 100 Wigner sampled geometries, 50 from the lowest energy conformer of each type (*anti* and *syn*), were generated at 298 K. Vertical excitations calculations were performed on each sampled structure. TD-DFT is well known to poorly replicate experimental excitations for cyanine dyes due to the missing double excitation contribution and predicts the $\lambda_{max,abs}$ roughly 250 – 300 nm lower than experimentally observed. Compared to ωB97XD[13]/6-31+G(d,p), CIS(D)[14]/cc-pvdz-RI[15] vertical excitations, calculated with ORCA 4.2.1[16] to leverage the Resolution of Identity approximation, give substantially improved agreement with experiment for dyes **4.10** and **4.11** with an error around 100 – 150 nm. Therefore, CIS(D) was chosen to plot absorbance spectra.

II. Vertical Excitation Energies calculated at TD-DFT and CIS(D) levels of theory

Vertical excitation energies were calculated at both the TD-DFT and CIS(D) levels of theory. These methods were benchmarked against the experimental $\lambda_{max,abs}$ at 896 nm for **4.11** and 938 nm for **4.10** (Table 4.1 and 4.2).

Table 4.1. Vertical excitation energies for the first three excited states are given for dye **4.11** with ωB97XD/6-31+G(d,p) and CIS(D)/cc-pvdz-RI. **4.11-H_2O-symmetric** was computed based on the **4.11-Gas** geometry in IEF-PCM water.

		ωB97XD/6-31+G(d,p)		**CIS(D)/cc-pvdz-RI**	
		wavelength (nm)	**Oscillator Strength**	**wavelength (nm)**	**Oscillator Strength**
4.11-Gas	Excitation 1	620.9	1.93	781.1	1.39
	Excitation 2	401.6	0.40	476.4	0.42
	Excitation 3	400.2	0.63	474.9	0.68
4.11-H_2O-symmetric	Excitation 1	672.6	2.03	780.2	1.38
	Excitation 2	413.0	0.48	485.9	0.43
	Excitation 3	412.1	0.78	484.5	0.69
4.11-H_2O	Excitation 1	588.9	1.80	620.1	1.43
	Excitation 2	434.1	0.83	511.0	0.72
	Excitation 3	366.7	0.48	351.5	0.05
4.11-Highlighted 775 nm	Excitation 1	678.7	2.08	774.8	1.46
	Excitation 2	410.5	0.27	463.4	0.27
	Excitation 3	408.1	0.95	459.7	0.75
4.11-Highlighted 523 nm	Excitation 1	507.4	1.68	523.2	1.37
	Excitation 2	450.4	0.82	523.4	0.80
	Excitation 3	355.7	0.30	352.2	0.21

Table 4.2. Vertical excitation energies for the first three excited states are given for dye **4.10** with ωB97XD/6-31+G(d,p) and CIS(D)/cc-pvdz-RI.

		ωB97XD/6-31+G(d,p)		CIS(D)/cc-pvdz-RI	
		wavelength (nm)	**Oscillator Strength**	**wavelength (nm)**	**Oscillator Strength**
4.10-Gas-conf0	Excitation 1	637.2	1.86	799.0	1.36
	Excitation 2	489.2	0.12	637.4	0.08
	Excitation 3	486.4	0.54	635.1	0.45
4.10-H_2O-A	Excitation 1	681.3	1.89	776.6	1.32
	Excitation 2	492.7	0.28	636.2	0.14
	Excitation 3	491.2	0.60	633.6	0.44
4.10-H_2O-B	Excitation 1	680.5	1.89	774.0	1.33
	Excitation 2	499.9	0.45	658.1	0.28
	Excitation 3	483.7	0.42	634.4	0.29
4.10-H_2O-C	Excitation 1	679.7	1.89	772.6	1.33
	Excitation 2	501.1	0.46	659.6	0.29
	Excitation 3	482.1	0.42	631.7	0.28
4.10-Highlighted 790 nm	Excitation 1	688.3	2.00	790.5	1.36
	Excitation 2	494.6	0.48	638.3	0.32
	Excitation 3	466.4	0.42	561.6	0.33
4.10-Highlighted 575 nm	Excitation 1	560.7	1.91	574.6	1.64
	Excitation 2	509.6	0.46	576.8	0.38
	Excitation 3	404.2	0.20	449.1	0.20

III. Desymmetrization Parameters

Bond length alternation and charge alternation plots were used to illustrate desymmetrization of the solvated structures of **4.10** and **4.11** (Figure 4.24). The parameters Δl and Δq were defined as:

$$\Delta l_v = |l_v - l_{v+1}| \qquad (7)$$

Where l_v is the length of the vth C-C bond along the extended polymethine chain labeled in Figure S1. Bond lengths at equivalent positions on the symmetrical heterocycle are averaged (i.e. 1 and 1').

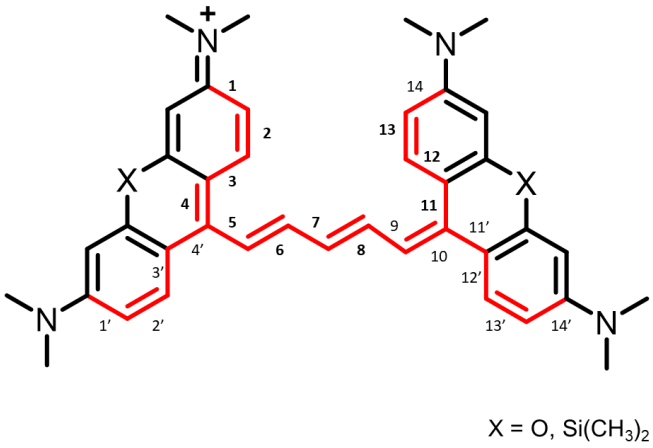

Figure 4.28. Labeled vth C-C bond used to calculate BLA along the polymethine chain.

CA is calculated as:

$$\Delta q_\mu = | q_\mu - q_{\mu+1} | \qquad (8)$$

Where q_μ is the charge of the μth atom, including the nitrogens, labeled in Figure 4.28. Charges at equivalent atoms in the symmetrical heterocycle are averaged (i.e. 1 and 1').

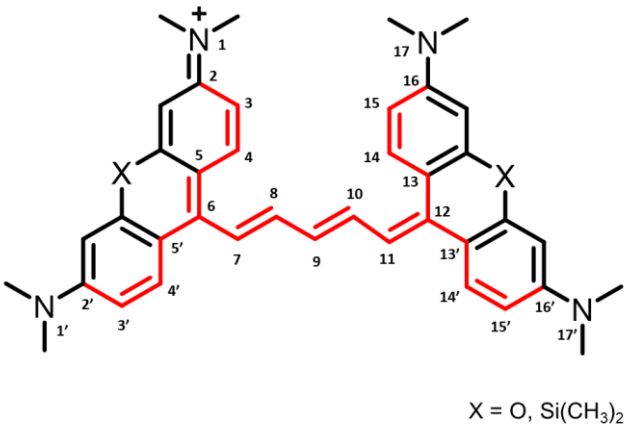

Figure 4.29. Labeled μth atom used to calculate CA along the polymethine chain.

IV. Desymmetrization analysis and optical properties of 4.11

Analogous desymmetrization and optical property analysis performed on **4.10** was conducted for **4.11**. Figure 4.30 shows the lowest energy conformers of **4.11** in the gas phase (**4.11-Gas**) and solvent (**4.11-H_2O**).

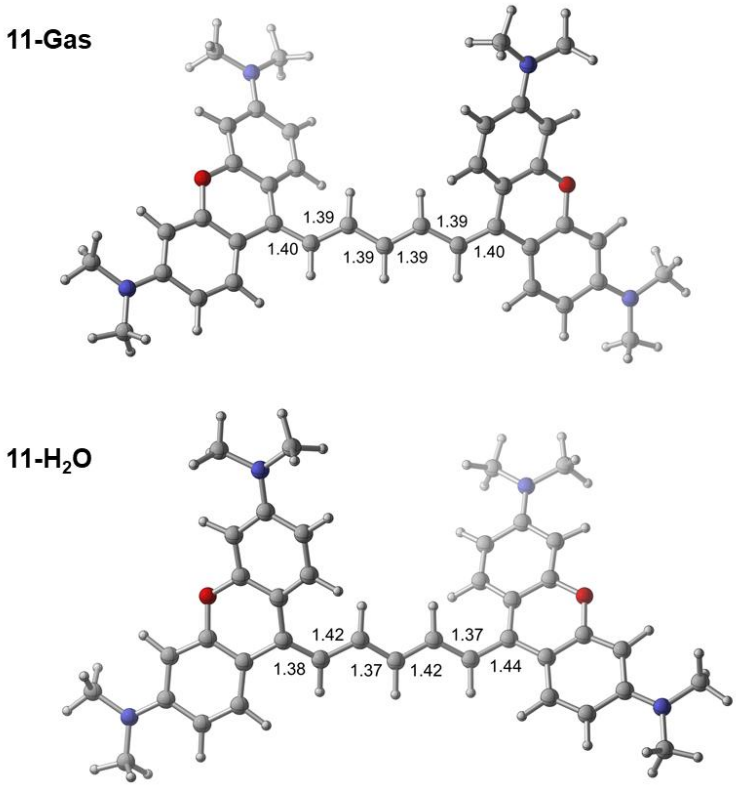

Figure 4.30. The lowest energy conformers, optimized with M062X[4]/6-31+G(d,p), of **4.11-Gas** and **4.11-H_2O** are shown. While bond lengths are equal in the gas phase structure, there is a significant deviation in the solvated geometry.

VI. Equilibrium Geometries

11-Gas

Charge	1
Multiplicity	1
Stoichiometry	C39H41N4O2(+1)
Number of Basis Functions	1060
Electronic Energy (Eh)	-1879.35995596
Sum of electronic and zero-point Energies (Eh)	-1878.633274

Sum of electronic and thermal Energies (Eh)	-1878.590441
Sum of electronic and enthalpy Energies (Eh)	-1878.589497
Sum of electronic and thermal Free Energies (Eh)	-1878.71341
Number of Imaginary Frequencies	0
Mean of alpha and beta Electrons	159

Molecular Geometry in Cartesian Coordinates

C	13.223633	-1.627347	-1.069216
C	12.303468	-1.742174	-2.128637
C	10.939734	-1.422285	-1.857200
C	10.533474	-1.099608	-0.585625
C	11.425303	-1.067457	0.513869
C	12.784343	-1.272109	0.195807
C	11.050080	-0.754618	1.873054
C	12.133531	-0.344487	2.738845
C	13.465151	-0.564231	2.333597
C	11.972773	0.214097	4.028807
C	13.037480	0.536348	4.832084
C	14.377380	0.293862	4.403682
C	14.562118	-0.271419	3.128328
N	15.435086	0.601621	5.200881
C	15.220482	1.190490	6.512598
C	16.786524	0.348466	4.733123
C	9.736987	-0.846674	2.358936
C	8.716581	-1.632451	1.823496
C	7.428116	-1.708615	2.350944
N	12.705742	-2.104073	-3.377098
C	14.116504	-2.326082	-3.642832
C	11.755665	-2.122766	-4.476749
C	6.470990	-2.584349	1.839673
C	5.143313	-2.628654	2.264275
C	4.144442	-3.477753	1.763813
C	4.417534	-4.728527	1.095201
C	3.402429	-5.349655	0.337707
C	1.792679	-3.814332	1.103392
C	2.746441	-3.126299	1.879788
C	5.624605	-5.460559	1.207574
C	5.840220	-6.637522	0.533591

C	4.837114	-7.183083	-0.321982
C	3.596070	-6.520457	-0.377216
C	0.443848	-3.496225	1.094489
C	-0.039032	-2.451754	1.904458
C	0.906676	-1.746693	2.708405
C	2.239011	-2.073167	2.676910
N	-1.358716	-2.124786	1.925042
C	-1.835297	-1.043675	2.772096
C	-2.296525	-2.864833	1.099125
N	5.059269	-8.326034	-1.025998
C	3.984657	-8.908602	-1.810865
C	6.313507	-9.045395	-0.878927
O	13.758205	-1.128581	1.130718
O	2.152667	-4.824384	0.265923
H	14.286215	-1.776441	-1.205978
H	10.215358	-1.392965	-2.660465
H	9.503153	-0.800671	-0.431937
H	10.976526	0.419168	4.402656
H	12.846292	0.978479	5.800932
H	15.542783	-0.490681	2.728073
H	14.706179	2.155512	6.438458
H	14.633711	0.526363	7.157235
H	16.186212	1.356499	6.986743
H	17.002660	0.914940	3.819538
H	17.493498	0.656038	5.501551
H	16.942000	-0.717599	4.529618
H	9.514512	-0.368200	3.307443
H	8.944152	-2.285836	0.982613
H	7.161129	-1.064410	3.187159
H	14.514555	-3.117047	-2.998051
H	14.238854	-2.639174	-4.678307
H	14.705580	-1.414041	-3.484287
H	10.920401	-2.797183	-4.261415
H	11.356547	-1.122830	-4.687472
H	12.258993	-2.485694	-5.371345
H	6.777317	-3.218635	1.009243
H	4.842618	-1.845696	2.953237
H	6.385146	-5.112212	1.896615
H	6.770766	-7.166866	0.690790
H	2.757062	-6.907435	-0.939620
H	-0.203205	-4.078281	0.452195
H	0.580839	-0.942014	3.354178
H	2.914009	-1.506006	3.307004
H	-1.636026	-1.247552	3.830353
H	-1.368589	-0.089525	2.502349
H	-2.911504	-0.943007	2.643048

H	-3.297436	-2.464149	1.249221
H	-2.045422	-2.774010	0.035711
H	-2.307433	-3.927924	1.367210
H	3.623659	-8.199428	-2.563540
H	4.358962	-9.790501	-2.327893
H	3.140099	-9.209613	-1.178334
H	6.313275	-9.896759	-1.557573
H	7.164333	-8.406635	-1.137749
H	6.451158	-9.419550	0.143106

Frequencies (Top 10 out of 252)

1. 7.2599 cm-1 (Symmetry: A)
2. 12.3729 cm-1 (Symmetry: A)
3. 12.5488 cm-1 (Symmetry: A)
4. 32.0596 cm-1 (Symmetry: A)
5. 33.7145 cm-1 (Symmetry: A)
6. 35.7408 cm-1 (Symmetry: A)
7. 37.5865 cm-1 (Symmetry: A)
8. 50.9758 cm-1 (Symmetry: A)
9. 56.6067 cm-1 (Symmetry: A)
10. 66.7526 cm-1 (Symmetry: A)

11-H_2O-symmetric (**11-Gas** geometry with solvated TD-DFT vertical excitation, note coordinates have been translated)

Charge	1
Multiplicity	1
Stoichiometry	C39H41N4O2(+1)
Number of Basis Functions	1060
Electronic Energy (Eh)	-1879.60837738

Mean of alpha and beta Electrons	159

Molecular Geometry in Cartesian Coordinates

C	5.274128	2.432737	1.205006
C	4.279209	3.087111	1.956134
C	3.094874	2.353851	2.265098
C	2.903512	1.087249	1.769953
C	3.850440	0.444138	0.936277
C	5.060292	1.143745	0.744325
C	3.692762	-0.876211	0.372486
C	4.914220	-1.516806	-0.062653
C	6.086576	-0.748120	-0.205583
C	5.027275	-2.876865	-0.435907
C	6.200181	-3.422054	-0.893904
C	7.371928	-2.620096	-1.040635
C	7.280931	-1.261376	-0.685954
N	8.533440	-3.153759	-1.504402
C	8.605776	-4.561697	-1.859229
C	9.709923	-2.312450	-1.636136
C	2.453287	-1.517486	0.226753
C	1.208369	-0.892275	0.158474
C	0.000326	-1.568793	-0.006148
N	4.457144	4.358236	2.407831
C	5.715379	5.040706	2.160381
C	3.458633	4.979163	3.262028
C	-1.208675	-0.893265	-0.168549
C	-2.452966	-1.519404	-0.236849
C	-3.693096	-0.878217	-0.378740
C	-3.852029	0.442864	-0.940471
C	-5.061440	1.142190	-0.744759
C	-6.085281	-0.750790	0.205591
C	-4.913248	-1.519343	0.058939
C	-2.906933	1.087293	-1.775352
C	-3.099476	2.354627	-2.268074
C	-4.283170	3.087380	-1.955336
C	-5.276385	2.431875	-1.202906
C	-7.278289	-1.264262	0.689010
C	-7.368344	-2.623186	1.043071
C	-6.196808	-3.424944	0.893091
C	-5.025188	-2.879582	0.432028
N	-8.528634	-3.157358	1.509209
C	-8.599011	-4.564888	1.866054
C	-9.704627	-2.316076	1.645509

N	-4.461926	4.359215	-2.404570
C	-5.718948	5.042056	-2.151947
C	-3.465411	4.981123	-3.260380
O	6.104847	0.581098	0.084478
O	-6.104459	0.578606	-0.083358
H	6.232182	2.887407	0.991886
H	2.349118	2.774491	2.926706
H	2.021379	0.538763	2.079066
H	4.167711	-3.530259	-0.343422
H	6.224570	-4.474269	-1.144799
H	8.119389	-0.583152	-0.769525
H	8.392042	-5.203037	-0.996517
H	7.903762	-4.807166	-2.664117
H	9.612418	-4.786184	-2.207489
H	10.008737	-1.893994	-0.667710
H	10.534861	-2.910222	-2.019595
H	9.530025	-1.486538	-2.334410
H	2.456871	-2.583323	0.021629
H	1.167061	0.195869	0.162895
H	0.001016	-2.657616	-0.007506
H	5.914746	5.112563	1.085717
H	5.657823	6.050654	2.562744
H	6.556148	4.523713	2.639746
H	2.482581	5.007994	2.766686
H	3.353985	4.450259	4.217476
H	3.760780	6.004291	3.469820
H	-1.168514	0.194923	-0.170397
H	-2.455554	-2.585752	-0.034353
H	-2.025353	0.539447	-2.087163
H	-2.355029	2.776560	-2.930346
H	-6.233941	2.886151	-0.986795
H	-8.116357	-0.585907	0.775524
H	-6.220444	-4.477213	1.143836
H	-4.165820	-3.532879	0.337146
H	-8.384372	-5.206930	1.004141
H	-7.896684	-4.808367	2.671310
H	-9.605409	-4.790305	2.214421
H	-10.529259	-2.914846	2.028077
H	-9.523570	-1.492298	2.346050
H	-10.004606	-1.894644	0.678784
H	-5.915533	5.110540	-1.076572
H	-5.661446	6.053228	-2.551189
H	-6.561367	4.527339	-2.630881
H	-3.768774	6.006044	-3.467479
H	-2.488427	5.010606	-2.766881
H	-3.362188	4.452583	-4.216142

11-H_2O

Charge	1
Multiplicity	1
Stoichiometry	C39H41N4O2(+1)
Number of Basis Functions	1060
Electronic Energy (Eh)	-1879.40850782
Sum of electronic and zero-point Energies (Eh)	-1878.683353
Sum of electronic and thermal Energies (Eh)	-1878.640325
Sum of electronic and enthalpy Energies (Eh)	-1878.639381
Sum of electronic and thermal Free Energies (Eh)	-1878.76438
Number of Imaginary Frequencies	0
Mean of alpha and beta Electrons	159

Molecular Geometry in Cartesian Coordinates

C	-5.212829	2.451570	1.194220
C	-4.217213	3.060658	1.984705
C	-3.050694	2.298146	2.271133
C	-2.871881	1.048687	1.715060

C	-3.815144	0.459773	0.847193
C	-5.007900	1.183127	0.671101
C	-3.667348	-0.841337	0.201157
C	-4.936478	-1.472042	-0.162476
C	-6.084315	-0.675522	-0.294425
C	-5.102760	-2.840279	-0.454699
C	-6.308254	-3.370696	-0.862822
C	-7.451485	-2.538083	-1.026152
C	-7.309721	-1.170367	-0.719722
N	-8.642703	-3.047789	-1.454762
C	-8.786420	-4.476833	-1.675551
C	-9.810014	-2.186996	-1.521763
C	-2.467048	-1.447532	-0.093637
C	-1.175116	-0.847916	-0.059388
C	-0.013606	-1.522705	-0.324410
N	-4.380922	4.321399	2.483015
C	-5.652220	5.001882	2.306850
C	-3.417842	4.855706	3.431878
C	1.246780	-0.859327	-0.359763
C	2.441980	-1.496189	-0.551419
C	3.726470	-0.851800	-0.529545
C	3.933159	0.474832	-1.011449
C	5.182342	1.110723	-0.796198
C	6.089911	-0.850188	0.149576
C	4.864160	-1.540238	-0.005712
C	2.996049	1.217665	-1.783945
C	3.239075	2.498422	-2.197070
C	4.470023	3.157057	-1.869114
C	5.452486	2.409443	-1.183056
C	7.229491	-1.427933	0.678369
C	7.204573	-2.776951	1.092716
C	5.967607	-3.491331	0.967562
C	4.854556	-2.886176	0.451568
N	8.303800	-3.376897	1.599316
C	9.542350	-2.623740	1.733924
C	8.255753	-4.767498	2.033977
N	4.692557	4.436209	-2.237876
C	5.974623	5.062494	-1.947028
C	3.679983	5.182848	-2.974658
O	-6.054026	0.669623	-0.043188
O	6.202306	0.459265	-0.186356
H	-6.162091	2.930721	0.993046
H	-2.298039	2.679072	2.948882
H	-1.991666	0.482551	1.998345
H	-4.261983	-3.515806	-0.335397
H	-6.373462	-4.434372	-1.051643

H	-8.134582	-0.474097	-0.797745
H	-8.083628	-4.831275	-2.436993
H	-8.620259	-5.049848	-0.754622
H	-9.796277	-4.678395	-2.028517
H	-10.656501	-2.764609	-1.888832
H	-10.068696	-1.778403	-0.536337
H	-9.643181	-1.350658	-2.209793
H	-2.497905	-2.457238	-0.494430
H	-1.100750	0.222314	0.123225
H	-0.040960	-2.594955	-0.513334
H	-5.893541	5.103981	1.244079
H	-5.581197	6.000777	2.733930
H	-6.474643	4.467442	2.800952
H	-3.388616	4.271701	4.361127
H	-2.413055	4.872812	2.999094
H	-3.696128	5.879698	3.675536
H	1.237543	0.211517	-0.160854
H	2.424425	-2.579705	-0.621449
H	2.075847	0.739409	-2.095902
H	2.498401	3.001608	-2.804324
H	6.431752	2.810997	-0.959658
H	8.116015	-0.813851	0.762713
H	5.899967	-4.521214	1.291888
H	3.940286	-3.464201	0.393878
H	9.411341	-1.767829	2.405228
H	10.309586	-3.273850	2.148455
H	9.885701	-2.258201	0.760214
H	7.980449	-5.429713	1.207034
H	9.242139	-5.056618	2.389857
H	7.539922	-4.903372	2.851327
H	6.170038	5.067131	-0.869657
H	6.793711	4.538627	-2.452060
H	5.953193	6.091693	-2.298183
H	4.030569	6.203260	-3.113121
H	3.497098	4.742007	-3.960497
H	2.737816	5.215333	-2.419524

Frequencies (Top 10 out of 252)

1. 6.0816 cm-1 (Symmetry: A)
2. 11.1143 cm-1 (Symmetry: A)
3. 12.4646 cm-1 (Symmetry: A)
4. 26.2643 cm-1 (Symmetry: A)
5. 32.8531 cm-1 (Symmetry: A)
6. 35.4086 cm-1 (Symmetry: A)
7. 40.1896 cm-1 (Symmetry: A)
8. 45.4988 cm-1 (Symmetry: A)

9. 51.4999 cm-1 (Symmetry: A)
10. 56.8884 cm-1 (Symmetry: A)

11-H_2O-syn

Charge	1
Multiplicity	1
Stoichiometry	C39H41N4O2(+1)
Number of Basis Functions	1060
Electronic Energy (Eh)	-1879.4085816
Sum of electronic and zero-point Energies (Eh)	-1878.683168
Sum of electronic and thermal Energies (Eh)	-1878.640227
Sum of electronic and enthalpy Energies (Eh)	-1878.639283
Sum of electronic and thermal Free Energies (Eh)	-1878.763416
Number of Imaginary Frequencies	0
Mean of alpha and beta Electrons	159

Molecular Geometry in Cartesian Coordinates

C	-5.300592	2.444126	0.988266
C	-4.404225	3.480907	0.658609
C	-3.293110	3.149181	-0.165832
C	-3.063459	1.843402	-0.546198
C	-3.898830	0.777601	-0.151347
C	-5.049221	1.146143	0.568319
C	-3.690248	-0.626922	-0.491987
C	-4.913281	-1.430275	-0.475456
C	-6.022657	-0.974742	0.252998
C	-5.062678	-2.683907	-1.100537
C	-6.214867	-3.433742	-0.993206

C	-7.314274	-2.971019	-0.216300
C	-7.191744	-1.709369	0.398398
N	-8.448385	-3.718703	-0.079457
C	-9.587544	-3.170574	0.634706
C	-8.593279	-4.961769	-0.818090
C	-2.472873	-1.203464	-0.774883
C	-1.184036	-0.632452	-0.566955
C	-0.013944	-1.251017	-0.916630
N	-4.612774	4.760246	1.087064
C	-3.762303	5.834854	0.602509
C	-5.840425	5.089828	1.790124
C	1.256641	-0.672590	-0.631524
C	2.451120	-1.278600	-0.907436
C	3.741388	-0.734871	-0.582006
C	4.022805	0.662914	-0.620895
C	5.262009	1.141047	-0.123779
C	6.030331	-1.056405	0.257257
C	4.807562	-1.604994	-0.197143
C	3.179017	1.649425	-1.205410
C	3.490467	2.980880	-1.192056
C	4.702706	3.447860	-0.584424
C	5.598695	2.480430	-0.078336
C	7.100777	-1.823051	0.679545
C	7.002590	-3.231073	0.669145
C	5.764618	-3.811223	0.236371
C	4.720949	-3.023556	-0.165498
N	8.034123	-4.010154	1.061204
C	9.279385	-3.396176	1.499175
C	7.903127	-5.461958	1.076945
N	4.991152	4.765393	-0.534165
C	6.260595	5.209367	0.024490
C	4.070341	5.748305	-1.092412
O	-6.003604	0.227725	0.906500
O	6.205762	0.286180	0.340187
H	-6.209486	2.624455	1.547381
H	-2.626263	3.921757	-0.525651
H	-2.233605	1.642185	-1.214318
H	-4.254424	-3.073425	-1.710871
H	-6.272392	-4.379941	-1.515379
H	-7.989541	-1.275285	0.986940
H	-9.322118	-2.929279	1.669761
H	-9.969025	-2.260464	0.153478
H	-10.384574	-3.911759	0.653762
H	-8.558611	-4.797985	-1.902698
H	-7.806829	-5.674559	-0.548879
H	-9.553678	-5.409317	-0.568282

H	-2.471184	-2.241535	-1.096869
H	-1.110754	0.320823	-0.047156
H	-0.042301	-2.209198	-1.433600
H	-3.849448	5.970245	-0.483504
H	-4.055980	6.762297	1.091336
H	-2.713246	5.641682	0.846566
H	-6.727580	4.916786	1.166523
H	-5.937199	4.494693	2.703940
H	-5.814993	6.140887	2.072554
H	1.249781	0.285960	-0.114476
H	2.418071	-2.287446	-1.308117
H	2.279802	1.334020	-1.719932
H	2.821393	3.679460	-1.676748
H	6.562655	2.746349	0.334147
H	7.990020	-1.308383	1.017894
H	5.641182	-4.886031	0.230499
H	3.801656	-3.509800	-0.468467
H	9.994586	-4.179043	1.741519
H	9.705092	-2.770658	0.707513
H	9.122853	-2.778334	2.390512
H	7.699254	-5.851442	0.074386
H	8.837813	-5.893147	1.428642
H	7.101452	-5.779881	1.751417
H	6.299569	6.295944	-0.005256
H	6.361581	4.886788	1.065905
H	7.104994	4.813941	-0.550950
H	4.455782	6.744329	-0.885817
H	3.971171	5.632191	-2.177081
H	3.081216	5.660862	-0.633484

Frequencies (Top 10 out of 252)

1. 7.2826 cm-1 (Symmetry: A)
2. 11.1374 cm-1 (Symmetry: A)
3. 14.7612 cm-1 (Symmetry: A)
4. 31.3951 cm-1 (Symmetry: A)
5. 33.3138 cm-1 (Symmetry: A)
6. 37.1210 cm-1 (Symmetry: A)
7. 40.1592 cm-1 (Symmetry: A)
8. 49.2097 cm-1 (Symmetry: A)
9. 57.1731 cm-1 (Symmetry: A)
10. 60.9654 cm-1 (Symmetry: A)

10-Gas

Charge	1
Multiplicity	1
Stoichiometry	C43H53N4Si2(+1)
Number of Basis Functions	1204
Electronic Energy (Eh)	-2467.51304465
Sum of electronic and zero-point Energies (Eh)	-2466.645072
Sum of electronic and thermal Energies (Eh)	-2466.591806
Sum of electronic and enthalpy Energies (Eh)	-2466.590862
Sum of electronic and thermal Free Energies (Eh)	-2466.73763
Number of Imaginary Frequencies	0
Mean of alpha and beta Electrons	183

Molecular Geometry in Cartesian Coordinates

C	-4.831619	2.802390	0.414678
C	-4.073492	3.621727	-0.461155
C	-3.231473	2.965979	-1.390360
C	-3.124848	1.587476	-1.395455

C	-3.848739	0.776518	-0.498624
C	-4.742710	1.418100	0.394393
C	-3.724616	-0.685289	-0.574481
C	-4.903834	-1.544791	-0.405846
C	-5.960813	-1.202885	0.474277
C	-5.015435	-2.750475	-1.127223
C	-6.111968	-3.579818	-1.004956
C	-7.166380	-3.260282	-0.114130
C	-7.049043	-2.051765	0.619050
N	-8.249827	-4.075732	0.024068
C	-8.337077	-5.304515	-0.744900
C	-9.330336	-3.706512	0.920817
C	-2.494007	-1.290070	-0.831541
C	-1.242083	-0.671145	-0.715080
C	-0.033040	-1.324120	-0.942454
N	-4.173776	4.982788	-0.427741
C	-5.126338	5.621064	0.463305
C	-3.445879	5.784720	-1.393476
C	1.190956	-0.692582	-0.737189
C	2.429282	-1.332812	-0.883078
C	3.676213	-0.754992	-0.644652
C	3.831643	0.702610	-0.546502
C	4.755954	1.309068	0.340089
C	5.924087	-1.335907	0.345961
C	4.841886	-1.639894	-0.517119
C	3.106875	1.544435	-1.413394
C	3.241090	2.920306	-1.384346
C	4.113695	3.541474	-0.459605
C	4.872756	2.690794	0.384812
C	6.998347	-2.208423	0.449952
C	7.075919	-3.404047	-0.309207
C	5.996563	-3.685057	-1.182933
C	4.914173	-2.832437	-1.264568
N	8.145715	-4.243102	-0.210729
C	9.252632	-3.912715	0.668772
C	8.194058	-5.455485	-1.008580
N	4.240820	4.899584	-0.401825
C	5.222255	5.502078	0.482718
C	3.509096	5.734125	-1.336473
Si	-5.790355	0.345003	1.522636
C	-4.861240	-0.054679	3.104611
C	-7.448904	1.137218	1.888631
Si	5.805067	0.194657	1.426438
C	4.900188	-0.216990	3.019315
C	7.485616	0.948334	1.773204
H	-5.518251	3.270131	1.112429

H	-2.683001	3.533004	-2.132010
H	-2.509617	1.120231	-2.158635
H	-4.251666	-3.023932	-1.848672
H	-6.159646	-4.473462	-1.614271
H	-7.835717	-1.777914	1.314351
H	-7.493362	-5.969708	-0.527410
H	-9.256062	-5.824910	-0.480331
H	-8.355092	-5.102887	-1.822857
H	-8.980415	-3.627742	1.957072
H	-9.781888	-2.750429	0.630246
H	-10.102418	-4.473075	0.880933
H	-2.479673	-2.363845	-0.997548
H	-1.198515	0.361391	-0.372088
H	-0.045270	-2.355365	-1.291549
H	-4.914121	5.374714	1.509580
H	-5.049207	6.701258	0.349776
H	-6.157715	5.323397	0.235654
H	-3.764959	5.572585	-2.422151
H	-3.626974	6.838852	-1.189149
H	-2.367387	5.605004	-1.319046
H	1.171884	0.338713	-0.388447
H	2.391761	-2.404363	-1.059565
H	2.467668	1.104017	-2.172860
H	2.689601	3.512167	-2.104024
H	5.582238	3.131479	1.077275
H	7.805303	-1.963510	1.132671
H	6.013469	-4.566802	-1.810909
H	4.129767	-3.076234	-1.974420
H	8.926077	-3.844501	1.713329
H	10.006678	-4.695024	0.599775
H	9.718913	-2.961573	0.385095
H	7.342652	-6.109873	-0.788373
H	8.193801	-5.229897	-2.081959
H	9.108295	-5.998487	-0.774837
H	5.163536	6.585575	0.391905
H	5.025555	5.238927	1.527948
H	6.243240	5.189868	0.229152
H	3.714477	6.780389	-1.115323
H	3.803181	5.536704	-2.375486
H	2.429039	5.573292	-1.243433
H	-3.894676	-0.514211	2.876183
H	-4.679451	0.851931	3.690200
H	-5.432387	-0.754279	3.722903
H	-7.990513	1.367969	0.967002
H	-8.071959	0.474011	2.497347
H	-7.321968	2.065103	2.455783

H	3.920249	-0.653028	2.802041
H	5.469408	-0.939274	3.612790
H	4.748246	0.681770	3.625167
H	8.012629	1.187250	0.845215
H	7.388026	1.866943	2.360899
H	8.108112	0.261575	2.355801

Frequencies (Top 10 out of 300)

1. 5.1354 cm-1 (Symmetry: A)
2. 10.5764 cm-1 (Symmetry: A)
3. 12.4656 cm-1 (Symmetry: A)
4. 20.4226 cm-1 (Symmetry: A)
5. 21.5135 cm-1 (Symmetry: A)
6. 31.1438 cm-1 (Symmetry: A)
7. 35.4318 cm-1 (Symmetry: A)
8. 50.5128 cm-1 (Symmetry: A)
9. 53.2121 cm-1 (Symmetry: A)
10. 54.4448 cm-1 (Symmetry: A)

10-H_2O-A

Charge	1
Multiplicity	1
Stoichiometry	C43H53N4Si2(+1)
Number of Basis Functions	1204
Electronic Energy (Eh)	-2467.561984
Sum of electronic and zero-point Energies (Eh)	-2466.696555
Sum of electronic and thermal Energies (Eh)	-2466.642793
Sum of electronic and enthalpy Energies (Eh)	-2466.641849
Sum of electronic and thermal Free Energies (Eh)	-2466.791762

Number of Imaginary Frequencies	0
Mean of alpha and beta Electrons	183

Molecular Geometry in Cartesian Coordinates

C	-4.778240	2.712996	0.369823
C	-3.955782	3.530931	-0.451075
C	-3.097748	2.870596	-1.365530
C	-3.030479	1.490261	-1.398510
C	-3.810171	0.678682	-0.547402
C	-4.726067	1.326731	0.320335
C	-3.704141	-0.783650	-0.632519
C	-4.902350	-1.629603	-0.511217
C	-5.986808	-1.279484	0.332152
C	-5.000971	-2.832311	-1.240511
C	-6.110056	-3.652246	-1.158921
C	-7.192696	-3.325619	-0.303106
C	-7.089474	-2.118381	0.436406
N	-8.285422	-4.131933	-0.202233
C	-8.360233	-5.356413	-0.981445
C	-9.392552	-3.756114	0.660910
C	-2.475039	-1.403745	-0.853127
C	-1.221173	-0.794696	-0.695648
C	-0.008561	-1.444680	-0.909996
N	-4.008544	4.889499	-0.380729
C	-3.186931	5.694159	-1.269400
C	-4.962468	5.538876	0.503392
C	1.200140	-0.789277	-0.686661
C	2.457205	-1.392959	-0.834030
C	3.682166	-0.766939	-0.603907
C	3.780519	0.695909	-0.523332
C	4.686746	1.352067	0.348618
C	5.958620	-1.248403	0.381946
C	4.882346	-1.607425	-0.468334
C	3.003307	1.500389	-1.383646
C	3.063673	2.881066	-1.355847
C	3.911562	3.549301	-0.437604
C	4.731758	2.738648	0.392898
C	7.063736	-2.082056	0.499680
C	7.177967	-3.292805	-0.232553
C	6.103473	-3.628690	-1.095126
C	4.991766	-2.813918	-1.190101
N	8.273175	-4.093737	-0.118739
C	9.372052	-3.708355	0.750790

C	8.358119	-5.323495	-0.888616
N	3.957363	4.908212	-0.372469
C	4.901341	5.565726	0.516376
C	3.138180	5.705406	-1.270161
Si	-5.846816	0.266858	1.390177
C	-7.509165	1.082932	1.672117
C	-5.007723	-0.148920	3.018308
Si	5.803963	0.302095	1.431720
C	4.954097	-0.110101	3.055150
C	7.460708	1.126358	1.722514
H	-5.477225	3.185089	1.052264
H	-2.498586	3.437822	-2.066767
H	-2.393093	1.025277	-2.144538
H	-4.213061	-3.115786	-1.931410
H	-6.142872	-4.545338	-1.770300
H	-7.896255	-1.839419	1.106191
H	-8.339101	-5.148417	-2.057902
H	-7.530307	-6.030904	-0.741849
H	-9.292948	-5.866964	-0.749260
H	-9.830442	-2.798509	0.355479
H	-10.164379	-4.520947	0.598621
H	-9.073270	-3.674279	1.706361
H	-2.464586	-2.474727	-1.035964
H	-1.177811	0.231646	-0.335922
H	-0.004886	-2.470530	-1.273861
H	-2.124453	5.460260	-1.140833
H	-3.453289	5.534039	-2.321541
H	-3.334884	6.746286	-1.033177
H	-4.790194	5.255719	1.547591
H	-4.843686	6.617451	0.419644
H	-5.995662	5.282957	0.239064
H	1.149559	0.237074	-0.327827
H	2.452742	-2.464144	-1.015693
H	2.374003	1.029349	-2.132699
H	2.467319	3.442530	-2.064067
H	5.423194	3.216887	1.078744
H	7.863742	-1.796326	1.174720
H	6.144913	-4.524947	-1.701323
H	4.210783	-3.104625	-1.885806
H	10.148766	-4.468831	0.696624
H	9.806427	-2.749441	0.444618
H	9.045072	-3.624412	1.793704
H	7.528269	-5.998738	-0.650960
H	8.345192	-5.123163	-1.966640
H	9.290393	-5.829581	-0.645167
H	4.778287	6.643364	0.427161

H	4.722202	5.286071	1.560353
H	5.937682	5.313473	0.261100
H	3.279029	6.759159	-1.036857
H	3.413108	5.542680	-2.319675
H	2.076018	5.466509	-1.148455
H	-7.996938	1.324251	0.723359
H	-8.170208	0.424297	2.244373
H	-7.390541	2.007623	2.246047
H	-4.036354	-0.621357	2.841661
H	-4.848965	0.758370	3.609743
H	-5.626507	-0.838407	3.601362
H	3.986144	-0.587485	2.873135
H	5.571309	-0.794327	3.646007
H	4.786895	0.799088	3.641314
H	8.119972	0.473036	2.302872
H	7.954761	1.365235	0.776394
H	7.333989	2.053207	2.291209

Frequencies (Top 10 out of 300)

1. 3.5127 cm-1 (Symmetry: A)
2. 6.6114 cm-1 (Symmetry: A)
3. 10.3205 cm-1 (Symmetry: A)
4. 16.4164 cm-1 (Symmetry: A)
5. 19.8651 cm-1 (Symmetry: A)
6. 29.6449 cm-1 (Symmetry: A)
7. 32.9063 cm-1 (Symmetry: A)
8. 47.6907 cm-1 (Symmetry: A)
9. 50.0771 cm-1 (Symmetry: A)
10. 51.3146 cm-1 (Symmetry: A)

10-H_2O-conf0-anti

Charge	1
Multiplicity	1
Stoichiometry	C43H53N4Si2(+1)
Number of Basis Functions	1204
Electronic Energy (Eh)	-2467.56200589

Sum of electronic and zero-point Energies (Eh)	-2466.696271
Sum of electronic and thermal Energies (Eh)	-2466.642683
Sum of electronic and enthalpy Energies (Eh)	-2466.641739
Sum of electronic and thermal Free Energies (Eh)	-2466.789428
Number of Imaginary Frequencies	0
Mean of alpha and beta Electrons	183

Molecular Geometry in Cartesian Coordinates

C	-4.671604	2.775445	1.023473
C	-3.715542	3.173867	1.996309
C	-2.803528	2.186542	2.445608
C	-2.816037	0.915314	1.902737
C	-3.732942	0.534580	0.900126
C	-4.698360	1.491862	0.495623
C	-3.708727	-0.834587	0.369792
C	-4.962694	-1.542329	0.065426
C	-6.109551	-0.864248	-0.419083
C	-5.055078	-2.937429	0.248866
C	-6.214974	-3.638619	-0.019343
C	-7.362671	-2.976724	-0.525398
C	-7.266790	-1.573459	-0.716309
N	-8.507682	-3.657450	-0.807823
C	-9.676400	-2.947231	-1.299520
C	-8.574069	-5.092426	-0.587547
C	-2.504131	-1.506611	0.165718
C	-1.236365	-0.908181	0.117222
C	-0.057503	-1.613099	-0.113160
N	-3.693167	4.440985	2.494176
C	-4.704869	5.403016	2.088711
C	-2.745795	4.792775	3.538838
C	1.163130	-0.952660	-0.231699
C	2.392305	-1.610847	-0.384446
C	3.636368	-0.988448	-0.482131
C	3.745934	0.444896	-0.781762
C	4.765741	1.262551	-0.230823
C	6.027716	-1.291456	0.277981

C	4.843902	-1.810797	-0.304309
C	2.858960	1.039607	-1.704033
C	2.927215	2.380745	-2.032272
C	3.896496	3.223459	-1.433214
C	4.820880	2.613963	-0.542527
C	7.138984	-2.107895	0.447890
C	7.150739	-3.464325	0.029532
C	5.966912	-3.964356	-0.570361
C	4.852623	-3.160199	-0.713680
N	8.251415	-4.249849	0.189648
C	8.229566	-5.632206	-0.258479
C	9.461969	-3.699176	0.775713
N	3.955773	4.553383	-1.718432
C	5.021806	5.372439	-1.165078
C	3.030996	5.131000	-2.679481
Si	-5.994910	0.979430	-0.761351
C	-5.373636	1.268626	-2.510116
C	-7.626991	1.851259	-0.469157
Si	6.019129	0.473314	0.922195
C	5.397435	0.502123	2.694510
C	7.701177	1.285432	0.781195
H	-5.412965	3.493171	0.688098
H	-2.098150	2.407334	3.236837
H	-2.129873	0.177782	2.307925
H	-4.215548	-3.489219	0.660223
H	-6.235496	-4.703753	0.174637
H	-8.123911	-1.034182	-1.105945
H	-10.481218	-3.661585	-1.462127
H	-10.021213	-2.196796	-0.578358
H	-9.466056	-2.444126	-2.250377
H	-8.419236	-5.343168	0.468653
H	-9.558187	-5.450538	-0.883878
H	-7.821648	-5.621021	-1.183833
H	-2.543421	-2.557560	-0.106777
H	-1.161233	0.174143	0.204460
H	-0.090619	-2.697486	-0.202184
H	-4.681198	5.567428	1.006107
H	-5.712531	5.072258	2.368928
H	-4.505311	6.353269	2.580543
H	-2.920207	4.214623	4.454907
H	-1.716044	4.619007	3.208966
H	-2.853899	5.850149	3.772978
H	1.154262	0.131979	-0.140460
H	2.366641	-2.692684	-0.288038
H	2.130621	0.421489	-2.220179
H	2.240198	2.770718	-2.772785

H	5.602744	3.220527	-0.097753
H	8.025298	-1.692617	0.916150
H	5.923762	-4.982601	-0.936135
H	3.983159	-3.585791	-1.205000
H	8.068924	-5.700446	-1.341109
H	9.186083	-6.095477	-0.024002
H	7.439832	-6.200151	0.246250
H	9.848759	-2.862597	0.181900
H	9.285213	-3.346583	1.798432
H	10.223343	-4.476165	0.809395
H	4.889655	6.398504	-1.503122
H	4.996154	5.367289	-0.069973
H	6.009215	5.024410	-1.492079
H	1.992795	4.968775	-2.370815
H	3.204912	6.203882	-2.737133
H	3.167539	4.702639	-3.680313
H	-4.418281	0.759055	-2.669779
H	-5.230145	2.338313	-2.692805
H	-6.095399	0.886681	-3.239141
H	-7.518482	2.930641	-0.616120
H	-7.992733	1.674905	0.546428
H	-8.383870	1.498005	-1.176821
H	4.414095	0.026921	2.766411
H	6.089772	-0.035220	3.350427
H	5.310708	1.532788	3.052863
H	8.062939	1.269879	-0.250878
H	7.654646	2.326419	1.117006
H	8.431578	0.769376	1.412537

Frequencies (Top 10 out of 300)

1. 8.4678 cm-1 (Symmetry: A)
2. 11.1503 cm-1 (Symmetry: A)
3. 11.6581 cm-1 (Symmetry: A)
4. 16.1969 cm-1 (Symmetry: A)
5. 21.0512 cm-1 (Symmetry: A)
6. 31.3307 cm-1 (Symmetry: A)
7. 31.6561 cm-1 (Symmetry: A)
8. 50.3171 cm-1 (Symmetry: A)
9. 52.9196 cm-1 (Symmetry: A)
10. 55.7017 cm-1 (Symmetry: A)

10-H_2O-B

Charge	1
Multiplicity	1
Stoichiometry	C43H53N4Si2(+1)
Number of Basis Functions	1204
Electronic Energy (Eh)	-2467.56202176
Sum of electronic and zero-point Energies (Eh)	-2466.696423
Sum of electronic and thermal Energies (Eh)	-2466.642749
Sum of electronic and enthalpy Energies (Eh)	-2466.641805
Sum of electronic and thermal Free Energies (Eh)	-2466.790732
Number of Imaginary Frequencies	0
Mean of alpha and beta Electrons	183

Molecular Geometry in Cartesian Coordinates

C	-4.719363	2.874815	0.421024
C	-3.884320	3.656061	-0.423923
C	-3.048566	2.956198	-1.330274
C	-3.013832	1.575083	-1.333959
C	-3.806467	0.798973	-0.459981
C	-4.700722	1.487861	0.400460
C	-3.736333	-0.664181	-0.520090
C	-4.943816	-1.485164	-0.354746
C	-6.011487	-1.091473	0.492458
C	-5.073064	-2.709563	-1.044387
C	-6.193539	-3.507312	-0.922167
C	-7.258777	-3.136130	-0.061877
C	-7.125136	-1.907982	0.638323
N	-8.361935	-3.919651	0.079248
C	-9.450760	-3.498998	0.945691

C	-8.462626	-5.173014	-0.650238
C	-2.521075	-1.313179	-0.762271
C	-1.256227	-0.734387	-0.620236
C	-0.059071	-1.415192	-0.854820
N	-3.906247	5.015263	-0.383299
C	-4.839332	5.705739	0.492622
C	-3.065665	5.782385	-1.288027
C	1.166441	-0.796996	-0.645590
C	2.406068	-1.437538	-0.825877
C	3.653032	-0.857904	-0.621247
C	3.808210	0.598961	-0.492432
C	4.758424	1.185929	0.380845
C	5.940761	-1.454647	0.274417
C	4.832493	-1.739594	-0.561000
C	3.044438	1.462935	-1.303578
C	3.159848	2.839043	-1.226837
C	4.053907	3.439447	-0.306213
C	4.860118	2.567991	0.473545
C	7.023643	-2.325431	0.318848
C	7.080057	-3.500864	-0.474060
C	5.973250	-3.761353	-1.320879
C	4.884876	-2.909422	-1.344646
N	8.153423	-4.339683	-0.430487
C	9.285509	-4.031451	0.426371
C	8.182113	-5.527511	-1.266660
N	4.153493	4.793844	-0.192502
C	5.153457	5.381134	0.683637
C	3.357774	5.653214	-1.052487
Si	-5.834470	0.480275	1.506143
C	-7.479560	1.334419	1.774993
C	-4.992037	0.093464	3.139396
Si	5.859329	0.051838	1.394367
C	5.026135	-0.401992	3.015646
C	7.549289	0.804481	1.689259
H	-5.400590	3.377786	1.099321
H	-2.443253	3.494055	-2.049035
H	-2.395070	1.080142	-2.076084
H	-4.301781	-3.028704	-1.738129
H	-6.249804	-4.417952	-1.505227
H	-7.917100	-1.595788	1.311066
H	-10.239325	-4.248218	0.910903
H	-9.117366	-3.397705	1.984993
H	-9.871393	-2.540587	0.620148
H	-7.636681	-5.846888	-0.396152
H	-9.397335	-5.662939	-0.384324
H	-8.455520	-5.007091	-1.733998

H	-2.536554	-2.383742	-0.945294
H	-1.182587	0.289647	-0.258534
H	-0.089452	-2.438055	-1.225914
H	-4.702081	6.779258	0.378658
H	-5.878989	5.461740	0.243847
H	-4.662169	5.446828	1.542244
H	-3.340617	5.612133	-2.336211
H	-3.183466	6.841886	-1.068691
H	-2.009889	5.520893	-1.158536
H	1.153012	0.226050	-0.274473
H	2.363986	-2.505205	-1.024314
H	2.379656	1.044437	-2.053365
H	2.569337	3.448897	-1.899125
H	5.586624	2.993047	1.158164
H	7.851163	-2.096025	0.982151
H	5.969923	-4.627534	-1.970740
H	4.075524	-3.140718	-2.030446
H	10.033432	-4.814934	0.319154
H	9.746354	-3.074766	0.152881
H	8.986936	-3.983660	1.480081
H	8.143163	-5.269445	-2.331826
H	9.107084	-6.069689	-1.079312
H	7.341505	-6.193555	-1.040452
H	5.068028	6.465358	0.639571
H	5.001184	5.068715	1.722510
H	6.170260	5.101125	0.381656
H	3.542828	6.691686	-0.784034
H	3.613836	5.517114	-2.110843
H	2.288296	5.452876	-0.925976
H	-7.969009	1.557878	0.822765
H	-8.148323	0.703659	2.369340
H	-7.340866	2.272335	2.322307
H	-4.030494	-0.401060	2.969911
H	-4.813343	1.013584	3.704717
H	-5.619475	-0.568436	3.744728
H	4.038301	-0.836512	2.832855
H	5.629183	-1.133063	3.563496
H	4.902674	0.485662	3.644180
H	8.033497	1.071927	0.745666
H	7.466440	1.706291	2.304325
H	8.195923	0.101075	2.223644

Frequencies (Top 10 out of 300)

1. 5.2062 cm-1 (Symmetry: A)
2. 8.2405 cm-1 (Symmetry: A)

3. 11.2697 cm-1 (Symmetry: A)
4. 16.4160 cm-1 (Symmetry: A)
5. 19.6030 cm-1 (Symmetry: A)
6. 30.4527 cm-1 (Symmetry: A)
7. 33.5858 cm-1 (Symmetry: A)
8. 45.4200 cm-1 (Symmetry: A)
9. 51.3909 cm-1 (Symmetry: A)
10. 51.6315 cm-1 (Symmetry: A)

10-H_2O-C

Charge	1
Multiplicity	1
Stoichiometry	C43H53N4Si2(+1)
Number of Basis Functions	1204
Electronic Energy (Eh)	-2467.56205573
Sum of electronic and zero-point Energies (Eh)	-2466.696225
Sum of electronic and thermal Energies (Eh)	-2466.642661
Sum of electronic and enthalpy Energies (Eh)	-2466.641717
Sum of electronic and thermal Free Energies (Eh)	-2466.789375
Number of Imaginary Frequencies	0
Mean of alpha and beta Electrons	183

Molecular Geometry in Cartesian Coordinates

C	-4.674465	2.978531	0.373357
C	-3.804346	3.749765	-0.445165
C	-2.970174	3.041173	-1.346343
C	-2.970270	1.659963	-1.368757
C	-3.797556	0.892142	-0.519521
C	-4.690174	1.592074	0.334025
C	-3.761769	-0.570937	-0.598123
C	-4.989736	-1.365734	-0.460996
C	-6.062430	-0.956687	0.372749
C	-5.135130	-2.580177	-1.165293
C	-6.274856	-3.353677	-1.069557
C	-7.345606	-2.967291	-0.222772
C	-7.196054	-1.749482	0.492247
N	-8.468039	-3.726967	-0.107728
C	-8.584802	-4.970518	-0.851590
C	-9.561312	-3.290485	0.745296
C	-2.557825	-1.245539	-0.831633
C	-1.282829	-0.699671	-0.660461
C	-0.097549	-1.404943	-0.887700
N	-3.792415	5.108104	-0.385451
C	-2.908837	5.865908	-1.256482
C	-4.725967	5.810685	0.480460
C	1.137819	-0.817880	-0.652954
C	2.366227	-1.482689	-0.828367
C	3.622340	-0.932642	-0.603866
C	3.807064	0.518804	-0.450161
C	4.760484	1.071364	0.441643
C	5.889092	-1.590646	0.301661
C	4.783750	-1.838905	-0.548969
C	3.070622	1.411446	-1.255163
C	3.214749	2.783504	-1.155574
C	4.111912	3.350103	-0.216879
C	4.891318	2.449428	0.556765
C	6.955227	-2.482276	0.339326
C	6.996884	-3.643509	-0.474944
C	5.893035	-3.867688	-1.335754
C	4.821084	-2.994796	-1.353595
N	8.054402	-4.502900	-0.438059
C	8.067934	-5.675723	-1.295343
C	9.184882	-4.230986	0.432960
N	4.239081	4.700387	-0.080380
C	5.247298	5.251808	0.809434
C	3.473616	5.590141	-0.936849
Si	-5.868604	0.599940	1.406383
C	-7.498722	1.489207	1.651421
C	-5.068803	0.176801	3.051895

Si	5.825177	-0.103197	1.447796
C	4.961773	-0.568001	3.050120
C	7.526798	0.607286	1.777826
H	-5.354832	3.489555	1.046475
H	-2.338976	3.573123	-2.047033
H	-2.351372	1.159716	-2.107132
H	-4.360241	-2.909935	-1.849906
H	-6.341752	-4.256961	-1.662848
H	-7.991749	-1.426410	1.155378
H	-8.554999	-4.794051	-1.933260
H	-7.779153	-5.665797	-0.590194
H	-9.535065	-5.441165	-0.606922
H	-9.955097	-2.319798	0.422562
H	-10.365637	-4.021497	0.690287
H	-9.242658	-3.206696	1.790742
H	-2.595750	-2.312334	-1.032145
H	-1.190875	0.316693	-0.281810
H	-0.145970	-2.421114	-1.274927
H	-1.864742	5.569741	-1.108607
H	-3.164974	5.724111	-2.313597
H	-2.999437	6.924083	-1.018746
H	-4.573534	5.538870	1.530769
H	-4.564137	6.881993	0.378364
H	-5.765695	5.591075	0.210626
H	1.142338	0.199487	-0.266268
H	2.303870	-2.546200	-1.043299
H	2.404560	1.018965	-2.017802
H	2.644391	3.416154	-1.824160
H	5.620205	2.847795	1.254810
H	7.780869	-2.280516	1.013853
H	5.879325	-4.721752	-2.001375
H	4.013632	-3.198057	-2.050482
H	8.980979	-6.238579	-1.110458
H	7.213194	-6.329842	-1.087998
H	8.042666	-5.398004	-2.355999
H	9.664255	-3.277360	0.181473
H	8.879192	-4.198224	1.485230
H	9.920063	-5.025083	0.316026
H	5.185517	6.338218	0.782283
H	5.083130	4.926486	1.842469
H	6.259390	4.954574	0.507858
H	3.675699	6.619891	-0.647763
H	3.741775	5.466871	-1.993876
H	2.398651	5.409843	-0.828504
H	-7.962008	1.736259	0.691972
H	-8.194692	0.866585	2.222687

H	-7.350348	2.416445	2.214143
H	-4.116279	-0.339347	2.896713
H	-4.879563	1.086719	3.630165
H	-5.724370	-0.475545	3.637526
H	3.967532	-0.978379	2.847300
H	5.542297	-1.321064	3.592487
H	4.848610	0.310878	3.692778
H	8.150105	-0.119394	2.308849
H	8.029921	0.879743	0.845631
H	7.455143	1.500195	2.407099

Frequencies (Top 10 out of 300)

1. 7.3232 cm-1 (Symmetry: A)
2. 11.0440 cm-1 (Symmetry: A)
3. 12.8667 cm-1 (Symmetry: A)
4. 17.4570 cm-1 (Symmetry: A)
5. 20.8633 cm-1 (Symmetry: A)
6. 30.9810 cm-1 (Symmetry: A)
7. 34.1983 cm-1 (Symmetry: A)
8. 48.1281 cm-1 (Symmetry: A)
9. 51.2924 cm-1 (Symmetry: A)
10. 53.6366 cm-1 (Symmetry: A)

VIII. Sampled structures corresponding to Highlighted Peaks

The coordinates of Wigner sampled structures corresponding to the peaks highlighted in Figure S24 are given.

11-Highlighted 775 nm

Charge	1
Multiplicity	1
Stoichiometry	C39H41N4O2(+1)
Number of Basis Functions	1060
Electronic Energy (Eh)	-1879.3164343
Mean of alpha and beta Electrons	159

Molecular Geometry in Cartesian Coordinates

C	-5.347210	2.428743	0.964350
C	-4.406773	3.478174	0.674987
C	-3.237585	3.167546	-0.112906
C	-3.028397	1.840443	-0.447903
C	-3.922908	0.758994	-0.127499
C	-5.085006	1.161590	0.534232
C	-3.714077	-0.599177	-0.528063
C	-4.905393	-1.417212	-0.475841
C	-6.040397	-0.927846	0.299821
C	-5.057520	-2.711481	-1.047034
C	-6.155962	-3.430780	-0.818667
C	-7.250030	-2.991867	-0.069505
C	-7.187909	-1.719384	0.559424
N	-8.500702	-3.780768	-0.018010
C	-9.682966	-3.099473	0.590755
C	-8.541568	-5.041543	-0.668204
C	-2.447867	-1.106202	-0.778517
C	-1.197490	-0.681026	-0.506003
C	-0.016228	-1.311154	-0.915210
N	-4.550151	4.786659	1.016609
C	-3.884020	5.843196	0.242697
C	-5.837019	5.148160	1.735671
C	1.248126	-0.762171	-0.679789
C	2.530914	-1.298947	-0.947156
C	3.820863	-0.830151	-0.567215
C	4.050817	0.696365	-0.524177
C	5.320408	1.169393	-0.150065
C	6.066087	-1.013803	0.202336
C	4.833849	-1.576296	-0.218486
C	3.192184	1.701541	-1.172222
C	3.510717	3.021173	-1.190160
C	4.668399	3.491841	-0.509471
C	5.563928	2.596497	0.007973
C	7.141104	-1.876273	0.514654
C	7.046877	-3.218342	0.577903
C	5.806766	-3.819625	0.153563
C	4.749239	-2.992986	-0.197741
N	8.071780	-4.006440	0.858376
C	9.391124	-3.481010	1.356623
C	7.869090	-5.548363	1.095530
N	4.975027	4.818337	-0.420520
C	6.253250	5.346654	0.092346
C	3.995515	5.661409	-0.933781
O	-6.074620	0.268893	0.912375

O	6.221909	0.317002	0.382030
H	-6.270200	2.638136	1.552680
H	-2.483363	3.809120	-0.366923
H	-2.372256	1.688897	-1.174076
H	-4.264140	-3.100690	-1.714879
H	-6.306735	-4.347946	-1.550657
H	-8.019239	-1.165319	1.004164
H	-9.484566	-3.021260	1.718321
H	-9.849072	-2.131605	0.123842
H	-10.572470	-3.718888	0.582086
H	-8.684264	-4.927883	-1.633031
H	-7.665106	-5.610155	-0.601211
H	-9.446725	-5.627077	-0.053584
H	-2.547221	-2.062804	-1.229725
H	-1.045098	0.315915	-0.021324
H	-0.070183	-2.227423	-1.326250
H	-3.832048	5.516462	-0.933287
H	-4.223006	6.788172	0.372285
H	-2.882471	5.577567	0.742416
H	-6.766473	4.809380	1.234827
H	-5.792000	4.518793	2.687622
H	-5.877600	6.232206	2.036250
H	1.219124	0.057207	-0.131220
H	2.598150	-2.370343	-1.288767
H	2.337629	1.341304	-1.772187
H	2.755705	3.705613	-1.570836
H	6.527806	2.985492	0.194663
H	7.995301	-1.481299	1.067288
H	5.508433	-4.886089	0.303851
H	3.714790	-3.510048	-0.348353
H	10.171268	-4.341188	1.454338
H	9.872879	-2.969477	0.436011
H	9.448408	-2.861430	2.301140
H	7.615317	-5.966904	0.083845
H	8.719830	-5.781270	1.548338
H	7.006736	-5.734889	1.759353
H	6.264485	6.398519	0.172594
H	6.480000	4.987887	1.222716
H	7.013630	4.872110	-0.563136
H	4.351171	6.595373	-0.385305
H	4.145904	5.648926	-2.008020
H	2.880091	5.605602	-0.439786

11-Highlighted 523 nm

Charge	1
Multiplicity	1
Stoichiometry	C39H41N4O2(+1)
Number of Basis Functions	1060
Electronic Energy (Eh)	-1879.24568955
Mean of alpha and beta Electrons	159

Molecular Geometry in Cartesian Coordinates

C	-5.163785	2.415337	1.278480
C	-4.161082	3.088290	2.043987
C	-2.984707	2.195327	2.334281
C	-2.773900	0.983505	1.722299
C	-3.794859	0.441352	0.945115
C	-5.004758	1.114738	0.817945
C	-3.661362	-0.887570	0.169432
C	-4.963737	-1.495739	-0.130943
C	-6.125229	-0.637659	-0.307384
C	-5.092751	-2.923605	-0.449074
C	-6.303484	-3.335743	-0.898993
C	-7.475198	-2.467567	-1.067287
C	-7.291576	-1.148223	-0.668988
N	-8.661270	-2.980591	-1.545431
C	-8.793249	-4.333131	-1.899980
C	-9.799433	-2.111053	-1.593738
C	-2.531579	-1.491541	-0.179434
C	-1.241394	-0.912511	-0.109442
C	-0.097092	-1.496859	-0.261242
N	-4.383987	4.291523	2.549440
C	-5.759381	4.870102	2.494466
C	-3.303943	4.868795	3.435119
C	1.268734	-0.937122	-0.322858
C	2.454908	-1.484978	-0.410497
C	3.687817	-0.825174	-0.530609
C	3.948100	0.474388	-0.987640
C	5.221075	1.103394	-0.958159

C	6.130143	-0.848259	0.152045
C	4.840315	-1.464795	0.073361
C	3.046324	1.231979	-1.766787
C	3.195298	2.439822	-2.225525
C	4.462247	3.091917	-1.927107
C	5.491730	2.383940	-1.322125
C	7.308990	-1.376615	0.643844
C	7.239146	-2.675690	1.124666
C	5.926167	-3.352617	1.212820
C	4.793320	-2.819735	0.607435
N	8.389607	-3.316492	1.582094
C	9.599452	-2.523058	1.613646
C	8.334854	-4.725981	2.056274
N	4.623650	4.277444	-2.420192
C	5.889307	5.053353	-2.139949
C	3.542670	5.126289	-2.995519
O	-6.058580	0.626530	0.029632
O	6.218022	0.392951	-0.251704
H	-6.173463	2.858504	1.302303
H	-2.341795	2.738469	2.817920
H	-1.996201	0.345111	1.822662
H	-4.226558	-3.695368	-0.252626
H	-6.444749	-4.235323	-1.316801
H	-8.135877	-0.544554	-0.836254
H	-8.136388	-4.641832	-2.661886
H	-8.680060	-4.998571	-0.955068
H	-9.767808	-4.441554	-2.400233
H	-10.745427	-2.529378	-2.058278
H	-10.028157	-1.812509	-0.409028
H	-9.579576	-1.438781	-2.259624
H	-2.618651	-2.588607	-0.429691
H	-1.103409	0.055279	0.056695
H	-0.001628	-2.663792	-0.195736
H	-6.047452	5.116985	1.483613
H	-5.729106	5.988958	2.847589
H	-6.487748	4.391029	3.118338
H	-3.271201	4.150534	4.164388
H	-2.191998	5.147170	2.916897
H	-3.734452	5.975532	3.861811
H	0.912662	0.225016	0.015047
H	2.333619	-2.506650	-0.543634
H	2.088282	0.776785	-1.963132
H	2.506422	2.888961	-2.910211
H	6.566319	2.782778	-1.186815
H	8.181114	-0.810640	0.568767
H	5.951231	-4.293611	1.889293

H	3.941050	-3.346540	0.702959
H	9.343308	-1.706734	2.164305
H	10.313591	-3.067428	2.246003
H	10.170488	-2.358642	0.545813
H	7.966604	-5.258530	1.200919
H	9.312418	-4.820449	2.573652
H	7.743361	-4.897470	2.927092
H	5.988256	5.021568	-0.963317
H	6.750900	4.564592	-2.530576
H	6.005327	6.043729	-2.581198
H	4.035009	6.172491	-3.103322
H	3.224220	4.740098	-3.982326
H	2.707408	4.970539	-2.502719

10-Highlighted 790 nm

Charge	1
Multiplicity	1
Stoichiometry	C43H53N4Si2(+1)
Number of Basis Functions	1204
Electronic Energy (Eh)	-2467.36564114
Mean of alpha and beta Electrons	183

Molecular Geometry in Cartesian Coordinates

C	-4.775630	2.752947	0.333307
C	-3.998269	3.641792	-0.502178
C	-3.160628	2.963942	-1.285232
C	-3.070759	1.530788	-1.401656
C	-3.802263	0.714912	-0.471039
C	-4.795013	1.359831	0.411542
C	-3.667424	-0.767794	-0.517354
C	-4.826492	-1.634742	-0.357806
C	-5.964063	-1.330112	0.423932
C	-4.853987	-2.821790	-1.099454
C	-5.895376	-3.690993	-1.036118
C	-7.077854	-3.381385	-0.243256

C	-7.028843	-2.157381	0.560051
N	-8.157510	-4.205349	-0.179124
C	-8.166154	-5.464702	-0.973054
C	-9.252479	-3.796824	0.714226
C	-2.375248	-1.364731	-0.776704
C	-1.112762	-0.729222	-0.614774
C	0.020016	-1.423761	-0.846713
N	-4.242428	4.942737	-0.588069
C	-3.340982	5.781426	-1.301514
C	-5.066241	5.625530	0.495086
C	1.294520	-0.868885	-0.727199
C	2.496531	-1.384245	-0.903641
C	3.671604	-0.795606	-0.579243
C	3.747392	0.714047	-0.493045
C	4.714897	1.410530	0.211066
C	5.976166	-1.235979	0.451944
C	4.853609	-1.666500	-0.436374
C	2.988925	1.562708	-1.334443
C	3.176622	2.898286	-1.405641
C	4.028475	3.553774	-0.493469
C	4.808207	2.742926	0.388933
C	7.069660	-2.095371	0.599424
C	7.134673	-3.301037	-0.217436
C	6.064713	-3.599000	-1.059217
C	4.925843	-2.844880	-1.128706
N	8.240344	-4.083810	-0.106054
C	9.321601	-4.033554	0.874950
C	8.068487	-5.254454	-0.914415
N	4.140014	4.875583	-0.497787
C	4.928464	5.615923	0.381317
C	3.318842	5.672082	-1.465798
Si	-5.816676	0.268724	1.497102
C	-7.573521	1.103761	1.697147
C	-5.125827	-0.173691	3.089265
Si	5.844804	0.386928	1.436164
C	4.830146	0.006379	3.109026
C	7.549340	1.137857	1.784695
H	-5.539720	3.051048	0.949393
H	-2.778833	3.599341	-2.038301
H	-2.442057	1.169935	-2.052217
H	-3.966240	-2.936539	-1.672585
H	-5.881274	-4.612873	-1.606288
H	-8.086955	-1.859991	0.963156
H	-7.771490	-5.315546	-2.025874
H	-7.387362	-6.332757	-0.569279
H	-9.279193	-6.107190	-1.007588

H	-9.887045	-2.894206	0.425233
H	-9.959469	-4.719624	0.685003
H	-8.898587	-3.652093	1.775851
H	-2.316494	-2.378267	-0.944852
H	-1.127328	0.385713	-0.442902
H	-0.183719	-2.445384	-1.135724
H	-2.186286	5.740386	-1.187512
H	-3.498525	5.790579	-2.530539
H	-3.503313	6.663262	-1.072234
H	-4.658418	5.360559	1.520528
H	-4.908289	6.559879	0.118145
H	-6.130292	5.313792	0.350061
H	1.192958	0.200910	-0.482051
H	2.341859	-2.481704	-1.106209
H	2.427339	0.854353	-1.999670
H	2.627315	3.420913	-2.146827
H	5.503407	3.369423	0.960382
H	7.972092	-1.989951	1.327468
H	6.095444	-4.665676	-1.371692
H	4.181367	-3.200693	-1.638603
H	9.947357	-4.896027	0.935920
H	9.919357	-3.199852	0.825329
H	8.801011	-3.952894	1.926893
H	7.273072	-6.214002	-0.662870
H	8.035171	-5.138953	-1.878314
H	9.081469	-5.637843	-1.021134
H	4.970656	6.702687	0.215330
H	4.912523	5.387508	1.574949
H	6.159180	5.332202	0.072053
H	3.477349	6.775046	-1.121630
H	3.393672	5.548085	-2.516262
H	2.149649	5.687969	-1.303113
H	-8.328083	1.594978	0.888235
H	-8.241998	0.839795	2.538430
H	-7.342641	1.923781	2.378450
H	-4.050689	-0.686487	3.015970
H	-5.133923	0.861605	3.596711
H	-5.887025	-0.536479	3.703193
H	3.882664	-0.567155	3.004285
H	5.670450	-0.257684	4.087233
H	4.711952	1.101301	3.371034
H	8.286986	0.428132	2.301781
H	8.184548	1.199209	0.721285
H	7.566186	2.097410	2.190905

10-Highlighted 575 nm

Charge	1
Multiplicity	1
Stoichiometry	C43H53N4Si2(+1)
Number of Basis Functions	1204
Electronic Energy (Eh)	-2467.39145308
Mean of alpha and beta Electrons	183

Molecular Geometry in Cartesian Coordinates

C	4.840453	2.693572	-0.775401
C	3.849522	3.218861	-1.691182
C	2.800140	2.403244	-2.060221
C	2.864376	1.065088	-1.630887
C	3.809361	0.462227	-0.783743
C	4.817550	1.384668	-0.343796
C	3.783971	-0.937520	-0.542057
C	4.849324	-1.671876	-0.250304
C	6.097989	-1.095207	0.230641
C	4.917314	-3.064934	-0.505568
C	5.974685	-3.804660	-0.305286
C	7.246979	-3.277906	0.269008
C	7.193415	-1.780733	0.629589
N	8.309530	-3.985317	0.619870
C	9.511111	-3.256413	1.157026
C	8.405402	-5.444863	0.216266
C	2.416763	-1.469927	-0.336684
C	1.219984	-0.908299	-0.215126
C	-0.037449	-1.516803	-0.166045
N	3.941042	4.521919	-2.058776
C	5.104925	5.432509	-1.654602
C	3.085395	5.047517	-3.178425
C	-1.246856	-0.846886	-0.050311
C	-2.544336	-1.484787	0.038906
C	-3.679559	-0.925717	0.257566

C	-3.770656	0.526556	0.788323
C	-4.754343	1.434400	0.348755
C	-6.066777	-1.092200	-0.390920
C	-4.871928	-1.772453	0.207825
C	-2.864722	1.015989	1.822905
C	-2.947278	2.300360	2.251905
C	-3.909420	3.294650	1.750952
C	-4.892246	2.741235	0.822028
C	-7.230587	-1.880296	-0.564649
C	-7.254690	-3.269957	-0.268381
C	-6.067520	-3.819553	0.306355
C	-4.827246	-3.121467	0.407560
N	-8.401325	-3.974958	-0.449943
C	-8.358401	-5.361357	-0.121771
C	-9.658869	-3.333154	-0.827412
N	-3.934386	4.527932	2.173969
C	-4.912586	5.416058	1.652102
C	-2.873627	5.036856	3.040819
Si	6.073884	0.714579	0.821661
C	5.428322	0.851763	2.539567
C	7.798014	1.370992	0.679146
Si	-6.133466	0.789012	-0.790894
C	-5.495644	0.814867	-2.616138
C	-7.735643	1.674100	-0.536193
H	5.477215	3.322862	-0.162904
H	2.199312	2.921518	-2.761113
H	2.080454	0.252375	-1.951283
H	4.058446	-3.396604	-1.083768
H	5.955520	-4.869863	-0.522123
H	7.954974	-1.232207	0.994070
H	10.190236	-4.256235	1.294950
H	10.116428	-2.601740	0.418816
H	9.214925	-2.646553	1.993810
H	8.417574	-5.604451	-1.034512
H	9.468646	-6.061987	0.762163
H	7.521902	-6.052267	0.551180
H	2.390625	-2.555340	-0.203988
H	1.169379	0.228019	-0.171549
H	0.039927	-2.562979	-0.002684
H	5.309757	5.492479	-0.446728
H	6.067082	4.919938	-2.121567
H	4.840085	6.501605	-2.018828
H	3.162754	4.520731	-4.252856
H	2.084855	4.939449	-2.748100
H	3.225963	6.097855	-3.290503
H	-1.218999	0.291016	0.033058

H	-2.423101	-2.408651	-0.281569
H	-2.217316	0.164532	2.036599
H	-2.196233	2.326258	3.003383
H	-5.758236	3.298746	0.473510
H	-8.212044	-1.583224	-1.084883
H	-5.906618	-4.877656	0.455584
H	-3.782527	-3.500582	0.446567
H	-8.526026	-5.564198	0.875943
H	-9.326815	-5.724146	-0.696389
H	-7.390892	-6.037246	-0.685644
H	-10.230861	-2.716749	-0.053876
H	-9.190582	-2.486392	-1.585911
H	-10.284622	-4.039295	-1.360752
H	-4.667839	6.250338	2.200922
H	-4.730702	5.571306	0.562744
H	-5.969596	4.910340	1.803426
H	-1.797193	4.825560	2.586763
H	-2.978443	6.004442	3.261355
H	-2.777200	4.584730	4.126004
H	4.487350	0.135652	2.564763
H	5.238232	1.854807	2.751231
H	6.060353	0.680805	3.570692
H	7.606518	2.485992	0.873600
H	8.535517	1.481098	-0.096784
H	8.488469	1.027537	1.502322
H	-4.640884	0.046218	-2.700487
H	-6.276430	0.981547	-3.406919
H	-5.081013	1.970003	-2.622335
H	-8.233962	1.694449	0.524770
H	-7.704932	2.668569	-0.983210
H	-8.496986	1.359014	-1.376384

4.5.3 Synthetic Procedures

Materials: Chemical reagents were purchased from Acros Organics, Alfa Aesar, Fisher Scientific, Sigma-Aldrich, or TCI and used without purification unless noted otherwise. Anhydrous and deoxygenated solvents (THF) were dispensed from a Grubb's-type Phoenix Solvent Drying System. Oxygen was removed by three consecutive freeze–pump–thaw cycles in air-free glassware directly before use.

Instrumentation: Thin layer chromatography was performed using Silica Gel 60 F_{254} (EMD Millipore) plates. Flash chromatography was executed with technical grade silica gel with 60 Å pores and 40 – 63 μm mesh particle size (Sorbtech Technologies). Solvent was removed under reduced pressure with a Büchi Rotovapor with a Welch self-cleaning dry vacuum pump and further dried with a Welch DuoSeal pump. Nuclear magnetic resonance (^{1}H-NMR, ^{13}C-NMR) spectra were taken on Bruker Avance 300, AV-400, AV-500 and processed with MestReNova or TopSpin software. All ^{1}H NMR and ^{13}C NMR peaks are reported in ppm in reference to their respective solvent signals. High resolution mass spectra (electrospray ionization (ESI)) were obtained on a Thermo Scientific Q Exactive™ Plus Hybrid Quadrupole-Orbitrap™ M with Dionex UltiMate 3000 RSLCnano System

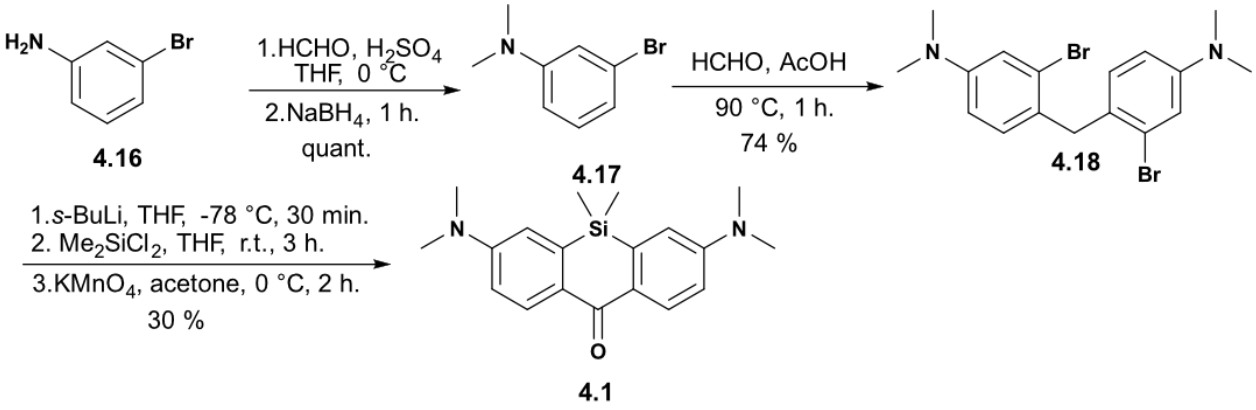

Scheme 4.3. Synthesis of silicon-xanthone **4.1** following previous literature procedure.[18]

3-bromo-*N*,*N*-dimethylaniline (4.17)

Sulfuric acid (3M, 1.2 mL, 3.5 mmol, 2 eq) was added dropwise at 0° C to an aqueous solution of formaldehyde (37% in H_2O, 0.700 mL, 5.22 mmol, 3 eq) in THF (4.7 mL). The solution was left to stir for 10 minutes before 3-bromoaniline (300 mg, 0.19 mL, 1.7 mmol, 1 eq) was added dropwise. Sodium borohydride (263 mg, 6.96 mmol, 4 eq) was added portion wise over 30

minutes, at which point the reaction was warmed to room temperature and left to stir for 1 hr. The solution was quenched with saturated $NaHCO_3$ (10 mL), extracted with dichloromethane (3 x 10 mL), dried over $MgSO_4$, filtered and evaporated to dryness. The crude product was purified via silica gel chromatography with hexanes: ethyl acetate (50:1 → 25:1) to afford pure **3-bromo-*N*,*N*-dimethylaniline** (388 mg, 1.95 mmol, quant) as a yellowish liquid. ^{1}H-NMR matched literature.[18] ^{1}H-NMR (400 MHz, Chloroform-*d*): δ 7.07 (ddd, *J* = 8.3, 7.6, 0.5 Hz, 1H), 6.90 – 6.72 (m, 2H), 6.62 (ddd, *J* = 8.5, 2.4, 1.0 Hz, 1H), 2.94 (s, 6H).

4,4′-Methylene-bis(3-bromo-*N*,*N*-dimethylaniline) (4.18)

3-bromo-*N*,*N*-dimethylaniline **4.16** (2.00 g, 10.0 mmol, 1 eq) was dissolved in glacial acetic acid (23.0 mL) and aqueous formaldehyde solution (37%, 0.74 mL, 5.0 mmol, 0.5 eq) was added dropwise. The mixture was heated to 90 °C and turned deep red in color. After 1 h, the reaction was quenched with a saturated $NaHCO_3$ solution, extracted with dichloromethane (3 x 5 mL), dried over $MgSO_4$, filtered and evaporated to give a dark red oil. The crude product was purified via silica gel chromatography with hexanes: ethyl acetate (25:1 →15:1 → 9:1) to afford pure **4,4′-methylene-bis(3-bromo-*N*,*N*-dimethylaniline)-one** as a white solid (1.12 g, 2.72 mmol, 74%). ^{1}H-NMR matched literature.[18] ^{1}H-NMR (300 MHz, Chloroform-*d*): δ 6.94 (d, *J* = 2.7 Hz, 2H), 6.85 (d, *J* = 8.6 Hz, 2H), 6.58 (dd, *J* = 8.5, 2.7 Hz, 2H), 4.00 (s, 2H), 2.91 (s, 12H).

3,7-Bis(*N*,*N*-dimethylamino)-5,5-dimethyldibenzo[b,e]silin10(5H)-one (4.1)

4,4′-Methylene-bis(3-bromo-*N*,*N*-dimethylaniline) **4.18** (250 mg, 0.61 mmol, 1 equiv.) was dissolved in THF (6 mL, anhydrous) and cooled to -78 °C. *sec*-BuLi (1.47 M in cyclohexane, 1.74 mL, 2.56 mmol, 4.2 eq) was added dropwise over 30 minutes and the mixture was stirred for an

additional 30 minutes. A solution of dichlorodimethylsilane (0.08 mL, 0.7 mmol, 1.2 eq) in THF (2.75 mL, anhydrous) was added slowly down the sides of the reaction flask and the reaction was warmed to room temperature. After 3h, the reaction was quenched via acidification with 2M HCl solution (2 mL) and turns from yellow to a deep dark blue/green. Saturated $NaHCO_3$ solution (5 mL) was added and then the solution was extracted with dichloromethane (3 x 20 mL), dried over $MgSO_4$, filtered and evaporated to give blue/green oil. Due to the instability of this intermediate, the crude mixture was pushed forward to the next reaction. The blue/green oil was dissolved in acetone (3.7 mL) and cooled to 0 °C. $KMnO_4$ (231 mg, 1.46 mmol, 2.4 eq) was added slowly over 30 min turning the solution purple. After stirring for two hours, TLC confirmed consumption of starting material. The crude mixture was extracted in excess amounts of dichloromethane (3 x 50 mL) until little color was seen in the organic layer, dried over $MgSO_4$, filtered and evaporated to give a blue/green solid. The crude product was purified via silica gel chromatography with hexanes: ethyl acetate (95:5) to afford pure **3,7-bis(*N*,*N*-dimethylamino)-5,5-dimethyldibenzo[b,e]silin10(5H)-one** as a yellow-green solid (55 mg, 0.17 mmol, 30%). ^{1}H-NMR matched literature.[18] ^{1}H-NMR (400 MHz, Chloroform-*d*): δ 8.39 (d, *J* = 9.0 Hz, 2H), 6.84 (dd, *J* = 9.0, 2.8 Hz, 2H), 6.79 (d, *J* = 2.9 Hz, 2H), 3.09 (s, 12H), 0.46 (s, 6H).

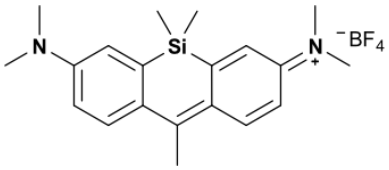

***N*-(7-(dimethylamino)-5,5,10-trimethyldibenzo[b,e]silin-3(5H)-ylidene)-*N*-methylmethanaminium (4.3)**

3,7-Bis(*N*,*N*-dimethylamino)-5,5-dimethyldibenzo[b,e]silin10(5H)-one **4.1** (20 mg, 0.06 mmol, 1 eq) was dissolved in THF (0.15 mL, anhydrous) and cooled to 0° C. MeMgBr (1.15 M in THF,

0.32 mL, 0.37 mmol, 6 eq) was added dropwise over 30 min and the solution turned bright orange. The reaction was warmed to room temperature and left to stir overnight, at which point it was quenched with 5% fluoroboric acid solution. After quenching, the solution turned dark blue and was extracted with dichloromethane (3 x 5 mL), dried over $MgSO_4$, filtered and evaporated. Crude product was purified through a 9:1 dichloromethane: ethanol column to afford pure **3** in a nearly 1:1.5 ratio of cation (methyl) and neutral (alkene) state, as a dark blue-green crystalline solid (25 mg, 0.10 mmol, 87%). ^{1}H-NMR (400 MHz, Chloroform-d) δ 8.17 (d, J = 9.6 Hz, 2H), 7.59 (d, J = 8.7 Hz, 2H), 7.07 (d, J = 2.9 Hz, 2H), 7.00 (d, J = 2.8 Hz, 2H), 6.89 – 6.84 (m, 4H), 5.42 (s, 2H), 3.37 (s, 9H), 3.02 (s, 12H), 2.91 (s, 3H), 0.50 (s, 4H), 0.43 (s, 6H). HRMS (ESI) *m/z* calc for $C_{20}H_{27}N_2Si^+$: 323.1938; found 323.1940. UV−vis (dichloromethane): (λ_{max}/nm) = 646 nm. Fluorescence (dichloromethane): λ_{max} (emission) = 673 nm.

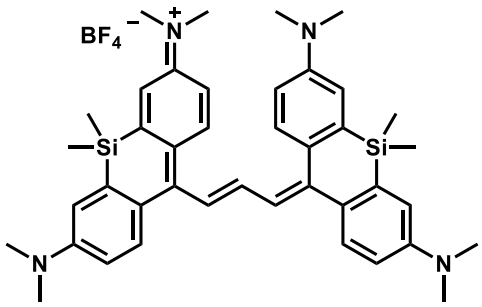

(E)-*N*-(10-(3-(3,7-bis(dimethylamino)-5,5-dimethyldibenzo[b,e]silin-10(5H)-ylidene)prop-1-en-1-yl)-7-(dimethylamino)-5,5-dimethyldibenzo[b,e]silin-3(5H)-ylidene)-*N*-methylmethanaminium (4.7)

Compound **4.3** (50 mg, 0.15 mmol, 2 eq) was added to a Schlenk flask along with *N*,*N*-diphenylformamidine (16 mg, 0.10 mmol, 1 eq) and then acetic anhydride (0.300 mL, 3.20 mmol) and 2,6-lutidine (0.052 mL, 0.45 mmol, 3 eq) was added. The solution was freeze pump thawed then heated to 140 °C. After 15 minutes, the reaction was cooled to r.t and concentrated directly

onto silica. The product was purified via silica gel chromatography with dichloromethane: ethanol (99:1 → 98:2 → 97:3) to afford pure **7** as a dark blue solid (7 mg, 0.01 mol, 9%). ^{1}H NMR (400 MHz, Chloroform-d) δ 7.84 (d, J = 9.0 Hz, 4H), 7.77 (t, J = 12.9 Hz, 2H), 7.36 (d, J = 12.9 Hz, 2H), 6.95 (d, J = 2.8 Hz, 4H), 6.85 (dd, J = 9.0, 2.8 Hz, 4H), 3.17 (s, 24 H), 0.43 (s, 12H). HRMS (ESI) *m/z* calc for $C_{41}H_{51}N_4Si_2^+$: 655.3647; found 655.3638. UV−vis (dichloromethane): (λ_{max}/nm) = 854 nm. Fluorescence (dichloromethane): λ_{max} (emission) = 913 nm.

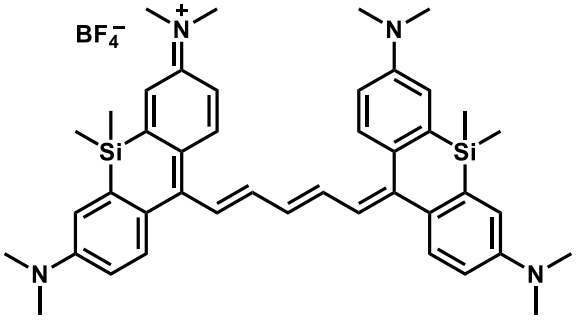

***N*-(10-((1E,3E)-5-(3,7-bis(dimethylamino)-5,5-dimethyldibenzo[b,e]silin-10(5H)-ylidene)penta-1,3-dien-1-yl)-7-(dimethylamino)-5,5-dimethyldibenzo[b,e]silin-3(5H)-ylidene)-*N*-methylmethanaminium (4.10)**

Compound **4.3** (50 mg, 0.15 mmol, 2 eq) was added to a Schlenk flask along with malonaldehyde bis(phenylimine) monohydrochloride (18 mg, 0.10 mmol, 1 eq) and then acetic anhydride (0.300 mL, 3.20 mmol) and 2,6-lutidine (0.052 mL, 0.45 mmol, 3 eq) was added. The solution was freeze pump thawed then heated to 140 °C. After 15 minutes, the reaction was cooled to r.t and concentrated directly onto silica. The product was purified via silica gel chromatography with dichloromethane: ethanol (99:1 → 98:2 → 97:3) to afford pure product as a blue-green solid (20 mg, 0.02 mmol, 32%). ^{1}H-NMR (400 MHz, Chloroform-*d*): δ 7.67 (d, *J* = 9.0 Hz, 3H), 7.17 (d, *J* = 8.0 Hz, 7H), 6.98 (d, *J* = 2.8 Hz, 3H), 6.77 (dd, *J* = 9.0, 2.8 Hz, 4H), 3.16 (s, 24H), 0.47 (s, 12H).

HRMS (ESI) *m/z* calc for $C_{43}H_{53}N_4Si_2^+$: 681.3803; found 681.3789. UV−vis (dichloromethane): (λ_{max}/nm) = 938 nm. Fluorescence (dichloromethane): λ_{max} (emission) = 1006 nm.

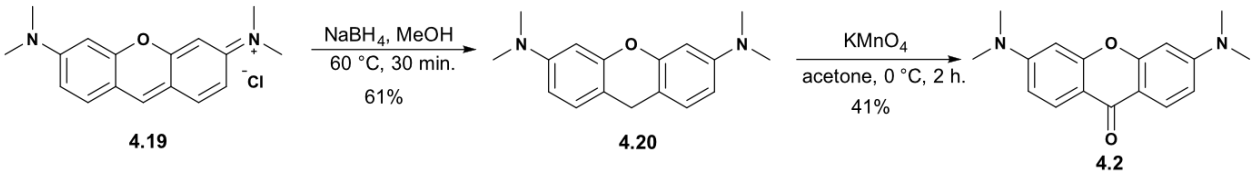

Scheme 4.4. Synthesis of oxygen-xanthone **4.2** following previous literature procedure.[19]

***N*3,*N*3,*N*6,*N*6-tetramethyl-9H-xanthene-3,6-diamine (4.20)**

Pyronin Y (**4.19**, 50 mg, 0.2 mmol, 1eq) was dissolved in MeOH (15 mL) by heating to 60 °C. After the solid was dissolved, sodium borohydride (38 mg, 1.0 mmol, 6 eq) was added slowly in portions over 30 minutes. The solution was stirred for 30 minutes, cooled to rt, then concentrated down to give dark purple solid. The solid was extracted into dichloromethane (3 x 10 mL), dried over Na_2SO_4, filtered and concentrated to afford pure ***N*3,*N*3,*N*6,*N*6-tetramethyl-9H-xanthene-3,6-diamine (4.20)** as a dark purple solid (28 mg, 0.10 mmol, 61%) ^{1}H-NMR matched literature.[19] ^{1}H-NMR (300 MHz, Chloroform-*d*): δ 7.05 (d, *J* = 8.2 Hz, 2H), 6.55 – 6.42 (m, 4H), 3.90 (s, 2H), 2.97 (s, 12H).

3,6-bis(dimethylamino)-9H-xanthen-9-one (4.2)

Compound **4.20** (25 mg, 0.10 mmol, 1 eq) was dissolved in acetone (0.910 mL). The solution was freeze pump thawed, followed by slow portion-wise addition of $KMnO_4$ (14 mg, 0.10 mmol, 1 eq) at 0 °C. Upon consumption of starting material (approx..2 hr), the solution was filtered over a pad of Celite and washed with acetone (20 mL). The filtrate was collected and concentrated to afford pure **3,6-bis(dimethylamino)-9H-xanthen-9-one (4.2)**, as a reddish brown solid (10 mg, 0.04

mmol, 41%). ^{1}H-NMR matched literature.[19] ^{1}H NMR (300 MHz, Chloroform-*d*): δ 8.17 (d, *J* = 9.0 Hz, 2H), 6.73 (dd, *J* = 9.0, 2.4 Hz, 2H), 6.52 (d, *J* = 2.5 Hz, 2H), 3.14 (s, 12H).

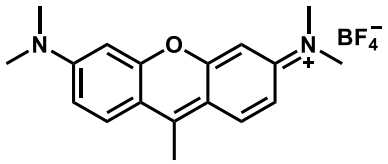

***N*-(6-(dimethylamino)-9-methyl-3H-xanthen-3-ylidene)-*N*-methylmethanaminium (4.4)**

3,6-bis(dimethylamino)-9H-xanthen-9-one **4.2** (65 mg, 0.23 mmol, 1 eq) is dissolved in THF (1.45 mL) at 0° C and MeMgBr (1.0 M in THF, 1.40 mL, 1.40 mmol, 6 eq) was added dropwise. The mixture was warmed to room temperature and left to stir overnight. The reaction was quenched with 5% fluoroboric acid (1 mL, 0.6 mmol) turning the solution bright pink, then extracted with dichloromethane (3 x 5 mL), dried over $MgSO_4$, filtered and evaporated to afford pure **4.4** as a magenta solid (42 mg, 0.12 mmol, 50%). ^{1}H-NMR matched literature.[20] ^{1}H NMR (300 MHz, Chloroform-*d*): δ 8.07 (d, *J* = 9.6 Hz, 2H), 7.16 (dd, *J* = 9.6, 2.6 Hz, 2H), 6.81 (d, *J* = 2.6 Hz, 2H), 3.37 (s, 12H), 2.99 (s, 3H).

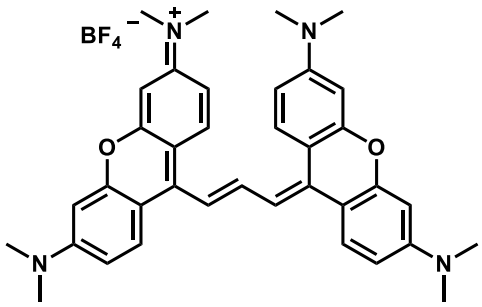

(E)-*N*-(9-(3-(3,6-bis(dimethylamino)-9H-xanthen-9-ylidene) prop-1-en-1-yl)-6-(dimethylamino)-3H-xanthen-3-ylidene)-*N*-methylmethanaminium (4.8)

Compound **4.4** (50 mg, 0.14 mmol, 1 eq) was split into two different portions. To one portion was added acetic anhydride (0.200 mL, 2.1 mmol) and triethylorthoformate (0.036 mL, 0.20 mmol, 1.5 eq). To the second portion, was added acetic anhydride (0.200 mL, 2.1mmol) and triethylamine

(0.015 mL, 0.10 mmol, 0.7 eq). Both portions were separately freeze-pump thawed. The portion containing triethylorthoformate was heated to 140 °C for 15 min before the second portion containing triethylamine was added. After 25 min, the reaction was cooled to r.t. and concentrated directly onto silica. The product was purified via silica gel chromatography with dichloromethane: ethanol (99:1 →98:2) to afford pure **4.4** as a dark purple solid (20 mg, 0.04 mmol, 26%). ^{1}H-NMR matched literature.[20] ^{1}H-NMR (400 MHz, Chloroform-*d*): δ 8.16 – 8.03 (m, 1H), 7.86 (d, *J* = 9.2 Hz, 4H), 7.18 (d, *J* = 13.1 Hz, 2H), 6.78 (dd, *J* = 9.3, 2.7 Hz, 4H), 6.50 (d, *J* = 2.5 Hz, 4H), 3.15 (s, 24H).

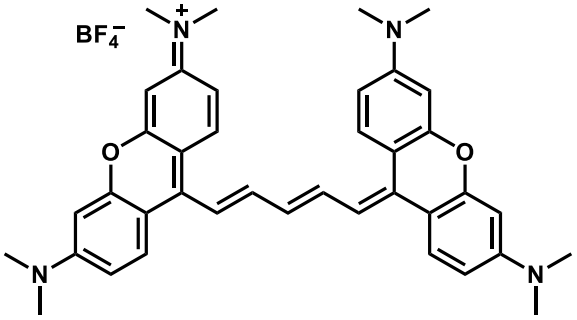

***N*-(10-((1E,3E)-5-(3,7-bis(dimethylamino)-5,5-dimethyldibenzo[b,e]silin-10(5H)-ylidene)penta-1,3-dien-1-yl)-7-(dimethylamino)-5,5-dimethyldibenzo[b,e]silin-3(5H)-ylidene)-N-methylmethanaminium (4.11)**

Compound **4.4** (50 mg, 0.10 mmol, 2 eq) was added to a Schlenk flask along with malonaldehyde bis(phenylimine) monohydrochloride (20 mg, 0.10 mmol, 1 eq) and then solubilized with triethylamine (1.10 mL, 8.0 mmol, 56 eq) and acetic anhydride (0.500 mL, 5.0 mmol, 38 eq). The solution was freeze pump thawed and then heated to 90 °C. After 15 minutes, the reaction was cooled to r.t. and concentrated directly onto silica. The product was purified via silica gel chromatography with dichloromethane: ethanol (99:1 →98:2) to afford pure **4.11** as a dark purple solid. (13 mg, 0.02 mmol, 28%). ^{1}H-NMR matched literature.[20] ^{1}H-NMR (400 MHz, Chloroform-

d): δ 7.85 (d, *J* = 9.3 Hz, 4H), 7.60 (t, *J* = 12.9 Hz, 2H), 6.90 (d, *J* = 13.5 Hz, 2H), 6.82 (dd, *J* = 9.2, 2.7 Hz, 4H), 6.50 (d, *J* = 2.5 Hz, 4H), 3.15 (s, 24H).

4.6 Spectra Relevant to Chapter Four

4.6.1 ^{1}H NMR Spectra

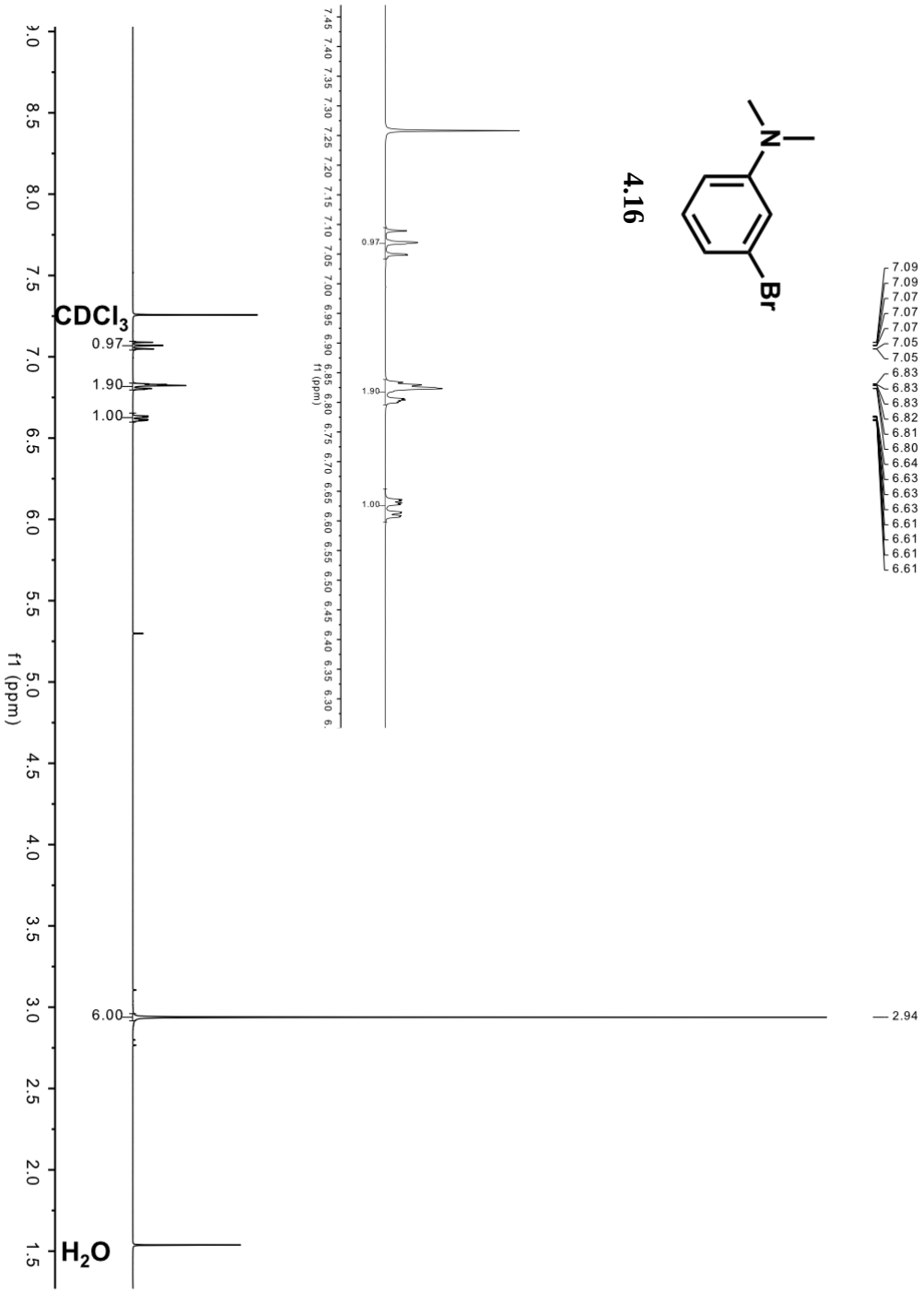

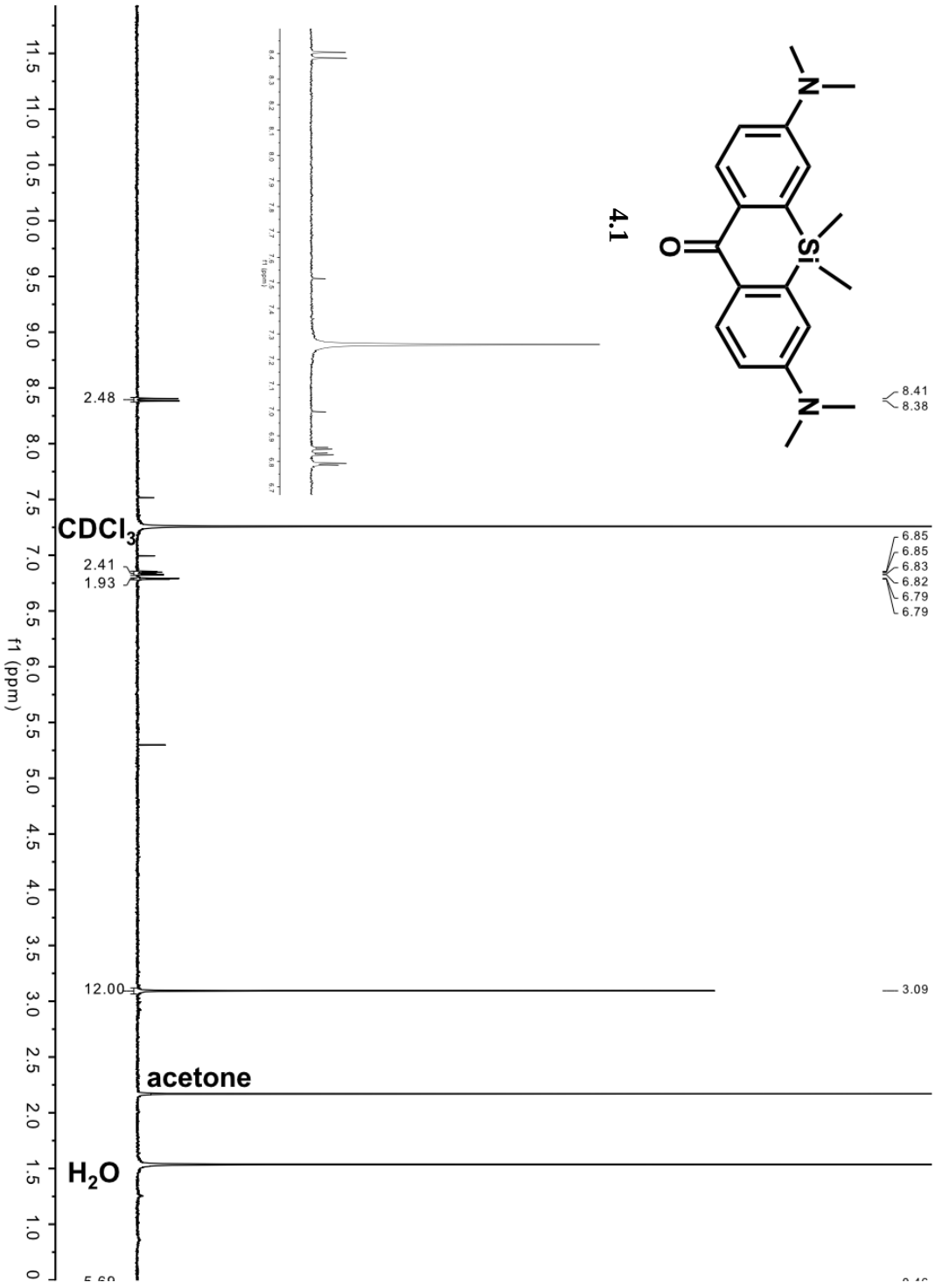
4.1
O
Si
N
N
2.48
CDCl3
2.41
1.93
12.00
acetone
H2O
8.41
8.38
6.85
6.85
6.83
6.82
6.79
6.79
3.09
f1 (ppm)

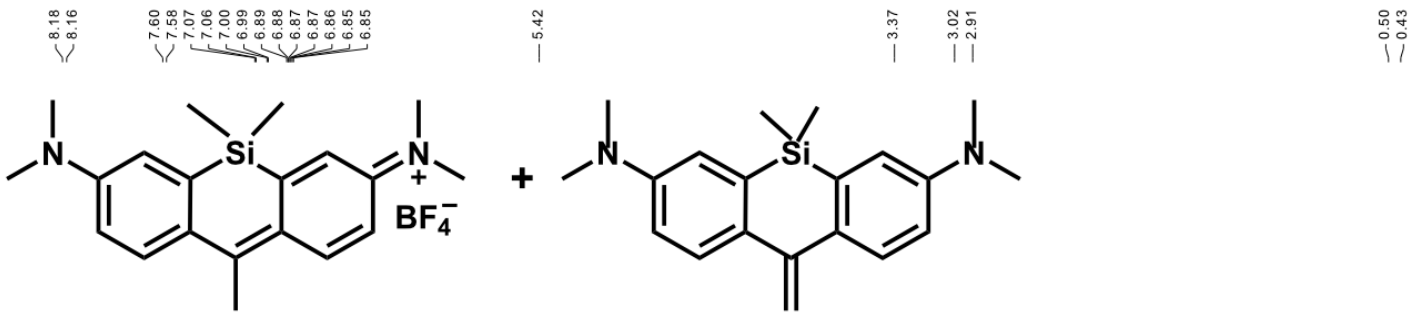
8.18
8.16
7.60
7.58
7.07
7.06
7.00
6.99
6.89
6.88
6.87
6.87
6.86
6.85
6.85
5.42
3.37
3.02
2.91
0.50
0.43
Si
N
N
+
BF4−
+
N
Si
N

4.3

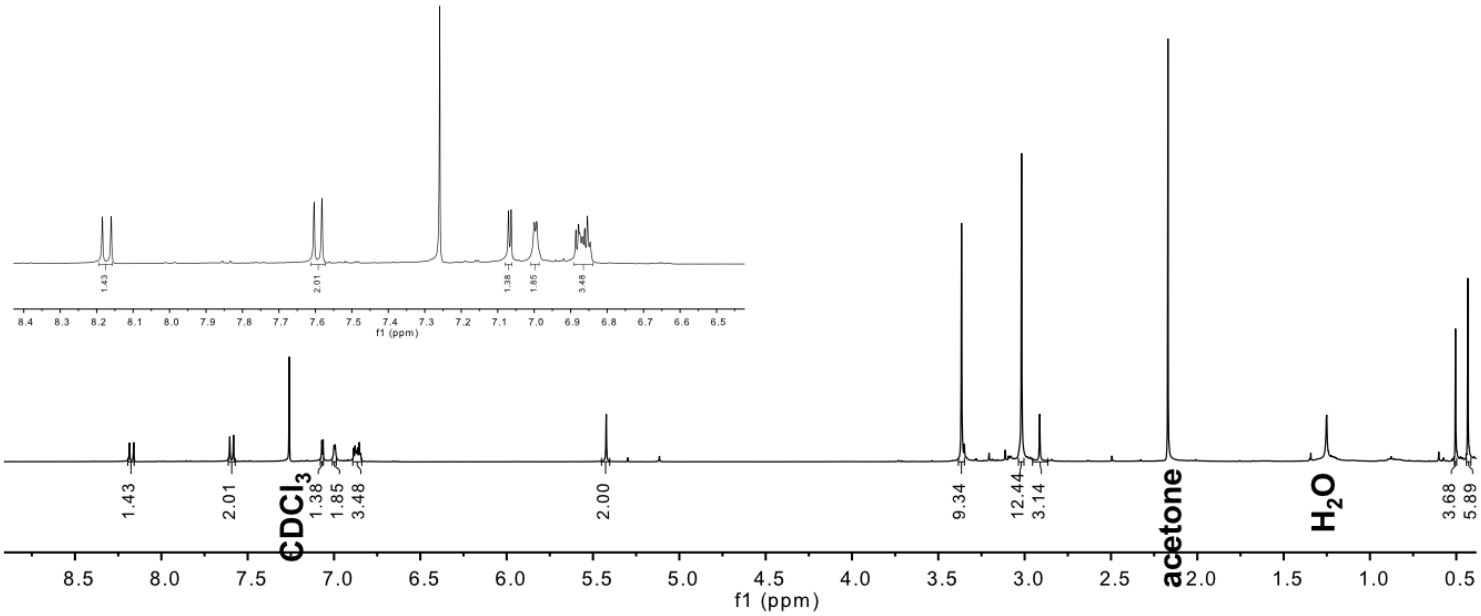
1.43
2.01
1.38
1.85
3.48
2.00
9.34
12.44
3.14
3.68
5.89
CDCl3
acetone
H2O
f1 (ppm)

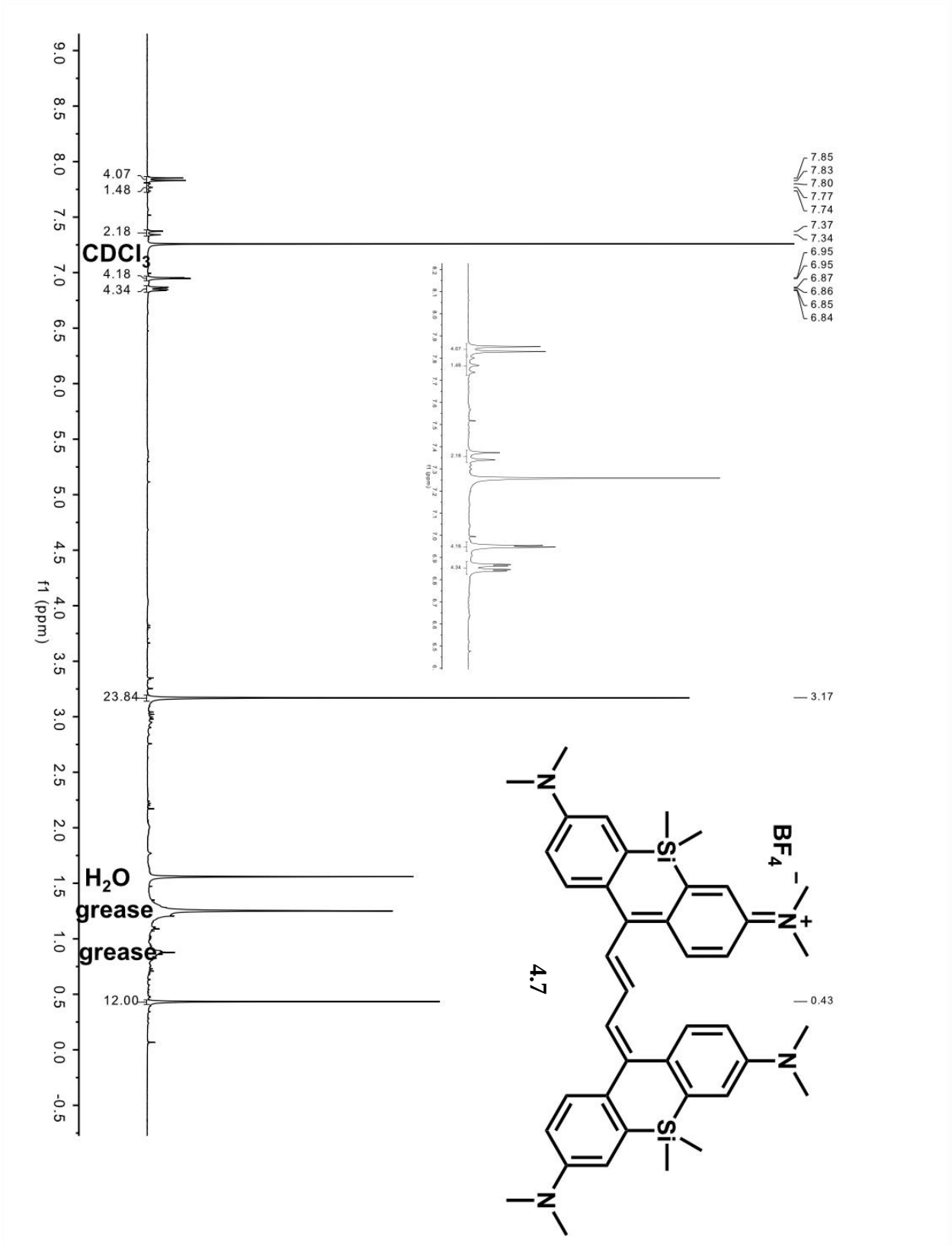
4.07
1.48
2.18
CDCl3
4.18
4.34
23.84
H2O
grease
grease
12.00
7.85
7.83
7.80
7.77
7.74
7.37
7.34
6.95
6.95
6.87
6.86
6.85
6.84
3.17
0.43
f1 (ppm)
BF4
4.7

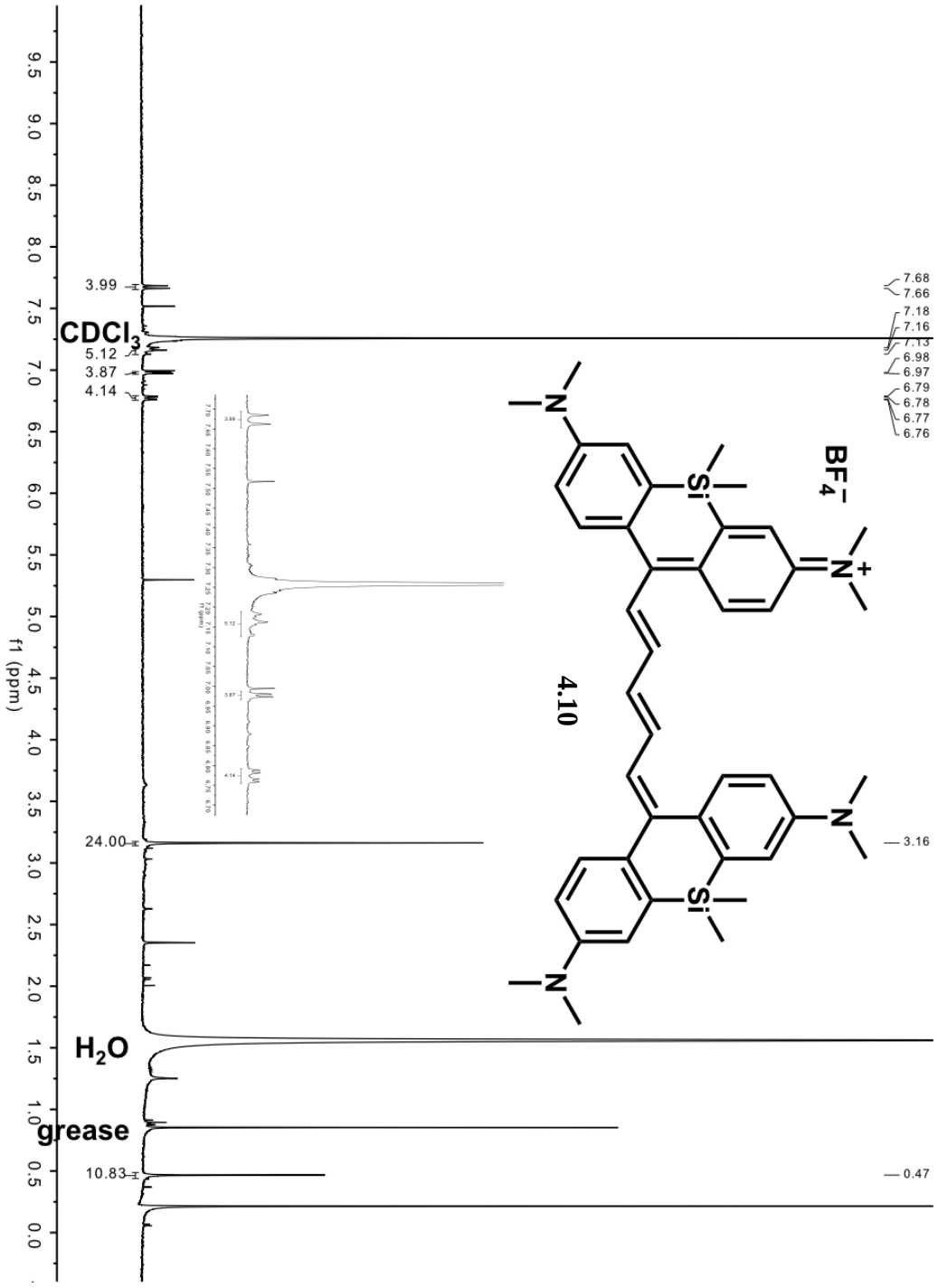
3.99
CDCl3
5.12
3.87
4.14
24.00
H2O
grease
10.83
7.68
7.66
7.18
7.16
7.13
6.98
6.97
6.79
6.78
6.77
6.76
3.16
0.47
f1 (ppm)
BF4−
4.10

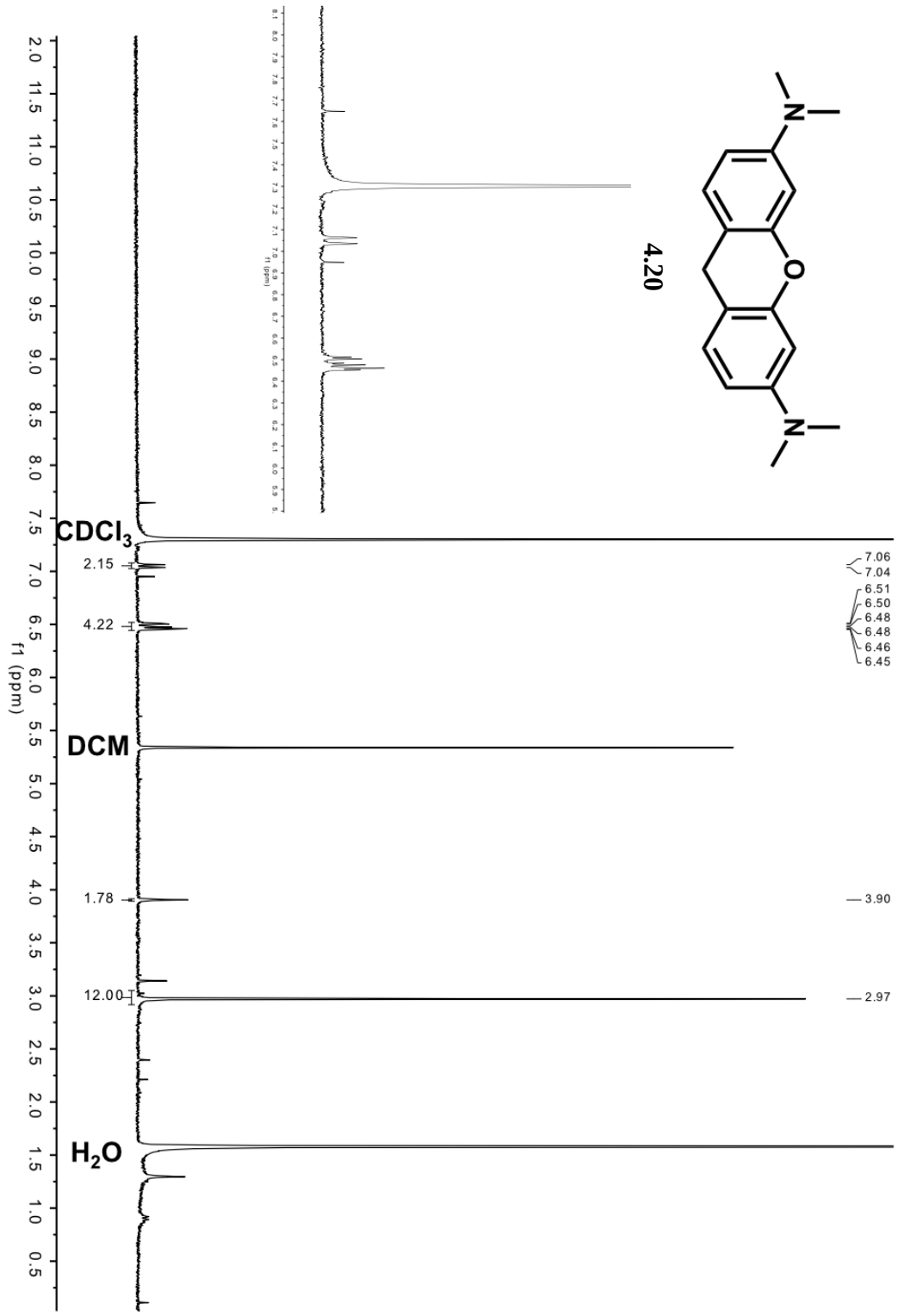
4.20
CDCl3
2.15
4.22
DCM
1.78
12.00
H2O
7.06
7.04
6.51
6.50
6.48
6.48
6.46
6.45
3.90
2.97
f1 (ppm)

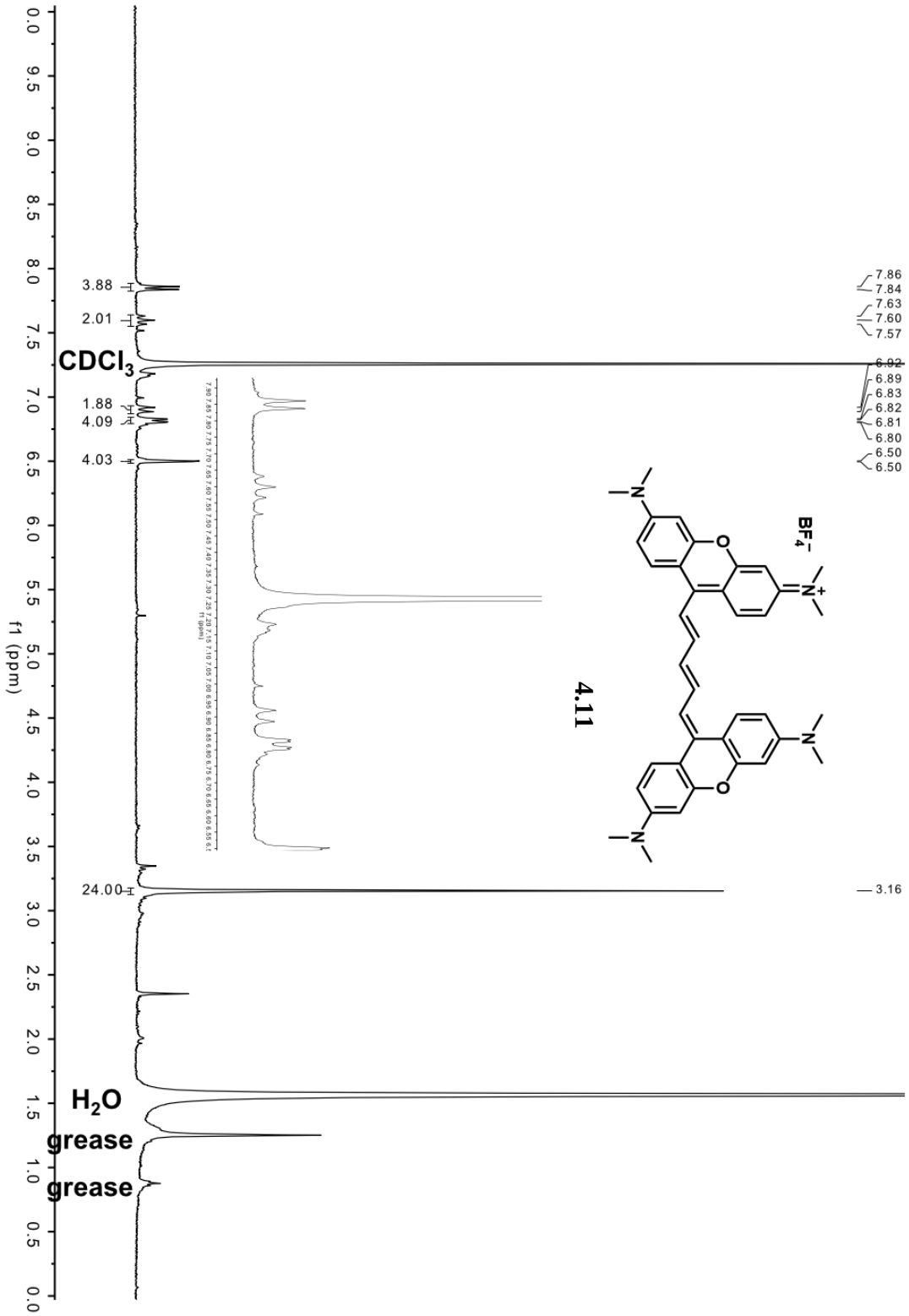
3.88
2.01
CDCl3
1.88
4.09
4.03
24.00
H2O
grease
grease
7.86
7.84
7.63
7.60
7.57
6.92
6.89
6.83
6.82
6.81
6.80
6.50
6.50
3.16
BF4−
4.11
f1 (ppm)

References:

(1) Lavis, L. D.; Raines, R. T. Bright Ideas for Chemical Biology. *ACS Chem. Bio.* **2008**, *3* (3), 142-155.

(2) Frangioni, J. V.; John V. Frangioni. In Vivo Near-Infrared Fluorescence Imaging. *Curr. Opin. Chem. Biol.* **2003**, *7* (5), 626–634.

(3) Weissleder, R. A Clearer Vision for in Vivo Imaging. *Nat. Biotechnol.* **2001**, *19* (4), 316–317.

(4) Fu, M.; Xiao, Y.; Qian, X.; Zhao, D.; Xu, Y. A Design Concept of Long-Wavelength Fluorescent Analogs of Rhodamine Dyes: Replacement of Oxygen with Silicon Atom. *Chem. Commun.* **2008**, *15*, 1780-1782.

(5) Grimm, J. B.; Brown, T. A.; Tkachuk, A. N.; Lavis, L. D. General Synthetic Method for Si-Fluoresceins and Si-Rhodamines. *ACS Cent. Sci* **2017**, *3*, 975–985.

(6) Lukinavičius, G.; Umezawa, K.; Olivier, N.; Honigmann, A.; Yang, G.; Plass, T.; Mueller, V.; Reymond, L.; Corrêa Jr, I. R.; Luo, Z.-G.; et al. A Near-Infrared Fluorophore for Live-Cell Super-Resolution Microscopy of Cellular Proteins. *Nat. Chem.* **2013**, *5* (2), 132–139.

(7) Kushida, Y.; Nagano, T.; Hanaoka, K. Silicon-Substituted Xanthene Dyes and Their Applications in Bioimaging. *Analyst*. **2015**, *140*, 685-695.

(8) Choi, A.; Miller, S. C. Silicon Substitution in Oxazine Dyes Yields Near-Infrared Azasiline Fluorophores That Absorb and Emit beyond 700 Nm. *Org. Lett.* **2018**, *20* (15), 4482–4485.

(9) Ikeno, T.; Nagano, T.; Hanaoka, K. Silicon-Substituted Xanthene Dyes and Their Unique Photophysical Properties for Fluorescent Probes. *Chem. Asian J.*. **2017**, *12* (13), 1435-1446.

(10) Li, C.; Wang, T.; Li, N.; Li, M.; Li, Y.; Sun, Y.; Tian, Y.; Zhu, J.; Wu, Y.; Zhang, D.; et al. Hydrogen-Bonding-Induced Bathochromic Effect of Si-Coumarin and Its Use in Monitoring Adipogenic Differentiation. *Chem. Commun* **2019**, *55*, 11802.

(11) Bricks, J. L.; Kachkovskii, A. D.; Slominskii, Y. L.; Gerasov, A. O.; Popov, S. V. Molecular Design of near Infrared Polymethine Dyes: A Review. *Dye. Pigment.* **2015**, *121*, 238–255.

(12) Detty, M. R.; Murray, B. J. Telluropyrylium Dyes. 1. 2,6-Diphenyltelluropyrylium Dyes. *J. Org. Chem.* **1982**, *47* (27), 5235–5239.

(13) Shandura, M. P.; Poronik, Y. M.; Kovtun, Y. P. Substituted Xanthylocyanines. II. Pyroninocyanines. *Dye. Pigment.* **2005**, *66* (3), 171–177.

(14) Pastierik, T.; Šebej, P.; Medalová, J.; Štacko, P.; Klán, P. Near-Infrared Fluorescent 9-Phenylethynylpyronin Analogues for Bioimaging. *J. Org. Chem.* **2014**, *79* (8), 3374–3382.

(15) Tolbert, L. M.; Zhao, X. Beyond the Cyanine Limit: Peierls Distortion and Symmetry Collapse in a Polymethine Dye. *J. Am. Chem. Soc.* **1997**, *119* (14), 3253-3258.

(16) Tolbert, L. M. Solitons in a Box: The Organic Chemistry of Electrically Conducting Polyenees. *Acc. Chem. Res.* **1992**, *25*, 561-568.

(17) Vasyluk, S. V.; Viniychuk, O. O.; Poronik, Y. M.; Kovtun, Y. P.; Shandura, M. P.; Yashchuk, V. M.; Kachkovsky, O. D. Breaking of Symmetrical Charge Distribution in Xanthylocyanine Chromophores Detecting by Their Absorption Spectra. *J. Mol. Struct.* **2011**, *990* (1–3), 6–13.

(18) Bernardo, B.; Cheyns, D.; Verreet, B.; Schaller, R. D.; Rand, B. P.; Giebink, N. C. Delocalization and Dielectric Screening of Charge Transfer States in Organic Photovoltaic

Cells. *Nat. Commun.* **2014**, *5* (1), 1–7.

(19) Parker, C. A.; Hatchard, C. G. Triplet-Singlet Emission in Fluid Solutions. Phosphorescence of Eosin. *Trans. Faraday Soc.* **1961**, *57* (0), 1894–1904.

(20) Hu, H.; Przhonska, O. V; Terenziani, F.; Painelli, A.; Fishman, D.; Ensley, T. R.; Reichert, M.; Webster, S.; Bricks, J. L.; Kachkovski, A. D.; et al. Two-Photon Absorption Spectra of a near-Infrared 2-Azaazulene Polymethine Dye: Solvation and Ground-State Symmetry Breaking. *Phys. Chem. Chem. Phys* **2013**, *15*, 7666.

(21) Zhao, Y.; Truhlar, D. G. The M06 Suite of Density Functionals for Main Group Thermochemistry, Thermochemical Kinetics, Noncovalent Interactions, Excited States, and Transition Elements: Two New Functionals and Systematic Testing of Four M06-Class Functionals and 12 Other Functionals. *Theor. Chem. Acc.* **2008**, *120* (1–3), 215–241.

(22) Gaussian 16, Revision A.03, Frisch, M. J.; Trucks, G. W.; Schlegel, H. B.; Scuseria, G. E.; Robb, M. A.; Cheeseman, J. R.; Scalmani, G.; Barone, V.; Petersson, G. A.; Nakatsuji, H.; Li, X.; Caricato, M.; Marenich, A. V.; Bloino, J.; Janesko, B. G.; Gomperts, R.; Mennucci, B.; Hratchian, H. P.; Ortiz, J. V.; Izmaylov, A. F.; Sonnenberg, J. L.; Williams-Young, D.; Ding, F.; Lipparini, F.; Egidi, F.; Goings, J.; Peng, B.; Petrone, A.; Henderson, T.; Ranasinghe, D.; Zakrzewski, V. G.; Gao, J.; Rega, N.; Zheng, G.; Liang, W.; Hada, M.; Ehara, M.; Toyota, K.; Fukuda, R.; Hasegawa, J.; Ishida, M.; Nakajima, T.; Honda, Y.; Kitao, O.; Nakai, H.; Vreven, T.; Throssell, K.; Montgomery, J. A., Jr.; Peralta, J. E.; Ogliaro, F.; Bearpark, M. J.; Heyd, J. J.; Brothers, E. N.; Kudin, K. N.; Staroverov, V. N.; Keith, T. A.; Kobayashi, R.; Normand, J.; Raghavachari, K.; Rendell, A. P.; Burant, J. C.; Iyengar, S. S.; Tomasi, J.; Cossi, M.; Millam, J. M.; Klene, M.; Adamo, C.; Cammi, R.;

Ochterski, J. W.; Martin, R. L.; Morokuma, K.; Farkas, O.; Foresman, J. B.; Fox, D. J. Gaussian, Inc., Wallingford CT, 2016.

(23) Head-Gordon, M.; Rico, R. J.; Oumi, M.; Lee, T. J. A Doubles Correction to Electronic Excited States from Configuration Interaction in the Space of Single Substitutions. *Chem. Phys. Lett.* **1994**, *219* (1–2), 21–29.

(24) Head-Gordon, M.; Maurice, D.; Oumi, M. A Perturbative Correction to Restricted Open Shell Configuration Interaction with Single Substitutions for Excited States of Radicals. *Chem. Phys. Lett.* **1995**, *246* (1–2), 114–121.

(25) Neese, F. Software Update: The ORCA Program System, Version 4.0. *WIREs Comput. Mol. Sci.* **2018**, *8* (1).

(26) Neese, F. The ORCA Program System. *WIREs Comput. Mol. Sci.* **2012**, *2* (1), 73–78.

(27) Thimsen, E.; Sadtler, B.; Berezin, M. Y. Shortwave-Infrared (SWIR) Emitters for Biological Imaging: A Review of Challenges and Opportunities. *Nanophotonics* **2017**, *6* (5), 1043–1054.

(28) Terenziani, F.; Przhonska, O. V.; Webster, S.; Padilha, L. A.; Slominsky, Y. L.; Davydenko, I. G.; Gerasov, A. O.; Kovtun, Y. P.; Shandura, M. P.; Kachkovski, A. D.; et al. Essential-State Model for Polymethine Dyes: Symmetry Breaking and Optical Spectra. *J. Phys. Chem. Lett* **2010**, *1* (12), 1800–1804.

(29) Nani, R. R.; Kelley, J. A.; Ivanic, J.; Schnermann, M. J. Reactive Species Involved in the Regioselective Photooxidation of Heptamethine Cyanines. *Chem. Sci.* **2015**, *6* (11), 6556–6563. https://doi.org/10.1039/c5sc02396c.

(30) Cosco, E. D.; Caram, J. R.; Bruns, O. T.; Franke, D.; Day, R. A.; Farr, E. P.; Bawendi, M. G.; Sletten, E. M. Flavylium Polymethine Fluorophores for Near- and Shortwave Infrared

Imaging. *Angew. Chemie - Int. Ed.* **2017**, *56* (42), 13126–13129.

(31) Semonin, O. E.; Johnson, J. C.; Luther, J. M.; Midgett, A. G.; Nozik, A. J.; Beard, M. C. Absolute Photoluminescence Quantum Yields of IR-26 Dye, PbS, and PbSe Quantum Dots. *J. Phys. Chem. Lett.* **2010**, *1* (16), 2445–2450. https://doi.org/10.1021/jz100830r.

(32) Schrödinger Release 2019-4: Maestro, Schrödinger, LLC, New York, NY, 2019. No Title.

(33) Harder, E.; Damm, W.; Maple, J.; Wu, C.; Reboul, M.; Xiang, J. Y.; Wang, L.; Lupyan, D.; Dahlgren, M. K.; Knight, J. L.; et al. OPLS3: A Force Field Providing Broad Coverage of Drug-like Small Molecules and Proteins. *J. Chem. Theory Comput.* **2016**, *12* (1), 281–296.

CHAPTER FIVE

Exploring Additional Flav7 Scaffolds and Counterion Exchange for Multiplexed Imaging

Material in this chapter was adapted from: Monica Pengshung, Emily D. Cosco, Zhumin Zhang, Ellen M. Sletten*. Counterion Pairing Effects on a Flavylium Heptamethine Dye. *Manuscript in preparation.*

5.1 Abstract

The ability to apply SWIR fluorophores to multiplex imaging *in vivo* highlights the potential of fluorophores within this region of the electromagnetic spectrum. To establish dyes with different λ_{max} and develop efficient methods to deliver them into biological systems are essential to improving upon the multiplex setup. Throughout our studies, we have made many strides in effecting photophysical changes to the Flav7 scaffold which has been discussed already in Chapter 2 (substituent identity), Chapter 3 (substituent position) and Chapter 5 (4' linker modification for aggregation). Herein, we will discuss exploring other substituents at the 6 position of the flavylium heterocycle to further diversify the toolbox of SWIR fluorophores we have developed, while also corroborating the *para*- position and red-shifted properties we had attributed to this position. Delivery of imaging agents is also essential to ensure *in vivo* applications, however, high aggregation states within nanoparticles are detrimental to advantageous photophysical properties. Counterion exchange has proved beneficial for reducing aggregation for indolenine cyanine dye and so we performed a similar procedure with the Flav7 scaffold. These studies led to an important understanding of the ion-pairing relationship between the flavylium heptamethine scaffold and anion. Exploring the development of materials for *in vivo* imaging paved the way to further fundamental photophysical understanding for future predictive measures.

5.2 Introduction

Fluorescence imaging in the short-wave infrared (SWIR, 1000- 2000 nm) region of the electromagnetic region has recently gained a lot of interest due to the high resolution images obtained.[1–3] In particular, multiplexed imaging in the SWIR is an attractive tool for non-invasive diagnostics.[4–6] Small molecule fluorophores for the SWIR have showcased potential for expanding the number of targets for multiplexed imaging.[7] Small structural changes can be exploited for developing fluorophores with different $\lambda_{max,abs}$ that can be excited individually but collected with the same detector (Figure 5.1A). In Chapter 2, we developed fluorophores that had $\lambda_{max,abs}$ ranging from 980 nm to 1060 nm through subtle structural modifications of a flavylium heptamethine scaffold (Flav7).[8] Within these derivatives, two stood out as they matched commercially available laser lines, those of MeOFlav7 (Figure 5.1B, **5.1**, $\lambda_{max,abs}$ = 984 nm) and JuloFlav7 (**5.2,** $\lambda_{max,abs}$ = 1061 nm). With the addition of ICG (**5.3,** $\lambda_{max,abs}$ = 787 nm), three colored excitation multiplexed imaging could be achieved *in vivo* (Figure 5.1B). Inspired by the success of these studies, herein we will focus on developing additional SWIR fluorophores with varying $\lambda_{max,abs}$ in order to obtain more channels.

Concurrently, improvements on reducing aggregation are crucial to enhancing multiplexed imaging. Despite their excellent photophysical characteristics, a limitation of polymethine fluorophores is the presence of a quenched aggregate state at high concentrations. The aromatic moieties of the polymethine scaffold can easily undergo π-π interactions in polar solvents, forming multi-dye aggregated states. Aggregation can potentially be advantageous, such as the formation of J-aggregates which are known to have even further red-shifted absorption maxima and improved photophysical properties.[9] However, the overwhelming majority of aggregation in fluorophores can be classified as H-aggregates, in which photophysical properties such as efficient excitation

and emission are diminished (Figure 5.1C).[9] H-aggregates, which represent face-to-face stacking and a cancellation of molecular dipoles, are characterized by a broad blue-shifted absorption spectrum and can become a hinderance to the utility of polymethine dyes.

Minimizing aggregate states can be achieved through increasing solubility or shielding the charged fluorophore so it can no longer stack upon itself. For example, attaching solubilizing groups such as sulfonates can increase water solubility for biological applications.[11–14] The attachment of sterically bulky moieties can also enable solubility in more non-polar solvents, allowing processing for the development of materials for solar cells and all optical signal processing.[15,16] Other methods to decrease self-aggregation involve shielding the polymethine scaffolds such as through sterically bulky moieties, installed through functionalization of Zincke salts, which has shown to prevent aggregation in indocarbocyanine derivatives.[17] Host-guest complexes have also been utilized, wherein a host can shield the dye guest from stacking with itself.[18] Finally, strategies to control aggregation based on the relationship between counterion and dye have been applied in nanomaterials for imaging[19–21] and in solid state applications.[22] Inspired by the simplicity of this method, we opted to further explore the association between counterion and dye.

This chapter aims to address two major aspects of multiplexed imaging, the fluorophore design and nanoparticle formulation (Figure 5.1a). By developing these two aspects in parallel, we hope to improve upon our current work by creating more channels to image as well as enhance our resolution by reducing aggregation within our delivery vehicle.

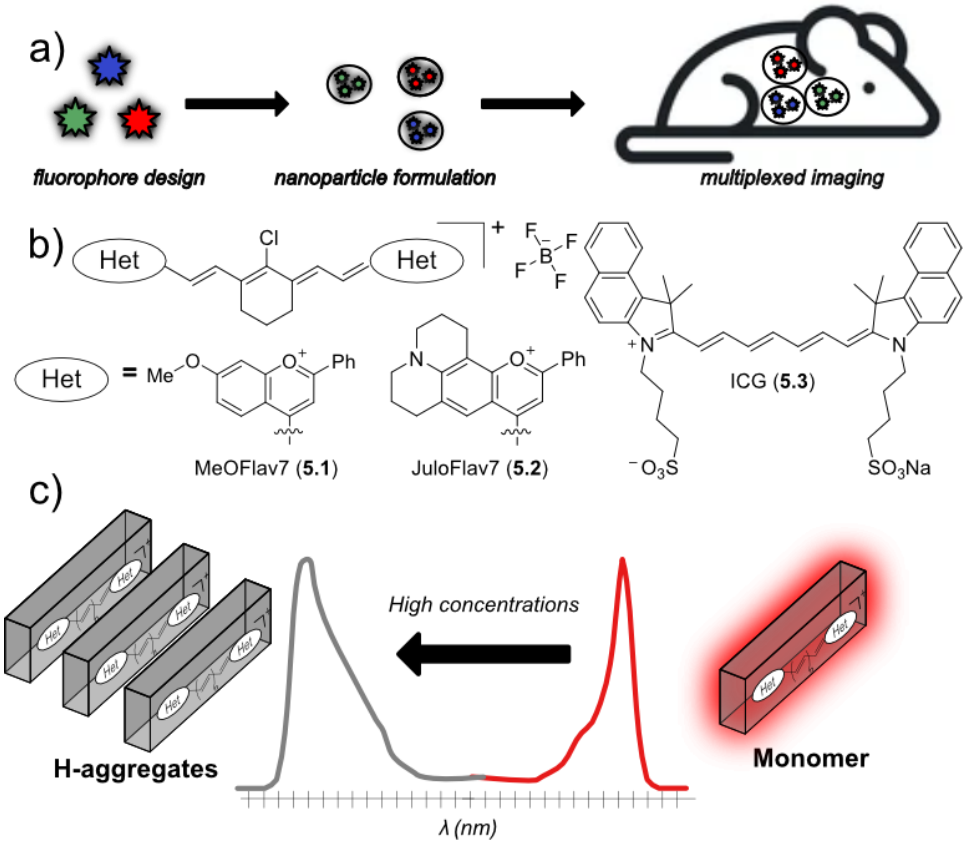

Figure 5.1 A) General scheme of multiplexed imaging and the two aspects explored herein: fluorophore design and nanoparticle formulation. B) Structures of fluorophores previously explored in Chapter 2 for multiplexed imaging, MeOFlav7 (**5.1**), JuloFlav7 (**5.2**), and ICG (**5.3**). C) H-aggregates (gray) at high concentrations are characterized by blue-shifted and broadened absorption from the monomeric peak (red).

5.3 Modification at the 6-position of the Flav7 scaffold

5.3.1. Synthesis of diphenylamino 6-substituted Flav7

Previous work exploring the different positions of Flav7 (Chapter 3) indicated that the 6-position has the most potential for red-shifting $\lambda_{max,abs}$. This position also showed more predictability in comparison to the 5 and 8 position which was complicated by steric bulk of the substituent. Thus, we thought this would be the most logical position to explore other substituents. We opted to focus on the two substituents that could provide the most extreme change in absorption maxima at the 6-position, a diphenylamino and methoxy. A diphenylamino was chosen instead of

the julolidine despite its further red shift, due to the ease in installing a diphenylamino substituent though a Buchwald Hartwig amination. We began by installing a diphenylamino substituent to a 6-triflated flavone (**5.5**) to yield 6-diphenylamino flavone (**5.6**). From there, the addition of methyl-Grignard followed be quenching with a tetrafluorboric acid solution yielded 6-diphenylamino flavylium (**5.7**). Upon reaction with heptamethine linker (**5.8**) in the presence of base, 6-diphenylamino flavylium heptamethine (**5.9**) could be yielded (Scheme 5.1).

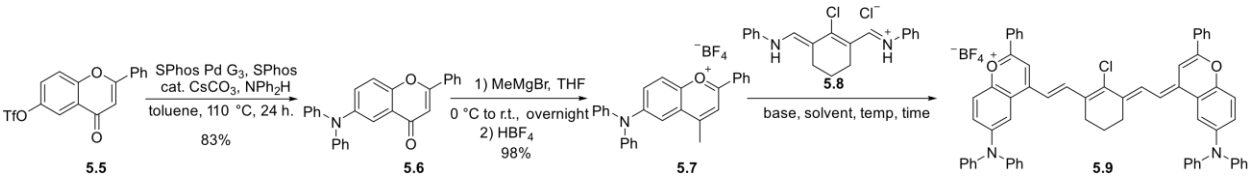

Scheme 5.1 Synthetic route of 6-subtsituted diphenylamine Flav7 (**5.9**)

Purification of **5.9** proved difficult due to its instability in washing with solvent (toluene, THF, EtOAc), silica gel chromatography, and high-performance liquid chromatography (HPLC). Due to the low stability of the chromophore we opted to optimize the reaction to obtain the cleanest crude sample. The reaction conversion was determined by UV-VIS spectroscopy and monitored by the ratio of desired product peak (Figure 5.2, **5.9,** 1053 nm) vs. linker peak (**5.8,** 550 nm). Commonly, n-butanol:toluene is used as the solvent system for flavylium heptamethine reactions but this showed low conversion (1:6, Entry 1, Table 5.1) and high amounts of degradation (< 450 nm) after heating at 100 °C for 10 min. To optimize, we started by exploring solvents (1,4-dioxane, acetic anhydride, DCE, DMF, Entry 2-5, Table 5.1) and found that DMF showed the highest conversion (Entry 5) with a ratio of 1.1:1 between desire product and linker (Table 5.1). Attempts to heat to 100 °C to promote higher conversion resulted in degradation instead, as shown by an increasing absorption peak below 450 nm (Entry 6, Table 5.1). Higher temperatures appeared to be detrimental to desire product thus we explored other routes to increase conversion.

Polymethine dyes are formed by the nucleophilic attack of the heterocycle to electrophilic linker, thus the first step is heterocycle deprotonation to form a more reactive reagent. The formation of **5.9** appeared to stall at an approximately ~1:1 ratio by absorption spectra (**5.9**: **5.8**), suggestive that conversion was limited by the deprotonation step of the heterocycle. A stronger base (2,6-lutidine) with lowered temperatures (r.t.) was attempted, but little conversion and mainly degradation was seen after 14 h (Entry 7, Table 5.1). We hypothesize that the reactivity match between base and heterocycle is crucial to effective deprotonation and that 2,6-di-*tert*-butyl-4-methylpyridine was the most efficient match. Due to degradation of **5.9,** base strength could not be increased more, thus we returned to a more extensive solvent screen. In our initial screen, we found that DMF allowed for the highest conversion without degradation. We logically explored solvents that were structurally similar to DMF and found that both DMAC and NMP showed a slightly higher conversion ratio (Entry 8 and 9, Table 5.1) at 80 °C after 45 min (Figure 5.2).

Table* 5.*1 Reaction optimization for **5.9**.

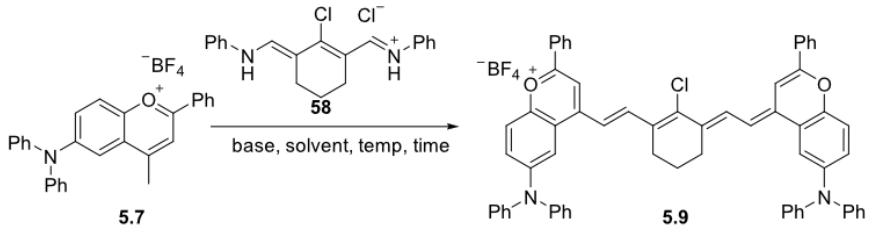

Entry	base	solvent	temp (°C)	time	results*
1	2,6-di*t*bu-4-MePyr	n-bu:tol	100	10 min	1:6
2	2,6-di*t*bu-4-MePyr	Ac_2O	100	10 min	deg.
3	2,6-di*t*bu-4-MePyr	1,4-dioxane	100	30 min	1:1.25
4	2,6-di*t*bu-4-MePyr	DCE	70	15 min	1:2
5	2,6-di*t*bu-4-MePyr	DMF	80	30 min	1:1.1
6	2,6-di*t*bu-4-MePyr	DMF	100	30 min	deg
7	2,6-lutidine	DMF	r.t	14 h	deg
8	2,6-di*t*bu-4-MePyr	DMAC	80	45 min	1.2:1
9	2,6-di*t*bu-4-MePyr	NMP	80	45 min	1.3:1

*Ratios are based on UV-Vis spectra of product: linker (1054 nm: 550 nm).

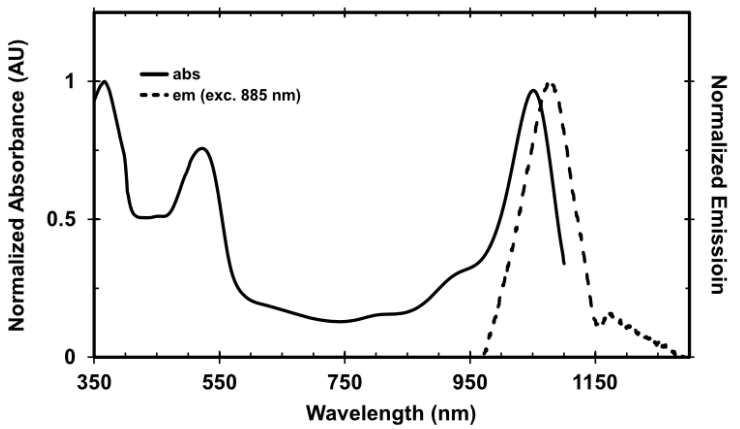

Figure 5.2. Normalized absorbance spectra and emission of crude sample of **5.9** in DCM.

With a crude sample of **5.9** in hand, we evaluated the photophysical properties and found $\lambda_{max,abs}$ at 1053 nm and $\lambda_{max,em}$ at 1077 nm in DCM. This is only a 5 nm red-shifted from the dimethylamino variant (6-Flav7, **5.10**) at 1048 nm (Table 5.2), which suggests that electron donation of the diphenylamino substituent is not optimal at this position. In contrast, data presented in Chapter 2 showed that exchanging a dimethylamino substituent at the 7-position (**5.11**) with a diphenylamino (**5.12**) presented with a 20 nm red-shift (Table 5.1). Furthermore, earlier data presented in Chapter 3 showed that electron donation is maximized at the 6-position hence the red-shifted $\lambda_{max,abs}$ when the dimethylamino substituent is placed at 7 (**5.11**) vs. 6 (**5.10**) position (1027 nm vs. 1048 nm). However, there is no difference when a diphenylamino substituent is placed at either position (**5.12** vs. **5.9**), suggesting that in the 6-position the phenyl substituents off the amine does not allow complete electron donation into the chromophore. It has been observed that diphenylamino groups can showcase a lower donating ability than dialkylamino groups due to a partial delocalization of the amine lone electron pair to the phenyls when arranged in a nonplanar manner.[23] Computational modeling to understand the planarity of the diphenylamino substituent at both positions could help shed light on why there is such unpredictable variation in λ_{max}.

Table 5.2. Photophysics of diphenylamino (**5.9** & **5.12**) and dimethylamino derivatives (**5.10**-**5.11**) in DCM

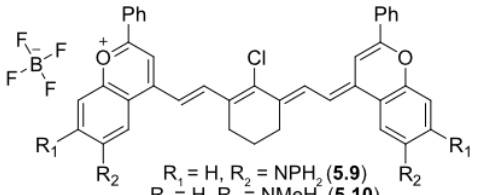

R_1 = H, R_2 = NPH_2 (**5.9**)
R_1 = H, R_2 = $NMeH_2$ (**5.10**)
R_1 = $NMeH_2$, R_2 = H(**5.11**)
R_1 = NPH_2, R_2 = H (**5.12**)

Compound	$\lambda_{max,\ abs}$ (nm)	$\lambda_{max,em}$(nm)	Φ_F (%)
5.9	1053	1077	0.09 ± 0.01
5.10 (6-Flav7)	1048	1080	0.12 ± 0.01
5.11 (Flav7)	1027	1053	0.61 ± 0.02
5.12	1047	1078	0.58 ± 0.02

Quantum yield of fluorescence (Φ_F) was also obtained as it does not require a pure sample. A value of 0.09 ± 0.01% was obtained in DCM for **5.9**, similar to the observed Φ_F for **5.10** (0.12 ± 0.01 %). We believe that TICT with the diphenylamino substituent at the 6-position could similarly contribute to the low Φ_F as was previously seen for the dimethylamino congener.[24] Unfortunately, the diphenylamino substituent did not impart a large red-shift in λ_{max} at the 6-position, contrast to what was seen at the 7-position. These studies show that the diphenylamino substituent does not act similarly at both positions due to possible changes in the planarity of the phenyl substituent.

5.3.2 Synthesis of Methoxy 6-Substituted Flav7

We also opted to explore the methoxy substituent as it would help confirm the identity of the 6-position. In the *meta* position, a methoxy moeity would act as an electron withdrawing group which can be observed in the $\lambda_{max,abs}$ of MeOFlav7 (**5.1**) at 984 nm, which is similar to IR-27 (**5.13**), the unsubstituted version of these fluorophores (Table 5.3). At the *para* position, a methoxy group would act as an electron donor such that a red-shifted $\lambda_{max,abs}$ should be observed. To synthesize this variant, 6-hydroxyflavone (**5.14**) was methylated via methyl iodide to provide 6-

methoxyflavone (**5.15**) followed by methyl-Grignard addition to yield 6-methoxyflavylium (**5.16).** Following other Flav7 derivatives, 6-MeOFlav7 (**5.16**) was synthesized by addition of linker (**5.8**) in the presence of 2,6-di-*tert*-butyl-4-methylpyridine in n:butanol:toluene (Scheme 6.2). Attempts to purify this compound through silica gel chromatography yielded similar results to MeOFlav7 (**5.1**) in which there appeared to be degradation upon the column. Thus, crude solid was washed with hot toluene to provide as clean as sample as possible.

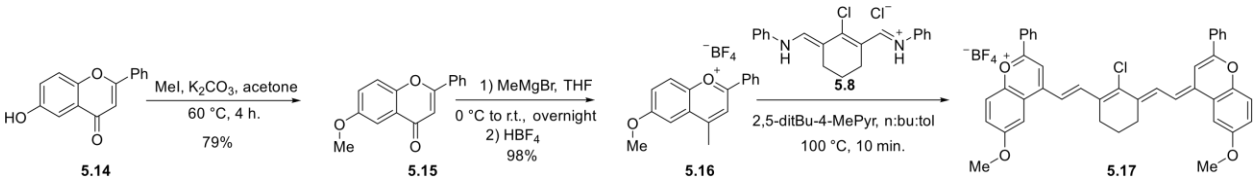

Scheme 5.2 Synthetic route of 6-substituted methoxy Flav7 (**5.17**)

Flavylium dye **5.17** has a $\lambda_{max,abs}$ of 1003 nm and a $\lambda_{max,em}$ of 1024 nm in DCM (Figure 5.3), which is red-shifted ~20 nm from IR-27 (**5.13**) demonstrating that the methoxy group acts as an electron donating group when placed at the 6 position (Table 5.3). This further supports the theory that the 6 position represents the *para* position of the Flav7 scaffold. The Φ_F in DCM was 0.44 ± 0.03% which is approximately four-fold higher than the dimethylamino variant (**5.10**). This large difference in Φ_F was not observed in the 7-position which shows only a one-fold difference, with the dimethylamino (**5.11**) derivative being brighter. A possible theory for the higher Φ_F is a lack of TICT with the methoxy substituent, though **5.17** is still two-fold higher than the azetidine variant which is also hypothesized to lack TICT. Other examples of methoxy substituents on the flavone scaffold has shown improved fluorescence quantum yield though the origins of the enhancement remain unknown.[25] Thus, the methoxy substituent at the 6-position helped support the assignment of the 6-position as the *para* position as well as increased brightness.

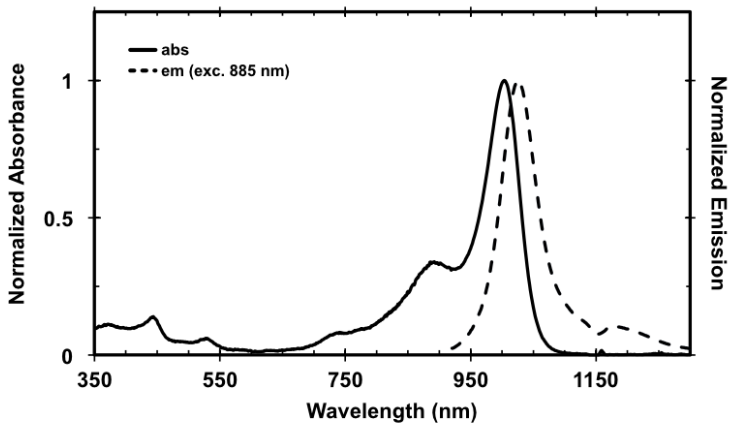

Figure 5.3. Normalized absorbance spectra and emission of crude sample of **5.17** in DCM.

Table 5.3. Photophysics of methoxy (**5.1** & **5.17**) derivatives and IR-27 (**5.13**) in DCM.

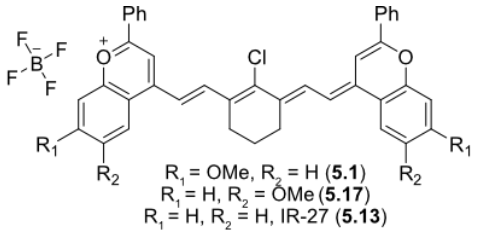

Compound	$\lambda_{max,\ abs}$ (nm)	$\lambda_{max,em}$(nm)	Φ_F (%)
5.1	984	1008	0.52 ± 0.01
5.13 (IR-27)	987	1011	0.35 ± 0.01
5.17	1003	1024	0.44 ± 0.02

We opted to explore the 6-position of the Flav7 scaffold to not only develop more fluorophores for multiplexed imaging but also to better understand the underlying structural relationship to photophysical properties. A methoxy (**5.17**) and diphenylamino (**5.9**) variant of 6-Flav7 was developed but due to difficulties in purification were utilized crude. Substitution at the 6-position proved more difficult than at the 7-position and 6-substituted dyes were less stable under similar reaction conditions. The diphenylamino substituent at the 6-postion (**5.9**) was less electron donating than expected as it provided a very small red-shift (~5 nm) from the dimethylamino congener suggestive that the phenyl substituents do not fully donate into the chromophore.

However, Φ_F was within the same range likely due to TICT for 6-amino substituted Flav7 fluorophores. The methoxy substituent at the 6-position proved to be electron donating as predicted for the *para* position with a red-shifted $\lambda_{max, abs}$ of ~16 nm from IR-27 (**5.13**). Surprisingly, Φ_F was also four-fold higher for **5.17** which suggests that TICT was not occurring but also that methoxy substituents at this position increase fluorescence. This result highlights that despite its reduced red-shifting abilities, a methoxy substituent could be beneficial for increasing brightness. Herein, we were able to gain more insight into the 6-position of the flavylium heptamethine scaffold that could help further our predictive measures in order to design fluorophores for multiplex imaging.

5.4 Counterion exchange of Flav7 for nanoparticle formulation

5.4.1 Background

To improve upon multiplexed imaging *in vivo*, we focused on two main aspects: development of SWIR fluorophores with varying λ_{max} and delivery through nanoparticle formulations. Thus far, we have discussed our attempts to develop predictive measures and expand the toolbox of fluorophores for multiplex imaging. However, a major limitation for *in vivo* imaging with Flav7 derivatives is the large amount of aggregation that occurs upon encapsulation of the dye in nanoparticles. To address this issue, we turned to counterion exchange as it has shown to decrease aggregation with similar indolenine cyanine dyes (Cy3 and Cy5).[26] Kylmchenko and coworkers found that larger bulky hydrophobic counterions could reduce aggregation and improve photophysical properties in poly(lactic-co-gycolic acid) (PLGA) nanoparticles. We turned to performing a similar counterion exchange with the intent to reduce aggregation in delivery vehicles and gain a better understanding of the relationship between counterion and fluorophore.

The association between ion and dye is crucial to the delocalization of the charge throughout the fluorophore. A perfectly delocalized charge often referred to as the “ideal

polymethine state" or "cyanine state", gives rise to the characteristic narrow monomer absorption spectrum and is characterized by a lack of bond length alternation (BLA).[23] If symmetric delocalization of charge breaks, known as "crossing the cyanine limit", then a dipolar asymmetric state is reached which is represented by a broadened absorption spectrum, and maximal BLA with diminished absorption coefficient and quantum yields (Figure 5.4A).[24,25] This phenomenon occurs predominately in longer chained polymethine dyes ($n \geq 3$) though there are few instances where large heterocycles can cause a similar effect.[26–28] Counterion identity can play a major role in which of these two states dominate depending on the solvent wherein more nonpolar solvents allow for more intimate ion pairing.[23,29–31] The position of the anion has been shown through crystal structures to localize either at the terminal heterocycle, polarizing the dye and causing an asymmetric state, or to be localized at the linker maintaining an ideal polymethine state. Thus, counterion exchange can dramatically alter the photophysical properties of polymethine dyes.

With this in mind, we explore the photophysical effects of ion pairing on flavylium heptamethine fluorophore, Flav7 (**5.11**), which absorbs and emits light in the SWIR region and shown favorable photophysical characteristics for *in vivo* imaging.[8] However, Flav7 (**5.11**) has low solubility in water, requiring encapsulation in nanoparticle formulations for *in vivo* imaging, where high amounts of aggregation are observed. To reduce aggregation in nanoparticles, we looked to perform counterion exchange on the Flav7 structure containing a tetrafluoroborate counterion, from here on referred to as Flav7·BF_4 (**5.11**) (Figure 5.4B). Furthermore, we were interested in whether this counterion exchange would affect the "ideal polymethine state" in more nonpolar solvents, as has been previously shown.

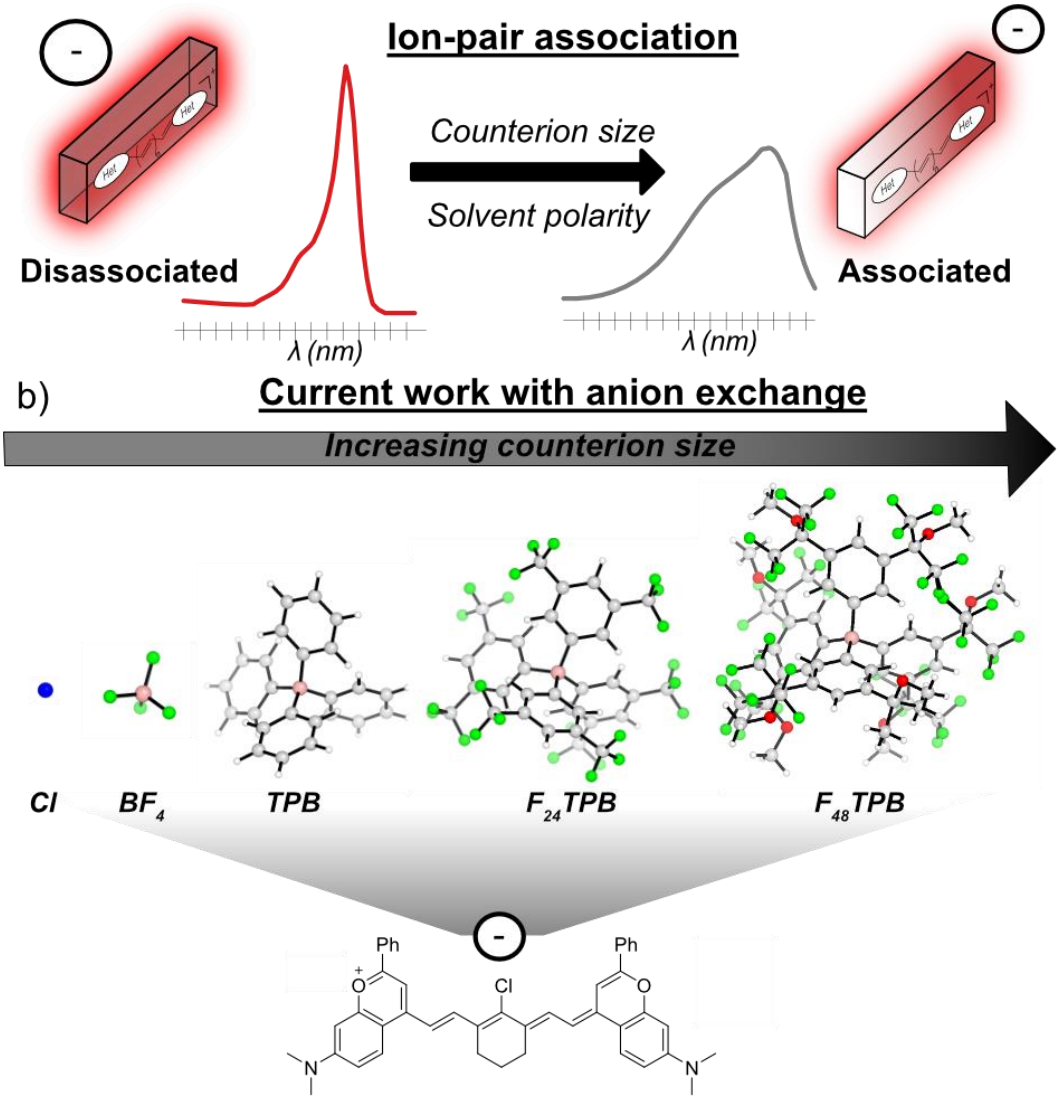

Figure 5.4. A) Ion-pair association can be tuned with counterion size and solvent to favor an associated state vs. a disassociated state. B) Current work exploring anion exchange with Flav7 (**6.11**).

5.4.2 Synthesis and Photophysical Characterization in DCM [1]

Counterions of varying sizes were exchanged with the original tetrafluoroborate (BF_4, 3.3 Å) anion by treating Flav7·BF_4 (**5.11**) in DCM with a series of sodium salts of the counterions of interest (Scheme 5.3). The counterions used were selected due to their varied sizes: chloride (Cl,

[1] Counterion exchange and characterization was done by Emily Cosco and Zhumin Zhang.

1.8 Å), tetraphenyl borate (TPB, 10.8 Å), tetrakis[3,5-bis(trifluoromethyl)phenyl]borate (F_{24}TPB, 12.4 Å) and tetrakis[3,5-bis(1,1,1,3,3,3-hexafluoro-2-methoxy-2-propyl)phenyl]borate (F_{48}TBP, 16.0 Å).[36,37] Photophysical characterization of the resulting Flav7 salts (**5.11, 5.18-5.21**), Scheme 5.3) in DCM revealed no change in $\lambda_{max,abs}$ with all species absorbing at 1027 nm (Table 5.4). Slight variations (~5 nm) were seen in $\lambda_{max,em}$ values, ranging from 1049 nm to 1053 nm. The most notable change between **5.18**–**5.21** was seen within absorption coefficients, with values ranging from 180,000 M^{-1} cm^{-1} for the TPB salt (**5.19**) to 283000 M^{-1} cm^{-1} for the F_{24}TPB salt (**5.20**). These values differ up to 25% from the original Flav7·BF_4 (**5.11**) (241000 M^{-1} cm^{-1}), but are all still within the typical range of polymethine dyes.[38] The quantum yields of fluorescence (Φ_F) ranged from 0.49 ± 0.03 % to 0.61 ± 0.02 % but were all within a similar range. Overall, the counterion exchange of Flav7·BF_4 (**5.11**) seemed to change photophysical properties minimally in DCM (Figure 5.5A). Based on similar work with indolenine cyanine dyes[35], this behavior is expected because DCM is polar enough to dissociate the ion and dye; thus, the size of counterion has little effect on the polymethine scaffold.

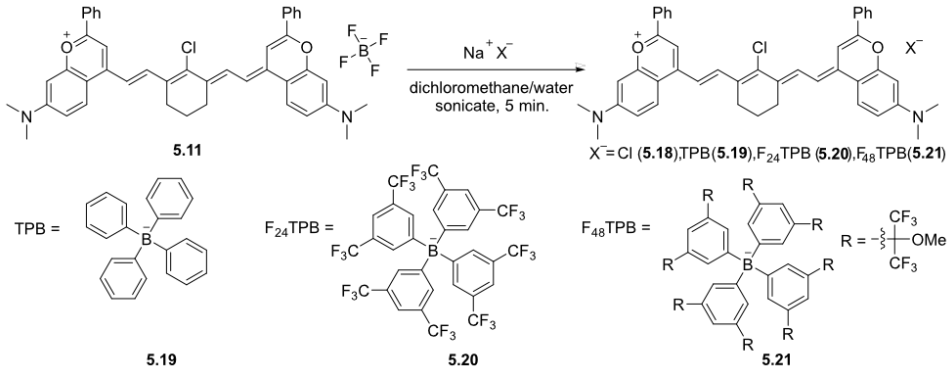

Scheme 5.3. Counterion exchange of Flav7 to other derivatives of different sized counterions.

Table 5.4. Photophysics of derivatives of Flav7 with varying counterions sizes

Solvent	**Dichloromethane**				**4:6 Tol:DCM**			**6:4 Tol:DCM**				**Toluene**			
Compound (anion)	Abs (nm)	Em (nm)	Φ_F (%)[a]	ε (M^{-1} cm^{-1})[a]	Abs (nm)	Em (nm)	Φ_F (%)[a]	Abs (nm)	Em (nm)	Φ_F (%)[a]	ε (M^{-1} cm^{-1})[a]	Abs (nm)	Em (nm)	Φ_F (%)[a]	ε (M^{-1} cm^{-1})[a]
5.1 (BF_4)	1027	1053	0.61	241,000	1030	1054	0.38	1033	1056	0.45	-	-	-	-	-
5.2 (Cl)	1027	1051	0.56	240,000	1029	1052	0.32	1035	1056	0.30	-	-	-	-	-
5.3 (TPB)	1027	1049	0.50	180,000	1030	1053	0.37	1035	1057	0.45	6,900	-	-	-	-
5.4 (F_{24}TPB)	1027	1051	0.55	283,000	1030	1052	0.37	1035	1055	0.48	190,000	1037	1057	0.34	66,000
5.5 (**F_{48}**TPB)	1027	1050	0.49	250,000	1030	1051	0.36	1035	1054	0.51	319,000	1035	1054	0.41	173,000

[a] Taken as an average of three replicates. Error is reported in supporting information. Dashes indicate that data could not be measured due to low solubility of compound in corresponding solvent.

5.4.3 Counterion effect on aggregation in nanoparticles

Counterion exchange has been shown to help prevent aggregation in cyanine dyes, and other fluorophores scaffolds upon nanoparticle encapsulation.[26,39] With the different Flav7 counterion species (**5.11, 5.18-5.22**) in hand, we sought to understand how the increase in counterion size impacted dye loading within nanomaterials. We investigated two nanoparticle systems: poly(ethylene glycol)-phospholipid (PEG-phospholipid) micelles and poly(lactic-*co*-glycolic acid) (PLGA) polymer nanoparticles. First, the PEG-phospholipid micelles were formulated by encapsulation of **5.11**, **5.19-5.21** with 18:0 PEG2000 PE using sonication. In contrast to previous reports using indolenine based cyanine dyes[39], increased H-aggregation and a decrease in the amount of monomer dye present was observed with increasing counterion size

(Figure 5.5B). We sought to increase the volume of nanoparticles by utilizing larger PLGA formulations to further prevent aggregation. Only **5.11** and **5.21** were chosen as they represented the control and largest counterion respectively, but only H-aggregation was observed (Figure 5.5C). Surprisingly, the larger counterion F_{48}TBP showed the highest amount of the H-aggregated species regardless of formulation chosen. Despite the reduction of aggregation seen with indolenine cyanine dyes previously, counterion exchange had the opposite effect with Flav7 derivatives, suggestive that the ion-pairing relationship differs between the two scaffolds. To better understand the association between the counterion and Flav7 scaffold, further photophysical insight was needed.

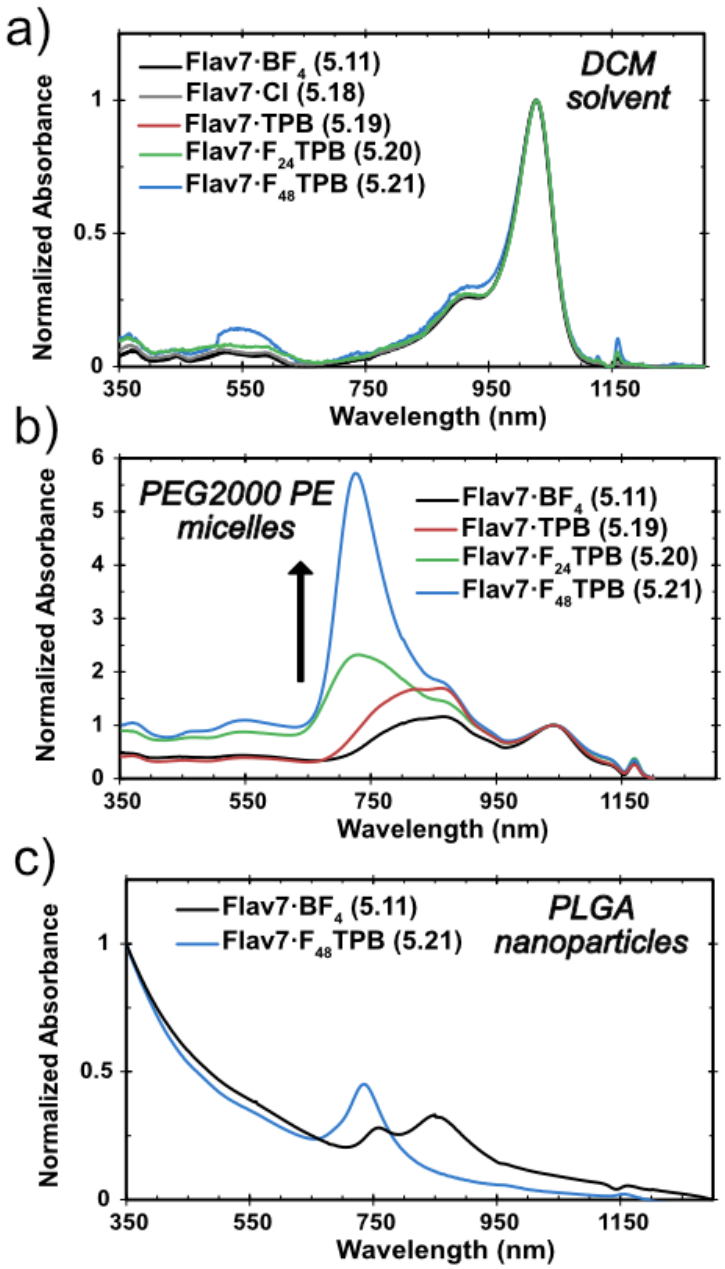

Figure 5.5. A) Normalized absorbance of **5.11, 5.18-5.21** in DCM. B) Normalized absorption spectra of PEG2000 PE micelles **5.11, 5.19-5.21**, fabricated by a solution method. C) Normalized absorption spectra of PLGA nanoparticles **5.11** and **5.21**.

5.4.4 Counterion-dye pairing relationships

The ion-pair relationship can be explored by observing whether anion exchange has an impact on symmetry breaking. In indole based cyanine dyes, the relationship between anion and dye scaffold has been shown to be very crucial in whether fluorophores maintain its symmetrical state.[33,35,40] If the anion sits in the middle of the polymethine linker then complete delocalization is observed, however if the ion is skewed to one side then a dipolar electronic state is achieved. In more nonpolar solvents, anion size has been shown to more substantially impact the symmetry of polymethine dyes due to the closer association between the cationic dye and the anion.[33] Flav7 derivatives **5.11, 5.18**–**5.21** were tested for their solubility in more non-polar solvents, such as toluene, by analyzing absorption spectra. We anticipated that the larger counterions (TPB, F_{24}TPB, and F_{48}TPB) would improve solubility in non-polar solvents as they could more effectively counteract the dipolar nature of the Flav7 polymethine scaffold. Observing the absorption spectra in toluene, we found that the solubility of the fluorophore increased with counterion size (Figure 5.6A/B). A fluorophore that is soluble shows a linear relationship between absorbance (O.D) and concentration with no change in spectral shape which can be quantified by the Beer Lambert law, thus we are able to obtain absorption coefficients for fluorophores that are sufficiently soluble. Flav7·F_{24}TPB (**5.20**) and Flav7·F_{48}TPB (**5.21**) showed comparable absorption bands to when solubilized in DCM (Figure 5.6C). Both salts had a slight increase in $\lambda_{max,abs}$ of approximately 10 nm ($\lambda_{max,abs}$ = 1035–1037 nm), but surprisingly showed no change to $\lambda_{max,em}$. The absorption coefficient for **5.20** and **5.21** showed a decrease of 77% and 31% respectively when comparing toluene to DCM, with Flav7·F_{24}TPB (**5.20**) at 66,000 M^{-1} cm^{-1} and Flav7·F_{48}TPB (**5.21**) at 173,000 M^{-1} cm^{-1}. The Φ_F also decreased in toluene with Flav7·F_{24}TPB (**5.20**) at 0.34% (compared to 0.55% in DCM), whereas Flav7·F_{48}TPB (**5.21**) was more comparable at 0.41% (TOL) vs 0.49% (DCM).

Flav7·F_{24}TPB (**5.20**) showed diminished photophysical properties in TOL vs. DCM (Table 6.4), whereas the larger Flav7·F_{48}TPB (**5.21**) showed a lesser change between the two solvents, suggestive that the larger F_{48}TPB counterion helps maintain an "ideal polymethine state".

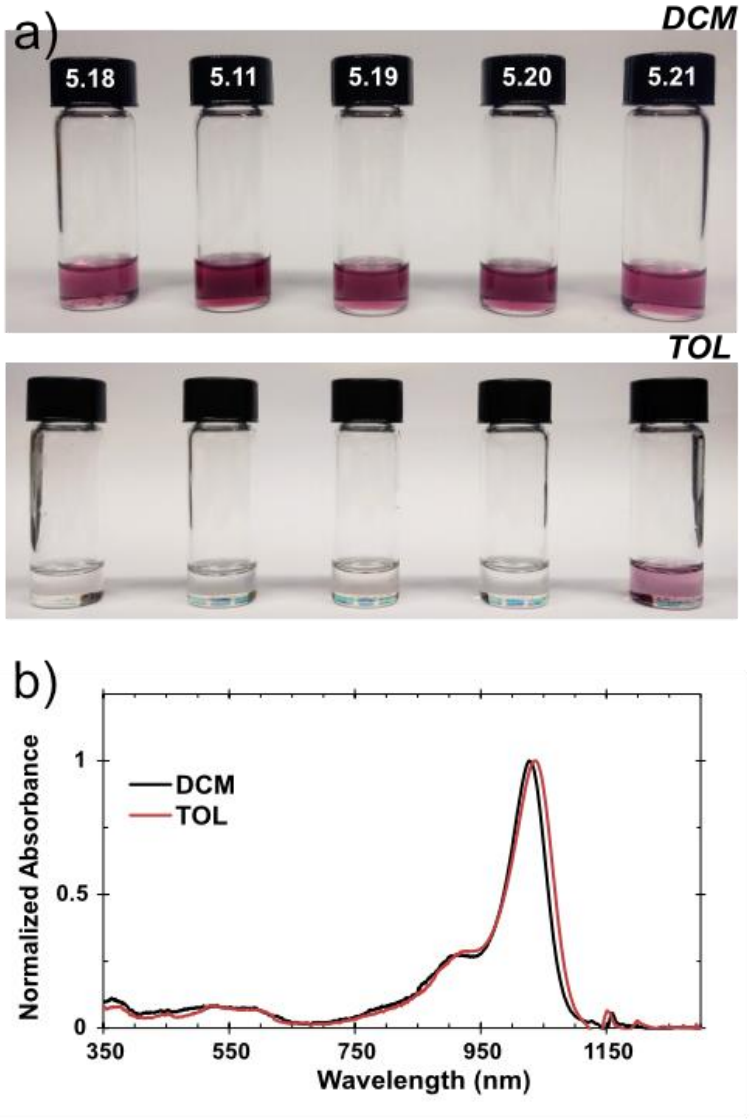

Figure 5.6. A) Vial pictures of **5.11, 5.18-5.21** in DCM (top) and TOL (bottom) at a concentration of 0.05mM. B) Normalized absorbance spectra in dichloromethane (black) and toluene (red) of B) F_{24}TPB (**5.20**)

To further explore these effects, photophysical properties were also analyzed in mixtures of toluene and DCM. In a mixture of 6:4 TOL:DCM, the absorption and emission spectra more

closely resembled that of the toluene soluble derivatives, with a $\lambda_{max,abs}$ at 1035 nm and an unchanging $\lambda_{max,em}$ (Table 5.4). There is also an observable trend in broadness of the blue-shifted shoulder in the absorption spectra (Figure 5.7A). Flav7·Cl (**5.18**) shows the most prominent broadening of the shoulder (Figure 5.7A, gray) whereas Flav7·F_{48}TPB (**5.21**) (Figure 5.7A, blue) is the narrowest, with a noticeable trend between counterion size and broadness of spectra. Looking at the full width half max (FWHM) there is a small range from **5.21** at 583 cm^{-1} to 683 cm^{-1} for **5.18** (Figure 5.7E). Due to limits in solubility of the Flav7 derivatives with smaller counterions (Cl and BF_4, **5.18** and **5.11** respectively), absorption coefficients could not be obtained. The other derivatives (**5.19**– **5.21**) showed increasing absorption coefficients as the size of counterion increased, ranging from 6,900 to 319,000 M^{-1} cm^{-1}. The Φ_F could be characterized for all derivatives as smaller concentrations are needed to determine Φ_F. The variation in Φ_F was less than that of the absorption coefficient, with Flav7·Cl (**5.18**) being the lowest at 0.31% and the other derivatives ranging from 0.45–0.51%. In the 6:4 TOL:DCM mixture, the broadened absorption spectra and decreased ε and Φ_F values present for the Flav7 derivatives with smaller counterions suggests the presence of a symmetry broken state in comparison to those with larger counterions. Emission spectra (Figure 5.7B) show no change in spectra width, which is consistent with the observation that emission comes from the "cyanine" state. In contrast, when increasing the amount of DCM (4:6 TOL:DCM), for all compounds, there is no change to the absorption spectra width showcased by a smaller range of FWHM (635-667 cm^{-1}) and the $\lambda_{max,abs}$ lies between the DCM value (1027 nm) and the toluene value (1033 nm) at 1030 nm (Figure 5.7C/E). The difference in FWHM of 6:4 TOL:DCM and 4:6 TOL:DCM show a decreasing value (Figure 5.7F). Furthermore, the Φ_F, though slightly lowered (0.32–0.38%) from the values in DCM, are all within

the same range regardless of counterion size (Figure 5.7D). The addition of more DCM gives rise to more dissociated ion-pairs in which the nature of the anion is less relevant.

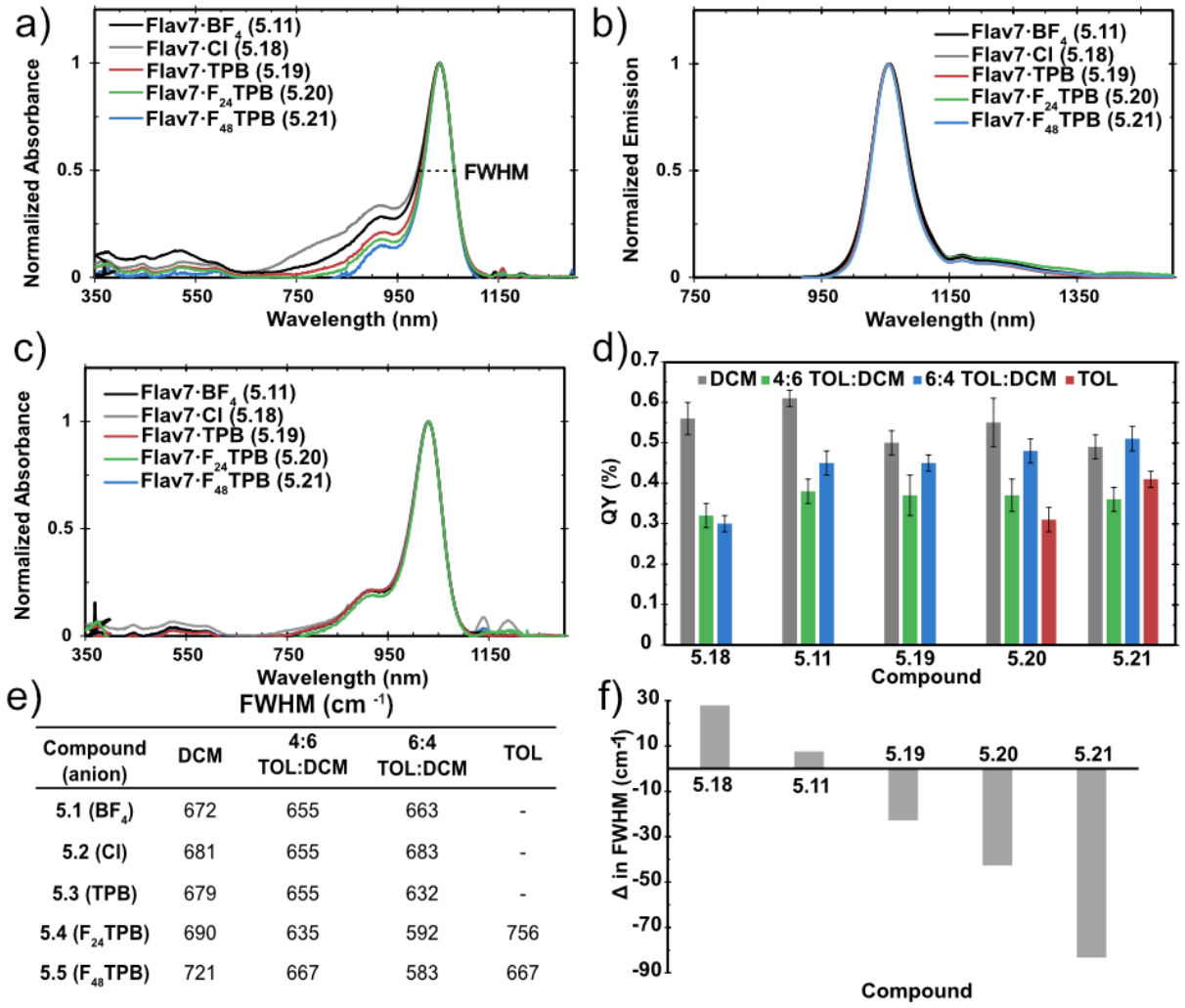

Compound (anion)	DCM	4:6 TOL:DCM	6:4 TOL:DCM	TOL
5.1 (BF_4)	672	655	663	-
5.2 (Cl)	681	655	683	-
5.3 (TPB)	679	655	632	-
5.4 (F_{24}TPB)	690	635	592	756
5.5 (F_{48}TPB)	721	667	583	667

Figure 5.7. A/B) Normalized absorbance spectra (A) and emission spectra (B) of Flav7 derivatives (**5.1-5.5**) in a mixture of 6:4 TOL: DCM. C) Normalized absorbance spectra of Flav7 derivatives (**5.1-5.5**) in a mixture of 4:6 TOL:DCM. D) Difference of full width half maxima (FWHM, nm) in 6:4 TOL:DCM and 4:6 TOL:DCM of Flav7 derivatives (**5.11, 5.18-5.21**)

Though symmetry breaking occurs within more nonpolar solvents, the change in the Flav7 scaffold is subtle, especially in comparison to what has been previously observed by the Maury group with indolenine cyanine dyes. In DCM, indolenine cyanine dyes (**5.22-5.23**) showed similar

absorption spectra regardless of counterion ($^{-}$Br vs. $^{-}B(C_6F_5)_4$), similar to what was observed in Flav7. Changing the solvent to toluene showed broadened and weaker absorption spectra for the small counterion $^{-}$Br (**5.22**).[35] On the other hand, the larger counterion ($^{-}B(C_6F_5)_4$, **5.23**) showed no broadening of absorption spectra or major changes in photophysical properties. When observing the $^{-}$Br derivative (**5.22**), FWHM was largest at 2337 cm^{-1} for pure toluene vs. 658 cm^{-1} for DCM. In 4:6 TOL:DCM, FWHM was reported at 655 cm^{-1} then increased to 910 cm^{-1} upon increasing thetoluene amount to 6:4 TOL:DCM (Figure 5.8). In comparison, the changes between FWHM for Flav7 derivatives between 4:6 TOL:DCM and 6:4 TOL:DCM are small (>100 cm^{-1}). The photophysical changes for Flav7 are more subtle and complicated by the low solubility of the fluorophore in toluene, but comparison of these data indicates that ion-pairing relationships could be less consequential in the Flav7 scaffold in comparison to indolenine cyanine dyes (Figure 5.8). These findings help explain why our initial exploration of counterion exchange in nanomaterials saw no significant changes in aggregation for Flav7 in comparison to literature precedent with indolenine dyes. Thus, different heterocycles (indolenine vs. flavylium) in polymethine fluorophores could play a major role in aggregation properties.

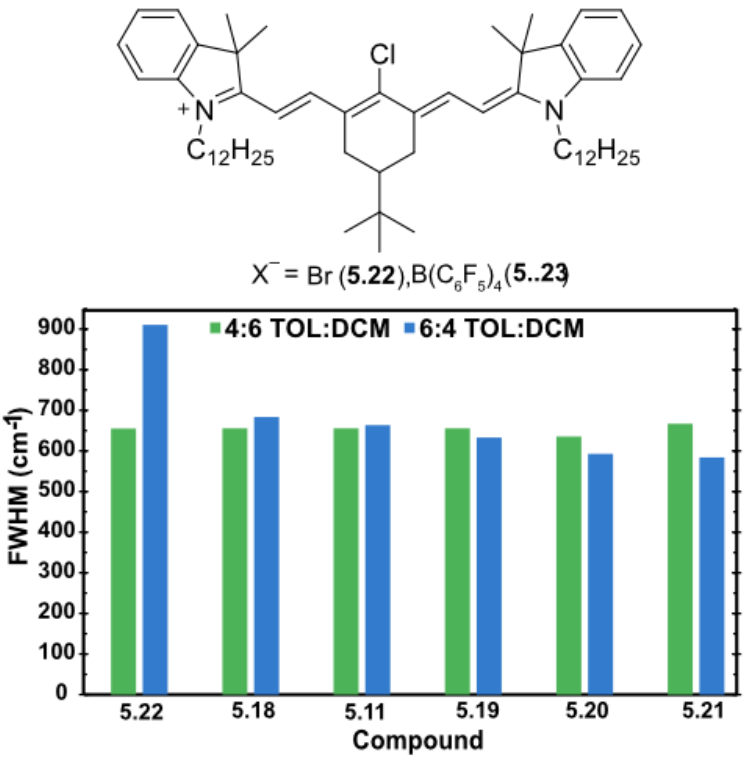

Figure 5.8. Comparison of FWHM (cm^{-1}) from previous work (**5.22**) and current work (**5.11, 5.18-5.21**) in 4:6 TOL:DCM (green) and 6:4 TOL:DCM (blue).

Properties of the SWIR polymethine dye Flav7 was explored by exchanging the anion from tetrafluoroborate to larger, more weakly coordinating anions. When applied to nanomaterial formulations, undesirable H-aggregation was unaffected with increasing counterion size, demonstrating the propensity for Flav7 to aggregate is not overcome by the steric bulk or positioning of the counterion. These findings contrast with previous work with indolinine cyanine dyes, suggestive that different heterocycles on polymethine fluorophores effect the ion-pair relationship. To understand these differences photophysical characteristics was explored in in different solvents. All dyes showed similar photophysical properties in DCM but increasing solubility in toluene was observed for larger counterion derivatives. This allowed for photophysical characterization of Flav7 F_{24}TPB (**5.20**) and Flav7 F_{48}TPB (**5.21**) in toluene.

Despite the solubility of Flav7 F_{24}TPB (**5.20**), ε and Φ_F were decreased compared to what was observed in DCM. On the other hand, Flav7 F_{48}TPB (**5.21**) showed more comparable photophysics in toluene and DCM. In mixtures of 6:4 TOL:DCM, we observed a similar trend: dyes with increasing counterion size had photophysical characteristics more comparable to pure DCM. Yet, when DCM was in a higher ratio (4:6 TOL:DCM), the photophysical properties were more similar across all derivatives. Thus, counterion exchange of Flav7 showed small changes in ion-pairing relationships depending on the anion size and solvent. Again, this contrasts what has been previously observed in indolenine cyanine dyes, suggestive that ion-pairing relationships differ depending on heterocycle identity. Overall, counterion exchange allowed us further insight into the photophysical properties of Flav7 dyes while also enabling higher solubility in non-polar solvents like toluene, which could be utilized in the future as a simple post-synthetic modification for helping increase solubility.

5.5 Conclusion

Our initial studies of excitation multiplexed imaging allowed for high resolution real time *in vivo* imaging with at least three channels. To expand on this technology, fluorophores with different $\lambda_{max, abs}$ need to be developed as well as improvement on the delivery vehicle to reduce the amount of aggregation and decrease brightness. To address these issues, we focused on developing derivatives with 6-Flav7 and showed that substituents do not act similarly to the 7-position. Exchanging the dimethylamino substituent for a diphenylamino at the 6-position showed nearly no change to $\lambda_{max, abs}$ which could be attributed to the planarity of the phenyl substituents. Interestingly, when this same substituent was replaced with a methoxy group there was a four-fold increase in fluorescence, suggestive that methoxy groups at the 6-position could be beneficial for the development of brighter dyes. We also explored counterion exchange as a method to reduce

aggregation in nanoparticles and found that in contrast to indolenine cyanine dyes, the flavylium heptamethine scaffold showed high amounts of H-aggregates regardless of counterion size. To better understand this phenomenon, ion-pairing relationship was explored through polarity studies and observation of symmetry breaking. Though larger counterions helped with solubility in toluene there was little changes to the symmetrical state. In contrast to cyanine dyes, ion-pairing relationships appear to be less important for the Flav7 scaffold possibly due to the difference in heterocycles. This explains why counterion exchange did not help in reducing aggregation in nanoparticle. We attempted to improve upon excitation multiplexed imaging *in vivo* through developing additional SWIR fluorophores and decreasing aggregation within nanoparticles. Though these studies did not necessarily accomplish these goals, they helped provide fundamental understandings that could inform future studies.

5.6 Experimental Procedures

5.6.1 Photophysical Procedures:

Absorbance spectra were collected on a JASCO V-770 UV-Visible/NIR spectrophotometer with a 2000 nm/min scan rate after blanking with the appropriate solvent. Photoluminescence spectra were obtained on a Horiba Instruments PTI QuantaMaster Series fluorometer. Quartz cuvettes (1 cm) were used for absorbance and photoluminescence measurements. Absorption coefficients in dichloromethane were calculated with serial dilutions with Hamilton syringes in volumetric glassware. Error was taken as the standard deviation of the triplicate experiments. Relative quantum yields were determined in dichloromethane relative to IR-26.

Fluorescence quantum yield measurements:

The fluorescence quantum yield (Φ_F) of a molecule or material is defined as follows:

$$\Phi_F = \frac{P_E}{P_A} \qquad (1)$$

Where P_E and P_A represent the number of photons emitted and absorbed, respectively. To determine the quantum yield, we used a relative method with IR-26 as a known standard in the same region of the electromagnetic spectrum.

To compare an unknown to a reference with a known quantum yield, the following relationship was used:

$$\Phi_{F,x} = \Phi_{F,r}\,(m_x / m_r)(\eta_x^2 / \eta_r^2)$$

Where m represents the slope of the line (y = mx + b) obtained from graphing integrated fluorescence intensity versus optical density across a series of samples, η is the refractive index of the solvent and the subscripts x and r represent values of the unknown and reference, respectively. The $\Phi_{F,r}$ of IR-26 was taken to be 0.05%, as previously determined.[41]

To obtain a plot of integrated fluorescence intensity versus absorbance for the reference and unknown, five solutions and a solvent blank were prepared with absorbance maxima between 0.01 and 0.1 au. Absorbance and emission spectra (with an excitation wavelength of 885 nm) were acquired for all samples. IR-26 and the unknown dyes were diluted in dichloromethane to concentrations with optical densities less than 0.1 to minimize effects of reabsorption. The baseline corrected (at 1500 nm) fluorescence traces were integrated, and the raw integrals were corrected by subtracting the integral over an identical range from fluorescence traces of the blank solvent. The integrated fluorescence intensities were then plotted against the baseline corrected absorbance values at the relevant wavelength (885 nm), and the slope and error in slope were obtained (R^2 > 0.99 for all traces).

5.6.2 Synthetic Proceduures

Materials: Chemical reagents were purchased from Acros Organics, Alfa Aesar, Fisher Scientific, Sigma-Aldrich, or TCI and used without purification unless noted otherwise. Anhydrous and deoxygenated solvents (THF) were dispensed from a Grubb's-type Phoenix Solvent Drying System. Oxygen was removed by three consecutive freeze–pump–thaw cycles in air-free glassware directly before use.

Instrumentation: Thin layer chromatography was performed using Silica Gel 60 F254 (EMD Millipore) plates. Flash chromatography was executed with technical grade silica gel with 60 Å pores and 40 – 63 μm mesh particle size (Sorbtech Technologies). Solvent was removed under reduced pressure with a Büchi Rotovapor with a Welch self-cleaning dry vacuum pump and further dried with a Welch DuoSeal pump. Nuclear magnetic resonance (^{1}H-NMR, ^{13}C-NMR) spectra were taken on Bruker Avance 300, AV-400, AV-500 and processed with MestReNova or TopSpin software. All ^{1}H NMR and ^{13}C NMR peaks are reported in ppm in reference to their respective solvent signals. High resolution mass spectra (electrospray ionization (ESI)) were obtained on a Thermo Scientific Q Exactive™ Plus Hybrid Quadrupole-Orbitrap™ M with Dionex UltiMate 3000 RSLCnano System

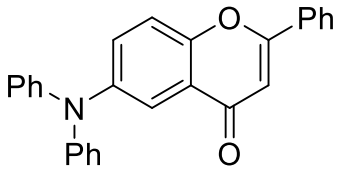

6-(diphenylamino)-2-phenyl-4H-chromen-4-one (5.6)

Flavone **5.5** (200 mg, 0.50 mmol, 1 eq), SPhos-Pd-G3 (45 mg, 0.10 mmol, 0.1 eq), SPhos (20 mg, 0.10 mmol, 0.1 eq) and cesium carbonate (240 mg, 0.80 mmol, 1.5 eq) was evacuated and

subsequently purged with nitrogen for three cycles. Anhydrous toluene (5 mL) was added to solubilize all solids and then diphenylamine (0.40 mL, 0.80 mmol, 1.5 eq) was added. The solution was heated to 110 °C in a heating block and turned from a cloudy brown to clear orange-yellow. After 24 hours of stirring, the solution was concentrated down to give an orange red solid. The crude product was purified via silica gel chromatography with hexanes: ethyl acetate (9:1→ 4:1) to afford pure **6-(diphenylamino)-2-phenyl-4H-chromen-4-one** (110 mg, 0.40 mmol, 83%) as a yellow/green solid. ^{1}H NMR (400 MHz, Acetonitrile-d_3) δ 7.54 – 7.48 (m, 2H), 7.46 (t, J = 1.6 Hz, 1H), 7.11 (dd, J = 5.3, 2.0 Hz, 3H), 7.04 (s, 1H), 6.89 – 6.81 (m, 5H), 6.70 – 6.61 (m, 7H), 6.37 (s, 1H).

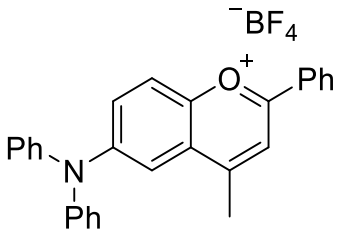

6-(diphenylamino)-4-methyl-2-phenylchromenylium (5.7)

6-(diphenylamino)-2-phenyl-4H-chromen-4-one **5.6** (110 mg, 0.40 mmol, 1 eq) was dissolved in THF (5.3 mL, anhydrous) and cooled to 0 °C. MeMgBr (1.4 M in THF/toluene, 0.60 mL, 0.80 mmol, 2 eq) was added dropwise over 30 min turning the solution from yellow to orange brown. The mixture was warmed to room temperature and left to stir overnight, at which point was quenched with 5% fluoroboric acid solution, turning the solution purple, then extracted with dichloromethane (3 x 15 mL), dried over $NaSO_4$, filtered and evaporated. The crude solid was washed with cold ethyl acetate (50 mL) to afford pure **5.7** as a purple solid (96 mg, 0.35 mmol, 98%). ^{1}H NMR (400 MHz, Acetonitrile-d_3) δ 8.45 – 8.36 (m, 3H), 8.07 (d, J = 9.5 Hz, 1H), 7.89 – 7.82 (m, 2H), 7.74 (dd, J = 8.5, 7.2 Hz, 2H), 7.50 – 7.41 (m, 5H), 7.33 – 7.23 (m, 5H), 2.78 – 2.76 (m, 3H).

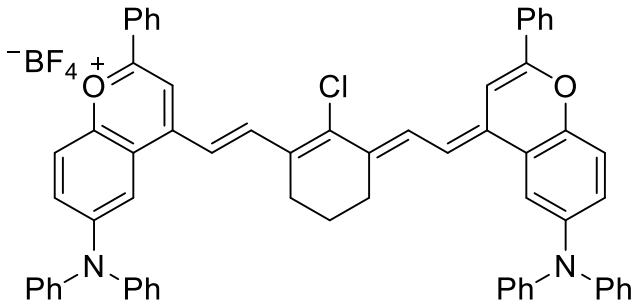

4-((E)-2-((E)-2-chloro-3-(2-((E)-6-(diphenylamino)-2-phenyl-4H-chromen-4-ylidene)ethylidene)cyclohex-1-en-1-yl)vinyl)-6-(diphenylamino)-2-phenylchromenylium (5.9)

A Schlenk flask was charged with flavylium **5.7** (80 mg, 0.20 mmol, 1 eq), 2,6-di-*tert*-butyl-4-methylpyridine (240 mg, 1.1 mmol, 5 eq), N-[(3-(anilinomethylene)-2-chloro-1-cyclohexen-1-yl)methylene]aniline hydrochloride **5.8** (25 mg, 0.1 mmol, 0.3 eq) and DMAC (2.5 mL). The dark magenta solution was freeze pump thawed 3x and then heated to 80 °C in an oil bath for 45 min. The reaction was monitored by UV-Vis for the disappearance of the 550nm peak and formation of 1053 peak.

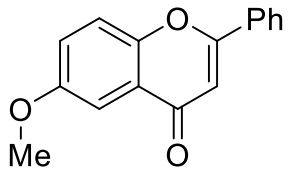

6-methoxy-2-phenyl-4H-chromen-4-one (5.15)

Flavone **5.14** (50 mg, 0.2 mmol, 1 eq) and K_2CO_3 (90 mg, 0.6 mmol, 3 eq) were dissolved in acetone (2 mL, 0.1M) to give a cloudy yellow solution. Iodomethane (0.02 mL, 0.2 mmol, 1.5 eq) was added and left to stir at r.t. for 7 h. NH_4Cl solution was added and the reaction was extracted into EtOAc (3 x 10 mL), dried over Na_2SO_4, filtered and concentrated to give a yellow solid. The crude product was purified via silica gel chromatography with hexanes: ethyl acetate (9:1→ 4:1) to afford pure **6-(diphenylamino)-2-phenyl-4H-chromen-4-one** (42 mg, 0.40 mmol, 79 %) as a

powdery white solid. ^{1}H NMR (400 MHz, Chloroform-*d*) δ 7.95 – 7.92 (m, 2H), 7.61 (d, *J* = 3.1 Hz, 1H), 7.55 – 7.49 (m, 4H), 7.30 (dd, *J* = 9.1, 3.1 Hz, 1H), 6.83 (s, 1H), 3.92 (s, 3H). ^{13}C NMR (101 MHz, Chloroform-*d*) δ 178.21, 163.06, 156.96, 151.01, 131.80, 131.45, 128.98, 126.18, 124.51, 123.73, 119.47, 106.75, 104.79, 55.88.

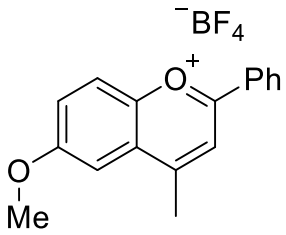

6-methoxy-4-methyl-2-phenylchromenylium (5.16)

6-methoxy-2-phenyl-4H-chromen-4-one **5.15** (40 mg, 0.2 mmol, 1 eq) was dissolved in THF (2.0 mL, anhydrous) and cooled to 0 °C. MeMgBr (1.4 M in THF/toluene, 0.2 mL, 0.3 mmol, 2 eq) was added dropwise over 30 min turning the solution from yellow to orange brown. The mixture was warmed to room temperature and left to stir overnight, at which point was quenched with 5% fluoroboric acid solution, turning the solution darker orange, then extracted with dichloromethane (3 x 15 mL), dried over $NaSO_4$, filtered and evaporated. The crude solid was washed with cold ethyl acetate (50 mL) to afford pure **5.16** as a green/yellow solid (96 mg, 0.35 mmol, 98%). ^{1}H NMR (400 MHz, Acetonitrile-d_3) δ 8.62 (d, *J* = 0.7 Hz, 1H), 8.52 – 8.47 (m, 2H), 8.29 (d, *J* = 9.4 Hz, 1H), 7.98 – 7.90 (m, 2H), 7.84 – 7.76 (m, 2H), 7.66 (d, *J* = 2.9 Hz, 1H), 4.10 (s, 3H), 3.15 (d, *J* = 0.7 Hz, 3H).

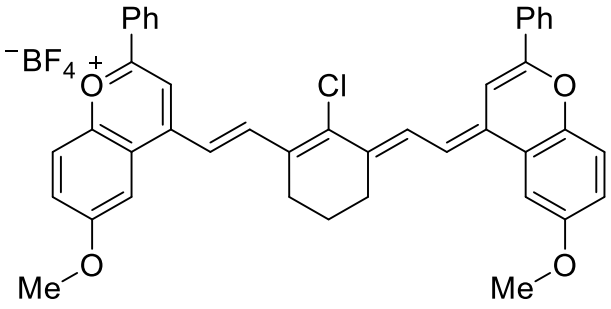

4-((E)-2-((E)-2-chloro-3-(2-((E)-6-methoxy-2-phenyl-4H-chromen-4-ylidene)ethylidene)cyclohex-1-en-1-yl)vinyl)-6-methoxy-2-phenylchromenylium (6.17)

A Schlenk flask was charged with flavylium **5.16** (10 mg, 0.04 mmol, 1 eq), 2,6-di-*tert*-butyl-4-methylpyridine (25 mg, 0.1 mmol, 3 eq), N-[(3-(anilinomethylene)-2-chloro-1-cyclohexen-1-yl)methylene]aniline hydrochloride **5.8** (6 mg, 0.02 mmol, 0.4 eq) and n-butanol:toluene (0.100 mL: 0.200 mL). The dark magenta solution was freeze pump thawed 3x and then heated to 100 °C in an oil bath for 10 min. The reaction was monitored by UV-Vis for the disappearance of the 550nm peak and formation of 1003 peak.

5.6.3 Nanoparticle fabrication methods[2]

Micelles with heptamethine dyes (DMSO method) 0.4 mg of each heptamethine dye was dissolved in 4 mL DMSO and added to 2 mL of a 6 mg/mL solution of 18:0 PEG2000 PE (1,2-distearoyl-*sn*-glycero-3-phosphoethanolamine-*N*-[methoxy(polyethylene glycol)-2000] ammonium salt (Avanti Polar Lipids) in a 50 mL falcon tube. The solution was sonicated in a probe sonicator for 3 min on ice. The solution was then transferred to a 10 kDa MW cutoff filter (Amicon Ultra-15) and centrifuged at 4,000 rpm. Sequential washes with 1x PBS were performed, until the remaining DMSO consisted of <1%. The micelles were then concentrated by centrifugation (4,000 rpm) to ~12.5 mL.

PLGA nanoparticle preparation. Dye (1mg/mL) and PLGA (50:50 lactide:glycolide ratio) (30 mg/mL) wre dissolved in a solution of 3:7 (v/v) of ethanol:DCM. A separate solution of 0.1% PVA in water was sonicated until completely dissolved then filtered with a 0.22μm PFTE syringe filter. The dye solution (0.100 mL) was added dropwise into the PVA solution (1.5 mL) over ice. This

[2] Micelle formulation was performed by Emily Cosco.

mixture was sonicated in a probe sonicator (40%) for 3 min at 0 ºC. The sonicated solution was then stirred at 1,300 rpm for 1 hour while open to air. The evaporated solution was centrifuged at 18,000 x *g* for 20 min, washed twice with an equal volume of PBS, and finally the centrifuged pellet was resuspended and stored in 0.5 mL PBS.

5.7 Spectra related to Chapter Five

5.7.1 ^{1}H NMR

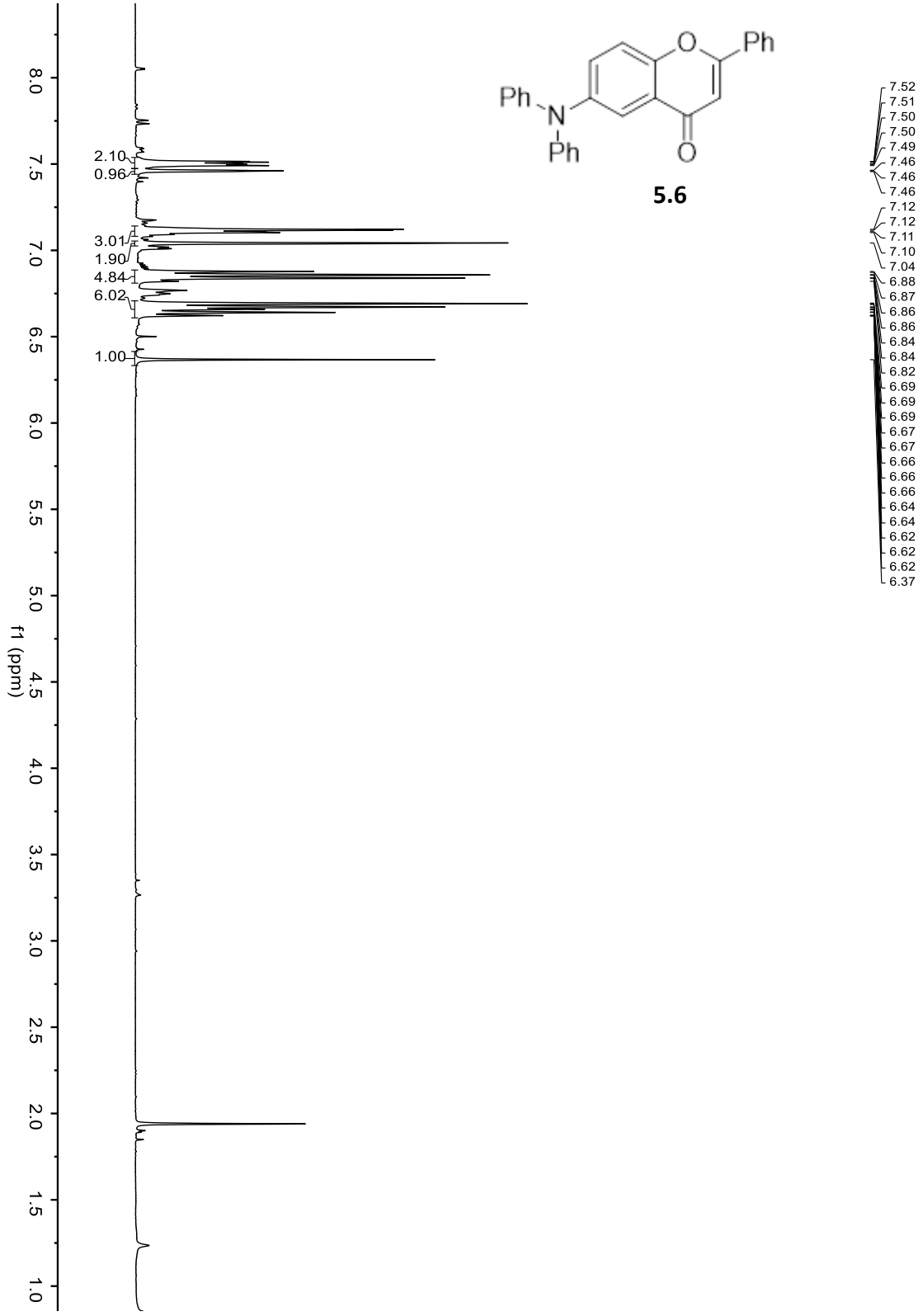

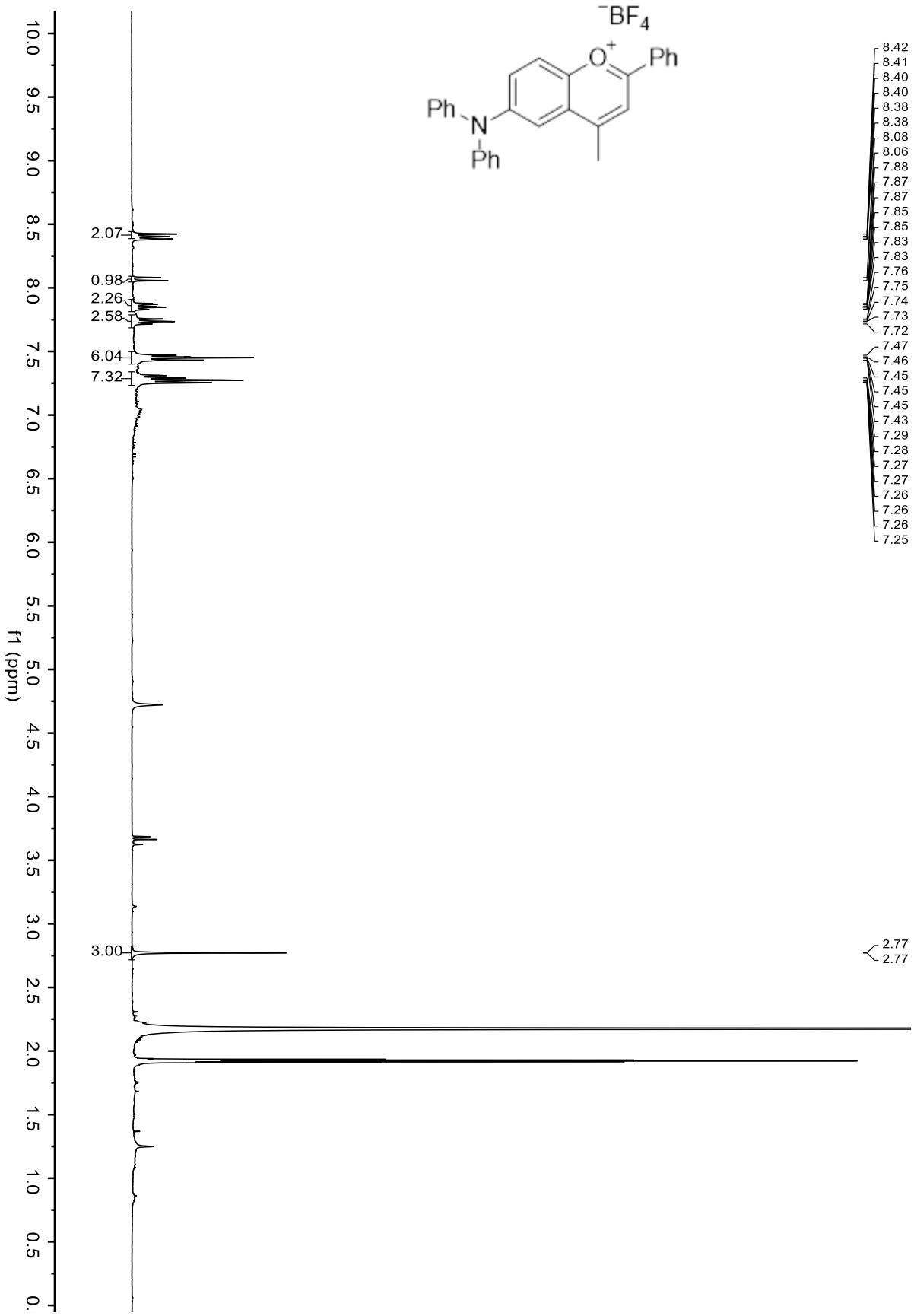
$^{-}BF_4$
O
+
Ph
Ph
N
Ph
f1 (ppm)
10.0
9.5
9.0
8.5
8.0
7.5
7.0
6.5
6.0
5.5
5.0
4.5
4.0
3.5
3.0
2.5
2.0
1.5
1.0
0.5
0.
2.07
0.98
2.26
2.58
6.04
7.32
3.00
8.42
8.41
8.40
8.40
8.38
8.38
8.08
8.06
7.88
7.87
7.87
7.85
7.85
7.83
7.83
7.76
7.75
7.74
7.73
7.72
7.47
7.46
7.45
7.45
7.45
7.43
7.29
7.28
7.27
7.27
7.26
7.26
7.26
7.25
2.77
2.77

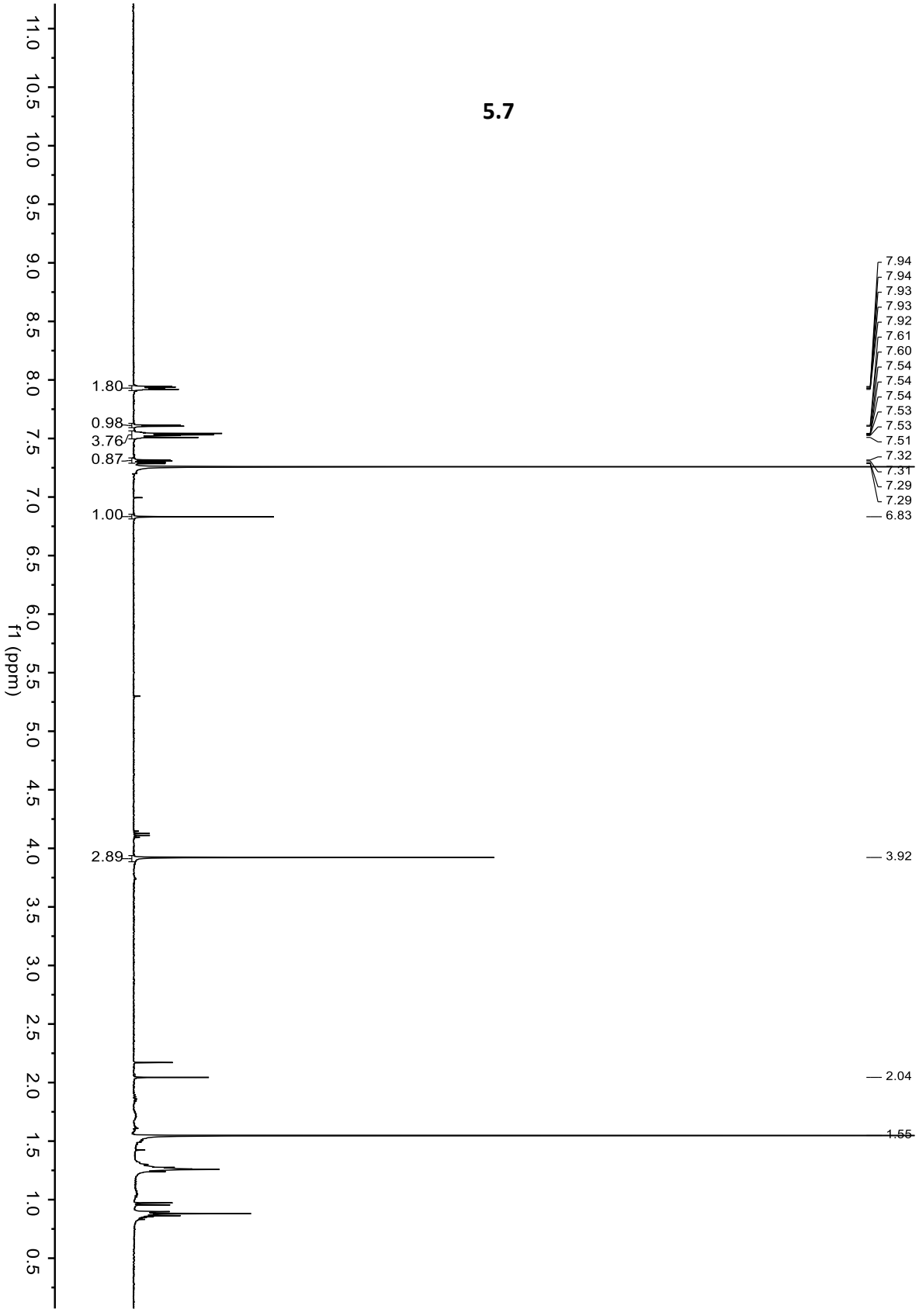
5.7
f1 (ppm)
11.0
10.5
10.0
9.5
9.0
8.5
8.0
7.5
7.0
6.5
6.0
5.5
5.0
4.5
4.0
3.5
3.0
2.5
2.0
1.5
1.0
0.5
1.80
0.98
3.76
0.87
1.00
2.89
7.94
7.94
7.93
7.93
7.92
7.61
7.60
7.54
7.54
7.54
7.53
7.53
7.51
7.32
7.31
7.29
7.29
6.83
3.92
2.04
1.55

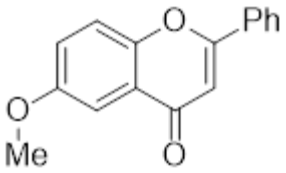
O
Ph
O
Me
O

5.15

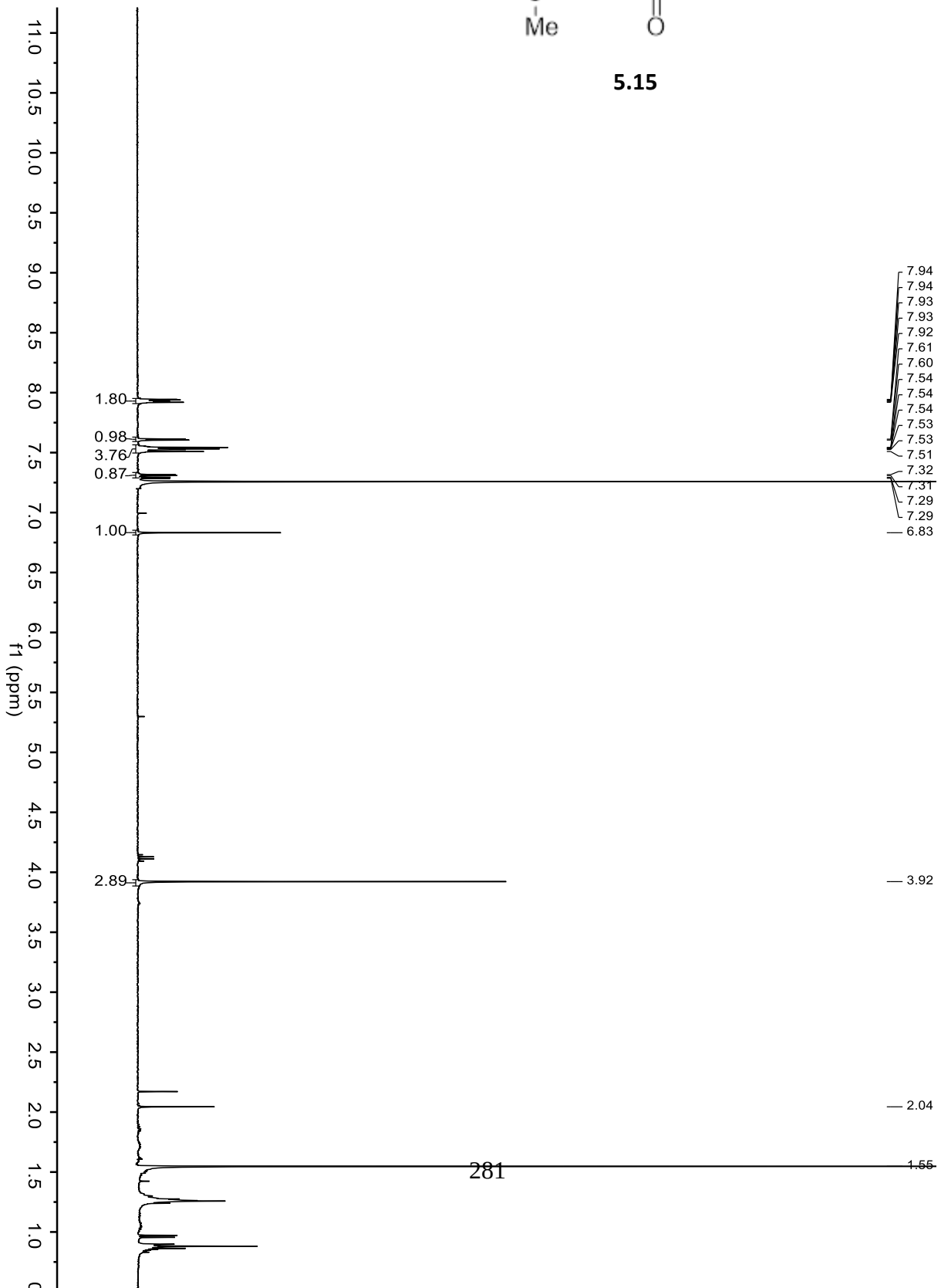
f1 (ppm)
11.0
10.5
10.0
9.5
9.0
8.5
8.0
7.5
7.0
6.5
6.0
5.5
5.0
4.5
4.0
3.5
3.0
2.5
2.0
1.5
1.0
1.80
0.98
3.76
0.87
1.00
2.89
7.94
7.94
7.93
7.93
7.92
7.61
7.60
7.54
7.54
7.54
7.53
7.53
7.51
7.32
7.31
7.29
7.29
6.83
3.92
2.04
1.55

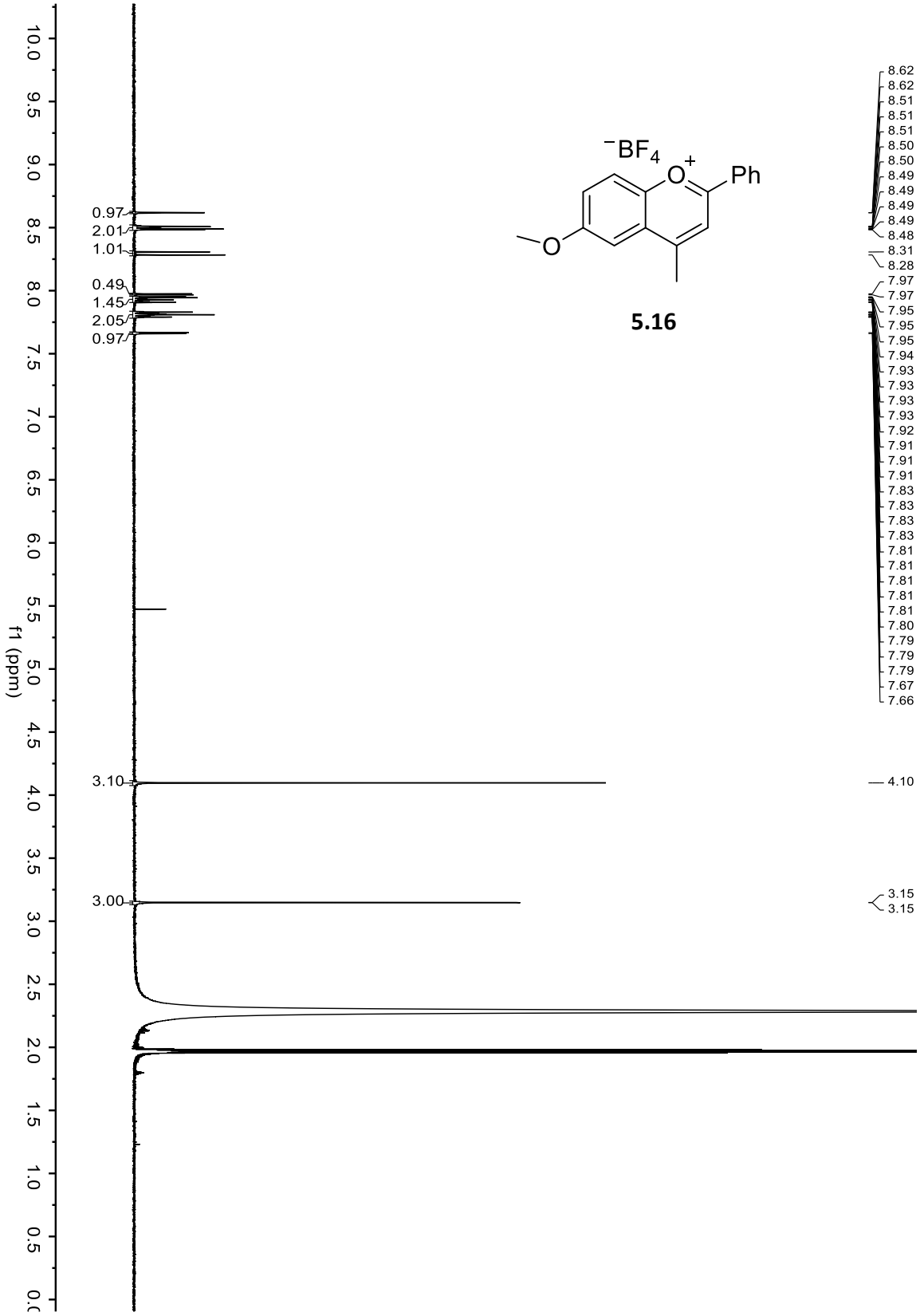
$^{-}BF_4$
O
+
Ph
O
5.16
f1 (ppm)
10.0
9.5
9.0
8.5
8.0
7.5
7.0
6.5
6.0
5.5
5.0
4.5
4.0
3.5
3.0
2.5
2.0
1.5
1.0
0.5
0.0
0.97
2.01
1.01
0.49
1.45
2.05
0.97
3.10
3.00
8.62
8.62
8.51
8.51
8.51
8.50
8.50
8.49
8.49
8.49
8.49
8.48
8.31
8.28
7.97
7.97
7.95
7.95
7.95
7.94
7.93
7.93
7.93
7.93
7.92
7.91
7.91
7.91
7.83
7.83
7.83
7.83
7.81
7.81
7.81
7.81
7.81
7.80
7.79
7.79
7.79
7.67
7.66
4.10
3.15
3.15

5.7.1 ^{2}C NMR

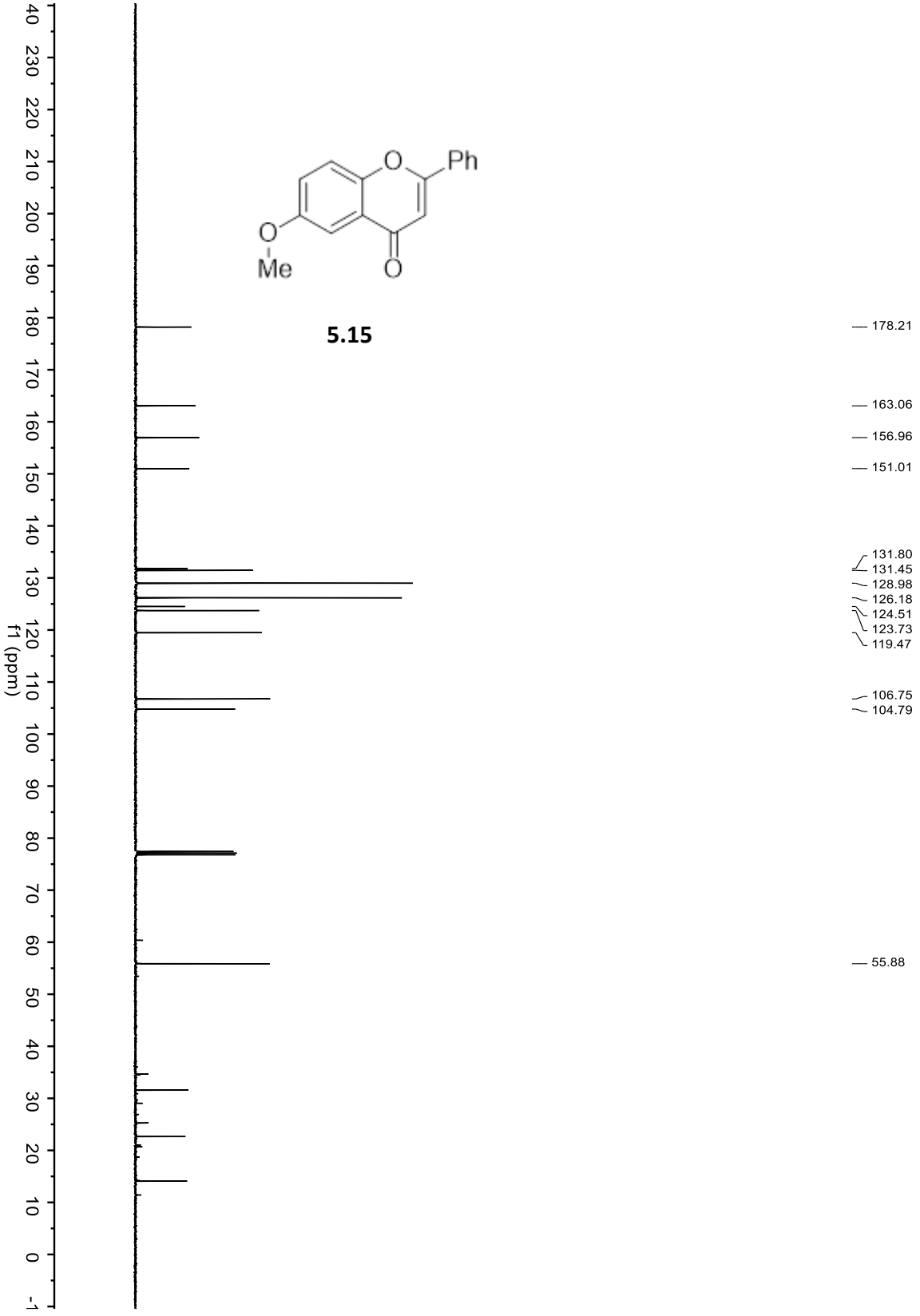
O
Ph
O
Me
O
5.15
178.21
163.06
156.96
151.01
131.80
131.45
128.98
126.18
124.51
123.73
119.47
106.75
104.79
55.88
f1 (ppm)

5.8 References

(1) Wang, S.; Li, B.; Zhang, F. Molecular Fluorophores for Deep-Tissue Bioimaging. *ACS Cent. Sci.* **2020**, *6* (8).

(2) He, S.; Song, J.; Qu, J.; Cheng, Z. Crucial Breakthrough of Second Near-Infrared Biological Window Fluorophores: Design and Synthesis toward Multimodal Imaging and Theranostics. *Chem. Soc. Rev.* **2018**, *47 (12)* 4258-4278.

(3) Zhu, S.; Tian, R.; Antaris, A. L.; Chen, X.; Dai, H. Near-Infrared-II Molecular Dyes for Cancer Imaging and Surgery. *Adv. Mater.* **2019**, *31* (24), 1900321.

(4) Shcherbakova, D. M.; Verkhusha, V. V. Near-Infrared Fluorescent Proteins for Multicolor in Vivo Imaging. *Nat. Methods* **2013**, *10* (8), 751–754.

(5) Kosaka, N.; Ogawa, M.; Sato, N.; Choyke, P. L.; Kobayashi, H. In Vivo Real-Time, Multicolor, Quantum Dot Lymphatic Imaging. *J. Invest. Dermatol.* **2009**, *129* (12), 2818–2822.

(6) Zavaleta, C. L.; Smith, B. R.; Walton, I.; Doering, W.; Davis, G.; Shojaei, B.; Natan, M. J.; Gambhir, S. S. Multiplexed Imaging of Surface Enhanced Raman Scattering Nanotags in Living Mice Using Noninvasive Raman Spectroscopy. *Proc. Natl. Acad. Sci. U. S. A.* **2009**, *106* (32), 13511–13516.

(7) Lei, Z.; Sun, C.; Pei, P.; Wang, S.; Li, D.; Zhang, X.; Zhang, F. Stable, Wavelength-Tunable Fluorescent Dyes in the NIR-II Region for In Vivo High-Contrast Bioimaging and Multiplexed Biosensing. *Angew. Chemie Int. Ed.* **2019**, *58*, 8166–9171.

(8) Cosco, E. D.; Caram, J. R.; Bruns, O. T.; Franke, D.; Day, R. A.; Farr, E. P.; Bawendi, M. G.; Sletten, E. M. Flavylium Polymethine Fluorophores for Near- and Shortwave Infrared Imaging. *Angew. Chemie - Int. Ed.* **2017**, *56* (42), 13126–13129.

(9) Bricks, J. L.; Slominskii, Y. L.; Panas, I. D.; Demchenko, A. P. Fluorescent J-Aggregates of Cyanine Dyes: Basic Research and Applications Review. *Methods Appl. Fluoresc.* **2018**, *6* (1).

(10) Hestand, N. J.; Spano, F. C. Expanded Theory of H- and J-Molecular Aggregates: The Effects of Vibronic Coupling and Intermolecular Charge Transfer. *Chem. Rev.* **2018**, *118* (15), 7069-7163.

(11) Kang, J.; Kaczmarek, O.; Liebscher, J.; Dähne, L. Prevention of H-Aggregates Formation in Cy5 Labeled Macromolecules. *Int. J. Polym. Sci.* **2010**, 264781.

(12) Biaggne, A.; Knowlton, W. B.; Yurke, B.; Lee, J.; Li, L. Substituent Effects on the Solubility and Electronic Properties of the Cyanine Dye Cy5: Density Functional and Time-Dependent Density Functional Theory Calculations. *Molecules* **2021**, *26* (3), 524.

(13) Jradi, F. M.; O'Neil, D.; Kang, X.; Wong, J.; Szymanski, P.; Parker, T. C.; Anderson, H. L.; El-Sayed, M. A.; Marder, S. R. A Step Toward Efficient Panchromatic Multi-Chromophoric Sensitizers for Dye Sensitized Solar Cells. *Chem. Mater.* **2015**, *27* (18), 6305–6313.

(14) Funabiki, K.; Mase, H.; Hibino, A.; Tanaka, N.; Mizuhata, N.; Sakuragi, Y.; Nakashima, A.; Yoshida, T.; Kubota, Y.; Matsui, M. Synthesis of a Novel Heptamethine-Cyanine Dye for Use in near-Infrared Active Dye-Sensitized Solar Cells with Porous Zinc Oxide

Prepared at Low Temperature. *Energy Environ. Sci.* **2011**, *4* (6), 2186–2192.

(15) Bouit, P. A.; Wetzel, G.; Berginc, G.; Loiseaux, B.; Toupet, L.; Feneyrou, P.; Bretonnière, Y.; Kamada, K.; Maury, O.; Andraud, C. Near IR Nonlinear Absorbing Chromophores with Optical Limiting Properties at Telecommunication Wavelengths. *Chem. Mater.* **2007**, *19* (22), 5325–5335.

(16) Hales, J. M.; Matichak, J.; Barlow, S.; Ohira, S.; Yesudas, K.; Brédas, J.-L. L.; Perry, J. W.; Marder, S. R. Design of Polymethine Dyes with Large Third-Order Optical Nonlinearities and Loss Figures of Merit. *Science.* **2010**, *327* (5972), 1485–1488.

(17) Li, D. H.; Schreiber, C. L.; Smith, B. D. Sterically Shielded Heptamethine Cyanine Dyes for Bioconjugation and High Performance Near-Infrared Fluorescence Imaging. *Angew. Chem. Int. Ed. Engl.* **2020**, *59* (29), 12154–12161.

(18) Gadde, S.; Batchelor, E. K.; Weiss, J. P.; Ling, Y.; Kaifer, A. E. Control of H- and J-Aggregate Formation via Host-Guest Complexation Using Cucurbituril Hosts. *J. Am. Chem. Soc.* **2008**, *130* (50), 17114–17119.

(19) Andreiuk, B.; Reisch, A.; Bernhardt, E.; Klymchenko, A. S. Fighting Aggregation-Caused Quenching and Leakage of Dyes in Fluorescent Polymer Nanoparticles: Universal Role of Counterion. *Chem. – An Asian J.* **2019**, *14* (6), 836–846.

(20) Adarsh, N.; Klymchenko, A. S. Ionic Aggregation-Induced Emission Dye with Bulky Counterions for Preparation of Bright near-Infrared Polymeric Nanoparticles. *Nanoscale* **2019**, *11* (29), 13977–13987.

(21) Aparin, I. O.; Melnychuk, N.; Klymchenko, A. S. Ionic Aggregation-Induced Emission: Bulky Hydrophobic Counterions Light Up Dyes in Polymeric Nanoparticles. *Adv. Opt. Mater.* **2020**, *8* (14), 2000027.

(22) Hales, J. M.; Barlow, S.; Kim, H.; Mukhopadhyay, S.; Brédas, J. L.; Perry, J. W.; Marder, S. R. Design of Organic Chromophores for All-Optical Signal Processing Applications. *Chemistry of Materials*. **2014**, *26* (1), 549-560.

(23) Bureš, F. Fundamental Aspects of Property Tuning in Push-Pull Molecules. *RSC Adv.* **2014**, *4* (102), 58826-58851.

(24) Chen, C. T.; Chiang, C. L.; Lin, Y. C.; Chan, L. H.; Huang, C. H.; Tsai, Z. W.; Chen, C. T. Ortho-Substituent Effect on Fluorescence and Electroluminescence of Arylamino-Substituted Coumarin and Stilbene. *Org. Lett.* **2003**, *5* (8), 1261–1264.

(25) Miao, J.; Cui, H.; Jin, J.; Lai, F.; Wen, H.; Zhang, X.; Ruda, G. F.; Chen, X.; Yin, D. Development of 3-Alkyl-6-Methoxy-7-Hydroxy-Chromones (AMHCs) from Natural Isoflavones, a New Class of Fluorescent Scaffolds for Biological Imaging. *Chem. Commun.* **2015**, *51* (5), 881–884. h

(26) Reisch, A.; Klymchenko, A. S. Fluorescent Polymer Nanoparticles Based on Dyes: Seeking Brighter Tools for Bioimaging. *Small* **2016**, *12* (15), 1968–1992.

(27) Tolbert, L. M.; Zhao, X. Beyond the Cyanine Limit: Peierls Distortion and Symmetry Collapse in a Polymethine Dye. *J. Am. Chem. Soc.* **1997**, *119* (14), 3253-3258.

(28) Pascal, S.; Haefele, A.; Monnereau, C.; Charaf-Eddin, A.; Jacquemin, D.; Le Guennic, B.;

Andraud, C.; Maury, O. Expanding the Polymethine Paradigm: Evidence for the Contribution of a Bis-Dipolar Electronic Structure. *J. Phys. Chem. A* **2014**, *118* (23), 4038–4047.

(29) Lepkowicz, R. S.; Przhonska, O. V.; Hales, J. M.; Fu, J.; Hagan, D. J.; Van Stryland, E. W.; Bondar, M. V.; Slominsky, Y. L.; Kachkovski, A. D. Nature of the Electronic Transitions in Thiacarbocyanines with a Long Polymethine Chain. *Chem. Phys.* **2004**, *305* (1–3), 259–270.

(30) Vasyluk, S. V.; Viniychuk, O. O.; Poronik, Y. M.; Kovtun, Y. P.; Shandura, M. P.; Yashchuk, V. M.; Kachkovsky, O. D. Breaking of Symmetrical Charge Distribution in Xanthylocyanine Chromophores Detecting by Their Absorption Spectra. *J. Mol. Struct.* **2011**, *990* (1–3), 6–13.

(31) Pengshung, M.; Neal, P.; Atallah, T. L.; Kwon, J.; Caram, J. R.; Lopez, S. A.; Sletten, E. M. Silicon Incorporation in Polymethine Dyes. *Chem. Commun.* **2020**, *56* (45), 6110–6113.

(32) Deng, Y.; Wei, X.-J.; Wang, H.; Sun, Y.; Noël, T.; Wang, X. Disulfide-Catalyzed Visible-Light-Mediated Oxidative Cleavage of C=C Bonds and Evidence of an Olefin-Disulfide Charge-Transfer Complex. *Angew. Chemie Int. Ed.* **2016**, 1–6.

(33) Bouit, P. A.; Aronica, C.; Toupet, L.; Guennic, B. Le; Andraud, C.; Maury, O. Continuous Symmetry Breaking Induced by Ion Pairing Effect in Heptamethine Cyanine Dyes: Beyond the Cyanine Limit. *J. Am. Chem. Soc.* **2010**, *132* (12), 4328–4335.

(34) Eskandari, M.; Roldao, J. C.; Cerezo, J.; Milián-Medina, B.; Gierschner, J.; Carlos

Roldao, J.; Cerezo, J.; Gierschner, J. Counterion-Mediated Crossing of the Cyanine Limit in Crystals and Fluid Solution: Bond Length Alternation and Spectral Broadening Unveiled by Quantum Chemistry. *J. Am. Chem. Soc.***2020**, *142* (6), 2835–2843.

(35) Pascal, S.; Chi, S.; Perry, J. W.; Andraud, C.; Maury, O. Impact of Ion-Pairing Effects on Linear and Nonlinear Photophysical Properties of Polymethine Dyes. *ChemPhysChem* **2020**, *21* (23), 2536–2542.

(36) Melnychuk, N.; Klymchenko, A. S. DNA-Functionalized Dye-Loaded Polymeric Nanoparticles: Ultrabright FRET Platform for Amplified Detection of Nucleic Acids. *J. Am. Chem. Soc.* **2018**, *140* (34), 10856–10865.

(37) Shulov, I.; Oncul, S.; Reisch, A.; Arntz, Y.; Collot, M.; Mely, Y.; Klymchenko, A. S. Fluorinated Counterion-Enhanced Emission of Rhodamine Aggregates: Ultrabright Nanoparticles for Bioimaging and Light-Harvesting. *Nanoscale* **2015**, *7* (43), 18198–18210.

(38) Julia L. Bricks; Alexei D.Kachkovskii; Yurii L.Slominskii; Andrii O.Gerasov; Sergei V.Popov; Bricks, J. L.; Kachkovskii, A. D.; Slominskii, Y. L.; Gerasov, A. O.; Popov, S. V. Molecular Design of near Infrared Polymethine Dyes: A Review. *Dye. Pigment.* **2015**, *121*, 238–255.

(39) Andreiuk, B.; Reisch, A.; Lindecker, M.; Follain, G.; Peyriéras, N.; Goetz, J. G.; Klymchenko, A. S. Fluorescent Polymer Nanoparticles for Cell Barcoding In Vitro and In Vivo. *Small* **2017**, *13* (38), 1701582.

(40) Gayton, J.; Autry, S.; Fortenberry, R.; Hammer, N.; Delcamp, J. Counter Anion Effect on

the Photophysical Properties of Emissive Indolizine-Cyanine Dyes in Solution and Solid State. *Molecules* **2018**, *23* (12), 3051.

(41) Semonin, O. E.; Johnson, J. C.; Luther, J. M.; Midgett, A. G.; Nozik, A. J.; Beard, M. C. Absolute Photoluminescence Quantum Yields of IR-26 Dye, PbS, and PbSe Quantum Dots. *J. Phys. Chem. Lett.* **2010**, *1* (16), 2445–2450.

CHAPTER SIX

Structural Modifications in Polymethine Dyes for J-aggregation

6.1 Abstract

Structural modifications in polymethine fluorophores give rise to modest changes in photophysical properties. Thus far, we have explored substituent identity (Chapter 2, 5), substituent position (Chapter 3), or exchange of heteroatom (Chapter 4) as avenues to affect photophysical properties but have yet to develop materials that can absorb beyond 1100 nm. Towards this end, we turned to J-aggregates, slip-stacked formations of dye, which can display bathochromic shifts up to ~200 nm from their respective solubilized monomeric form. Despite the potential for far-red shifted materials, very few aggregates for the SWIR have been developed. The largest hurdle to the development of SWIR J-aggregates is a lack of understanding of what causes monomeric fluorophores to aggregate in an appropriate manner. Herein, we explored derivatives of a thiazole-based cyanine to examine how structure effects aggregate arrangement. The fundamental understanding from this study could then be applied to the Flav7 structure to yield an unprecedented aggregate with $\lambda_{max,abs}$ at 1350 nm.

6.2 Introduction

Supramolecular assemblies of fluorophores bring about new photophysical features that are difficult to obtain with single monomer chromophores. When monomeric fluorophores pack in a slip-stacked manner, efficient transition dipole coupling is achievable throughout a number of molecules, a phenomena known as J-aggregation.[1] With respect to the monomer, J-aggregates have advantageous photophysical features such as strongly red-shifted absorption maxima ($\lambda_{max, abs}$) and emission ($\lambda_{max, em}$), narrower bandwidths, small Stokes shifts, high absorption coefficients (ε) and

enhanced quantum yield of fluorescence (Φ_F) (Figure 6.1A).[1] However, fluorophores more commonly stack in a face to face manner, known as H-aggregation, which is commonly associated with a more blue-shifted broad absorption spectra and diminished photophysical properties (Figure 6.1A). Preferentially forming either H or J aggregates can be an arduous task as it depends on the structure of the molecule as well as environmental conditions. To favor J-aggregation and gain enhanced photophysical properties first necessitates a better understanding of these assemblies.

Originally discovered in cyanine dyes, J-aggregates have now been explored in a wide variety of different fluorophore scaffolds such as perylene bisimides, BODIPYs, phthalocyanines and porphyrins.[2–4] However, polymethine dyes are still the staple scaffold for J-aggregation due to their rigidity, planarity, and high polarizability which allow for strong attractive dispersion forces between monomers.[1] Furthermore, as polymethine fluorophores can be developed to absorb and emit in the short-wave infrared (SWIR, 1000- 2000 nm) region of the electromagnetic spectrum, the ability to aggregate these molecules could yield extremely red-shifted fluorophores (> 1100 nm).[5] Organic materials that absorb within this region are of considerable interest to biomedical and material scientists, due to the high depth penetration of light through heterogenous materials and lack of competing molecules.[6–9]

Currently, there are few examples of SWIR polymethine aggregates. Commercially available IR-140 (Figure 6.1B, **6.1**) has been utilized as a SWIR contrast agent *in vivo* by stabilizing J-aggregation within hollow mesoporous nanoparticles.[10] Though the monomer absorbs within the near-infrared (NIR, 700- 1000 nm) at 826 nm (DMSO), the aggregate is over ~200 nm redshifted with a $\lambda_{max,\ abs}$ at 1042 nm. J-aggregation of IR-140 pushed the $\lambda_{max,\ abs}$ into the SWIR, allowing for higher contrast *in vivo* imaging. Zhang and coworkers, have also showcased that FD-1080 (Figure 6.1B, **6.2**) could form J-aggregates in the presence of 1,2-dimyristoyl-sn-flycero-3-

phosphocholine (DMPC) with a $\lambda_{max, abs}$ of 1360 nm, a nearly ~300 nm red-shift from the monomer (1064 nm).[11] These examples showcase the potential of SWIR aggregates but there is still a major lack of understanding of which fluorophore structures can aggregate efficiently and how this correlates to photophysical properties.

Predictive measures of how structural modifications can affect J-aggregate formation have been mainly focused on trimethine and pentamethine dyes for the visible (VIS, 400- 700 nm) and NIR regions.[12–14] For example, benzimidazole carbocyanine fluorophores are a commonly utilized scaffold (Figure 6.1B). The amphiphilic character of these molecules promotes self-assembly into ordered structures. Daehne and coworkers exploited this amphiphilicity by changing the length of alkyl chains in either the hydrophobic (Figure 6.1B, red) or hydrophilic (blue) portion of the molecule (**6.3**-**6.5**). The balance between different intermolecular forces gives way to different packing structures; tubes (**6.3**), ribbons (**6.4**), or planar sheets (**6.5**) which results in variation of photophysical properties.[14] Other modifications with the benzimidazole carbocyanine scaffold have shown that the exchange of a chlorine substituent to bromine (**6.3)** can also lead to size changes of tubular aggregates.[15] Similarly, thiacarbocyanines dyes are another class of monomers that have been extensively investigated for their J-aggregation properties. Modification of the *meso*-alkyl substituents (methyl vs. ethyl) showed that varying bulk at this position can determine morphology of aggregate formation.[16] These important observations have not yet been fully explored in heptamethine dyes but could help design J-aggregates for the SWIR region.

A systematic understanding of key structural modifications for the thiacarbocyanine heptamethine structure should be explored and their effect on aggregate arrangement could help establish predictive measures for SWIR aggregates. Herein, we explored a number of different modifications on the thiazole cyanine scaffold focusing on steric bulk at the 4’ position of the

linker (red), polarizability at the 7 position of the heterocycle (green), and substituents off the nitrogen (blue) (Figure 6.1C).

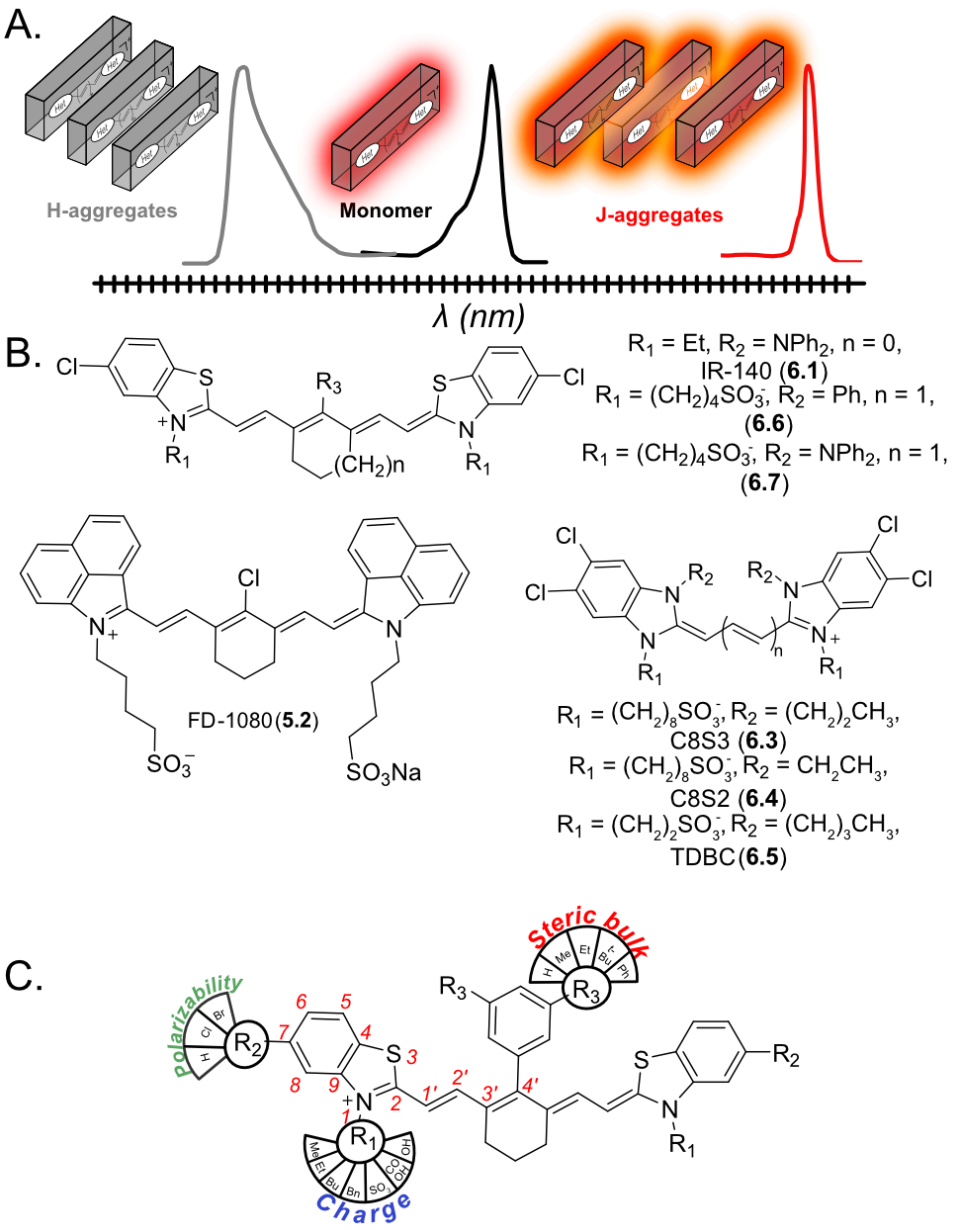

Figure 6.1. A) Monomeric polymethine dyes (black) can aggregate in a slip-stack manner to produce J-aggregates (red) or H-aggregates (gray). B) Other polymethine fluorophores which form J-aggregates include IR-140 (**6.1**), FD-1080 (**6.2**), benzimidazole carbocyanine (**5.3**-**5.5**) and thiazole based (**5.6**-**5.7**). C) Current work within this chapter includes altering steric bulk at the 4' position (R_3, red), polarizability at the 7 position (R_2, green) and charge based on the N substituent (R_1, blue)

6.3. Results and Discussion

6.3.1. 4' Linker Modification[1]

Currently, commercially available heptamethine fluorophores have been mainly investigated for J-aggregate properties. Variants of IR-140 (Figure 6.1B, **6.6**-**6.7**) with different 4' substituents have suggested that steric bulk at this position correlates with aggregate architecture, similar to the previously reported *meso*-alkyl variants of thiacarbocyanine trimethine dyes.[17] The difference between a phenyl (**6.6**) and diphenylamino (**6.7**) at the 4' position can change the slip stack from 4-5 Å to 7-10 Å, respectively. This difference in slip stack results in a bright state closer to the band edge for **6.7**, though no emission was detected for either of these aggregates. However, the structural comparison is inconclusive due to the major differences between **6.6** and **6.7**. Thus, we started our studies by exploring small structural changes to the thiacarbocyanine heptamethine scaffold.

We utilized **6.6** and added increasing steric bulk to the 4' phenyl position (Scheme 6.1, **6.8**-**6.13**). Of note, the molecules explored herein, differ from the previously explored **6.6** which has a butyl sulfonate off the nitrogen. Rather, derivatives **6.8**-**6.13** contain a propyl sulfonate. Thus, to ensure a true comparison, **6.9** was synthesized to model **6.6**. A modular synthesis was developed in which a Suzuki coupling could be utilized to attach the appropriate boronic acid (**6.14**-**6.18**) to linker **6.19** to yield **6.20**-**6.24**. Addition of sodium acetate and 3-(5-chloro-2-methylbenzo[d]thiazol-3-ium-3-yl)propane-1-sulfonate (**6.25**) with the appropriate linker (**6.20**-**6.24**) gave dyes **6.8**-**6.13**. The diphenylphenyl 4' substituted dye (**6.13**) had low stability on silica gel and could be not further purified. Thus, all aggregation data for **6.13** utilized crude samples.

[1] Aggregation was done in collaboration with Austin Bailey.

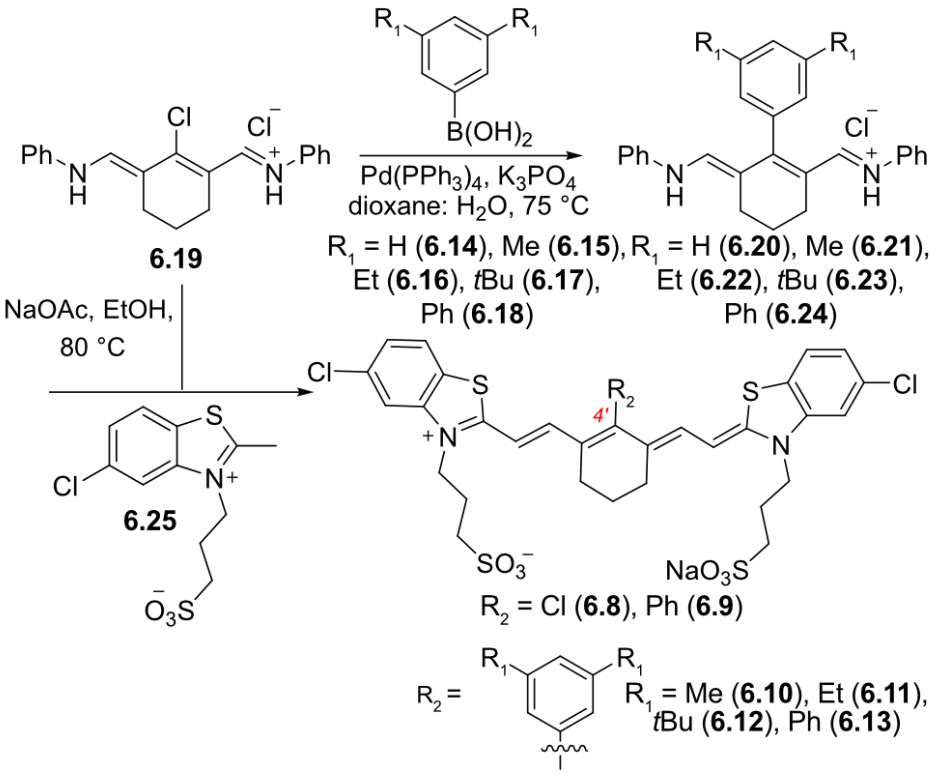

Scheme 6.1. Synthesis of varying steric bulk thiazole cyanines (**6.8**-**13**) starting from linker **6.19** by coupling of boronic acids (**6.14**-**6.18)** to yield modular linkers (**6.20**-**6.24**). More detailed synthetic procedures and yields can be found in the supporting info.

Next, we began to explore monomer photophysical properties. The 4'phenyl substituted thiazole cyanines (Table 1, **6.9**-**6.13**) showed no change to λ_{max} and slight variation in Φ_F (5.1 – 6.7%). Notably, as steric bulk increased the ε also decreased going from ~10^5 to ~10^4 M^{-1} cm^{-1}. Overall, the substituents off the phenyl ring appear to be too far away from the chromophore to play a major role in changing λ_{max}. The 4'Cl substituted version (Figure 6.2A, **6.8**) showed $\lambda_{max,abs}$ of 828 nm and $\lambda_{max,em}$ of 834 nm, a red-shift from **6.9**-**6.13**. The ε and Φ_F were found to be significantly lower with a ε of 15,000 M^{-1} cm^{-1} and Φ_F of 0.57%. The electron donating properties of the Cl contribute to an expected red-shift ~30 nm, but a surprising decrease in both ε and Φ_F.

The lowered solubility and stability of **6.8** in EtOH could contribute to these diminished photophysical properties.

Table 6.1. Photophysical properties of thiazole cyanines (**6.8**-**6.13**) in EtOH.

Compound	R	$\lambda_{max,\ abs}$ (nm)	$\lambda_{max,em}$(nm)	Φ_F (%)	ε (x 10^5 M^{-1} cm^{-1})
6.8	Cl	828	834	0.57 ± 0.01	0.15 ± 0.01
6.9	Ph	798	813	5.2 ± 0.2	1.1 ± 0.1
6.10	3,5-diMePh	798	814	6.6 ± 0.4	2.0 ± 0.1
6.11	3,5-diEtPh	798	812	5.1 ± 0.2	0.25 ± 0.02
6.12	3,5-ditBuPh	798	813	6.7 ± 0.6	0.63 ± 0.06
6.13	3,5-diPhPh	798	813	5.9 ± 0.6	N/A

Aggregates were formed by dissolving samples of monomeric dye in MeOH, 0.9% NaCl solution was added and then the sample was shaken vigorously for 10 sec. The percent methanol in each trial was 10, 30, 50 or 70%. The 4'Cl substituted fluorophore (**6.8**) showed no signs of J-aggregation but did form blue-shifted H-aggregate peaks (Figure 6.2B, $\lambda_{max\ abs}$ = 717 nm) with increasing amount of salt solution (Figure 6.2B, blue to black). Exchanging the Cl for a phenyl substituent (**6.9**) showed a sharp J-aggregate peak at 1008 nm in 10 % MeOH (Figure 6.2C, black). Upon increasing the percentage of MeOH, H-aggregates at 700 nm (Figure 6.2C, green and blue) were preferentially formed. Additional steric bulk where R = Me (methyl, **6.10**) showed two distinct J-aggregate peaks depending on the percentage of methanol used (Figure 6.2D, 10 % MeOH, black, 1028 nm and 30% MeOH, red, $\lambda_{max\ abs}$ = 1000 nm). Extension of the steric bulk to R = *t*Bu (*tert*-butyl), (**6.12**) showed three J-aggregate peaks. At 10% MeOH (Figure 6.2E, black) $\lambda_{max\ abs}$ of aggregate was at 973 nm, increasing the percent of MeOH blue-shifted $\lambda_{max,abs}$ to 958 nm (50% MeOH, Fig 6.2e, green). Interestingly, there was also no H-aggregation observed even at 70% MeOH. The bulkiest substituent R = Ph (phenyl, Figure 6.2F, **6.13**) showed predominately

H-aggregate formation in most percentages of MeOH (Figure 6.2F). Unfortunately, we currently do not have data from a thorough screen of R = Et (ethyl, **6.11**). However, a sample of aggregate formulated at 10% MeOH was made with a $\lambda_{max,abs}$ at 988 nm (Figure 6.2G, green)

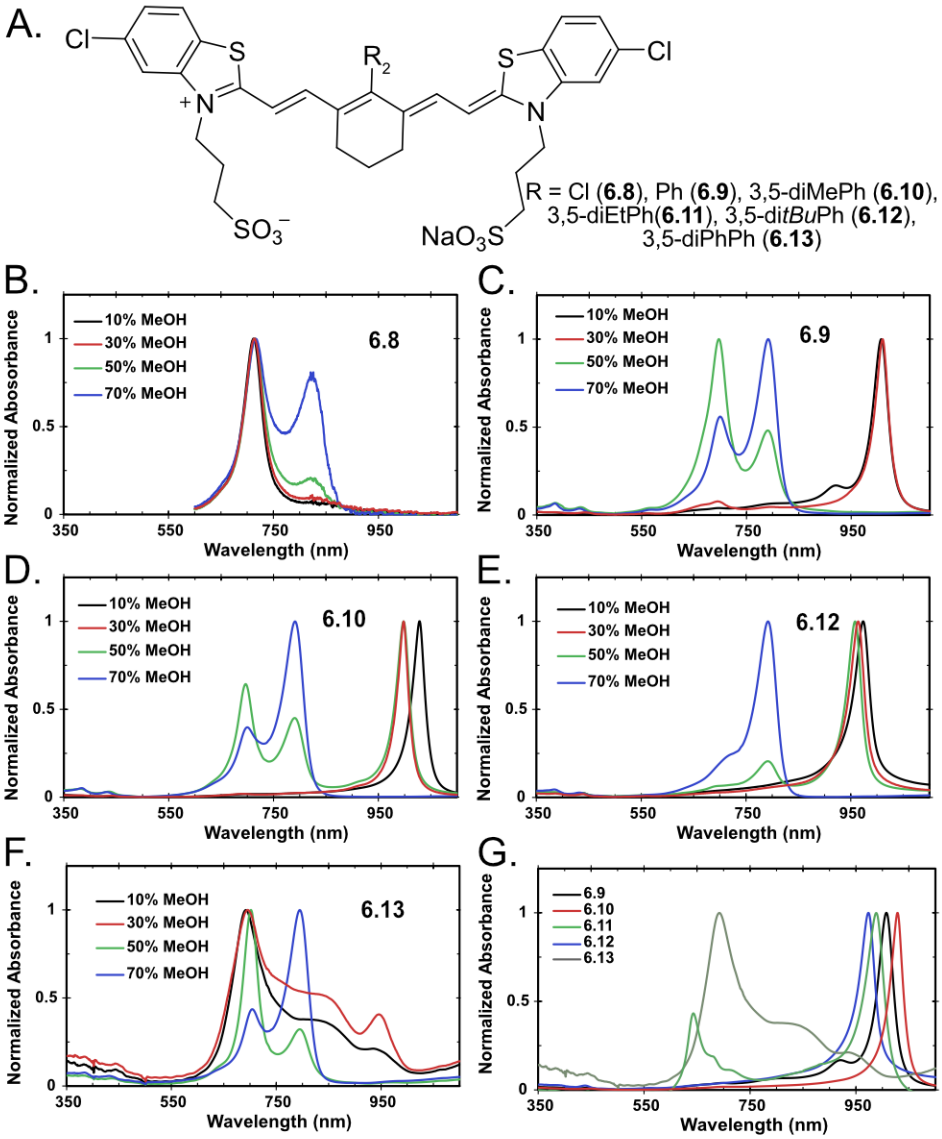

Figure 6.2. A) Structures of thiazole cyanine fluorophores (**6.8**-**6.13**) with varying steric bulk. B-F) Normalized absorbance screens of changing bulk at 4' position with varying amounts of MeOH (10%, black ; 30%, red; 50%, green; 70%, blue) and 0.9% NaCl solution at 0.2 mM concentration of fluorophore (**6.8**-**6.10, 6.12**-**6.13**). G) Normalized absorbance of **6.8**-**6.13** in 10% MeOH and 0.9 NaCl solution at 0.2 mM.

Comparing the J-aggregates at 10% MeOH (Figure 6.2G) showed a significant change in λ_{max} depending on the steric bulk of the substituent. Interestingly, the J-aggregates of the methyl substituted fluorophore (**6.10**) showed the most red-shifted λ_{max} followed by the hydrogen (**6.9)**, ethyl (**6.11)**, and *tert*-butyl (**6.12)**. The $\lambda_{max,abs}$ ranges from 973 nm to 1028 nm, suggestive that changing the steric bulk at the 4' position invokes a major change in the aggregate assembly (Figure 6.3A). These studies show that the 4' position appears to be crucial to J-aggregate formation of heptamethine fluorophores, and that larger steric bulk helps promote favorable slip-stack assembly. However, there is a limit to bulk tolerated in J-aggregation formation as **6.13** primarily forms H-aggregates. Overall, exchange of the Cl substituent (**6.8)** for a phenyl derivative (**6.9**-**6.11**), appeared to generally promote J-aggregation. Further insight into the packing morphology could provide an understanding of why **6.13** does not form orderly slip-stacked assemblies in comparison to **6.9**-**6.12**.

Commonly, SWIR fluorophores show low Φ_F due to the energy-gap law in which the overlap of wave functions at longer wavelengths allows for increased nonradiative transitions. Despite the enhanced photophysical properties of J-aggregates from monomeric fluorophores, it can still be difficult to obtain emissive materials as showcased by the lack of emission reported for **6.6** and **6.7**. Excitation of aggregates (**6.9**-**6.12**) at 885 nm showed weak emission with small Stoke shifts (Figure 6.3A). Upon absorption matching, integrated intensity of emission appears to show that aggregates of **6.12** are the most emissive (Figure 6.3B), whereas **6.11** is the least fluorescent, however further studies and quantitative Φ_F are needed to support these data.

A.

Compound	R	$\lambda_{max,\ abs}$ (nm)	$\lambda_{max,em}$(nm)
6.8	Cl	-	-
6.9	Ph	1007	1030
6.10	3,5-diMePh	1028	1030
6.11	3,5-diEtPh	988	1018
6.12	3,5-ditBuPh	973	975
6.13	3,5-diPhPh	-	-

B.

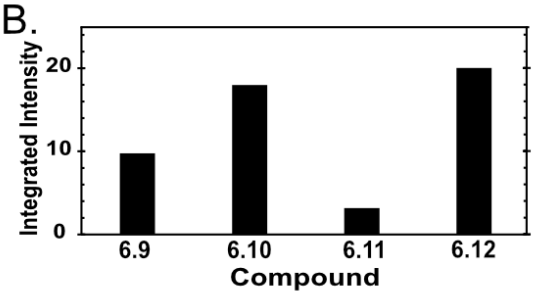

Figure 6.3. A) Table of λ_{max} of **6.8**-**6.13** aggregates in 10% MeOH and 90% NaCl (0.9%) solution at 0.2 mM in a 3 mm cuvette. B) Integrated intensity of fluorescence for **6.9**-**6.12** aggregates upon excitation at 885 nm.

Interestingly, these studies also showed that increasing steric bulk afforded more robust J-aggregates, evident by the J-aggregate peaks present at 50% MeOH for both **6.10** and **6.12**. Of note, is the absence of any H-aggregation within trials of **6.12** showing that the bulk of the *tert*-butyl substituent prevents face-to-face stacking of monomeric fluorophores. As H-aggregation diminishes advantageous photophysical properties at high concentrations of fluorophore, the prevention of H-aggregates is crucial for applications requiring high concentrations of dye. Thus, we envision that the sterically bulky *tert*-butyl substituted linker could also be useful for preventing H-aggregation in other fluorophore scaffolds.

These studies show that changing the substituent at the 4' position of heptamethine dyes can play an important role in aggregate formation by favoring slip stacked J-aggregates while also changing λ_{max}. Though the monomer showed no changes in $\lambda_{max\ abs}$ for the series of phenyl substituted dyes (**6.9**-**6.13)**, aggregates showed a significant change in $\lambda_{max\ abs}$ spanning about ~50

nm, which could be attributed to differences in packing formation. Further studies to understand the arrangement of J-aggregates through CyroEM, temperature dependence and complete photophysical characterization are currently underway. As the methyl substituent off the phenyl appeared to give the most red-shifted aggregate, this linker was utilized for the remaining thiazole cyanine fluorophores explored from here on.

6.3.2. Heterocycle Modification

We were pleasantly surprised that such a small structural change could provide such drastic changes in aggregate properties, thus we wanted to further explore other structural modification. Aggregates are formed by favorable van der waals interactions, thus polarizability of the fluorophore could be crucial to promoting J-aggregation. Larger more polarizable atoms readily participate in these interactions and could play a major role in the assembly of J-aggregates. Due to the modular synthesis, heterocycle modification, specifically halogenation of the 7 position of the thiazole heterocycle could be readily explored to modulate polarizability. As a control, a non-substituted thiazole heterocycle was also synthesized. To start, commercially available 2-methylthiazoles with either a chlorine, bromine or hydrogen at the 7 position were purchased and reacted with 1,3-propane sultone to yield heterocycles (**6.25**-**6.27**). Upon reaction of these heterocycles with linker **6.21** in sodium acetate and ethanol, dyes (**6.10, 6.28**-**6.29**) could be obtained (Scheme 6.2).

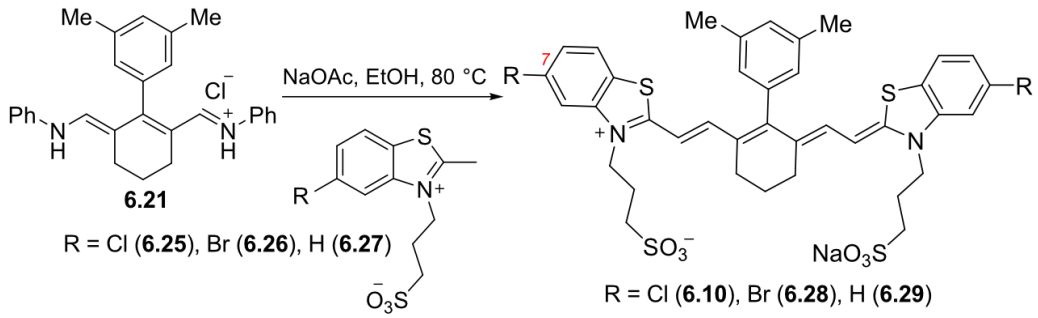

Scheme 6.2. Synthesis of varying halogenated thiazole cyanine dyes (**6.10, 6.28-6.29**) by reaction of linker **6.21** with heterocycles **6.25-6.27**.

Photophysical properties of the monomer (Table 6.2, **6.10, 6.28-6.29**) in EtOH showed a similar λ_{max} for the brominated (**6.28**) and chlorinated version (**6.10**) and a slight blue-shift for the non-substituted version (**6.29)**. The ε was within the range of typical polymethine dyes at 124,000 to 200,000 M^{-1} cm^{-1} and Φ_F between 6.6 – 7.6%.[5] Ultimately, no major differences in photophysical properties were observed upon changing the substituent at the 7 position of the thiazole heterocycle.

Table 6.2. Photophysical properties of thiazole heptamethine dyes with different substituents at the 7-position (**6.10, 6.28-6.29**) in EtOH.

Compound	R	$\lambda_{max,\ abs}$ (nm)	$\lambda_{max,em}$(nm)	Φ_F (%)	ε (x 10^5 M^{-1} cm^{-1})
6.10	Cl	798	814	6.6 ± 0.4	2.0 ± 0.1
6.28	Br	798	814	5.7 ± 0.6	1.24 ± 0.05
6.29	H	791	806	7.6 ± 0.6	1.3 ± 0.1

For these fluorophores, aggregation was performed focusing on 10% MeOH as it showed the best J-aggregation properties in the previous screens (Figure 6.4). In comparison to the Cl-substituted thiazole cyanine **6.10** which exhibits a sharp J-aggregate at 1028 nm, the bromine variant **6.28** showed a broader, blue-shifted peak at 980 nm (Figure 6.4, black). In contrast, the unsubstituted version (**6.29,** green) showed a sharp H-aggregate peak at 669 nm, a blue-shift from

the monomer of 122 nm, along with a small J-aggregate peak at 979 nm. Though preliminary data, these results suggest that halogenation at the 7 position could be crucial to forming orderly J-aggregates in thiazole cyanine dyes. The lack of substituent in **6.29** seems to favor H-aggregation, though this peak is uncharacteristically sharp and narrow. Whereas, the broader absorption spectra of **6.28** suggests a more disordered packing arrangement than **6.10** suggestive that the bromine effects aggregate distribution. Due to the unusual absorption spectra of these aggregates, we were interested in exploring their emission. Upon exciting aggregates of **6.28**-**6.29** at 885 nm, we found that the **6.28** aggregates showed little emission (Figure 6.5) whereas **6.10** was the most emissive of the series. Surprisingly, the small J-aggregate peak observed for **6.29** was also emissive though approximately two-fold less than **6.10**.

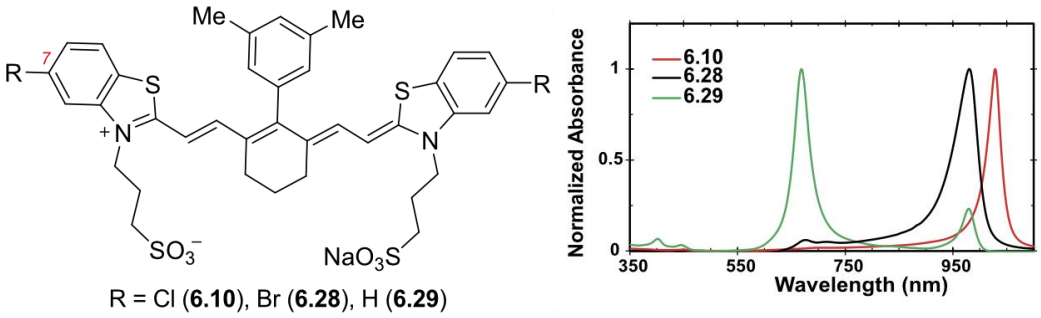

Figure 6.4. Normalized absorbance screens of changing the substituent at the 7 position with 10% MeOH and 0.9% NaCl solution at 0.2 mM concentration of fluorophore (**6.10, 6.28**-**6.29**).

A.

Compound	R	$\lambda_{max,\ abs}$ (nm)	$\lambda_{max,em}$(nm)
6.10	Cl	1028	1030
6.28	Br	980	-
6.29	H	979	977

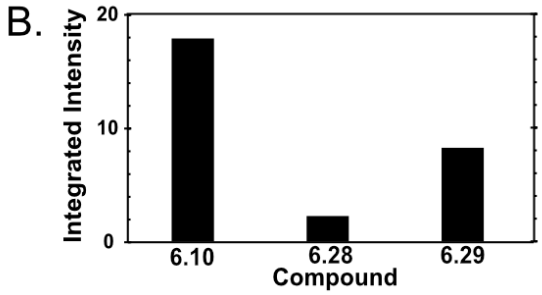

Figure 6.5. A) Photophysical properties of aggregates (**6.10**, **6.28**-**6.29**) in 10% MeOH and 90% NaCl (0.9%) solution at 0.2mM in a 3 mm cuvette. B) Integrated intensity of fluorescence for **6.10, 6.28**-**6.29** upon excitation at 885 nm.

Halogenation of benzimidazole carbocyanine dyes and its effect on aggregation has been previously explored.[15] These studies showed no change in $\lambda_{max\ abs}$ and minimal change in spectral width. The molecular packing of **6.3** was unchanged however the diameter of self-assembled nanotubes formed from these monomers varied from 18.1 ± 0.02 nm (Br) to 13.1 ± 0.02 nm (Cl). A fluorinated version was also synthesized but showed poor aggregation assembly, which was hypothesized to be due to a lack of halogen bond formation. To confirm whether halogen bond is generally important to aggregation formation, a fluorinated version of thiazole heptamethine dye should be synthesized. Though a non-substituted benzimidazole carbocyanine was not reported, our data suggests that a lack of substituent at this position could lead to preferential face to face stacking arrangements. More systematic studies of aggregation conditions should be conducted to better understand the different aggregate formations, along with complete photophysical characterization. Additional halogenation at the 6 position, similar to what is seen on benzimidazole carbocyanine dyes could be another viable route to increase polarizability and

develop more robust aggregates. Exchanging the sulfur heteroatom for an oxygen or selenium is another method to investigate the role of polarizability for promoting J-aggregates. Ultimately, we believe that polarizability of the heterocycle could be a viable route to developing J-aggregate formations. Despite the limited data thus far, it appears that substituents at the 7 position, especially halogenation could be crucial for aggregation packing parameters and the uncharacteristically sharp H-aggregate of **6.29** is of considerable interest.

6.3.3. N-substituent Modification

Thus far we have found that structural modifications effect $\lambda_{max,abs}$ of aggregate formations, and have only briefly touched upon emission. One of the major advantages of J-aggregates is the enhanced brightness of these materials, though emissive SWIR J-aggregates have rarely been reported. For example, **6.6** and **6.7** were shown to have no emission despite the structural similarities to IR-140 (**6.1**). Structurally, IR-140 has an ethyl substituent off the nitrogen within the thiazole heterocycle, in contrast to **6.7** which contains a butyl sulfonate moiety. Yet, IR-140 shows considerable emission in the aggregate state, whereas **6.7** aggregates have been previously reported to show no fluorescence. Intrigued by this observation, we sought to explore whether substituents off the nitrogen could play a role in the emissive state of aggregates. To do this, we applied a similar synthesis that combined heterocycles (**6.25, 6.30**-**6.36**) with linker **6.21** in ethanol with sodium acetate to provide dyes **6.10, 6.37**-**6.43** (Scheme 6.3).

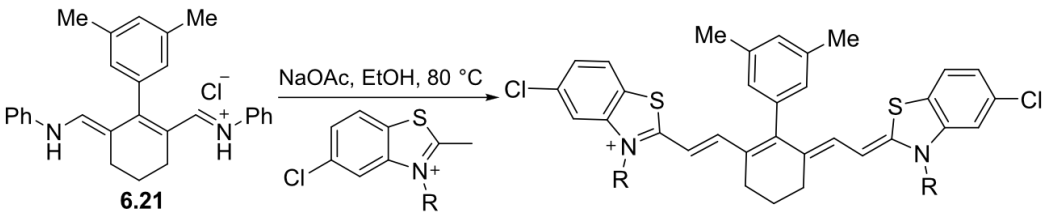

Scheme 6.3. Synthesis of varying N-substituted thiazole cyanine dyes (**6.10, 6.37**-**6.43**) by reaction of linker **6.21** with heterocycles **6.25, 6.30**-**6.36**.

The photophysical properties of the monomer were obtained in EtOH and displayed little variation in $\lambda_{max\ abs}$ ranging from 789-798 nm and $\lambda_{max\ em}$ ranging from 806-818 nm (Table 6.3). These results suggest that the substituent at the nitrogen position contributes very little to the effective conjugation of the chromophore. The other photophysical properties were within a similar range with ε ranging from 110,000-244,000 M^{-1} cm^{-1} and Φ_F from 6.2% - 8.6% (Table 6.3). Overall, the substituent at the nitrogen played little role in the photophysical properties of these monomers.

Table 6.3. Photophysical properties of *N*-substituted variants **6.10, 6.36**-**6.43** in EtOH.

Compound	R	$\lambda_{max,\ abs}$ (nm)	$\lambda_{max,em}$(nm)	Φ_F (%)	ε (x 10^5 M^{-1} cm^{-1})
6.37	Me	789	806	7.0 ± 0.4	1.98 ± 0.01
6.38	Et	791	806	8.6 ± 0.4	2.03 ± 0.07
6.39	Bu	793	810	6.6 ± 0.7	1.44 ± 0.03
6.40	Bn	798	810	7.4 ± 0.4	2.07 ± 0.06
6.10	$(CH_2)_3SO_3^-$	797	814	6.6 ± 0.4	2.0 ± 0.1
6.41	$(CH_2)_4SO_3^-$	796	812	6.5 ± 0.6	1.19 ± 0.03
6.42	$(CH_2)_3COO^-$	794	818	6.7 ± 0.4	1.1 ± 0.1
6.43	$(CH_2)_3OH$	795	817	6.2 ± 0.6	2.44 ± 0.1

For clarity only the 10% MeOH aggregates are represented in Figure 6.6 as they represent the sharpest and most uniform J-aggregates obtained. Substituents that were more hydrophobic (R = Me, Et, Bu and Bn, **6.37**-**6.40**) also resulted in cationic monomers. The smaller alkyl chains, R = Me (Figure 6.6A, methyl, **6.37**, black) and Et (Figure 6.6A, ethyl, **6.38**, red) showed the narrowest and sharpest aggregates at 1032 nm and 1011 nm, respectively. Furthermore, **6.38** aggregates showed a slight shoulder peak around ~912 nm. Larger alkyl chains like R = Bu (Figure 6.6A, butyl, **6.39**, green) showed a broader less defined aggregate peak at 999 nm, and R = Bn (Figure 6.6A, benzyl, **6.40**, blue) showed the least defined aggregate. More hydrophilic and anionic charged monomers with either sulfonates or carboxylates gave defined narrow aggregates as shown in Figure 6.6B. Of note is that the three-methylene spacer (**6.10**, black) and four methylene spacer (**6.41**, red) with a sulfonate group, showed slight changes in aggregate properties with $\lambda_{max,\ abs}$ at 990 nm and 998 nm, respectively. When the nitrogen was substituted with a propyl carboxylate (**6.42**, green), we observed interesting spectral results with a shoulder at 927 nm and a narrow peak at 1008 nm. This uncharacteristic shoulder was present regardless of percentage of MeOH. A more polar but still cationic substituent with a three-methylene spacer and alcohol (**6.43**, blue) showed a sharp aggregate peak at 1006 nm, comparable to the anionic variants (**6.10, 6.41**-**6.42**).

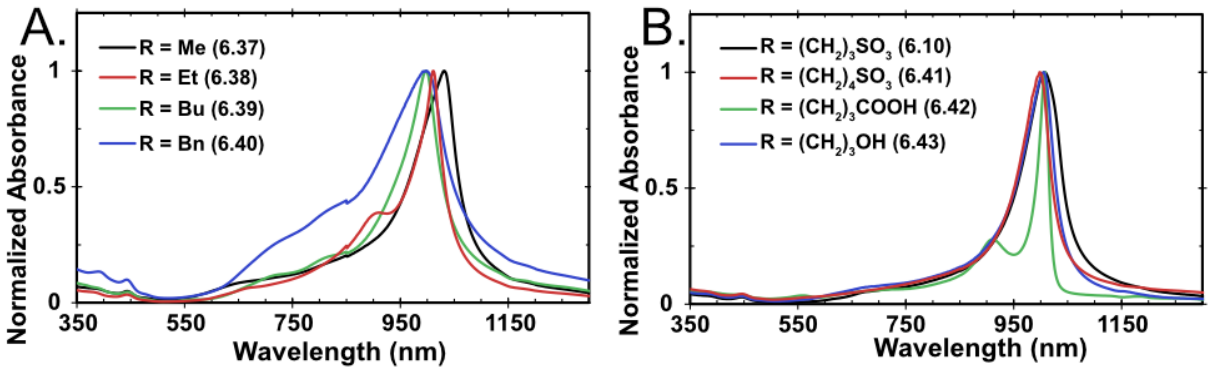

Figure 6.6 A/B) Normalized absorbance screens of changing the nitrogen substituent in 10% MeOH and 0.9% NaCl solution at 0.2 mM concentration of fluorophore (**6.10, 6.37**-**6.43**) at time = 0 min.

Generally, the cationic monomers (**6.37**-**6.40**) showed broader less defined absorption spectra when aggregated, suggestive that their morphology is less ordered. On the other hand, the anionic monomers (**6.10, 6.41**-**6.42**) had sharper aggregate peaks, though **6.43** which is a cationic monomer with a more polar substituent showed similarly narrow absorption spectra. These studies suggest that aggregation morphology could be dictated by polarity of *N*-substituent which would support previous studies performed by Daehne and coworkers on benzimidazole carbocyanine dyes.[14] Time studies to test stability was also performed over the course of seven days and interestingly for R = Me, Et, $(CH_2)_3SO_3^-$, and $(CH_2)_4SO_3^-$ (**6.37**-**6.38, 6.10, 6.41**), a second blue-shifted shoulder appeared within 24 h. The cationic monomers (**6.37**-**6.40, 6.43**) were significantly less stable showing broadened less defined absorption spectra at 48 h. Whereas, the anionic versions (**6.10**, **6.41**-**6.42)** were more stable showing little change in absorption even after seven days. This suggests that aggregation morphology and stability is impacted by both the charge and polarity of the *N*-substituent.

We were initially interested in changing the *N*-substituent because we hypothesized it would have an impact on the emission properties due to the differences observed for IR-140 (**6.1**)

and **6.7**. Upon exciting aggregate formations of **6.10, 6.37**-**6.43** at 885 nm, we found that there was emission regardless of the substituent (Table 6.4). This contradicted our initial hypothesis and prompted us to investigate the emission of commercially available Cy7-Ph (**6.6**) further. We found that J-aggregates of **6.6** do show emission, although it is extremely low which is possibly one of the reasons that it was undetected beforehand. Due to the difficulties of reabsorption of the excitation wavelength with small Stokes shift, we are unable at present to obtain quantitative Φ_F of these aggregates. Thus, we performed an absorption matching study instead to gain a sense of the difference in emission intensity between **6.10, 6.37**-**6.43** (Figure 6.7A). Comparing integrated fluorescence intensity, **6.10** shows the highest fluorescence whereas **6.41** was the least emissive (Figure 6.7B). Surprisingly, the only difference between these two is one methylene spacer but there is nearly a 3-fold difference in fluorescence intensity. Compounds **6.42**-**6.43** also showed slightly higher intensity fluorescence, whereas more hydrophobic cationic monomers (**6.37**-**6.43**) showed similar fluorescence intensity. The weak emission of the butyl sulfonate (**6.41**) correlates with the low emission of previously studied **6.6.** However, a quantifiable comparison is still needed to better understand how the morphology could impact emissive properties.

Table 6.4. Photophysical properties of **6.10, 6.37**-**6.43** aggregates in 10% MeOH and 0.9% NaCl solution.

Compound	R	$\lambda_{max,\ abs1}$ (nm)	$\lambda_{max,\ abs2}$ (nm)	$\lambda_{max,em}$(nm)
6.37	Me	1032	901	1013
6.38	Et	1011	909	998
6.39	Bu	999	-	983
6.40	Bn	999	-	989
6.10	$(CH_2)_3SO_3^-$	990	930	998
6.41	$(CH_2)_4SO_3^-$	998	935	990
6.42	$(CH_2)_3COO^-$	1008	927	997
6.43	$(CH_2)_3OH$	1006	928	1000

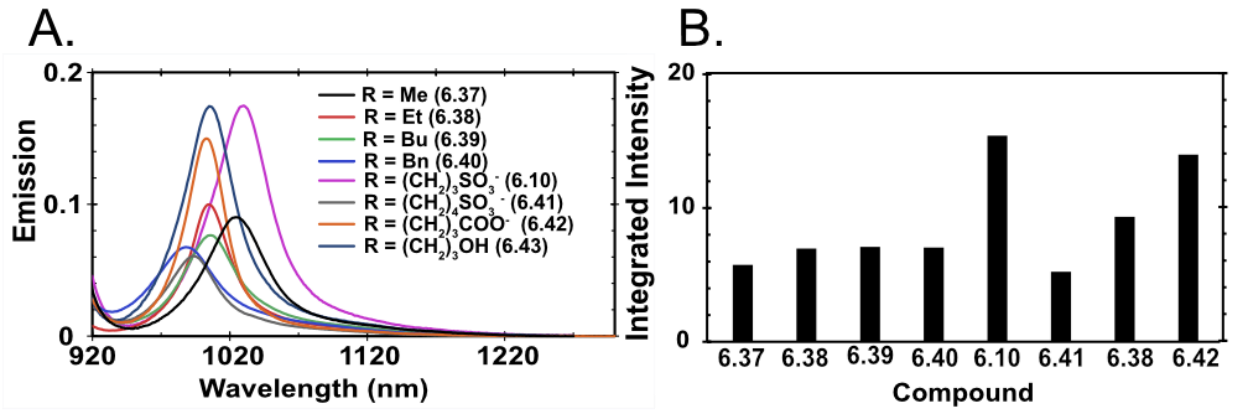

Figure 6.7. A) Emission of thiazole cyanines aggregates (**6.10**, **6.37-43**) in 10% MeOH and 0.9% NaCl solution and B) integrated fluorescence intensity.

J- aggregates are known to have small Stokes shift, but some of these aggregates showed what appeared to be anti-Stokes shift (Table 6.4), a phenomenon when an emitted photon has more energy than the absorbed photon.[18] This phenomenon is rarely seen in J-aggregates thus it is possible that there are multiple aggregate species and the most blue-shifted formulation is the only emissive species. The presence of secondary shoulder peaks contributes to this theory of multiple aggregate species present. Furthermore, excitation closer to the aggregate peak (~1000 nm) showed no emission, suggestive that the emissive aggregate species is more blue-shifted. Further exploration into the possibility of multiple aggregate species need to be explored through modification of environmental conditions.

Despite the lack of photophysical changes within the monomers, the aggregates showed considerable differences. We hypothesize that aggregate morphology depends on the nitrogen substituent and could account for the observed differences in photophysical properties. To confirm this theory, complete photophysical characterization of the aggregates is needed as well as, CyroEM of aggregate assemblies. By making small structural changes to the *N*-substituent, we have found that charge of monomer effects stability of aggregate and polarity influences the

spectral width. We also observed drastic differences in emissive properties depending on *N*-substituent thus we aim to further understand how these modifications alter photophysical properties. By making small and subtle systematic structural modifications to the monomer we have found that large differences are possible upon J-aggregate formation. A better understanding of these structural modifications could lend itself to aggregating other heptamethine fluorophores, particularly SWIR fluorophores such as flavylium heptamethine dyes.

6.3.4. Aggregating Flav7 and other scaffolds[2]

The previous work presented herein has explored a thiazole cyanine scaffold that is already well precedented to aggregate. However, these J-aggregates show $\lambda_{max,\ abs}$ = ~1000 nm and ultimately, we aim to aggregate dyes that have monomeric absorption in the SWIR such that their aggregates can absorb beyond 1300 nm. From the insight we have gathered from our studies on the thiazole heptamethine dyes, we found that the *tert*-butyl phenyl linker **6.12** provided the most robust J-aggregates with formations observable even at 50% MeOH. Thus, we hypothesized that addition of this steric bulk to a SWIR polymethine monomer could readily provide J-aggregate assemblies above 1300 nm. We focused on Flav7, a dye that has already been explored extensively within our lab as a SWIR imaging agent. By reacting flavylium heterocycle (**6.44**) with linker **6.12** in the presence of sodium acetate in n:butanol:toluene we could prepare **6.45** (Scheme 6.4).

[2] Cesar Garcia and Austin Bailey contributed to the synthesis and aggregation studies within this section.

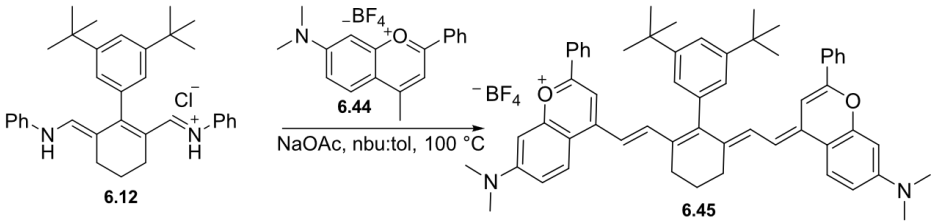

Scheme 6.4. Synthesis of Flav7 derivative (**6.45**) by addition of *tert*-butyl phenyl linker (**6.12**) and flavylium heterocycle (**6.44**).

To attempt aggregation of **6.45**, we utilized EtOH instead of MeOH due to previous studies showing low stability of Flav7 in MeOH, and deuterated water (D_2O) in order to avoid absorption of water in the SWIR. Studies with 30% and 50% EtOH show a strong absorption peak at 1354 nm and a secondary peak at 1300 nm (Figure 6.8, black). In contrast, Flav7 with a Cl at the 4' position (**6.46**, green) showed no aggregation at all, and when the 4' was reduced to a H (**6.47,** red) only broad absorption or bluer aggregates (~1150 nm) were formed (Figure 6.8). Sadly, aggregates of **6.45** showed no emission but we were still delighted that this small structural change based upon our previous studies proved fruitful in developing an aggregate beyond 1300 nm. To this end, ongoing work on other fluorophore scaffolds utilizing a similar strategy is currently underway to test the generalizability of this method. By aggregating SWIR monomeric fluorophores, we aim to achieve aggregates even beyond 1350 nm.

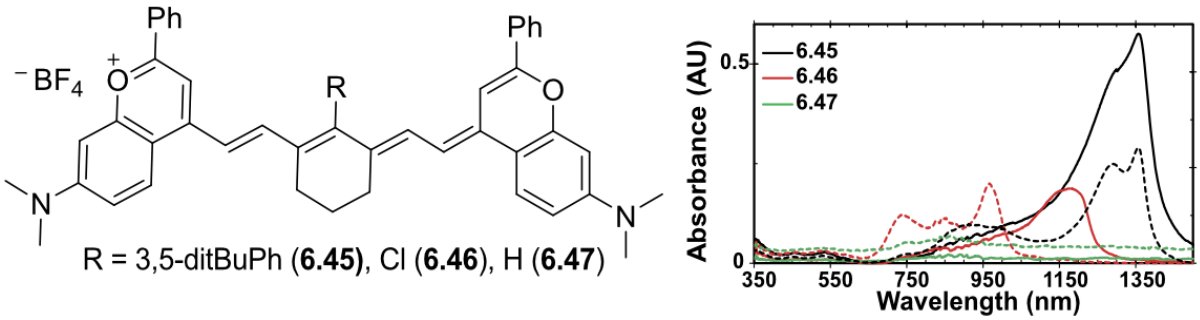

Figure 6.8. Absorbance spectra of Flav7 derivatives (**6.45-6.47**) aggregates in 30% (solid) and 50% (dotted) MeOH with D_2O.

6.4 Conclusion

Once a simple physical phenomenon that was of intellectual interest, J-aggregation of fluorophores has become a fruitful endeavor for biomedical and material applications. The ability for J-aggregates to provide absorption in the SWIR is beyond what is achievable with monomeric fluorophores alone. However, an understanding of structural modifications and its effect on aggregation properties has been scarce in the literature, especially for developing materials for the SWIR. Herein, we showed through different modifications with a well-known thiazole cyanine scaffold that aggregation morphology could be altered. We opted to explore substituent changes at the 4' position of the linker, 7 position of the heterocycle and off the nitrogen within the benzothiazole. Slip stack angles modified by changing the steric bulk at the 4' position (**6.9**-**6.12**) help promote J-aggregation but too large of a substituent (**6.13**) has an opposite effect and promotes H-aggregate formation. Halogenation of the heterocycle (**6.10, 6.28**), particularly at the 7 position, appears to be essential for inducing J-aggregation whereas lack of a halogen (**6.29**) increases H-aggregation. Finally, we explored nitrogen substituent of the fluorophore and found that cationic versions (**6.37**-**6.40, 6.43**) were less stable over time in comparison to the anionic monomers (**6.10**, **6.41**-**6.42**). More hydrophobic substituents show broader absorption spectra which suggests less ordered J-aggregate formation. There was also a large variation in fluorescence intensity, surprisingly the brightest and dimmest aggregates having only one methylene spacer difference (**6.10** vs **6.41**). The fundamental understanding, we gained from these studies allowed us to aggregate a SWIR monomeric fluorophore by simply adding a 4'phenyl linker with 3,5 *tert*-butyl substituent (**6.45**) that could absorb at 1350 nm. We have shown through systematic exploration

of structural modifications could lead to new avenues for fine-tuning aggregation properties, which could then be applied to the development of SWIR materials for absorption beyond 1300 nm.

6.5 Experimental Procedures

6.5.1 Photophysical Procedures

Absorbance spectra were collected on a JASCO V-770 UV-Visible/NIR spectrophotometer and JASCO V-730 UV-Visible/NIR with a 2000 nm/min scan rate after blanking with the appropriate solvent. Photoluminescence spectra were obtained on a Horiba Instruments PTI QuantaMaster Series fluorometer. Quartz cuvettes (1 cm) were used for absorbance and photoluminescence measurements. Absorption coefficients in ethanol were calculated with serial dilutions with Hamilton syringes and volumetric glassware. Error was taken as the standard deviation of three independent replicates.

Fluorescence quantum yield measurements:

The fluorescence quantum yield (Φ_f) of a molecule or material is defined as followed:

$$\Phi_F = \frac{P_E}{P_A} \qquad (1)$$

where PE, PA are the number of photons emitted and absorbed respectively. To determine absolute quantum yield, the number of photons absorbed and emitted are measured independently. The quantum yield measurements are performed with a Horiba petite integrating sphere. The spectra are measured with a Horiba fluorimeter PTI QM-400. The sample optical density is kept below 0.1 to avoid fluorescence quenching and reabsorption effects. The experimental setup is adjusted and tested on standard dyes. Emission spectra are baseline corrected. The emission background for the blank is normalized by the transmission ratio of the blank and sample at the excitation line.

6.5.2 Synthetic Procedures

Materials: Chemical reagents were purchased from Acros Organics, Alfa Aesar, Fisher Scientific, Sigma-Aldrich, or TCI and used without purification unless noted otherwise. Anhydrous and deoxygenated solvents (THF) were dispensed from a Grubb's-type Phoenix Solvent Drying System. Oxygen was removed by three consecutive freeze–pump–thaw cycles in air-free glassware directly before use.

Instrumentation: Thin layer chromatography was performed using Silica Gel 60 F_{254} (EMD Millipore) plates. Flash chromatography was executed with technical grade silica gel with 60 Å pores and 40 – 63 μm mesh particle size (Sorbtech Technologies). Solvent was removed under reduced pressure with a Büchi Rotovapor with a Welch self-cleaning dry vacuum pump and further dried with a Welch DuoSeal pump. Nuclear magnetic resonance (^{1}H-NMR, ^{13}C-NMR) spectra were taken on Bruker Avance 300, AV-400, AV-500 and processed with MestReNova or TopSpin software. All ^{1}H NMR and ^{13}C NMR peaks are reported in ppm in reference to their respective solvent signals. High resolution mass spectra (electrospray ionization (ESI)) were obtained on a Thermo Scientific Q Exactive™ Plus Hybrid Quadrupole-Orbitrap™ M with Dionex UltiMate 3000 RSLCnano System

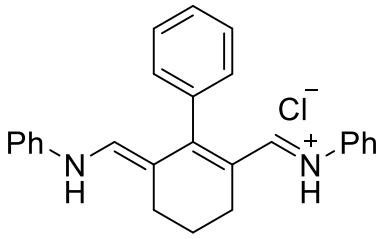

***N*-((E)-((E)-6-((phenylamino)methylene)-3,4,5,6-tetrahydro-[1,1'-biphenyl]-2-yl)methylene)benzenaminium chloride (6.20)**

N-((E)-((E)-2-chloro-3-((phenylamino)methylene)cyclohex-1-en-1-yl)methylene)benzenaminium chloride **6.19** (500 mg, 1.40 mmol, 1.0 eq), phenyl boronic acid **6.14** (340 mg, 2.8 mmol, 2.0 eq), tetrakis(triphenylphosphine)palladium(0) (160 mg, 0.1 mmol, 0.1 eq) and tripotassium phosphate K_3PO_4 (890 mg, 4.1 mmol, 3.0 eq) was dissolved in a 13:2 mixture of 1,4-dioxane: water (12.4 mL: 2.6 mL). The solution was freeze-pump-thawed x3 then heated at 75 °C for 5h. Upon cooling to room temperature, the reaction was quenched via addition of $NaHCO_3$ solution then extracted into DCM (3 x 20 mL), dried over Na_2SO_4, filtered and evaporated to give a dark red oil. The crude product was purified via silica gel chromatography with hexanes: ethyl acetate (9:1) to afford ***N*-((E)-((E)-6-((phenylamino)methylene)-3,4,5,6-tetrahydro-[1,1'-biphenyl]-2-yl)methylene)benzenaminium chloride** as a dark red oil. Acidification with 2M HCl (2 mL) gave the salt version as a dark red solid (304 mg, 0.76 mmol, 54 %) and was utilized crude in the next reaction.

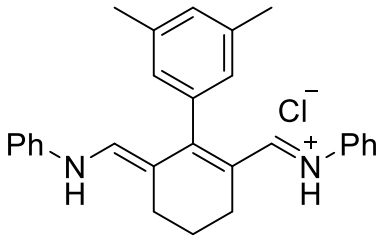

***N*-((E)-((E)-3',5'-dimethyl-6-((phenylamino)methylene)-3,4,5,6-tetrahydro-[1,1'-biphenyl]-2-yl)methylene)benzenaminium chloride (6.21)**

N-((E)-((E)-2-chloro-3-((phenylamino)methylene)cyclohex-1-en-1-yl)methylene)benzenaminium chloride **6.19** (500 mg, 1.4 mmol, 1.0 eq), 3,5-dimethylphenyl boronic acid **6.15** (420 mg, 2.8 mmol, 2.0 eq), tetrakis(triphenylphosphine)palladium(0) (160 mg, 0.14 mmol, 0.1 eq) and tripotassium phosphate K_3PO_4 (890 mg, 4.2 mmol, 3.0 eq) was dissolved

in a 13:2 mixture of 1,4-dioxane: water (12.5 mL: 2.5 mL). The solution was freeze-pump-thawed x3 then heated at 75 °C for 5 h. Upon cooling to room temperature, the reaction was quenched via addition of $NaHCO_3$ solution then extracted into DCM (3 x 20 mL), dried over Na_2SO_4, filtered and evaporated to give a dark red oil. The crude product was purified via silica gel chromatography with hexanes: ethyl acetate (9:1) to afford ***N*-((E)-((E)-3',5'-dimethyl-6-((phenylamino)methylene)-3,4,5,6-tetrahydro-[1,1'-biphenyl]-2-yl)methylene)benzenaminium chloride** as a dark red oil. Acidification with 2M HCl (2 mL) gave the salt version as a dark red solid (300 mg, 0.70 mol, 50 %) and was utilized crude in the next reaction.

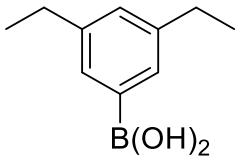

(3,5-diethylphenyl)boronic acid (6.16)

Bromo-3,5-diethyl benzene (0.200 mL, 1.0 mmol, 1 eq) was dissolved in THF (3.0 mL, anhydrous) and cooled to -78 °C. A solution of *n*-BuLi (1.2M in hexanes, 1.5 mL, 2.0 mmol, 1.7 eq) was added dropwise slowly turning solution yellow then left to stir for 30 min. To a second flask was combined triisopropyl borate (0.530 mL, 2.3 mmol, 2 eq) in THF (17.25 mL, anhydrous) then added slowly to first flask at -78 °C. After 2h of stirring at -78 °C, reaction was quenched with H_2O and acidified with 3M H_2SO_4 (2 mL) until pH = 2. This created a biphasic solution and the top phase was removed and extracted into EtOAc (3 x 10 mL), dried over Na_2SO_4, filtered and evaporated to give pure **(3,5-diethylphenyl)boronic acid** as a white solid (160 mg, 0.8 mmol,

78%) ^{1}H-NMR matched literature.[13] ^{1}H NMR (400 MHz, DMSO-d_6) δ 7.86 (s, 2H), 7.40 (d, J = 1.8 Hz, 2H), 7.02 (t, J = 1.8 Hz, 1H), 2.52 (q, J = 7.6 Hz, 4H), 1.21 – 1.06 (m, 6H).

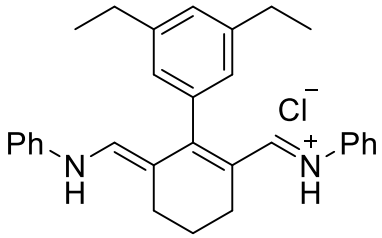

***N*-((E)-((E)-3',5'-diethyl-6-((phenylamino)methylene)-3,4,5,6-tetrahydro-[1,1'-biphenyl]-2-yl)methylene)benzenaminium chloride (6.22)**

N-((E)-((E)-2-chloro-3-((phenylamino)methylene)cyclohex-1-en-1-yl)methylene)benzenaminium chloride **6.19** (250 mg, 0.7 mmol, 1.0 eq), 3,5-diethyllphenyl boronic acid **6.16** (250 mg, 1.4 mmol, 2.0 eq), tetrakis(triphenylphosphine)palladium(0) (80 mg, 0.10 mmol, 0.1 eq) and tripotassium phosphate K_3PO_4 (460 mg, 2.1 mmol, 3.0 eq) was dissolved in a 13:2 mixture of 1,4-dioxane: water (6.3 mL: 1.2 mL). The solution was freeze-pump-thawed x3 then heated at 75 °C for 5 h. Upon cooling to room temperature, the reaction was quenched via addition of $NaHCO_3$ solution then extracted into DCM (3 x 10 mL), dried over Na_2SO_4, filtered and evaporated to give a dark red oil. The crude product was purified via silica gel chromatography with hexanes: ethyl acetate (9:1) to afford ***N*-((E)-((E)-3',5'-diethyl-6-((phenylamino)methylene)-3,4,5,6-tetrahydro-[1,1'-biphenyl]-2-yl)methylene)benzenaminium chloride** as a dark red oil. Acidification with 2M HCl (2 mL) gave the salt version as a dark red solid (90 mg, 0.20 mmol, 27 %) and was utilized crude in the next reaction.

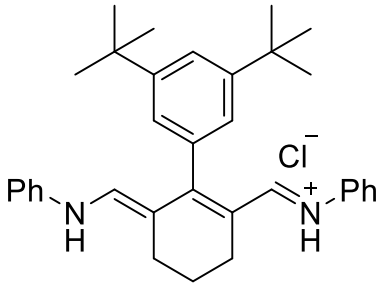

***N*-((E)-((E)-3',5'-di-tert-butyl-6-((phenylamino)methylene)-3,4,5,6-tetrahydro-[1,1'-biphenyl]-2-yl)methylene)benzenaminium chloride (6.23)**

N-((E)-((E)-2-chloro-3-((phenylamino)methylene)cyclohex-1-en-1-yl)methylene)benzenaminium chloride **6.19** (150 mg, 0.4 mmol, 1.0 eq), 3,5-ditertbutyllphenyl boronic acid **6.17** (200 mg, 0.8 mmol, 2.0 eq), tetrakis(triphenylphosphine)palladium(0) (50 mg, 0.04 mmol, 0.1 eq) and tripotassium phosphate K_3PO_4 (270 mg, 1.3 mmol, 3.0 eq) was dissolved in a 13:2 mixture of 1,4-dioxane: water (3.75 mL: 0.75 mL). The solution was freeze-pump-thawed x3 then heated at 100 °C for 5 h. Upon cooling to room temperature, the reaction was quenched via addition of $NaHCO_3$ solution then extracted into DCM (3 x 20 mL), dried over Na_2SO_4, filtered and evaporated to give a dark red oil. The crude product was purified via silica gel chromatography with hexanes: ethyl acetate (9:1) to afford pure ***N*-((E)-((E)-3',5'-di-tert-butyl-6-((phenylamino)methylene)-3,4,5,6-tetrahydro-[1,1'-biphenyl]-2-yl)methylene)benzenaminium chloride** as a dark red oil. Acidification with 2M HCl (2 mL) gave the salt version as a dark red solid (78 mg, 0.15 mmol, 38 %). ^{1}H NMR (400 MHz, Methanol-d_4) δ 7.66 (t, J = 1.7 Hz, 1H), 7.56 – 7.44 (m, 2H), 7.44 – 7.36 (m, 1H), 7.33 – 7.21 (m, 6H), 7.21 – 7.11 (m, 2H), 7.02 (dd, J = 8.6, 1.1 Hz, 3H), 2.72 (t, J = 6.1 Hz, 4H), 2.07 (t, J = 6.1 Hz, 2H), 1.35 (s, 18H).

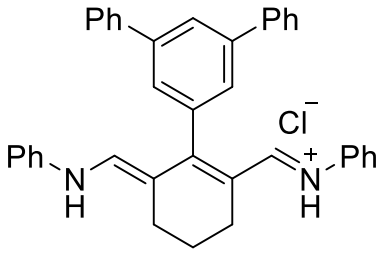

***N*-((E)-((E)-5'-phenyl-6-((phenylamino)methylene)-3,4,5,6-tetrahydro-[1,1':3',1''-terphenyl]-2-yl)methylene)benzenaminium chloride (6.24)**

N-((E)-((E)-2-chloro-3-((phenylamino)methylene)cyclohex-1-en-1-yl)methylene)benzenaminium chloride **6.19** (150 mg, 0.41 mmol mmol, 1.0 eq), 3,5-ditertbutyllphenyl boronic acid **6.18** (230 mg, 0.84 mmol, 2.0 eq), tetrakis(triphenylphosphine)palladium(0) (50 mg, 0.04 mmol, 0.1 eq) and tripotassium phosphate K_3PO_4 (260 mg, 1.20 mmol, 3.0 eq) was dissolved in a 13:2 mixture of 1,4-dioxane: water (3.7 mL: 0.7 mL). The solution was freeze-pump-thawed x3 then heated at 75 °C for 5h. Upon cooling to room temperature, the reaction was quenched via addition of $NaHCO_3$ solution then extracted into DCM (3 x 10 mL), dried over Na_2SO_4, filtered and evaporated to give a dark red oil. The crude product was purified via silica gel chromatography with hexanes: ethyl acetate (9:1) to afford ***N*-((E)-((E)-5'-phenyl-6-((phenylamino)methylene)-3,4,5,6-tetrahydro-[1,1':3',1''-terphenyl]-2-yl)methylene)benzenaminium chloride** as a dark red oil which was pushed forward crude.

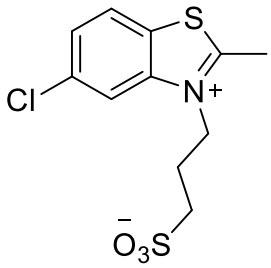

3-(5-chloro-2-methylbenzo[d]thiazol-3-ium-3-yl)propane-1-sulfonate (6.25)

5-chloro-2-methylbenzothiazole (500 mg, 2.7 mmol, 1 eq) and 1,3-propane sultone (403 mg, 3.3 mmol, 1.2 eq) are heated at 120 °C for 3 h. Precipitate formed during the reaction is refluxed slightly in MeOH in order to dissolve solid than excess Et_2O is added to precipitate solid. The product was collected via vacuum filtration and washed with excess Et_2O to afford pure **3-(5-chloro-2-methylbenzo[d]thiazol-3-ium-3-yl)propane-1-sulfonate** as a fluffy white solid (300 mg, 1.0 mmol, 36%). ^{1}H NMR (400 MHz, Deuterium Oxide) δ 8.15 (d, *J* = 1.9 Hz, 1H), 8.00 (d, *J* = 8.8 Hz, 1H), 7.63 (dd, *J* = 8.8, 1.8 Hz, 1H), 4.72 (dd, *J* = 6.6, 4.1 Hz, 1H), 3.06 (s, 2H), 2.99 (t, *J* = 7.1 Hz, 2H), 2.30 – 2.15 (m, 2H). ^{13}C NMR (101 MHz, Deuterium Oxide) δ 178.2 , 141.7 , 135.9 , 129.10 , 127.6 , 124.9 , 116.4 , 47.9 , 47.3 , 23.0 , 16.4 .

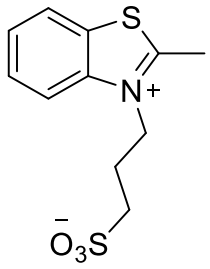

3-(2-methylbenzo[d]thiazol-3-ium-3-yl)propane-1-sulfonate (6.26)

2-methylbenzothiazole (0.430 mL , 3.40 mmol, 1 eq) and 1,3-propane sultone (490 mg, 4.0 mmol, 1.2 eq) were heated at 120 °C for 3h. Yellow fluffy precipitate formed during the reaction is refluxed slightly in MeOH in order to dissolve solid than excess Et_2O is added to precipitate solid. Product is collected via vacuum filtration and washed with excess Et_2O to afford pure **3-(2-methylbenzo[d]thiazol-3-ium-3-yl)propane-1-sulfonate** as a fluffy white solid (220 mg, 0.81 mmol, 24%). ^{1}H NMR (400 MHz, Methanol-d_4) δ 8.37 (d, *J* = 8.6 Hz, 1H), 8.26 (dt, *J* = 8.1, 0.8

Hz, 1H), 7.90 (ddd, *J* = 8.5, 7.3, 1.2 Hz, 1H), 7.79 (ddd, *J* = 8.2, 7.3, 1.0 Hz, 1H), 5.04 – 4.91 (m, 2H), 3.07 – 2.92 (m, 2H), 2.42 – 2.27 (m, 2H). ^{1}H NMR matched literature.[21]

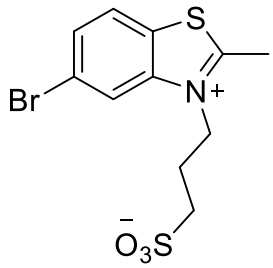

3-(5-bromo-2-methylbenzo[d]thiazol-3-ium-3-yl)propane-1-sulfonate (6.27)

5-bromo-2-methylbenzothiazole (500 mg, 2.20 mmol, 1 eq) and 1,3-propane sultone (320 mg, 2.6 mmol, 1.2 eq) are heated at 120 °C for 6h. Brown solid precipitate formed during the reaction is refluxed slightly in MeOH in order to dissolve solid than excess Et_2O is added to precipitate solid. Product is collected via vacuum filtration and washed with excess Et_2O to afford pure **3-(5-bromo-2-methylbenzo[d]thiazol-3-ium-3-yl)propane-1-sulfonate** as a beige solid (156 mg, , 0.44 mmol, 20%). ^{1}H NMR (400 MHz, Methanol-d_4) δ 8.67 (d, *J* = 1.7 Hz, 1H), 8.22 – 8.02 (m, 1H), 7.93 (dd, *J* = 8.7, 1.7 Hz, 1H), 4.97 – 4.90 (m, 1H), 3.22 (s, 2H), 3.05 – 2.96 (m, 2H), 2.41 – 2.22 (m, 2H). ^{13}C NMR (101 MHz, Deuterium Oxide) δ 177.9, 141.8, 131.8, 124.9, 119.3, 68.7, 47.9, 47.3, 24.2, 23.0, 16.4.

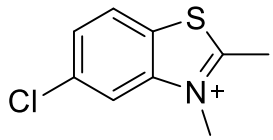

5-chloro-2,3-dimethylbenzo[d]thiazol-3-ium iodide (6.30)

5-chloro-2-methylbenzothiazole (500 mg, 2.7 mmol, 1 eq) and methyl iodide (0.850 mL, 14 mmol, 5 eq) was left at r.t for 4 d. Precipitate formed during the reaction is refluxed slightly in MeOH in

order to dissolve solid than excess Et_2O is added to precipitate solid. Product is collected via vacuum filtration and washed with excess Et_2O to afford pure **5-chloro-2,3-dimethylbenzo[d]thiazol-3-ium iodide** as a fluffy white solid (97 mg, 0.3 mmol, 11%). ^{1}H NMR (400 MHz, DMSO-d_6) δ 8.50 (d, J = 1.9 Hz, 1H), 8.43 (d, J = 8.8 Hz, 1H), 7.84 (dd, J = 8.8, 1.9 Hz, 1H), 4.15 (s, 3H), 3.15 (s, 3H). ^{13}C NMR (101 MHz, DMSO-d_6) δ 179.6, 143.0, 134.7, 128.8, 128.1, 126.5, 117.4, 37.0, 17.9.

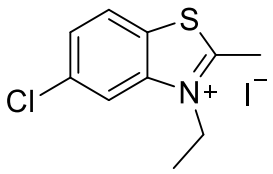

5-chloro-3-ethyl-2-methylbenzo[d]thiazol-3-ium iodide (6.31)

5-chloro-2-methylbenzothiazole (500 mg , 2.5 mmol, 1 eq) and iodoethane (2.1 g, 14 mmol, 5 eq) was heated at 110 °C for 24 h. Yellow solid precipitate formed during the reaction is refluxed slightly in MeOH in order to dissolve solid than excess Et_2O is added to precipitate solid. Product is collected via vacuum filtration and washed with excess Et_2O to afford pure **5-chloro-3-ethyl-2-methylbenzo[d]thiazol-3-ium iodide** as a pale orange solid (429 mg, 1.3 mmol, 47%). ^{1}H NMR (400 MHz, DMSO-d_6) δ 8.56 (d, J = 1.9 Hz, 1H), 8.45 (d, J = 8.8 Hz, 1H), 7.84 (dd, J = 8.8, 1.9 Hz, 1H), 4.72 (q, J = 7.3 Hz, 2H), 3.19 (s, 3H), 1.40 (t, J = 7.3 Hz, 3H). ^{13}C NMR (101 MHz, DMSO-d_6) δ 179.3, 141.9, 134.9, 128.8, 128.6, 126.7, 117.1, 45.4, 17.5, 13.7.

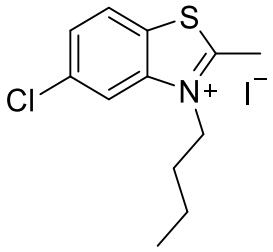

3-butyl-5-chloro-2-methylbenzo[d]thiazol-3-ium iodide (6.32)

5-chloro-2-methylbenzothiazole (500 mg, 2.7 mmol, 1 eq) and iodobutane (1.5 mL, 14 mmol, 5 eq) was left at r.t for 4 d. Green/blue precipitate formed during the reaction is refluxed slightly in MeOH in order to dissolve solid than excess Et_2O is added to precipitate solid. Product is collected via vacuum filtration and washed with excess Et_2O to afford pure **3-butyl-5-chloro-2-methylbenzo[d]thiazol-3-ium iodide** as a pale green solid (190 mg, 0.50 mmol, 19%). ^{1}H NMR (400 MHz, DMSO-d_6) δ 8.56 (d, J = 1.9 Hz, 1H), 8.44 (d, J = 8.8 Hz, 1H), 7.84 (dd, J = 8.7, 1.9 Hz, 1H), 4.72 – 4.58 (m, 2H), 3.19 (s, 3H), 1.76 (tt, J = 9.6, 3.7 Hz, 2H), 1.46 – 1.35 (m, 2H), 0.90 (t, J = 7.3 Hz, 3H). ^{13}C NMR (101 MHz, DMSO-d_6) δ 179.4 , 142.3 , 135.0 , 128.9 , 128.5, 126.6, 117.3, 49.7, 30.2, 19.7, 17.6, 14.0.

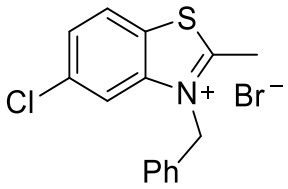

3-benzyl-5-chloro-2-methylbenzo[d]thiazol-3-ium bromide (6.33)

5-chloro-2-methylbenzothiazole (500 mg, 2.5 mmol, 1 eq) and benzyl bromide (0.600 mL , 5.0 mmol, 2 eq) was heated at 120 °C for 5h. Dark yellow solid precipitate formed during the reaction is refluxed slightly in MeOH in order to dissolve solid than excess Et_2O is added to precipitate solid. Product is collected via vacuum filtration and washed with excess Et_2O to afford pure **3-**

benzyl-5-chloro-2-methylbenzo[d]thiazol-3-ium bromide as a pale yellow solid (509 mg, 1.4 mmol, 57%). ^{1}H NMR (400 MHz, DMSO-d_6) δ 8.54 (d, J = 8.8 Hz, 1H), 8.43 (d, J = 1.9 Hz, 1H), 7.84 (dd, J = 8.8, 1.9 Hz, 1H), 7.39 – 7.32 (m, 3H), 7.28 (dd, J = 7.9, 1.7 Hz, 2H), 6.08 (s, 2H), 3.22 (s, 3H). ^{13}C NMR (101 MHz, DMSO-d_6) δ 180.8, 142.4, 135.0, 133.0, 129.6, 129.0 (d, J = 3.5 Hz), 128.8, 127.5, 127.0, 117.4, 52.4, 18.1.

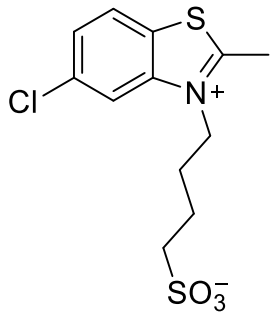

4-(5-chloro-2-methylbenzo[d]thiazol-3-ium-3-yl)butane-1-sulfonate (6.34)

5-chloro-2-methylbenzothiazole (500 mg, 3 mmol, 1 eq) and 1,4-butane sultone (0.330 mL, 3.3 mmol, 1.2 eq) was c. Gray brown solid precipitate formed during the reaction is refluxed slightly in MeOH in order to dissolve solid than excess Et_2O is added to precipitate solid. Product is collected via vacuum filtration and washed with excess Et_2O to afford pure **3-benzyl-5-chloro-2-methylbenzo[d]thiazol-3-ium bromide** as a light gray solid (260 mg, 0.93 mmol, 31%). ^{1}H NMR (400 MHz, Deuterium Oxide) δ 8.12 (d, J = 1.8 Hz, 1H), 7.99 (d, J = 8.8 Hz, 1H), 7.61 (dd, J = 8.8, 1.8 Hz, 1H), 4.58 (t, J = 7.9 Hz, 2H), 3.05 (s, 3H), 2.84 (t, J = 7.5 Hz, 2H), 1.97 (p, J = 7.9 Hz, 2H), 1.80 (q, J = 7.6 Hz, 2H). ^{13}C NMR (101 MHz, Deuterium Oxide) δ 177.8, 141.7, 135.8, 129.0, 127.5, 124.8, 116.5, 49.9, 49.2, 26.2, 21.3, 16.5.

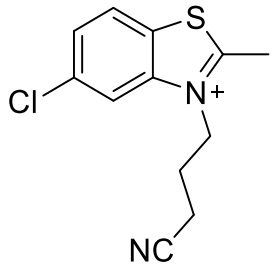

5-chloro-3-(3-cyanopropyl)-2-methylbenzo[d]thiazol-3-ium bromide (6.48)

5-chloro-2-methylbenzothiazole (100 mg, 0.5 mmol, 1 eq) and 4-bromobutyronitrile (0.110 mL, 1.10 mmol, 2 eq) was heated at 110 °C for 24h. Purple blue solid precipitate formed during the reaction is refluxed slightly in MeOH in order to dissolve solid than excess Et_2O is added to precipitate solid. Product is collected via vacuum filtration and washed with excess Et_2O to afford **4-(5-chloro-2-methylbenzo[d]thiazol-3-ium-3-yl)butanoate bromide** as a pale blue solid (125 mg, 0.4 mmol, 76%). ^{1}H NMR (400 MHz, DMSO-d_6) δ 8.61 (d, J = 1.9 Hz, 1H), 8.47 (d, J = 8.8 Hz, 1H), 7.84 (dd, J = 8.7, 1.9 Hz, 1H), 4.76 – 4.64 (m, 2H), 3.21 (s, 3H), 2.76 (dd, J = 8.1, 7.1 Hz, 2H), 2.22 – 2.09 (m, 2H). ^{13}C NMR (101 MHz, DMSO-d_6) δ 180.3, 142.3, 135.0, 128.9, 128.5, 126.7, 120.3, 117.1, 48.4, 24.0, 17.7, 14.2.

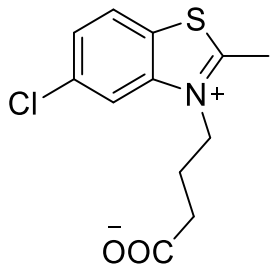

4-(5-chloro-2-methylbenzo[d]thiazol-3-ium-3-yl)butanoate (6.35)

4-bromobutyronitrile (300 mg, 0.90 mmol, 4 eq) was refluxed in 6M HCl (2 mL) in H_2O (2 mL) at 100 °C. The dark solution is washed with DCM (3 x 10mL) to remove dark coloration. H_2O was removed to give beige tan solid. The solid was dissolved in MeOH than excess Et_2O is added to

precipitate solid. The product was collected via vacuum filtration and washed with excess Et_2O to afford pure **4-(5-chloro-2-methylbenzo[d]thiazol-3-ium-3-yl)butanoate** as a pale tan solid (220 mg, 0.80 mmol, 98%). ^{1}H NMR (400 MHz, Methanol-d_4) δ 8.53 (d, J = 1.8 Hz, 1H), 8.28 (d, J = 8.8 Hz, 1H), 7.81 (dd, J = 8.8, 1.8 Hz, 1H), 4.81 – 4.69 (m, 2H), 3.21 (dt, J = 4.8, 2.4 Hz, 1H), 2.61 (dd, J = 6.9, 5.9 Hz, 2H), 2.24 – 2.11 (m, 2H). ^{13}C NMR (101 MHz, Methanol-d_4) δ 174.4, 142.2, 136.1, 128.9, 128.0, 125.2, 116.7, 48.8, 29.2, 22.8.

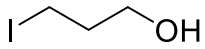

3-iodopropan-1-ol (6.49)

3-chloro-1-propanol (1.1 mL, 11 mmol, 1 eq) was dissolved in acetone (10 mL, 1M) and sodium iodide was added (8 g, 50 mmol, 5 eq) and refluxed for 24 h. The orange solution was concentrated down into an orange solid and then washed with Et_2O (100 mL) until all orange color was removed. The organic solution was washed with $NaHSO_3$ solution (3 x 20 mL) and brine (3 x 20 mL), dried over Na_2SO_4, filtered and concentrated to give **3-iodopropan-1-ol** as a clear pale yellow liquid. ^{1}H NMR matched literature.[22] ^{1}H NMR (400 MHz, Chloroform-d) δ 3.74 (t, J = 5.9 Hz, 1H), 3.30 (t, J = 6.7 Hz, 1H), 2.04 (tt, J = 6.7, 5.9 Hz, 1H).

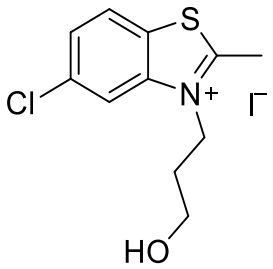

5-chloro-3-(3-hydroxypropyl)-2-methylbenzo[d]thiazol-3-ium iodide (6.36)

5-chloro-2-methylbenzothiazole (100 mg, 0.5 mmol, 1 eq) and 1,3-chloropropanol **5.16** (0.26 mL, 2.8 mmol , 5 eq) was heated at 110 °C for 5 h. The resulting brown tar was dissolved slightly in MeOH than excess Et_2O was added to precipitate the product as a yellow solid. The product was collected via vacuum filtration and washed with excess Et_2O to afford **4-(5-chloro-2-methylbenzo[d]thiazol-3-ium-3-yl)butanoate bromide** as a pale yellow solid (45 mg, 0.11 mmol, 23%). ^{1}H NMR (400 MHz, DMSO-d_6) δ 8.51 (d, *J* = 1.9 Hz, 1H), 8.44 (d, *J* = 8.8 Hz, 1H), 7.84 (dd, *J* = 8.8, 1.9 Hz, 1H), 4.78 – 4.64 (m, 2H), 4.24 (br s, 1H), 3.48 (t, *J* = 5.7 Hz, 2H), 3.19 (s, 3H), 2.04 – 1.87 (m, 2H). ^{13}C NMR (101 MHz, DMSO-d_6) δ 179.7, 142.3, 134.9, 128.8, 128.5, 126.6, 117.2, 57.8, 47.6, 30.5, 17.6.

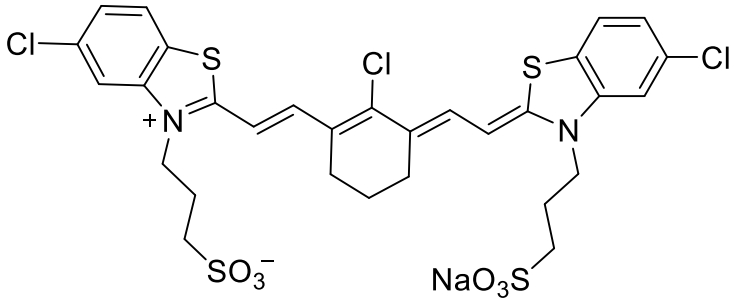

3-(5-chloro-2-((E)-2-((E)-2-chloro-3-((Z)-2-(5-chloro-3-(3-sulfonatopropyl)benzo[d]thiazol-2(3H)-ylidene)ethylidene)cyclohex-1-en-1-yl)vinyl)benzo[d]thiazol-3-ium-3-yl)propane-1-sulfonate (6.8)

3-(5-chloro-2-methylbenzo[d]thiazol-3-ium-3-yl)propane-1-sulfonate **6.25** (100 mg, 0.3 mmol, 1 eq), **6.19** (6 mg, 0.2 mmol, 0.5 eq), NaOAc (30 mg, 0.4 mmol, 1.2 eq) was dissolved in EtOH (6.6 mL, 0.05 M). The dark magenta solution was freeze-pump-thawed x3, then heated to 80 °C for 1h turning the solution green. The reaction was monitored by UV-Vis for the appearance of product (~800 nm) and loss of linker (~550 nm). The crude product was purified via silica gel chromatography with a gradient of 19:1 → 9:1 → 17:3 dichloromethane: methanol to afford **3-(5-**

chloro-2-((E)-2-((E)-2-chloro-3-((Z)-2-(5-chloro-3-(3-sulfonatopropyl)benzo[d]thiazol-2(3H)-ylidene)ethylidene)cyclohex-1-en-1-yl)vinyl)benzo[d]thiazol-3-ium-3-yl)propane-1-sulfonate as a shiny green brown solid (130 mg, 0.2 mmol, 58%). ^{1}H NMR (400 MHz, DMSO-d_6) δ 7.92 (s, 3H), 7.49 (d, *J* = 2.3 Hz, 1H), 7.37 – 7.29 (m, 3H), 6.85 (d, *J* = 8.7 Hz, 1H), 6.72 (d, *J* = 13.9 Hz, 2H), 4.50 (s, 4H), 2.76 (s, 4H), 2.55 (t, *J* = 6.5 Hz, 6H), 1.97 – 1.86 (m, 6H).

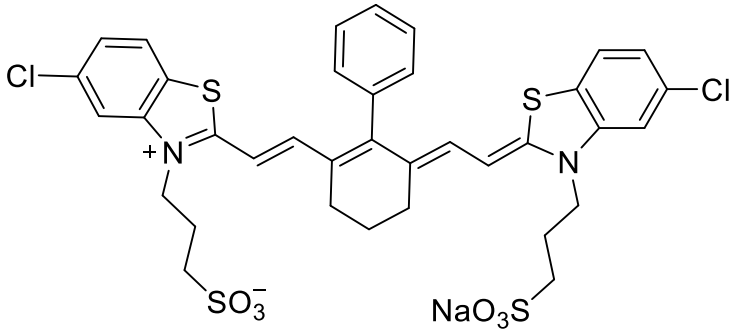

3-(5-chloro-2-((E)-2-((E)-6-((Z)-2-(5-chloro-3-(3-sulfonatopropyl)benzo[d]thiazol-2(3H)-ylidene)ethylidene)-3,4,5,6-tetrahydro-[1,1'-biphenyl]-2-yl)vinyl)benzo[d]thiazol-3-ium-3-yl)propane-1-sulfonate (6.9)

3-(5-chloro-2-methylbenzo[d]thiazol-3-ium-3-yl)propane-1-sulfonate **6.25** (100 mg, 0.33 mmol, 1 eq), **6.14** (65 mg, 0.16 mmol, 0.5 eq), NaOAc (32 mg, 0.40 mmol , 1.2 eq) was dissolved in EtOH (6.5 mL, 0.5 M). The dark magenta solution was freeze-pump-thawed x3, then heated to 80 °C for 1h turning the solution green. The reaction was monitored by UV-Vis for the appearance of product (~800 nm) and lost of linker (~550 nm). The crude product was purified via silica gel chromatography with a gradient of 19:1 → 9:1 → 17:3 →4:1 dichloromethane: methanol to afford pure product **3-(5-chloro-2-((E)-2-((E)-6-((Z)-2-(5-chloro-3-(3-sulfonatopropyl)benzo[d]thiazol-2(3H)-ylidene)ethylidene)-3,4,5,6-tetrahydro-[1,1'-**

biphenyl]-2-yl)vinyl)benzo[d]thiazol-3-ium-3-yl)propane-1-sulfonate as a shiny green brown solid (12 mg, 0.03 mmol, 9%). ^{1}H NMR (400 MHz, DMSO-d_6) δ 7.88 (d, *J* = 1.9 Hz, 2H), 7.82 (d, *J* = 8.5 Hz, 2H), 7.53 – 7.47 (m, 3H), 7.29 (dd, *J* = 8.5, 1.9 Hz, 2H), 7.24 (dd, *J* = 7.4, 2.0 Hz, 1H), 6.67 (d, *J* = 13.3 Hz, 2H), 6.58 (d, *J* = 13.4 Hz, 2H), 4.46 (t, *J* = 7.9 Hz, 4H), 2.64 (d, *J* = 7.6 Hz, 4H), 2.51 (t, *J* = 6.7 Hz, 4H), 1.93 (t, *J* = 7.4 Hz, 4H), 1.87 (t, *J* = 5.9 Hz, 2H).

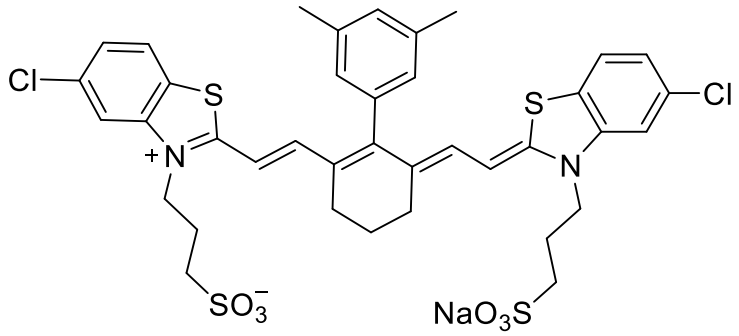

3-(5-chloro-2-((E)-2-((E)-6-((Z)-2-(5-chloro-3-(3-sulfonatopropyl)benzo[d]thiazol-2(3H)-ylidene)ethylidene)-3',5'-dimethyl-3,4,5,6-tetrahydro-[1,1'-biphenyl]-2-yl)vinyl)benzo[d]thiazol-3-ium-3-yl)propane-1-sulfonate (6.21)

3-(5-chloro-2-methylbenzo[d]thiazol-3-ium-3-yl)propane-1-sulfonate **6.25** (100 mg, 0.30 mmol, 1 eq), **6.15** (70 mg, 0.20 mmol, 0.5 eq), NaOAc (30 mg, 0.4 mmol, 3 eq) was dissolved in EtOH (6.6 mL, 0.5M). The dark magenta solution was freeze-pump-thawed x3, then heated to 80 °C for 1h turning the solution green.The reaction was monitored by UV-Vis for the appearance of product (~800 nm) and loss of linker (~550 nm). The crude product was purified via silica gel chromatography with a gradient of 19:1 → 9:1 → 17:3 dichloromethane: methanol to afford pure product **3-(5-chloro-2-((E)-2-((E)-6-((Z)-2-(5-chloro-3-(3-sulfonatopropyl)benzo[d]thiazol-2(3H)-ylidene)ethylidene)-3',5'-dimethyl-3,4,5,6-tetrahydro-[1,1'-biphenyl]-2-yl)vinyl)benzo[d]thiazol-3-ium-3-yl)propane-1-sulfonate** as a shiny green brown solid (45 mg,

0.10 mmol, 33%). ^{1}H NMR (400 MHz, DMSO-d_6) δ 7.88 (d, J = 1.9 Hz, 2H), 7.83 (d, J = 8.5 Hz, 2H), 7.30 (dd, J = 8.5, 1.9 Hz, 2H), 7.15 – 7.13 (m, 1H), 6.88 – 6.85 (m, 2H), 6.74 (d, J = 13.3 Hz, 2H), 6.57 (d, J = 13.4 Hz, 2H), 4.46 (t, J = 7.8 Hz, 4H), 2.63 (t, J = 6.2 Hz, 4H), 2.52 (d, J = 6.7 Hz, 3H), 2.33 (s, 6H), 1.94 (t, J = 7.4 Hz, 4H), 1.85 (t, J = 6.3 Hz, 1H).

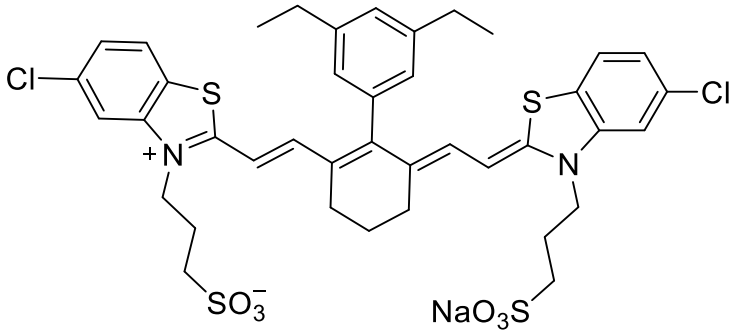

3-(5-chloro-2-((E)-2-((E)-6-((Z)-2-(5-chloro-3-(3-sulfonatopropyl)benzo[d]thiazol-2(3H)-ylidene)ethylidene)-3',5'-diethyl-3,4,5,6-tetrahydro-[1,1'-biphenyl]-2-yl)vinyl)benzo[d]thiazol-3-ium-3-yl)propane-1-sulfonate (6.22)

3-(5-chloro-2-methylbenzo[d]thiazol-3-ium-3-yl)propane-1-sulfonate **6.25** (30 mg, 0.10 mmol, 1 eq), **5.16** (20 mg, 0.04 mmol, 0.5 eq), NaOAc (9 mg, 0.10 mmol, 1.2 eq) was dissolved in EtOH (2.7 mL, 0.3M). The dark magenta solution was freeze-pump-thawed x3, then heated to 80 °C for 1h turning the solution green. The reaction was monitored by UV-Vis for the appearance of product (~800 nm) and loss of linker (~550 nm). The crude product was purified via silica gel chromatography with a gradient of 19:1 → 9:1 → 17:3 dichloromethane: methanol to afford pure product **3-(5-chloro-2-((E)-2-((E)-6-((Z)-2-(5-chloro-3-(3-sulfonatopropyl)benzo[d]thiazol-2(3H)-ylidene)ethylidene)-3',5'-diethyl-3,4,5,6-tetrahydro-[1,1'-biphenyl]-2-yl)vinyl)benzo[d]thiazol-3-ium-3-yl)propane-1-sulfonate** as a shiny green brown solid (10 mg, 0.01 mmol, 12%). ^{1}H NMR (400 MHz, DMSO-d_6) δ 7.88 (d, J = 1.9 Hz, 2H), 7.82 (d, J = 8.5 Hz,

2H), 7.29 (dd, *J* = 8.5, 1.9 Hz, 2H), 7.18 (s, 1H), 6.91 (s, 2H), 6.79 (s, 2H), 6.57 (d, *J* = 13.4 Hz, 2H), 4.46 (t, *J* = 7.8 Hz, 4H), 2.64 (d, *J* = 7.6 Hz, 8H), 2.53 – 2.49 (m, 4H), 1.94 (s, 4H), 1.86 (d, *J* = 5.9 Hz, 2H), 1.25 – 1.18 (m, 6H).

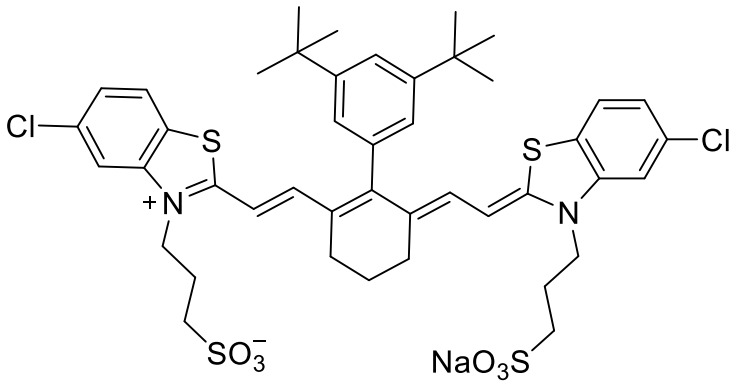

3-(5-chloro-2-((E)-2-((E)-3',5'-di-tert-butyl-6-((Z)-2-(5-chloro-3-(3-sulfonatopropyl)benzo[d]thiazol-2(3H)-ylidene)ethylidene)-3,4,5,6-tetrahydro-[1,1'-biphenyl]-2-yl)vinyl)benzo[d]thiazol-3-ium-3-yl)propane-1-sulfonate (6.23)

3-(5-chloro-2-methylbenzo[d]thiazol-3-ium-3-yl)propane-1-sulfonate **6.25** (12 mg, 0.04 mmol, 1 eq), **6.17** (10 mg, 0.02 mmol, 0.5 eq), NaOAc (4 mg, 0.05 mmol, 1.2 eq) was dissolved in EtOH (0.8 mL, 0.05M). The dark magenta solution was freeze-pump-thawed x3, then heated to 80 °C for 1h turning the solution green. The reaction was monitored by UV-Vis for the appearance of product (~800 nm) and loss of linker (~550 nm). The crude product was purified via silica gel chromatography with a gradient of 19:1 → 9:1 → 17:3 dichloromethane: methanol to afford pure product **3-(5-chloro-2-((E)-2-((E)-3',5'-di-tert-butyl-6-((Z)-2-(5-chloro-3-(3-sulfonatopropyl)benzo[d]thiazol-2(3H)-ylidene)ethylidene)-3,4,5,6-tetrahydro-[1,1'-biphenyl]-2-yl)vinyl)benzo[d]thiazol-3-ium-3-yl)propane-1-sulfonate** as a shiny green brown solid (10 mg, 0.02 mmol, 54 %). ^{1}H NMR (400 MHz, DMSO-d_6) δ 7.88 (d, *J* = 1.9 Hz, 2H), 7.82

(d, *J* = 8.5 Hz, 2H), 7.49 (t, *J* = 1.8 Hz, 1H), 7.29 (dd, *J* = 8.5, 1.9 Hz, 2H), 7.06 (d, *J* = 1.8 Hz, 2H), 6.78 (d, *J* = 13.2 Hz, 2H), 6.58 (d, *J* = 13.4 Hz, 2H), 4.46 (t, *J* = 7.8 Hz, 4H), 2.64 (d, *J* = 5.7 Hz, 4H), 2.52 (t, *J* = 6.6 Hz, 4H), 1.94 (t, *J* = 7.5 Hz, 4H), 1.87 (s, 2H), 1.33 (s, 18H).

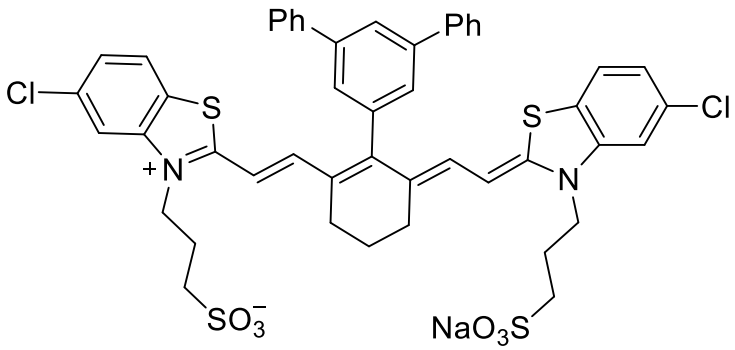

3-(5-chloro-2-((E)-2-((E)-6-((Z)-2-(5-chloro-3-(3-sulfonatopropyl)benzo[d]thiazol-2(3H)-ylidene)ethylidene)-5'-phenyl-3,4,5,6-tetrahydro-[1,1':3',1''-terphenyl]-2-yl)vinyl)benzo[d]thiazol-3-ium-3-yl)propane-1-sulfonate (6.24)

3-(5-chloro-2-methylbenzo[d]thiazol-3-ium-3-yl)propane-1-sulfonate **6.25** (10 mg, 0.04 mmol, 1 eq), **6.18** (10 mg, 0.02 mmol 0.5 eq), NaOAc (5 mg, 0.05 mmol, 1.2 eq) was dissolved in EtOH (0.8 mL, 0.05M). The dark magenta solution was freeze-pump-thawed x3, then heated to 80 °C for 1h turning the solution green. The reaction was monitored by UV-Vis for the appearance of product (~800 nm) and loss of linker (~550 nm). The crude product pushed through a silica gel column with a gradient of 19:1 → 9:1 → 17:3 dichloromethane: methanol to afford **3-(5-chloro-2-((E)-2-((E)-6-((Z)-2-(5-chloro-3-(3-sulfonatopropyl)benzo[d]thiazol-2(3H)-ylidene)ethylidene)-5'-phenyl-3,4,5,6-tetrahydro-[1,1':3',1''-terphenyl]-2-yl)vinyl)benzo[d]thiazol-3-ium-3-yl)propane-1-sulfonate** as a crude blue/green solid that was utilized as is for aggregation.

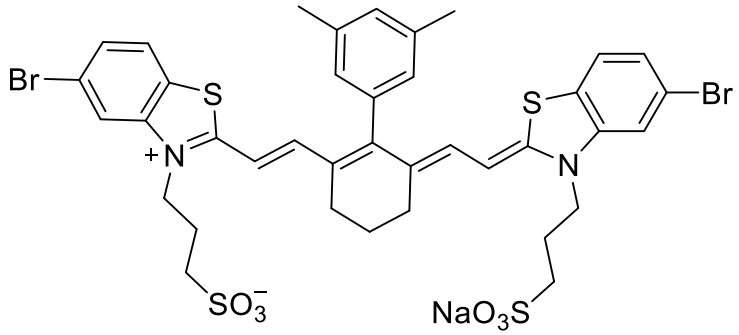

3-(5-bromo-2-((E)-2-((E)-6-((Z)-2-(5-bromo-3-(3-sulfonatopropyl)benzo[d]thiazol-2(3H)-ylidene)ethylidene)-3',5'-dimethyl-3,4,5,6-tetrahydro-[1,1'-biphenyl]-2-yl)vinyl)benzo[d]thiazol-3-ium-3-yl)propane-1-sulfonate (6.28)

3-(5-bromo-2-methylbenzo[d]thiazol-3-ium-3-yl)propane-1-sulfonate **6.26** (20 mg, 0.05 mmol, 1 eq), **5.21** (10 mg, 0.02 mmol, 0.5 eq), NaOAc (5 mg, 0.05 mmol, 1.2 eq) was dissolved in EtOH (1.0 mL, 0.05 M). The dark magenta solution was freeze-pump-thawed x3, then heated to 80 °C for 1h turning the solution green. The reaction was monitored by UV-Vis for the appearance of product (~800 nm) and loss of linker (~550 nm). The crude product was purified via silica gel chromatography with a gradient of 19:1 → 9:1 → 17:3 dichloromethane: methanol to afford pure product **3-(5-bromo-2-((E)-2-((E)-6-((Z)-2-(5-bromo-3-(3-sulfonatopropyl)benzo[d]thiazol-2(3H)-ylidene)ethylidene)-3',5'-dimethyl-3,4,5,6-tetrahydro-[1,1'-biphenyl]-2-yl)vinyl)benzo[d]thiazol-3-ium-3-yl)propane-1-sulfonate** as a shiny green brown solid (10 mg, 0.03 mmol, 54%). ^{1}H NMR (400 MHz, DMSO-d_6) δ 7.98 (d, J = 1.8 Hz, 2H), 7.77 (d, J = 8.5 Hz, 2H), 7.41 (dd, J = 8.5, 1.7 Hz, 2H), 7.14 (s, 1H), 6.86 (d, J = 1.5 Hz, 2H), 6.74 (d, J = 13.3 Hz, 2H), 6.57 (d, J = 13.4 Hz, 2H), 4.45 (t, J = 7.7 Hz, 4H), 2.66 – 2.59 (m, 4H), 2.51 (t, J = 6.7 Hz, 4H), 2.33 (s, 6H), 1.93 (t, J = 7.4 Hz, 2H), 1.86 (d, J = 10.5 Hz, 2H).

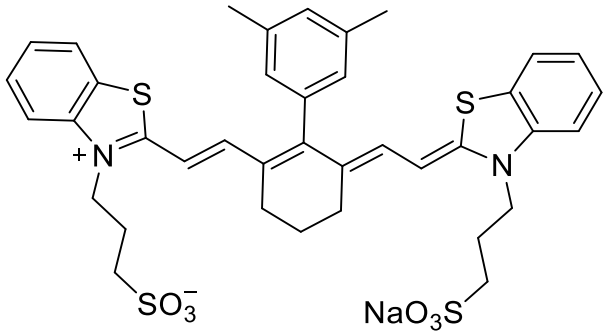

3-((Z)-2-((E)-2-(3',5'-dimethyl-6-((E)-2-(3-(3-sulfonatopropyl)benzo[d]thiazol-3-ium-2-yl)vinyl)-4,5-dihydro-[1,1'-biphenyl]-2(3H)-ylidene)ethylidene)benzo[d]thiazol-3(2H)-yl)propane-1-sulfonate (6.29)

3-(2-methylbenzo[d]thiazol-3-ium-3-yl)propane-1-7 **6.27** (20 mg, 0.10 mmol, 1 eq), **6.21** (20 mg, 0.04 mmol, 0.5 eq), NaOAc (10 mg , 0.08 mmol, 1.2 eq) was dissolved in EtOH (1.4 mL, 0.05M). The dark magenta solution was freeze-pump-thawed x3, then heated to 80 °C for 1h turning the solution green. The reaction was monitored by UV-Vis for the appearance of product (~800 nm) and loss of linker (~550 nm). The crude product was purified via silica gel chromatography with a gradient of 19:1 → 9:1 → 17:3 dichloromethane: methanol to afford pure product **3-((Z)-2-((E)-2-(3',5'-dimethyl-6-((E)-2-(3-(3-sulfonatopropyl)benzo[d]thiazol-3-ium-2-yl)vinyl)-4,5-dihydro-[1,1'-biphenyl]-2(3H)-ylidene)ethylidene)benzo[d]thiazol-3(2H)-yl)propane-1-sulfonate** as a shiny green brown solid (12 mg, 0.01 mmol, 15%). ^{1}H NMR (400 MHz, DMSO-d_6) δ 7.84 (dd, J = 8.1, 1.2 Hz, 2H), 7.70 (d, J = 8.3 Hz, 2H), 7.44 (ddd, J = 8.5, 7.3, 1.3 Hz, 2H), 7.29 – 7.20 (m, 2H), 7.14 (d, J = 1.6 Hz, 1H), 6.87 (d, J = 1.6 Hz, 2H), 6.76 (d, J = 13.3 Hz, 2H), 6.53 (d, J = 13.4 Hz, 2H), 4.49 (t, J = 7.7 Hz, 4H), 2.62 (d, J = 6.9 Hz, 5H), 2.51 (t, J = 6.7 Hz, 4H), 2.35 (s, 6H), 1.96 (t, J = 5.8 Hz, 3H), 1.91 – 1.82 (m, 2H).

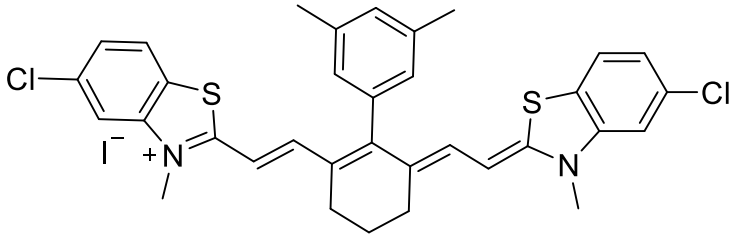

5-chloro-2-((E)-2-((E)-6-((Z)-2-(5-chloro-3-methylbenzo[d]thiazol-2(3H)-ylidene)ethylidene)-3',5'-dimethyl-3,4,5,6-tetrahydro-[1,1'-biphenyl]-2-yl)vinyl)-3-methylbenzo[d]thiazol-3-ium iodide (6.37)

5-chloro-2,3-dimethylbenzo[d]thiazol-3-ium iodide **6.30** (100 mg, 0.3 mmol, 1 eq), **6.21** (60mg , 0.2 mmol, 0.5 eq), NaOAc (30 mg, 0.4 mmol, 1.2 eq) was dissolved in EtOH (5.3 mL, 0.5 M). The dark magenta solution was freeze-pump-thawed x3, then heated to 80 °C for 1h turning the solution green. The reaction was monitored by UV-Vis for the appearance of product (~800 nm) and lost of linker (~550 nm). The crude product was purified via silica gel chromatography with a gradient of 99:1 → 49:1 → 97:3 dichloromethane: methanol to afford pure product **5-chloro-2-((E)-2-((E)-6-((Z)-2-(5-chloro-3-methylbenzo[d]thiazol-2(3H)-ylidene)ethylidene)-3',5'-dimethyl-3,4,5,6-tetrahydro-[1,1'-biphenyl]-2-yl)vinyl)-3-methylbenzo[d]thiazol-3-ium iodide** as a shiny green brown solid (40 mg, 0.05 mmol, 18%). ^{1}H NMR (400 MHz, DMSO-d_6) δ 7.84 (d, J = 8.5 Hz, 2H), 7.76 (d, J = 2.0 Hz, 2H), 7.31 (dd, J = 8.5, 1.9 Hz, 2H), 7.18 – 7.14 (m, 1H), 6.89 – 6.75 (m, 2H), 6.73 (d, J = 13.5 Hz, 2H), 6.34 (d, J = 13.5 Hz, 2H), 3.74 (s, 6H), 2.60 (t, J = 6.1 Hz, 4H), 2.33 (s, 6H), 1.91 – 1.82 (m, 2H).

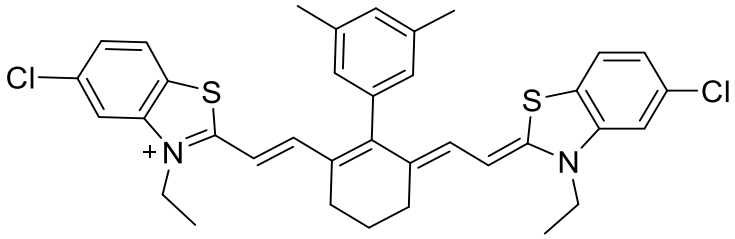

5-chloro-2-((E)-2-((E)-6-((Z)-2-(5-chloro-3-ethylbenzo[d]thiazol-2(3H)-ylidene)ethylidene)-3',5'-dimethyl-3,4,5,6-tetrahydro-[1,1'-biphenyl]-2-yl)vinyl)-3-ethylbenzo[d]thiazol-3-ium iodide (6.38)

5-chloro-3-ethyl-2-methylbenzo[d]thiazol-3-ium iodide **6.31** (100 mg, 0.3 mmol, 1 eq), **6.21** (60 mg, 0.2 mmol 0.5 eq), NaOAc (, 30 mg, 0.4 mmol, 1.2 eq) was dissolved in EtOH (5.3 mL, 0.5M). The dark magenta solution was freeze-pump-thawed x3, then heated to 80 °C for 1h turning the solution green. The reaction was monitored by UV-Vis for the appearance of product (~800 nm) and loss of linker (~550 nm).The crude product was purified via silica gel chromatography with a gradient of 99:1 → 49:1 → 97:3 dichloromethane: methanol to afford pure product **5-chloro-2-((E)-2-((E)-6-((Z)-2-(5-chloro-3-ethylbenzo[d]thiazol-2(3H)-ylidene)ethylidene)-3',5'-dimethyl-3,4,5,6-tetrahydro-[1,1'-biphenyl]-2-yl)vinyl)-3-ethylbenzo[d]thiazol-3-ium iodide** a shiny green brown solid (38 mg, 0.05 mmol , 17%). ^{1}H NMR (400 MHz, DMSO-d_6) δ 7.86 (d, J = 8.6 Hz, 2H), 7.79 (d, J = 1.9 Hz, 2H), 7.37 – 7.31 (m, 2H), 7.20 – 7.12 (m, 1H), 6.88 – 6.79 (m, 2H), 6.76 (d, J = 13.4 Hz, 2H), 6.36 (d, J = 13.4 Hz, 2H), 4.35 (q, J = 7.0 Hz, 4H), 2.61 (t, J = 6.0 Hz, 4H), 2.34 (s, 6H), 1.86 (d, J = 6.0 Hz, 2H), 1.22 (t, J = 7.1 Hz, 6H).

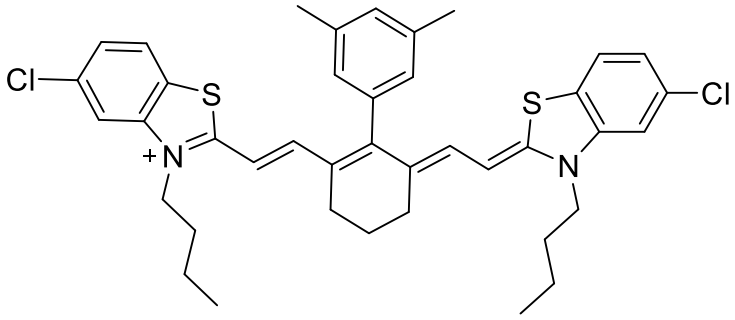

3-butyl-2-((E)-2-((E)-6-((Z)-2-(3-butyl-5-chlorobenzo[d]thiazol-2(3H)-ylidene)ethylidene)-3',5'-dimethyl-3,4,5,6-tetrahydro-[1,1'-biphenyl]-2-yl)vinyl)-5-chlorobenzo[d]thiazol-3-ium iodide (6.39)

5-chloro-3-butyl-2-methylbenzo[d]thiazol-3-ium iodide **6.32** (100 mg, 0.3 mmol, 1 eq), **6.21** (60 mg, 0.2 mmol, 0.5 eq), NaOAc (30 mg, 0.3 mmol, 1.2 eq) was dissolved in EtOH (5.0 mL, 0.5M). The dark magenta solution was freeze-pump-thawed x3, then heated to 80 °C for 1h turning the solution green. The reaction was monitored by UV-Vis for the appearance of product (~800 nm) and loss of linker (~550 nm). The crude product was purified via silica gel chromatography with a gradient of 99:1 → 49:1 → 97:3 dichloromethane: methanol to afford pure product **3-butyl-2-((E)-2-((E)-6-((Z)-2-(3-butyl-5-chlorobenzo[d]thiazol-2(3H)-ylidene)ethylidene)-3',5'-dimethyl-3,4,5,6-tetrahydro-[1,1'-biphenyl]-2-yl)vinyl)-5-chlorobenzo[d]thiazol-3-ium iodide** as a shiny green brown solid (48 mg, 0.06 mmol, 20%). ^{1}H NMR (400 MHz, DMSO-d_6) δ 7.90 (d, *J* = 8.5 Hz, 2H), 7.83 (d, *J* = 1.9 Hz, 2H), 7.36 (dd, *J* = 8.5, 1.9 Hz, 2H), 7.20 (s, 1H), 6.89 – 6.86 (m, 2H), 6.79 (d, *J* = 13.3 Hz, 2H), 6.38 (d, *J* = 13.4 Hz, 2H), 4.35 (t, *J* = 7.5 Hz, 4H), 2.64 (t, *J* = 6.0 Hz, 4H), 2.38 (s, 6H), 1.91 (t, *J* = 6.1 Hz, 2H), 1.65 (p, *J* = 7.3 Hz, 4H), 1.45 – 1.35 (m, 4H), 0.93 (t, *J* = 7.3 Hz, 6H).

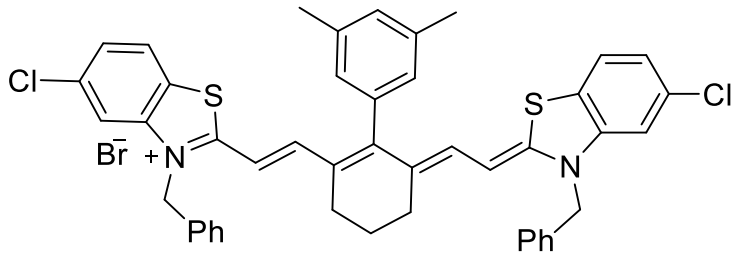

3-benzyl-2-((E)-2-((E)-6-((Z)-2-(3-benzyl-5-chlorobenzo[d]thiazol-2(3H)-ylidene)ethylidene)-3',5'-dimethyl-3,4,5,6-tetrahydro-[1,1'-biphenyl]-2-yl)vinyl)-5-chlorobenzo[d]thiazol-3-ium iodide (6.40)

5-chloro-3-benzyl-2-methylbenzo[d]thiazol-3-ium iodide **6.33** (100 mg, 0.3 mmol, 1 eq), **6.21** (60 mg, 0.2 mmol, 0.5 eq), NaOAc (30 mg, 0.3 mmol, 1.2 eq) was dissolved in EtOH (5.6 mL, 0.5M). The dark magenta solution was freeze-pump-thawed x3, then heated to 80 °C for 1h turning the solution green. The reaction was monitored by UV-Vis for the appearance of product (~800 nm) and loss of linker (~550 nm)The crude product was purified via silica gel chromatography with a gradient of 99:1 → 49:1 → 97:3 dichloromethane: methanol to afford pure product **3-benzyl-2-((E)-2-((E)-6-((Z)-2-(3-benzyl-5-chlorobenzo[d]thiazol-2(3H)-ylidene)ethylidene)-3',5'-dimethyl-3,4,5,6-tetrahydro-[1,1'-biphenyl]-2-yl)vinyl)-5-chlorobenzo[d]thiazol-3-ium iodide** s a shiny green brown solid (52 mg, 0.06 mmol, 21%). ^{1}H NMR (400 MHz, DMSO-d_6) δ 7.90 (d, J = 8.6 Hz, 2H), 7.76 (d, J = 1.9 Hz, 2H), 7.39 – 7.31 (m, 6H), 7.31 – 7.22 (m, 3H), 7.22 – 7.11 (m, 5H), 6.85 – 6.80 (m, 2H), 6.74 (d, J = 13.3 Hz, 2H), 6.38 (d, J = 13.4 Hz, 2H), 5.63 (s, 4H), 2.45 – 2.39 (m, 4H), 2.34 (s, 6H), 1.74 (d, J = 10.8 Hz, 2H).

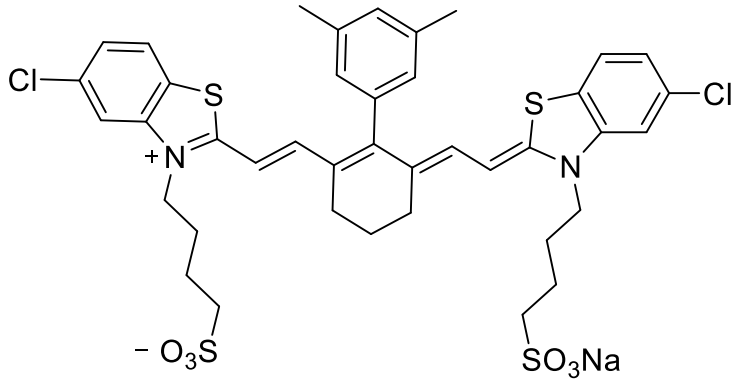

4-(5-chloro-2-((E)-2-((E)-6-((Z)-2-(5-chloro-3-(4-sulfonatobutyl)benzo[d]thiazol-2(3H)-ylidene)ethylidene)-3',5'-dimethyl-3,4,5,6-tetrahydro-[1,1'-biphenyl]-2-yl)vinyl)benzo[d]thiazol-3-ium-3-yl)butane-1-sulfonate (6.41)

4-(5-chloro-2-methylbenzo[d]thiazol-3-ium-3-yl)butane-1-sulfonate **6.34** (100 mg, 0.3 mmol, 1 eq), **6.21** (70 mg, 0.2 mmol, 0.5 eq), NaOAc (30 mg, 0.3 mmol, 1.2 eq) was dissolved in EtOH (5.3 mL, 0.5M). The dark magenta solution was freeze-pump-thawed x3, then heated to 80 °C for 1h turning the solution green. The reaction was monitored by UV-Vis for the appearance of product (~800 nm) and loss of linker (~550 nm). The crude product was purified via silica gel chromatography with a gradient of 19:1 → 1:9 → 17:3 → 4:1 → 3:7 dichloromethane: methanol to afford pure product **4-(5-chloro-2-((E)-2-((E)-6-((Z)-2-(5-chloro-3-(4-sulfonatobutyl)benzo[d]thiazol-2(3H)-ylidene)ethylidene)-3',5'-dimethyl-3,4,5,6-tetrahydro-[1,1'-biphenyl]-2-yl)vinyl)benzo[d]thiazol-3-ium-3-yl)butane-1-sulfonate** as a shiny green brown solid (60 mg, 0.07 mmol, 23%). ^{1}H NMR (400 MHz, DMSO-d_6) δ 7.85 (s, 1H), 7.83 (s, 1H), 7.30 (dd, J = 8.5, 1.9 Hz, 2H), 7.14 (s, 1H), 6.88 – 6.82 (m, 2H), 6.75 (d, J = 13.3 Hz, 2H), 6.41 (d, J = 13.4 Hz, 1H), 4.31 (s, 4H), 2.62 (t, J = 6.3 Hz, 4H), 2.34 (s, 6H), 1.87 (s, 2H), 1.70 (s, 12H).

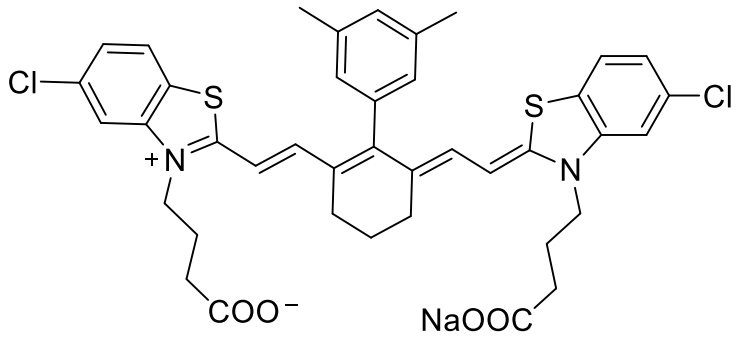

4-(2-((E)-2-((E)-6-((Z)-2-(3-(3-carboxylatopropyl)-5-chlorobenzo[d]thiazol-2(3H)-ylidene)ethylidene)-3',5'-dimethyl-3,4,5,6-tetrahydro-[1,1'-biphenyl]-2-yl)vinyl)-5-chlorobenzo[d]thiazol-3-ium-3-yl)butanoate (6.42)

4-(5-chloro-2-methylbenzo[d]thiazol-3-ium-3-yl)butanoate **6.35** (100 mg, 0.4 mmol, 1 eq), **6.21** (80 mg, 0.2 mmol, 0.5 eq), NaOAc (30 mg, 0.4 mmol, 1.2 eq) was dissolved in EtOH (6.3 mL, 0.5M). The dark magenta solution was freeze-pump-thawed x3, then heated to 80 °C for 1h turning the solution green. The reaction was monitored by UV-Vis for the appearance of product (~800 nm) and loss of linker (~550 nm). The crude product was purified via silica gel chromatography with a gradient of 1:9 → 17:3 → 4:1 → 3:7 dichloromethane: methanol to afford pure product **5-(2-((E)-2-((E)-6-((Z)-2-(3-(4-carboxylatobutyl)-5-chlorobenzo[d]thiazol-2(3H)-ylidene)ethylidene)-3',5'-dimethyl-3,4,5,6-tetrahydro-[1,1'-biphenyl]-2-yl)vinyl)-5-chlorobenzo[d]thiazol-3-ium-3-yl)pentanoate** a shiny green brown solid (61 mg, 0.08 mmol, 26%). ^{1}H NMR (400 MHz, DMSO-d_6) δ 12.39 (s, 2H), 7.87 (s, 1H), 7.85 (s, 3H), 7.32 (dd, J = 8.5, 1.9 Hz, 2H), 7.16 (s, 1H), 6.84 (d, J = 1.6 Hz, 2H), 6.76 (d, J = 13.4 Hz, 2H), 6.48 (d, J = 13.4 Hz, 2H), 4.26 (t, J = 8.1 Hz, 4H), 3.12 (d, J = 3.2 Hz, 4zH), 2.62 (t, J = 6.3 Hz, 4H), 2.34 (s, 6H), 1.83 (t, J = 7.7 Hz, 6H).

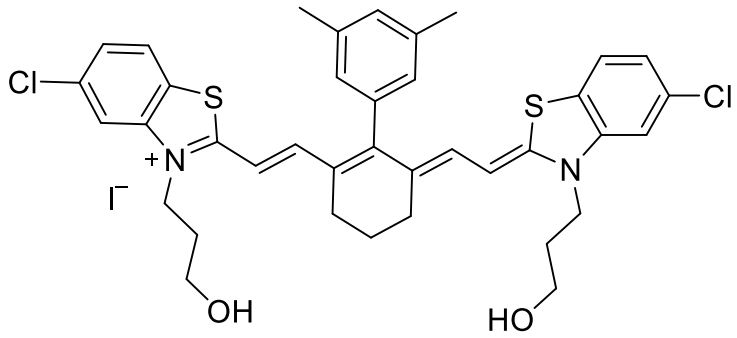

5-chloro-2-((E)-2-((E)-6-((Z)-2-(5-chloro-3-(3-hydroxypropyl)benzo[d]thiazol-2(3H)-ylidene)ethylidene)-3',5'-dimethyl-3,4,5,6-tetrahydro-[1,1'-biphenyl]-2-yl)vinyl)-3-(3-hydroxypropyl)benzo[d]thiazol-3-ium (6.43)

5-chloro-3-(3-hydroxypropyl)-2-methylbenzo[d]thiazol-3-ium iodide **6.36** (100 mg, 0.3 mmol, 1 eq), **6.21** (60 mg, 0.2 mmol, 0.5 eq), NaOAc (30 mg, 0.3 mmol, 1.2 eq) was dissolved in EtOH (4.6 mL, 0.5 M). The dark magenta solution was freeze-pump-thawed x3, then heated to 80 °C for 1h turning the solution green. The reaction was monitored by UV-Vis for the appearance of product (~800 nm) and loss of linker (~550 nm). The crude product was purified via silica gel chromatography with a gradient of 99:1 → 49:1 → 97:3 → 24:1 dichloromethane: methanol to afford pure product **5-chloro-2-((E)-2-((E)-6-((Z)-2-(5-chloro-3-(3-hydroxypropyl)benzo[d]thiazol-2(3H)-ylidene)ethylidene)-3',5'-dimethyl-3,4,5,6-tetrahydro-[1,1'-biphenyl]-2-yl)vinyl)-3-(3-hydroxypropyl)benzo[d]thiazol-3-ium** as a shiny green brown solid (30 mg, 0.04 mmol, 12%). ^{1}H NMR (400 MHz, DMSO-d_6) δ 7.86 (d, J = 8.5 Hz, 2H), 7.75 (d, J = 2.0 Hz, 2H), 7.31 (d, J = 1.9 Hz, 2H), 7.18 – 7.12 (m, 1H), 6.86 – 6.82 (m, 2H), 6.74 (d, J = 13.4 Hz, 2H), 6.42 (d, J = 13.4 Hz, 2H), 4.32 (t, J = 7.2 Hz, 4H), 3.48 – 3.42 (m, 4H), 2.58 (t, J = 6.2 Hz, 4H), 2.34 (s, 6H), 1.90 – 1.76 (m, 6H).

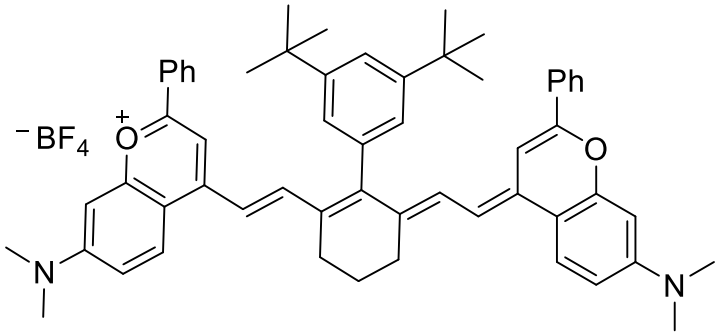

4-((E)-2-((E)-3',5'-di-tert-butyl-6-(2-((E)-7-(dimethylamino)-2-phenyl-4H-chromen-4-ylidene)ethylidene)-3,4,5,6-tetrahydro-[1,1'-biphenyl]-2-yl)vinyl)-7-(dimethylamino)-2-phenylchromenylium tetrafluoroborate (6.45)

Flavylium heterocycle **6.44** (100 mg, 0.4 mmol, 1 eq), **6.12** (60 mg, 0.2 mmol, 0.5 eq), NaOAc (80 mg, 0.8 mmol, 3 eq) were dissolved in n-butanol: toluene (2.1 mL: 1.0 mL). The dark magenta solution was freeze-pump-thawed x3, then heated to 100 °C for 15 min. Reaction was monitored by UV-Vis for the appearance of product (~1000 nm) and loss of linker (~550 nm). The crude product was purified via silica gel chromatography with a gradient of 99:1 up to 9:1 dichloromethane: ethanol to afford product **4-((E)-2-((E)-3',5'-di-tert-butyl-6-(2-((E)-7-(dimethylamino)-2-phenyl-4H-chromen-4-ylidene)ethylidene)-3,4,5,6-tetrahydro-[1,1'-biphenyl]-2-yl)vinyl)-7-(dimethylamino)-2-phenylchromenylium tetrafluoroborate** as a dark purple solid that could be utilized crude for aggregation.

6.6 Spectra relevant to Chapter Six

6.6.1 ^{1}H NMR Spectra

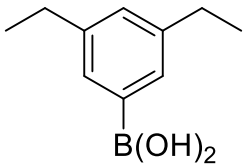

6.16

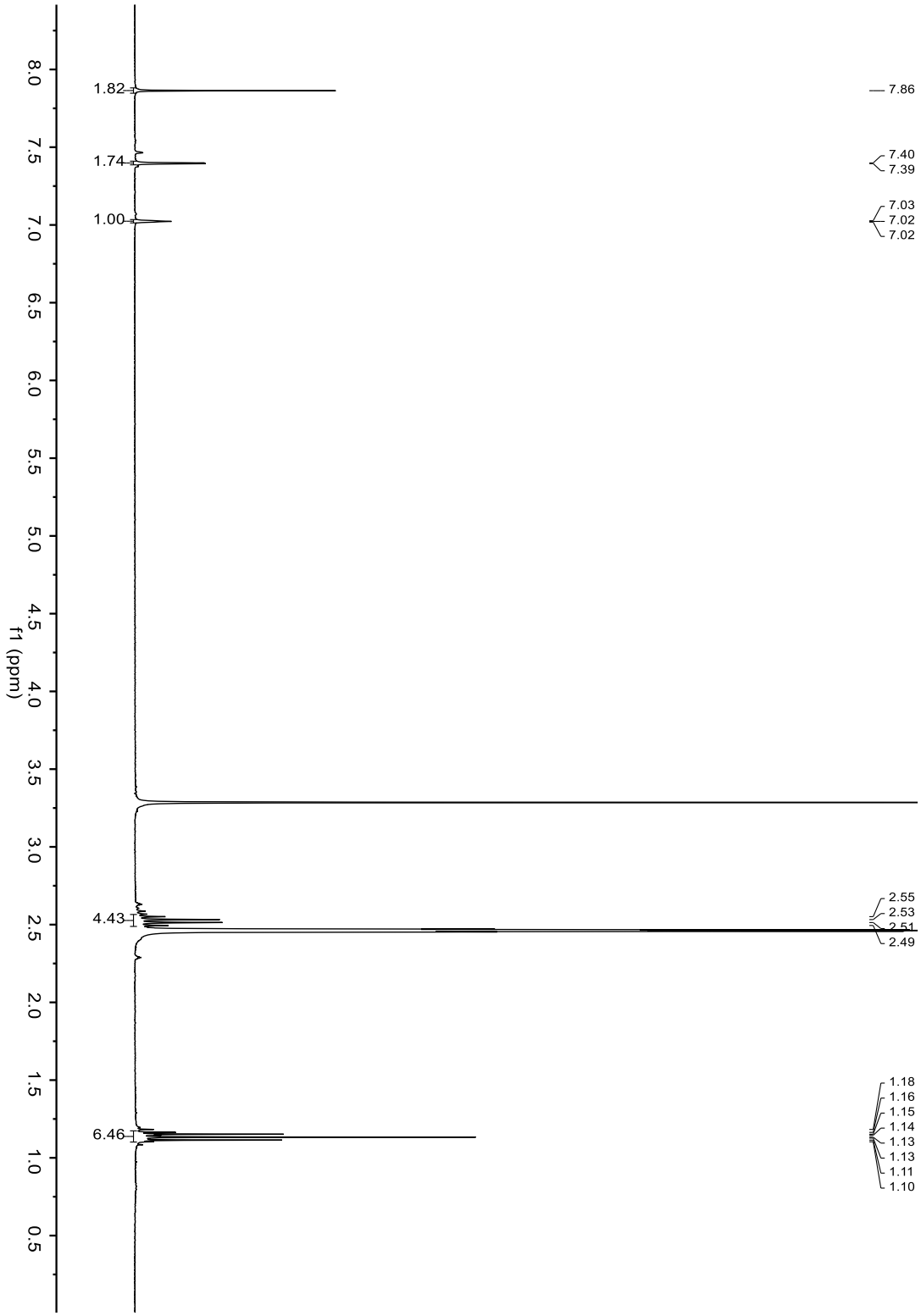
f1 (ppm)
8.0
7.5
7.0
6.5
6.0
5.5
5.0
4.5
4.0
3.5
3.0
2.5
2.0
1.5
1.0
0.5
1.82
1.74
1.00
4.43
6.46
7.86
7.40
7.39
7.03
7.02
7.02
2.55
2.53
2.51
2.49
1.18
1.16
1.15
1.14
1.13
1.13
1.11
1.10

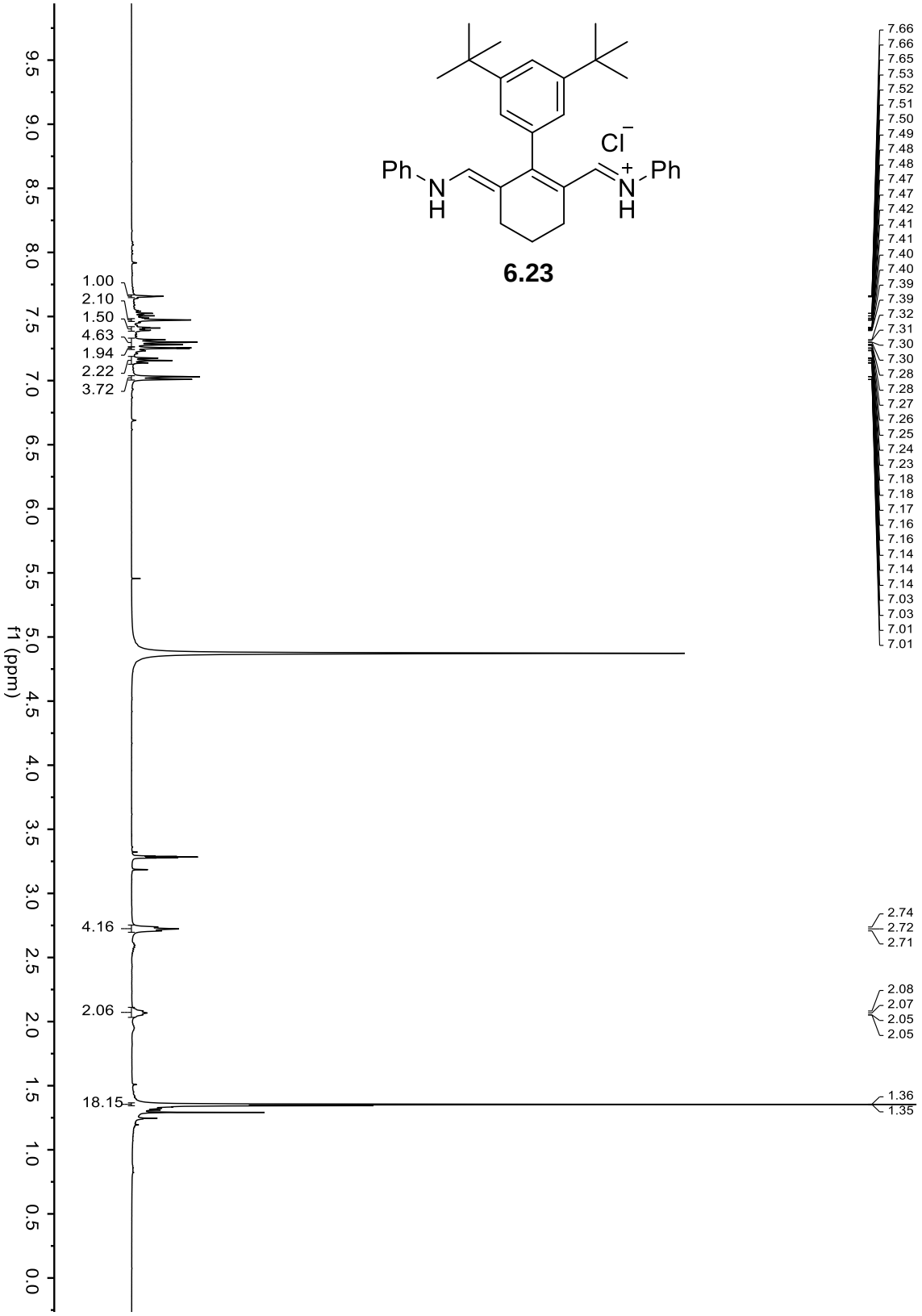
Cl⁻
Ph
N
H
+
N
H
Ph
6.23
f1 (ppm)
1.00
2.10
1.50
4.63
1.94
2.22
3.72
4.16
2.06
18.15
7.66
7.66
7.65
7.53
7.52
7.51
7.50
7.49
7.48
7.48
7.47
7.47
7.42
7.41
7.41
7.40
7.40
7.39
7.39
7.32
7.31
7.30
7.30
7.28
7.28
7.27
7.26
7.25
7.24
7.23
7.18
7.18
7.17
7.16
7.16
7.14
7.14
7.14
7.03
7.03
7.01
7.01
2.74
2.72
2.71
2.08
2.07
2.05
2.05
1.36
1.35

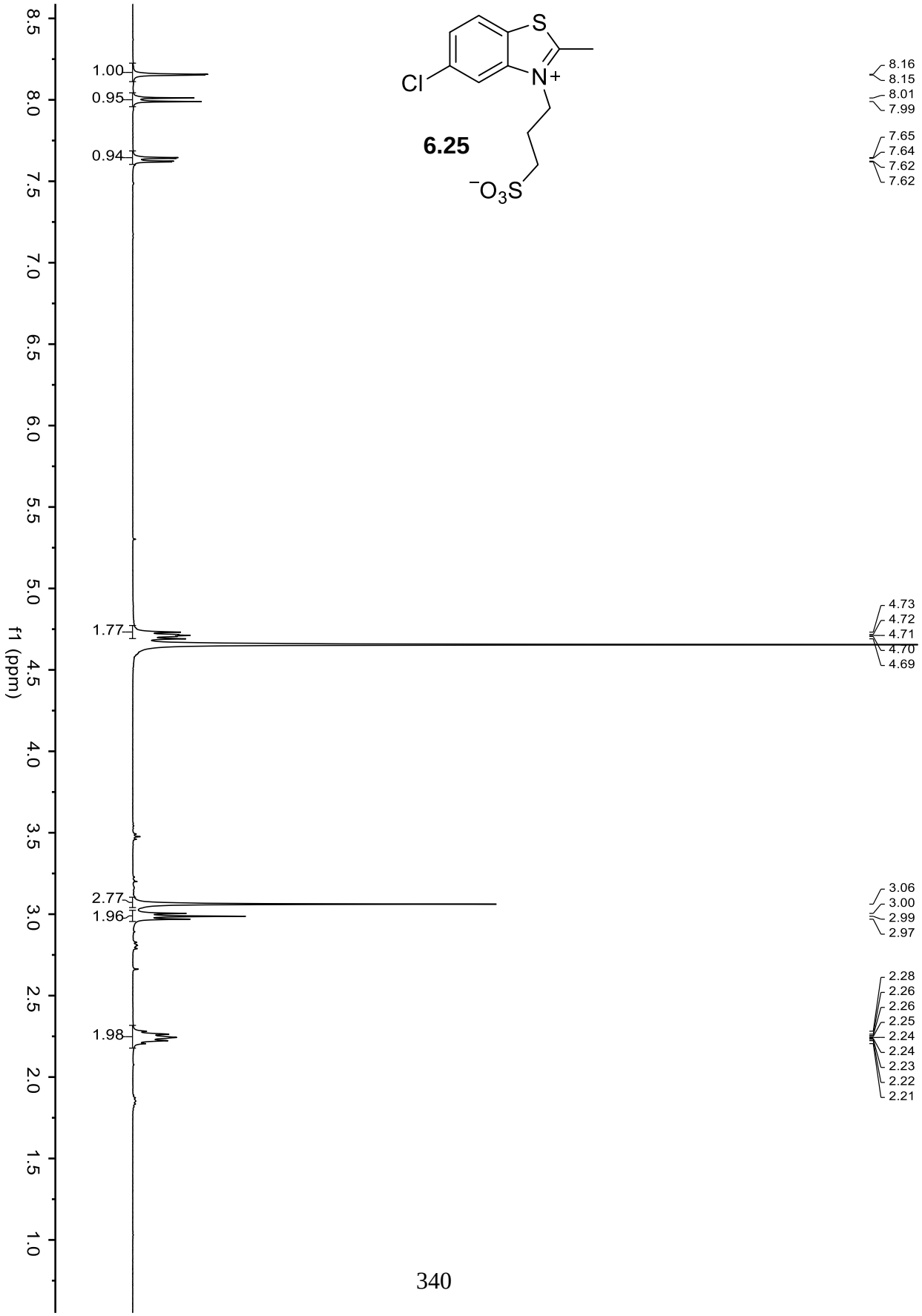
6.25
Cl
S
N+
$^{-}O_3S$
1.00
0.95
0.94
1.77
2.77
1.96
1.98
8.16
8.15
8.01
7.99
7.65
7.64
7.62
7.62
4.73
4.72
4.71
4.70
4.69
3.06
3.00
2.99
2.97
2.28
2.26
2.26
2.25
2.24
2.24
2.23
2.22
2.21
f1 (ppm)
8.5
8.0
7.5
7.0
6.5
6.0
5.5
5.0
4.5
4.0
3.5
3.0
2.5
2.0
1.5
1.0

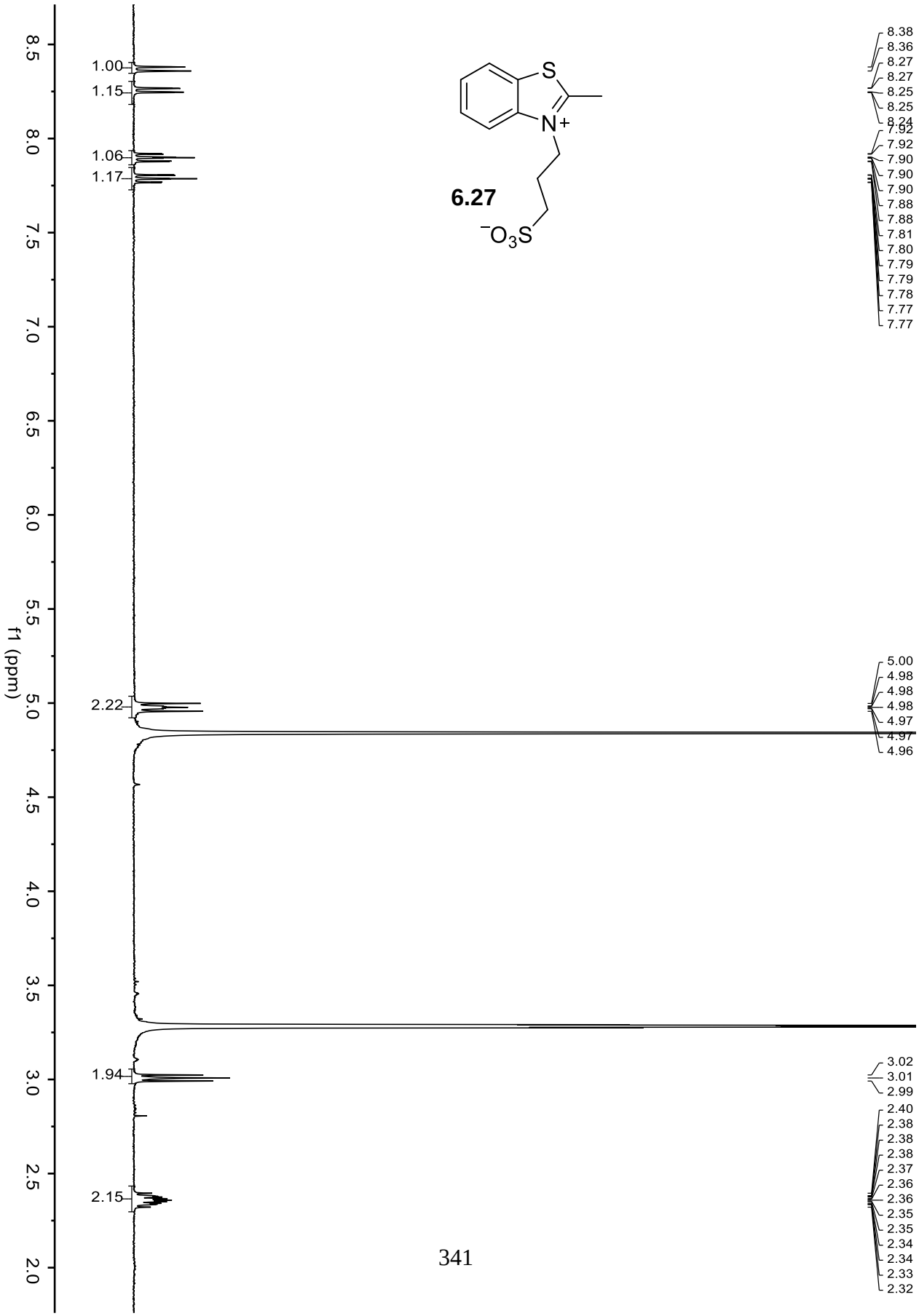
8.5
8.0
7.5
7.0
6.5
6.0
5.5
5.0
4.5
4.0
3.5
3.0
2.5
2.0
f1 (ppm)
1.00
1.15
1.06
1.17
2.22
1.94
2.15
S
N+
6.27
⁻O3S
8.38
8.36
8.27
8.27
8.25
8.25
8.24
7.92
7.92
7.90
7.90
7.90
7.88
7.88
7.81
7.80
7.79
7.79
7.78
7.77
7.77
5.00
4.98
4.98
4.98
4.97
4.97
4.96
3.02
3.01
2.99
2.40
2.38
2.38
2.38
2.37
2.36
2.36
2.35
2.35
2.34
2.34
2.33
2.32

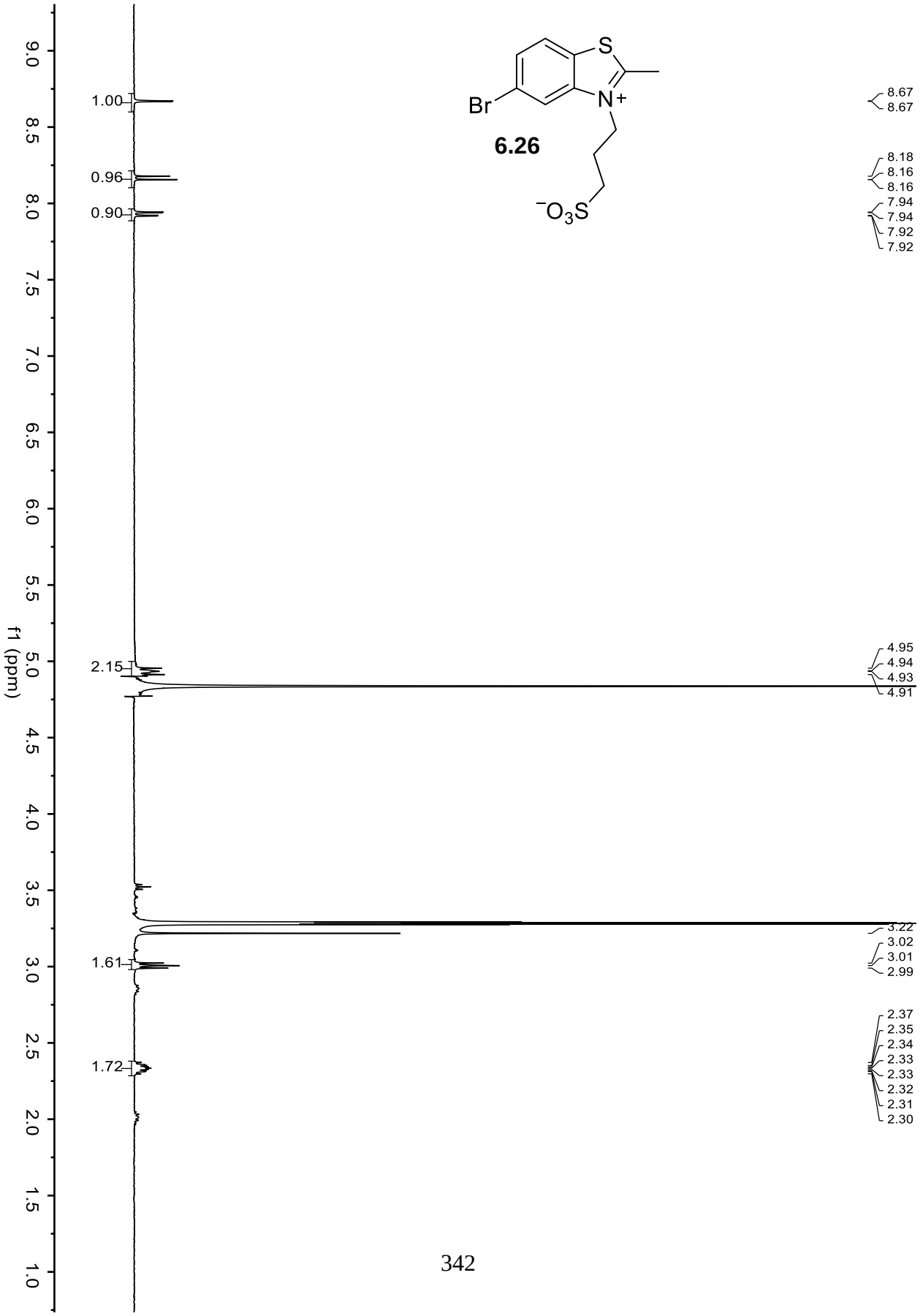
6.26
Br
S
N+
$^{-}O_3S$
1.00
0.96
0.90
2.15
1.61
1.72
8.67
8.67
8.18
8.16
8.16
7.94
7.94
7.92
7.92
4.95
4.94
4.93
4.91
3.22
3.02
3.01
2.99
2.37
2.35
2.34
2.33
2.33
2.32
2.31
2.30
f1 (ppm)

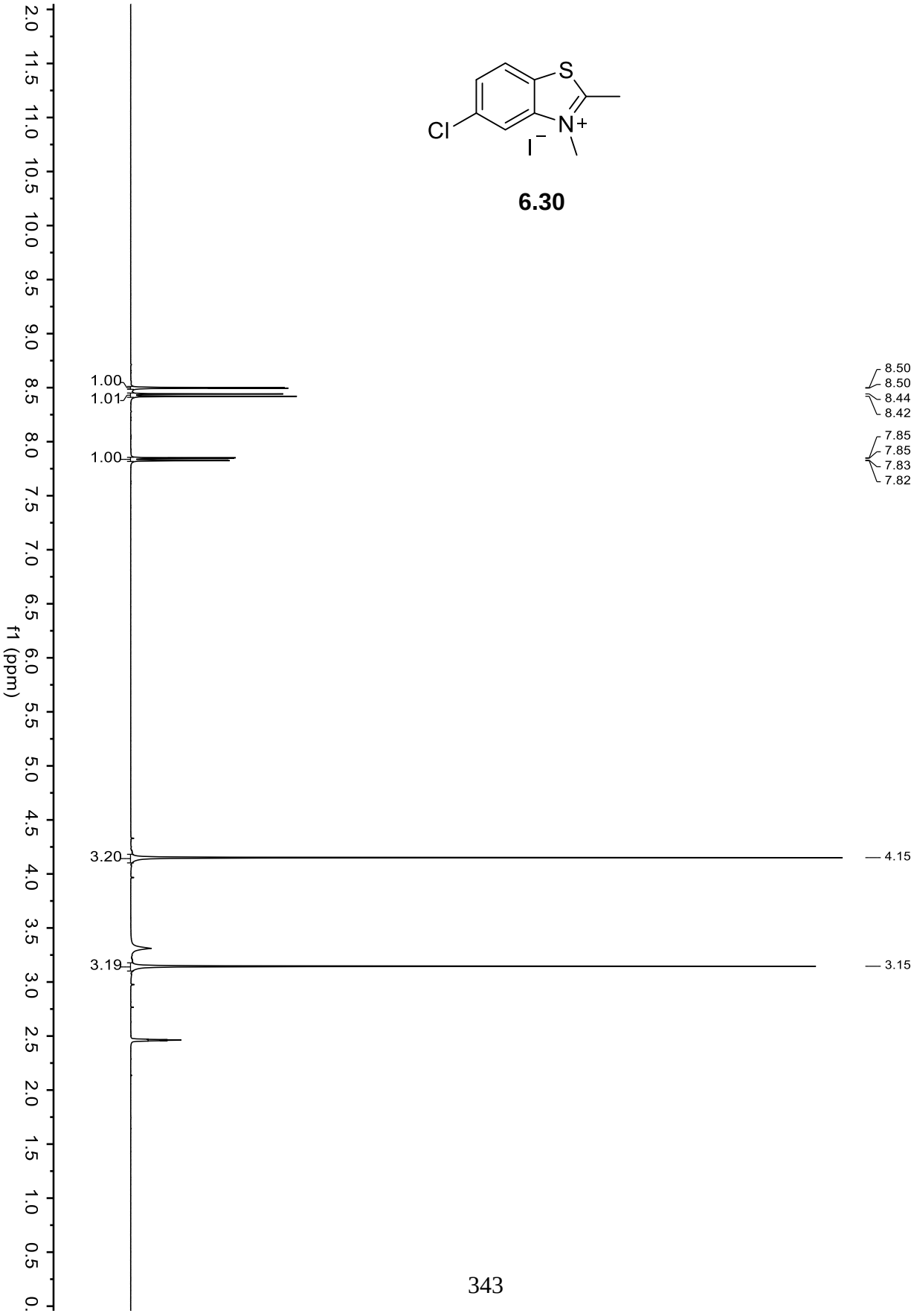
S
Cl
N+
I−
6.30
1.00
1.01
1.00
3.20
3.19
8.50
8.50
8.44
8.42
7.85
7.85
7.83
7.82
4.15
3.15
f1 (ppm)

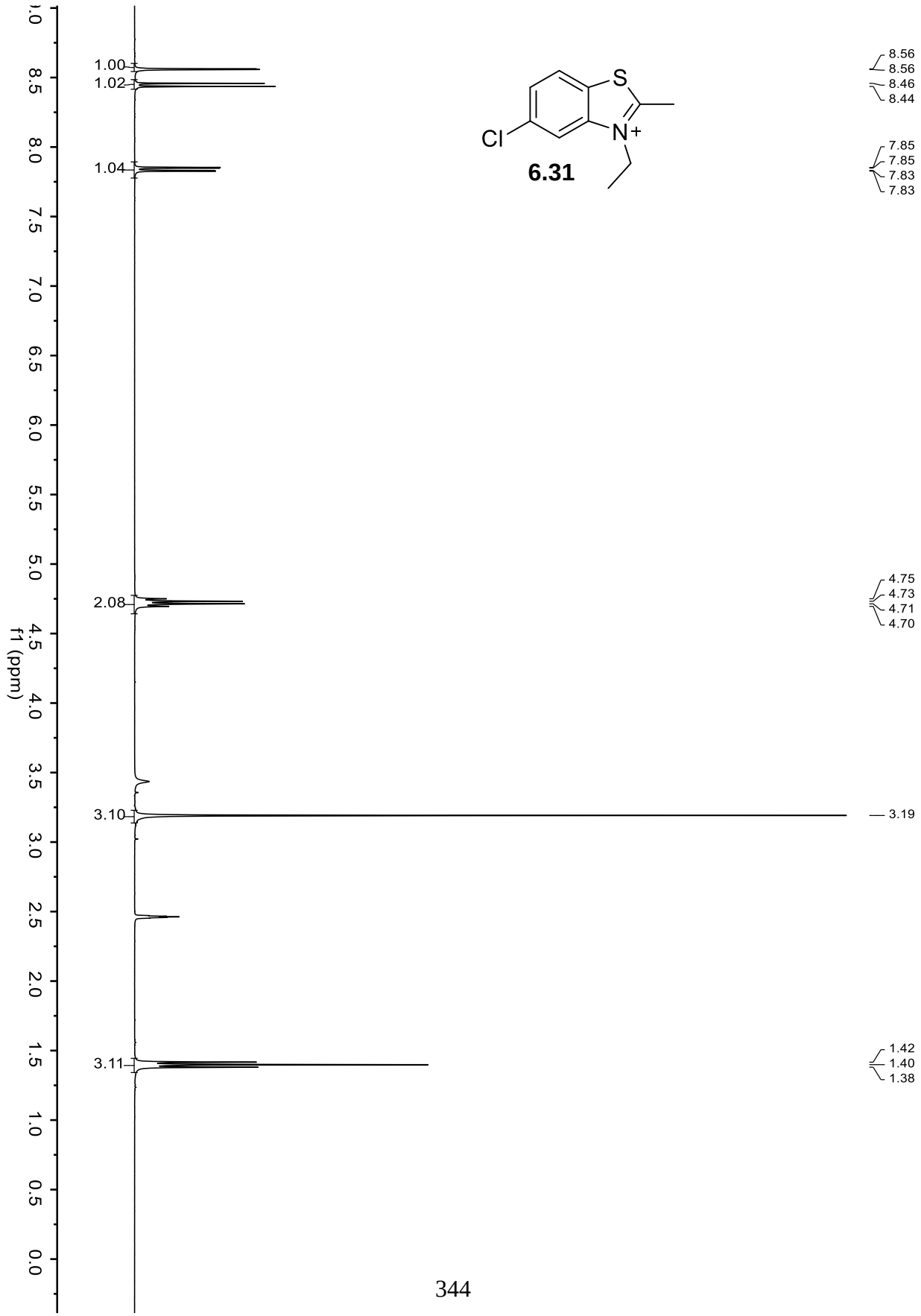
1.00
1.02
1.04
2.08
3.10
3.11
8.56
8.56
8.46
8.44
7.85
7.85
7.83
7.83
4.75
4.73
4.71
4.70
3.19
1.42
1.40
1.38
Cl
S
N+
6.31
f1 (ppm)

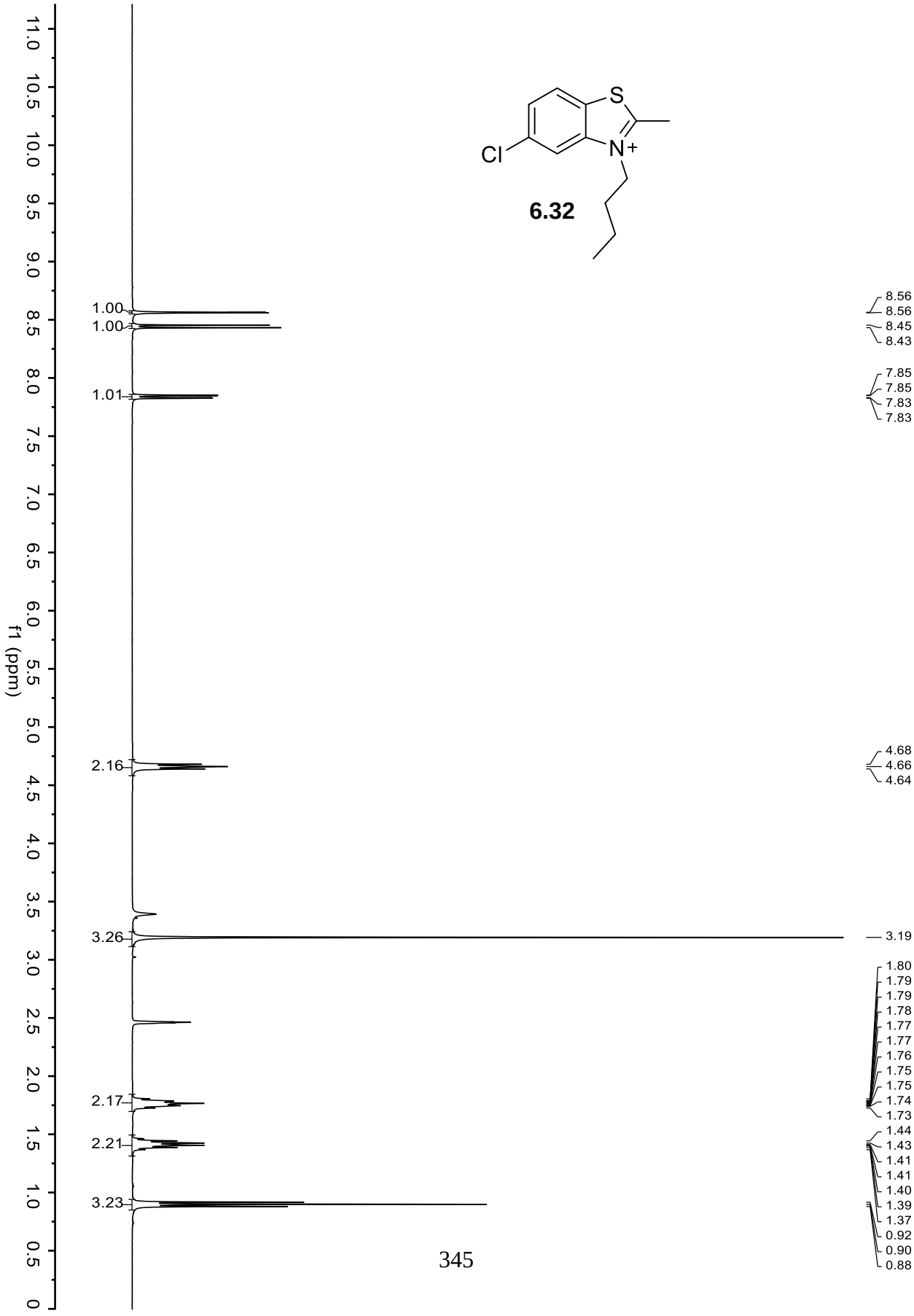
S
Cl
N+
6.32
f1 (ppm)
11.0
10.5
10.0
9.5
9.0
8.5
8.0
7.5
7.0
6.5
6.0
5.5
5.0
4.5
4.0
3.5
3.0
2.5
2.0
1.5
1.0
0.5
0
1.00
1.00
1.01
2.16
3.26
2.17
2.21
3.23
8.56
8.56
8.45
8.43
7.85
7.85
7.83
7.83
4.68
4.66
4.64
3.19
1.80
1.79
1.79
1.78
1.77
1.77
1.76
1.75
1.75
1.74
1.73
1.44
1.43
1.41
1.41
1.40
1.39
1.37
0.92
0.90
0.88

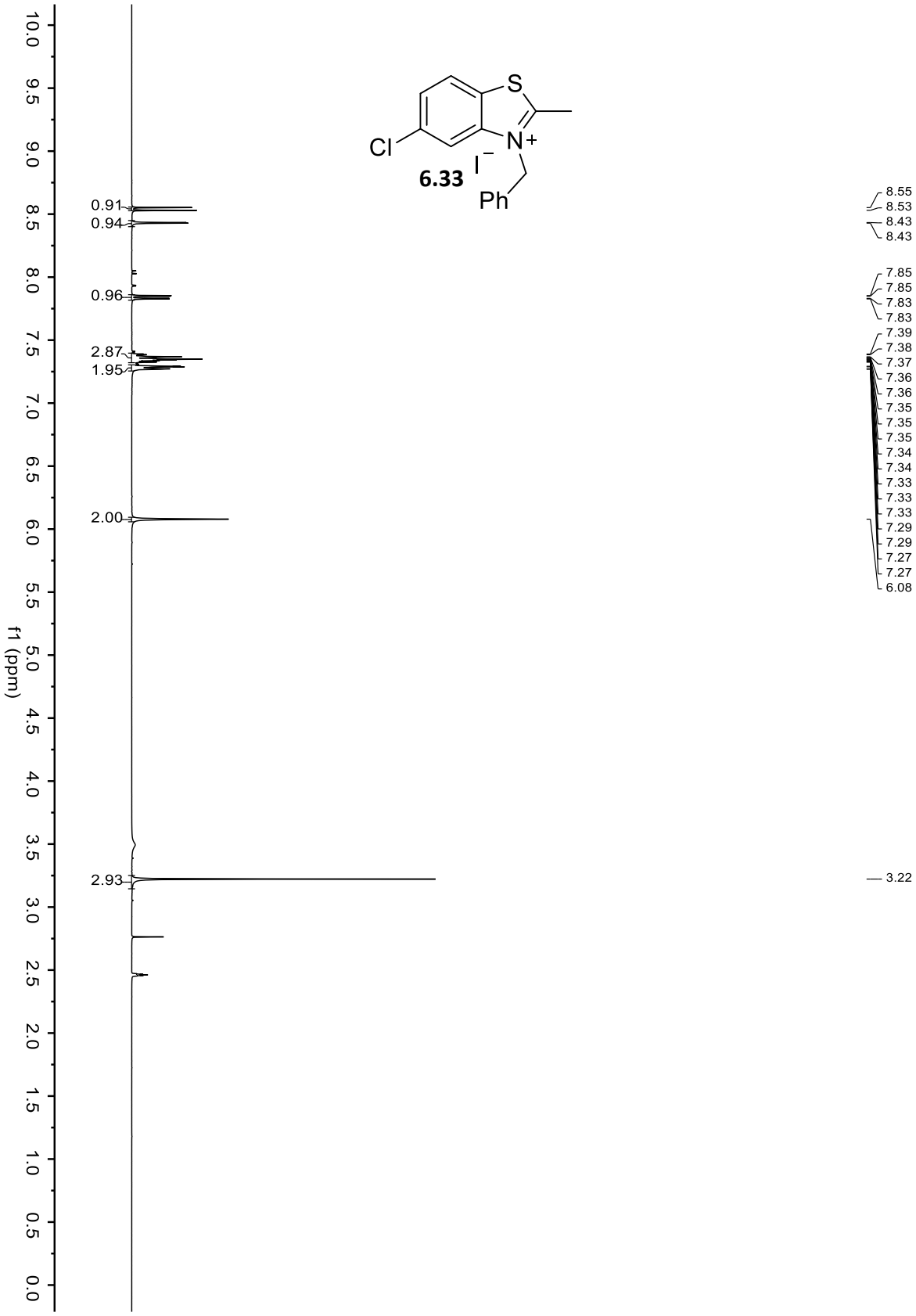
S
Cl
N+
I−
6.33
Ph
f1 (ppm)
10.0
9.5
9.0
8.5
8.0
7.5
7.0
6.5
6.0
5.5
5.0
4.5
4.0
3.5
3.0
2.5
2.0
1.5
1.0
0.5
0.0
0.91
0.94
0.96
2.87
1.95
2.00
2.93
8.55
8.53
8.43
8.43
7.85
7.85
7.83
7.83
7.39
7.38
7.37
7.36
7.36
7.35
7.35
7.35
7.34
7.34
7.33
7.33
7.33
7.29
7.29
7.27
7.27
6.08
3.22

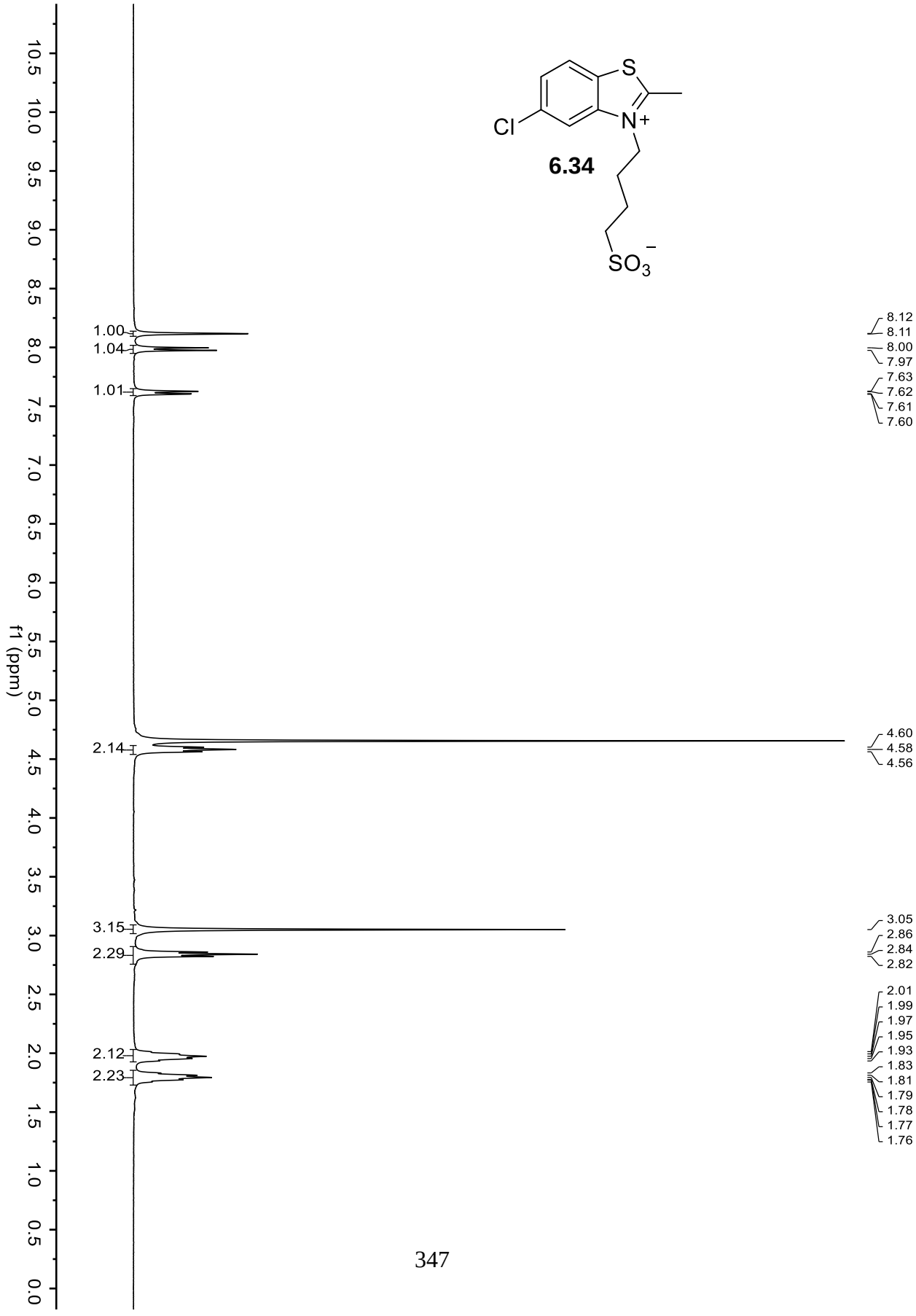
6.34
Cl
S
N+
SO3−
f1 (ppm)
10.5 10.0 9.5 9.0 8.5 8.0 7.5 7.0 6.5 6.0 5.5 5.0 4.5 4.0 3.5 3.0 2.5 2.0 1.5 1.0 0.5 0.0
1.00
1.04
1.01
2.14
3.15
2.29
2.12
2.23
8.12
8.11
8.00
7.97
7.63
7.62
7.61
7.60
4.60
4.58
4.56
3.05
2.86
2.84
2.82
2.01
1.99
1.97
1.95
1.93
1.83
1.81
1.79
1.78
1.77
1.76

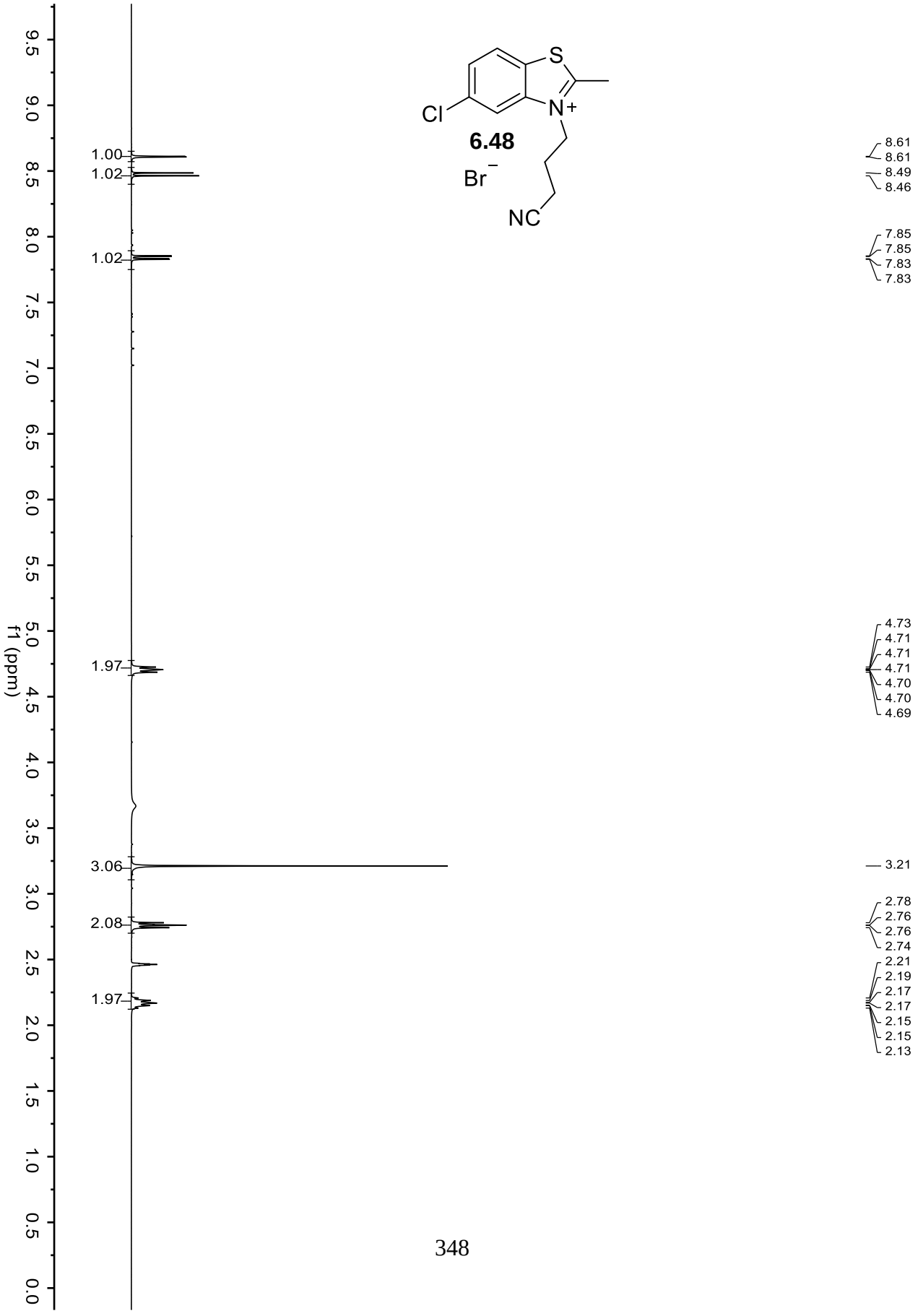
S
Cl
N+
6.48
Br−
NC
1.00
1.02
1.02
1.97
3.06
2.08
1.97
8.61
8.61
8.49
8.46
7.85
7.85
7.83
7.83
4.73
4.71
4.71
4.71
4.70
4.70
4.69
3.21
2.78
2.76
2.76
2.74
2.21
2.19
2.17
2.17
2.15
2.15
2.13
f1 (ppm)

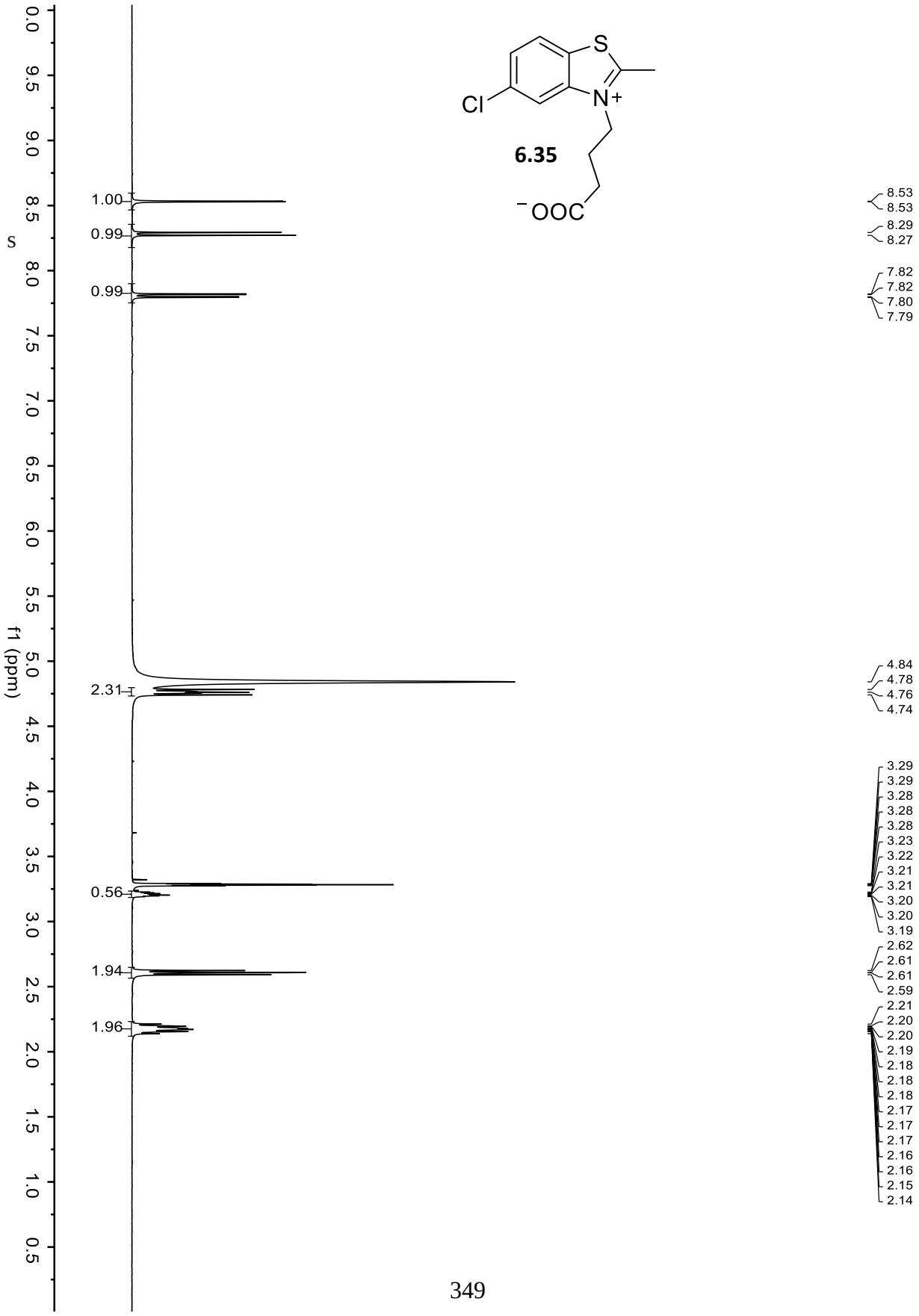
S
Cl
N+
6.35
−OOC
1.00
0.99
0.99
2.31
0.56
1.94
1.96
f1 (ppm)
8.53
8.53
8.29
8.27
7.82
7.82
7.80
7.79
4.84
4.78
4.76
4.74
3.29
3.29
3.28
3.28
3.28
3.23
3.22
3.21
3.21
3.20
3.20
3.19
2.62
2.61
2.61
2.59
2.21
2.20
2.20
2.19
2.18
2.18
2.18
2.17
2.17
2.17
2.16
2.16
2.15
2.14

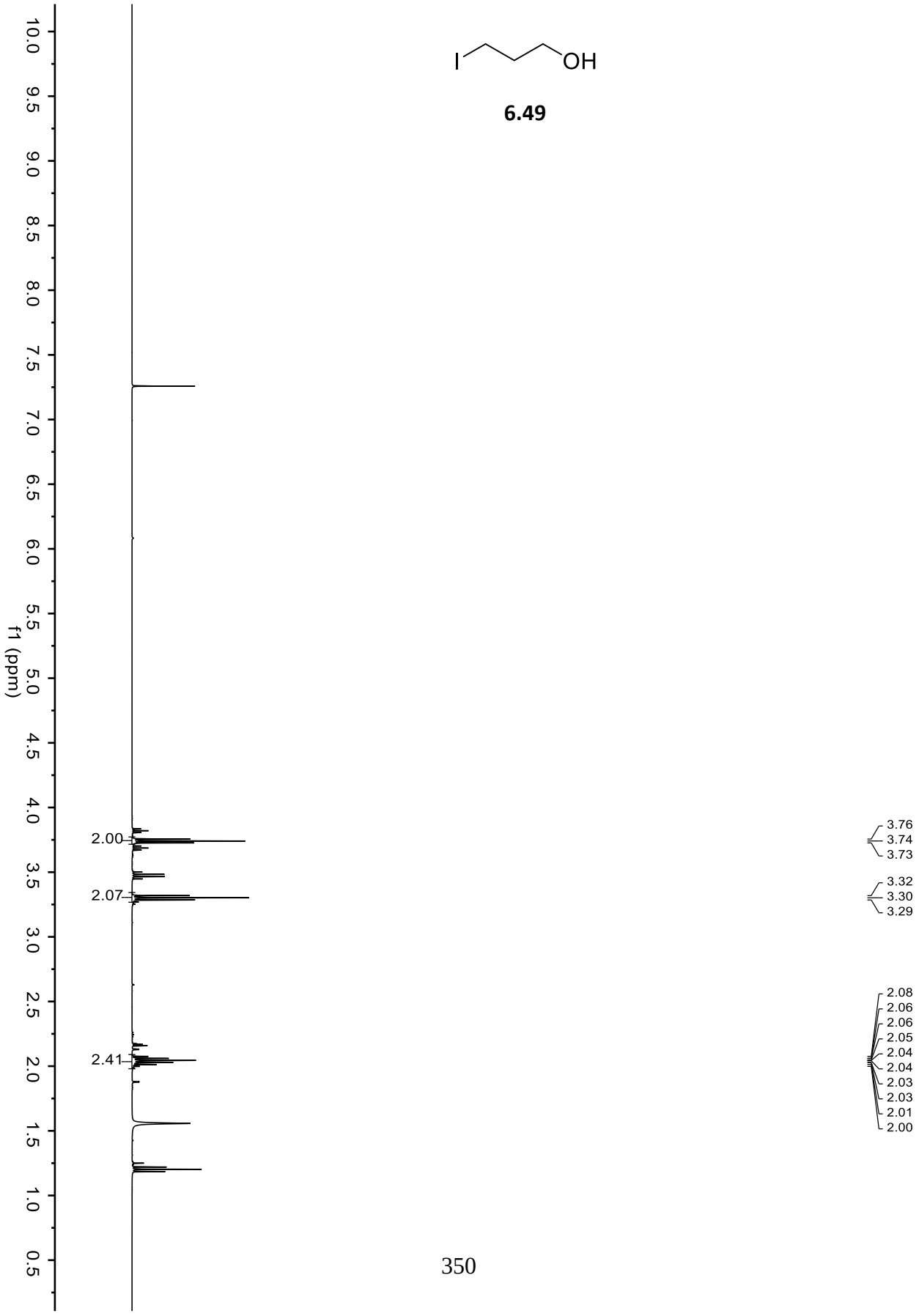
I
OH
6.49
f1 (ppm)
10.0
9.5
9.0
8.5
8.0
7.5
7.0
6.5
6.0
5.5
5.0
4.5
4.0
3.5
3.0
2.5
2.0
1.5
1.0
0.5
2.00
2.07
2.41
3.76
3.74
3.73
3.32
3.30
3.29
2.08
2.06
2.06
2.05
2.04
2.04
2.03
2.03
2.01
2.00

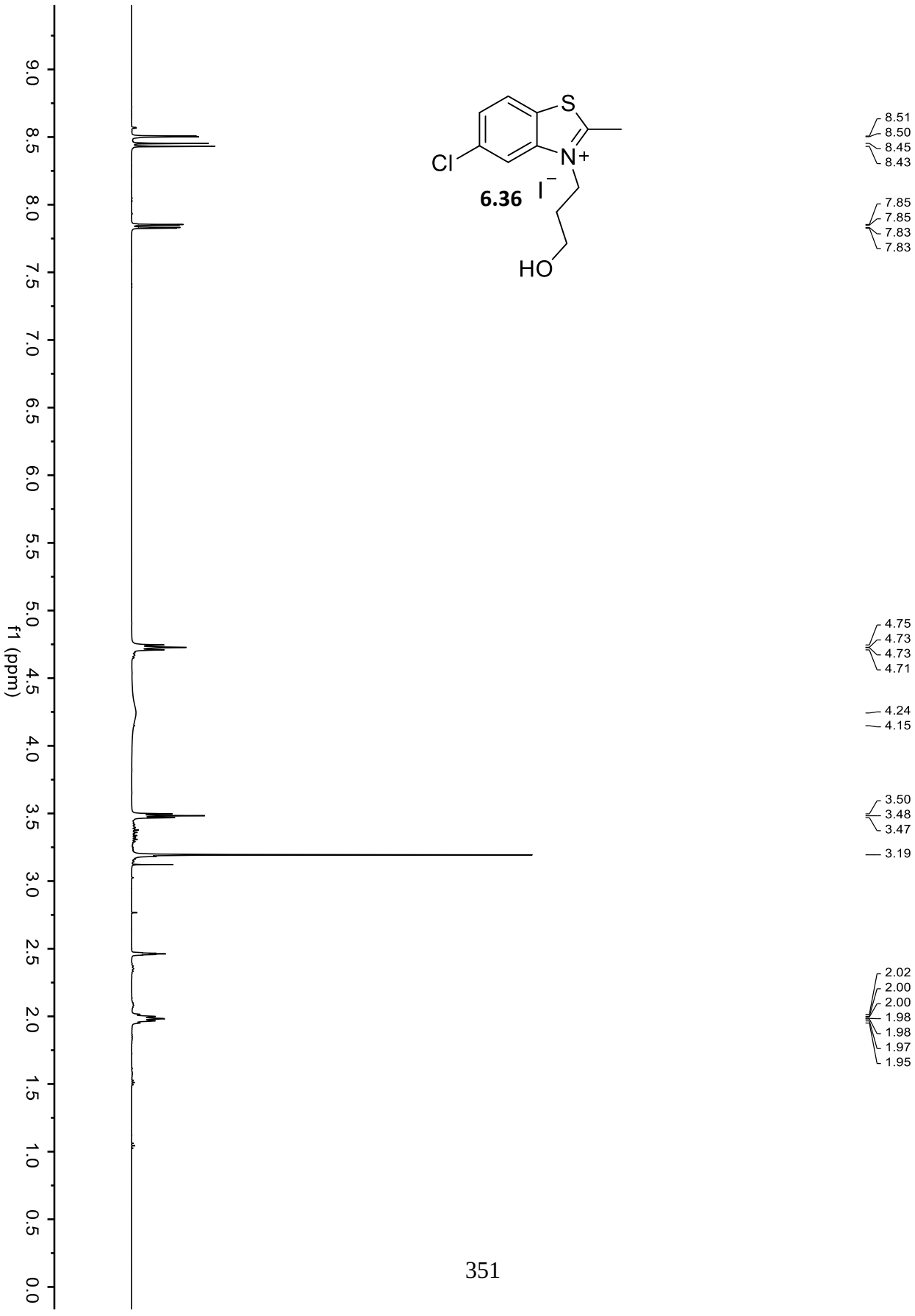
9.0
8.5
8.0
7.5
7.0
6.5
6.0
5.5
5.0
4.5
4.0
3.5
3.0
2.5
2.0
1.5
1.0
0.5
0.0
f1 (ppm)
S
Cl
N+
I−
HO
6.36
8.51
8.50
8.45
8.43
7.85
7.85
7.83
7.83
4.75
4.73
4.73
4.71
4.24
4.15
3.50
3.48
3.47
3.19
2.02
2.00
2.00
1.98
1.98
1.97
1.95

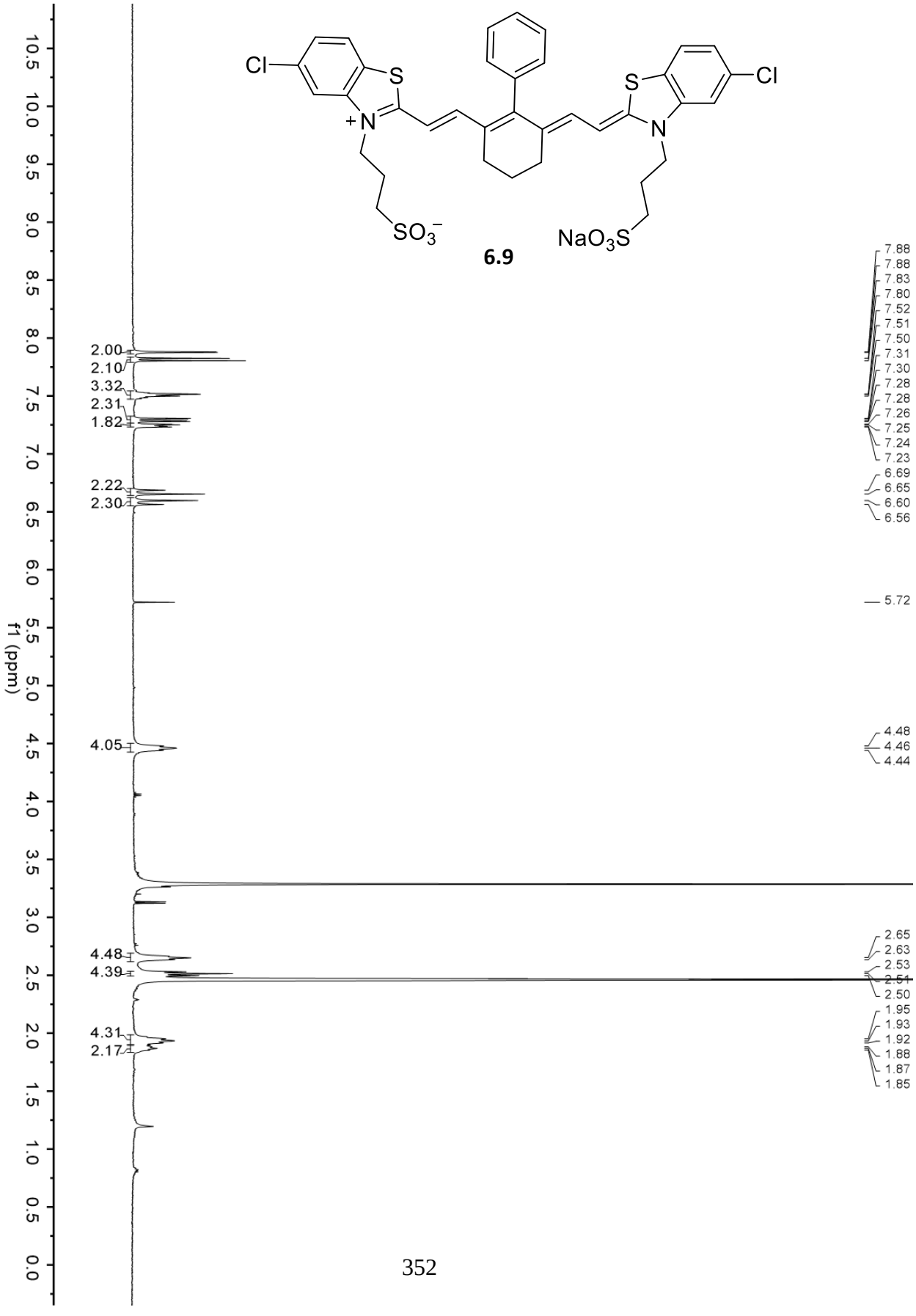
Cl
S
+N
SO3−
S
N
Cl
NaO3S
6.9
f1 (ppm)
10.5 10.0 9.5 9.0 8.5 8.0 7.5 7.0 6.5 6.0 5.5 5.0 4.5 4.0 3.5 3.0 2.5 2.0 1.5 1.0 0.5 0.0
2.00
2.10
3.32
2.31
1.82
2.22
2.30
4.05
4.48
4.39
4.31
2.17
7.88
7.88
7.83
7.80
7.52
7.51
7.50
7.31
7.30
7.28
7.28
7.26
7.25
7.24
7.23
6.69
6.65
6.60
6.56
5.72
4.48
4.46
4.44
2.65
2.63
2.53
2.51
2.50
1.95
1.93
1.92
1.88
1.87
1.85

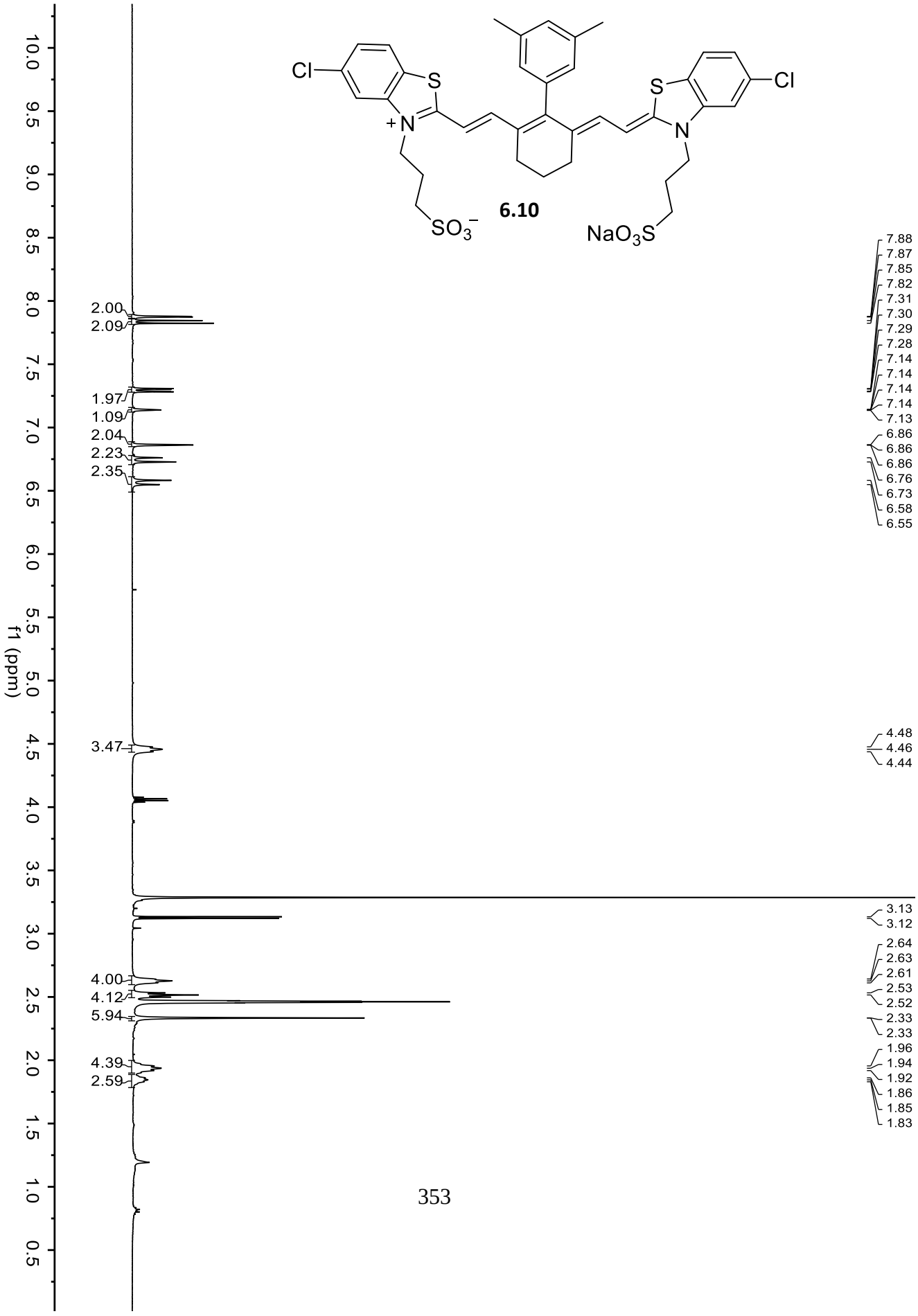
Cl
S
+N
S
N
Cl
SO3−
NaO3S
6.10
f1 (ppm)
10.0
9.5
9.0
8.5
8.0
7.5
7.0
6.5
6.0
5.5
5.0
4.5
4.0
3.5
3.0
2.5
2.0
1.5
1.0
0.5
2.00
2.09
1.97
1.09
2.04
2.23
2.35
3.47
4.00
4.12
5.94
4.39
2.59
7.88
7.87
7.85
7.82
7.31
7.30
7.29
7.28
7.14
7.14
7.14
7.14
7.13
6.86
6.86
6.86
6.76
6.73
6.58
6.55
4.48
4.46
4.44
3.13
3.12
2.64
2.63
2.61
2.53
2.52
2.33
2.33
1.96
1.94
1.92
1.86
1.85
1.83

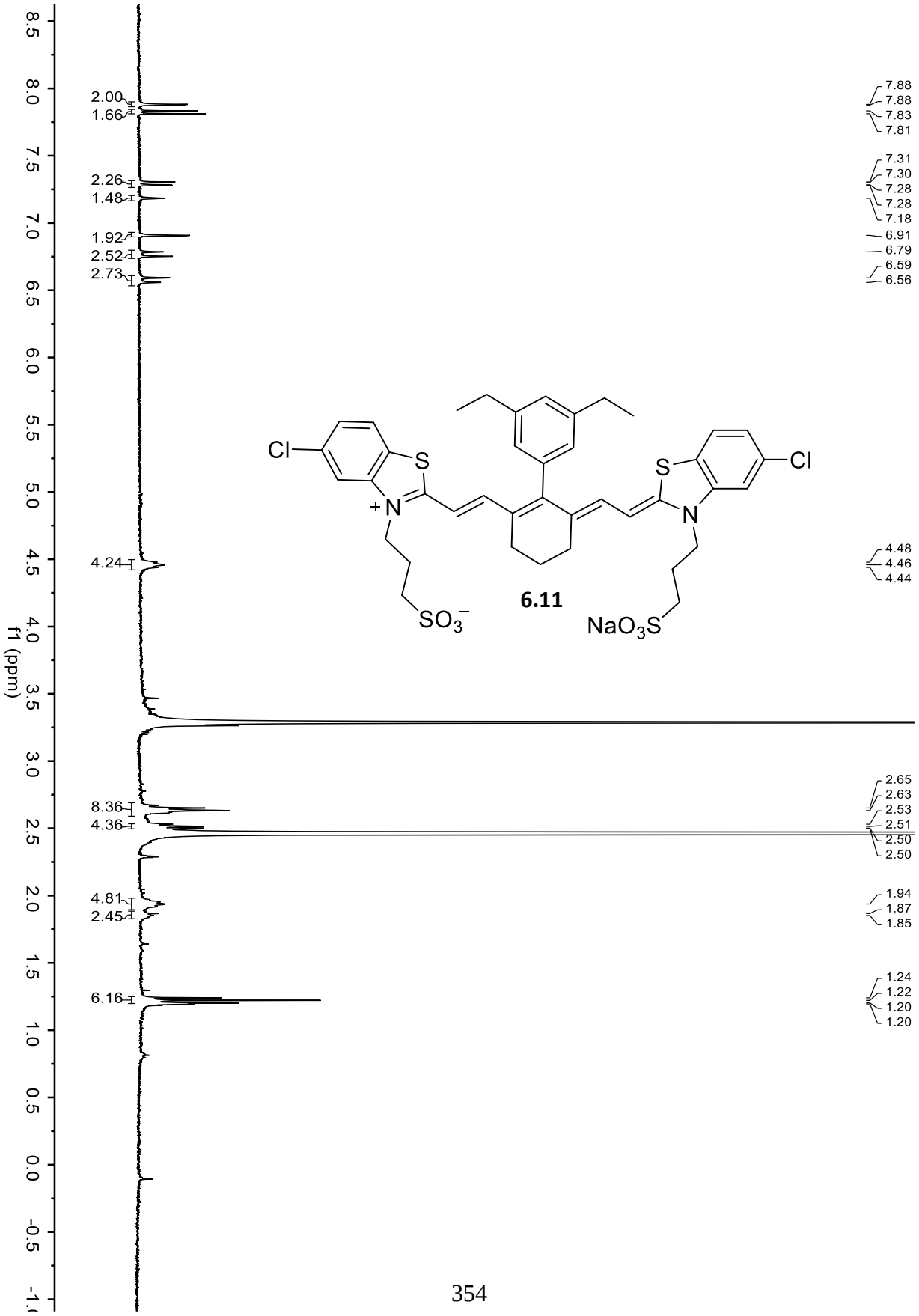
f1 (ppm)
8.5
8.0
7.5
7.0
6.5
6.0
5.5
5.0
4.5
4.0
3.5
3.0
2.5
2.0
1.5
1.0
0.5
0.0
-0.5
2.00
1.66
2.26
1.48
1.92
2.52
2.73
4.24
8.36
4.36
4.81
2.45
6.16
7.88
7.88
7.83
7.81
7.31
7.30
7.28
7.28
7.18
6.91
6.79
6.59
6.56
4.48
4.46
4.44
2.65
2.63
2.53
2.51
2.50
2.50
1.94
1.87
1.85
1.24
1.22
1.20
1.20
Cl
S
+N
SO3−
S
N
Cl
NaO3S
6.11

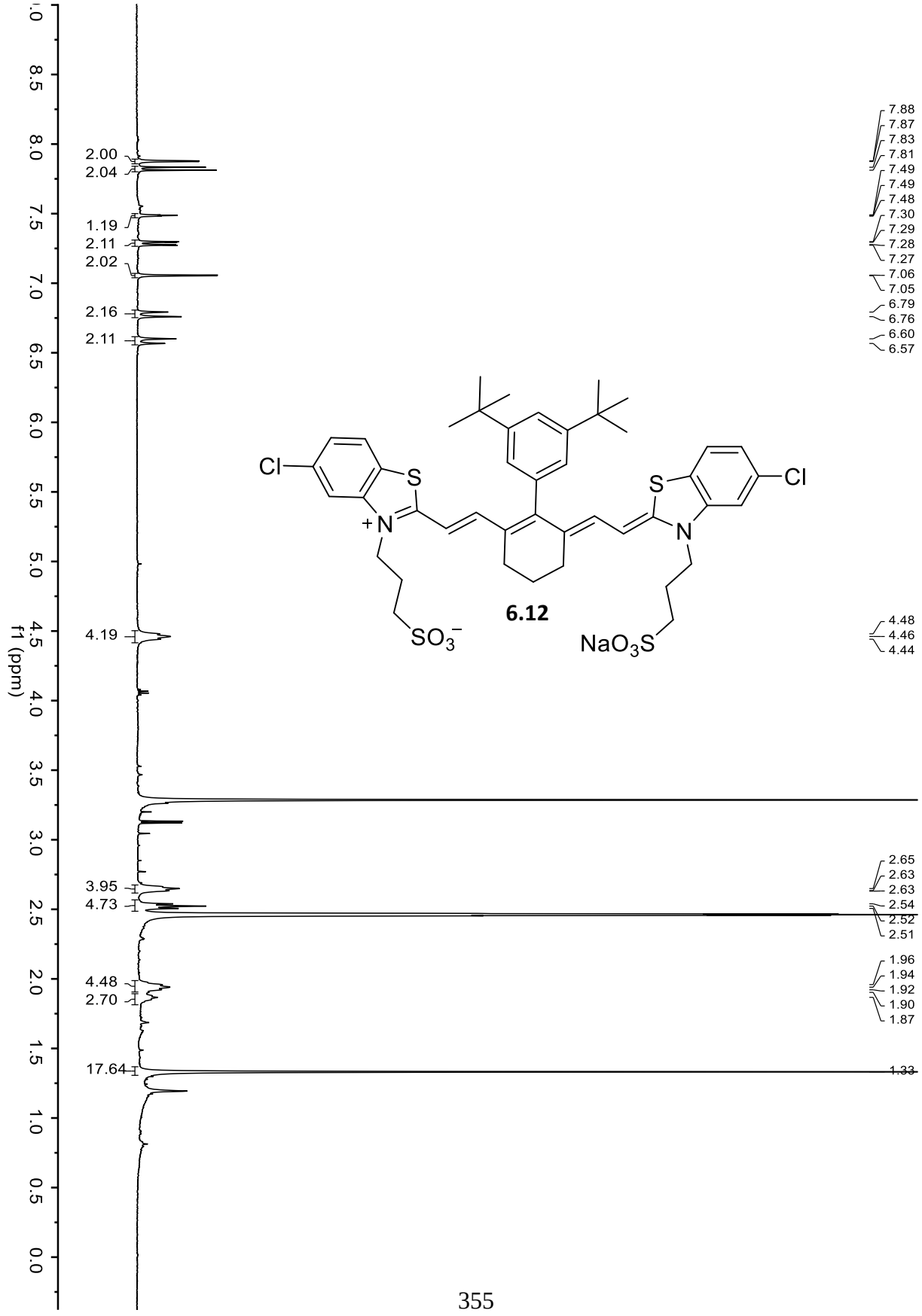
9.0
8.5
8.0
7.5
7.0
6.5
6.0
5.5
5.0
4.5
4.0
3.5
3.0
2.5
2.0
1.5
1.0
0.5
0.0
f1 (ppm)
2.00
2.04
1.19
2.11
2.02
2.16
2.11
4.19
3.95
4.73
4.48
2.70
17.64
7.88
7.87
7.83
7.81
7.49
7.49
7.48
7.30
7.29
7.28
7.27
7.06
7.05
6.79
6.76
6.60
6.57
4.48
4.46
4.44
2.65
2.63
2.63
2.54
2.52
2.51
1.96
1.94
1.92
1.90
1.87
1.33
Cl
S
+N
SO3−
S
N
Cl
NaO3S
6.12

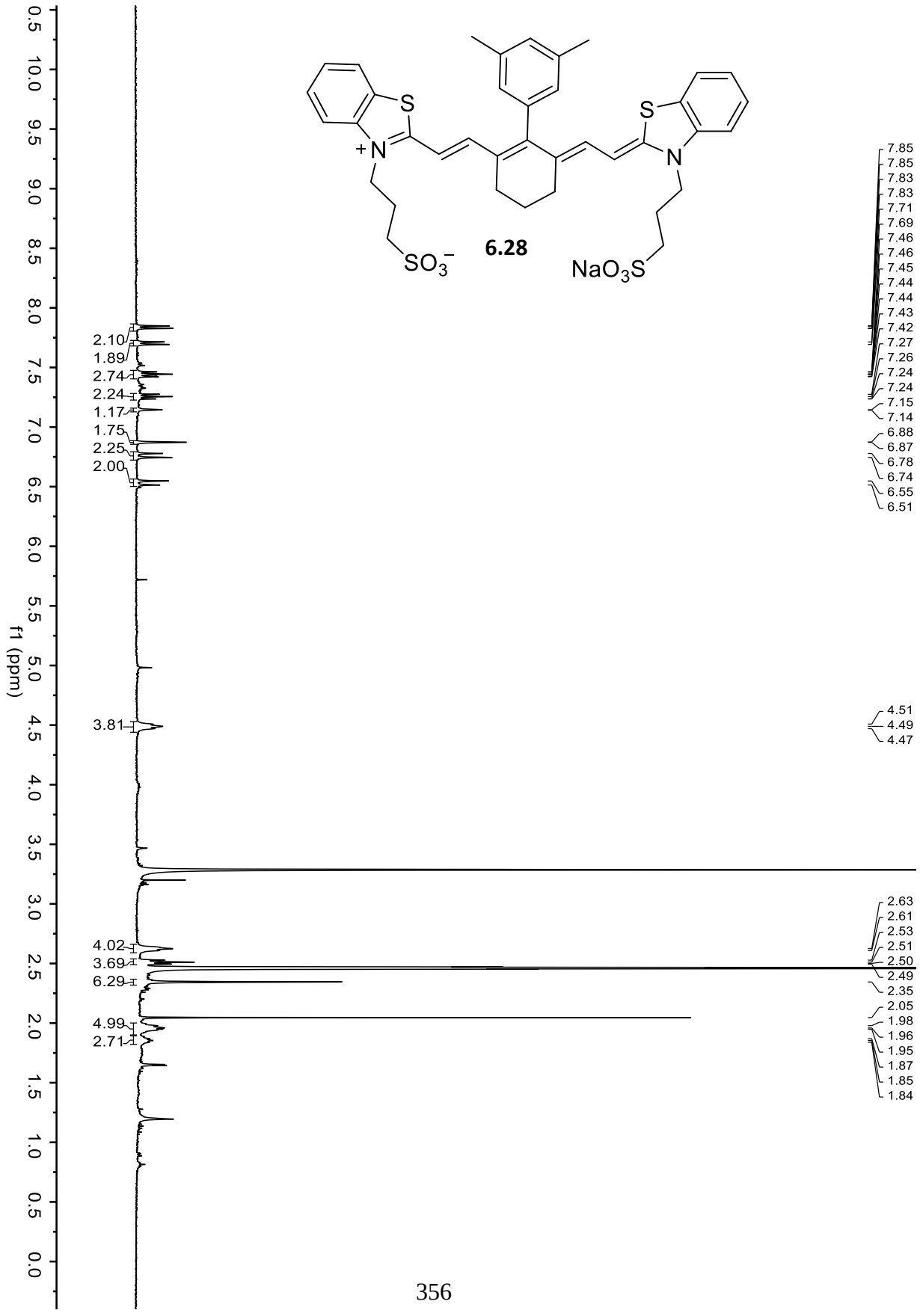
6.28
f1 (ppm)
2.10
1.89
2.74
2.24
1.17
1.75
2.25
2.00
3.81
4.02
3.69
6.29
4.99
2.71
7.85
7.85
7.83
7.83
7.71
7.69
7.46
7.46
7.45
7.44
7.44
7.43
7.42
7.27
7.26
7.24
7.24
7.15
7.14
6.88
6.87
6.78
6.74
6.55
6.51
4.51
4.49
4.47
2.63
2.61
2.53
2.51
2.50
2.49
2.35
2.05
1.98
1.96
1.95
1.87
1.85
1.84

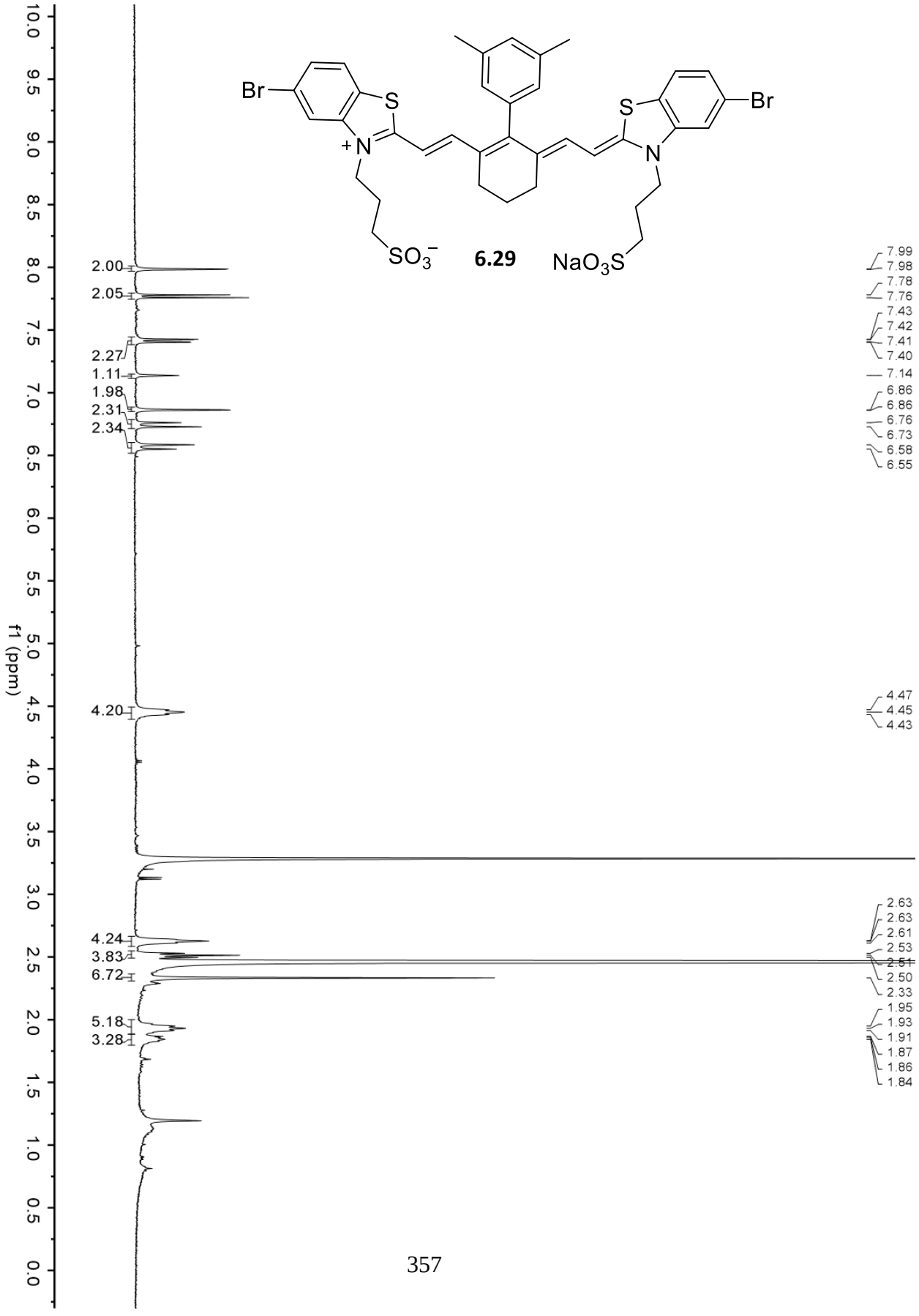
Br
S
+N
S
N
Br
SO3−
6.29
NaO3S
f1 (ppm)
10.0
9.5
9.0
8.5
8.0
7.5
7.0
6.5
6.0
5.5
5.0
4.5
4.0
3.5
3.0
2.5
2.0
1.5
1.0
0.5
0.0
2.00
2.05
2.27
1.11
1.98
2.31
2.34
4.20
4.24
3.83
6.72
5.18
3.28
7.99
7.98
7.78
7.76
7.43
7.42
7.41
7.40
7.14
6.86
6.86
6.76
6.73
6.58
6.55
4.47
4.45
4.43
2.63
2.63
2.61
2.53
2.51
2.50
2.33
1.95
1.93
1.91
1.87
1.86
1.84

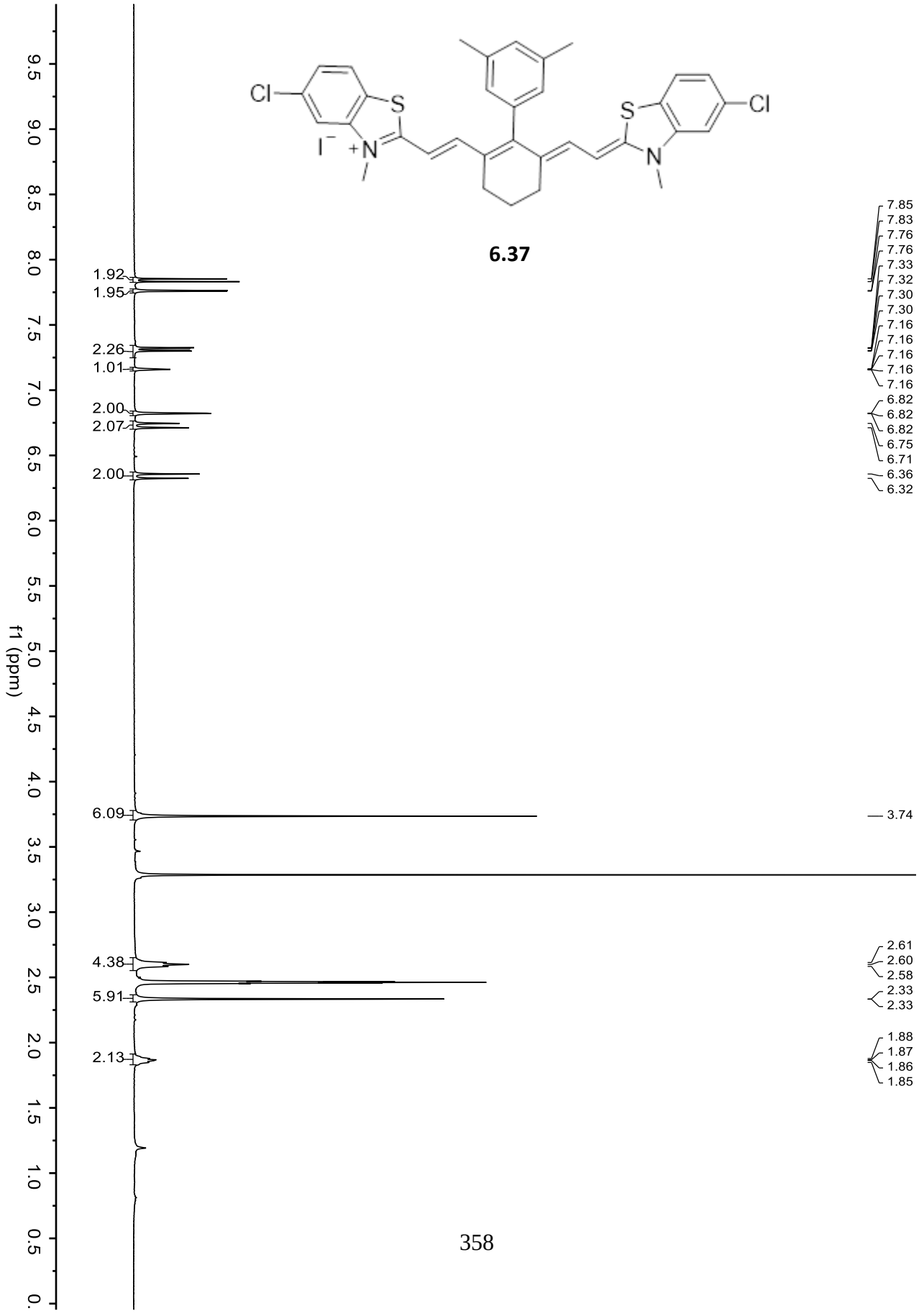
Cl
S
I⁻ +N
S
N
Cl
6.37
1.92
1.95
2.26
1.01
2.00
2.07
2.00
6.09
4.38
5.91
2.13
7.85
7.83
7.76
7.76
7.33
7.32
7.30
7.30
7.16
7.16
7.16
7.16
7.16
6.82
6.82
6.82
6.75
6.71
6.36
6.32
3.74
2.61
2.60
2.58
2.33
2.33
1.88
1.87
1.86
1.85
f1 (ppm)
9.5
9.0
8.5
8.0
7.5
7.0
6.5
6.0
5.5
5.0
4.5
4.0
3.5
3.0
2.5
2.0
1.5
1.0
0.5
0.

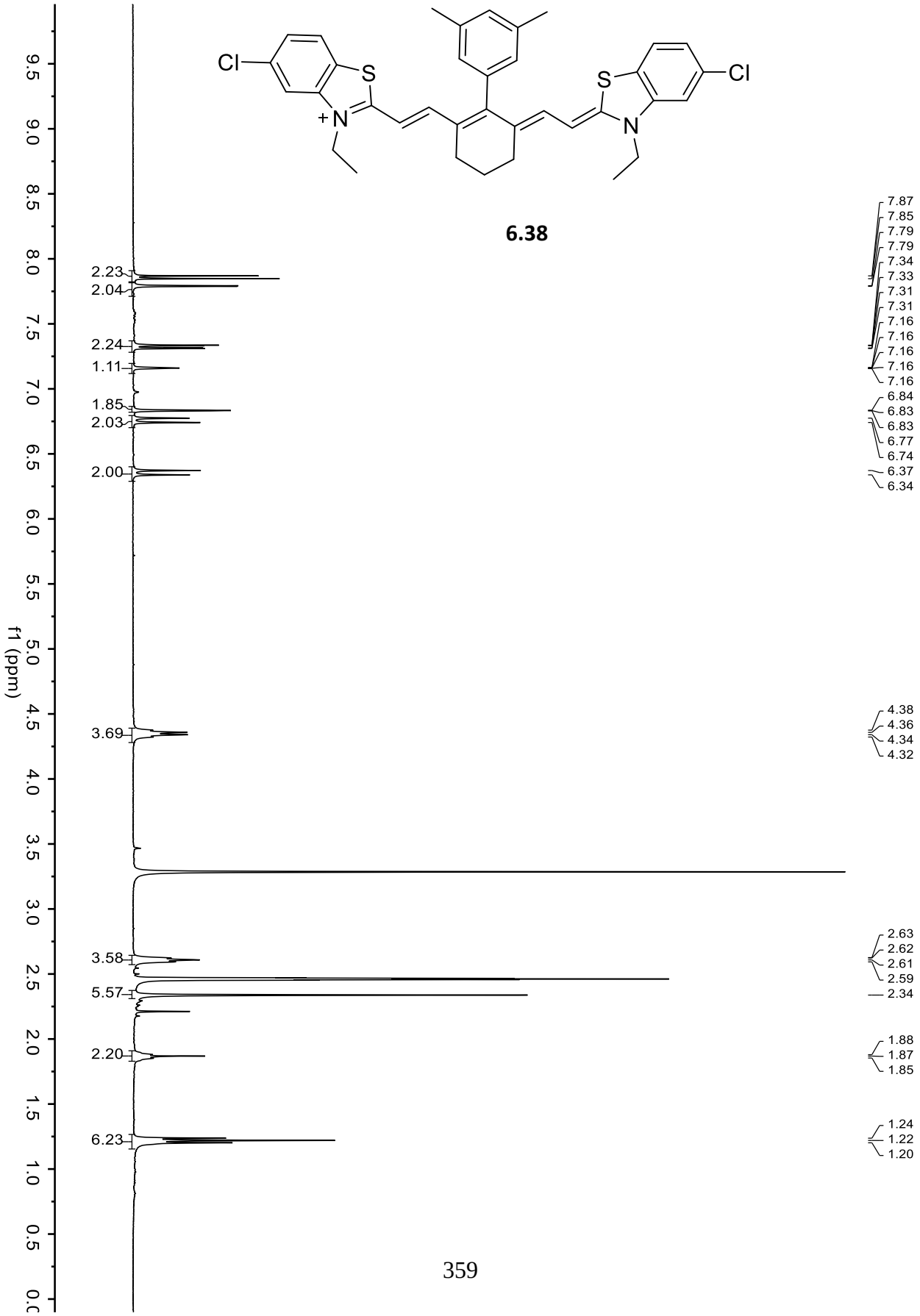
Cl
S
+N
S
N
Cl
6.38
f1 (ppm)
9.5
9.0
8.5
8.0
7.5
7.0
6.5
6.0
5.5
5.0
4.5
4.0
3.5
3.0
2.5
2.0
1.5
1.0
0.5
2.23
2.04
2.24
1.11
1.85
2.03
2.00
3.69
3.58
5.57
2.20
6.23
7.87
7.85
7.79
7.79
7.34
7.33
7.31
7.31
7.16
7.16
7.16
7.16
7.16
6.84
6.83
6.83
6.77
6.74
6.37
6.34
4.38
4.36
4.34
4.32
2.63
2.62
2.61
2.59
2.34
1.88
1.87
1.85
1.24
1.22
1.20

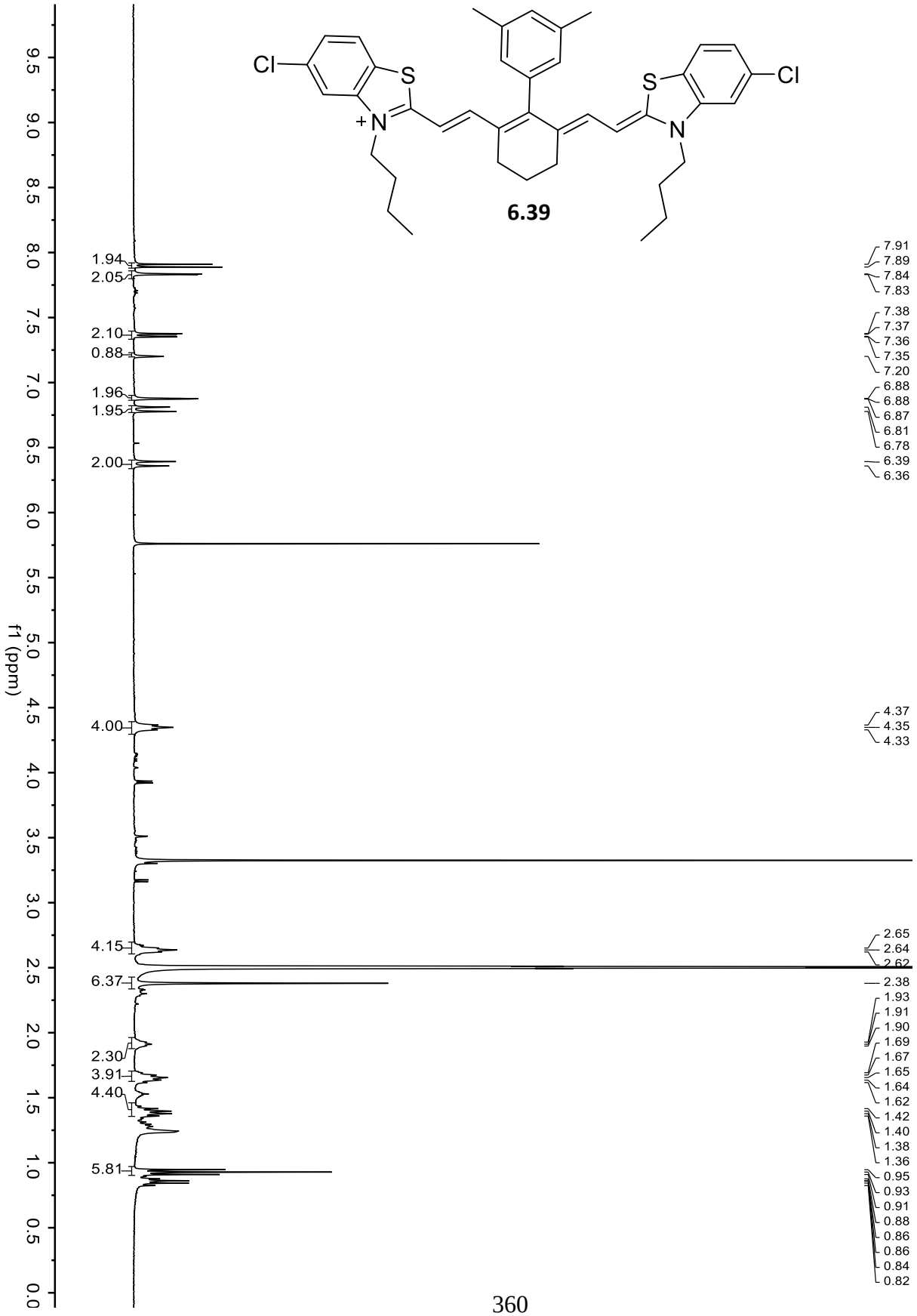
Cl
S
+N
S
N
Cl
6.39
f1 (ppm)
9.5
9.0
8.5
8.0
7.5
7.0
6.5
6.0
5.5
5.0
4.5
4.0
3.5
3.0
2.5
2.0
1.5
1.0
0.5
0.0
1.94
2.05
2.10
0.88
1.96
1.95
2.00
4.00
4.15
6.37
2.30
3.91
4.40
5.81
7.91
7.89
7.84
7.83
7.38
7.37
7.36
7.35
7.20
6.88
6.88
6.87
6.81
6.78
6.39
6.36
4.37
4.35
4.33
2.65
2.64
2.62
2.38
1.93
1.91
1.90
1.69
1.67
1.65
1.64
1.62
1.42
1.40
1.38
1.36
0.95
0.93
0.91
0.88
0.86
0.86
0.84
0.82

Cl
S
Br⁻ +N
Ph
S
Cl
N
Ph

6.40

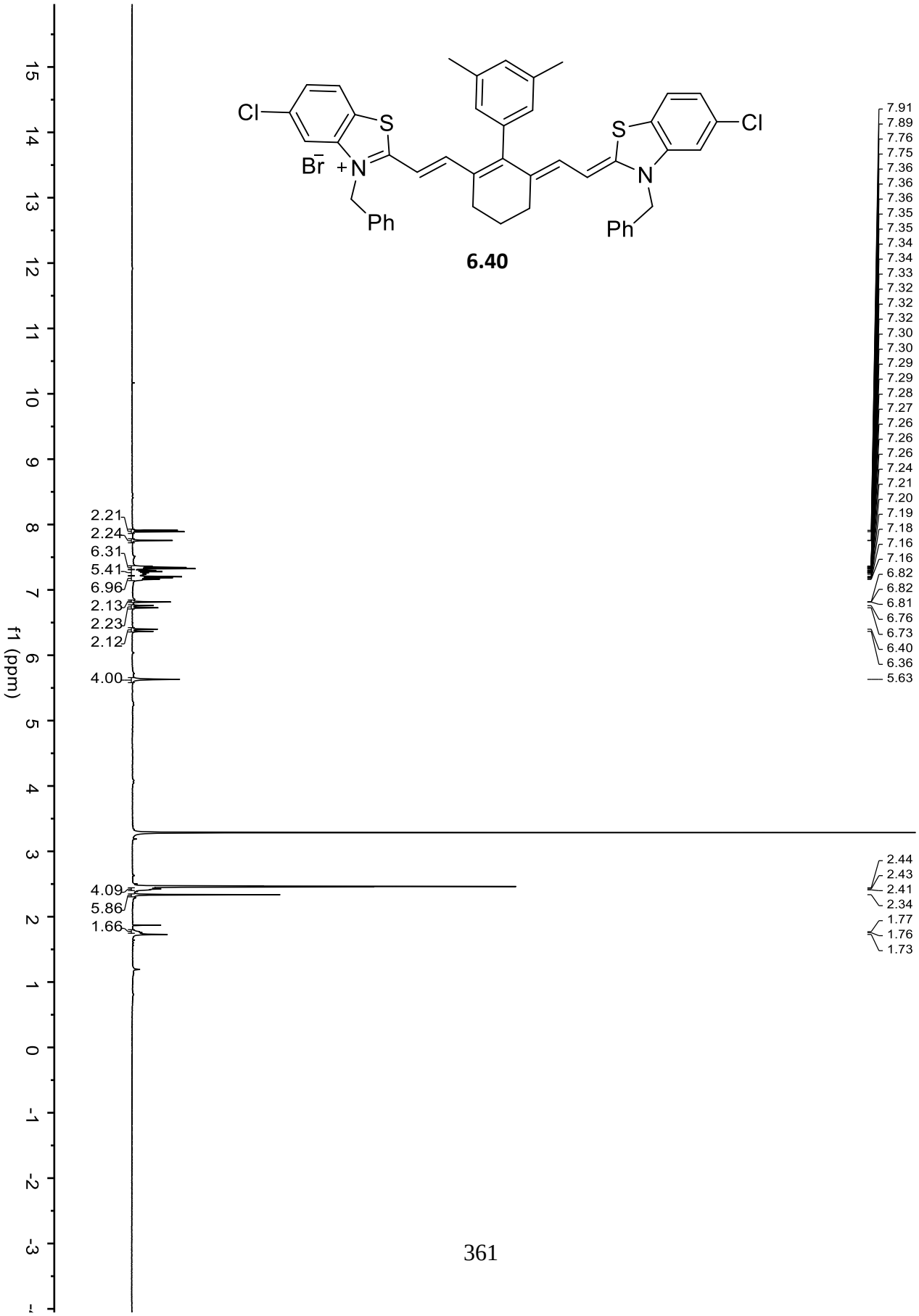
f1 (ppm)
15
14
13
12
11
10
9
8
7
6
5
4
3
2
1
0
-1
-2
-3
2.21
2.24
6.31
5.41
6.96
2.13
2.23
2.12
4.00
4.09
5.86
1.66
7.91
7.89
7.76
7.75
7.36
7.36
7.36
7.35
7.35
7.34
7.34
7.33
7.32
7.32
7.32
7.30
7.30
7.29
7.29
7.28
7.27
7.26
7.26
7.26
7.24
7.21
7.20
7.19
7.18
7.16
7.16
6.82
6.82
6.81
6.76
6.73
6.40
6.36
5.63
2.44
2.43
2.41
2.34
1.77
1.76
1.73

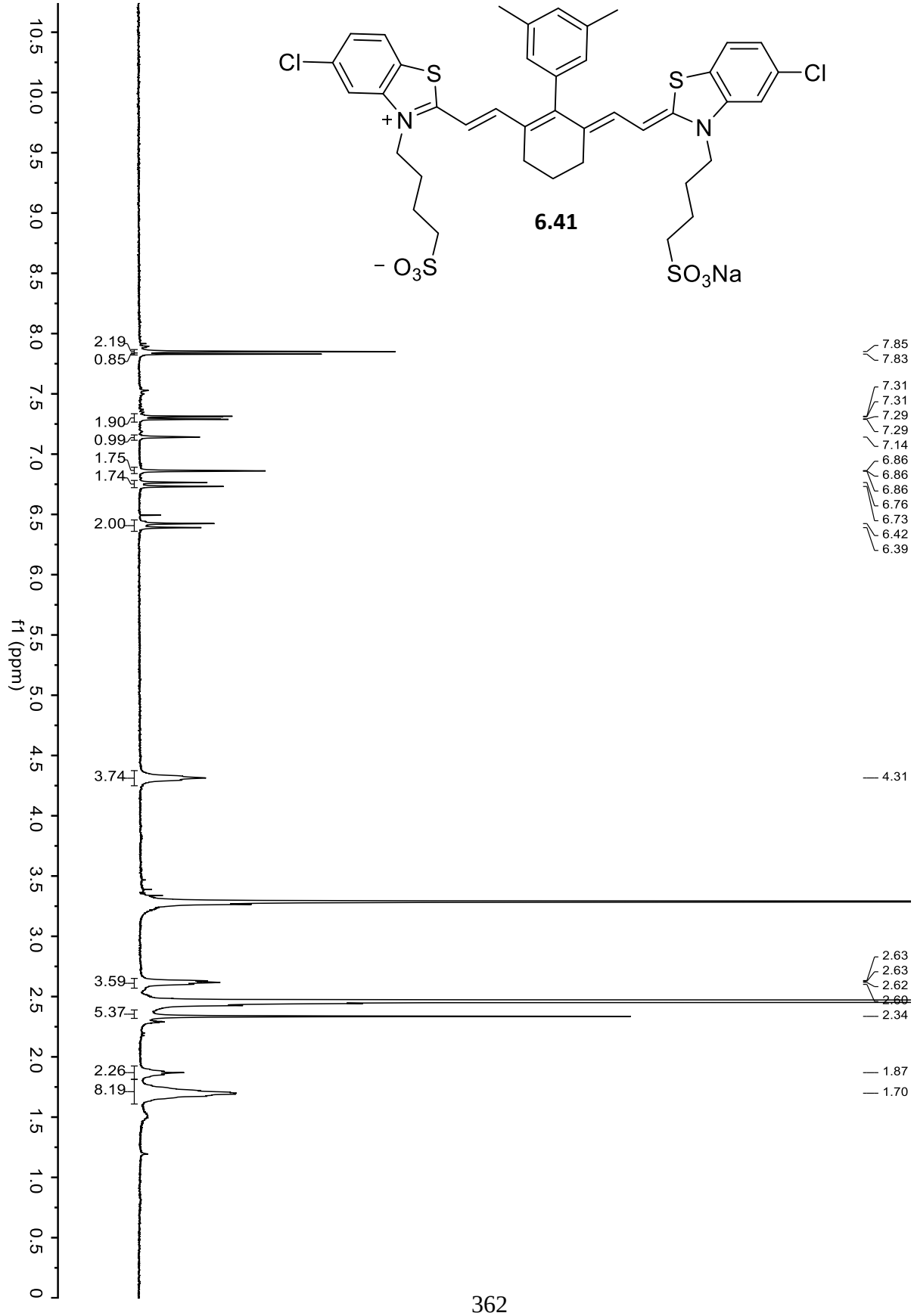
Cl
S
+N
S
N
Cl
6.41
− O3S
SO3Na
f1 (ppm)
2.19
0.85
1.90
0.99
1.75
1.74
2.00
3.74
3.59
5.37
2.26
8.19
7.85
7.83
7.31
7.31
7.29
7.29
7.14
6.86
6.86
6.86
6.76
6.73
6.42
6.39
4.31
2.63
2.63
2.62
2.60
2.34
1.87
1.70

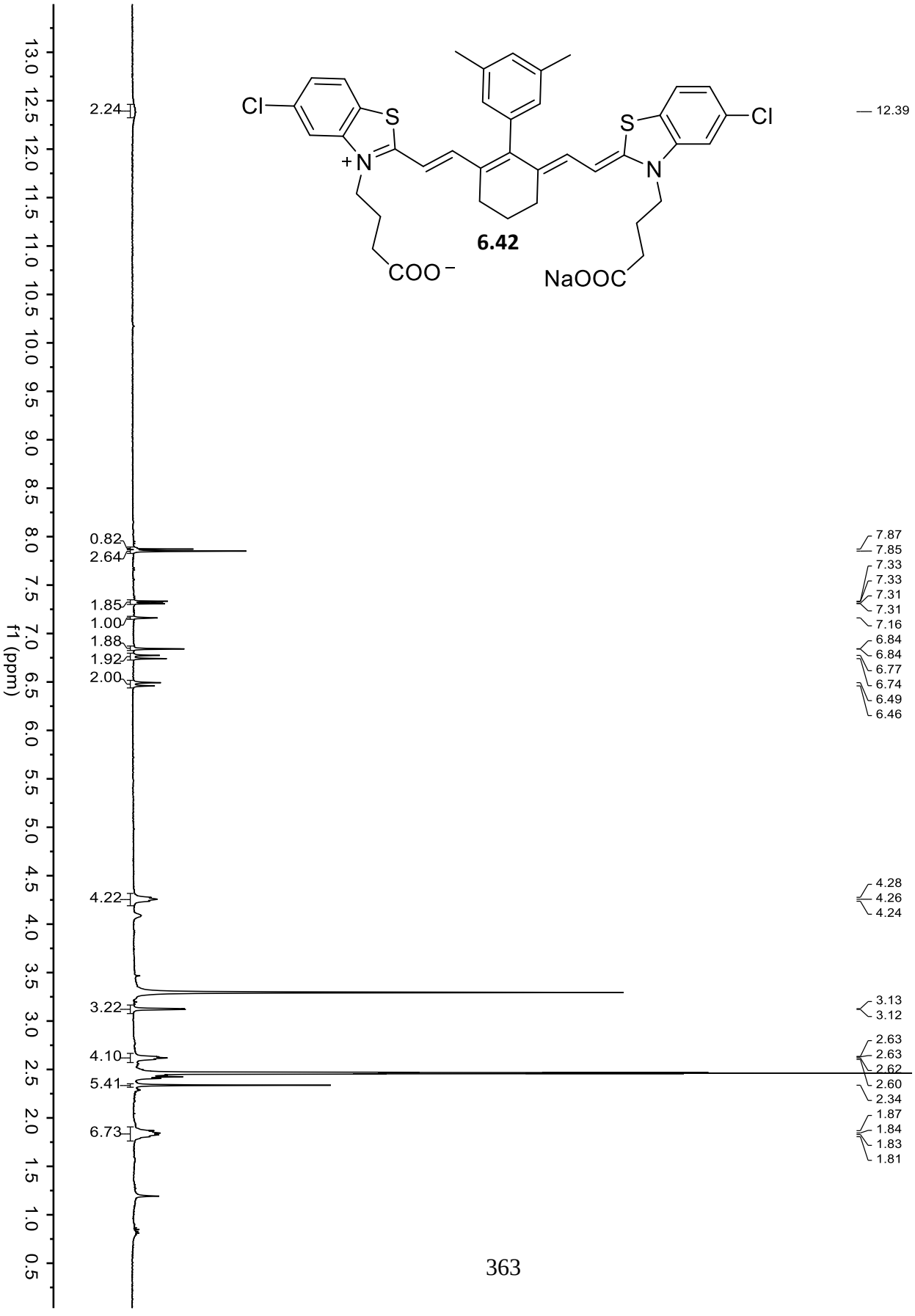
Cl
S
+N
S
N
Cl
COO⁻
NaOOC
6.42
f1 (ppm)
2.24
0.82
2.64
1.85
1.00
1.88
1.92
2.00
4.22
3.22
4.10
5.41
6.73
12.39
7.87
7.85
7.33
7.33
7.31
7.31
7.16
6.84
6.84
6.77
6.74
6.49
6.46
4.28
4.26
4.24
3.13
3.12
2.63
2.63
2.62
2.60
2.34
1.87
1.84
1.83
1.81

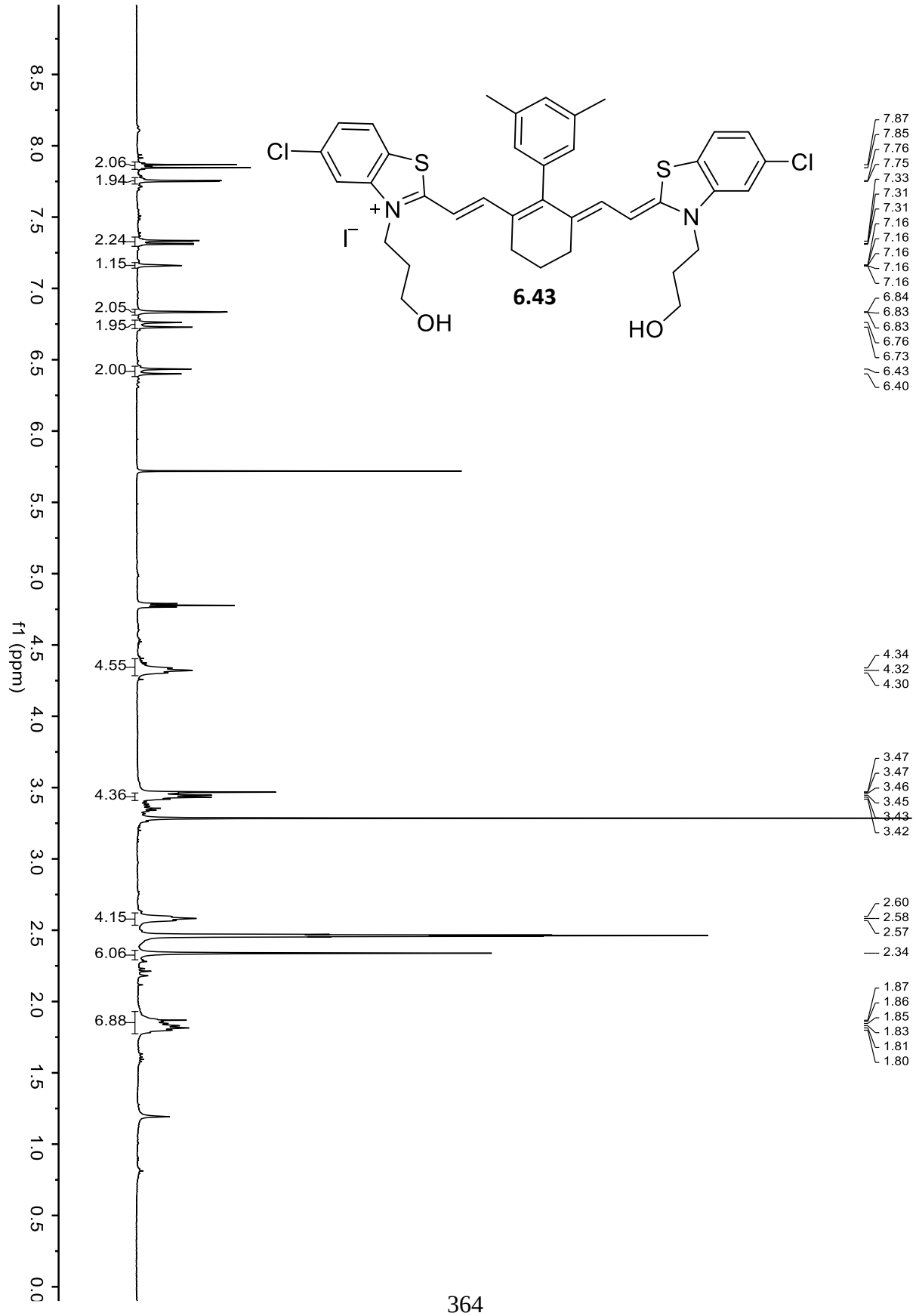
Cl
S
+N
I⁻
OH
S
N
Cl
HO
6.43
f1 (ppm)
8.5
8.0
7.5
7.0
6.5
6.0
5.5
5.0
4.5
4.0
3.5
3.0
2.5
2.0
1.5
1.0
0.5
0.0
2.06
1.94
2.24
1.15
2.05
1.95
2.00
4.55
4.36
4.15
6.06
6.88
7.87
7.85
7.76
7.75
7.33
7.31
7.31
7.16
7.16
7.16
7.16
7.16
6.84
6.83
6.83
6.76
6.73
6.43
6.40
4.34
4.32
4.30
3.47
3.47
3.46
3.45
3.43
3.42
2.60
2.58
2.57
2.34
1.87
1.86
1.85
1.83
1.81
1.80

6.6.2 ^{13}C NMR Spectra

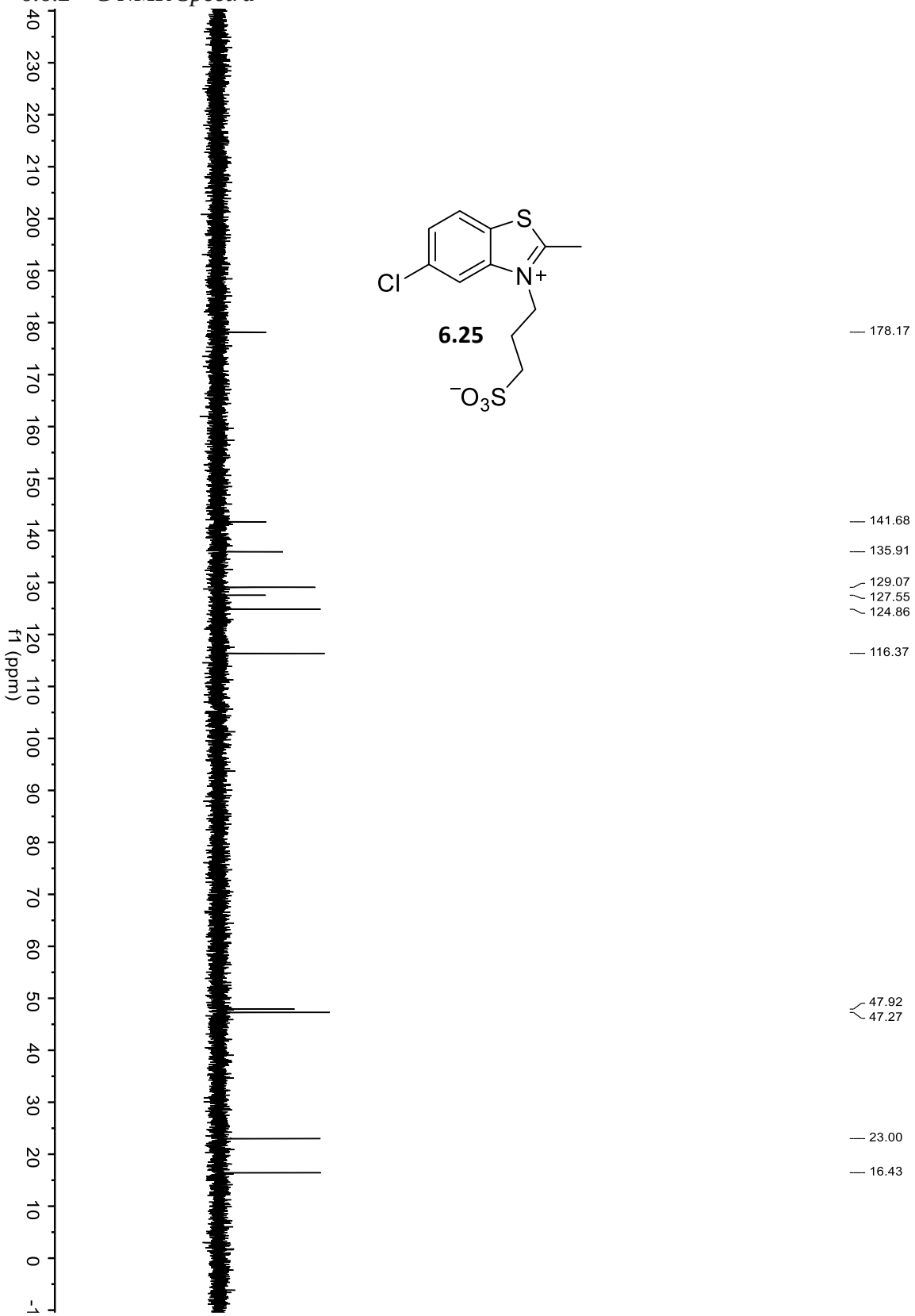

6.25

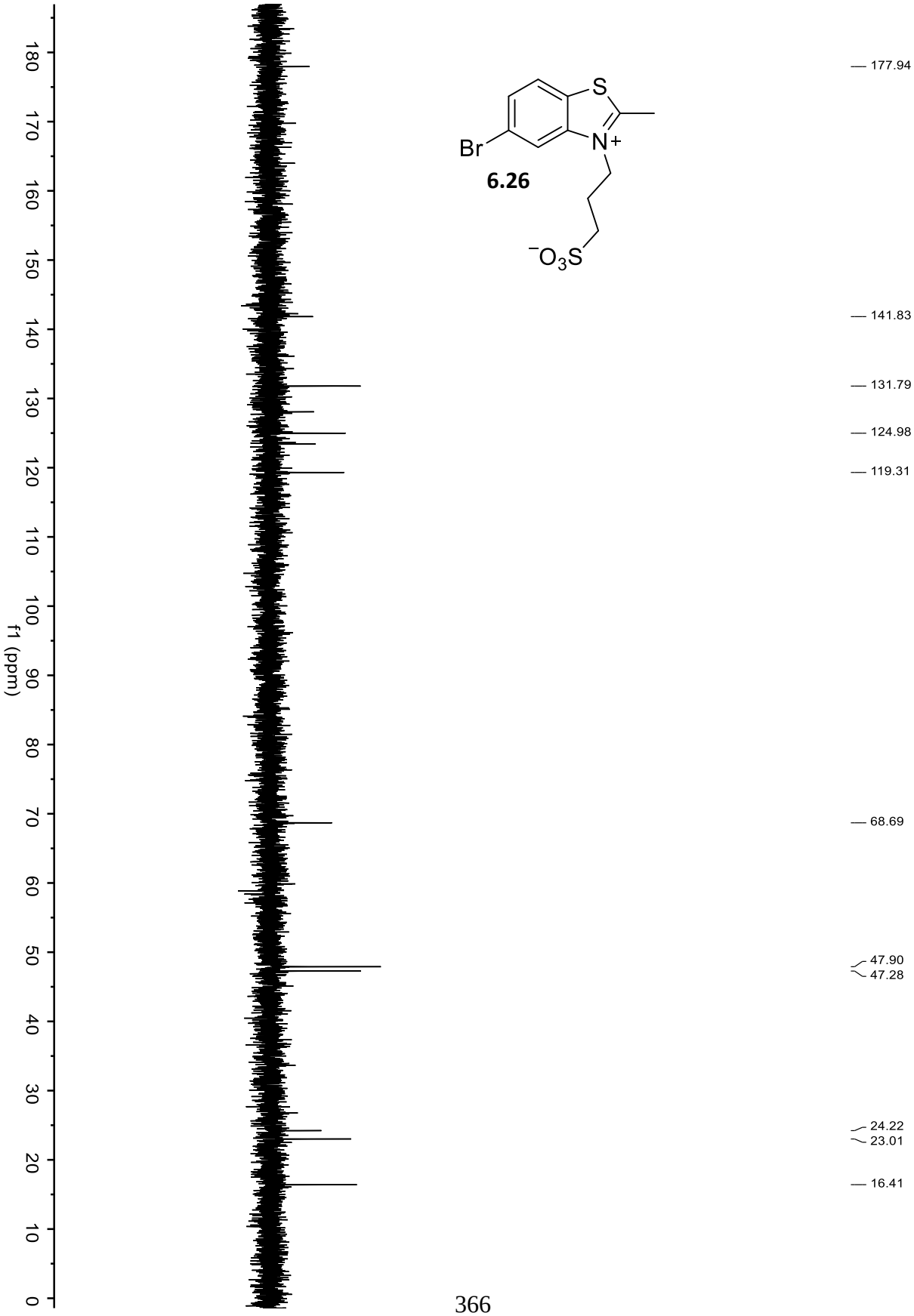
177.94
141.83
131.79
124.98
119.31
68.69
47.90
47.28
24.22
23.01
16.41
f1 (ppm)
Br
S
N+
$^{-}O_3S$
6.26

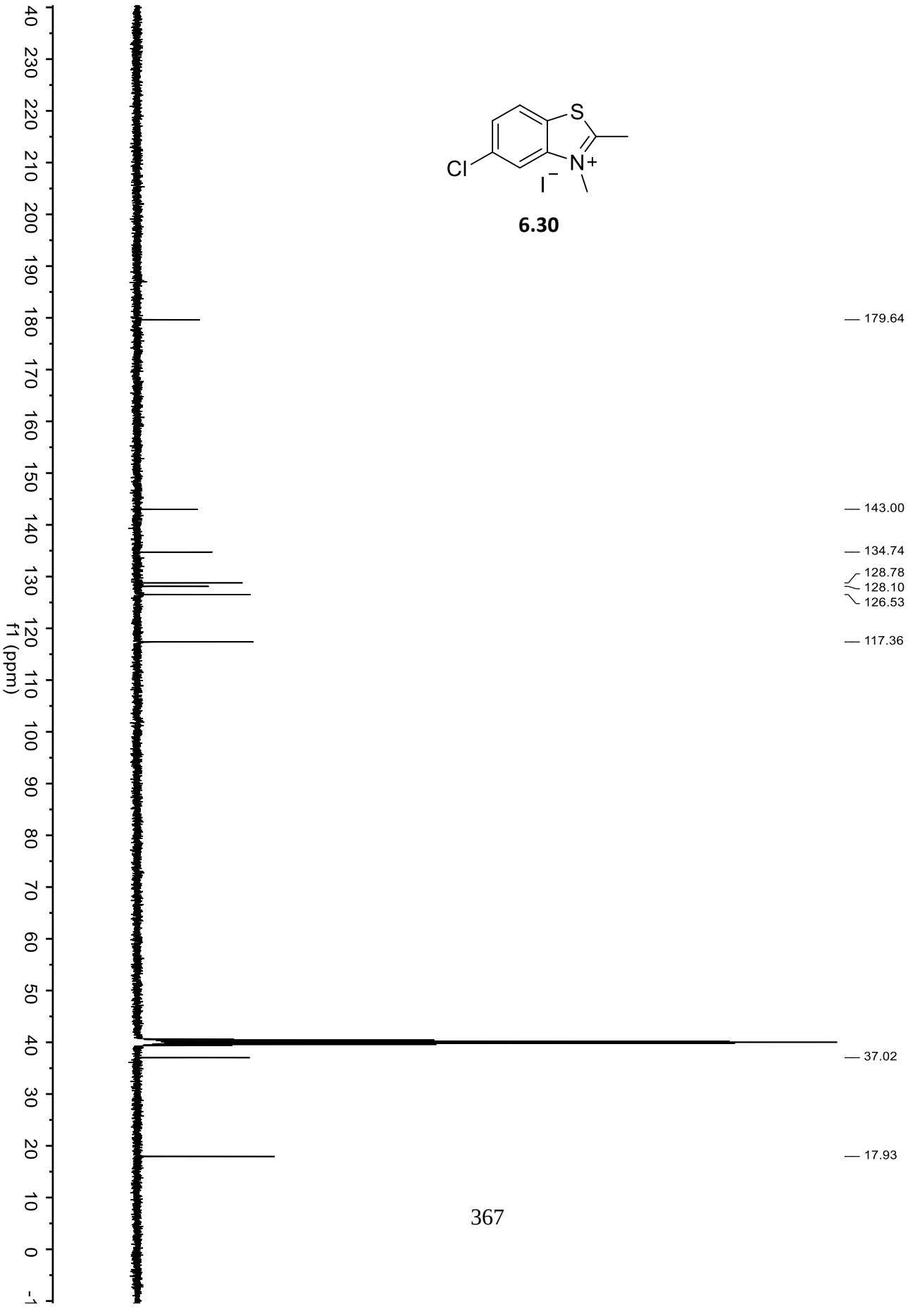
S
Cl
N+
I−
179.64
143.00
134.74
128.78
128.10
126.53
117.36
37.02
17.93
f1 (ppm)

6.30

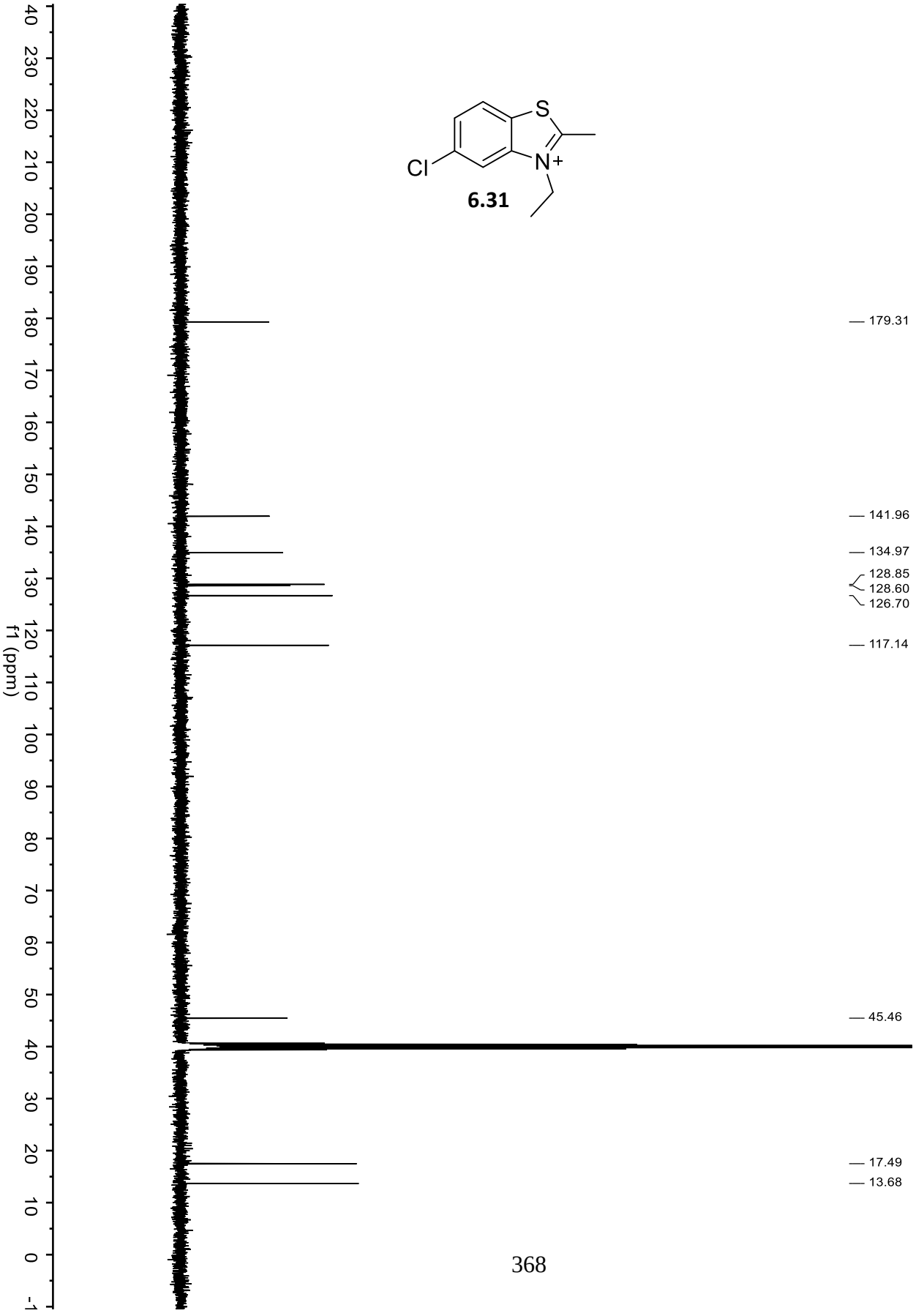
S
Cl
N+
6.31
179.31
141.96
134.97
128.85
128.60
126.70
117.14
45.46
17.49
13.68
f1 (ppm)

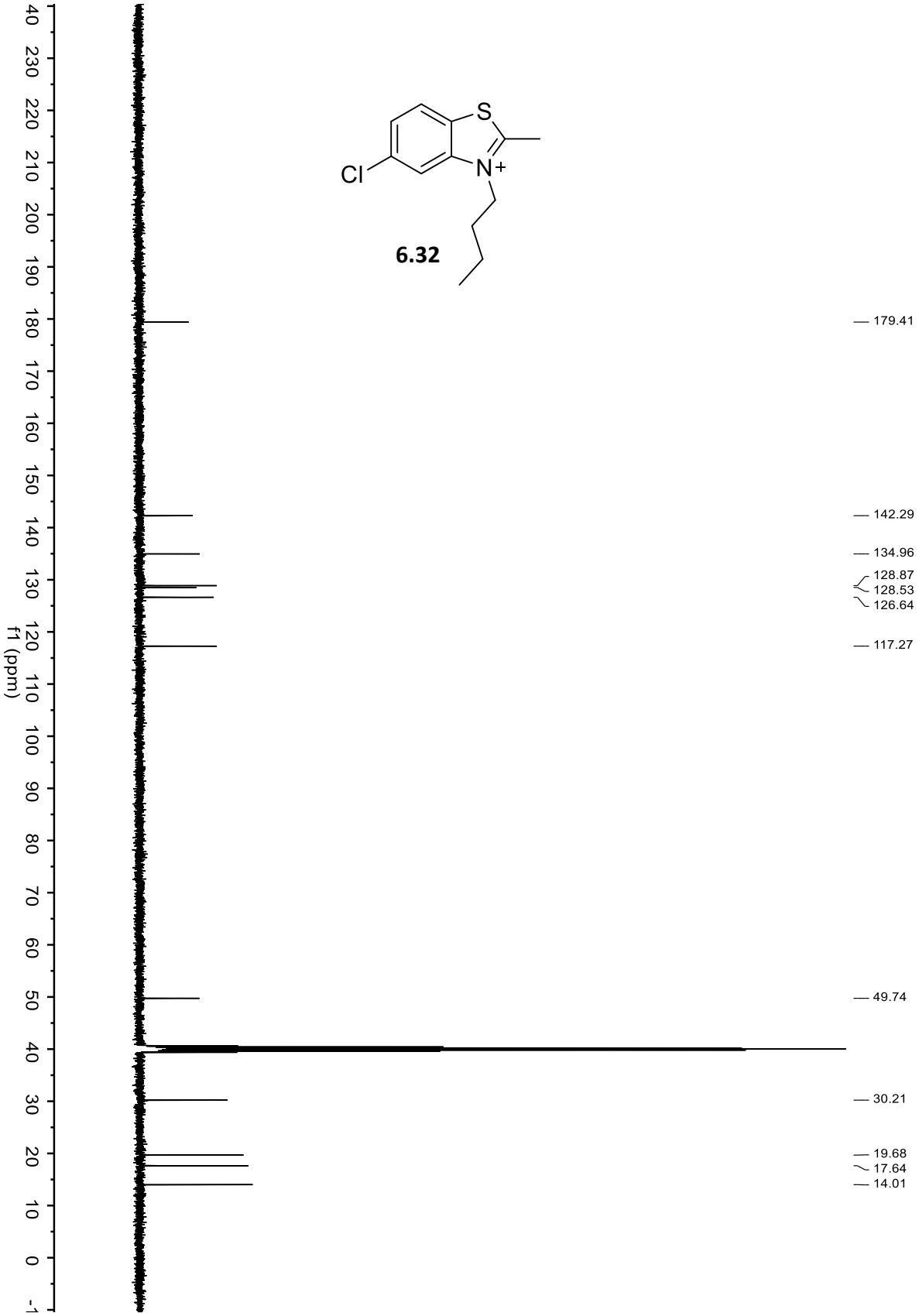
S
Cl
N+
6.32
179.41
142.29
134.96
128.87
128.53
126.64
117.27
49.74
30.21
19.68
17.64
14.01
f1 (ppm)

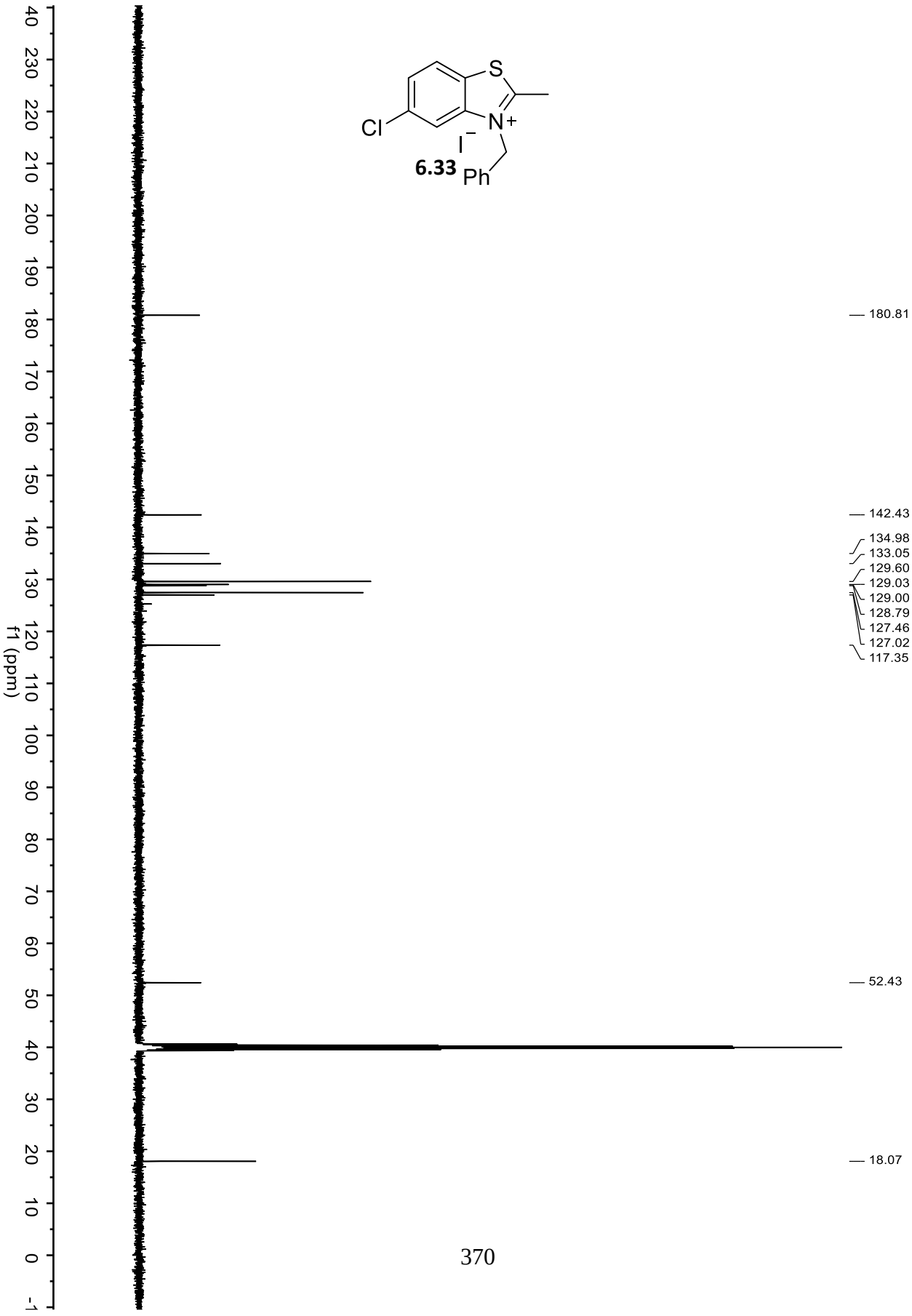
S
Cl
N+
I−
6.33
Ph
180.81
142.43
134.98
133.05
129.60
129.03
129.00
128.79
127.46
127.02
117.35
52.43
18.07
f1 (ppm)

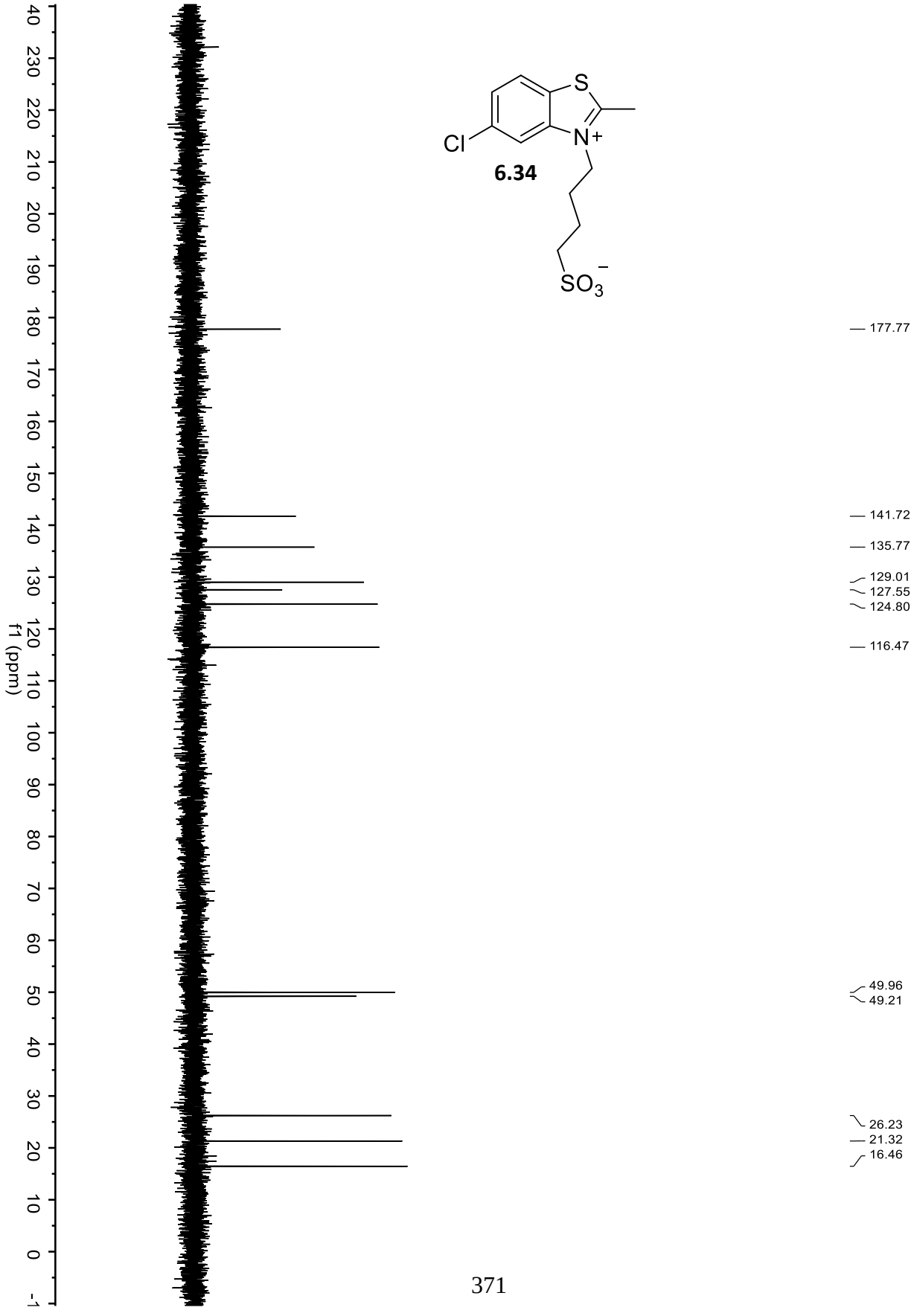
S
Cl
N+
6.34
SO3 −
177.77
141.72
135.77
129.01
127.55
124.80
116.47
49.96
49.21
26.23
21.32
16.46
f1 (ppm)

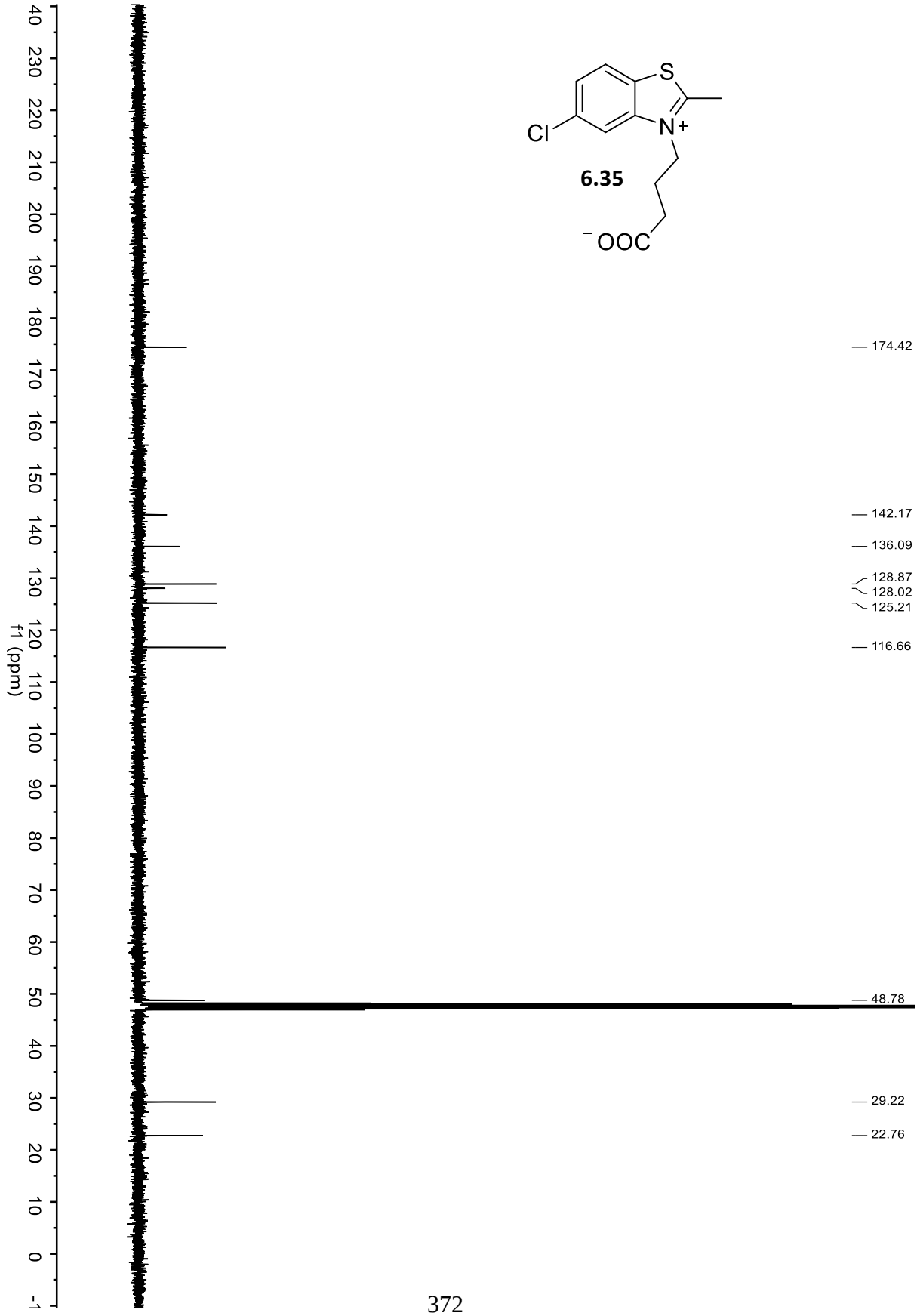
S
Cl
N+
6.35
⁻OOC
174.42
142.17
136.09
128.87
128.02
125.21
116.66
48.78
29.22
22.76
f1 (ppm)

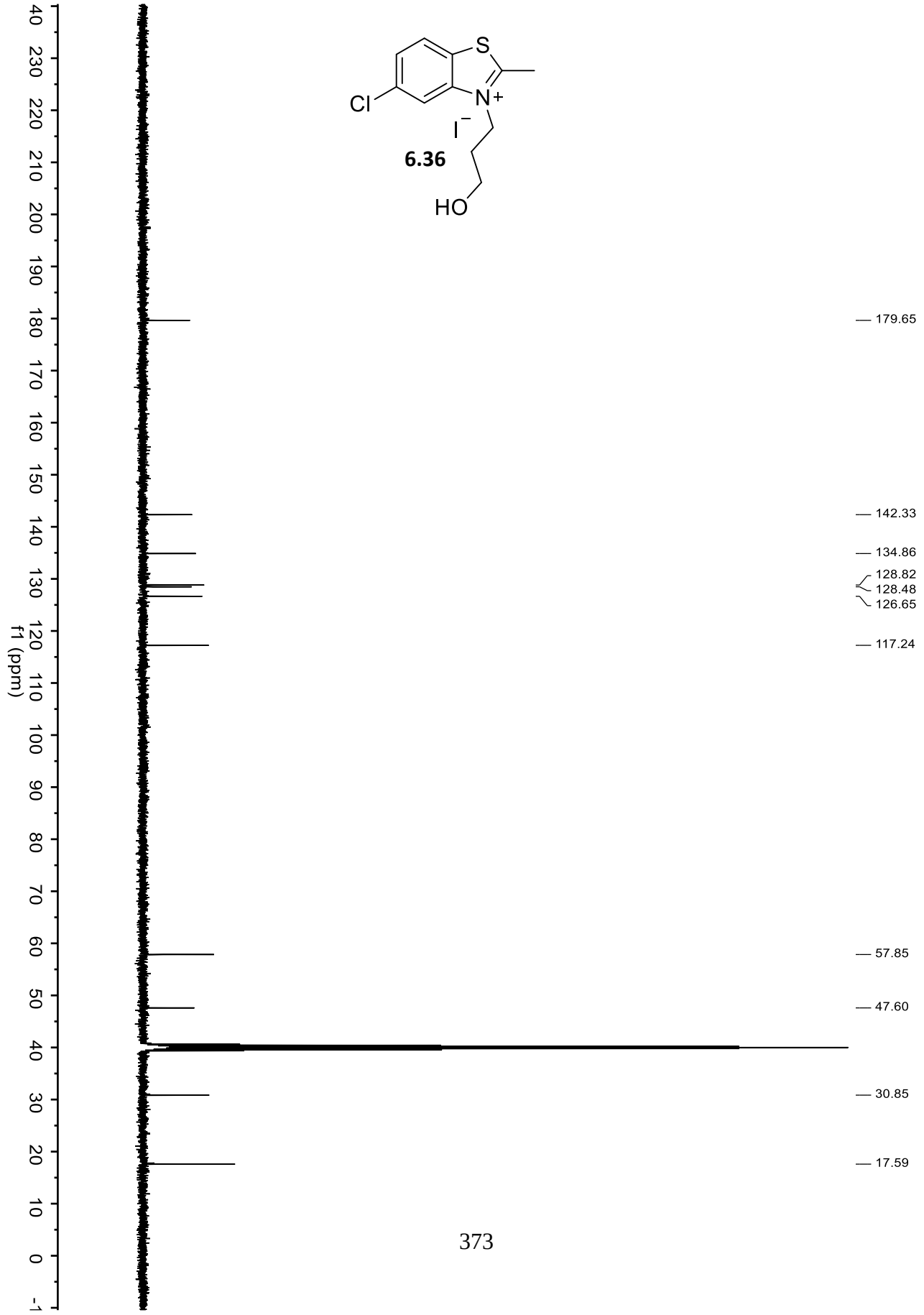
S
Cl
N+
I−
6.36
HO
179.65
142.33
134.86
128.82
128.48
126.65
117.24
57.85
47.60
30.85
17.59
f1 (ppm)

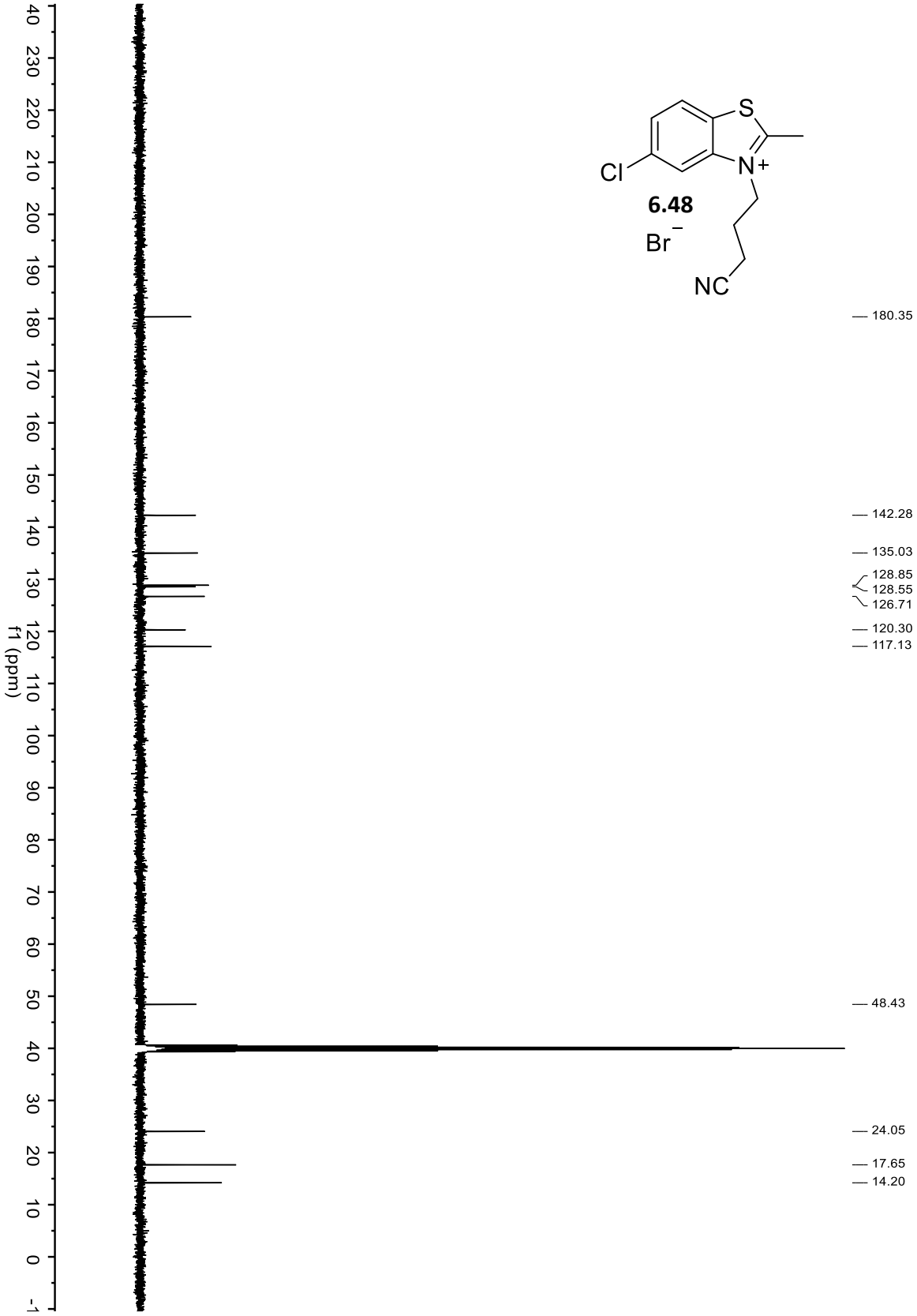
S
Cl
N+
6.48
Br−
NC
180.35
142.28
135.03
128.85
128.55
126.71
120.30
117.13
48.43
24.05
17.65
14.20
f1 (ppm)

6.7 References

(1) Bricks, J. L.; Slominskii, Y. L.; Panas, I. D.; Demchenko, A. P. Fluorescent J-Aggregates of Cyanine Dyes: Basic Research and Applications Review. *Methods Appl. Fluoresc.* **2018**, *6* (1).

(2) Chen, Z.; Liu, Y.; Wagner, W.; Stepanenko, V.; Ren, X.; Ogi, S.; Würthner, F. Near-IR Absorbing J-Aggregate of an Amphiphilic BF_2 -Azadipyrromethene Dye by Kinetic Cooperative Self-Assembly. *Angew. Chemie Int. Ed.* **2017**, *56* (21), 5729–5733.

(3) Würthner, F.; Kaiser, T. E.; Saha-Möller, C. R. J-Aggregates: From Serendipitous Discovery to Supramolecular Engineering of Functional Dye Materials. *Angew. Chemie Int. Ed.* **2011**, *50* (15), 3376–3410.

(4) Kaiser, T. E.; Wang, H.; Stepanenko, V.; Würthner, F. Supramolecular Construction of Fluorescent J-Aggregates Based on Hydrogen-Bonded Perylene Dyes. *Angew. Chemie Int. Ed.* **2007**, *46* (29), 5541–5544.

(5) Bricks, J. L.; Kachkovskii, A. D.; Slominskii, Y. L.; Gerasov, A. O.; Popov, S. V. Molecular Design of near Infrared Polymethine Dyes: A Review. *Dye. Pigment.* **2015**, *121*, 238–255.

(6) Thimsen, E.; Sadtler, B.; Berezin, M. Y. Shortwave-Infrared (SWIR) Emitters for Biological Imaging: A Review of Challenges and Opportunities. *Nanophotonics* **2017**, *6* (5), 1043–1054. https://doi.org/10.1515/nanoph-2017-0039.

(7) Ding, B.; Xiao, Y.; Zhou, H.; Zhang, X.; Qu, C.; Xu, F.; Deng, Z.; Cheng, Z.; Hong, X. Polymethine Thiopyrylium Fluorophores with Absorption beyond 1000 Nm for Biological

Imaging in the Second Near-Infrared Subwindow. *J. Med. Chem.* **2019**, *62*, 2049–2059.

(8) Gieseking, R. L.; Mukhopadhyay, S.; Risko, C.; Marder, S. R.; Brédas, J. L. 25th Anniversary Article: Design of Polymethine Dyes for All-Optical Switching Applications: Guidance from Theoretical and Computational Studies. *Adv. Mater.* **2014**, *26* (1), 68-84.

(9) Saccone, D.; Galliano, S.; Barbero, N.; Quagliotto, P.; Viscardi, G.; Barolo, C. Polymethine Dyes in Hybrid Photovoltaics: Structure-Properties Relationships. *European J. Org. Chem.* **2016**, *2016* (13), 2244–2259.

(10) Chen, W.; Cheng, C. A.; Cosco, E. D.; Ramakrishnan, S.; Lingg, J. G. P.; Bruns, O. T.; Zink, J. I.; Sletten, E. M. Shortwave Infrared Imaging with J-Aggregates Stabilized in Hollow Mesoporous Silica Nanoparticles. *J. Am. Chem. Soc.* **2019**, *141* (32), 12475–12480.

(11) Sun, C.; Li, B.; Zhao, M.; Wang, S.; Lei, Z.; Lu, L.; Zhang, H.; Feng, L.; Dou, C.; Yin, D.; et al. J-Aggregates of Cyanine Dye for NIR-II in Vivo Dynamic Vascular Imaging beyond 1500 Nm. *J. Am. Chem. Soc.* **2019**, *141* (49), 19221–19225.

(12) Berlepsch, H. V; Bö, C. Tubular J-Aggregates of a New Thiacarbocyanine Cy5 Dye for the Far-Red Spectral Region-a Spectroscopic and Cryo-Transmission Electron Microscopy Study †. *Phys. Chem. Chem. Phys* **2018**, *20*, 18969.

(13) V. Berlepsch, H.; Böttcher, C. Supramolecular Structure of TTBC J-Aggregates in Solution and on Surface. *Langmuir* **2013**, *29* (16), 4948–4958.

(14) Kirstein, S.; Daehne, S. J-Aggregates of Amphiphilic Cyanine Dyes: Self-Organization of Artificial Light Harvesting Complexes. *Int. J. Photoenergy* **2006**, *2006*, 1–21. ht

(15) Rn Kriete, B.; Bondarenko, A. S.; Jumde, V. R.; Franken, L. E.; Minnaard, A. J.; Jansen, T. L. C.; Knoester, J.; Pshenichnikov, M. S. Steering Self-Assembly of Amphiphilic Molecular Nanostructures via Halogen Exchange. *J. Phys. Chem. Lett* **2017**, *10*.

(16) Shapiro, B. I.; Sokolova, L. S.; Kuz'min, V. A.; Tolmachev, A. I.; Slominskii, Y. L.; Briks, Y. L. Effect of Meso-Alkyl Substituents in the Polymethine Chain of Thiacarbocyanines on the Morphology of Dye Aggregates. *Nanotechnologies Russ.* **2012**, *7* (5–6), 205–212.

(17) Deshmukh, A. P.; Koppel, D.; Chuang, C.; Cadena, D. M.; Cao, J.; Caram, J. R. Design Principles for Two-Dimensional Molecular Aggregates Using Kasha's Model: Tunable Photophysics in Near and Short-Wave Infrared. *J. Phys. Chem. C.* **2019**, *123*, 18702-18710.

(18) Zhu, X.; Su, Q.; Feng, W.; Li, F. Anti-Stokes Shift Luminescent Materials for Bio-Applications. *Chem. Soc. Rev* **2017**, *46*, 1025.

(19) Salon, J.; Wolinska, E.; Raszkiewicz, A.; Patonay, G.; Strekowski, L. Synthesis of Benz[e]Indolium Heptamethine Cyanines Containing C-Substituents at the Central Portion of the Heptamethine Moiety. An Efficient Procedure for the Synthesis of near-Infrared Dyes 5a-d Is Described. *J. Heterocycl. Chem.* **2005**, *42* (5), 959–961.

(20) Wiedemann, T.; Voit, G.; Tchernook, A.; Roesle, P.; Göttker-Schnetmann, I.; Mecking, S. Monofunctional Hyperbranched Ethylene Oligomers. *J. Am. Chem. Soc.* **2014**, *136* (5), 2078–2085.

(21) Chen, J.; Fang, Y.; Sun, L.; Zeng, F.; Wu, S. An Activatable Probe for Detecting

Alcoholic Liver Injuryviamultispectral Optoacoustic Tomography and Fluorescence Imaging. *Chem. Commun.* **2020**, *56* (75), 11102–11105.

(22) Zeng, C.; Shen, G.; Yang, F.; Chen, J.; Zhang, X.; Gu, C.; Zhou, Y.; Fan, B. Rhodium-Catalyzed Generation of Anhydrous Hydrogen Iodide: An Effective Method for the Preparation of Iodoalkanes. *Org. Lett.* **2018**, *20* (21), 6859–6862.